Digital Airborne Camera

Introduction and Technology

Edited by

Rainer Sandau
DLR, Berlin, Germany

With contributions by Ulrich Beisl, Bernhard Braunecker, Michael Cramer, Hans Driescher, Andreas Eckardt, Peter Fricker, Michael Gruber, Stefan Hilbert, Karsten Jacobsen, Walfried Jagschitz, Herbert Jahn, Werner Kirchhofer, Klaus J. Neumann, Rainer Sandau, and Maria von Schönermark

Springer

Editor
Dr. Rainer Sandau
Deutsches Zentrum for
Luft- und Raumfahrt e.V.
(DLR)
Rutherfordstr. 2
12489 Berlin
Germany
rainer.sandau@dlr.de

This is a translation of the book in German "Digitale Luftbildkamera – Einführung und Grundlagen", by Rainer Sandau, published by Wichmann Verlag, 2005; including some new additions in chapter 7 (Examples)

ISBN 978-1-4020-8877-3 e-ISBN 978-1-4020-8878-0
DOI 10.1007/978-1-4020-8878-0
Springer Dordrecht Heidelberg London New York

Library of Congress Control Number: 2009940584

Cover illustration: Transparent view of the ADS40 camera made by Leica Geosystems AG.

Printed on acid-free paper

Springer is part of Springer Science+Business Media (www.springer.com)

Preface

Digital airborne cameras are now penetrating the market of photogrammetry and remote sensing. Owing to rapid progress in the last 10 years in fields such as detector technology, computer power, memory capacity, and measurement of position and orientation, it is now possible to acquire, with the new generation of digital airborne cameras, different sets of geometric and spectral data with high resolution within a single flight. This is a decisive advantage over aerial film cameras. The linear characteristic of the optoelectronic converters is at the root of this transformation from an imaging camera to a measuring instrument that captures images. The direct digital processing chain from the airborne camera to the derived products involves no chemical film development or digitisation in a photogrammetric film scanner. Causes of failure, expensive investments and prohibitive staff costs are avoided. The effective use of this new technology, however, requires knowledge of the characteristics, possibilities and restrictions of the formation of images and the generation of information from them.

This book describes all the components of a digital airborne camera, from the object to be imaged to the mass memory device on which the imagery is written in the air. Thus natural processes influencing image quality are considered, such as the reflection of the electromagnetic energy from the sun by the object being imaged and the influence of the atmosphere. The essential features and related parameters of the new technology are discussed and placed in a system framework. The complex interdependencies between the components, for example, optics, filters, detectors, analogue and digital electronics, and software, become apparent. The book describes several systems available on the market at the time of writing.

The book will appeal to all who want to be informed about the technology of the new generation of digital airborne cameras. Groups of potential readers include: managers who have to decide about investment in and use of the new cameras; camera operators whose knowledge of the features of the cameras is essential to the quality of the data acquired; users of derived products who want to order or effectively process the new digital data sets; and scientists and university students, in photogrammetry, remote sensing, geodesy, cartography, geospatial and environmental sciences, forestry, agriculture, urban planning, land use monitoring and other fields, who need to prepare for the use of the new cameras and their imagery.

This book is a translation of the publication in German, *Digitale Luftbildkamera – Einführung und Grundlagen*, published in 2005 by Herbert Wichmann Verlag in Heidelberg. Only Chapter 7 was extended to three example camera systems which are being marketed worldwide and are also roughly representative of the bandwidth of the implementation variations. I would like to acknowledge Wichmann Verlag's gracious agreement to transfer the English-language rights to Springer.

I would like also to acknowledge the help that the contributors to this book received from a number of individuals:

Ms. Ute Dombrowski (DLR, Berlin, Germany), who was very supportive in typing large parts of the manuscript, dealing with figures and tables, editing the chapters of the various authors, and combining the results into a book.

Dr. A. Stewart Walker (BAE Systems, San Diego, USA), who proof-read the entire manuscript in order to polish and homogenise the usage of the English language in the translation from German carried out by the authors.

Dipl.-Ing. Dieter Zeuner (formerly Applanix, Toronto, Canada), who contributed to the translation of the German version.

Prof. Dr.-Ing. Hans-Peter Röser (Unversität Stuttgart, Institut für Photogrammetrie, Germany; formerly DLR, Berlin, Germany), who led the DLR team during the joint development of the ADS40 with Leica and LH Systems.

Ms. Petra van Steenbergen of the publisher, who supported the creation of the book through pleasant, patient collaboration.

Berlin, Germany Rainer Sandau
April 2009

Contents

Contributors

Editor

Dr. Rainer Sandau

List of Authors

	Section
Dr. Ulrich Beisl Leica Geosystems AG, Heerbrugg, Switzerland	2.9
Dr. Bernhard Braunecker Leica Geosystems AG, Heerbrugg, Switzerland	4.2, 4.3
Dr. Michael Cramer Universität Stuttgart, Institut für Photogrammetrie, Stuttgart, Germany	2.10, 4.9
Dr. Hans Driescher Deutsches Zentrum für Luft- und Raumfahrt (DLR), Berlin, Germany	4.5
Dr. Andreas Eckardt Deutsches Zentrum für Luft- und Raumfahrt (DLR), Berlin, Germany	2.8
Dipl.-Ing. Peter Fricker Leica Geosystems AG, Heerbrugg, Switzerland	7.1
Dr. Michael Gruber Microsoft Photogrammetry, Graz, Austria	7.3
Dipl.-Ing. Stefan Hilbert Deutsches Zentrum für Luft- und Raumfahrt (DLR), Berlin, Germany	4.4, 4.6
Dr. Karsten Jacobsen Leibniz Universität Hannover, Institut für Photogrammetrie und GeoInformation, Hannover, Germany	2.10
Dipl.-Ing. Walfried Jagschitz Leica Geosystems AG, Heerbrugg, Switzerland	4.10

Prof. Dr. Herbert Jahn Deutsches Zentrum für Luft- und Raumfahrt (DLR), Berlin, Germany	2, 2.1 – 2.7
Dipl.-Ing. Werner Kirchhofer Leica Geosystems AG, Heerbrugg, Switzerland	4.7, 4.8
Dipl.-Ing. Klaus J. Neumann Intergraph AG, Aalen, Germany	7.2
Dr. Rainer Sandau Deutsches Zentrum für Luft- und Raumfahrt (DLR), Berlin, Germany	1, 4, 4.1–4.3, 4.10, 7
Dr. Maria von Schönermark Universität Stuttgart, Institut für Raumfahrtsysteme, Germany	3
Dipl.-Ing. Udo Tempelmann Leica Geosystems AG, Heerbrugg, Switzerland	5, 6

Chapter 1
Introduction

1.1 From Analogue to Digital Airborne Cameras

The use of aerial photography dates back to the middle of the nineteenth century. By studying applications during this period, one can easily identify the level of technology at each particular time. Continuous efforts have been made to employ the best technologies available in either the area of photographic technique or the methods of getting the camera airborne.

It is interesting that around 1,500 Leonardo da Vinci designed the first flying systems and also described the process of a “Camera Obscura”, which were quite remarkable instruments for their time and indicative of astounding foresight. Their implementation, however, had to wait. The technical possibilities were limited, since the components to build these systems were not yet available, owing to the lack of differentiated natural and engineering sciences.

Three hundred years went by before further progress was made. In 1783 the first hot-air balloon was successfully flown by the Montgolfiers brothers. In 1837 Daguerre was able to produce the first images. Then in 1858 the French Daguerrotypist and writer Gaspare Tournachon, also called Nadar, took the first aerial photographs, over Paris from a balloon at an altitude of 300 m (Albertz, 2001). Balloons were used for reconnaissance purposes until the middle of the twentieth century.

Kites were also soon utilized to take photos from an unmanned platform and in 1888 Arthur Batut in France was able to take aerial photographs in this way for the first time. The time release for this camera was arranged by a fuse line.

Even carrier-pigeons were used to take photographs from the air. In 1903 Dr. Julius Neubauer patented a miniature camera to be strapped to pigeons’ bodies, activated by a timer mechanism (Fig. 1.1-1). Rockets were also used as carriers of small cameras. In 1897 Alfred Nobel secured a patent for a “Photo Rocket”. As early as 1904, Alfred Maul, an engineer from Dresden, deployed the first “Photo Rockets”, which lifted cameras to an altitude of 800 m.

Due to progress made in the field of aviation technology, the aircraft became a useful platform from which to take aerial photographs. The first aerial photograph acquired from an aircraft – an oblique – was taken in 1909 over Centocelli in Italy

R. Sandau (ed.), *Digital Airborne Camera*, DOI 10.1007/978-1-4020-8878-0_1,

Fig. 1.1-1 Carrier pigeon with miniature camera (source: Archive Deutsches Museum)

by Wilbur Wright. Four years later, also in Italy, the first maps were produced from aerial photographs (Falkner, 1994).

During World War I these cameras were developed even further and in 1915 the first cyclical camera system for systematic serial photographs was developed by Oskar Messter (Albertz, 1999). This system could produce photographs at a scale of 1:10,000, covering an area of 400 square km, taken at an altitude of 3,000 m and using no more than 1.5 h of flying time (Willmann, 1968).

After World War I the first commercial companies to make maps using aerial photographs as the major source of information were established. Colour film was soon developed and slowly introduced into photogrammetry. In 1925, the Wild company produced the C2 camera, which used panchromatic glass plates with a format of 10×15 cm. It was used as a handheld camera (Fig. 1.1-2) or installed as a convergent dual camera system by means of a special mount.

Before the beginning of World War II the standard format in aerial photography both for film and plates was 18×18 cm. During the Second World War aerial photography underwent rapid development. Infrared film was introduced for the purpose of detecting enemy positions.

During the 1970s, with the introduction of electronic computer-controlled technology, manual, graphical methods of map production were replaced by computer-assisted mapping technology, which opened up tremendous possibilities. The refinement of these developments has been an ongoing process that still continues today. The 1980s and 1990s were characterised mainly by their steady progress in the application of computers to both the stereo plotter itself and map-making systems in general.

Analogue aerial photography and photogrammetry were developed over many decades and have now reached a very high standard. This very mature development has included the introduction of large format aerial cameras, analytical and digital stereo restitution systems and photogrammetric scanners, all of which are described in the appropriate literature and are considered to be well known to the reader. Examples are highly efficient analogue aerial camera systems, the Leica RC30 from Leica Geosystems and the RMK TOP from Carl Zeiss. Today we live in a world of digital map production and of integration of digital map data into digital databases.

Fig. 1.1-2 Use of the Wild C2 handheld aerial camera

This facilitates merging of this data with data from other sources and data that has been generated with other remote sensing sensors, opening the opportunity to meet new requirements and generate new products.

With the beginning of photography from space, the attempt was soon made to eliminate film as the medium to "store" data. The problem of returning the film to Earth proved to be complicated and onerous. To eliminate this, digital scanners were developed, which allowed transmission of the image signal directly and in digital form from the satellite back to Earth. Starting from single-detector whiskbroom scanners, rapid development took place, which eventually brought us via multi-element whiskbroom scanners to pushbroom scanners and matrix systems, technologies which are still used today in space-based photogrammetry and remote sensing worldwide. They allow the generation of multispectral and stereo images with a high degree of geometric and radiometric resolution. ERTS (Earth Resource Technology Satellite) was the first civil Earth observation satellite, launched in 1972 to acquire images from the Earth's surface. Later this system was renamed Landsat-1. Its sensor system MSS (Multispectral Scanner System) consisted of a single-detector whiskbroom scanner. In 1980 the first CCD lines for satellite image acquisition were implemented on METEOR-PRIRODA-5. The sensor system MSU-E (Multispectral Scanning Unit-Electronic) worked in a pushbroom mode. In 1986 SPOT-1 became the first satellite to acquire time-generated stereo images via "off-track imaging". To generate stereo images the single line pushbroom scanner HRV (High Resolution Visible) took two strips of images from two neighbouring orbits oriented towards the area which was to be photographed in stereo. MOMS-02 was the first sensor system to use the three-line stereo method (In-Track-Stereo) patented by Otto Hofmann in 1979 (Hofmann, 1982). In 1993 MOMS-02 was flown on the Space Shuttle Mission STS 55 and in 1996 it was installed in the PRIRODA-Module of the MIR Space Station. MOMS-02 used one objective lens for each stereo channel. The first space-based mission of a Three-Line Stereo System, which had the three stereo lines arranged on the focal plane behind one single wide-angle objective lens, was achieved with BIRD (Bi-Spectral Infrared Detection) in 2001 (Briess, 2001). WAOSS-B (Wide-Angle Optoelectronic Stereo Scanner-BIRD) is the modified version of WAOSS, a sensor system on the Russian Mars 96 Mission that was designed to observe the dynamics in the atmosphere and on the surface of Mars (Sandau, 1998). Unfortunately this mission failed in its initial launch stage.

Most of the sensor systems which were developed for space-based applications gave rise also to versions developed for use in aircraft [for example, Sandau and Eckardt (1996)]. As a result they have been used for test purposes or/and for scientific or commercial applications. Examples of a number of different German sensor systems are:

- MEOSS: the satellite version was also used on aircraft
- MOMS-02: DPA (Digital Photogrammetry Assembly) as the airborne version
- WAOSS: WAAC (Wide-Angle Airborne Camera) as the airborne version
- HRSC: HRSC-A and HRSC-AX as airborne versions (HRSC – High Resolution Stereo Camera – was the second German stereo camera for the failed Mars 96 Mission; it is now part of the ESA-Mission Mars Express, launched in 2003).

The development of these different techniques and sensors evolved in parallel with the increased utilisation of aerial photographs in digital map production. If film images are to be entered into digital databases, they must be converted into digital form using photogrammetric scanners. Owing to the development of space-based sensor technologies as mentioned above and the strong development trends in other high technology fields essential to this application, it eventually became practicable and economically feasible to go beyond scanning and replace the conventional film used in aerial photography with direct digital imagery. Owing to the many significant advances in key technological disciplines such as optics, mechanics, critical materials, micro-electronics, micro-mechanics, detector and computer technologies, signal processing, communication and navigation, we now have financially realistic solutions for digital airborne camera systems accepted on the market.

One concept considered for a digital camera system is to replace the conventional film by suitable digital matrices or blocks of matrices. Another is to implement single or multiple detector lines to create the digital image data. The first ideas along these lines were indicated in a dissertation at the University of New Brunswick (Derenyi, 1970). Independently from this, Otto Hoffmann developed and patented the Three Line Concept of a Digital Airborne Camera system (Hofmann, 1982, 1988). This Three Line Concept has already been utilized in spaceborne camera systems (e.g. MOMS-02, WAOSS) and for experimental purposes in airborne cameras (e.g. MEOSS, DPA, WAAC, HRSC).

The first commercially available digital airborne camera systems, the ADS40 from Leica Geosystems (formerly LH Systems) and the DMC from Intergraph (formerly Z/I Imaging), were introduced in the year 2000 at the ISPRS Congress in Amsterdam. Other digital airborne camera systems were introduced into the market later. Section 1.5 gives examples of commercial systems presently available on the market.

Reasonably priced digital airborne camera systems which immediately deliver the image in digital form are only one attractive reason to switch from conventional film cameras to digital camera systems. There are other significant economic reasons for doing so as described in Fig. 1.1-3. The direct digital approach using the digital airborne camera system eliminates the processes of developing the conventional film and scanning each individual photograph into digital form. This direct approach eliminates sources of errors and inaccuracies. Most importantly, it results in significant savings in investment and costs related to personnel.

If the correct design concept is applied, the digital airborne camera system is able to deliver stereo information, RGB data RGB data and IR data simultaneously during one flight. With conventional analogue aerial cameras it is necessary to fly the area more than once owing to different film requirements (panchromatic, colour and FCIR), or to have multiple cameras in the aircraft.

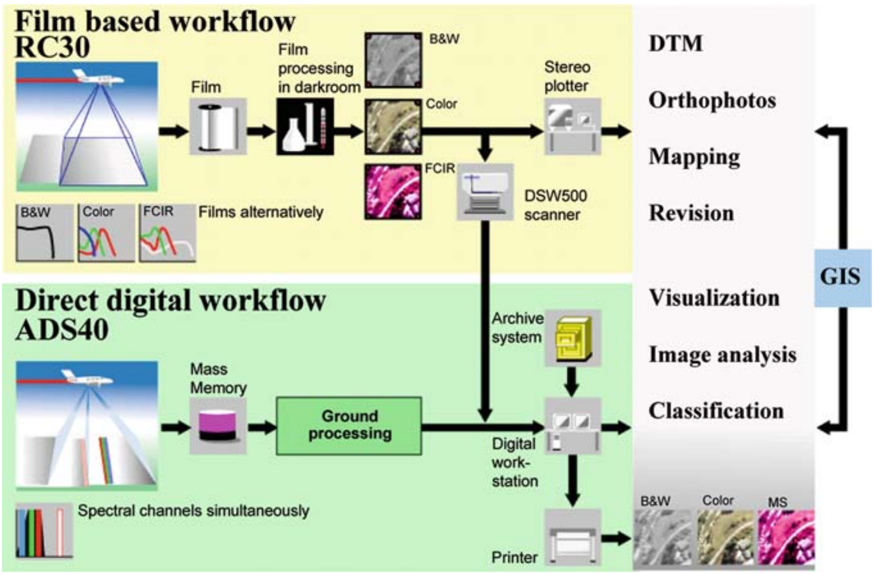

Fig. 1.1-3 Comparison between the workflows for analogue and digital airborne cameras

The thematic interpretation of image data can be significantly improved too, because with digital technology the filter values required for specific applications can be taken into consideration at the time of the design of the system.

These last two arguments in favour of a digital image generated directly by the digital airborne camera system strongly indicate that photogrammetry and remote sensing continue to coalesce. In many cases topographic information (e.g. digital terrain models) is essential to expedite thematic interpretation (remote sensing) of the data within a specific area; for photogrammetric applications, such as cartography, the colour information is often necessary for a finished product. With the new task of preprocessing the flight data in digital form, the interface between the company flying the imagery and the company processing the digital imagery into a final product may now shift in such a way that the former takes over more processing activities than ever before (see Chapter 6). The future will show whether the flying operation becomes involved in the overall process of generating the final product, and to what extent it is willing to do so or capable thereof.

Working directly from digital imagery instead of film is opening up other very significant possibilities in remote sensing. As can be seen from Fig. 1.1-4, film records light rays in an s-shaped logarithmic curve. This so called DlogE curve shows the relationship between the relative illumination (exposure) and the resulting density in the photograph, the density D as a function of the logarithm of the exposure E. The term relative illumination is used because the value depends on the exposure setting (exposure time, aperture, etc.) and the film processing (developing, fixing, washing etc.). The CCD elements, which function as optoelectronic converters, present themselves in a linear curve. This opens up the possibility of measuring within the spectral ranges selected by different filters. The photons hitting the detector elements within a specific, selected filter range can be counted and therefore can be interpreted as an actual physical measuring unit.

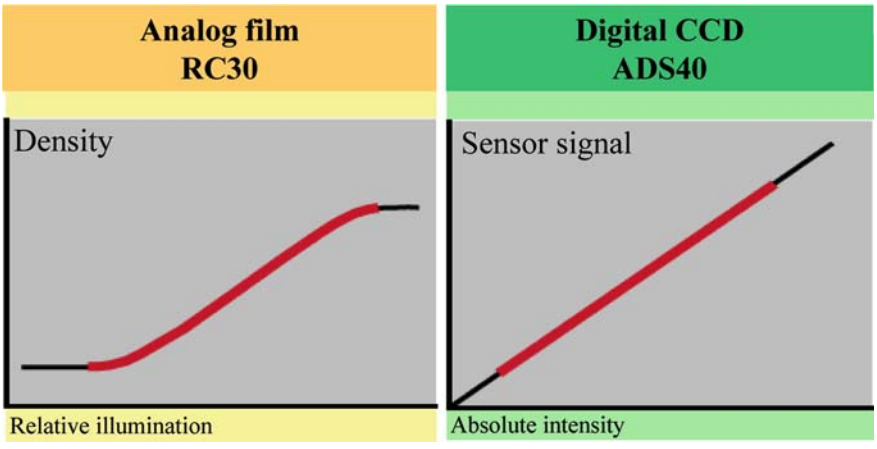

Fig. 1.1-4 Characteristics of CCD detectors and film materials (qualitative)

Modern electro-optical converters allow dynamic ranges of 1:4,000 (12-bit dynamic capacity) or better. With this capability it is possible to span illumination ranges from high reflectance to very low reflectance apparent in deep shadows in a single image (see Fig. 1.1-5). This is also relevant in the matching procedures of digital image processing. The histograms in Fig. 1.1-5 represent the number of pixels within the respective illumination ranges. If one "zooms" in radiometrically within specific areas, details will be very recognisable. The high dynamic range combined with the linear "curves" are characteristic of the quality of modern electro-optical converters (CCD detectors) and therefore also the quality of the new digital airborne camera systems.

The digital image technology used in modern airborne camera systems, through appropriate system design and configuration, enables speedy transition from the traditional photographic camera to a measuring system that captures images. This opens up completely new application areas for digital airborne imaging sensors. The fact that the new digital airborne cameras can be used for classical photogrammetry as well as for airborne remote sensing creates opportunities in market segments which so far have not been explored. This will also result in a significant increase in the processing of such digital imagery and will result in the development of completely new "intelligent" methods to deal with such data. This trend is strongly supported by ongoing development of and improvement to existing and newly available digital photogrammetric workstations, on which software to deal with these digital images is being installed (Ackermann, 1995). The introduction and progress

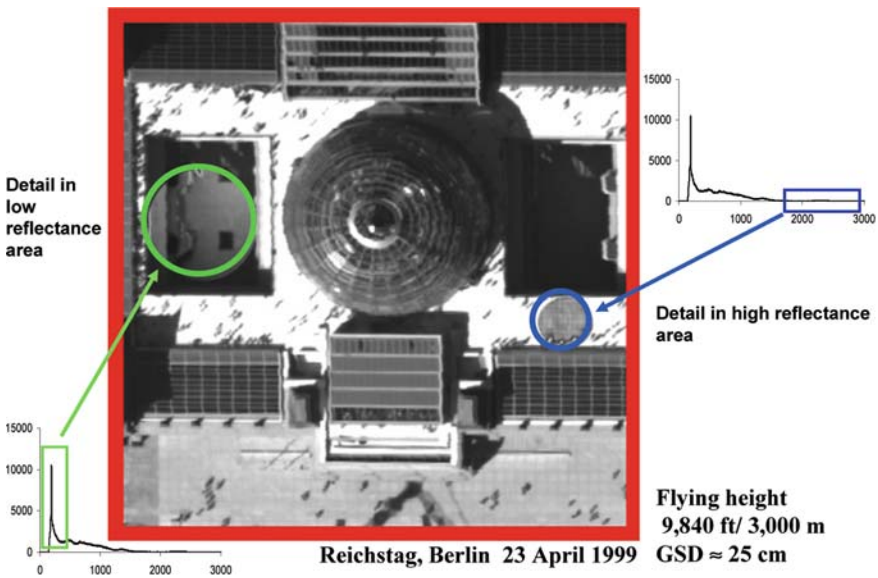

Fig. 1.1-5 The large dynamic range of the digital sensor provides the unique opportunity to resolve details in the dark as well as the bright areas of the image (Fricker et al., 2000)

of digital airborne camera systems in photogrammetry and remote sensing, facilitated by the immense progress in diverse fields of technology, obviously has far reaching consequences in these respective fields, which no doubt will also have a significant influence on education, on the structure of companies active in these fields and on the development of new job opportunities.

1.2 Applications for Digital Airborne Cameras in Photogrammetry and Remote Sensing

Geometric data are derived with the aid of photogrammetry through measurement in image material. The task of digital photogrammetry lies in the use of methods of image processing, such as automatic point measurement, co-ordinate transformation, image matching to derive elevation data and differential image rectification to produce orthoimages with a cartographically compatible geometry. Remote sensing is the contact-free imaging or measurement of objects for generating qualitative or quantitative data on their occurrence, their state or changes in their state. Further comments and remarks can be found in Albertz (2001), Hildebrandt (1996), Konecny (2003), Kraus (1988, 1990) and others. New digital sensor systems can provide all data for

- determining the sizes and shapes of objects with the aid of photogrammetry,
- making the photographed content accessible to thematic evaluation through analysis and interpretation for a specific purpose,
- determining the meaning of the recorded data through semantic evaluation.

Two parameters are particularly characteristic of photogrammetry and remote sensing: geometric resolution, which is best expressed by ground sample distance (GSD) in the case of digital systems, and radiometric resolution. Figure 1.2-1 shows which spectral resolutions and GSDs are required for topographic mapping and for selected thematic (remote sensing) applications (Röser et al., 2000). Spectral resolution is shown only in qualitative terms. The following is a rough classification of the different types of imagery and their suitability for various tasks:

- panchromatic imagery to recognise and survey the structure of the earth's surface and objects located on it
- multispectral imagery for making a rough classification of the chemical and biophysiological properties of the earth's surface and of objects situated on it
- hyperspectral imagery for identifying and making a refined classification of the geological, chemical and biophysiological properties of the earth's surface and of objects situated on it.

A principle that applies to all applications is that as few spectral channels as possible should be used.

Revisit rate is another parameter that affects the monitoring of application-specific changes. Figure 1.2-2 shows the required revisit rates for selected applications. Figures 1.2-1 and 1.2-2 show that topographic maps with a revisit

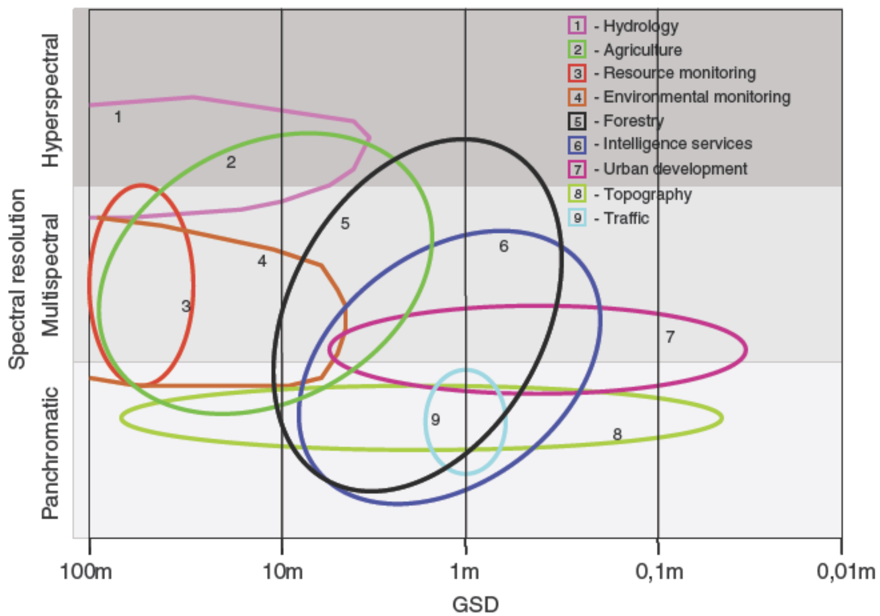

Fig. 1.2-1 Spectral and geometric resolutions required for various applications (Röser et al., 2000)

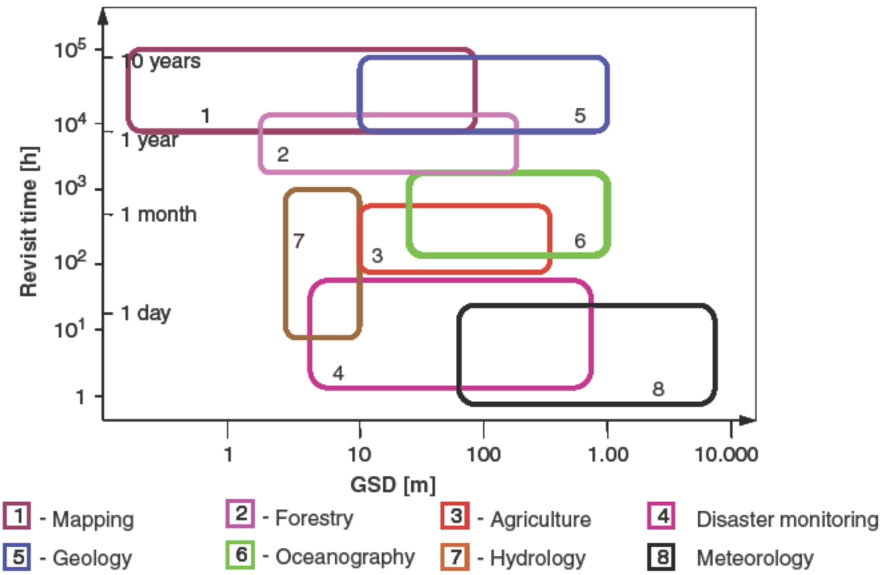

Fig. 1.2-2 Required geometric resolutions and revisit rates (Röser et al., 2000)

Table 1.2-1 Ground pixel size and achievable planimetric mapping scales

GSD	Mapping scale
5 cm	1:500
10 cm	1:1,000
25 cm	1:2,500
50 cm	1:5,000
1 m	1:10,000
2.5 m	1:25,000
5 m	1:50,000
10 m	1:100,000
50 m	1:500,000

rate of 1–10 years with a GSD in the range of 5 cm–50 m are required. The associated map scales for selected applications are in the 1:500–1:500,000 range (Table 1.2-1).

The stereo angles achieved with an airborne camera influence the accuracy of object point determination. Larger stereo angles correspond to larger potential height resolution but may lead to problems as a result of the larger radial offset in the image.

Experience gained with analogue airborne cameras has shown that different stereo angles are required to achieve optimum results for topography or for object extraction applications. It was found that large stereo angles often do not yield the desired precision in hilly or mountainous, built-up or wooded areas. Good images that can be readily correlated are required in digital photogrammetry. Table 1.2-2 shows the stereo angle ranges for various terrains and situations.

Table 1.2-2 Stereo angles for various applications

Topographic applications	Stereo angle
Flat terrain and high height accuracy	30°–60°
Hilly terrain	20°–40°
Mountainous areas	10°–25°
Object extraction applications	
Natural landscape	30°–50°
Suburban areas	20°–40°
Urban areas	10°–25°
Woodland	10°–25°

Remote sensing applications give rise to a modified filter design with regard to the spectral requirements. This is illustrated in Fig. 1.2-3.

The blue spectral channel with 460 ± 30 nm is placed in the weak absorption range of chlorophyll of green vegetation in water or on the surface (maximum between 430 and 450 nm). This channel is important for observing water bodies. The 560 ± 25 nm green spectral channel lies in the reflectance maximum of green

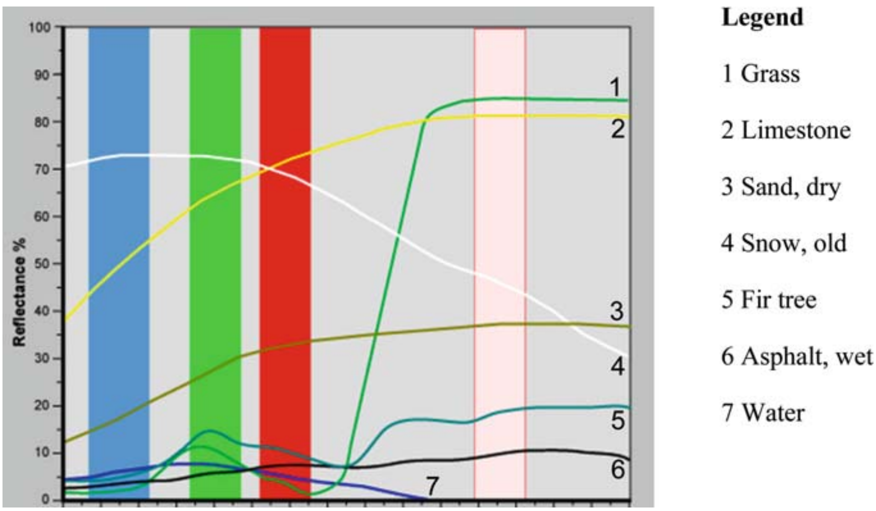

Fig. 1.2-3 Illustration of a filter design mainly for observing vegetation

vegetation and is also used to detect chlorophyll in water bodies. The second absorption band of chlorophyll lies in the 635 ± 25 nm red spectral channel (maximum at 650 nm).

At 860 ± 25 nm, the NIR channel lies on the plateau of vegetation curves and, in conjunction with the red channel, which ends in front of the vegetation edge ("red edge"), provides data on the state of the vegetation.

The spectral responsivity of colour film is broad-banded for the various spectral channels, and the spectral channels overlap (Fig. 1.2-4). This overlap of the spectral

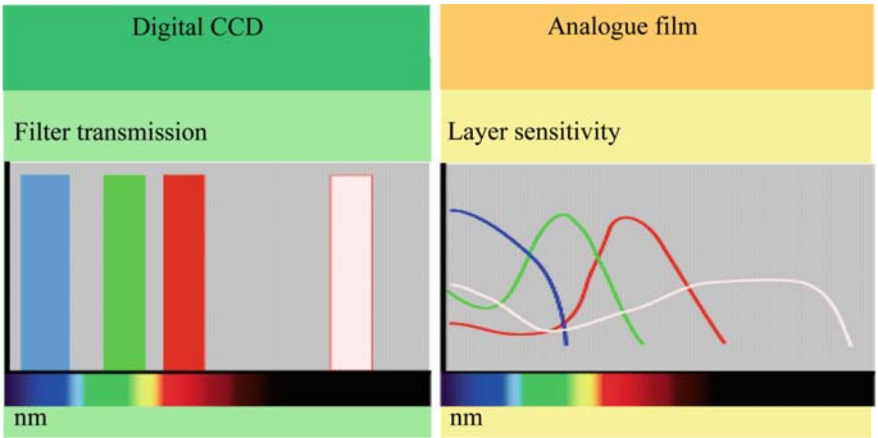

Fig. 1.2-4 Spectral responsivity of colour film material and of a detector system designed for photogrammetry and remote sensing (Leica, 2004)

channels is good for the colour film impression or infrared colour film impression, but it does not support remote sensing applications. The central wavelengths and the spectral bandwidths for multispectral and true-colour images differ. Multispectral applications require non-overlapping, narrow spectral bands, and, for observing vegetation, also an infrared channel near the vegetation edge (red edge). In contrast, the true-colour channels are rather more adjusted to spectral visual sensitivity and for this reason are broad-banded and overlapping.

Hence, a sensor system or digital airborne camera for photogrammetry and remote sensing must be equipped with filters that generate narrow spectral channels which are separated from each other. The true-colour images can be derived from the RGB channels designed in this manner using a process of colour transformation, possibly in conjunction with a panchromatic channel (see Section 2.7).

The absorption filters mounted during the manufacture of CCD matrices are also not so well suited to the multispectral applications discussed above.

The bandpass response of typical narrow-band absorption filters is shown in the right-hand part of Fig. 1.2-5. Absorption filter Absorption filters cannot be produced as perfectly and with such narrow bands as interference filters (see Section 4.3.2). The transitions are not sufficiently steep. For instance, the green filter does not completely absorb the red and blue parts of the spectrum. The interference filters shown on the left-hand sides of Figs. 1.2-4 and 1.2-5 can be implemented with much greater precision. It should be mentioned, however, that a considerable amount of effort is involved in manufacturing them (many metal oxide layers have to be vapour-plated on to the glass bases in a vacuum).

Summing up, it can be said that modern digital detector components enable digital airborne cameras for photogrammetry and remote sensing to be developed and manufactured. Often they make it possible to improve the quality of the results achieved using analogue airborne cameras and to expand the range of applications.

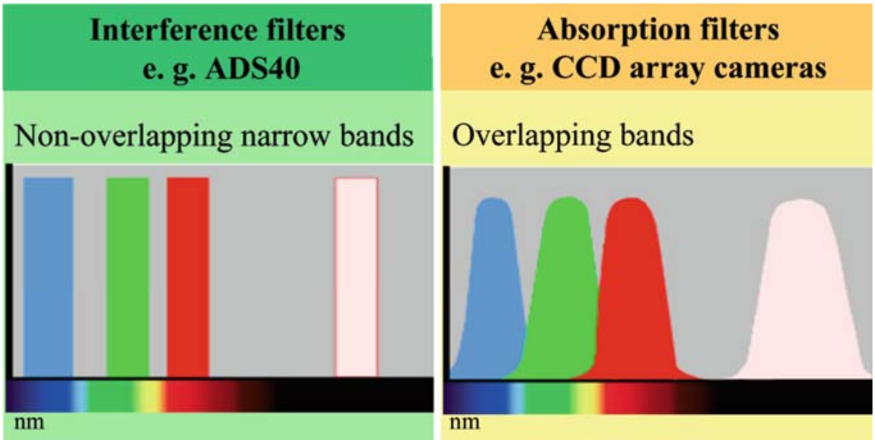

Fig. 1.2-5 Comparison of spectral responsivities of detectors fitted with absorption filters and a detector system designed for photogrammetry and remote sensing (Leica, 2004)

1.3 Aircraft Camera or Satellite Camera

Digital airborne sensors suitable for photogrammetry and remote sensing applications currently occupy a position between analogue airborne cameras, which potentially have higher geometric resolution but limited spectral variability, dependent on the available film material, on the one hand, and satellite systems, which have a lower geometric resolution, but in many instances a higher spectral resolution, on the other.

Figure 1.3-1 is a schematic representation of the performance of sensor systems based on the key parameters: geometric and spectral resolution. Analogue airborne cameras can provide virtually any resolution down to about 1 cm. Digital airborne cameras are already capable of a ground sample distance (GSD) below 5 cm. Satellite systems using panchromatic systems (roughly comparable to black-and-white film) have reached a GSD below 0.5 m. Figure 1.3-2 illustrates the development of GSD of satellite systems. From 80 m GSD achieved by ERTS (later renamed Landsat-1) – the first satellite launched for civil earth observation in 1972 – we have advanced to 0.41 m GSD.

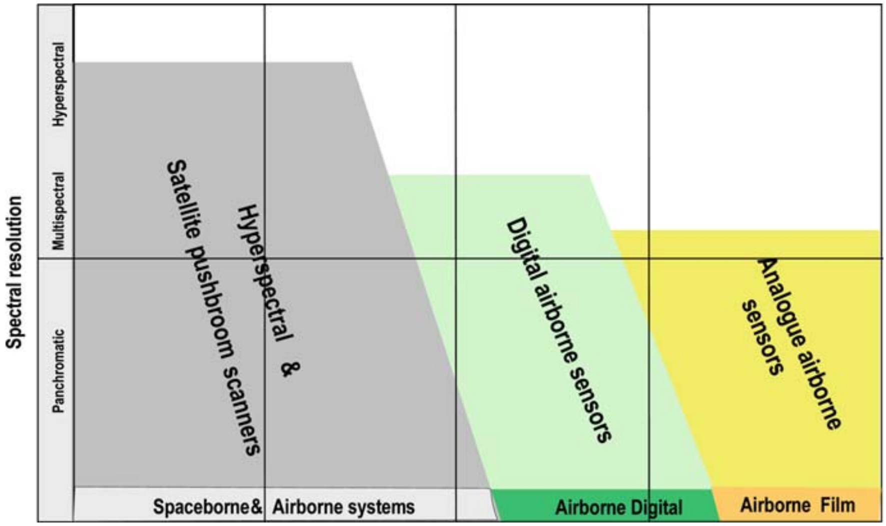

Fig. 1.3-1 Performance for sensor systems

Table 1.3-1 shows characteristics of selected satellite systems, such as the coarser GSD of multispectral channels, swath width, scene size and revisit time (time interval until the next opportunity to photograph the same area), indicating the potential geometric and time coverage.

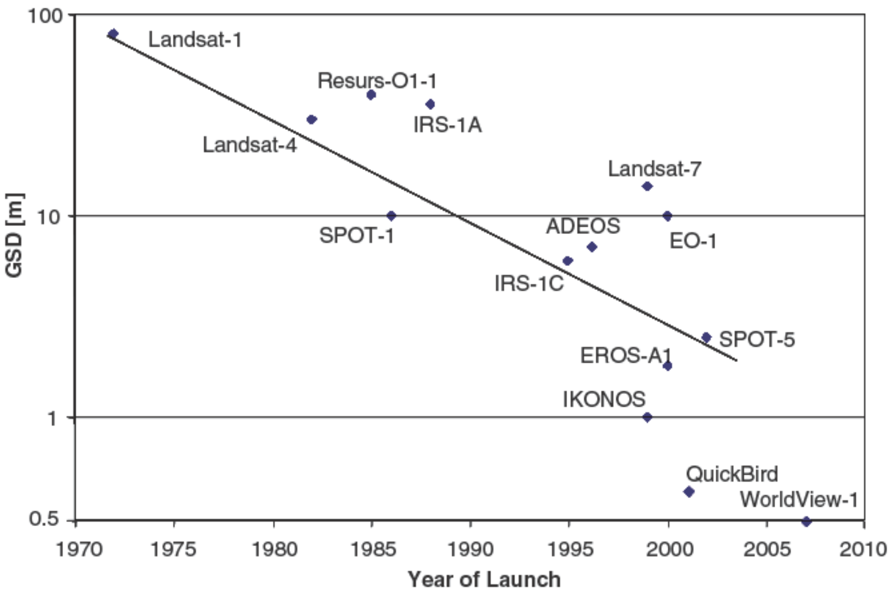

Fig. 1.3-2 GSD development of civil satellite systems in the panchromatic channel

Table 1.3-1 Selected imaging satellite systems

Satellite	Launch	Orbit altitude (km)	GSD [m] PAN	GSD [m] MS (R, G, B, SWIR)	Swath width (km)	Revisit (days)	Scene size (km × km)
Landsat-7	1999	705	14	28	185	16	185 × 185
SPOT-5	1999	832	5/3.5[a]	10	60	5	60 × 60
IKONOS	1999	680	1	4	13	1–3	11 × 11
QuickBird	2001	450	0.62	2.5	16.5	1–3.5	16.5 × 16.5
WorldView-1	2007	496	0.5	–	17.6	1.7–4.6	Max. 60 × 110

[a] In "supermode" with staggered line array, GSD = 3.5 m.

The connection between GSD and repeat rate is represented in Fig. 1.3-3 (Konecny, 2003). Every 30 min, such geostationary satellites as Meteosat and GOES, orbiting the earth at an altitude of roughly 36,000 km, supply images of a complete hemisphere in three spectral channels (one of them in the thermal IR) with a GSD of 5 km. NOAA satellites circling the earth in polars orbit at an altitude of 850 km provide images in five channels with a GSD of 1 km once every 12 h for meteorological purposes.

Owing to the high probability of an overcast sky, sun-synchronous satellites, for example, Landsat, SPOT and IRS, which have repeat rates of less than one month,

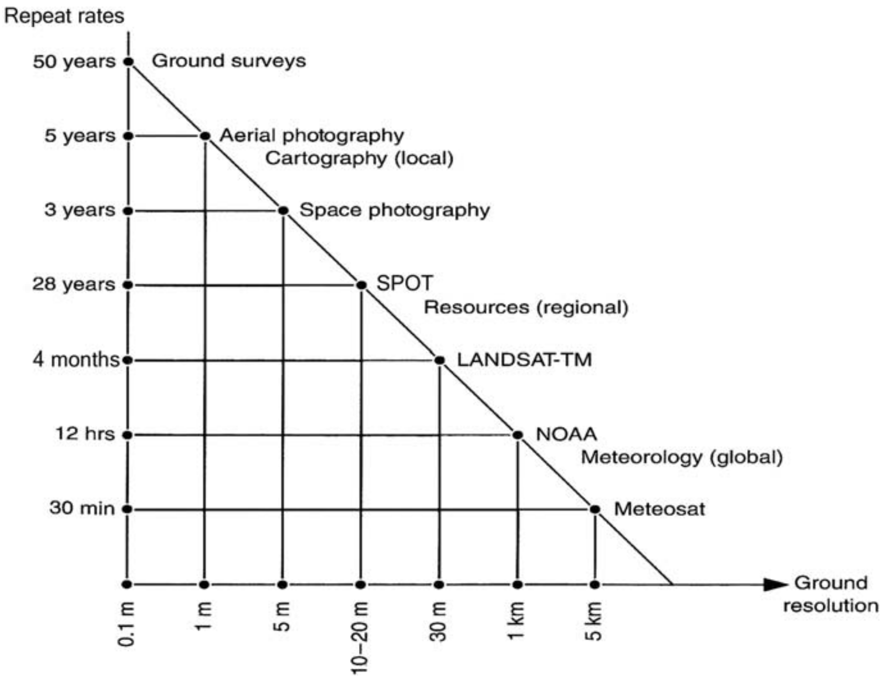

Fig. 1.3-3 Connection between repeat rate and ground resolution (Konecny, 2003)

can supply images of intermediate resolution (5–14 m pan and 10–28 m MS) only a few times a year. But coverage of large areas is possible only at intervals of several years. High-resolution satellite systems (IKONOS with 1 m GSD or Russian photographic systems with a resolution of 2 m) are approaching the resolution range of aerial images obtained from high-flying aircraft. The highest resolutions in the decimeter to centimeter range are obtained with low-flying airborne cameras or ground surveys at correspondingly longer time intervals.

Figure 1.3-4 illustrates the huge differences in altitude from which civil earth observation systems and aircraft systems carry out imaging operations. The difference of about 1:200 (3–600 km) illustrates, in qualitative terms at least, that satellite systems are much more complex and costly to make than aircraft systems to achieve comparable GSDs. This is also reflected in the costs of the image products and explains why more than 80% of the earth is mapped with airborne cameras. The main reason lies in the ratio between the focal lengths, which, like the altitude ratio, is 1:200. Figure 1.3-4 gives an impression on the flight hight ranges of airborne and spaceborne sensors. Speed differences also play a role. An aircraft, for instance, flies at a speed of 70 m/s, whereas the ground track of an LEO satellite at an altitude of roughly 600 km is approximately 7 km/s. The speed ratio and hence the ratio of the integration times is 1:100.

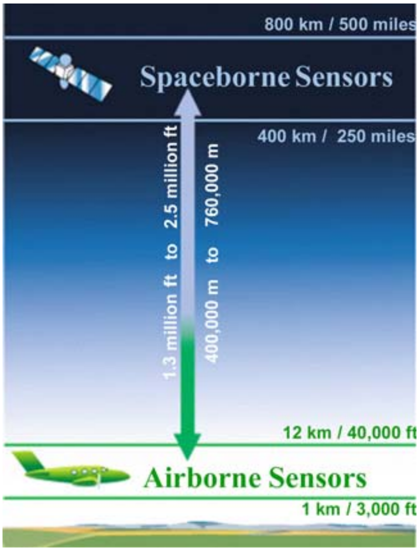

Fig. 1.3-4 General situation for flighing hight of airborne and space borne sensors

1.3.1 Detection, Recognition, Identification

The information the human brain is able to derive from an image depends on the number of picture dots (pixels) in a pixel conglomerate. Image interpreters typically use the following decision levels:

- Detection: discovering the existence of an object
- Recognition: classifying the object as belonging to a type group
- Identification: identifying the object type.

The number of pixels occupied by the object determines the certainty of the decision regarding the existence of an object or even its identification. Information about the object type is not substantially improved, nor the likelihood of identification of a certain object type substantially increased, if, for instance, a the number of pixels viewed is a 100 times the number required to reach a decision. In other words, the object's size and structure determine the required pixel size or GSD. In this respect, there are optimal applications for high-resolution sensors with small GSDs and for sensors with larger GSDs. The critical question is how many pixels are needed to achieve a certain decision quality. Figure 1.3-5 illustrates the issue sketched in the foregoing.

Figure 1.3-6 is an example in which the identification of a car about 5 m in length is used to illustrate the relationships. The component pictures in Fig. 1.3-7 which are to be recognised and identified are once again highlighted.

Figure 1.3-8 shows the situations in which decisions would have to be made when viewing the image material obtained by the QuickBird satellite with GSD = 0.8 m,

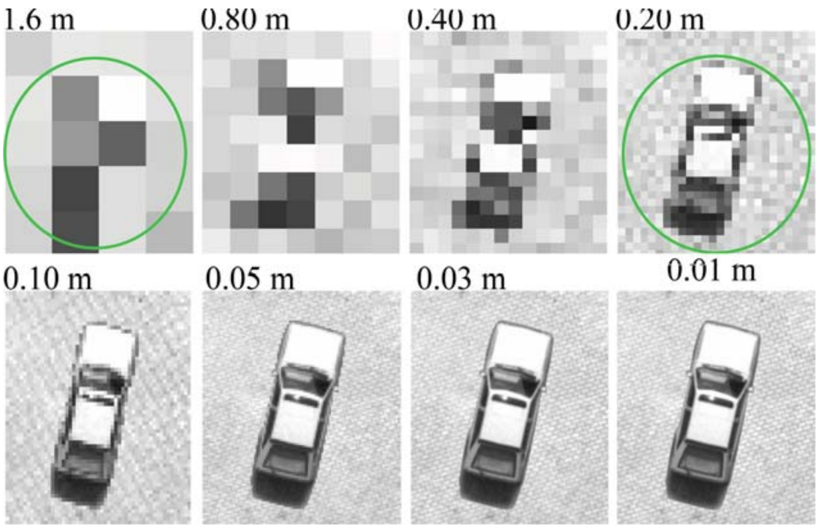

Fig. 1.3-5 GSD and object identification (Leica, 2004)

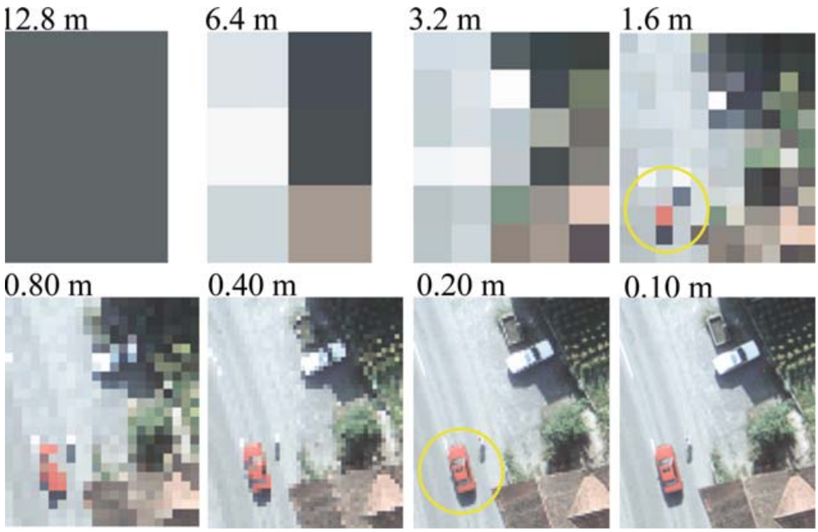

Fig. 1.3-6 GSD and object identification using a car about 5 m long (Leica, 2004)

a digital airborne camera with GSD = 0.2 m and an analogue airborne camera with a simulated GSD = 0.1 m.

The number of object pixels required for the three decision levels is not consistently defined. Practitioners sometimes refer to the Johnson criteria (Johnson, 1985), which have been modified somewhat over the years. Table 1.3-2 shows the number of object pixels required for a decision probability of 50% for the object's one- and two-dimensional expansion (Holst, 1996).

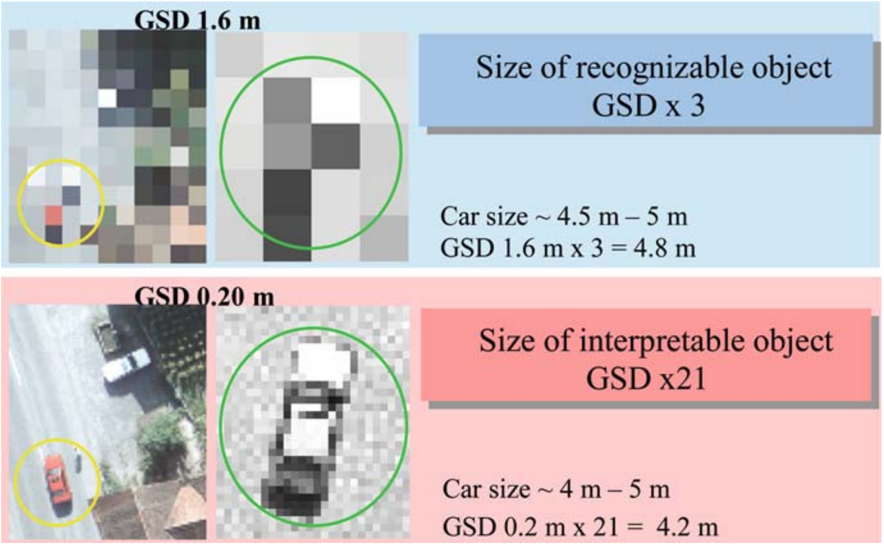

Fig. 1.3-7 Component images for reconition and identification from Fig. 1.3-5 as an illustration (Leica, 2004)

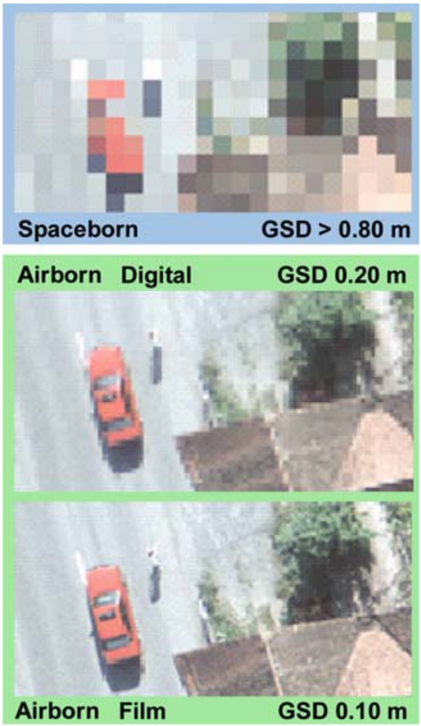

Fig. 1.3-8 Images from QuickBird, GSD GSD = 0.8 m, a digital airborne camera, GSD = 0.2 m, and an analogue airborne camera, simulated GSD = 0.1 m (Leica, 2004)

Table 1.3-2 Decision thresholds derived from the Johnson criterion

Decision	Description	One-dimensional N_{50}	2D N_{50}
Detection	The pixel represents an object being sought with good probability	1	0.75
Recognition	Allocation to a specific class with hierarchical certainty	4	3
Identification	Specification within a class with hierarchical certainty	8	6

Table 1.3-3 Factors for changing the outcome probabilities in Table 1.3-2

Outcome probability	Factor
1.00	3.0
0.95	2.0
0.80	1.5
0.50	1.0
0.30	0.75
0.10	0.50
0.02	0.25
0	0

Table 1.3-3 shows the requisite factors by which the values in Table 1.3-2 need to be multiplied to obtain an outcome probability other than 50% (Ratches, 1975).

It is contended, therefore, that aircraft and satellite systems are complementary. Some essential characteristics of satellite systems are:

- Fixed orbit: area coverage being predictable but dependent on cloud cover
- Applicable without having to invest a great deal of effort into preparation
- Fixed GSD, current minimum 0.5 m panchromatic and 2 m multispectral
- Known costs per scene.

Essential characteristics of aircraft systems:

- Flexible application on demand
- Usable even in unfavourable weather (flying below the clouds)
- GSD adaptable to the task at hand by varying flight altitude
- Stereo data easily acquired.

Data from airborne and satellite sensors is complementary in many applications. Different sensors and platforms have to be used owing to the great variety of objects to be observed and/or surveyed with respect to size, shape, texture and colour or to properties that can be differentiated only with multispectral or hyperspectral sensors. Given the increasingly expanding fields of application and the use of GIS stations, it is necessary to fuse all types of sensor date in order to meet the demand for information quickly and reliably. Data fusion and GIS have a high potential for creating new lines of business.

1.4 Matrix Concept or Line Concept

The technological possibilities, potential quality expectations and possible applications in photogrammetry and remote sensing discussed in Sections 1.1, 1.2, and 1.3 apply to digital airborne cameras regardless of any specific design concept. The extent to which possibilities become concrete solutions, however, depends on the basic underlying concept, based on either detector lines or detector matrices. Extensive variations are, of course, possible within the basic concepts, some of which are discussed in Section 1.5.

The key difference between the basic concepts is shown in Fig. 1.4-1. The line variant generates long, continuous strips of images, whereas the matrix variant generates rectangular, in most cases square, images that can be joined to form image strips. Matrix-based cameras are used like analogue film cameras to implement stereoscopic applications with overlaps such as 60% in the direction of flight. In most cases, the three-line concept is used in line-based airborne cameras (Hofmann, 1988). Figure 1.4-2 shows a schematic representation of the procedure.

In the case of the three-line camera, all objects on the ground are photographed from three different directions. This redundancy results in robust solutions in triangulation or in creating DEMs (digital elevation models). In photographs taken with a matrix camera at 60% forward overlap, 60% of the objects appear in three photographs.

In the line camera, the convergence angles are a function of the distance *d* from the nadir line

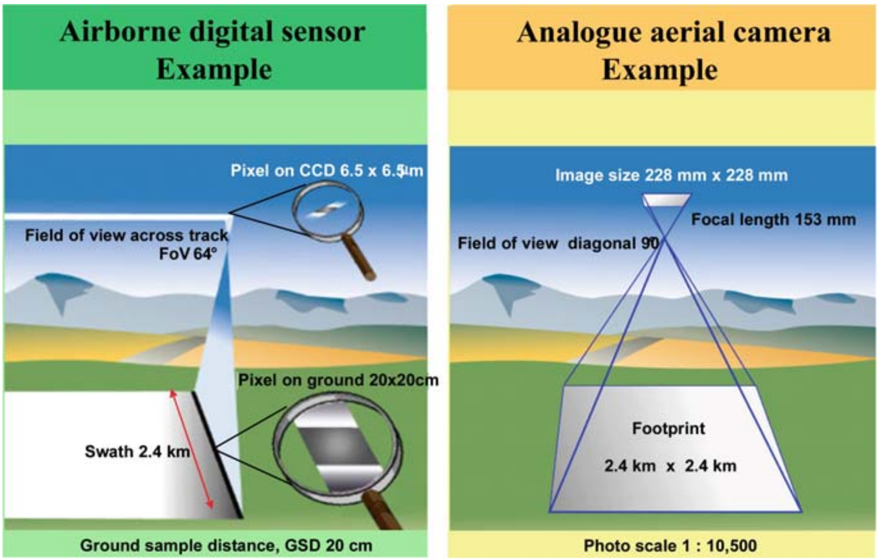

Fig. 1.4-1 Sample systems exemplifying the line concept and the matrix concept (Leica, 2004)

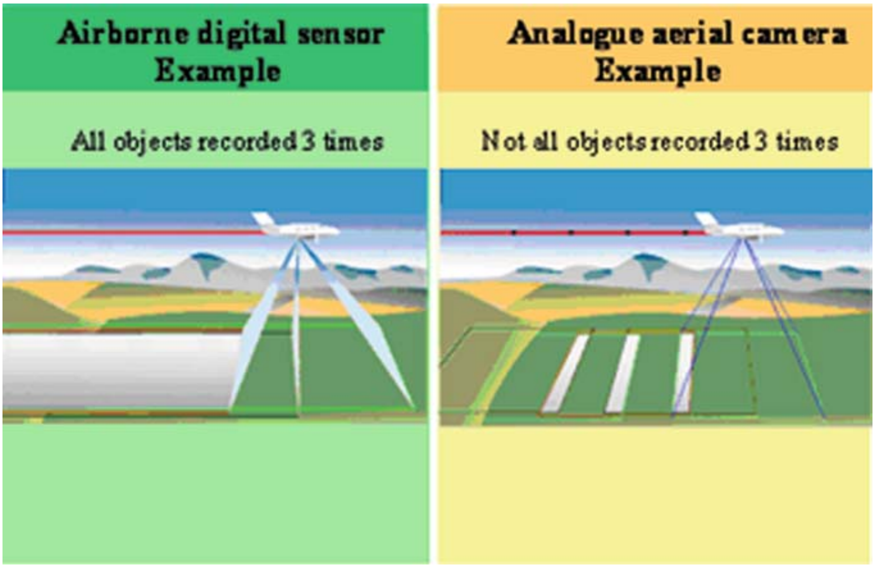

Fig. 1.4-2 Different principles of photography are used in line and matrix cameras for making 3D measurements (Leica, 2004)

$$\gamma_Z = \arctan \frac{d}{f}. \tag{1.4-1}$$

In Fig. 1.4-3, the ADS40 camera, in which the forward and backward view angles are different owing to the asymmetrical arrangement of the stereo lines, is used as an example to illustrate the situation. The range of stereo angles – 14.2°, 28.4° and

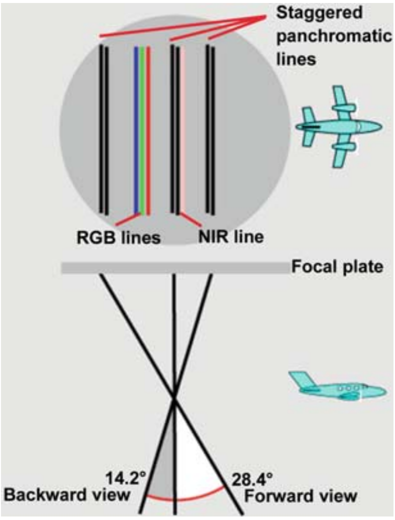

Fig. 1.4-3 Implementing an asymmetrical array of stereo lines (Leica, 2004)

42.6° – of the implementation shown covers the angles listed in Table 1.2-2, which are required for various applications in photogrammetry and remote sensing.

In the matrix camera, the angle of convergence is a function of the overlap o and hence variable

$$\gamma_m = \arctan \frac{s(1-o)}{f}. \tag{1.4-2}$$

In (1.4-2), s is the format width of the matrix in the direction of flight and f the focal length again. To illustrate various perspectives in line and matrix cameras, schematic representations of tall buildings are shown in Fig. 1.4-4. As with a film camera, the relief displacement of the central perspective produced with a matrix camera has two components. The cross-track shift is a function of the distance from the image centre at right angles to the flight direction and of the height difference. In the direction of flight, the shift is a function of the distance from the image centre in the direction of flight and of the height difference.

A special case of central perspective is used in the line camera, namely line perspective. The essential difference is that the shift component in the direction of flight is constant for equal height differences all along the image strip. The line perspective makes it possible to see images in three dimensions, similar to the way we see normal stereoscopic pairs, and also to measure the parallax for determining the height. The uniform perspective for the longitudinal direction of the entire image strip is advantageous.

Line cameras operating according to the pushbroom principle are designed such that sufficient energy impinges on the detectors given the smallest permissible GSDs

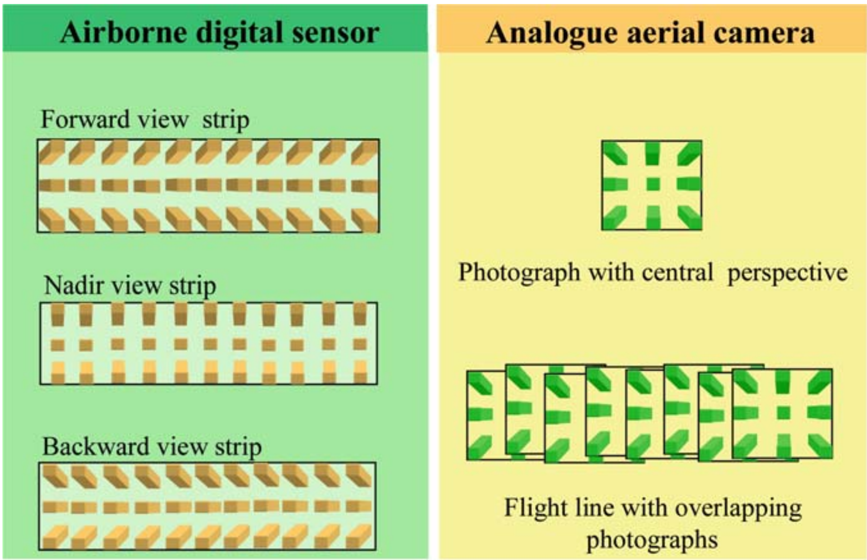

Fig. 1.4-4 Differences in perspectives of line and matrix cameras (Leica, 2004)

and reasonable illumination to satisfy the condition

$$t_{\text{int}} \leq t_{\text{dwell}} \tag{1.4-3}$$

where t_{int} is the integration time and t_{dwell} is the dwell time or time of flying over a GSD. FMC (forward motion compensation) is not required. With matrix cameras, it is permissible to incorporate TDI mode in the radiometric design when designing the system. TDI is explained in Section 4.4.2. Suffice it to say here that the energy reflected by an object on the ground is pushed forward to the pixels of each successive matrix line. In n shifting and signal accumulation stages, one obtains an n-fold integration time, increases the signal n-fold and increases the SNR by the factor $\sqrt{n}$. The reflected radiation is accumulated by the object from n different angles, however, which influences the precision of height measurements. During this n-fold integration time, the roll, pitch and yaw also cause image migration, which can be ameliorated through platform stabilisation. It is expedient to use FMC, therefore, only if the image migration brought about by changes in the aircraft's attitude does not cause greater image migration in the direction of flight than that compensated by FMC. Nor may cross-track image migration become greater than the pixel dimension during the integration time. Only then does pixel smearing still remain within acceptable limits (see also Sections 2.4, 4.1 and 4.10.1).

In most matrix cameras, integration time is controlled by mechanical shutters. In line cameras, integration time is controlled electronically; moving parts are not required. Exterior orientation is the same across the whole matrix in matrix cameras. Individual matrix photographs have to be connected when making image strips, using pass points at the von Gruber locations. In line cameras, exterior orientation is the same for all the lines in the focal plane, but it changes with each line recorded. This is illustrated in Fig. 1.4-5. The consequences for sensor orientation are described in Section 2.10.

Whereas the requirements which the position and attitude measuring technology for matrix cameras has to meet correspond to those of analogue airborne cameras, additional aspects need to be taken into account in the use of multiple-line cameras. The three-line camera is based on the fact that at least three lines are needed to establish correct orientation with the aid of pass points at the von Gruber locations (Hofmann, 1986), but this procedure requires a great deal of computing time. GPS and IMU systems can support the process of determining the exact orientation of all lines (see Section 4.9). Cost-effectiveness is a decisive factor when selecting IMU systems.

Georeferencing following high-precision measurement of external orientation at each recording position is possible by using measured data on its own, because this is not a cost-effective solution. Economical measuring systems can be used and georeferencing results computed within an acceptable time frame in georeferencing using bundle block adjustment with a relatively small number of linkage points by incorporating position and attitude values of relatively low precision. In the meantime, GPS receivers are also used in analogue airborne cameras and matrix cameras for navigation purposes and for supporting the generation of image strips. As a rule,

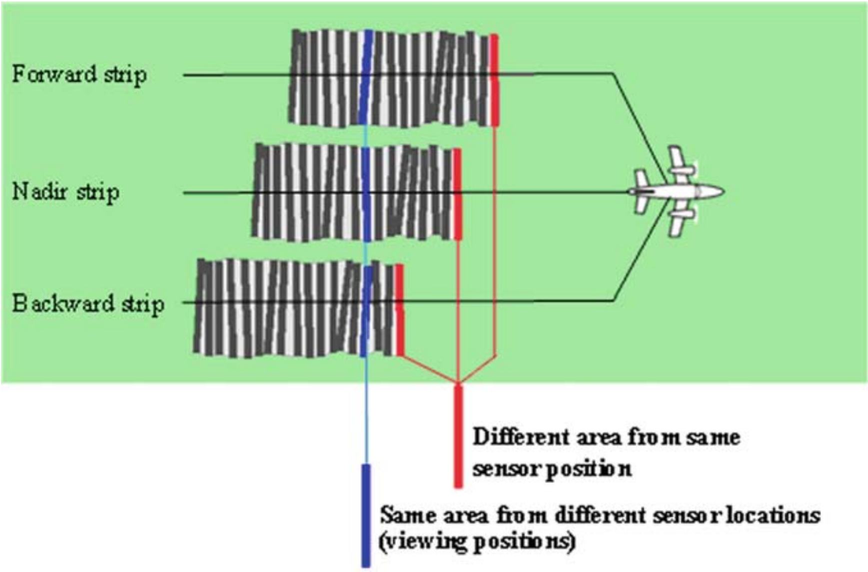

Fig. 1.4-5 Schematic representation of external orientation change for each new line recorded (Leica, 2004)

differential position determination using kinematic phase measurement is employed in all camera types. Real-time solutions are nor required.

Figure 1.4-6 shows this photo flight situation typical of airborne cameras. The sensor head of the ADS40 multiple-line camera contains an integrated IMU selected according to the foregoing criteria. Aspects of the rectification of multiple-line camera images sketched here are discussed in further detail in Sections 2.10 and 4.9.

Resolution values and performance that should be as close as possible to those of analogue airborne cameras are among the principal characteristics of digital airborne cameras. Resolution and performance are defined by GSD (ground sample distance, see Section 2.5) and swath width. This applies to both multispectral and panchromatic channels.

Instead of an airborne camera film, it would be ideal to have a matrix with 80,000 $\times$ 80,000 detector elements array in the focal plane. This matrix should have detectors spaced roughly 2–3 μm apart, with spectral responsivities alternating between blue, green, red and NIR (near infrared). The 20,000 $\times$ 20,000 colour detectors would correspond to analogue aerial photographs in a 23 $\times$ 23 cm format that have been digitized with an 11.5-μm grid. A detector size of 16 $\times$ 16 cm to 24 $\times$ 24 cm would be large enough for lenses used in analogue airborne cameras to be combined directly with the matrix. The surface would have to be extremely even with tolerances in the range of a few micrometres (see Sections 4.2 and 4.5). Such a matrix cannot be manufactured at an acceptable price today. But there are alternatives based on different approaches for the two basic concepts (matrix or line). The basic ideas behind the two alternatives are shown in Fig. 1.4-7. In each case,

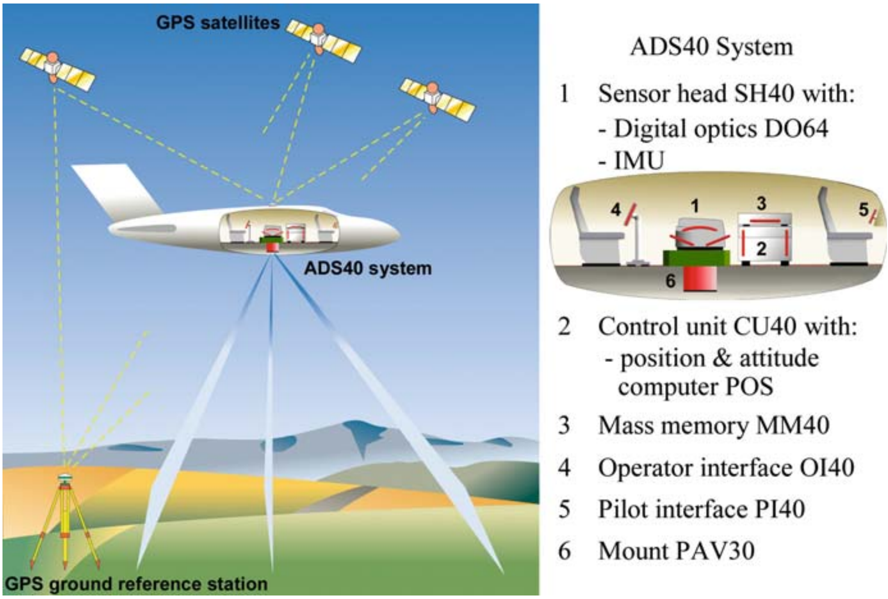

Fig. 1.4-6 Schematic representation illustrating the use of differential GPS in aerial photography in conjunction with an ADS40 (Leica, 2004)

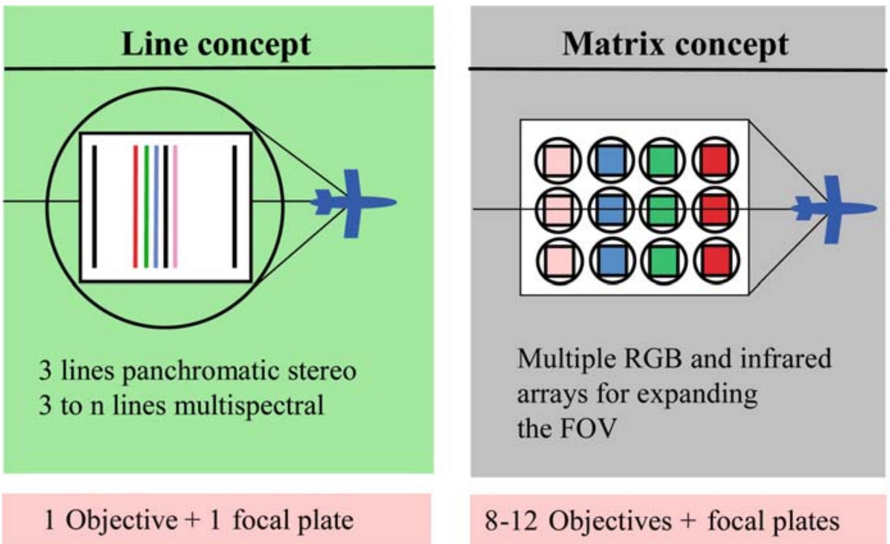

Fig. 1.4-7 Alternative solutions for digital airborne cameras (Leica, 2004)

a Cartesian coordinate system is constructed, the axes of which represent spectral resolution along the flight track and geometric resolution across the track in combination with the swath width, thus representing the number of detector elements schematically.

Since it is easier to construct an array comprising a multitude of faultless detector elements in a single dimension (line) with good yield than in two dimensions simultaneously (matrix), lines are bound to provide higher resolutions at a given stage in technological development. The current state of the art is lines with 12,000 detector elements which, in staggered array (see Section 2.5), can accomplish 24,000 scanning operations along the line (see Section 2.5 and Chapter 7).

Matrices with roughly 9,000 $\times$ 9,000 detector elements are available today, although their application in digital airborne cameras is not yet economical. Currently, matrices with about 7 $\times$ 4 k are used (see Section 1.5). Thus, depending on the required number of sampling points in the swath direction, the appropriate number of matrix cameras is arranged side by side. As shown in Section 1.5, several variants are possible.

There are also two basic concepts (matrix or line) with respect to the spectral co-ordinates shown in the flight direction in Fig. 1.4-7. In the case of the matrix concept, the appropriate number of cameras must be used to achieve the required swath width with the specified GSD for each spectral channel or, if several channels are combined in a camera using special optical processes, then for each channel combination.

In the case of the line concept, additional lines – corresponding to the number of required spectral channels – are arranged in the focal plane between the lines (usually panchromatic) used in topographic mapping. It should be noted that in both alternative solutions shown in Fig. 1.4-7, the differences in angles of convergence and exposure time between the spectral channels, on the one hand, and between spectral channels and the panchromatic channels, on the other, lead to pixel cover problems during data processing or presentation. These systemic pixel cover problems arising from angles of convergence and varying recording time points also occur with analogue airborne cameras, however, when images from several flight missions using different films (panchromatic, colour, IR) are joined. A major advantage of digital airborne cameras is that all data obtained with analogue airborne cameras using three different films from three photo flights can be generated on a single flight. Here, the pixel cover problems result from the overlapping of the results obtained not on three photo flights but on only one. Also, greater differences in illumination conditions inevitably occur when images are generated on three flights in the case of analogue airborne cameras than those generated on a single flight using digital airborne cameras.

These systemic errors can be avoided only if the angles of convergence between channels and different time points of imaging can be avoided. This can be done with camera systems that convey the different spectral light components (R, G, B, NIR) to different detector systems (matrices or lines) via polychroitic beam-splitting devices. In large-format digital cameras (see Section 1.5) this can be achieved more readily by using detector lines and polychroitic beam splitting devices, which cover the airborne camera's entire FOV, rather than by using matrix-based multi-camera systems (see Chapter 7).

1.5 Selection of Commercial Digital Airborne Cameras

There are several cameras on the market that are sold and/or used as digital airborne cameras. A good survey of the different systems from different manufacturers is given in Petrie and Walker (2007). It gives also a classification of all systems.

We focus our attention here on the large-format cameras ADS80, DMC and UltraCam shown in Fig. 1.5-1, which are already being marketed worldwide and which are also representative of the various approaches.

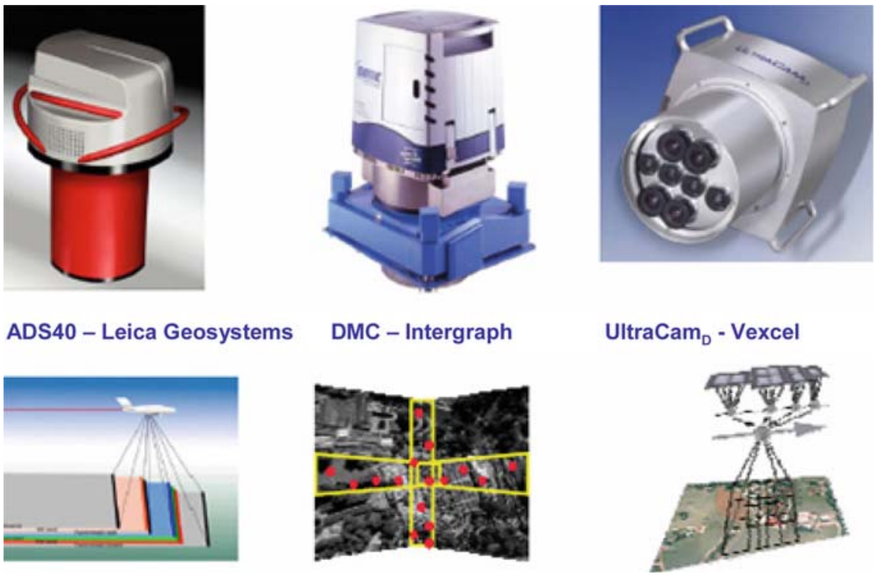

Fig. 1.5-1 Commercial large-format (Cramer, 2004)

1.5.1 ADS80

The multiple-line scanner ADS40 (Airborne Digital Sensor) made by Leica Geosystems (Leica, 2004) was developed in cooperation with Institut für Weltraumsensorik und Planetenerkundung of Deutsches Zentrum für Luft- und Raumfahrt in Berlin. The scanner is based on the three-line concept and is an adaptation of the WA0SS stereo camera developed for the Russian Mars 96 mission (Sandau, 1998), so the ADS40 represents the latest technologies available. It is supplied in various focal plan variants (see Section 7.1). To illustrate the basic principle of the scanner's construction, some details of one of its variants are examined here. The panchromatic CCD line directed vertically downward consists of two lines with 12,000 detector elements each, the elements being spaced 6.5 μm apart and staggered against each other by half a detector width. A synthetic 3.25 μm grid with 24,000 sampling points in the ground track across the direction of flight is produced through this staggered arrangement. Two similar CCD lines directed forwards and backwards and, with the 62.7 mm f/4 lens, yield stereo angles of 28.4° and 14.2° respectively. The FOV is 64° in the cross-track direction, so a swath width of 2.4 km can be achieved a flight altitude of 1,500 m,. At a distance of 14.2° from the central CCD line, there are narrow-banded, spectrally separated R, G and B lines with 12,000 detector elements each, suitable for generating true-colour images as well as for thematic interpretation in remote sensing applications. In addition, 2° from the central line, there is a line that is sensitive in the near infrared range (NIR). The filter design and the linear characteristic of the CCD detector elements give the digital airborne camera the quality of an imaging and measuring instrument. The RGB channel are perfectly co-registered through special optical means and there are no chromatic fringes. Table 1.5-1 shows some parameters of the ADS40 in comparison with the other two digital airborne cameras detailed here. Further details are given in Chapter 7.

Table 1.5-1 Comparison of parameters of digital airborne cameras (camera head)

	ADS40	DMC	UltraCam_D
Dynamic range	12 bits	12 bits	12 bits
Frame frequency	800 s^{-1}	0.5 s^{-1}	0.77 s^{-1}
Shutter	N/A	1/300–1/50 s	1/500–1/60 s
FMC	N/A	Electronic (TDI)	Electronic (TDI)
Detector type	CCD line	CCD matrix	CCD matrix
Element spacing	6.5 μm	12 μm	9 μm
Spectral channels	Pan, R, G, B, NIR	Pan, R, G, B, NIR	Pan, R, G, B, NIR
Panchromatic system			
Detector size (y · x)	2 × 12,000 staggered	7 × 4 k	4,008 × 2,672
Number of detectors	3	4	9
Number of lenses	1	4	4
Image format (y · x)	24,000 × strip length	13,824 × 7,680	11,500 × 7,500
Focal length, f#	62.7 mm, f/4	120 mm, f/4	100 mm, f/5.6
FOV (y · x)	64° × N/A	69.3° × 42°	55° × 37°
Multispectral system			
Detector size (y · x)	12,000	3,072 × 2,048	4,008 × 2,672
Number of detectors	4	4	4
Number of lenses	1	4	4
Image format (y · x)	12,000 × strip length	3,072 × 2,048	3,680 × 2,400
Focal length, Focal length f#	62.7 mm, f/4	25 mm, f/4	28 mm, f/4
FOV (y · x)	64° × N/A	69.3° × 42°	61° × 42°

N/A – not applicable

1.5.2 DMC

The matrix-based camera system DMC (Digital Mapping Camera) from Intergraph (Intergraph, 2008) uses four 7 × 4 k matrices behind four lenses whose optical axes are slightly inclined in order to produce a panchromatic image of 13,824 × 7680 pixels in central perspective from the butterfly-shaped component images (see Section 7.2). The system's FOV is 69° × 42°, its pixel size is 12 μm and its focal length 120 mm. The maximum repetition rate of two frames per second makes for large image scales and small GSDs. In addition to the four panchromatic cameras, there are four multispectral cameras for R, G, B and NIR with matrix sizes of 3 × 2 k. The focal lengths of 25 mm ensure that the multispectral coverage of each exposure is the same as that of the image array from the four panchromatic cameras. Pan-sharpening is used to produce colour images. Figure 1.5-2 shows the DMC's lens array: the inner four lenses generate the panchromatic image, whereas the outer four lenses, the four colour separations. Some of the parameters of the DMC are shown in Table 1.5-1 in comparison with the two other digital airborne cameras covered here.

Fig. 1.5-2 The DMC as seen from below. The four inner cameras generate the panchromatic image (Z/I Imaging, 2003)

1.5.3 UltraCam

The Vexcel UltraCam approach (see Section 7.3) uses nine CCD matrices with 4,008 × 2,672 detector elements to generate a panchromatic image of 11,500 × 7,500

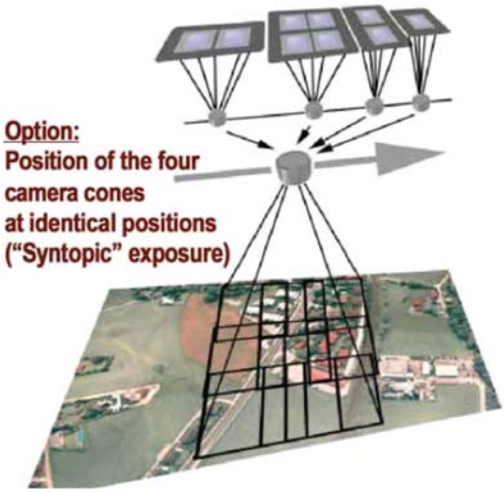

Fig. 1.5-3 The panchromatic image is made from nine component images (see Gruber and Manshold, 2008)

pixels (see Gruber and Manshold, 2008). Figure 1.5-3 shows how the patchwork-like montage of the composite image is produced.

The four colour images are generated with four additional cameras with focal lengths of 28 mm. The associated larger outer lenses can be seen in Fig. 1.5-1. Colour images of higher resolution are generated with the aid of pan-sharpening. Some of the parameters of the UltraCam$_D$ are shown in Table 1.5-1 in comparison with the two other digital airborne cameras covered here.

Chapter 2
Foundations and Definitions

2.1 Introduction

Some preliminary remarks are helpful before the foundations and definitions are provided in more detail. Optoelectronic imaging sensors are described by parameters or functions that characterise the geometric, radiometric and spectral quality of optical imaging and the quality of the analogue and digital processing of optical information.

Geometric imaging by the lens of a sensor (which will be considered in more detail in Section 4.2) is described, as a first approximation, by thin lens (ideal) imaging of an object. If one considers the image of a luminous point P which is located at distance g in front of the lens then this point is mapped at distance b behind the lens in a point P'. The relationship between g and b is given by

$$\frac{1}{f} = \frac{1}{g} + \frac{1}{b}, \tag{2.1-1}$$

where f is the focal length of the lens.

If the point P is located at distance G from the optical axis then the distance B of point P' from the optical axis is

$$B = \frac{b}{g} \cdot G \tag{2.1-2}$$

(see Fig. 2.1-1).

If the image is not observed in the image plane (at distance b from the lens), but in a shifted plane at distance $b \pm \varepsilon$, then the point P is imaged into a circle. The image becomes blurred, and the blur increases with increasing shift ε. This simple model of an imaging lens is sufficient for a coarse assessment of the imaging quality, but is not sufficient for a more precise analysis.

In general, real (multi-lens) optics have imaging errors which violate the ideal imaging equations (2.1-2) and (2.1-2). These errors are not considered here, but the reader is referred to McCluney (1994). In high-precision optics the errors are minimized by elaborate lens corrections. The remaining errors can be measured

R. Sandau (ed.), *Digital Airborne Camera*, DOI 10.1007/978-1-4020-8878-0_2,

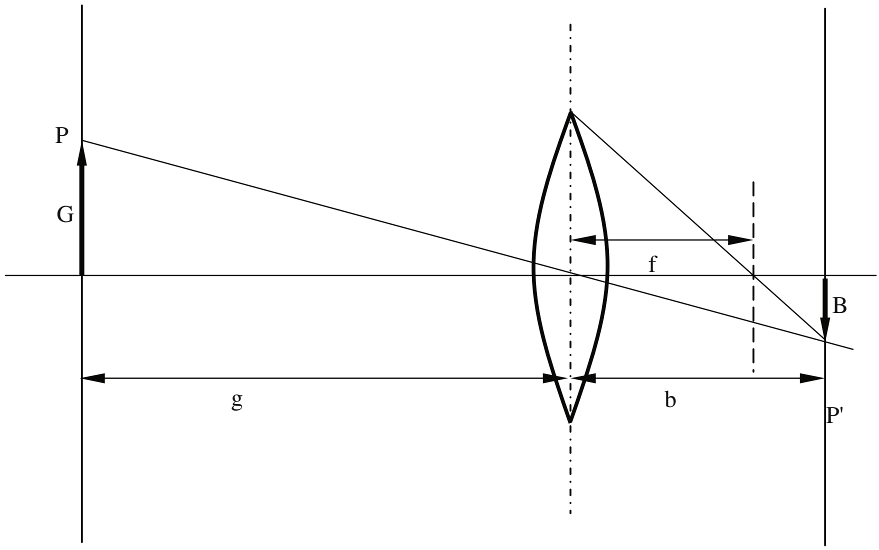

Fig. 2.1-1 Imaging by a thin lens

in a process of geometric calibration and corrected by software later. If there is a requirement to measure in images (photogrammetry), the geometric calibration and subsequent correction must be done very carefully.

Not all effects of optical imaging can be explained by the laws of geometric optics, because, if we use a better approximation, light is described by waves, which are characterised by parameters such as wavelength λ, frequency ν, amplitude A, and phase φ. This leads to phenomena of diffraction affecting the imaging quality. The point P is no longer mapped to a point P' but to a diffuse spot, the diameter of which characterises the geometric resolution of imaging. Existing lens errors (aberrations) lead to a further deterioration of the image quality. If aberrations are absent, the imaging lens is said to be diffraction-limited. Because diffraction is a wave phenomenon, image quality decreases with increasing wavelength λ. The approximation of geometric optics described at the beginning of this chapter is reached as $\lambda \to 0$. Only in this case will a point be mapped into a point.

Light as a waveform also has properties such as coherence and polarisation. In most cases these phenomena do not play an essential role in the design of a camera and they are not discussed here. Light is considered as incoherent and unpolarised. The (partial) coherence of radiation is responsible for the interference of light, which occurs especially in the use of laser radiation. Whereas for coherent light the wave amplitudes are superimposed, incoherent light is a superimposition of intensities (radiances and brightnesses). The amplitudes and phases of incoherent light are random functions of space and time (called white noise in the case of fully incoherent light) and the light must be described by statistical averages of quadratic quantities (intensities, correlation functions and so on). Real light is neither fully coherent nor totally incoherent – it is partially coherent – but that property will not be used in the following analysis.

Polarisation follows from the vector character of light. As with any other electromagnetic radiation obeying Maxwell's equations, light is described by electric and magnetic field vectors which are orthogonal to each other and to the direction of propagation (transverse fields). If one considers, for example, the electric vector in a given point of space as a function of time it can describe various curves. If it oscillates along a straight line the light is linearly polarised. But the vector also can describe an ellipse (elliptical polarisation) or a circle (circular polarisation) or even move randomly (unpolarised radiation). Natural radiation, which is often unpolarised, can become polarised after reflection or refraction at optical surfaces. This effect can give useful information on the properties of polarising media, but it can also lead to radiometric errors if it is not taken into account. If one wants to have precise radiometry, rather than just attractive pictures, then polarisation should be studied intensely.

Light is always a superimposition of wave trains with different wavelengths (and directions of propagation). Therefore, all physical quantities which describe the radiation, such as amplitudes, phases and intensities, depend on the wavelength λ or on the wavenumber $\sigma = 1/\lambda$. These functions $f(\lambda)$ characterise the spectral properties of light, and $f(\lambda)$ is the spectrum of the corresponding physical quantity f. If the function $f(\lambda)$ is concentrated in a small neighbourhood around a mean wavelength $\lambda 0$ then the radiation is (quasi-)monochromatic. Otherwise, the radiation is more or less broad-band. It can be decomposed into its spectral parts using filters, prisms or gratings, enabling useful information on light sources or on reflecting, refracting, absorbing, or scattering media to be obtained. Natural radiation in general is broad-band, whereas laser radiation can be extremely narrow-band. Connected with the spectrum is the colour of light, which is not a physical quantity but a phenomenon of visual perception. Many models have been developed to describe colour more or less correctly and these should be used if true colour images must be generated.

The physical value which is measured by a radiation detector is proportional to a time average of the quadratic amplitude of incoming radiation. It is a measure of the radiation energy in a certain spectral interval reaching the detector during the integration time and of the brightness too. When that energy must be measured (for ordinary cameras that is not the case – a good visual impression is enough), then a radiometric system must be considered. Radiometric systems need very careful design, because diverse errors can cause considerable deterioration of the quality of measurement.

The description of light by Maxwell's equations as a continuous phenomenon in space and time is only an approximation of its true nature. If one goes to the atomic range and investigates the emission and absorption of light by atoms and molecules, it becomes clear that light is emitted and absorbed only as discrete portions of energy (light quanta or photons). For our purposes it is sufficient to imagine a photon as a wave train of limited duration and extent with the wavelength λ and the frequency

$$\nu = c/\lambda, \tag{2.1-3}$$

where c is the velocity of light, and the energy

$$E = h \times \nu, \tag{2.1-4}$$

where h is Planck's constant.

Because the emission of a photon is a random event (i.e. the time of emission is a random variable), natural light is a more or less random superimposition of photons with a fluctuating photon number in space and time. These fluctuations are called photon noise, which is the ultimate limit of the radiometric measurement accuracy of an optoelectronic system.

After the optical system is adequately described, including the radiation source and the transmitting medium, it is necessary to study the properties of the detector and the signal processing electronics. Advanced optoelectronic detectors are assembled detector elements arranged regularly on a chip. The continuous radiation field is sampled by the limited area of a detector element. Owing to the size of the detector element and the spatial distribution of the sensitivity, the spatial information is blurred. This blur is superimposed on the blur generated by diffraction of light at the aperture of the optics. Sometimes the regular arrangement of the detector elements produces certain unwanted phenomena (aliasing), which can be reduced by a proper trade-off of optics and detector array. To achieve this, one has to consider the sampling theorem together with the parameters describing the blur, such as Point Spread Function (PSF) or Modulation Transfer Function (MTF). Here the Fourier transform plays an essential role.

In the following sections the characteristics of radiation, optics and sensors, which have been mentioned only briefly so far, will be discussed in more detail. The registration of incoherent and unpolarised radiation is of particular interest. The necessary theoretical foundation is presented together with practical questions, to which reference is made in later chapters.

Reference may be made to the following books for a deeper insight into the problems: Goodman (1985), McCluney (1994), Jahn and Reulke (1995) and Holst (1998a, b).

2.2 Basic Properties of Light

According to the wave theory of light, a light wave propagating in a medium can be described by the real part of a superimposition of plane waves

$$\mathbf{A}(\lambda) \cdot \exp\left[j \cdot (\mathbf{k} \cdot \mathbf{r} - \omega \cdot t)\right]. \tag{2.2-1}$$

Here, $\mathbf{k} = \frac{2\pi}{\lambda} \cdot \mathbf{e}$ is the wave vector described by the wavelength λ and the direction of propagation given by the unit vector $\mathbf{e}$. $\omega = 2\pi\nu$ is the circular frequency, which depends on the wavelength according to $c = \lambda \cdot \nu$ (2.1-3). The phase velocity c is the velocity of light in the transmitting medium. It is connected with the vacuum velocity of light via $c = c_{\mathrm{vac}}/n$ ($n = n(\lambda)$ is the refractive index). The amplitude **A,** a complex number, is actually a vector (the vector of the electric or magnetic field strength) which is orthogonal to the direction **e** of propagation (transverse waves). Because polarisation is not studied here, **A** is considered as a scalar variable. If the complex number **A** is written as $\mathbf{A}(\lambda) = |\mathbf{A}(\lambda)| \cdot \exp\left[j \cdot \varphi(\lambda)\right]$ with the (real number) amplitude $A = |\mathbf{A}|$ and the phase φ then the wave can be written as

$$A(\lambda) \cdot \cos\left[\frac{2\pi}{\lambda} \cdot (\mathbf{e} \cdot \mathbf{r} - c \cdot t) + \varphi(\lambda)\right]. \tag{2.2-2}$$

This wave propagates with velocity c in the direction **e**.

Radiometric quantities such as radiance and power flux are averaged squares of waves of the kind (2.2-2), i.e. they are proportional to the squared amplitude $A2(\lambda)$. In the case of incoherent radiation, these quantities can be added (and, especially, integrated over the wavelength), whereas, in the case of coherence, the complex-valued amplitudes $A(\lambda)$ must be integrated or added.

To estimate the amount of energy reaching a detector element during the time interval Δt, the necessary quantities describing the radiation are now briefly introduced. The power (measured in Watts [W]) in the wavelength interval $\Delta\lambda$ which is emitted by a surface element ΔF (with the unit vector **n** describing the surface normal) into the solid angle element $\Delta\Omega$ (around the direction **s**) is given by

$$\Delta\Phi_\lambda = L_\lambda \cdot \cos(\vartheta) \cdot \Delta F \cdot \Delta\Omega \cdot \Delta\lambda. \tag{2.2-3}$$

Here ϑ is the angle between vectors **n** and **s** (see Fig. 2.2-1).

The variable L_λ (measured in [W/(m^2·sr · nm)]) characterizing the radiation properties of the emitting surface is called spectral radiance. In general, L_λ depends on the position of the emitting surface element, the time of emission, the wavelength λ and the direction **s** of emission. In the (idealized) case of a Lambertian radiator, L_λ does not depend on the direction **s** of emission. For simplicity, this case is often

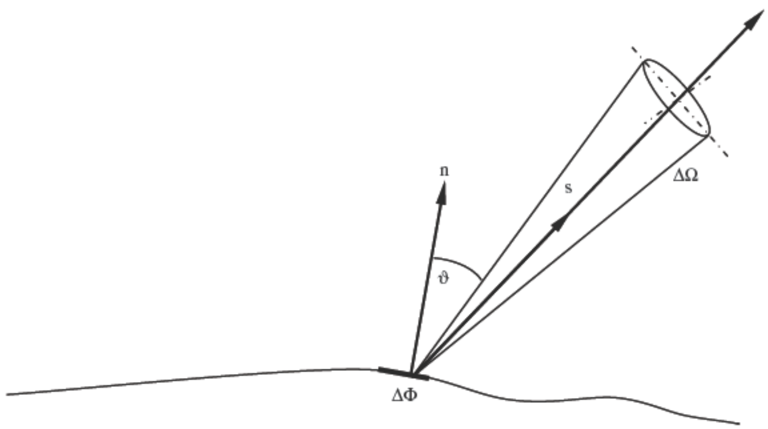

Fig. 2.2-1 Emission of radiation

used for coarse estimation. Strictly speaking, it holds only in the interior of a cavity whose walls have the constant temperature T. Such a cavity is filled with the so-called black body radiation with the radiance

$$B_{\lambda}(T) = \frac{2hc^2}{\lambda^5} \cdot \frac{1}{\exp\left(\frac{h \cdot c}{\lambda \cdot k \cdot T}\right) - 1}. \tag{2.2-4}$$

In (2.2-4) h is Planck's constant, k the Boltzmann constant, and T the absolute temperature.

For the purpose of calibration, black body radiation is often (especially in the infrared part of the spectrum) generated approximately by so-called black bodies. In reality, they always show deviations from Planck's law (2.2-4), which are described by the emissivity ε_{λ}. A light source which does not receive radiation emits the radiance

$$L_{\lambda} = \varepsilon_{\lambda} \cdot B_{\lambda}(T), \tag{2.2-5}$$

with $\varepsilon_{\lambda} < 1$.

An example of a near black body source is the sun. The photosphere of the sun approximately emits black body radiation with a temperature of about $T = 5{,}800$ K. Then the chromosphere absorbs some parts of that spectrum resulting in a radiance of type (2.2.5).

For the estimation of the radiant energy hitting a detector element, the optical mapping of a radiating surface by a lens is now considered. Let F_{O} be the object area (which is assumed here to be perpendicular to the principal axis) which is mapped on to a detector element of area F_{D}. Then, according to (2.1-2):

$$F_{\mathrm{D}} = \frac{b^2}{g^2} \cdot F_{\mathrm{O}}. \tag{2.2-6}$$

The radiation emitted by F_{O} and reaching F_{D} is collected by a lens of aperture D and area $F_{\mathrm{L}} = \frac{\pi}{4} \cdot D^2$. This radiation is contained in the solid angle (see Fig. 2.2-2)

$$\Omega_{\mathrm{O}} = \frac{F_{\mathrm{L}}}{g^2} \cdot \cos(\vartheta) = \frac{\pi}{4} \cdot \left(\frac{D}{g}\right)^2 \cdot \cos^3(\vartheta). \tag{2.2-7}$$

The detector element, therefore, receives approximately the power

$$\Delta\Phi_{\lambda} = L_{\lambda} \cdot \cos(\vartheta) \cdot F_{\mathrm{O}} \cdot \Omega_{\mathrm{O}} \cdot \Delta\lambda = \frac{\pi}{4} \cdot \left(\frac{D}{g}\right)^2 \cdot F_{\mathrm{O}} \cdot \cos^4(\vartheta) \cdot L_{\lambda} \cdot \Delta\lambda.$$

Using (2.2-6) and considering far away objects ($g >> f$; $b \approx f$), then one finally obtains

$$\Delta\Phi_{\lambda} = \frac{\pi}{4} \cdot \left(\frac{D}{f}\right)^2 \cdot F_{\mathrm{D}} \cdot \cos^4(\vartheta) \cdot L_{\lambda} \cdot \Delta\lambda = \frac{\pi}{4} \cdot \frac{F_{\mathrm{D}}}{f_{\#}^2} \cdot \cos^4(\vartheta) \cdot L_{\lambda} \cdot \Delta\lambda. \tag{2.2-8}$$

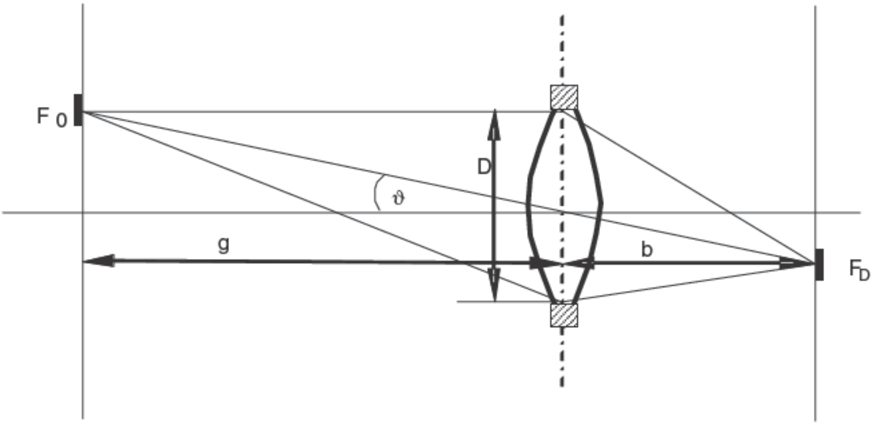

Fig. 2.2-2 Radiometric parameters of optical imaging

Here, $f_\# = f/D$ is the so-called f-number of the lens. This important parameter is responsible for the diffraction of light at the aperture of the lens (see below). Also characteristic of the amount of radiation which the detector element receives is the decrease in brightness with increasing distance from the principal axis, which is proportional to $\cos^4(\vartheta)$ in the approximation used here. The further a detector element is from the principal axis, the less energy it receives.

In (2.2-8) it was tacitly assumed that all the radiation hitting the lens can pass through it. But in reality there is absorption and scattering of radiation at the lens and also in the atmosphere. Furthermore, spectral filters can be used (e.g. R-, G- and B-filters for the generation of colour images). All these effects can be described by a transmission function $\tau_\lambda < 1$. Then (2.2-8) changes to

$$\Delta\Phi_\lambda = \frac{\pi}{4} \cdot \frac{F_\mathrm{D}}{f_\#^2} \cdot \cos^4(\vartheta) \cdot \tau_\lambda \cdot L_\lambda \cdot \Delta\lambda. \tag{2.2-9}$$

Owing to scattering of light in optical media (atmosphere, lenses etc.), unwanted light from other sources can hit the detector element. This cannot be avoided completely, but it can be reduced by adequate countermeasures (baffles). The remaining part of this disturbing radiation must be added to the right-hand side of (2.2-9). It generates a systematic error in the sensor data. In the domain of thermal infrared radiation, which is not considered here, one has to consider also the radiation emitted by lenses, housings and so on, i.e. the whole environment of the detector.

The total power received by the detector element is given by integration over the wavelength of (2.2-9):

$$\Phi = \frac{\pi}{4} \cdot \frac{F_\mathrm{D}}{f_\#^2} \cdot \cos^4(\vartheta) \cdot \int_0^\infty \tau_\lambda \cdot L_\lambda \cdot \mathrm{d}\lambda + \Phi_\mathrm{scatter}. \tag{2.2-10}$$

Formally, the integration is extended over all wavelengths from zero to infinity. But in reality only a part of that spectrum interacts with the detector element because of the limitation given by the transmission function τ_λ.

During a time interval Δt (integration time) the sensor element receives the energy

$$E = \Phi \cdot \Delta t. \tag{2.2-11}$$

Because the CCD or CMOS sensors considered here are quantum detectors, it is sometimes more adequate to consider light as a flux of energy quanta or photons. These detectors can be characterised by the quantum efficiency η^{qu}, which, on average, generates N^{el} electrons from the impinging (mean) number N^{ph} of photons.

To calculate the mean number of photons hitting the detector element, Equations (2.2-10) and (2.2-11) should be written as

$$E = \int_0^\infty e_\lambda \mathrm{d}\lambda, \tag{2.2-12}$$

with

$$e_\lambda = \frac{\pi}{4} \cdot \frac{F_\mathrm{D}}{f_\#^2} \cdot \cos^4(\vartheta) \cdot \tau_\lambda \cdot L_\lambda \cdot \Delta t + e_{\lambda,\mathrm{scatter}}. \tag{2.2-13}$$

According to quantum theory, the radiation energy at wavelength λ can only be a multiple of the energy $h \cdot \nu = h \cdot c/\lambda$ of a single photon (see (2.1-4) and (2.1-3)). If $n_\lambda \mathrm{d}\lambda$ is the mean number of photons in the interval [λ,λ+dλ], then it follows that

$$e_\lambda = n_\lambda \cdot \frac{h \cdot c}{\lambda}$$

and

$$n_\lambda = \frac{\lambda}{h \cdot c} \cdot e_\lambda = \frac{\pi}{4} \cdot \frac{F_\mathrm{D}}{f_\#^2} \cdot \cos^4(\vartheta) \cdot \tau_\lambda \cdot \frac{\lambda}{h \cdot c} \cdot L_\lambda \cdot \Delta t. \tag{2.2-14}$$

$N^{\mathrm{ph}} = \int_0^\infty n_\lambda \mathrm{d}\lambda$ is the total number of photons received by the detector element.

Now the mean number of electrons generated inside the detector element can be calculated if (2.2-14) is multiplied by the quantum efficiency and integrated over the wavelengths:

$$N^{\mathrm{el}} = \frac{\pi}{4} \cdot \frac{F_\mathrm{D}}{f_\#^2} \cdot \cos^4(\vartheta) \cdot \Delta t \cdot \int_0^\infty \eta_\lambda^{\mathrm{qu}} \cdot \tau_\lambda \cdot \frac{\lambda}{h \cdot c} \cdot L_\lambda \cdot \mathrm{d}\lambda. \tag{2.2-15}$$

This quantity is converted into a voltage by the read-out electronics. This voltage is fed into an analogue-to-digital converter, which generates a digital number proportional to N^{el}. This number can be stored and processed digitally.

The formulae presented above are sufficient for coarse estimation of the detector signal. For more precise investigations one must consider the space- and time-dependencies of the radiation quantities. The radiance L_λ and also the related quantities depend in general on space and time, which was neglected above. Because the integration time Δt of a CCD or CMOS sensor is very short in most cases, L_λ does not change much during this time and $\int\limits_t^{t+\Delta t} L_\lambda\left(t'\right)\mathrm{d}t'$ may be approximated by $L_\lambda(t)\Delta t$ as was done above.

Let X, Y be the coordinates in the object plane (e.g. on the surface of the Earth if the Earth is observed by a spaceborne or airborne sensor). Then L_λ is a function of X and Y. The corresponding coordinates in the image plane (or focal plane) where the detector is positioned are, according to (2.1-2)

$$x = -\frac{b}{g} \cdot X; \quad y = -\frac{b}{g} \cdot Y. \tag{2.2-16}$$

The quantities which are related to the measured values, therefore, are functions of x and y. They can change considerably from one detector element to another.

A point (X,Y) on the surface of a radiating object is mapped by the lens (in the approximation used in geometric optics) on to a point (x,y) in the image plane. The function $L_\lambda(X,Y)$ is then transformed into the function

$$L_\lambda^*\,(x,y) = L_\lambda\left(-\frac{g}{b} \cdot x, -\frac{g}{b} \cdot y\right), \tag{2.2-17}$$

which is a function of the coordinates x, y in the image plane.

Therefore, in the formulae presented above, $F_\mathrm{D} \cdot L_\lambda$ should be substituted by $\int\limits_{F_D}\!\int L_\lambda^*\left(x',y'\right)\mathrm{d}x'\mathrm{d}y' \approx F_\mathrm{D} \cdot L_\lambda^*\,(x,y)$. This is not true if diffraction is taken into account. The necessary modifications are considered in detail later when appropriate mathematics (Fourier transform) is available (Section 2.3).

At the end of this chapter the relationships between radiometry and photometry will be briefly considered.

If one considers measurement systems then, as above, one has to work with radiometric quantities. But in the past (and often today too) images have been evaluated visually. For this purpose certain photometric quantities are used which are connected with properties (especially the spectral sensitivity) of the human visual system. To present the relationships between the radiometric and photometric quantities a precise definition of the radiometric quantities already used is necessary.

The spectral radiance L_λ is the power of radiation emanating from a surface per unit wavelength interval (for example, 1 nm), per unit area (for example, 1 m^2)

and per unit solid angle (steradian, sr). It is a function of spatial coordinates *x, y*, time *t*, wavelength λ, zenith angle θ and azimuth angle ϕ. It has the dimension [W/(m^2·sr·nm)]. The radiance L [W/(m^2·sr)] is given by $\int L_\lambda \mathrm{d}\lambda$. The radiance, integrated over the area, is denoted as intensity I [W/sr]. The irradiance E [W/m^2] at a radiation receiving surface is

$$E = \int_\Omega L \cdot \cos\theta \cdot \mathrm{d}\Omega; \quad (\mathrm{d}\Omega = \sin\theta \cdot \mathrm{d}\theta \cdot \mathrm{d}\phi)\,,$$

which is the power per unit area received by a surface hit by impinging radiation which is confined to the solid angle Ω. Integration over the area (e.g. of a detector element) gives the radiant flux Φ[W]. Without integration over the wavelength one obtains related spectral quantities such as the spectral flux Φ_λ [W/nm]; $\Phi = \int \Phi_\lambda \mathrm{d}\lambda$.

Let Q_λ be any spectral radiometric quantity. Then the related photometric quantity Q_{phot} is given by

$$Q_{\mathrm{phot}} = 683 \cdot \int Q_\lambda \cdot V(\lambda)\,\mathrm{d}\lambda. \tag{2.2-18}$$

Here, $V(\lambda)$ is the human sensitivity for photopic vision (i.e. vision by the retinal cones). It is presented in Fig. 2.2-3. The relationships between the radiometric and photometric quantities are given in Table 2.2-1.

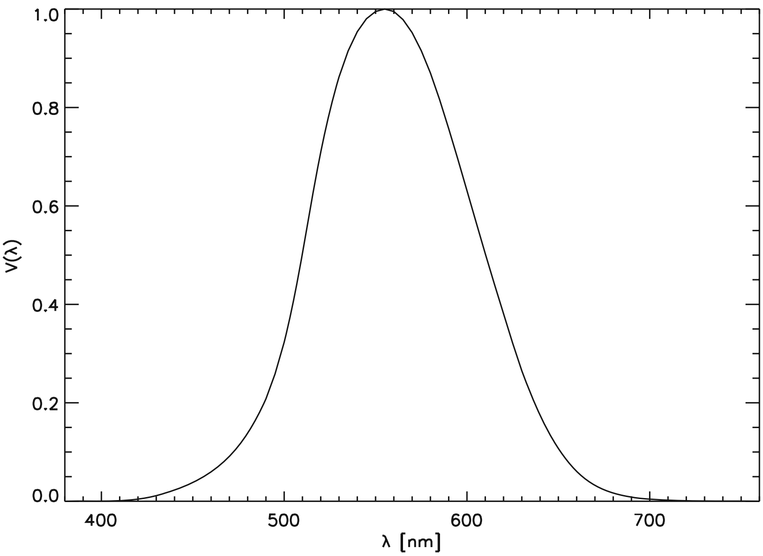

Fig. 2.2-3 Human sensitivity for photopic vision $V(\lambda)$

Table 2.2-1 Radiometric and photometric quantities

Radiometric quantity	Photometric quantity
radiant flux Φ_{rad} [W]	luminous flux Φ_{phot} [lumen (lm)]
radiation intensity I_{rad} [W/sr]	luminous intensity I_{phot} [candela (cd)]
irradiance E_{rad} [W/m^2]	illuminance E_{phot} [lux (lx)]
radiance L_{rad} [W/m^2·sr]	luminance L_{phot}[cd/m^2]

2.3 Fourier Transforms

In many scientific disciplines and especially in investigations of optical systems, it has turned out to be appropriate to understand functions of space and/or time as superimpositions of sinusoidal functions. One reason is that the shape of sinusoidal functions is not changed by linear systems. Only amplitude (the modulation) and phase are affected. Hence, important characteristics of optoelectronic systems such as Optical Transfer Function (OTF) and Modulation Transfer Function (MTF) have been introduced and these will be considered later (Section 2.4 covers linear systems).

The one-dimensional case is considered first. This is of interest in the study of signal processing in electronic circuits. Let $f(t)$ be a function of only one variable t (which may be time or any other coordinate). Under certain mathematical restrictions (which are not discussed here), the function $f(t)$ can be written as a superimposition of sinusoidal functions $\sin(2\pi\nu t)$ and $\cos(2\pi\nu t)$. Here, ν is the frequency of the sinusoidal functions, which are periodic functions with the period $T = 1/\nu$. The frequency ν as a physical quantity is a non-negative real number $(0 \leq \nu < \infty)$.

It is more elegant to use the complex-valued exponential function

$$e^{jx} = \cos(x) + j \cdot \sin(x)\,, \tag{2.3-1}$$

where j is the imaginary unit instead of the sinusoidal functions. Equation (2.3-1) can be resolved to give

$$\cos(x) = \frac{1}{2} \cdot \left[e^{jx} + e^{-jx}\right] \quad ; \quad \sin(x) = \frac{1}{2j} \cdot \left[e^{jx} - e^{-jx}\right]. \tag{2.3-2}$$

Now, the Fourier representation of function $f(t)$ can be written as

$$f(t) = \int_{-\infty}^{+\infty} F(\nu) \cdot e^{j2\pi\nu t} \mathrm{d}\nu. \tag{2.3-3}$$

$F(\nu)$ is the (complex-valued) spectrum of the function $f(t)$, which is defined for positive and negative "frequencies" ν. The occurrence of negative frequencies has no physical meaning: it only guarantees mathematical elegance. Using (2.3-2), one can transform (2.3-3) into a “physical” form with real valued quantities and non-negative frequencies:

$$f(t) = 2\int_{0}^{\infty} A(\nu)\cdot\cos\left[2\pi\nu\cdot t + \varphi(\nu)\right]\mathrm{d}\nu. \tag{2.3-4}$$

To obtain this formula, the complex-valued spectrum is written as

$$F(\nu) = A(\nu)\cdot e^{j\varphi(\nu)} \quad ; \quad A(\nu) = |F(\nu)|\,. \tag{2.3-5}$$

Equation (2.3-4) is the representation of $f(t)$ as a superimposition of sinusoidal oscillations. Here, each oscillation of frequency ν has the amplitude $2A(\nu)$ and the phase shift $\varphi(\nu)$. Therefore, $A(\nu)$ is the amplitude spectrum and $\varphi(\nu)$ the phase spectrum of the (real-valued) function $f(t)$.

If the spectrum $F(\nu)$ is known, then the function $f(t)$ can be calculated according to (2.3-3). Inversely, the spectrum can be computed as

$$F(\nu) = \int_{-\infty}^{+\infty} f(t)\cdot e^{-j2\pi\nu t}\mathrm{d}t, \tag{2.3-6}$$

if $f(t)$ is given. The signals $f(t)$ considered here are real-valued functions. For such functions the following symmetry relationships can be derived from (2.3-6):

$$F^{*}(\nu) = F(-\nu)\,; \quad |F(\nu)| = |F(-\nu)|\,; \quad \varphi(\nu) = -\varphi(-\nu)\,. \tag{2.3-7}$$

Here, F^{*} is the complex conjugate of F. Equation (2.3-7) characterises the fact mentioned above that non-negative frequencies are sufficient for the description of a real-valued signal $f(t)$.

A special class of functions $f(t)$ comprises of the periodic functions with

$$f^{p}(t+T) = f^{p}(T)\,. \tag{2.3-8}$$

T is the period of the function. The functions $f(t)$ considered up to this point can be interpreted as a special case of periodic functions with $T \to \infty$.

The periodic functions can be represented as a superimposition of sinusoidal functions with the discrete frequencies $n\cdot\nu = n/T$. The functions $\sin(2\pi\nu t)$ and $\cos(2\pi\nu t)$ are periodic with $T = 1/\nu$. The same is true for the functions $\sin(2\pi n\nu t)$ and $\cos(2\pi n\nu t)$ and also for every linear combination of those functions. The functions $\sin(2\pi n\nu t)$ and $\cos(2\pi n\nu t)$ ($n = 0,\ldots,\infty$) represent a fully orthogonal system of functions. Each periodic function can be represented as a superimposition of that system.

As for the Fourier integrals, the expansion of periodic functions $f^{\mathrm{p}}(t)$ in terms of exponential functions is more elegant:

$$f^{\mathrm{p}}(t) = \sum_{n=-\infty}^{+\infty} a_n \cdot e^{j2\pi \frac{n}{T} t}. \tag{2.3-9}$$

Equation (2.3-9) is the Fourier series of the periodic function $f^{\mathrm{p}}(t)$.

The orthogonal property of the basis functions $\exp(j2\pi nt/T)$ is expressed by the relationship

$$\int_{-T/2}^{+T/2} e^{j2\pi \frac{n-m}{T} t} \mathrm{d}t = T \cdot \delta_{n,m}. \tag{2.3-10}$$

Here, $\delta_{n,m}$ is the Kronecker symbol defined by

$$\delta_{n,m} = \begin{cases} 1 & \text{for} \quad n = m \\ 0 & \text{for} \quad n \neq m \end{cases}. \tag{2.3-11}$$

Using (2.3-10) the expansion (2.3-9) can be inverted with the result

$$a_n = \frac{1}{T} \cdot \int_{-T/2}^{+T/2} f^{\mathrm{p}}(t) \cdot e^{-j2\pi \frac{n}{T} t} \mathrm{d}t, \tag{2.3-12}$$

which is the analogue of (2.3-6). The Fourier coefficients that describe the discrete spectrum of the periodic function $f^{\mathrm{p}}(t)$ obey the symmetry relation

$$a_n^* = a_{-n}, \tag{2.3-13}$$

which is the analogue of (2.3-7). As for $F(\nu)$, one can introduce (discrete) amplitude and phase spectra according to

$$a_n = |a_n| \cdot e^{j\varphi_n}. \tag{2.3-14}$$

Next, we present some properties of Fourier integrals and Fourier series. Let $F(\nu)$ be the spectrum of a function $f(t)$. Let $G(\nu)$ be a spectrum which differs from $F(\nu)$ by a linear phase shift:

$$G(\nu) = F(\nu) \cdot e^{-j2\pi \nu t_0}. \tag{2.3-15}$$

Then, according to (2.3-3), the corresponding functions $f(t)$ and $g(t)$ are related by

$$g(t) = f(t - t_0), \tag{2.3-16}$$

which means that a linear phase shift corresponds to a time shift of the signal. Furthermore, a pure time shift of a signal $f(t)$ does not change the amplitude spectrum of that signal. In the periodic case the same is true: multiplication of the Fourier coefficients a_n by a linear phase $\exp(-j2\pi n\nu t_0)$ is equivalent to a time shift t_0.

If $f(t)$ is a voltage or a current then $f^2(t)$ is proportional to the electrical power. The integral over $f^2(t)$ is therefore proportional to the total energy contained in the signal. The following relationship holds (Parseval theorem):

$$\int_{-\infty}^{+\infty} f^2(t)dt = \int_{-\infty}^{+\infty} |F(\nu)|^2 \mathrm{d}\nu. \tag{2.3-17}$$

The total energy is decomposed into spectral parts $|F(\nu)|^2\mathrm{d}\nu$. $|F(\nu)|^2$, therefore, is called the power spectrum (energy spectrum would be better). In the periodic case the analogous formula is

$$\frac{1}{T} \cdot \int_{-T/2}^{+T/2} f^{\mathrm{p}^2}(t)dt = \sum_{n=-\infty}^{+\infty} |a_n|^2. \tag{2.3-18}$$

One derives (2.3-18) by inserting the Fourier series into the left hand side and using the orthogonality relationship (2.3-10). Analogously, (2.3-17) can be derived if one uses the Dirac delta function $\delta(t)$ instead of the Kronecker delta. One can envisage this function (mathematically not correct!) as an infinitely narrow signal with an infinitely large signal value concentrated at $t = 0$:

$$\delta(t) = \begin{cases} \infty & \text{for} \quad t = 0 \\ 0 & \text{elsewhere} \end{cases}$$

The δ-function is normalized to unity and cuts a single value out of a continuous function $f(t)$:

$$f(t) = \int_{-\infty}^{+\infty} f(t') \cdot \delta(t' - t)\,\mathrm{d}t' \;; \quad \text{especially:}$$
$$f(0) = \int_{-\infty}^{+\infty} f(t) \cdot \delta(t)\,\mathrm{d}t \;\text{ and } \int_{-\infty}^{+\infty} \delta(t)\,\mathrm{d}t = 1. \tag{2.3-19}$$

There are many representations of the δ-function as a boundary value of continuous funct-ions, for instance as a Gaussian with vanishing width (see Fig. 2.3-1):

$$\delta(t) = \lim_{\sigma \to 0} \frac{1}{\sigma\sqrt{2\pi}} \cdot e^{-\frac{t^2}{2\sigma^2}}. \tag{2.3-20}$$

If the Fourier transform (2.3-6) is applied to the δ-function, then from (2.3-5) it follows that:

$$\Delta(\nu) = 1 \quad \mathit{for} \quad -\infty < \nu < +\infty \tag{2.3-21}$$

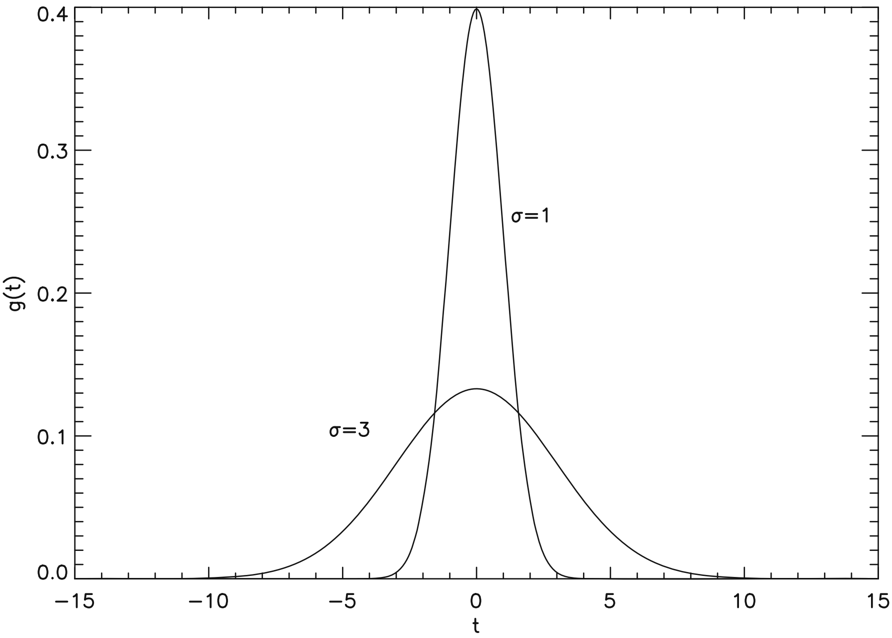

Fig. 2.3-1 Gaussian

and

$$\delta(t) = \int_{-\infty}^{+\infty} e^{j2\pi\nu t} \mathrm{d}\nu. \tag{2.3-22}$$

The spectrum of the δ-function contains arbitrarily high frequencies with constant amplitude, which is not possible in reality. The δ-function is a mathematical abstraction which does not represent a real signal. But it has many mathematical advantages, which can be used to derive formulae such as (2.3-17).

Another important function is the Gaussian (or normal distribution, see Fig. 2.3-1), which is often used for the description of optoelectronic signals:

$$g(t) = \frac{1}{\sigma\sqrt{2\pi}} \cdot e^{-\frac{t^2}{2\sigma^2}} . \tag{2.3-23}$$

Its spectrum is given by

$$G(\nu) = e^{-\frac{\nu^2}{2\kappa^2}} \quad \text{with} \quad \kappa = \frac{1}{2\pi\sigma}. \tag{2.3-24}$$

The spectrum of a Gaussian, therefore, is also a Gaussian but with another normalisation. The parameter σ describes the width of the bell-shaped function $g(t)$,

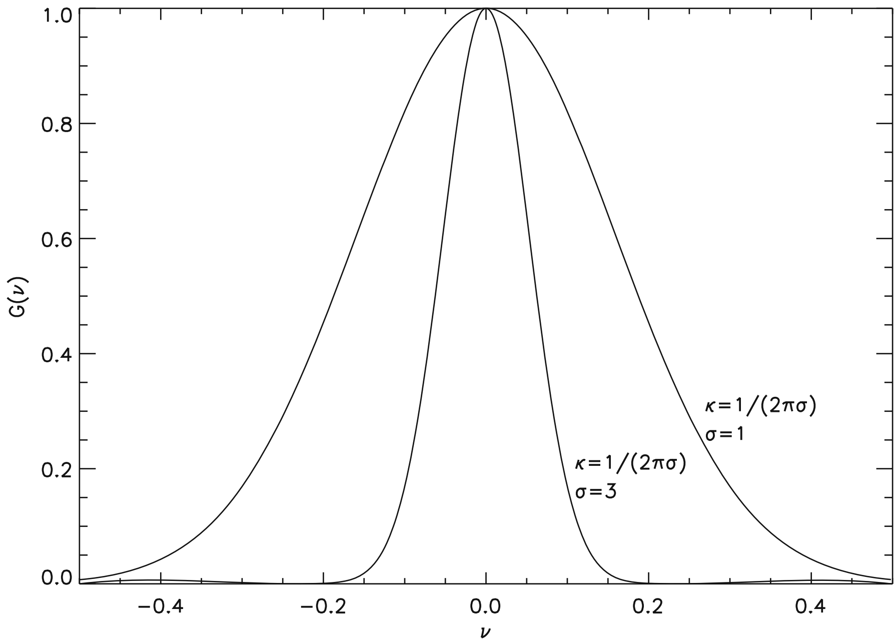

Fig. 2.3-2 Spectrum of Gaussian

whereas κ characterises the width of $G(\nu)$. The relationship $2\pi\sigma\kappa = 1$ (2.3-24) means that the broader the spectrum $G(\nu)$, the narrower is the signal $g(t)$ and conversely (see Fig. 2.3-2). In other words, the narrower and steeper a function, the greater the frequencies it must contain. This holds in general and not only for a Gaussian.

Another function used in the following is the "rectangular" function

$$r_\tau(t) = \begin{cases} \frac{1}{\tau} & \text{for} \quad -\frac{\tau}{2} \leq t \leq +\frac{\tau}{2} \\ 0 & \text{elsewhere} \end{cases} \tag{2.3-25}$$

with the width τ (Fig. 2.3-3). Its spectrum is given by

$$R_\tau(\nu) = \frac{\sin(\pi\nu\tau)}{\pi\nu\tau} \tag{2.3-26}$$

(see Fig. 2.3-4). This spectrum decreases very slowly with increasing frequency (proportional to $1/\nu$) owing to the discontinuities of $r_\tau(t)$. This behaviour is also expressed by zeroes $\nu_n = n/\tau$ of $R_\tau(\nu)$. The smaller τ is, the bigger are the zeroes.

Not only sinusoidal functions but also other periodic functions play an important role in the description of signals. Before special cases are addressed, however, a general relationship between continuous and discrete signal representations is given.

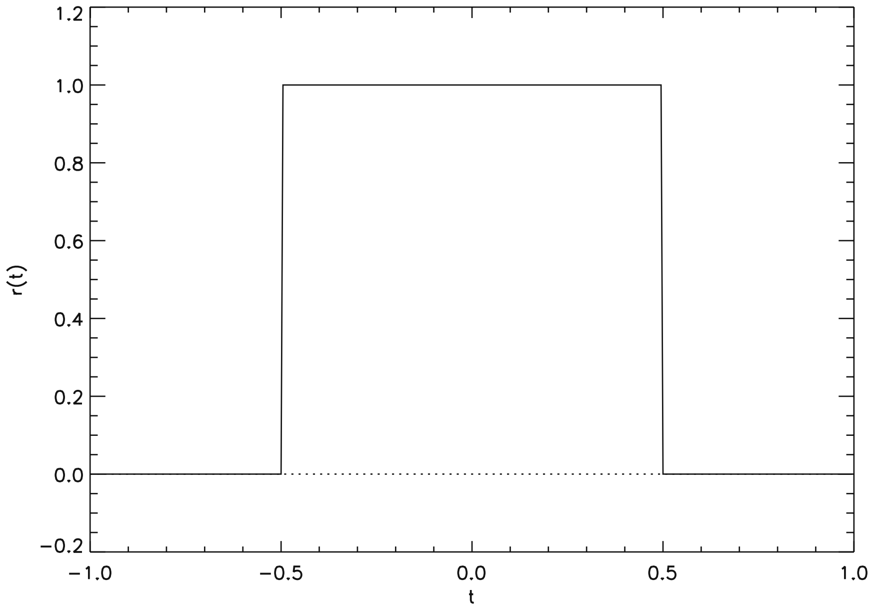

Fig. 2.3-3 Rectangular function ($\tau = 1$)

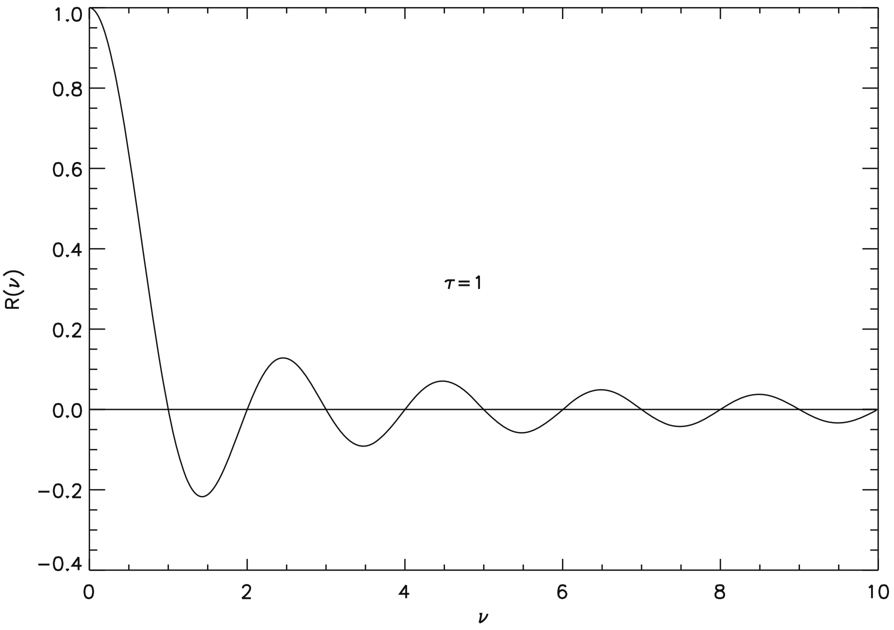

Fig. 2.3-4 Spectrum of the rectangular function ($\tau = 1$)

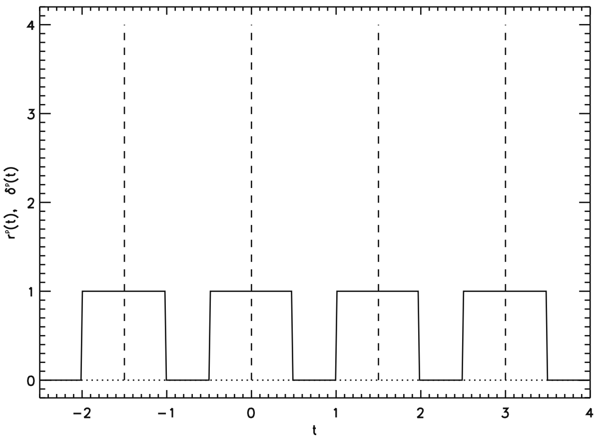

Fig. 2.3-5 Periodic rectangular signal ($\tau = 1, T = 1.5$) and Dirac-comb (*dashed*)

A periodic signal can be written as the periodic continuation of a function $f_\tau(t)$, which is concentrated in the interval $[-\tau/2, +\tau/2]$ (i.e. $f_\tau(t) = 0$ for $t \notin [-\tau/2, +\tau/2]$) (Fig. 2.3-5):

$$f_\tau^p(t) = \sum_{n=-\infty}^{+\infty} f_\tau(t - nT)\ ; \quad T \geq \tau. \tag{2.3-27}$$

Here, the period T is always greater than or equal to the width τ of the function $f_\tau(t)$. According to (2.3-6), the spectrum $F_\tau(\nu)$ of the function $f_\tau(t)$ can be written as

$$F_\tau(\nu) = \int\limits_{-\tau/2}^{+\tau/2} f_\tau(t) \cdot e^{-j2\pi\nu t} \mathrm{d}t.$$

Otherwise, according to (2.3-12), the Fourier coefficients are

$$a_n = \frac{1}{T} \cdot \int\limits_{-T/2}^{+T/2} f_\tau(t) \cdot e^{-j2\pi \frac{n}{T} t} \mathrm{d}t = \frac{1}{T} \cdot \int\limits_{-\tau/2}^{+\tau/2} f_\tau(t) \cdot e^{-j2\pi \frac{n}{T} t} \mathrm{d}t.$$

The comparison of these two formulae shows that the Fourier coefficients can be expressed through the spectrum $F_\tau(\nu)$ at the sampling points $\nu = n/T$:

$$a_n = \frac{1}{T} \cdot F_\tau\left(\frac{n}{T}\right). \tag{2.3-28}$$

The periodic function $f_\tau^{\mathrm{p}}(t)$ can therefore be represented as the Fourier series

$$f_\tau^{\mathrm{p}}(t) = \frac{1}{T} \sum_n F_\tau\left(\frac{n}{T}\right) \cdot e^{j2\pi \frac{n}{T} t}. \tag{2.3-29}$$

From (2.3-6) the spectrum of the periodic function $f_\tau^{\mathrm{p}}(t)$ is given by

$$F_\tau^{\mathrm{p}}(\nu) = \frac{1}{T}\sum_n F_\tau\left(\frac{n}{T}\right)\cdot\delta\left(\nu-\frac{n}{T}\right). \tag{2.3-30}$$

As is the case with the periodic functions $f_\tau^{\mathrm{p}}(t)$, their spectra $F_\tau^{\mathrm{p}}(\nu)$ can be represented by a defined number of quantities. This is also important in connection with the band-limited signals considered in Section 2.5.

We turn now to some special cases of periodic signals. For the description of time-discrete signals and especially for the sampling of continuous signals, periodic continuations of rectangular functions are used (Fig. 2.3-5):

$$r_\tau^{\mathrm{p}}(t) = \sum_{n=-\infty}^{+\infty} r_\tau(t-nT); \quad T \geq \tau. \tag{2.3-31}$$

The individual rectangles of the periodic signal (2.3-31) have the amplitude $1/\tau$. So, in the limit $\tau \to 0$ with

$$\delta(t) = \lim_{\tau\to 0} r_\tau(t) \tag{2.3-32}$$

the so-called Dirac comb can be introduced:

$$\delta^{\mathrm{p}}(t) = \sum_{n=-\infty}^{+\infty} \delta(t-nT), \tag{2.3-33}$$

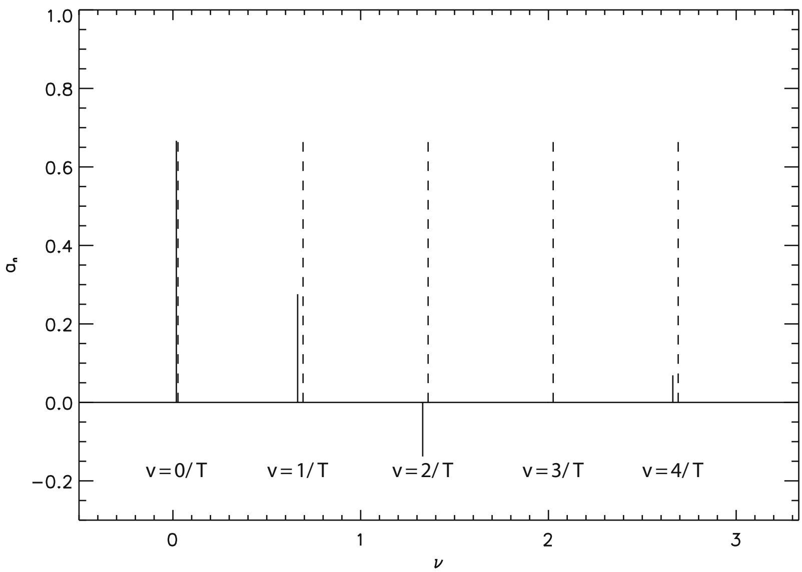

Fig. 2.3-6 Fourier coefficients for periodic rectangular function and Dirac-comb (*dashed*)

which is the periodic continuation of the delta function and the limit of (2.3-31) for $\tau \to 0$.

According to (2.3-9) the periodic function $\delta^{p}(t)$ can be represented by the Fourier series

$$\sum_{n=-\infty}^{+\infty} \delta(t-nT) = \frac{1}{T} \sum_{n=-\infty}^{+\infty} e^{j2\pi \frac{n}{T} t}. \tag{2.3-34}$$

This formula is a special case of (2.3-29) and is useful for many investigations of signals. The spectrum of the Dirac comb is given by

$$\Delta^{\mathrm{p}}(\nu) = \sum_{n} e^{-j2\pi nT\nu} = \frac{1}{T} \sum_{n} \delta\left(\nu - \frac{n}{T}\right). \tag{2.3-35}$$

Using these formulae and the spectrum $R_{\tau}(\nu)$ (2.3-26), we obtain the following results for the periodic continuations of rectangular functions (2.3-31):

$$a_n = \frac{1}{T} \cdot \frac{\sin\left(\pi \frac{n}{T} \tau\right)}{\pi \frac{n}{T} \tau} = \frac{1}{T} R_{\tau}\left(\frac{n}{T}\right) \text{ (Fourier coefficients)} \tag{2.3-36}$$

$$R_{\tau}^{\mathrm{p}}(\nu) = \frac{1}{T} \sum_{n} \frac{\sin\left(\pi \frac{n}{T} \tau\right)}{\pi \frac{n}{T} \tau} \cdot \delta\left(\nu - \frac{n}{T}\right) \text{ (spectrum).} \tag{2.3-37}$$

Periodicities can appear not only in the function $f(t)$ but also in the spectrum $F(\nu)$. Let $F^{\mathrm{p}}(\nu)$ be a periodic spectrum with the period ν_{p}. Then the equation $F^{\mathrm{p}}(\nu + \nu_{\mathrm{p}}) = F^{\mathrm{p}}(\nu)$ holds. Similarly to (2.3-29) and (2.3-12), the periodic spectrum can be described by the Fourier series

$$F^{\mathrm{p}}(\nu) = \sum_{n} c_n \cdot e^{-j2\pi \frac{n}{\nu_{\mathrm{p}}} \nu} \tag{2.3-38}$$

with the Fourier coefficients

$$c_n = \frac{1}{\nu_{\mathrm{p}}} \int_{-\nu_{\mathrm{p}}/2}^{+\nu_{\mathrm{p}}/2} F^{\mathrm{p}}(\nu) \cdot e^{j2\pi \frac{n}{\nu_{\mathrm{p}}} \nu} \mathrm{d}\nu. \tag{2.3-39}$$

This description will be helpful for the derivation of the sampling theorem (Section 2.5).

Following these representations of one-dimensional Fourier integrals and Fourier series, the two-dimensional case can now be addressed very briefly.

Let $f(x,y)$ be a function of two variables x and y. Then, analogously to (2.3-3) and (2.3-6), the 2D Fourier transform is defined by

$$f(x,y) = \cdot e^{j2\pi (k_x x + k_y y)} \mathrm{d}k_x \mathrm{d}k_y \tag{2.3-40}$$

$$F\left(k_x,k_y\right) = \cdot e^{-j2\pi (k_x x + k_y y)} \mathrm{d}x\mathrm{d}y. \tag{2.3-41}$$

Here, the integrals are taken from –∞ to +∞. The variables k_x, k_y are the spatial frequencies and $F\left(k_x,k_y\right)$ is the spatial frequency spectrum of the function $f(x,y)$. With the introduction of the amplitude and phase spectra according to

$$F\left(k_x,k_y\right) = \left|F\left(k_x,k_y\right)\right| \cdot e^{j\Phi\left(k_x,k_y\right)} \qquad (2.3\text{-}42)$$

one can obtain a representation with non-negative spatial frequencies:

$$f(x,y) = 2\int_0^\infty\int_0^\infty \left|F\left(k_x,k_y\right)\right| \cdot \cos\left[2\pi\left(k_x x + k_y y\right) + \Phi\left(k_x,k_y\right)\right] \mathrm{d}k_x \mathrm{d}k_y. \qquad (2.3\text{-}43)$$

This description gives a clear interpretation of the spatial frequencies. The function $\cos\left[2\pi\left(k_x x + k_y y\right) + \Phi\left(k_x,k_y\right)\right]$ is a wave with peaks and valleys. If the phase shift Φ, which characterises only the shift of the wave with respect to the point $x = 0$, $y = 0$, is neglected, then the peaks are given by $\cos\left[2\pi\left(k_x x + k_y y\right)\right] = 1$ or by the equations $k_x x + k_y y = n \quad (n = 0, \pm 1, \ldots)$. If one introduces the wave vector (or spatial frequency vector) $\mathbf{k} = \left(k_x,k_y\right)$ and the position vector $\mathbf{r} = (x,y)$, then this equation can be written more compactly as $\mathbf{k} \cdot \mathbf{r} = n$. These equations describe a variety of straight lines (see Fig. 2.3-7) which are perpendicular to the wave vector $\mathbf{k}$. The distance between two straight lines n and $n + 1$ is given by the "wavelength" $\Lambda = 1/k$. Here, $k = \sqrt{k_x^2 + k_y^2}$ is the length of the wave vector. The equation $\Lambda = 1/k$ is the equivalent of the equation $T = 1/\nu$ (T is period, ν is frequency) which characterises the sinusoidal oscillations. This justifies the term spatial frequency for k. The components k_x and k_y of the wave vector describe the actual spatial frequency k and the wave direction $\vartheta = \arctan\left(k_y/k_x\right)$.

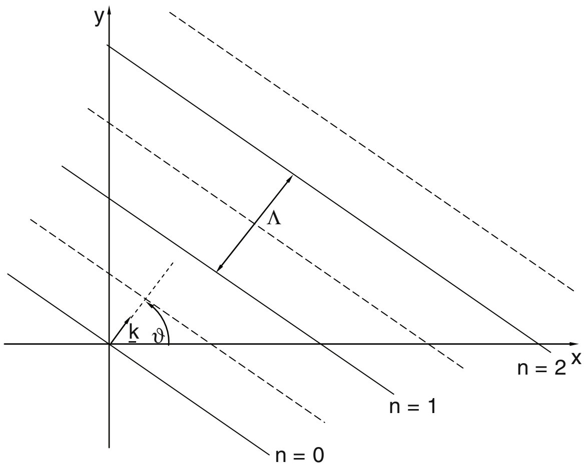

Fig. 2.3-7 Wave peaks and valleys (*dashed*)

As in the one-dimensional case, one can consider periodic functions $f^{\mathrm{p}}(x + X, y + Y) = f^{\mathrm{p}}(x, y)$. Similarly to (2.3-9) and (2.3-12), the Fourier series

$$f^{\mathrm{p}}(x,y) = \sum_{m}\sum_{n} a_{m,n} \cdot e^{j2\pi\left(\frac{m}{X}x + \frac{n}{Y}y\right)} \tag{2.3-44}$$

with the Fourier coefficients

$$a_{m,n} = \frac{1}{X \cdot Y} \int\limits_{-X/2}^{+X/2} \int\limits_{-Y/2}^{+Y/2} f^{\mathrm{p}}(x,y) \cdot e^{-j2\pi\left(\frac{m}{X}x + \frac{n}{X}y\right)} \mathrm{d}x\mathrm{d}y \tag{2.3-45}$$

is obtained.

In connection with the band-limited functions and the sampling theorem (Section 2.5), the periodic spectra with $F^{\mathrm{p}}\left(k_x + L_x, k_y + L_y\right) = F^{\mathrm{p}}\left(k_x, k_y\right)$ are of interest. Generalizing (2.3-38) and (2.3-39), we obtain the following formulae:

$$F\left(k_x,k_y\right) = \sum_{m}\sum_{n} c_{m,n} \cdot e^{-j2\pi\left(\frac{m}{L_x}k_x + \frac{n}{L_y}k_y\right)} \tag{2.3-46}$$

and

$$c_{m,n} = \frac{1}{L_x \cdot L_y} \int\limits_{-L_x/2}^{+L_y/2} \int\limits_{-L_y/2}^{+L_y/2} F\left(k_x,k_y\right) \cdot e^{j2\pi\left(\frac{m}{L_x}k_x + \frac{n}{L_y}k_y\right)}. \tag{2.3-47}$$

The integrals considered above of type

$$f(t) = \int F(\nu) \cdot e^{j2\pi\nu t} \mathrm{d}\nu \tag{2.3-48}$$

cannot always be represented in closed forms. Often one has to use numerical methods. For this purpose the Discrete Fourier Transform (DFT) is adequate, because it can be calculated very fast by the Fast Fourier Transform (FFT) algorithm.

The DFT is defined by the forward transform

$$f_k = \sum_{l=0}^{N-1} F_l \cdot e^{j\frac{2\pi}{N}k \cdot l}; \quad (k = 0,\ldots,N-1). \tag{2.3-49}$$

and the backward transform

$$F_l = \frac{1}{N}\sum_{k=0}^{N-1} f_k \cdot e^{-j\frac{2\pi}{N}k \cdot l}; \quad (l = 0,\ldots,N-1). \tag{2.3-50}$$

If the F_l ($l = 0,\ldots,N$-1) are given, the f_k can be computed (for arbitrary values of N) by the simple algorithm

$\boldsymbol{a} = 2\pi/\boldsymbol{N}$
for $\boldsymbol{k} = 0\ldots\boldsymbol{N}$-1 do begin
$\boldsymbol{a}_{\mathrm{k}} = \boldsymbol{a} \cdot \boldsymbol{k}$
Re_$\boldsymbol{f}_{\mathrm{k}} = 0$
Im_$\boldsymbol{f}_{\mathrm{k}} = 0$
for $\boldsymbol{l} = 0\ldots\boldsymbol{N}$-1 do begin
$\boldsymbol{a}_{\mathrm{kl}} = \boldsymbol{a}_{\mathrm{k}} \cdot \boldsymbol{l}$
sn = sin($\boldsymbol{a}_{\mathrm{kl}}$)
cs = cos($\boldsymbol{a}_{\mathrm{kl}}$)
Re_$\boldsymbol{f}_{\mathrm{k}}$ = Re_$\boldsymbol{f}_{\mathrm{k}}$ + [Re_$\boldsymbol{F}_{\mathrm{l}}$ · cs - Im_$\boldsymbol{F}_{\mathrm{l}}$ · sn]
Im_$\boldsymbol{f}_{\mathrm{k}}$ = Im_$\boldsymbol{f}_{\mathrm{k}}$ + [Re_$\boldsymbol{F}_{\mathrm{l}}$ · sn + Im_$\boldsymbol{F}_{\mathrm{l}}$ · cs]
end
end

(similarly for the backward transform). One needs O(N^2) arithmetical operations. If N is a power of two then the various algorithms of the FFT [see Wikipedia (2004)] can be used which need only O(N·log$N$) operations. For sufficiently large values of N, DFT calculations become practicable only if the FFT is used.

A simple example shows the possibility of approximating the integral (2.3-48) by the DFT. Let $|F(\nu)|$ be very small or even equal to zero for frequencies outside the interval $-\nu_g \le \nu \le +\nu_g$. Then

$$f\,(t) \approx \int_{-\nu_g}^{+\nu_g} F\,(\nu) \cdot e^{j2\pi\nu t} \mathrm{d}\nu.$$

If one approximates this integral by a sum of rectangles with heights $F(\nu_l)$ ($\nu_l = l \cdot \Delta\nu - \nu_g$, $l = 0,\ldots,N-1$) and widths $\Delta\nu = 2\nu_g/N$, then one obtains

$$f\,(t) \approx \Delta\nu \cdot e^{-j2\pi\nu_g t} \cdot \sum_{l=0}^{N-1} F\,(\nu_l) \cdot e^{j2\pi\, l\, \Delta\nu\, t}.$$

If it is sufficient to compute the function $f(t)$ only at the sampling points $t_k = k \cdot \Delta t - \tau$ ($k = 0,\ldots,N-1$), these values are given by

$$f\,(t_k) \approx \Delta\nu \cdot e^{-j2\pi\nu_g (k\Delta t - \tau)} \cdot \sum_{l=0}^{N-1} F\,(\nu_l) \cdot e^{-j2\pi\, l\, \Delta\nu\, \tau} \cdot e^{j2\pi\, \Delta\nu\, \Delta t\, kl}.$$

Finally, if $\Delta\nu \cdot \Delta t = 1/N$ ($\Delta t = {}^1\!/_{2}\nu_g$) is chosen and the abbreviation $G_l = F\,(\nu_l) \cdot e^{-j2\pi\, l\, \Delta\nu\, \tau}$ and the DFT

$$g_k = \sum_{l=0}^{N-1} G_l \cdot e^{j\frac{2\pi}{N} k \cdot l}; \quad (k = 0,\ldots,N-1)$$

are used, the required values $f(t_k)$ can be calculated according to

$$f\,(t_k) \approx \Delta\nu \cdot (-1)^k \cdot e^{j2\pi\,\nu_g\,\tau} \cdot g_k. \tag{2.3-51}$$

The same is true in the two-dimensional case if the 2D-DFT is introduced by

$$f_{k,l} = \sum_{m,n=0}^{N-1} F_{m,n} \cdot e^{j\frac{2\pi}{N}(k\,m+l\cdot n)}. \tag{2.3-52}$$

and

$$F_{m,n} = \frac{1}{N^2}\sum_{k,l=0}^{N-1} f_{k,l} \cdot e^{-j\frac{2\pi}{N}(m\cdot k+n\cdot l)}. \tag{2.3-53}$$

The precision of this approximation depends strongly on the size of N. As an example the values $f(t_k)$ (2.2-51) are calculated for the spectrum (2.3-24)

$$F\,(\nu) = e^{-\frac{\nu^2}{2\kappa^2}} \quad \text{with} \quad \kappa = \frac{1}{2\pi} \quad (\sigma = 1)\,.$$

Figure 2.3-8 shows the values $F(\nu_l)$ for $N = 8$, $\nu_g = 1$, $\Delta\nu = 0.25$ together with the function $F(\nu)$. Figure 2.3-9 shows the values $f(t_k)$ which have been calculated by (2.3-51) using the DFT. One can see that these few values are not sufficient for the

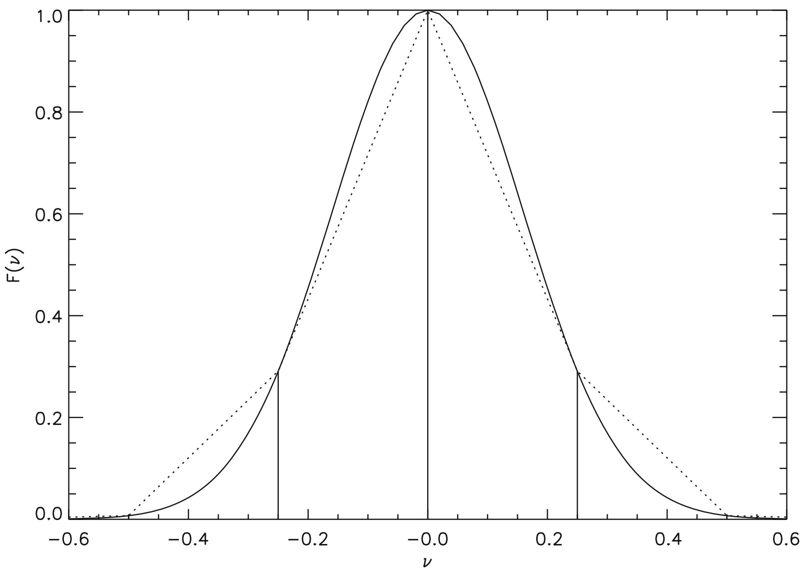

Fig. 2.3-8 Samples of spectrum $F(\nu)$ ($N = 8$)

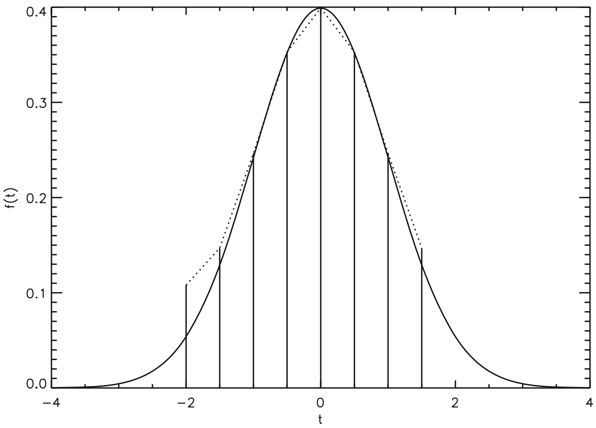

Fig. 2.3-9 Values $f(t_k)$ for the spectrum of Fig. 2.3-8 ($N = 8$) calculated with DFT

representation of the function $f(t)$. Better results are obtained with larger values of N and ν_g (see Figs. 2.3-10 and 2.3-11 for $N = 32$).

For practical purposes important examples of Fourier transforms are presented in Tables 2.3-1, 2.3-2, and 2.3-3.

Some of the results in Table 2.3-3 can be obtained using the formula

$$\sum_{n=0}^{N-1} q^n = \frac{q^N - 1}{q - 1}. \tag{2.3-54}$$

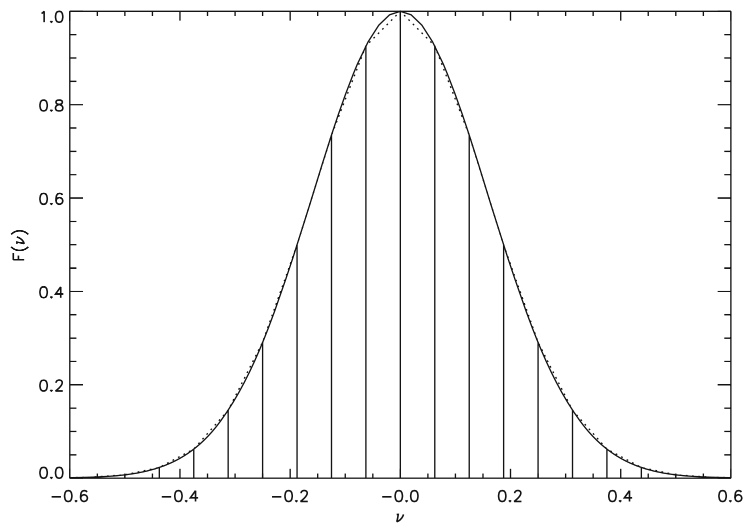

Fig. 2.3-10 Samples of spectrum $F(\nu)$ ($N = 32$)

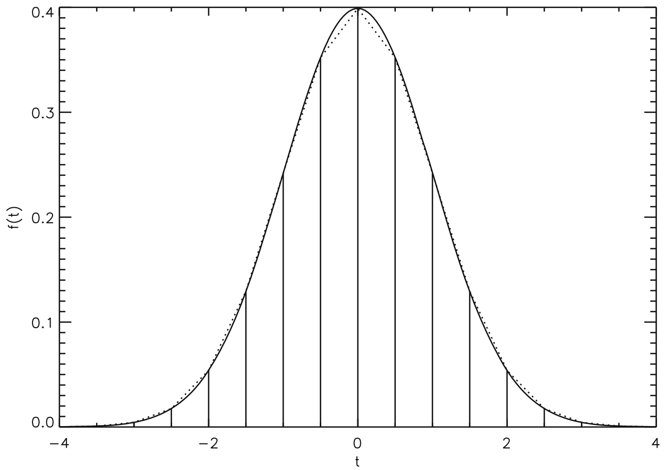

Fig. 2.3-11 Values $f(t_k)$ for the spectrum of Fig. 2.3-10 ($N = 32$) calculated with DFT

Table 2.3-1 One-dimensional Fourier transform

$F(\nu)$	$F(t)$
Const = 1	$\delta(t)$
$\delta(\nu - \nu 0)$	$\mathrm{Exp}(\mathrm{j}2\pi\nu 0 t)$
$\exp(-j2\pi\nu\tau)$	$\delta(t-\tau)$
$[\delta(\nu-\nu 0) - \delta(\nu+\nu 0)]/2j$	$\sin(2\pi\nu 0 t)$
$[\delta(\nu-\nu 0) + \delta(\nu+\nu 0)]/2$	$\cos(2\pi\nu 0 t)$
$\sum\limits_{n=-\infty}^{\infty} \delta\left(\nu - \frac{n}{T}\right) = T \cdot \sum\limits_{n=-\infty}^{\infty} \exp(\pm j2\pi N\nu t)$	$\sum\limits_{n=-\infty}^{\infty} \exp\left(\pm j2\pi n \frac{t}{T}\right) = T \cdot \sum\limits_{n=-\infty}^{\infty} \delta(t - nT)$
$\begin{cases} 1 & -\nu_g/2 \le \nu \le +\nu_g/2 \\ 0 & \text{elsewhere} \end{cases}$	$\nu_g \cdot \frac{\sin(\pi\nu_g t)}{\pi\nu_g t}$
$\tau \cdot \frac{\sin(\pi\nu\tau)}{\pi\nu\tau}$	$\begin{cases} 1 & -\tau/2 \le t \le +\tau/2 \\ 0 & \text{elsewhere} \end{cases}$
$\exp\left(-\frac{\nu^2}{2\kappa^2}\right)$	$\frac{1}{\sigma\sqrt{2\pi}} \exp\left(-\frac{t^2}{2\sigma^2}\right); \quad \sigma = \frac{1}{2\pi\kappa}$
$\frac{\tau}{1+j2\pi\nu\tau}$	$\begin{cases} \exp(-t/\tau) & t \ge 0 \\ 0 & t < 0 \end{cases}$

2.4 Linear Systems

Electronic and optical systems often can be described by so-called linear systems, which are studied in systems theory. A linear system describes the connection between an input signal $f_{\text{in}}(x,y,z,\ldots)$, which can depend on multiple variables, and an output signal $f_{\text{out}}(x,y,z,\ldots)$ in such a way that a superimposition

$$f_{\text{in}} = a \cdot f_{\text{in}}^{(1)} + b \cdot f_{\text{in}}^{(2)} \tag{2.4-1}$$

Table 2.3-2 Two-dimensional Fourier transform

$F(k_x,k_y)$	$f(x,y)$
Const = 1	$\delta(x)\cdot\delta(y)$
$\delta\left(k_x-k_x^0\right)\cdot\delta\left(k_y-k_y^0\right)$	$\exp\left\lfloor j2\pi\left(k_x^0x+k_y^0y\right)\right\rfloor$
$\exp\left\lfloor -j2\pi\left(k_xx_0+k_yy_0\right)\right\rfloor$	$\delta\left(x-x_0\right)\cdot\delta\left(y-y_0\right)$
$\frac{1}{2}\left[\delta\left(k_x-k_x^0\right)\cdot\delta\left(k_y-k_y^0\right)+\delta\left(k_x+k_x^0\right)\cdot\delta\left(k_y+k_y^0\right)\right]$	$\cos\left\lfloor 2\pi\left(k_x^0x+k_y^0y\right)\right\rfloor$
$\frac{1}{2j}\left[\delta\left(k_x-k_x^0\right)\cdot\delta\left(k_y-k_y^0\right)-\delta\left(k_x+k_x^0\right)\cdot\delta\left(k_y+k_y^0\right)\right]$	$\sin\left\lfloor 2\pi\left(k_x^0x+k_y^0y\right)\right\rfloor$
$\begin{cases}1 & -K/2\le k_x\le +K/2;\ -L/2\le k_y\le +L/2\\ 0 & \text{elsewhere}\end{cases}$	$K\cdot\frac{\sin(\pi Kx)}{\pi Kx}\cdot L\cdot\frac{\sin(\pi Ly)}{\pi Ly}$
$L_x\cdot\frac{\sin(\pi k_xL_x)}{\pi k_xL_x}\cdot L_y\cdot\frac{\sin(\pi k_yL_y)}{\pi k_yL_y}$	$\begin{cases}1 & -L_x/2\le x\le +L_x/2;\ -L_y\le y\le L_y/2\\ 0 & \text{elsewhere}\end{cases}$
$\begin{cases}1 & k_x^2+k_y^2\le K_g^2\\ 0 & \text{elsewhere}\end{cases}$	$\pi K_g^2\cdot 2\cdot\frac{J_1\left(2\pi K_g\sqrt{x^2+y^2}\right)}{2\pi K_g\sqrt{x^2+y^2}}$ [a]
$\exp\left(-\frac{k_x^2+k_y^2}{2\kappa^2}\right)$	$\frac{1}{2\pi\sigma^2}\exp\left(-\frac{x^2+y^2}{2\sigma^2}\right);\quad \sigma=\frac{1}{2\pi\kappa}$

[a] *J1(x)* is the Bessel function of first order

Table 2.3-3 One-dimensional DFT

$F_l\ (0\le l\le N–1)$	$f_k\ (0\le k\le N–1)$
Const = 1	$N\cdot\delta k,0$
$\delta_{l,n}(0\le n\le N-1)$	$\exp\left(j\frac{2\pi}{N}k\cdot n\right)$
$\frac{N}{2}\left[\delta_{l-n,0}+\delta_{l+n,0\vert N}\right]$ [a]	$\cos\left(\frac{2\pi}{N}k\cdot n\right)$
$\frac{N}{2j}\left[\delta_{l-n,0}-\delta_{l+n,0\vert N}\right]$ [a]	$\sin\left(\frac{2\pi}{N}k\cdot n\right)$
$\frac{\sin\left(\pi\frac{k_2-k_1+1}{N}\cdot l\right)}{\sin\left(\pi\frac{1}{N}\cdot l\right)}\cdot\exp\left[-j\pi\frac{k_1+k_2}{N}\cdot l\right]$	$\begin{cases}1 & k_1\le k\le k_2\\ 0 & \text{elsewhere}\end{cases}\quad (0\le k_1\le k_2\le N-1)$
$\frac{\exp(-\alpha\cdot N)-1}{\exp\left(-\alpha-j\frac{2\pi}{N}\cdot l\right)-1}$	$\exp(-\alpha\cdot k)$

[a] $\delta_{l+n,0|N}$ is the abbreviation for $\delta_{l+n,0|N}=\begin{cases}1 & l+n=0\quad\text{or}\quad l+n=N\\ 0 & \text{elsewhere}\end{cases}$.

of input signals leads to an analogous superimposition

$$f_{\text{out}}=a\cdot f_{\text{out}}^{(1)}+b\cdot f_{\text{out}}^{(2)} \tag{2.4-2}$$

of output signals (linearity).

This is not an introduction into systems theory. Only few basics are presented in order to understand optoelectronic systems. Of special importance are the shift-invariant linear systems which are defined by the following connection between input and output signals:

$$f_{\text{out}}(x,y,z,t) = \int\int\int\int h\left(x - x',y - y',z - z',t - t'\right) \cdot f_{\text{in}}\left(x',y',z',t'\right) \mathrm{d}x'\mathrm{d}y'\mathrm{d}z'\mathrm{d}t' \tag{2.4-3}$$

Equation (2.4-3) describes a four-dimensional system. Shift-invariance means that a shift of the input signal ($f_{\text{in}}(x',y',z',t') \rightarrow f_{\text{in}}(x'-a,y'-b,z'-c,t'-d)$) leads only to the same shift of the output signal without any other change.

One- and two-dimensional systems, which describe the transform of electrical and optical signals, are discussed here. One-dimensional systems are important for the understanding and design of the analogue-electronic signal processing units (front-end electronics) of a sensor. Here, the function $f(t)$ is a time-dependent electric quantity such as current or voltage. One of the important kinds of signal processing is the filtering of the signal $f(t)$ in order to reduce unwanted signal components such as disturbances and noise. It is defined by the convolution

$$f_{\text{out}}(t) = \int_{-\infty}^{+\infty} h\left(t - t'\right) \cdot f_{\text{in}}\left(t'\right) \mathrm{d}t', \tag{2.4-4}$$

i.e. by a linear system of the kind *Fehler! Verweisquelle konnte nicht gefunden werden*. One can write this operation symbolically as

$$f_{\text{out}} = h \otimes f_{\text{in}}. \tag{2.4-5}$$

The reaction of the filter (2.4-4) to a needle-shaped input impulse $\delta(t)$ (delta-function; see Chapter 2 .Chapter 3) is considered first. In this case the output signal $f_{\text{out}}(t) = h(t)$ is obtained. Therefore $h(t)$ is called the impulse response. Because the input signal $\delta(t)$ is concentrated at $t = 0$, there cannot be an output signal for $t < 0$ because of causality. Therefore

$$h(t) = 0 \quad \text{for} \quad t < 0. \tag{2.4-6}$$

The impulse response of a physical system must always fulfill the condition (2.4-6). This substantially restricts the possibilities of signal filtering.

Important for the understanding the filtering operation is the representation of the convolution (2.4-4) in frequency space. Applying the Fourier back-transform (2.3-6) to (2.4-4), one obtains the connection

$$F_{\text{out}}(\nu) = H(\nu) \cdot F_{\text{in}}(\nu), \tag{2.4-7}$$

which means that in frequency space the filter reduces to the simple multiplication of the input spectrum with the frequency response $H(\nu)$ of the filter. This is a fundamental advantage for systems analysis and synthesis.

If the frequency response $H(\nu)$ of the filter is written as

$$H(\nu) = |H(\nu)| \cdot e^{j\Phi_{\mathrm{H}}(\nu)} \tag{2.4-8}$$

and if $F_{\mathrm{in}}(\nu)$ and $F_{\mathrm{out}}(\nu)$ according to (2.3-5) are represented in the same way, then, from (2.4-7), the following relationships hold:

$$|F_{\mathrm{out}}(\nu)| = |H(\nu)| \cdot |F_{\mathrm{in}}(\nu)| \tag{2.4-9}$$

$$\varphi_{\mathrm{out}}(\nu) = \Phi_{\mathrm{H}}(\nu) + \varphi_{\mathrm{in}}(\nu)\,. \tag{2.4-10}$$

This means in particular that, if a sinusoidal input signal $f_{\mathrm{in}}(t) = \cos(2\pi\nu t)$ is filtered, the output signal has the same shape and frequency. There occur only an attenuation and a phase shift: $f_{\mathrm{out}}(t) = |H(\nu)|\cos(2\pi\nu t + \Phi_{\mathrm{H}}(\nu))$.

Non-sinusoidal functions, however, do not have this advantage: their shape is changed by filtering. This is the crucial advantage of sinusoidal functions for systems analysis and design.

Next, some examples are given. The ideal low pass filter has the frequency response

$$H(\nu) = A(\nu) \cdot e^{-j2\pi\nu\tau}; \quad A(\nu) = \begin{cases} 1 & \text{for} \quad -\nu_g \le \nu \le +\nu_g \\ 0 & \text{elsewhere} \end{cases}, \tag{2.4-11}$$

where ν_g is the cut-off-frequency (see Fig. 2.4-1).

The impulse response of this filter is

$$h(t) = 2\nu_g \frac{\sin\left[2\pi\nu_g(t-\tau)\right]}{2\pi\nu_g(t-\tau)}. \tag{2.4-12}$$

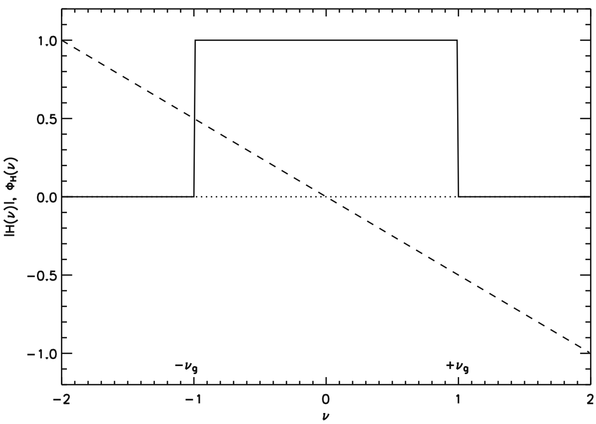

Fig. 2.4-1 Ideal low-pass filter: amplitude and phase response (*dashed*) for $\nu_g = 1$ [Hz], $\tau = 1/(4\pi)$ [s]

This function extends to infinity. It does not fulfill the causality condition (2.4-6)! This means that the ideal low pass filter does not exist in reality: one can only approximate it. A possibility for such an approximation is the allocation of values $h = 0$ for $t < 0$. Evidently, this approximation will become better as the time lag τ. Figure 2.4-2 shows this.

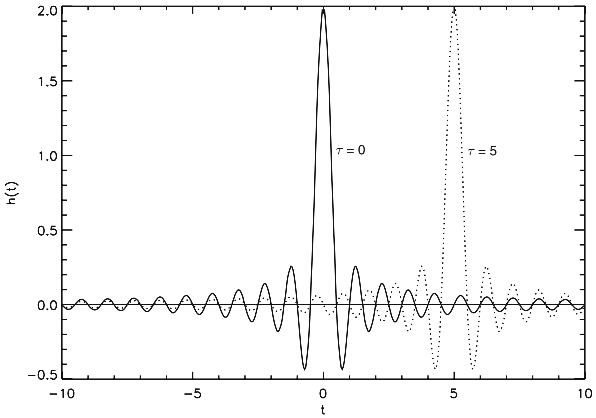

Fig. 2.4-2 Ideal low-pass filter: impulse response for $\tau = 0$ and $\tau = 5$ [s]

The so-called low-pass filter of first order (Figs. 2.4-3 and 2.4-4) has the impulse response

$$h(t) = \begin{cases} \frac{1}{\tau} e^{-t/\tau} & \text{for} \quad t \geq 0 \\ 0 & \text{elsewhere} \end{cases} \tag{2.4-13}$$

and the frequency response

$$H(\nu) = \frac{1}{1 + j2\pi\nu\tau}; \quad |H(\nu)| = \frac{1}{\sqrt{1 + (2\pi\nu\tau)^2}}; \quad \Phi_{\mathrm{H}} = -\arctan(2\pi\nu\tau). \tag{2.4-14}$$

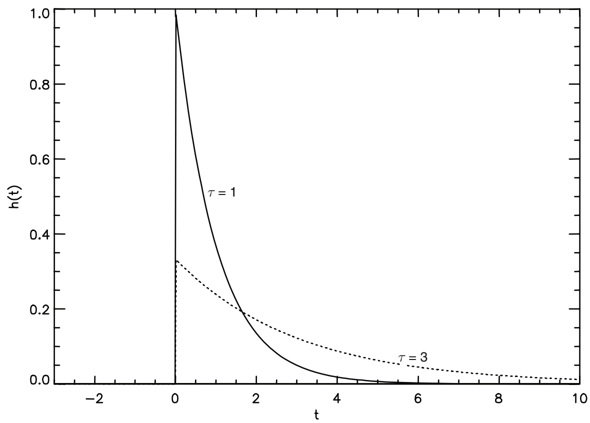

Fig. 2.4-3: Low-pass filter of first order: impulse response

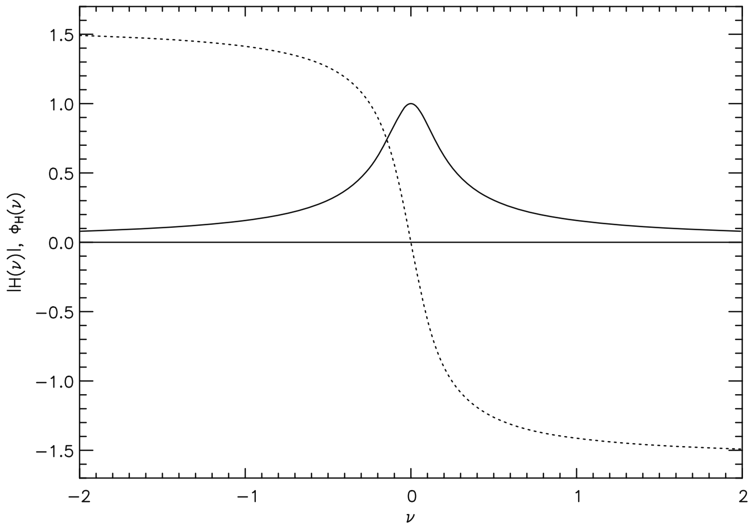

Fig. 2.4-4 Low-pass filter of first order. amplitude and phase response (*dotted*) ($\tau = 1$)

It can be implemented as an electric R-C-circuit. Its frequency response decreases very slowly with the frequency ($\sim 1/\nu$). Filters with a steeper descent (e.g. Butterworth filters) can be implemented with more complicated circuits.

In the two-dimensional case, which is important for optical imaging, the formulae (2.4-3) and (2.4-7) change to

$$f_{\text{out}}\left(x',y'\right) = \int\int h\left(x'-x,y'-y\right)\cdot f_{\text{in}}\,(x,y)\,\mathrm{d}x\mathrm{d}y \tag{2.4-15}$$

and

$$F_{\text{out}}\left(k_x,k_y\right) = H\left(k_x,k_y\right)\cdot F_{\text{in}}\left(k_x,k_y\right). \tag{2.4-16}$$

With a proper choice of the Equations (2.14-15) and (2.4-16), we can describe the alteration of radiometric quantities (intensities, radiances etc.) by diffraction of light at the aperture of an imaging system. But before the function $h(x,y)$ for diffraction-limited optical systems is introduced, we cover some more general considerations:

Let $f_{\text{in}}\,(x,y) = \delta\,(x-x_0)\cdot\delta\,(y-y_0)$ be the (idealized) intensity distribution of a light emitting point in the object plane of an optical system. Then, in the image plane, the intensity distribution $f_{\text{out}}\left(x',y'\right) = h\left(x'-x_0,y'-y_0\right)$ is obtained. The function $h(x,y)$ has a certain width because of diffraction. Therefore, the image of the point (x_0,y_0) is spread over a certain area (or blurred) and the function $h(x,y)$ is called the Point Spread Function (PSF).

If the optical system has circular symmetry, then the function h depends only on the distance $r = \sqrt{x^2+y^2}$ from the principal axis, i.e. it has the property

$h(x,y) = g(r)$. In this case the image of the light emitting point has circular symmetry around (x_0,y_0):

$$f_{\mathrm{out}}\left(x',y'\right) = g\left(\sqrt{\left(x'-x_0\right)^2 + \left(y'-y_0\right)^2}\right).$$

It can be shown that the frequency spectrum $H(k_x,k_y)$ of a circular symmetric function $h(x,y)$ is circular symmetric too:

$$H\left(k_x,k_y\right) = G(k) \quad \left(k = \sqrt{k_x^2 + k_y^2}\right).$$

Now, let the periodic intensity distribution

$$f_{\mathrm{in}}(x,y) = 1 + \cos\left[2\pi\left(k_x x + k_y y\right)\right]$$

be given in the object plane. Unity is added to the cosine function because radiation intensities cannot adopt negative values. Because it holds that $1 = \cos\left[2\pi\left(k_x^0 x + k_y^0 y\right)\right]$ with $k_x^0 = k_y^0 = 0$, the function f_{in} consists of two periodic parts which are both transformed into the output distribution. In a similar way to the one-dimensional case (see the remarks following (2.4-10)) the result

$$f_{\mathrm{out}}\left(x',y'\right) = |H(0,0)| + \left|H\left(k_x,k_y\right)\right| \cdot \cos\left[2\pi\left(k_x x' + k_y y'\right) + \Phi_{\mathrm{H}}\left(k_x,k_y\right)\right]$$

is obtained.

This means that there is also a periodic intensity distribution in the image plane, with, of course, different amplitude and phase. The function $|H(k_x,k_y)|$ attenuates the modulation of the sinusoidal intensity distribution and is therefore called the Modulation Transfer Function (MTF). Because f_{out} (as f_{in}) cannot adopt negative values, the MTF must fulfill the condition:

$$|H(0,0)| \geq \left|H\left(k_x,k_y\right)\right|. \tag{2.4-17}$$

The functions $H(k_x,k_y)$ and $\Phi_{\mathrm{H}}(k_x,k_y)$ are called the Optical Transfer Function (OTF) and the Phase Transfer Function (PTF), respectively.

Now the circular symmetric case is considered in more detail. As was shown above, in this case the OTF $H(k_x,k_y)$ depends only on the spatial frequency k. Thus H is a one-dimensional function. Furthermore, it can be shown that $H(k_x,k_y) = G(k)$ is a real-valued function. Let be $G(k) < 0$ for $k_1 < k < k_2$. Then $G(k) = |G(k)| \cdot \exp(j\pi)$ and $\Phi_{\mathrm{H}}(k) = \pi$ hold for $k_1 < k < k_2$. Since $\cos(x+\pi) = -\cos(x)$, the intensity distribution in the image plane becomes

$$f_{\mathrm{out}}\left(x',y'\right) = |G(0)| - |G(k)| \cdot \cos\left[2\pi\left(k_x x' + k_y y'\right)\right] (k_1 < k < k_2).$$

Thus there is contrast reversal in $k_1 < k < k_2$. Bright parts of the input wave appear dark and dark parts appear bright. Figures 2.4-5 and 2.4-6 illustrate this behaviour.

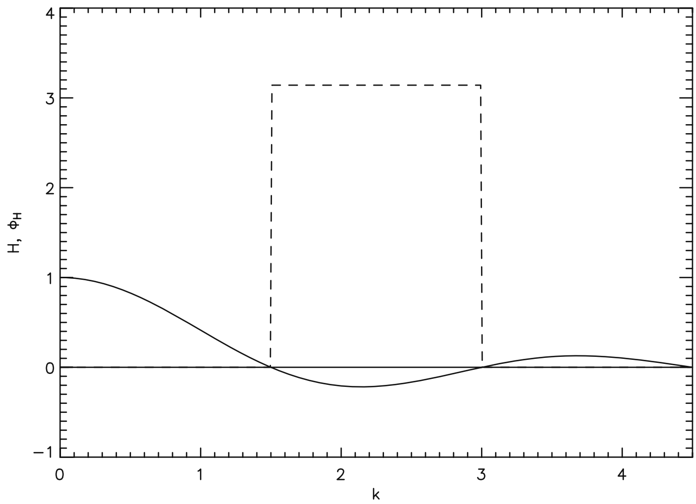

Fig. 2.4-5 Contrast reversal: OTF und PTF (*dashed*)

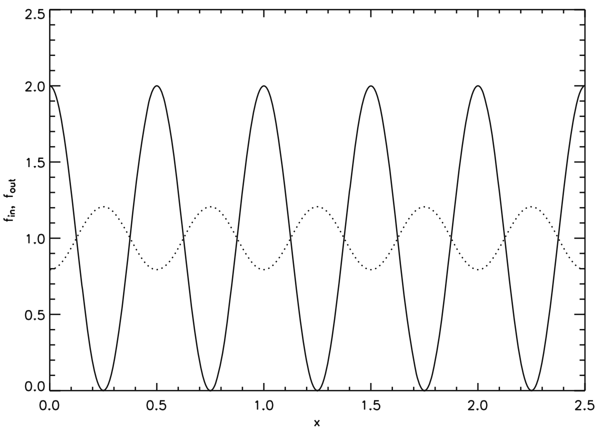

Fig. 2.4-6 Contrast reversal: intensity profiles in object plane and image plane (*dotted*) for $k = 2$

In the range from $k_1 = 1.5$ to $k_2 = 3$, $H(k) \leq 0$. At $k = k_1$ and $k = k_2$ the wave is extinguished.

In the following discussion, the functions $h(x,y)$ and $H(k_x,k_y)$ are given and analysed for optical imaging with a thin lens (see Fig. 2.1-2). Let $f_{\text{in}}(x,y) = L_\lambda(x,y)$ and $f_{\text{out}}(x,y) = L'_\lambda(x',y')$ be the spectral radiances in the object plane and the image plane, respectively. Then these radiances are connected by the relationship

$$L_\lambda{}'\left(x',y'\right) = L_\lambda\,(x,y)\,\mathrm{d}x\mathrm{d}y \qquad (2.4\text{-}18)$$

with

$$h_\lambda\left(x',y';x,y\right) = \text{const}\cdot\left[2\frac{J_1\left(\frac{\pi D}{\lambda b}\sqrt{\left(x'+\frac{b}{g}x\right)^2+\left(y'+\frac{b}{g}y\right)^2}\right)}{\frac{\pi D}{\lambda b}\sqrt{\left(x'+\frac{b}{g}x\right)^2+\left(y'+\frac{b}{g}y\right)^2}}\right]^2. \quad (2.4\text{-}19)$$

Here J_1 is the Bessel function of first order. The function h_λ is not shift-invariant. The reason for this is the scaling (down) with the factor b/g and the reversal of the coordinates. If one introduces new coordinates

$$X = -\frac{b}{g}x, \quad Y = -\frac{b}{g}y$$

in the object plane, then the PSF h_λ depends on $\sqrt{\left(x'-X\right)^2+\left(y'-Y\right)^2}$ and is shift-invariant and circular-symmetric too.

The diffraction image of a light emitting point at (x_0,y_0) with the radiance $L_\lambda(x,y) = \delta(x-x_0)\cdot\delta(y-y_0)$ is a circular spot (Airy spot) in the vicinity of the point (x'_0,y'_0) with $x_0{}' = -\frac{b}{g}x_0, \quad y_0{}' = -\frac{b}{g}y_0$. This spot is surrounded by bright and dark rings which become weaker with increasing distance from (x_0,y_0) (see Fig. 2.4-7).

The PSF

$$h_\lambda(r) = \text{const}\cdot\left[2\frac{J_1\left(\frac{\pi D}{\lambda b}r\right)}{\frac{\pi D}{\lambda b}r}\right]^2, \quad r = \sqrt{x^2+y^2} \quad (2.4\text{-}20)$$

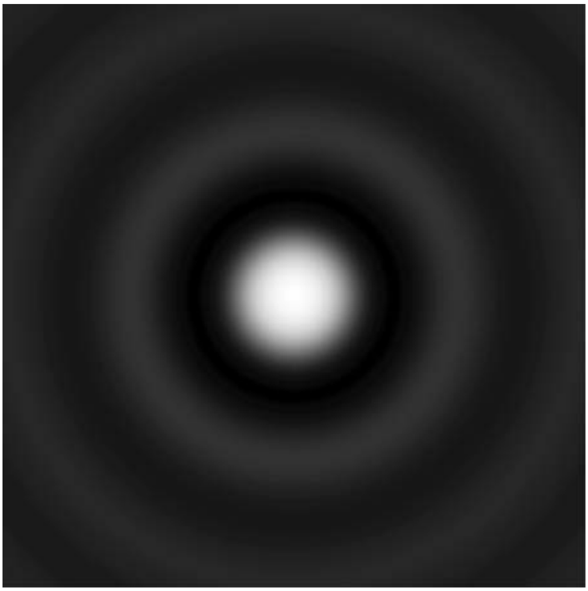

Fig. 2.4-7 Airy spot; rings enhanced for display

has its first zero at

$$r_0 = 1.22\frac{\lambda b}{D}. \tag{2.4-21}$$

or for $g >> f$, $b \approx f$ at

$$r_0 = 1.22\frac{\lambda f}{D} = 1.22 \cdot \lambda \cdot f_{\#}. \tag{2.4-22}$$

The radius r_0 is a measure of the thickness of the Airy spot. It is proportional to the wavelength λ: long-wave light is diffracted more strongly than short-wave light. For $\lambda \to 0$ the diffraction phenomena vanish. This is the limit of geometric optics. Furthermore, r_0 increases with the f-number $f_{\#} = f/D$: lenses with smaller f-numbers produce sharper images. This is well-known from photography.

Lenses with the PSF (2.4-20) are called diffraction-limited. Today's real lenses are generally not diffraction limited because of aberrations. Their blur is stronger than that of diffraction-limited lenses.

With the aid of the PSF, the geometric resolution of an optical system can now be defined. One can start from Rayleigh's criterion for diffraction-limited resolution: two point sources can be separated if the central maximum of the Airy spot of one source has the position of the first minimum of the other source, i.e. if the distance between the centres of the two Airy spots is equal to r_0. Then, the separable light sources have the distance $r_0 \cdot g/b$ in the object plane.

Figure 2.4-8 shows this case: the sum of the diffraction images of both points (dotted) has a central recess with an intensity value of 0.74. This means that the central value is lowered by about 26% with respect to the maximum. Such a difference between maximum and minimum of the diffraction image is often very detectable, which means that Rayleigh's value r_0 does not provide the ultimate resolution of a diffraction-limited optical system. Ultimately, the measurement precision (limited by noise and quantisation errors) determins whether two points can be separated. If

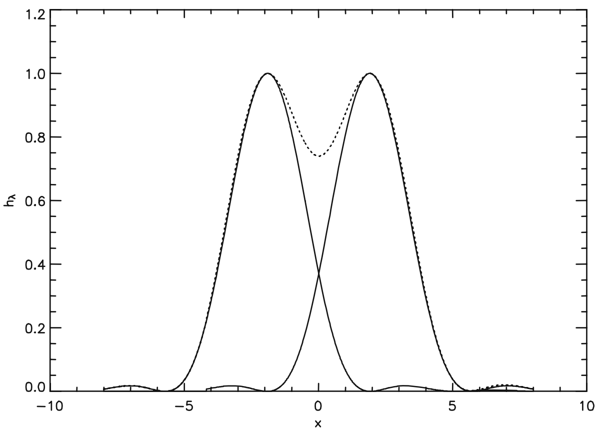

Fig. 2.4-8 Geometric resolution according to Rayleigh

the signal-to-noise ratio is very good then two points with a distance much smaller than r_0 can be separated if advanced methods of estimation theory are used. But r_0 is a good measure for coarse estimates (as a rule of thumb). In the general (not diffraction-limited) case, however, the PSF does not necessarily have a zero r_0. Then the geometric resolution may be defined by the distance d between two points for which the function

$$a_\lambda(r) = h_\lambda\left(r - \frac{d}{2}\right) + h_\lambda\left(r + \frac{d}{2}\right) \tag{2.4-23}$$

has the contrast

$$C = \frac{\max\{a_\lambda\} - a_\lambda(0)}{\max\{a_\lambda\}} = 0.26. \tag{2.4-24}$$

The PSF of a diffraction-limited optical system has been given only up to a constant factor (2.4-20), which describes the radiometric properties of the imaging that have been discussed in Section 2.2 and which are not of interest here. Often *const* is chosen so that $\iint h_\lambda(\mathrm{x,y})\mathrm{d_x d_y} = 1\left(\mathrm{const} = \frac{\pi}{4}\left(\frac{\mathrm{D}}{\lambda \cdot \mathrm{b}}\right)^2\right)$. Then the OTF is normalized to $H_\lambda(0{,}0) = 1$.

The OTF of the normalized PSF (2.4-20) is given by

$$H_\lambda\left(k_x, k_y\right) = G_\lambda(k) = \begin{cases} \frac{2}{\pi}\left[\arccos\left(\frac{\lambda b}{D}k\right) - \frac{\lambda b}{D}k \cdot \sqrt{1 - \left(\frac{\lambda b}{D}k\right)^2}\right] & \text{for} \quad k \le \dfrac{D}{\lambda b} \\ 0 & \text{elsewhere} \end{cases} \tag{2.4-25}$$

(see Fig. 2.4-9).

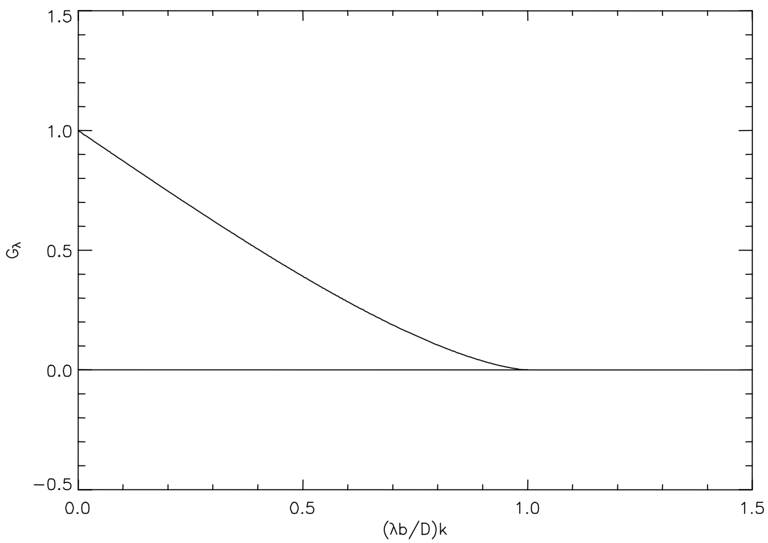

Fig. 2.4-9 MTF (=OTF) of a diffraction-limited optical system

Formula (2.4-25) shows that the OTF (or MTF) vanishes for spatial frequencies greater than the cut-off frequency

$$k_g = \frac{D}{\lambda b}. \tag{2.4-26}$$

The optical system operates as an exact band-limited spatial low-pass filter. A wavelike intensity distribution $f_{\text{in}}\,(x,y) = 1 + \cos\left[2\pi\,\left(k_x x + k_y y\right)\right]$ in the object plane cannot be seen in the image plane if the spatial frequency fulfills the condition $k = \sqrt{k_x^2 + k_y^2} > k_g$. In other words, the distance $\Lambda = 1/k$ between two wave peaks cannot be resolved if $\Lambda < 1/k_g$ holds. Thus a somewhat different definition of resolution via the smallest resolvable wavelength $\Lambda_g = 1/k_g$ can be given. This is not far from the definition given above, because $r_0 = 1.21{\cdot}\Lambda_g$. To measure the resolution, test images with thin lines on homogeneous backgrounds are used. Let Λ be the width of a line pair. Then a line pair cannot be resolved if the number of line pairs per mm [lp/mm] ($= k$) is greater than a certain value k_g (in the case of diffraction-limited systems k_g is given by (2.4-26)). Therefore, the cut-off frequency k_g defines the upper limit of line pairs per mm that can be resolved.

If one does not use sinusoidal functions for the measurement of the MTF, but instead makes use of patterns of rectangular stripes (which are easier to generate), then one obtains not the MTF directly but a related function which is known as the Contrast Transfer Function (CTF) (Holst, 1998b). The CTF is also an adequate measure of the quality of an optical system.

To introduce the CTF, (2.4-15) is a convenient starting point. Let $f_{\text{in}}(x,y) = f_{\text{in}}(x)$ be a function which depends only on x (but not on y). Then it follows that f_{out} too is a function of x alone and that the two functions are related by

$$f_{\text{out}}\left(x'\right) = \int_{-\infty}^{+\infty} q\left(x' - x\right) \cdot f_{\text{in}}\,(x)\,\mathrm{d}x. \tag{2.4-27}$$

Here

$$q\,(x) = \int_{-\infty}^{+\infty} h\,(x,y)\mathrm{d}y, \tag{2.4-28}$$

is the so-called Line Spread Function (LSF), which is the reaction of the optical system upon a line-shaped intensity distribution

$$f_{\text{in}}\,(x) = \delta\,(x - x_0)\,.$$

The function $c(x)$ is the response of the system (2.4-27) to an upright stripe pattern of the following kind:

$$f_{\text{in}}\,(x,y) = \sum_{n=-\infty}^{+\infty} r_L\,(x - n\Lambda); \quad \Lambda = 2L. \tag{2.4-29}$$

Here (a little bit different from (2.3-25))

$$r_L(x) = \begin{cases} 1 & \text{for} \quad -\frac{L}{2} \le x \le +\frac{L}{2} \\ 0 & \text{elsewhere} \end{cases}$$

is the rectangle function and $\Lambda = 2L$ is the period (or "wavelength"). A profile of the function (2.4-29) is shown in Fig. 2.4-10 (solid line). Putting (2.4-29) into (2.4-27), we obtain the following result (for $f_{\mathrm{out}}(x) = c(x)$):

$$c(x) = \sum_{n=-\infty}^{+\infty} q_n(x). \tag{2.4-30}$$

with

$$q_n(x) = \int\limits_{x-\left(2n+\frac{1}{2}\right)L}^{x-\left(2n-\frac{1}{2}\right)L} q(z)\mathrm{d}z. \tag{2.4-31}$$

An example for a Gaussian PSF or LSF

$$h(x,y) = \frac{1}{2\pi\sigma^2} e^{-\frac{x^2+y^2}{2\sigma^2}}; \quad q(x) = \frac{1}{\sigma\sqrt{2\pi}} e^{-\frac{x^2}{2\sigma^2}}$$

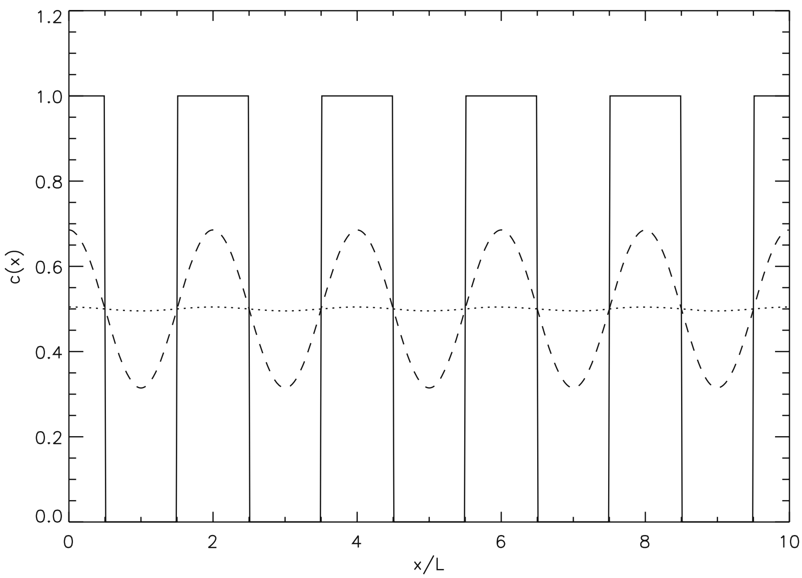

Fig. 2.4-10 Stripe pattern response $c(x)$ for $\sigma = L/2$ (*dashed*) and $\sigma = L$ (*dotted*)

is shown in Fig. 2.4-10. As mentioned above, the shape of the stripe pattern is not maintained after transmission through the optical system. Furthermore, one realizes that the contrast in the image plane almost vanishes for $\sigma = L$. The stripe pattern response $c(x)$ can be related to the OTF. Firstly, from (2.3-40) it follows that

$$q(x) = \int Q(k_x) e^{j2\pi k_x x} \mathrm{d}k_x \quad \text{with} \quad Q(k_x) = H(k_x, 0). \tag{2.4-32}$$

Here, $Q(k_x)$ is the spectrum of the LSF (which, analogously to the MTF, could be called the Line Modulation Transfer Function). Secondly, the quantities in (2.4-31) can be written as

$$q_n(x) = \int H(k_x, 0) \cdot L \frac{\sin(\pi k_x L)}{\pi k_x L} \cdot e^{j2\pi k_x x} \cdot e^{-j4\pi k_x n}.$$

From (2.4-30) and (2.3-34) the following result is obtained:

$$c(x) = \frac{1}{2} \sum_{n=-\infty}^{+\infty} H\left(\frac{n}{2L}, 0\right) \cdot \frac{\sin\left(n\frac{\pi}{2}\right)}{n\frac{\pi}{2}} \cdot e^{jn\pi \frac{x}{L}}. \tag{2.4-33}$$

This formula expresses the function $c(x)$ through the OTF $H(k_x,k_y)$ at the spatial frequencies $k_x = n/2L$, $k_y = 0$.

Now it is easy to introduce the CTF. The contrast (or the modulation) of the function $c(x)$ is given by $[\max\{c(x)\} - \min\{c(x)\}]/[\max\{r_L(x)\} + \min\{r_L(x)\}] = [\max\{c(x)\} - \min\{c(x)\}]$. The CTF is the contrast as a function of the spatial frequency $k_x = 1/2L$. It can be calculated using (2.4-33). The result is:

$$CTF(k_x) = \frac{4}{\pi} \cdot \sum_{n=0}^{\infty} \frac{(-1)^n}{2n+1} \cdot H[(2n+1)k_x, 0] = \frac{4}{\pi} \cdot \sum_{n=0}^{\infty} \frac{(-1)^n}{2n+1} \cdot Q[(2n+1)k_x]. \tag{2.4-34}$$

Figure 2.4-11 shows the CTF for a diffraction-limited system with the OTF (2.4-25) for some values of the cut-off frequency $k_g = \frac{D}{\lambda b}$.

2.5 Sampling

Thus far, one- or two-dimensional signals have been considered as continuous functions of space and/or time. Now we must take into account that for signal processing using digital computers a signal discretisation in space and/or time and in amplitude is necessary. This means that continuous signals will be sampled at discrete space or time points.

In the one-dimensional case the values $f(t_n)$ at the discrete points t_n are extracted from the continuous function $f(t)$. The questions are whether or how much information is lost because of sampling. It turns out that in the case of functions of finite support (band-limited functions) there is no loss of information if the sampling interval is small enough. Therefore, it can be useful (if aliasing must be avoided, see below) to apply band-limiting filters before sampling.

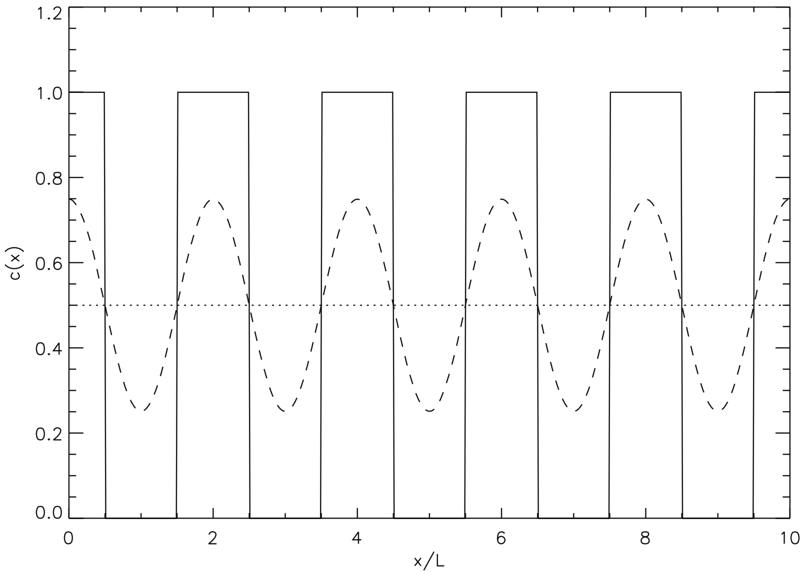

Fig. 2.4-11 CTF for a diffraction-limited optical system (*solid curve*: $k_g = 150\ \mathrm{mm}^{-1}$, *dotted curve*: $k_g = 100\ \mathrm{mm}^{-1}$, *dashed curve*: $k_g = 50\ \mathrm{mm}^{-1}$)

Let $f(t)$ be a function with the finite spectrum $F(\nu)$ with cut-off frequency ν_g:

$$F(\nu) = 0 \quad \text{for} \quad |\nu| > \nu_g. \tag{2.5-1}$$

Then the spectrum $F(\nu)$ can be continued in a periodic way and written as a Fourier series. Let ν_s be any frequency with $\nu_s \geq \nu_g$. If $2\nu_s$ is used as period, then, analogously to (2.3-9), inside the interval $-\nu_s < \nu < +\nu_s$, $F(\nu)$ can be represented as

$$F(\nu) = \sum_{n=-\infty}^{+\infty} a_n \cdot e^{-j2\pi \frac{n}{2\nu_s}\nu} \tag{2.5-2}$$

with

$$a_n = \frac{1}{2\nu_s} \int_{-\nu_s}^{+\nu_s} F(\nu) \cdot e^{j2\pi \frac{n}{2\nu_s}\nu} \mathrm{d}\nu. \tag{2.5-3}$$

Otherwise, the function $f(t)$ may be written as the Fourier integral

$$f(t) = \int_{-\nu_s}^{+\nu_s} F(\nu) \cdot e^{j2\pi\nu t} \mathrm{d}\nu \tag{2.5-4}$$

with finite limits.

Comparing (2.5-3) and (2.5-4), it can be seen that the Fourier coefficients a_n are proportional to the sampling values $f(t_n)$ of the signal $f(t)$:

$$a_n = \frac{1}{2\nu_s} f\left(\frac{n}{2\nu_s}\right). \tag{2.5-5}$$

If one chooses the sampling points according to

$$t_n = n \cdot \Delta t = \frac{n}{2\nu_s}, \tag{2.5-6}$$

then, since $\nu_s > \nu_g$, the distance Δt of sampling points must be smaller than

$$\Delta t_{\max} = \frac{1}{2\nu_g}. \tag{2.5-7}$$

in order not to lose information.

If the condition $\Delta t < \Delta t_{\max}$ is fulfilled and the sampling values $f(n \cdot \Delta t)$ are given, then the spectrum $F(\nu)$ may be calculated according to (2.5-2) and (2.5-5). The same must also be true for the function $f(t)$, because it is uniquely determined by $F(\nu)$. From (2.5-2), (2.5-4) and (2.5-5), Shannon's sampling theorem

$$f(t) = \sum_{n=-\infty}^{+\infty} f\left(\frac{n}{2\nu_s}\right) \cdot \frac{\sin\left[2\pi\nu_s\left(t - \frac{n}{2\nu_s}\right)\right]}{2\pi\nu_s\left(t - \frac{n}{2\nu_s}\right)} \tag{2.5-8}$$

or

$$f(t) = \sum_{n=-\infty}^{+\infty} f(n\Delta t) \cdot \frac{\sin\left[\frac{\pi}{\Delta t}(t - n\Delta t)\right]}{\frac{\pi}{\Delta t}(t - n\Delta t)} \quad ; \quad \Delta t = \frac{1}{2\nu_s}. \tag{2.5-8a}$$

is obtained.

The sampling theorem (2.5-8) allows the calculation of any value of $f(t)$ if all sampled values $f(n \cdot \Delta t)$ are given. Of course, in reality only a finite number of sampling values is available (e.g. $f(n \cdot \Delta t)$ for $-N \leq n \leq N$), resulting in an error which can be estimated if one has some knowledge about $f(t)$ for $|t| \to \infty$.

A different kind of errors arises if the sampling distance Δt is chosen greater than $\Delta t_{\max}$ (or $\nu_s < \nu_g$), called undersampling. Incorrect contributions at some frequencies inside $-\nu_g < \nu < \nu_g$ may occur which can substantially distort the function $f(t)$ (which is calculated from the sampling values using the sampling theorem or another interpolation formula).

This behaviour can be demonstrated using the function $\sin(2\pi\nu_g t)$ (see Fig. 2.5-1): the dotted curve in Fig. 2.5-1 is the function $\sin(2\pi\nu_g t)$ and the vertical bars are the sampling values. There is strong undersampling because the sampling distance is bigger than a whole period of the sine-function (less than half a period is allowed). Interpolation of the sampling values using Shannon's sampling theorem leads to a function which is presented as the solid curve in Fig. 2.5-1. This

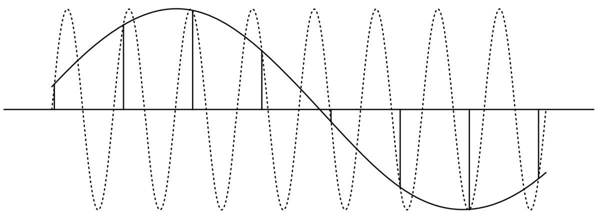

Fig. 2.5-1 Undersampling

is also a sine-function but with incorrect (too low) frequency. In sampled images (see Fig. 2.5-4), this effect may be seen impressively because the eye interpolates between the sampling points (picture elements, pixels).

Optoelectronic sensors sample images too. The problems that arise will be discussed now. It was shown in Section 2.4 that an optical system has band-limiting properties because of diffraction (see (2.4-25) and Fig. 2.4-9). Spatial frequencies $k > k_g$ of the scene will be cut off and do not occur in the image, which means that the scene is smoothed. If one samples images using optoelectronic sensors (e.g. CCD or CMOS sensors), this should be taken into account, especially when there are periodic structures in the scene that cause aliasing.

The optoelectronic detectors used today are assembled by detector elements arranged in a periodic way. Figure 2.5-2 shows (idealized) rectangular detector elements with central points (x_k, y_l) and linear dimensions δ_x, δ_y. The detector elements have the pitch Δ_x and Δ_y with $\Delta_x \geq \delta_x$ und $\Delta_y \geq \delta_y$. If the detector array according

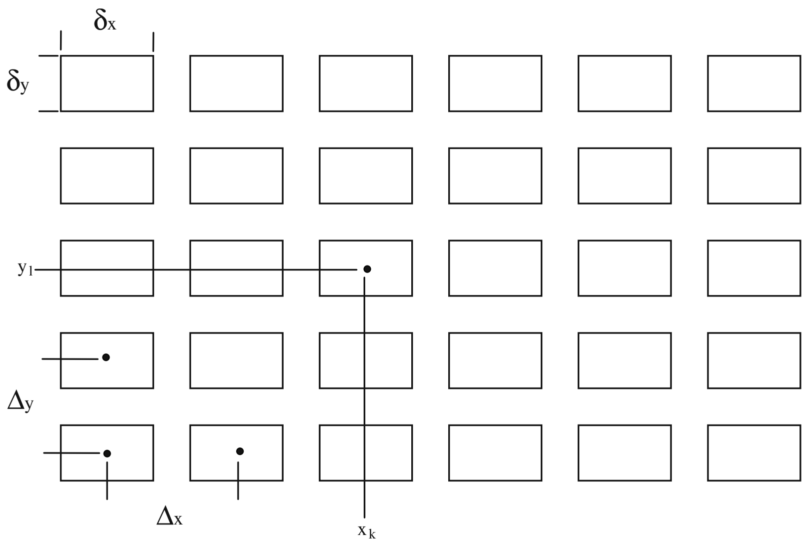

Fig. 2.5-2 Detector array

to (2.1-2) is projected on to the object plane (e.g. the surface of the Earth in the case of remote sensing) then $\Delta_x' = \Delta_x \cdot g/b$ and $\Delta_y' = \Delta_y \cdot g/b$ are called the Ground Sampling Distances (GSD) (in the x- and y- directions, respectively). The size of the projected detector element on the ground $\delta_x' \cdot \delta_y'$ defines the Instantaneous Field of View (IFOV), which may also be expressed through the angles $\approx \delta_x'/g = \delta_x/b$, $\approx \delta_y'/g = \delta_y/b$ (which do not depend on height).

Each detector element generates a single electrical signal which, after pre-processing and analogue-to-digital conversion, corresponds to one picture element (pixel) of the image generated in the computer and displayed on a screen or other medium. Therefore, sometimes the detector element itself is called a pixel.

Because the spatial information contained in the total radiation which the detector element receives is converted into a single signal value, some of that information is lost. Again, the integration of the radiation power over the detector area may be described by a PSF or OTF (see Section 2.4). It is assumed here that there is a constant light responsivity inside the detector element, whereas outside (i.e. in the gaps between the pixels, see Fig. 2.5-2) the responsivity vanishes (ideal case). Then, the integration over the pixel area may be described by the PSF

$$h_{\text{pix}}(x,y) = \begin{cases} \frac{1}{\delta_x \cdot \delta_y} & \text{for} \quad -\frac{\delta_x}{2} \le x \le +\frac{\delta_x}{2},\ -\frac{\delta_y}{2} \le y \le +\frac{\delta_y}{2} \\ 0 & \text{elsewhere} \end{cases} \tag{2.5-9}$$

or by the OTF

$$H_{\text{pix}}\left(k_x,k_y\right) = \frac{\sin\left(\pi\,\delta_x k_x\right)}{\pi\,\delta_x k_x} \cdot \frac{\sin\left(\pi\,\delta_y k_y\right)}{\pi\,\delta_y k_y}. \tag{2.5-10}$$

Owing to the rectangular detector elements these functions are not circular-symmetrical functions. Therefore, the image smoothing depends slightly on the direction.

In reality, the PSF and OTF will adopt slightly different values to (2.5-9) and (2.5-10), respectively. This is caused by the fact that the pixels are not exactly rectangular and the responsivity is not constant inside the pixel. Furthermore, there are physical effects such as diffusion of charge carriers between the pixels, which blur the information further. If one wants to determine the PSF exactly, one has to measure it. But here the precise shape of the PSF is not essential; to understand the problem, (2.5-9) is sufficient.

The sampling of the optical signal by a detector array may be described in two steps. Firstly, the (continuous) output signal $f_{\text{out}}(x,y)$ of the optical system is convolved with the PSF h_{pix} (see also (2.5-4)):

$$f_{\text{pix}} = h_{\text{pix}} \otimes f_{\text{out}} = h_{\text{pix}} \otimes h_{\text{opt}} \otimes f_{\text{in}} = h \otimes f_{\text{in}} \tag{2.5-11}$$

Here, h_{opt} is the PSF of the optical system and f_{pix} the continuous signal (in x,y) which contains the integration over the pixel area. The total PSF which contains the mapping of the input signal by the optics and the integration over the pixel, therefore, is given by the convolution of the PSFs of the optical system and the detector element.

The corresponding relationship in frequency space is

$$\begin{aligned} F_{\text{pix}}\left(k_x,k_y\right) &= H_{\text{pix}}\left(k_x,k_y\right)\cdot F_{\text{out}}\left(k_x,k_y\right) \\ &= H_{\text{pix}}\left(k_x,k_y\right)\cdot H_{\text{opt}}\left(k_x,k_y\right)\cdot F_{\text{in}}\left(k_x,k_y\right), \\ H\left(k_x,k_y\right) &= H_{\text{pix}}\left(k_x,k_y\right)\cdot H_{\text{opt}}\left(k_x,k_y\right). \end{aligned} \tag{2.5-12}$$

The second step consists of the sampling of the (smoothed) signal $f_{\text{pix}}(x,y)$ at the pixel centres $x_k = k\cdot\Delta x$ ($k = 0, \pm1, \pm2,\ldots$), $y_l = l\cdot\Delta y$ ($l = 0, \pm1, \pm2,\ldots$). The result is an array of values $f_{k,l} = f_{\text{pix}}(x_k,y_l)$ which are proportional to the gray values of the computer generated image.

Because the optical OTF has an upper cut-off frequency k_g (2.4-26), the same is true for the total OTF. Figure 2.5-3 shows this for the case $k_x = k$ ($k_y = 0$), $\Delta_x = \delta_x = 1/2k_g$, $k_g = D/(\lambda b)$, which means that the Nyquist frequency $k_{\text{nyq}}=1/2\Delta_x$ is equal to the cut-off frequency and that the sampling condition (2.5-13) is just fulfilled. According to (2.5-10), the OTF $H_{\text{pix}}(k_x,0)$ has the value $2/\pi \approx 0.64$ at the Nyquist frequency. One can enhance this value if one decreases the pixel size δ_x compared to the pixel pitch Δ_x. Then the total OTF corresponds better to that of the optical system.

In Fig. 2.5-3 the OTF of the optics is plotted dashed, $H_{\text{pix}}(k_x,0)$ is the dotted curve, and the total OTF $H = H_{\text{opt}}\cdot H_{\text{pix}}$ is the solid curve.

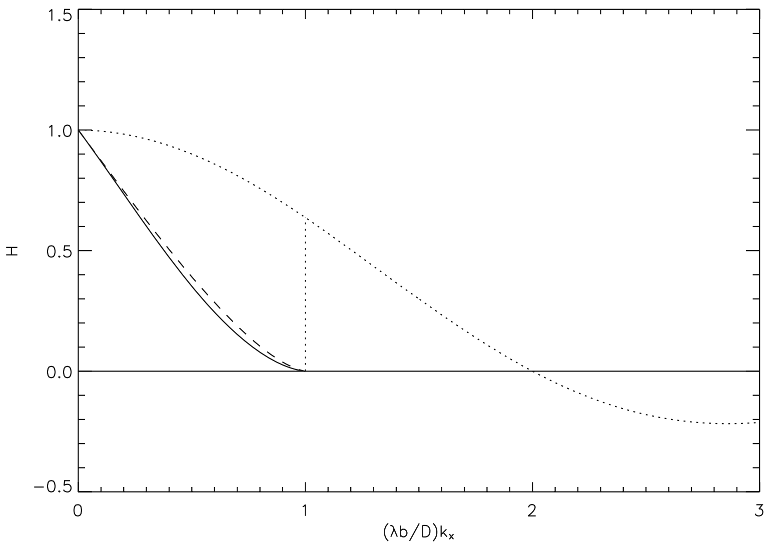

Fig. 2.5-3 Total OTF and OTFs of partial systems (description in the text)

If the sampling distances are chosen as

$$\mathrm{Max}\,\{\Delta x, \Delta y\} < \frac{1}{2k_g}, \tag{2.5-13}$$

the sampling condition is fulfilled and one can reconstruct the spatial signal $f_{\mathrm{pix}}(x,y)$ with the sampling values $f_{k,l} = f_{\mathrm{pix}}(k\Delta x, l\Delta y)$:

$$f_{\mathrm{pix}}(x,y) = \sum_k \sum_l f_{\mathrm{pix}}(k\Delta x, l\Delta y) \cdot \frac{\sin\left[\frac{\pi}{\Delta x}(x - k\Delta x)\right]}{\frac{\pi}{\Delta x}(x - k\Delta x)} \cdot \frac{\sin\left[\frac{\pi}{\Delta y}(y - l\Delta y)\right]}{\frac{\pi}{\Delta y}(y - l\Delta y)}. \tag{2.5-14}$$

When the sampling condition is fulfilled, the values $f_{k,l}$ represent the whole signal $f_{\mathrm{pix}}(x,y)$ (they do so only approximately, of course, because there is only a finite number of sampling values available). If it is not fulfilled, $f_{\mathrm{pix}}(x,y)$ contains too high frequencies and the sampling leads to the aforementioned aliasing errors, which may change periodic signal parts in their spatial frequency and direction. For example, the left-hand image in Fig. 2.5-4 shows a sinusoidal brightness distribution, which was sampled at the brightly marked points, whereas the right-hand image displays the brightness at the sampling points. One sees that the spatial frequency is too low and the wave direction is wrong too.

The undersampling of periodic structures generates patterns which are a special case of the well-known Moiré-patterns. These may arise when periodic structures are observed through other periodic structures (e.g. a fence through finely woven curtain).

Whereas insufficiently dense sampling points may lead to errors, unnecessarily dense sampling points are not corruptive (of course, the amount of data is higher). If the sampling distance has the maximum possible value $1/2k_g$ then all sampling points are necessary for the reconstruction of the whole function $f_{\mathrm{pix}}(x,y)$. If only one sampling value is absent, an exact reconstruction is no longer possible. But, if

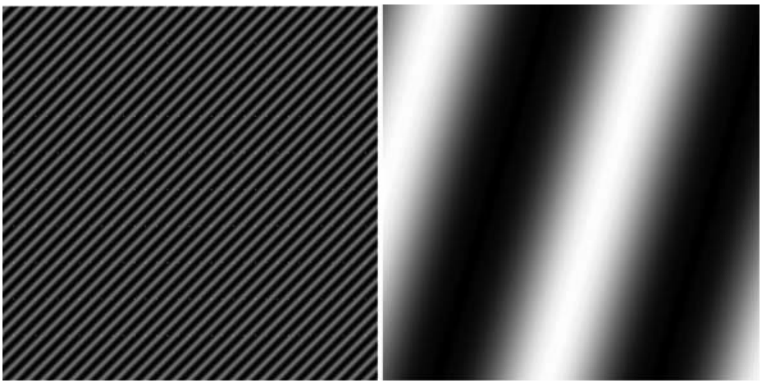

Fig. 2.5-4 Aliasing

the sampling distance is smaller than $1/2k_g$, a certain redundancy is available, which may be used to interpolate missing values, though this is not discussed here.

A detector array (Fig. 2.5-2) is not always used for imaging. If the imaging system is moving relative to the scene, a detector line is sufficient. Such a line sensor with N pixels in the x-direction samples the intensity field in the x-direction in the same way as an array sensor. Sampling in the y-direction becomes possible because of the relative motion of the sensor in that direction. Let $f(x,y)$ be the intensity distribution in the image plane. When the sensor is moving with constant velocity v (related to the image plane) in the y-direction, the intensity at a point (x_0,y_0) (e.g. the central point of a pixel) changes according to $f(x_0,y(t))$ with $y(t) = y_0 + v{\cdot}t$. If the pixel is exposed during the time Δt (exposure time, integration time), the intensity is integrated. As a result the signal

$$g\,(x_0,y_0) = \Delta t \cdot \frac{1}{\Delta t} \int\limits_0^{\Delta t} f(x_0,y_0 + v \cdot t)\mathrm{d}t$$

is generated in the detector element under consideration. This connection can also be written as a linear system

$$g\,(x_0,y_0) = \Delta t \cdot \int\limits_{y_0}^{y_0+v\cdot\Delta t} H_{\mathrm{mot}}\,(y_0 - y) \cdot f\,(x_0,y)\,\mathrm{d}y. \tag{2.5-15}$$

with the PSF of motion or scanning

$$H_{\mathrm{mot}}\,(\xi) = \begin{cases} \frac{1}{v\cdot\Delta t} & \text{for} \quad -v\Delta t \le \xi \le 0 \\ 0 & \text{elsewhere} \end{cases} \tag{2.5-16}$$

Compared to $f(x_0,y_0)$, the intensity $g(x_0,y_0)$ is blurred in the y-direction (along-track). The blur increases with the integration time Δt. It causes an asymmetry, which can be minimized if integration time and pixel dimensions ($\delta_y < \delta_x$) are chosen such that after the integration the effective pixel size in the y-direction $\delta_y{+}v{\cdot}\Delta t$ is (approximately) equal to δ_x Of course, a special sensor design is necessary for this to be accomplished.

If the integration time is chosen such that the pixel shift during this time is equal to the pixel size, it is called the dwell time $\Delta t_{\mathrm{dwell}}$. A point (x,y) of the optical signal then crosses the pixel once during that time (it dwells inside the pixel). In most cases one tries not to exceed the dwell time. Unfortunately, it is not possible to choose $\Delta t \ll \Delta t_{\mathrm{dwell}}$ in most cases, because then the signal-to noise ratio becomes too low (see Section 2.6).

If one uses two CCD lines (instead of one) with the second line shifted by ½ pixel with respect to the first one (staggered array, Fig. 2.5-5), the ground sample distance (GSD) can be halved in both directions (along track and across track). But to enhance the geometric resolution too, it must be kept in mind that the PSF

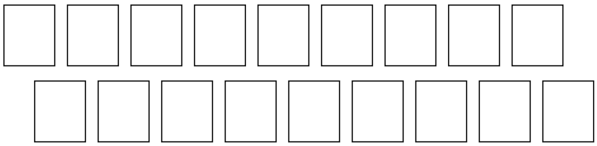

Fig. 2.5-5 Staggered array

of the optical system must be improved also (adequate enhancement of the cut-off frequency k_g)!

With sensor arrays the same effect is achievable if the array is shifted in the x- and y-directions by micro-scanning techniques. But this method is applicable only if there is no motion between object and sensor during consecutive measurements.

Sometimes the geometric resolution of an optical system is equated with the Ground Sampling Distance (GSD) (which corresponds to Δ_x or Δ_y in the image plane). But in general this is not true! In Section 2.4, Rayleigh's definition was used, but this is not the ultimate limit of achievable resolution. If the signal-to-noise ratio (SNR) is good, a central recess in the image of two neighbouring points which is much smaller than the recess of 26% at the Rayleigh distance r_0 (see Fig. 2.4-8 and (2.4-24)) can be detected. In the special case $\Delta = \Delta_x = \Delta_y = 1/2k_\mathrm{g}$ (no aliasing) there is $\Delta = r_0/2.42$. Therefore, for good SNR, the GSD corresponds to a better resolution than r_0 and can serve as a rule of thumb value for the geometric resolution. But ultimately the achievable resolution depends on the SNR.

In short, the sampling of functions may be described as follows (Fig. 2.5-6). In the two-dimensional case, sampling is the transition from $f(x,y)$ to $f_{m,n} = f(m\cdot\Delta x, n\cdot\Delta y)$. These functional characteristics are values from the continuum of real numbers. To process these numbers in digital computers they must be transformed to digital numbers. This is done with the aid of analogue-to-digital converters or units (ADC, ADU), which convert real numbers to integers. For instance, an 8-bit-ADU converts an input signal (voltage) U_E to a digital output value $U_\mathrm{A} = n\cdot\Delta U_\mathrm{A}(n = 0, 1, \ldots, 2^8-1)$, which corresponds to the digital number n. This operation may be

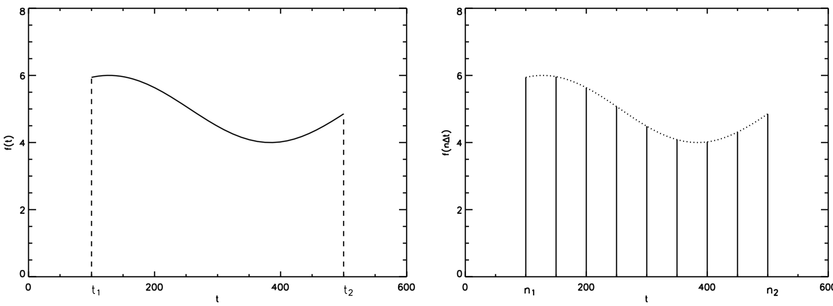

Fig. 2.5-6 One-dimensional sampling: continuous function $f(t)$ $(t_1 \leq t \leq t_2) \rightarrow$ (time-) discrete function $f_n = f(n\cdot\Delta \mathrm{t})$ $(n = n_1,\ldots,n_2)$

defined in the following manner. If the input signal U_E fulfills the condition $(n - \frac{1}{2})\cdot\Delta \le U_E < (n + \frac{1}{2})\cdot\Delta$, the output signal $U_A = n\cdot\Delta U_A$, or the integer n is assigned to U_E. Of course, this operation causes a (digitisation) error (except if, by chance, $U_E = n\cdot\Delta$ holds), which is studied in the next chapter.

2.6 Radiometric Resolution and Noise

In the above sections the necessity of a good dignal-to-noise ratio (SNR) has been mentioned. With good radiometric resolution the geometric resolution can be enhanced. Thus radiometry and geometry are not independent characteristics. To understand radiometric resolution correctly, the nature of random variables and random processes must be understood. If there were no noise, the radiometric resolution, i.e. the possibility to discriminate neighbouring values of intensity, would be arbitrarily large and one could separate any point sources that are close together.

A random process $\xi(t)$ is characterised by the fact that it is impossible to predict future values of $\xi(t)$ exactly. It is possible only to assign probabilities to such values. The reason for the randomness of noise is the fact that the physical signal carriers (photons, electrons etc.) perform random motions and are distributed randomly in space. For example, the photons in a light beam are emitted by randomly distributed emitting atoms or molecules in random moments of time. Therefore, the number received by a detector element during a time interval Δt fluctuates randomly. The electrons responsible for the signal transfer inside a wire have a chaotic velocity distribution (depending on the temperature of the wire) caused by interactions with ions and other electrons. Thus signal fluctuations are generated which are perceived as noise during radio reception. Therefore the name "noise" was chosen for these random processes.

Random fields $\xi(x,y,\ldots)$ are two- or multi-dimensional generalisations of random processes, whereas random variables are represented by numbers ξ_1, ξ_2, … , ξ_n. Here, the theory of random processes can be presented only very briefly.

Because optoelectronic imaging sensors are sampling systems, the following remarks are focused on a short discussion of random variables (e.g. $\xi_{k,l} = \xi(x_k,y_l)$ as sampling values of the random field $\xi(x,y)$).

Let ξ be a random variable which can take real numbers x. These values are described by the probability density $p_\xi(x)$. $p_\xi(x)\mathrm{d}x$ is the probability of the event that the value of ξ is a real number in the interval $[x,x+\mathrm{d}x]$ as the result of an experiment. Then the probability of the event that ξ takes a value x inside the interval $x_1 \le x \le x_2$ is given by

$$P_\xi\,\{x_1 \le x \le x_2\} = \int_{x_1}^{x_2} p_\xi\,(x)\mathrm{d}x. \qquad (2.6\text{-}1)$$

Because it is certain that ξ takes a value inside $-\infty < x < +\infty$ and because the unit probability is assigned to an event that will take place with certainty, the relationship

$$\int_{-\infty}^{+\infty} p_\xi\,(x)\mathrm{d}x = 1. \tag{2.6-2}$$

holds.

The function $p_\xi(x)$ allows one to define the so-called expected values. Let $f(\xi)$ be any function of the random variable ξ. Then the expected value of $f(\xi)$ is given by

$$\langle f\rangle = \int_{-\infty}^{+\infty} f\,(x)\,p_\xi\,(x)\mathrm{d}x. \tag{2.6-3}$$

If one carries out N experiments with the result that the random variable $f(\xi)$ takes the values $f_1,\ldots f_N$ then one can calculate the arithmetic mean value

$$\bar{f} = \frac{1}{N}\sum_{n=1}^{N} f_n. \tag{2.6-4}$$

If N is large then $\bar{f}$ is near to $\langle f\rangle$ with high probability. Therefore, the expected value is also called the statistical mean value.

In the following the expected value

$$\langle\xi\rangle = \int_{-\infty}^{+\infty} x\cdot p_\xi\,(x)\mathrm{d}x \tag{2.6-5}$$

of the random variable ξ itself and the expected value of squared variable $(\xi - \langle\xi\rangle)^2$

$$\sigma_\xi^2 = \left\langle(\xi - \langle\xi\rangle)^2\right\rangle = \int_{-\infty}^{+\infty} (x - \langle\xi\rangle)^2\cdot p_\xi\,(x)\mathrm{d}x, \tag{2.6-6}$$

which is the variance of the random variable ξ, are used. The standard deviation σ_ξ (the square root of the variance) is a measure of the deviation of ξ from the mean value $\langle\xi\rangle$ and therefore a measure of the width of the probability density $p_\xi(x)$.

The mean energy of the black body radiation of temperature T inside the wavelength interval $[\lambda, \lambda+\Delta\lambda]$ is considered by way of an example. This is received during the integration time Δt by a detector element. It is proportional to Planck's function $B_\lambda(T)$ (see Section 2.2). $B_\lambda(T)$ is not a random variable: it characterises the mean radiance of the black body radiation! Therefore, all radiometric quantities considered up to now must be understood as statistical mean values. The values obtained as the results of measurements fluctuate around these mean values. The standard deviation σ is a measure of that fluctuation. Therefore, it is useful to characterise the quality of a signal by the signal-to-noise ratio

$$\mathrm{SNR} = \frac{\langle S \rangle}{\sigma}. \tag{2.6-7}$$

Let $E = \Phi \cdot \Delta t$ be the energy which a detector element receives during the integration time Δt (Φ is the power of that radiation; see Section 2.2). If the detector is linear (a condition well fulfilled by CCD sensors) then the sensor output signal U is proportional to E: $U = K \cdot E$. During a measurement the (noisy) value $U = \langle U \rangle + \delta U$ is observed. Here, δU is a random variable with the mean value $\langle \delta U \rangle = 0$ and standard deviation σ_U. It is assumed that the noise δU is generated in the detector and/or the read-out electronics and that the input signal (the radiation) is noise-free (which means that the photon noise, which is developed in (2.6-20), (2.6-21), (2.6-22), (2.6-23) and (2.6-24), can be neglected). Then, an error $\delta E = \delta U/K$ and an error $\delta\Phi = \delta U/(K \cdot \Delta t)$ may be attributable to the random error δU. Those random variables have the standard deviations $\sigma_E = \sigma_U/K$ and $\sigma_\Phi = \sigma_U/(K \cdot \Delta t)$, respectively. They are measures of the quality with which the radiometric variable under consideration can be measured and define the achievable radiometric resolution. In particular, σ_Φ is called the Noise Equivalent Power (NEP). In this way, the radiometric resolution of other radiometric variables such as the radiance may also be estimated. For instance, if one measures the radiation in the wavelength interval $\Delta\lambda$ then according to (2.2-9) the relationship

$$\Phi = K_0 \cdot L_\lambda \; ; \quad K_0 = \frac{\pi}{4} \cdot \frac{F_D}{f_\#^2} \cdot \cos^4(\vartheta) \cdot \tau_\lambda \cdot \Delta\lambda$$

is true, and it holds that $\sigma_{L\lambda} = \sigma_U/(K_0 \cdot K \cdot \Delta t)$.

If the connection between U and E is non-linear (for CMOS sensors, for example), the radiometric resolution of E (and also of Φ or L_λ) may be determined if the probability density $p_U(u)$ of the random variable U is known. Let the connection between E and U be given by $E = f(U)$. Then, according to (2.6-3) and (2.5-6) the following relationships hold:

$$\sigma_E^2 = \left\langle (E - \langle E \rangle)^2 \right\rangle = \int \left[f(u) - \langle E \rangle \right]^2 \cdot p_U(u)\, \mathrm{d}u, \tag{2.6-8}$$

and

$$\langle E \rangle = \int f(u) \cdot p_U(u)\, \mathrm{d}u. \tag{2.6-9}$$

The linear relationship $E = U/K$ is a special case of $E = f(U)$. For practical purposes (with weak noise) the simpler relationships

$$\sigma_E \approx \left| f'(\langle U \rangle) \right| \cdot \sigma_U \tag{2.6-10}$$

and

$$\langle E\rangle \approx f\,(\langle U\rangle) \tag{2.6-11}$$

are sufficient. They can be obtained if the relationship $E = f(U) = f(\langle U\rangle + \delta U)$ is approximated by $f(\langle U\rangle) + \delta U{\cdot}f'(\langle U\rangle)$. Equation (2.6-10) shows that the radiometric resolution of E in the non-linear case (for weak noise) depends on the mean signal value $\langle U\rangle$ and therefore also on the received mean radiation energy. An example is the logarithmic relationship $U = C{\cdot}\ln E$ (which may hold approximately in the case of CMOS sensors) with $E = e^{U/C} = f\,(U)$ and $\sigma_E = \frac{1}{C}e^{\langle U\rangle/C}\cdot\sigma_U = \frac{1}{C}\langle E\rangle\cdot\sigma_U$. The relative radiometric error $\sigma_E/\langle E\rangle$ and the *SNR* $\langle E\rangle/\sigma_E$ do not depend on the mean energy $\langle E\rangle$.

To calculate the quantities (2.6-8) and (2.6-9) exactly (for strong noise), one needs the probability density $p_U(u)$. This may often be approximated by the Gaussian or normal distribution, which is certainly the most important probability distribution because of the central limit theorem: if a random variable ξ is the sum of (not necessarily independent) N random variables $\xi_1, \xi_2, \ldots, \xi_N$, which may have probability densities different from the normal distribution, then (under certain conditions) the probability density of ξ tends to the normal distribution with increasing number N.

The normal distribution is given by

$$p\,(x) = \frac{1}{\sigma\sqrt{2\pi}}e^{-\frac{(x-a)^2}{2\sigma^2}}. \tag{2.6-12}$$

with $\langle\xi\rangle = a$ and $\sigma_\xi = \sigma$.

Figure 2.6-1 shows the normal distribution for $a = 5$ and $\sigma = 1$. The probability that ξ takes a value in the interval $a–3\sigma < x < a+3\sigma$ has the value 0.9973. This

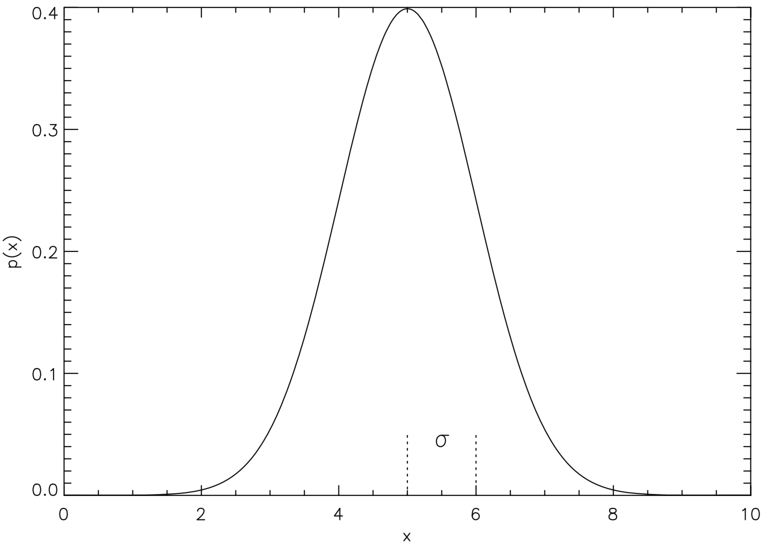

Fig. 2.6-1 Normal (Gaussian) distribution

so-called 3σ-interval is often taken as a measure of the domain of values of the random variable ξ, though it must be pointed out that values outside this interval (so-called outliers) may occur.

Many noise processes (and especially thermal noise) can be well described by normal distributions. In the case of thermal noise $\sigma^2 \sim T$ (see (2.6-29) and (2.6-30)). Thus this kind of noise may be reduced by the cooling of detectors and electronic circuits.

If several random variables $\xi_1, \xi_2, \ldots, \xi_N$ have to be considered, then the joint probability density $p_{\xi 1 \ldots \xi N}(x_1, \ldots x_N)$ must be used. For statistically independent random variables this distribution decays into a product of the single densities $p_{\xi i}(x_i)$. This means that the occurrence of a value of a random variable ξ_n is not influenced by all other random variables. This case is important because the output signal in most cases is a superimposition of several independent random processes (photon noise superimposed by several types of detector noise, for example, and by the noise of electronic components).

Let

$$\xi = \xi_1 + ... + \xi_N \tag{2.6-13}$$

be the sum of N independent random variables. Then the relationships

$$\langle \xi \rangle = \langle \xi_1 \rangle + ... + \langle \xi_N \rangle \tag{2.6-14}$$

and

$$\sigma_\xi^2 = \sigma_{\xi_1}^2 + ... + \sigma_{\xi_N}^2. \tag{2.6-15}$$

hold.

If, for instance, the ξ_n are the amplitudes of the radiation field with vanishing mean values ($\langle \xi_n \rangle = 0$), then, in the case of statistical independence (in optics called "incoherence"), the squared amplitudes sum up. This was already mentioned in Section 2.1. In the case of independent noise contributions, (2.6-15) shows that their variances are added. Especially important is the case where one physical parameter is measured several times. Then the relationships $\langle \xi_1 \rangle = \langle \xi_2 \rangle = \ldots = \langle \xi_N \rangle$ and $\sigma_{\xi_1} = \sigma_{\xi_2} = ... = \sigma_{\xi_N}$ hold and, therefore, according to (2.6-14) and (2.6-15), $\langle \xi \rangle = \mathrm{N} \cdot \langle \xi_\mathrm{n} \rangle$ and $\sigma_\xi = \sigma_{\xi_n} \cdot \sqrt{N}$. The *SNR* increases in proportion to the square root of N:

$$SNR_\xi = SNR_{\xi_n} \cdot \sqrt{N}. \tag{2.6-16}$$

This method is often used to increase the quality of measurement.

An important application of this method is the so-called TDI principle (Time Delay and Integration). If one uses an airborne or spaceborne CCD line sensor, the integration time is limited by the height-to-velocity ratio h/V and by the pixel size δ. To enhance the geometric resolution at given h/V substantially (which means that the pixel size must be diminished), the signal and the *SNR* are reduced. This limits the possibility of enhancing the geometric resolution. A solution is possible when

N detector elements ($n = 1,\ldots,N$) (along track) are coupled such that the amount of charge generated in a detector element n during the integration time can be shifted into the next element n+1. One has to ensure that the charge transfer is synchronized with the motion of the sensor. A portion of an object which is seen by element n during $t_n \leq t \leq t_n+\Delta t$ must be seen in the next interval $t_{n+1} \leq t \leq t_{n+1}+\Delta t$ by element n+1 to enhance the shifted amount of charge. Thus the signal will obtain the value $N{\cdot}S$ whereas the noise is increased only to the value $\sigma{\cdot}N$, which means that the increase of the SNR is N.

Until now random variables have been considered as real numbers with a continuum of values. The analogue-to digital conversion generates discrete values which are proportional to the integer numbers 0, ±1, ±2, …. These discrete random variables adopt only a finite number of values (or, in a limiting case, a countable number). Let ζ be a discrete random variable with the values $z_1, z_2, \ldots, z_N$. Then $P\{\zeta = z_n\} = P_n$ is the probability that ζ takes the value z_n in the result of an experiment. Now, instead of (2.6-2), the normalisation condition is

$$\sum_{n=1}^{N} P_n = 1. \tag{2.6-17}$$

Expected value and variance are calculated according to

$$\langle\zeta\rangle = \sum_{n=1}^{N} z_n \cdot P_n \tag{2.6-18}$$

and

$$\sigma_\zeta^2 = \sum_{n=1}^{N} (z_n - \langle\zeta\rangle)^2 \cdot P_n \tag{2.6-19}$$

(compare with (2.6-5) and (2.6-6)).

The following are two examples of discrete random variables, which are relevant for optoelectronic systems. The first example is the analogue-to-digital conversion of a (continuous) random variable $U = \langle U\rangle + \delta U$. Let U be normally distributed with the expected value a and the standard deviation σ_U. If U takes a value u inside the interval $z{\cdot}\Delta-\Delta/2 \leq u < z{\cdot}\Delta+\Delta/2$ (z is an integer number and Δ is the distance of discretisation or quantisation level) then the integer number $z = [u/\Delta+0.5]$ is assigned to u. Here, $[x]$ is the notation for the integer part of the real number x. Using the given normal distribution of U, one can calculate the probability P_z that the random number $\zeta = [U/\Delta+0.5]$ takes the value z. This probability [see Jahn and Reulke (1995)] essentially depends on the ratio Δ/σ_U and (weaker) on a/σ_U. For $\Delta/\sigma_U \leq 1$ the expected value and the standard deviation of ζ deviate from the same values of the continuous variable U/Δ only insignificantly. Therefore, for $\Delta/\sigma_U \leq 1$ the deterioration due to analogue-to-digital conversion is marginal. In most cases it is sufficient to choose $\Delta \approx \sigma_U$. If the noise is very small ($\sigma_U << \Delta$) or even vanishing ($U = \langle U \rangle$), then the discretisation of U results in an error ΔU with $|\Delta U| \leq \Delta/2$ ($\Delta U = 0$ in the special case $U = z \cdot \Delta$). If U is interpreted as a random variable which is evenly distributed inside the interval $z \cdot \Delta - \Delta/2 \leq u < z \cdot \Delta + \Delta/2$, i.e.

$$p_U(u) = \begin{cases} 1/\Delta & \text{if } (z - 1/2) \cdot \Delta \leq u < (z + 1/2) \cdot \Delta \\ 0 & \text{elsewhere} \end{cases}$$

then, according to (2.5-6), the standard deviation $\sigma = \Delta/\sqrt{12} \approx 0.289 \cdot \Delta$ is obtained as a measure of the quantisation error, which is sometimes used to characterise the quantisation noise.

As the second example of a discrete random variable the photon noise is now considered. Let N_{phot} be the number of photons received by the detector within the integration time Δt. N_{phot} is an integer number which can take the values $n = 0, 1, 2, \ldots$. The expected value $\langle N_{\text{phot}} \rangle$, which was considered in Section 2.2, is a real number. Often the Poisson distribution

$$P_n = \frac{a^n \cdot e^{-a}}{n!}; n = 0,1,2,\ldots \tag{2.6-20}$$

is chosen as the probability distribution of N_{phot}. According to (2.6-18) and (2.6-19), N_{phot} has the expected value

$$\langle N_{\text{phot}} \rangle = a \tag{2.6-21}$$

and the standard deviation

$$\sigma_{N_{\text{phot}}} = \sqrt{\langle N_{\text{phot}} \rangle}, \tag{2.6-22}$$

respectively. Therefore, the signal-to-noise ratio is $SNR = \sqrt{\langle N_{\text{phot}} \rangle}$. It can be enhanced only if the mean photon number can be increased (e.g. by an enlarged aperture or by a bigger integration time). In any case, the photon noise defines the ultimate limit of the achievable measurement precision; other noise contributions may be reduced, for example by cooling.

Figure 2.6-2 shows the Poisson distribution for two values of the parameter $a = \langle N_{\text{phot}} \rangle$. It is seen that the Poisson distribution approaches the normal distribution for large values of a. This can also be shown mathematically.

When the detector (e.g. CCD or CMOS sensor) is a quantum detector with a quantum detectivity η_{qu}, the generated number N_{el} of electrons is again a Poisson distributed random variable with

$$\langle N_{\text{el}} \rangle = \eta_{\text{qu}} \cdot \langle N_{\text{phot}} \rangle \tag{2.6-23}$$

and

$$\sigma_{N_{\text{el}}} = \sqrt{\langle N_{\text{el}} \rangle} = \sqrt{\eta_{\text{qu}}} \cdot \sigma_{N_{\text{phot}}}. \tag{2.6-24}$$

Let $N_{\max}$ be the maximum number of electrons that a detector element can contain. Then the optical system should be designed so that the maximum received

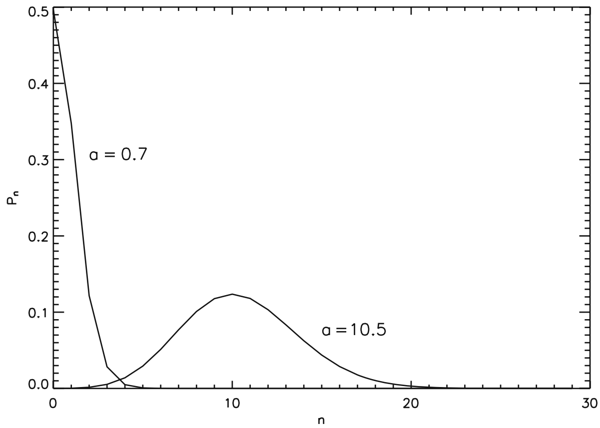

Fig. 2.6-2 Poisson distribution

photon number is small enough to ensure that the maximum generated electron number (up to outliers) remains below $N_{\max}$ (for example by choosing $\langle N_{\mathrm{el}} \rangle + 3\sigma_{\mathrm{Nel}} = N_{\max}$). The minimum value $N_{\min} \approx \langle N_{\mathrm{el}} \rangle_{\min}$ which has to be measured has a noise value $\sigma_{\min} = \sqrt{\langle N_{\mathrm{el}} \rangle_{\min}}$. As was shown above, this value should be chosen not bigger than the quantisation step Δ of the ADU. Δ corresponds to the least significant bit (LSB). To be able to measure the whole signal range from $\langle N_{\mathrm{el}} \rangle_{\min}$ to $\langle N_{\mathrm{el}} \rangle_{\max}$ precisely one needs (for $\sigma_{\min} \approx \Delta$)

$$D = \frac{N_{\max}}{\sigma_{\min}} \approx \frac{N_{\max}}{\Delta}. \tag{2.6-25}$$

steps of quantisation or $\log_2 \mathrm{D}$ bits, which the ADU must provide free of error. D (or $\log_2 D$) is called the dynamic range of the system. For example, a photon noise limited detector element with $N_{\max} = 100{,}000$ and $\langle N_{\mathrm{el}} \rangle_{\min} = 100$ has a dynamic range $D = 10{,}000$. One needs 14 bits to cover that range with high quality.

Often the so-called Power Spectrum is used in order to characterise noise processes. To introduce this quantity the random processes $\xi(t)$ must be briefly discussed. Let $\xi(t)$ take the value x at time t. Then $\xi(t)$ will be described by the probability density $p_\xi(x,t)$ (and by joint density functions $p_\xi(x_1,t_1;x_2,t_2;\ldots;x_N,t_N)$ of any order N, though these are not used here).

According to (2.6-5) and (2.6-6) the expected value and variance are given by

$$\langle \xi\,(t) \rangle = \int_{-\infty}^{+\infty} x \cdot p_\xi\,(x,t)\mathrm{d}x \tag{2.6-26}$$

and

$$\sigma_\xi^2\,(t) = \int_{-\infty}^{+\infty} (x - \langle \xi\,(t) \rangle)^2 \cdot p_\xi\,(x,t)\mathrm{d}x. \tag{2.6-27}$$

Now, both quantities depend on the time t.

An important sub-group of random processes consists of the stationary random processes. The statistical properties of these processes do not change with time. This means in particular that the probability density, the expected value and the variance do not depend on time. With the aid of the Fourier transform (2.3-3), a spectrum (the Power Spectrum) $S_\xi(\nu)$ may be assigned to the variance of the stationary process $\xi(t)$:

$$\sigma_\xi^2 = \int_0^\infty S_\xi\,(\nu)\mathrm{d}\nu. \tag{2.6-28}$$

To clarify the meaning of this quantity, an electrical resistance R with temperature T is considered. When its contacts are connected by a voltmeter one can measure a (weak) noisy voltage $U(t)$ with vanishing mean value $\langle U(t)\rangle$. The variance of this voltage is constant as long as the resistance and its temperature are not changed. The thermal noise (also called Johnson noise) is caused by the chaotic motion of the charge carriers, which becomes more intense with increasing temperature. The stationarity of the process $U(t)$ follows from the stability of the physical parameters R and T. The variance $\sigma_U{}^2 = \langle U^2\rangle$ is proportional to the electrical power. Therefore the name Power Spectrum was assigned to $S_U(\nu)$. Thermal noise has the constant Power Spectrum

$$S_U\,(\nu) = 4kTR \tag{2.6-29}$$

in a very wide range of frequencies (k is Boltzmann's constant).

The so-called white noise has a Power spectrum which is constant up to infinitely high frequencies. According to (2.6-28) its variance is infinitely large and therefore it does not exist in reality. Hence the spectrum (2.6-29) of thermal noise must decrease with increasing (high) frequencies. If a frequency range $\Delta\nu$ is filtered out of the noise then the observed effective noise voltage is given by

$$U_{\mathrm{eff}} = \sqrt{\langle U^2\rangle} = \sqrt{4kTR\Delta\nu}. \tag{2.6-30}$$

In most cases the frequency range of the thermal noise is much larger than that of the required signal. If ν_g is the cut-off frequency of the signal, the thermal noise may be reduced considerably if $\Delta\nu = \nu_g$ is chosen.

Shot noise is almost a white noise process too. It is generated when a current flows through a p-n transition of a semiconductor. If $I = \langle I\rangle + \delta I$ is the current, the Power Spectrum of the noisy current δI (in a very large frequency range) is given by

$$S_{\delta 1}\,(\nu) = 2e\,\langle I\rangle \tag{2.6-31}$$

(e is the elementary charge). The effective noise current in the frequency range $\Delta\nu$ is

$$\delta I_{\mathrm{eff}} = \sqrt{\langle(\delta I)^2\rangle} = \sqrt{2e\,\langle I\rangle\,\Delta\nu}. \tag{2.6-32}$$

If one uses a photo diode, the mean current $\langle I \rangle$ is composed of two parts. The main part is generated by the photons received (the required signal). The second part is the so-called dark current, which is also generated by thermal effects in the absence of light. This disturbing signal causes the (signal-independent) dark current noise. It increases with the temperature and hence may be reduced by cooling.

Another important noise process is the 1/f-noise (also called flicker noise). It arises from random adhesion of charges at impurities and defects in semiconductors. Its Power Spectrum has a $1/\nu$-dependency at low frequencies (sometimes up to MHz). Of course, for $\nu \to 0$ the spectrum must converge to a finite value, because otherwise the integral (2.6-28) would diverge. For the same reason $S_{1/\mathrm{f}}(\nu)$ has to decrease more rapidly than $1/\nu$ for high frequencies.

The so-called fixed pattern noise which appears in array and line sensors is not a genuine random process. It is caused by the non-uniformity of the detector elements and does not change with time (or only very slowly because of degradations). The Photo Response Non-Uniformity (PRNU) is caused by different pixel sizes and changes in quantum efficiency from pixel to pixel. The Dark Signal Non-Uniformity (DSNU) describes the change of the dark current from pixel to pixel. Because the dark current depends on the temperature of the detector, the DSNU may be reduced by cooling (the PRNU cannot be similarly reduced). Because both are constant in time they may be corrected when measured in the process of calibration. Of course, if the quantum efficiency vanishes in a pixel (dark pixel) then it cannot be corrected. Such values must be interpolated.

Next the spectral resolution of a sensor is considered briefly. In Section 2.2 it was shown that the mean electron number generated in the detector element is proportional to

$$\int_0^\infty \eta_\lambda^{\mathrm{qu}} \cdot \tau_\lambda \cdot \frac{\lambda}{h \cdot c} \cdot L_\lambda \mathrm{d}\lambda$$

Equation (2.2-15). The radiance L_λ, which describes the properties of the observed object, is filtered by the transmissions of atmosphere, optical materials and (colour) filters, and by the quantum efficiency. If the spectral filtering functions are combined in a joint spectral responsivity η_λ, the measured signal is proportional to

$$\int_0^\infty \eta_\lambda \cdot L_\lambda \mathrm{d}\lambda. \tag{2.6-33}$$

The spectral responsivity η_λ defines the spectral resolution of the sensor system (which includes the atmosphere). Normally the system transmits broad band radiation (panchromatic sensor). For instance, a CCD sensor based on silicon technology detects light in the whole visible and near infrared range of the spectrum up to (a little bit more than) 1 μm. By means of special narrow-band filters or spectrometric devices (such as prisms or gratings), this broad-band spectral range can be limited and made extremely narrow banded.

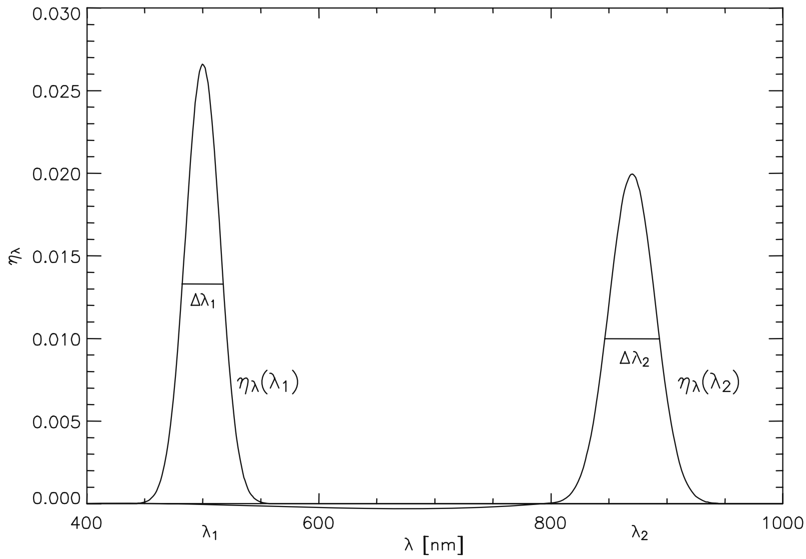

Fig. 2.6-3 Narrow-band filter

Let $\eta_\lambda(\lambda_0)$ be a narrow-band function with the mid-wavelength λ_0 (Fig. 2.6-3). This function cuts the part

$$S(\lambda_0) = \int_0^\infty \eta_\lambda\,(\lambda) \cdot L_\lambda \cdot \mathrm{d}\lambda \tag{2.6-34}$$

out of the radiance L_λ. This signal part may be approximated by

$$S(\lambda_0) = L_{\lambda_0} \cdot \int_0^\infty \eta_\lambda\,(\lambda_0)\,\mathrm{d}\lambda = \mathrm{const} \cdot L_{\lambda_0}, \tag{2.6-35}$$

This approximation will be better the less L_λ changes over the width of the function $\eta_\lambda(\lambda_0)$. If the filter is narrow banded enough, one has the possibility of measuring the radiance L_λ at the wavelength $\lambda = \lambda_0$. Of course, this is possible exactly only for $\eta_\lambda(\lambda_0) \rightarrow \mathrm{const} \cdot \delta(\lambda\text{–}\lambda_0)$.

Airborne or spaceborne sensors often use multiple filters with mid-wavelengths $\lambda_1, \ldots, \lambda_N$ and spectral widths $\Delta\lambda_1, \ldots, \Delta\lambda_N$. They are then called multispectral sensors. Hyperspectral sensors have many ($N > 100$, for example) narrow-band spectral channels.

The width $\Delta\lambda_0$ of a spectral channel with the responsivity $\eta_\lambda(\lambda_0)$ may be defined in various ways. A common measure is the half-height width, i.e. the width of $\eta_\lambda(\lambda_0)$ at $\max\{\eta_\lambda(\lambda_0)\}/2$ (see Fig. 2.6-3). The value $\lambda_0/\Delta\lambda_0$ is called the spectral resolution of the channel.

It must be mentioned that the width $\Delta\lambda$ of a spectral channel cannot be reduced to zero because as $\Delta\lambda \to 0$ the power of the radiation vanishes (see Section 2.2). One must always accept a trade-off between spectral and radiometric resolution, which are not independent.

2.7 Colour

Whereas the spectral and radiometric properties of light are physically well defined, this is not the case for colour. Colour is a phenomenon of perception which is generated in the visual system of the brain when three stimuli arrive from the colour detectors (cones) in the retina of the eyes. A quantification of this phenomenon is possible only via visual comparisons by test persons and therefore cannot be fully objective. In the past various approaches to solve this problem have been developed (Wyszecki, 1960), but these cannot be presented in this short introduction.

When light of wavelength $\lambda = 700.0$ nm is received by the eye, a red colour impression is generated. At $\lambda = 546.1$ nm the impression is green, and at $\lambda = 435.8$ nm, blue. These three colours are called the primary colours and are denoted by **R**, **G**, **B** if their intensities are in the relationship 73.04 : 1.40 : 1.00. This definition is given by the International Commission of Illumination, CIE (Commission Internationale de l'Eclairage). Any colour **F** can be generated by light with any spectral distribution in the wavelength range from λ_{min} » 380 nm to λ_{max} » 760 nm. It is assumed that **F** may be represented by a linear superimposition of the three primary colours **R**, **G**, **B**:

$$\mathrm{F} = R \cdot R + G \cdot G + B \cdot B. \tag{2.7-1}$$

This representation of colour may be interpreted as a vector equation with the three unit vectors **R**, **G**, **B**. The three colour values *R*, *G*, *B* which uniquely determine the colour **F** have to be determined by experiments with test persons. In such experiments the colour **F** is projected on to a test plate 1, whereas the superimposition $R'\cdot\mathbf{R}+G'\cdot\mathbf{G}+B'\times\mathbf{B}$ is projected on to a second test plate (both on black background). Then the three colour values *R*', *G*', *B*' are varied until the test person perceives the same colour on both test plates. The resulting values *R*, *G*, *B* are then the colour values which characterise the colour **F**. It turns out that not all colours **F** may be described by three non-negative colour values *R*, *G*, *B*. But the method can be changed so that the sum (e.g. $G'\cdot\mathbf{G}+B'\times\mathbf{B}$) of only two primary colours is projected on to test plate 2 whereas on test plate 1 **F** is superimposed with $R'\cdot\mathbf{R}$. From $\mathbf{F}+R\cdot\mathbf{R} = G\times\mathbf{G}+B\times\mathbf{B}$ again follows (2.7-1), but now *R* has a negative value. That means that Equation (2.7-1) holds in general if the colour values *R*, *G*, *B* can take negative values too.

The three colour values *R*, *G*, *B* which correspond to light with a continuous spectrum may be represented by a superimposition of the spectral colour values $R_\lambda \mathrm{d}\lambda$, $G_\lambda \mathrm{d}\lambda$, $B_\lambda \mathrm{d}\lambda$:

$$R = \int_{\lambda_{min}}^{\lambda_{max}} R_\lambda \mathrm{d}\lambda, \dots. \tag{2.7-2}$$

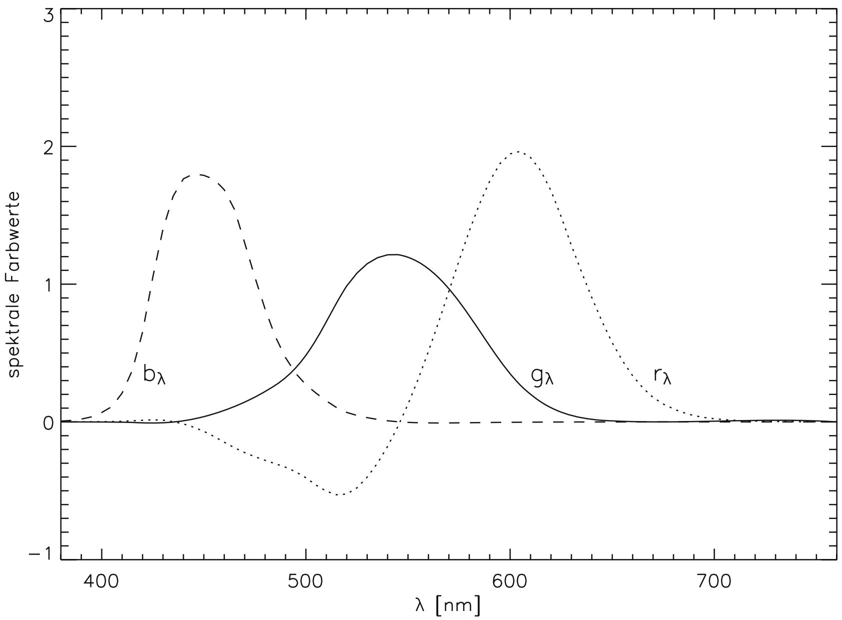

Fig. 2.7-1 Spectral value functions

Let r_λ, g_λ, b_λ be those spectral colour values (spectral value functions) which correspond to light with a spectrum of constant intensity (Fig. 2.7-1). Now the colour values for any (spectral) colour stimulus may be calculated. A colour stimulus φ_λ is defined by the spectral distribution of the light which causes the perception of a colour:

$$\varphi_\lambda = \beta_\lambda \cdot S_\lambda \tag{2.7-3}$$

Here, β_λ is the spectral reflectivity of the illuminated surface and S_λ is the spectral density of the illuminating light.

Then the following equations are true:

$$R = \int_{\lambda_{\min}}^{\lambda_{\max}} \beta_\lambda \cdot S_\lambda \cdot r_\lambda \mathrm{d}\lambda, \quad G = \int_{\lambda_{\min}}^{\lambda_{\max}} \beta_\lambda \cdot S_\lambda \cdot g_\lambda \mathrm{d}\lambda, \quad B = \int_{\lambda_{\min}}^{\lambda_{\max}} \beta_\lambda \cdot S_\lambda \cdot b \mathrm{d}\lambda.. \tag{2.7-4}$$

The spectral colour values (Fig. 2.7-1) have the drawback that they may have negative values. Therefore, they cannot be generated with optical filters. One can generate the colour values R, G, B with spectrometers but not with the so-called True Colour Sensors consisting of three filters only. With a spectrometer the spectral colour stimuli φ_λ may be measured with reflected light. They can then be multiplied with the spectral colour values r_λ, g_λ, b_λ, and finally the integrals (2.7-4) can be computed numerically. To measure colour also with three-colour sensors, the transition from the colour space of the primary colours **R**, **G**, **B** to the space of the so-called standard colours **X**, **Y**, **Z** must be performed.

The vectors **X**, **Y**, **Z** are connected with the vectors **R**, **G**, **B** via the linear transform

$$\begin{pmatrix} X \\ Y \\ Z \end{pmatrix} = \mathrm{A} \cdot \begin{pmatrix} R \\ G \\ B \end{pmatrix} \tag{2.7-5}$$

with

$$\mathrm{A} = \begin{pmatrix} 2.36460 & -0.51515 & 0.00520 \\ -0.89653 & 1.42640 & -0.01441 \\ -0.46807 & 0.08875 & 1.00921 \end{pmatrix} \tag{2.7-6}$$

If, analogously to (2.7-1), one writes

$$F = X \cdot X + Y \cdot Y + Z \cdot Z, \tag{2.7-7}$$

then one obtains the following connection between the primary colour values R, G, B and the normalized colour values X, Y, Z:

$$\begin{pmatrix} R \\ G \\ B \end{pmatrix} = \mathbf{A}^{\mathbf{T}} \cdot \begin{pmatrix} X \\ Y \\ Z \end{pmatrix} \quad \text{and} \quad \begin{pmatrix} r_\lambda \\ g_\lambda \\ b_\lambda \end{pmatrix} = \mathbf{A}^{\mathbf{T}} \cdot \begin{pmatrix} x_\lambda \\ y_\lambda \\ z_\lambda \end{pmatrix} \tag{2.7-8}$$

Here $\mathbf{A}^{\mathbf{T}}$ is the transpose of matrix **A** and x_λ, y_λ, z_λ are the standard spectral value functions (see Fig. 2.7-2), respectively. The normalized spectral value functions have non-negative values and may be implemented with suitable filters.

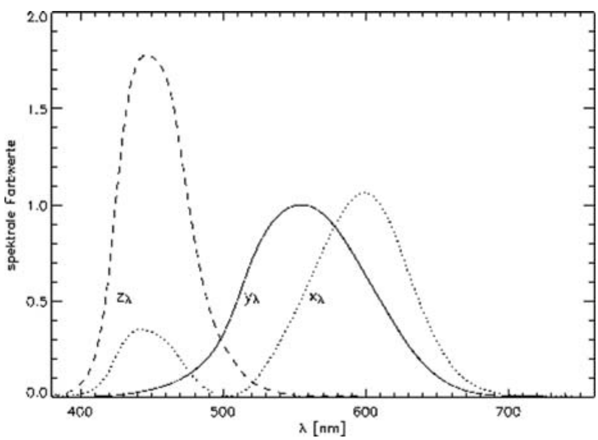

Fig. 2.7-2 Standard spectral value functions

Analogously to (2.7-4), the standard colour values obey the equations

$$X=C\cdot\int\limits_{\lambda_{\min}}^{\lambda_{\max}}\beta_\lambda\cdot S_\lambda\cdot x_\lambda \mathrm{d}\lambda,\quad Y=C\cdot\int\limits_{\lambda_{\min}}^{\lambda_{\max}}\beta_\lambda\cdot S_\lambda\cdot y_\lambda \mathrm{d}\lambda,\quad Z=C\cdot\int\limits_{\lambda_{\min}}^{\lambda_{\max}}\beta_\lambda\cdot S_\lambda\cdot z_\lambda \mathrm{d}\lambda. \tag{2.7-9}$$

The multiplier C is chosen so that the standard colour value Y has the value 100 for the fully matt-white reflecting surface ($\beta_\lambda = 1$):

$$C = \frac{100}{\int\limits_{\lambda_{\min}}^{\lambda_{\max}} S_\lambda \cdot y_\lambda d_\lambda} \cdot \lim_{x\to\infty} \tag{2.7-10}$$

The standard colour values X, Y, Z can be generated using digital cameras with filters x_λ, y_λ, z_λ implemented and, of course, with spectrometers.

The standard colour values X, Y, Z are an instrument-independent basis for the representation of colours on monitors and printers (see the remarks after Equation (2.7-13)). They offer the possibility of instrument-independent colour measurements, which can be achieved by transforming the **X**, **Y**, **Z** space into other colour spaces which are better adapted to the visual perception of humans.

If one looks at two neighboring plates with slightly different colours described by the values X_1,Y_1,Z_1 and X_2,Y_2,Z_2 then the colour distance

$$r_{1,2} = \sqrt{(X_1 - X_2)^2 + (Y_1 - Y_2)^2 + (Z_1 - Z_2)^2} \tag{2.7-11}$$

may be assigned to these colours. But it turns out that this distance does not correspond to an equal perception in different positions in colour space **X**, **Y**, **Z**. In other words, if one has two coloured plates 1 and 2 at a position in colour space **X**, **Y**, **Z** (for example, in the blue range) and two other plates 3 and 4 at another position (for example, in the red range), such that $r_{1,2} = r_{3,4}$, then the perception of these colour differences may be different. Researchers tried, therefore, to find other colour spaces with better properties in this regard. An example is the CIE $L^*a^*b^*$ colour space, which was modified on several occasions to provide a fully satisfactory solution.

The transition from **X**, **Y**, **Z** space to the CIE $L^*a^*b^*$ colour space is given by the following transformation:

$$\begin{aligned} L^* &= 116\cdot\left(\tfrac{Y}{Y_n}\right)^{1/3} - 16 \\ a^* &= 500\cdot\left[\left(\tfrac{X}{X_n}\right)^{1/3} - \left(\tfrac{Y}{Y_n}\right)^{1/3}\right] \\ b^* &= 200\cdot\left[\left(\tfrac{Y}{Y_n}\right)^{1/3} - \left(\tfrac{Z}{Z_n}\right)^{1/3}\right] \end{aligned} \tag{2.7-12}$$

Here, X_n, Y_n, Z_n are standard values obtained for the fully matt-white surface ($\beta_\lambda = 1$) at equal illumination (according to (2.7-10), $Y_n = 100$).

In CIE $L^*a^*b^*$ colour space L^* is proportional to brightness and a^* is the so-called green-red value, which changes from green ($a^* = -500$) to red ($a^* = +500$) for $b^* = 0$. Analogously b^* changes from yellow to blue and is called the yellow-blue value. The $L^*a^*b^*$ values are used for the objective assessment of colours and colour differences, which are measured using the distance

$$\Delta E = \sqrt{(\Delta L^*)^2 + (\Delta a^*)^2 + (\Delta b^*)^2}. \qquad (2.7\text{-}13)$$

The "equal distance property" of this measure is better than that of (2.7-11), but it is not ideal.

If the X, Y, Z values of an image are stored in a computer and one wants to make them visible, one has to use a colour output device such as monitor, printer or data projector. The problem is that all these devices have different colour spaces, which may be different even inside one category of devices (for example, from monitor to monitor). That means that a standard colour value X, Y, Z may stimulate the light emitting phosphors of each monitor differently, resulting in different impressions.

This problem is explained in more detail using the example of a cathode ray tube (CRT) monitor. To control the monitor there are three integer numbers R, G, B in the range [0,255]. These values are converted into three voltages which control three electron guns. The guns generate electron beams which activate the R, G, B phosphors on the screen to emit light with defined intensities I_R, I_G, I_B. This conversion is non-linear and, in general, differs from monitor to monitor. Methods exist, therefore, to standardize and calibrate monitors. If a monitor satisfies the sRGB standard defined by the International Electrotechnical Commission (IEC), the following transformation (www.srgb.com/basicsofsrgb.htm) holds. Firstly, the X, Y, Z values must be converted to R, G, B values by means of the linear transformation:

$$\begin{pmatrix} R \\ G \\ B \end{pmatrix} = \begin{pmatrix} 3.2406 & -1.5372 & -0.4986 \\ -0.9689 & 1.8758 & 0.0415 \\ 0.0557 & -0.2040 & 1.0570 \end{pmatrix} \cdot \begin{pmatrix} X \\ Y \\ Z \end{pmatrix}_{D65} \qquad (2.7\text{-}14)$$

Here, the X, Y, Z values are not normalized to 100 (see (2.7-10)) but to 1. The index D65 refers to the standard light D65 (see Fig. 2.7-3), which corresponds to mean daylight. To be precise, the objects should be illuminated with D65 light in order to measure their colours, because normal daylight or artificial light differs to some extent from D65.

It may happen that the R, G, B values from (2.7-14) take negative values or values which are greater than one. These values are set to zero or one, respectively. Then the non-linear transformations

$$R' = \begin{cases} 12.92 \cdot R & \text{if} \quad R \le 0.0031308 \\ 1.055 \cdot R^{0.4167} - 0.055 & \text{elsewhere} \end{cases} \qquad (2.7\text{-}15)$$

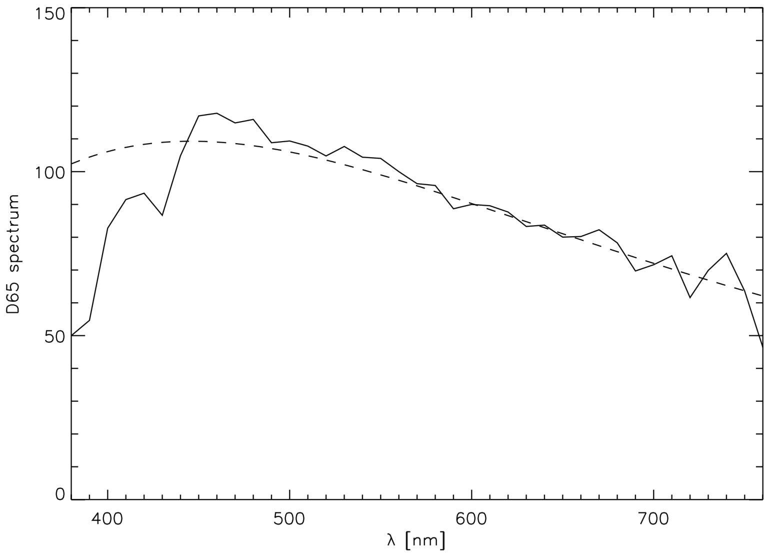

Fig. 2.7-3 Standard light D65 (*dashed line* shows black body radiation at 6,500 K)

and

$$R_{sRGB} = [255 \cdot R' + 0.5] \tag{2.7-16}$$

follow (analogously for G and B). $[x]$ is the integer part of the real number x.

Secondly, the values R_{sRGB}, G_{sRGB}, B_{sRGB} are transferred to the monitor. To assess the colours visually the monitor must be situated in a dark room.

If an sRGB monitor is used together with a true colour sensor and D65 illumination and the sRGB values have been generated according to (2.7-14), (2.7-15) and (2.7-16), the perceived colour impression should be nearly the same as if the illuminated object is being observed. This is the goal of the standardization. A parallel process exists for printers but is not considered here.

Cameras are commercially available that have standard spectral value functions, but most digital cameras have colour filters which deviate substantially from the standard spectral value functions (Fig. 2.7-2). This is especially true in the case of multispectral cameras such as Landsat-TM, SPOT and ADS40, in which relatively narrow spectral channels are implemented which are optimised not for the generation of true colour images but for purposes of remote sensing. With such sensors true colour can be created only approximately.

To discuss the problem in more detail, we consider a sensor with three narrow band RGB channels at λR, λG, λB. If the scene is illuminated with monochromatic light of wavelength λ which, for example, is positioned in the middle between λR and λG, then the sensor cannot detect any light and the colour which corresponds to the wavelength λ cannot be represented. The illuminated object is not seen by the sensor, but remains black. If the illumination is narrow-banded, therefore, overlapping spectral channels should be used. Airborne and spaceborne cameras for photogrammetry and remote sensing do not have this problem: the illumination is broad-banded and we can use narrow-band channels.

If a sensor has N spectral channels with the mid-wavelengths $\lambda 1, \ldots, \lambda N$, it generates N measurement values $S1, \ldots, SN$ (for every pixel). For normal digital cameras (red, green, and blue channel), $N = 3$. Multispectral sensors typically have $N < 10$ channels, whereas hyperspectral sensors may have $N > 100$ spectral channels, so we can generate three colour values X', Y', Z' according to

$$\begin{pmatrix} X' \\ Y' \\ Z' \end{pmatrix} = \begin{pmatrix} a_{1,1} & \ldots & a_{1,N} \\ a_{2,1} & \ldots & a_{2,N} \\ a_{3,1} & \ldots & a_{3,N} \end{pmatrix} \cdot \begin{pmatrix} S_1 \\ \ldots \\ \ldots \\ \ldots \\ S_N \end{pmatrix}. \qquad (2.7\text{-}17)$$

For certain classes of spectral data, this result may be adapted to the standard values X, Y, Z, which may be computed for these data according to (2.7-9). This approach was successfully implemented, for example, for the ADS40, in which the panchromatic channel added to the three colour channels R, G, B gives $N = 4$ (Pomierski et al., 1998). The procedure may also be applied to ordinary digital cameras ($N = 3$; colour calibration) if good true colour capability is required. This is especially useful if the output medium is calibrated too (for example, *sRGB* standard for monitors).

2.8 Time Resolution and Related Properties

In this section, we introduce formulae and relations to enable the user of airborne cameras to estimate the expected

- exposure times (integration times),
- data rates and volumes,
- camera viewing angles (FOV, IFOV) and
- stereo angles.

Figure 2.8-1 shows the array principle. It is assumed that the detector arrays (line or matrix) have been placed in the image plane of the lens. It is further assumed that the lens produces ideal geometric images without spherical aberration and, in the case of sensors with spectral filters, without chromatic aberration.

As shown in Fig. 2.8-1, the derivation can be performed using the theorem on intersecting lines and the ratio of the focal length of the lens f to the pixel size p with reference to the scanning distance GSD_y to flight altitude h_g (see (2.8-1)). For example, when $h_g = 1$ km, $f = 62$ mm and $p = 6.5$ µm, then $\mathrm{GSD}_y = 10.5$ cm. The distance GSD_y corresponds to the pixel size on the ground across the direction

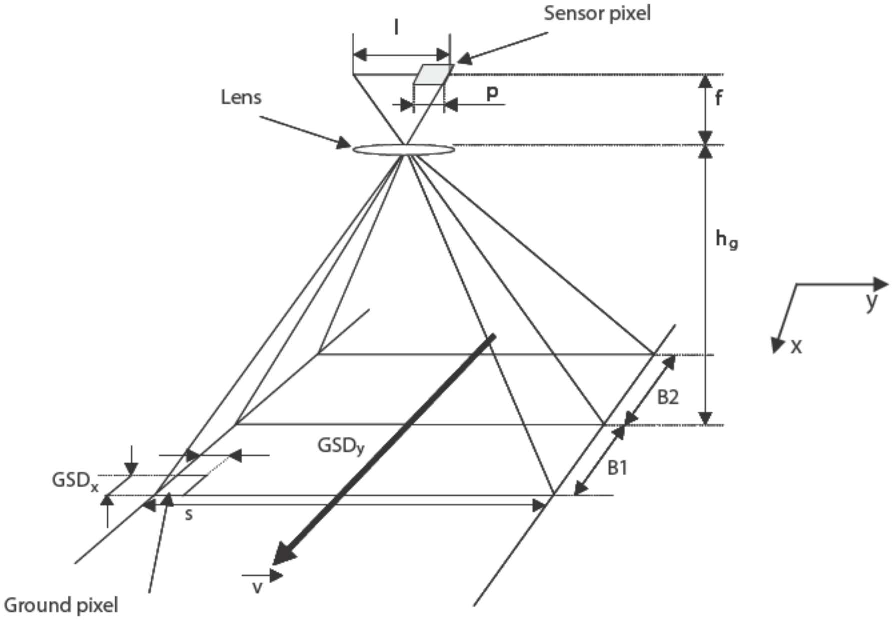

Fig. 2.8-1 Array principle illustrating the cinematic properties

of flight. In the flight direction, the pixel size is dependent on the sensor control (line camera) or the shutter control (matrix camera), with the exception of frame transfer matrix sensors. In some applications, the relationship (2.8-2) is unnecessary, since asymmetrical sampling is assumed. In the case of a quadratic pixel formation, (2.8-2) applies.

The sampling distance across the flight line is given by:

$$\mathrm{GSD}_y = \frac{p_y \cdot h_g}{f} \tag{2.8-1}$$

Where p is the cross-track pixel pitch; h_g, altitude above ground; f, focal length of the lens; and GSD_y, cross-track sampling distance.

The sampling distance GSD_x in direction of flight is given by

$$\mathrm{GSD}_x = \frac{p_x \cdot h_g}{f} \tag{2.8-2}$$

where p_x is the pixel size in the direction of flight. Note, the projection of the sensor pixel on the ground is smeared due to the aircraft velocity. The amount of smearing depends on the ratio of integration time and dwell time and needs to be restricted (see Equation 2.8-4). More quantitative assessment and the influence on the MTF is given in Section 4.10.2.

Flight speed v is an important variable in Fig. 2.8-1. As mentioned previously, in photogrammetry one usually tries to obtain square images. Dwell time (maximum cycle time for square sampling area) can be introduced for this approach. It is the time needed to bridge the extension of the pixel projection in the direction of flight. In line cameras, integration is started anew after each dwell time. In the case of a matrix system, the start of a new integration is delayed according to the number of pixels in the direction of flight and on the degree of overlap.

Geometric resolution in the case of integration times that correspond to the dwell time does not change as a result of smearing of an entire pixel. Equation (2.8-3) defines dwell time. This definition of the maximum possible cycle time (dwell time) sets the maximum possible integration time of both line and matrix cameras:

$$t_{\text{dwell}} = \frac{\text{GSD}_x}{v} \tag{2.8-3}$$

The data rates D_{line} and D_{matrix} refer to a collection of k sensors, each with a number N_P of pixels. The effective data rates of matrix and line cameras also differ, since matrix cameras are typically used with a 60% overlap to generate stereo images. The line camera data rate D_{line} in pixels per second is given by:

$$D_{\text{line}} = \frac{k \cdot N_p}{t_{\text{dwell}}} \tag{2.8-4}$$

The stereo matrix camera data rate D_{matrix} in pixels per second [results in 2.5 images per matrix frame] is:

$$D_{\text{matrix}} = \frac{k \cdot N_p \cdot 2.5}{t_{\text{dwell}}} \tag{2.8-5}$$

The data volume is also dependent on radiometric resolution [bits] and on image recording time [t_{image}]. The number of bits required is typically filled up to the next whole number byte limit. Thus, a 14-bit digital pixel value is represented by two bytes [16 bits]. A conversion convention is required for this form of representation. In most cases, the lowest-value bit of the 14-bit value is equated with the lowest-value bit of the 16-bit value. The data volume Dv in bytes is defined by:

$$\text{Dv[Byte]} = \frac{\text{pixel}}{s} \cdot t_{\text{image}} \cdot N_B \tag{2.8-6}$$

A finite number of pixels across the direction of flight is assumed for defining the FOV (field of view). For example, in a line camera this would be the number of pixels of the line sensor [Ns], and in the case of a matrix camera the cross-track dimension of the matrix. As shown in Fig. 2.8-1, this dimension determines the camera system's swath. The triangular relationships required for (2.8-7) and (2.8-8) can be readily understood if one imagines a plumb line from the nadir pixel along the system's optical axis:

$$\text{FOV} = 2 \cdot \arctan\left(\frac{0.5 \cdot Ns \cdot p}{f}\right) \tag{2.8-7}$$

The instantaneous field of view (IFOV) is given by:

$$\mathrm{IFOV} = \arctan\left(\frac{p}{f}\right) \tag{2.8-8}$$

The angle of convergence (stereo angle) describes the angle implemented by the sensor system to enable the camera to produce stereo images. This angle depends mainly on the focal length f of the lens. In the case of the line camera, the angle is determined by the distance Zs between the lines, which are parallel to each other. For the calculation (2.8-9) it is assumed that $Z's$ is defined as a nadir line. Thus, the angle of convergence can be calculated using Equation (2.8-9). In a three-line camera, the distances in relation to the nadir line are often implemented differently. Such a design has three different angles of convergence.

$$\alpha_{\mathrm{Stereo}} = \arctan\left(\frac{[\,|\,Zs - Z's\,|\,]}{f}\right) \tag{2.8-9}$$

In the case of the matrix camera, the angle of convergence depends on the focal length of the lens, the percentage of overlap, as discussed with respect to Equation (2.8-5), and the sensor [Equation (2.8-10)]. The assumption in (2.8-10) is that the minimum overlap is 50%, as otherwise there would be regions for which no stereo data can be generated. It can be very easily derived from Fig. 2.8-2. For this purpose, a relationship is established between the positions of the sensor and lens, on the one hand, and the overlapping area, on the other. As can be clearly seen from the figure, the convergence or stereo angle in matrix cameras can be influenced by the

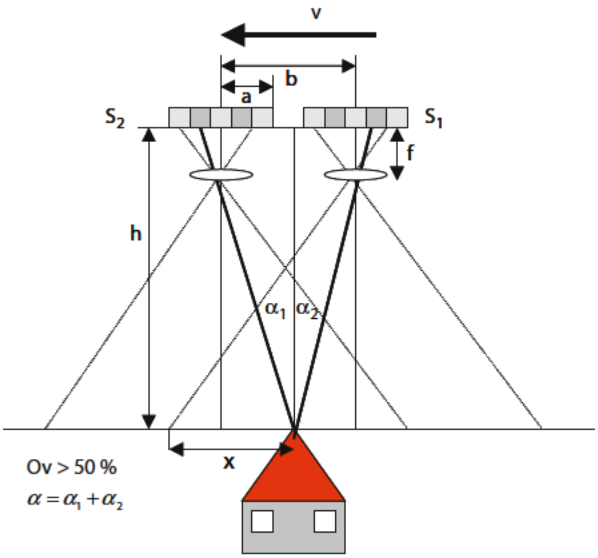

Fig. 2.8-2 Triangulation model, α is a function of the overlap *Ov*

percentage of overlap. But on the other hand, it is influenced by the minimum time required to read the matrix sensor. This imposes technological limits on the selection of the percentage overlap.

$$\alpha_{\mathrm{Stereo}} = \arctan\left(\frac{x}{h} + \frac{a}{f} \cdot (1 - 2Ov)\right) + \arctan\left(\frac{a}{f} - \frac{x}{h}\right) \tag{2.8-10}$$

An error parameter that directly influences the quality of stereo evaluation is the stereo base to flight altitude ratio (*B*/*h*). It can be clearly seen in Fig. 2.8-2 that in the case of matrix cameras, the base is dependent on the overlap set. Line cameras have fixed angles of convergence, which can also be combined. This is has been illustrated in Fig. 2.8-1. Bases B_1 and B_2 can be regarded separately or as a sum.

Thus, the general form (2.8-11) can be applied to both line and matrix cameras. Consequently, the error parameter *B/h* can be regarded as

$$\Delta \mathrm{err} = f\left(\frac{B}{h}\right) \tag{2.8-11}$$

The differences between the bases of a line camera make it possible, with the aid of an intelligent sensor control system, to include or exclude the lines with delay in order to generate relevant stereo data.

2.9 Comparison of Film and CCD

Imaging with film and solid-state detectors (which are summarily called CCDs in the following, although the radiometric quality of CMOS technology is almost equivalent) is described by different statistical theories. These have consequences for the characteristic curve and for different quality criteria, which can only be evaluated together with the camera system. Hence, a comparison can refer either, as in this section, to the fundamental physical boundaries, or to the practical consequences for a special camera system.

Knowledge of the fundamentals of the photographic imaging process, CCD technology and optical quantities is assumed here and can be drawn from, for example, Sections 2.4 and 4.3 of this book, Schwidefski and Ackermann (1976), Finsterwalder and Hofmann (1968), the *Manual of Photogrammetry* (McGlone et al., 2004), and the *Handbook of Optics* (Bass et al., 1995).

2.9.1 Comparison of the Imaging Process and the Characteristic Curve

Modern black and white film material features grain sizes in the range from 0.1 μm to 3 μm – a typical value is 0.5 μm (*Handbook of Optics*, Section 20.2). Each grain carries only 1-bit information (black/white) and it is necessary to invoke the concept of an "equivalent pixel", that is, a larger area, to allow the calculation of a gray value as the proportion of black grains to the total number of grains. This equivalent pixel size is defined, for example, by the MTF of the optics used, or by the pixel size of the film scanning process and is in practice larger than 4 μm [typical values for film scanning are 12–25 μm (McGlone et al., 2004, 402)].

A lower limit for the equivalent pixel is also the granularity of the film, which originates in a statistical clustering of grains and leads to variations in the gray value, even for homo-geneous illumination. In practice, at a transmission of 10% (corresponding to a logarithmic density of $D = 1$), the granularity lies between 0.8 μm for fine-grain film and 1.1 μm for coarse-grain film (Finsterwalder and Hofmann, 1968, 75).

Owing to the statistical distribution of the grains there is no aliasing in the original film.

At least three photons are theoretically necessary to blacken a grain, but in practice the figure is ten or more (Dierickx, 1999). A Poisson distribution can therefore be used to describe the likelihood that a grain is hit by a certain number of photons. The resulting cumulative distribution function for the event that three or more photons strike the grain (the characteristic curve) is non-linear. For a three-photon grain in the area of low exposure, it is initially proportional to the third power of the number of striking photons and only then reaches the linear part of the function (cf. Fig. 2.9-1). For a hypothetical one-photon grain, however, the density is proportional to the number of photons from the beginning, in the case of low exposure (Dierickx, 1999). The non-linear area at low exposure rates produces a gross fog level followed by a low contrast area.

The roughly linear part of the function comprises about two logarithmic units or 7 bits and is described by the contrast factor γ (maximum gradient of the characteristic curve), which for aerial films is in the range 0.9–1.5 (Finsterwalder and Hofmann,

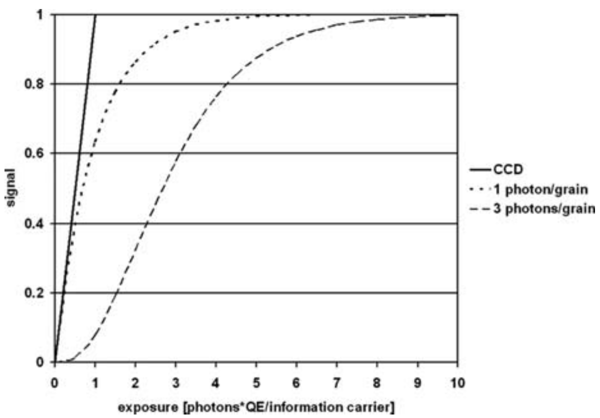

Fig. 2.9-1 Signal as a function of normalised exposure for an ideal CCD and two different models for film material

1968, 73). Above the linear part saturation occurs, followed by solarisation (a reversal of contrast in the case of extreme overexposure).

For statistical reasons, in contrast to a CCD, for a normalized exposure of 1 (i.e. the number of photons multiplied by the quantum efficiency is equal to the number of grains) complete blackening of film still does not occur, even for the one-photon grain. Correspondingly, the case of a normalized exposure of 3 and a three-photon grain does not show complete blackening either.

Compared to terrestrial photography, a steep characteristic curve is necessary because ground objects show low contrast when seen from the air. The ground reflectance typically lies between 2 and 40%, i.e. the object brightness dynamic range on the ground is 1:20. Due to superimposed aerial stray light, however, the object brightness dynamic range measured in the aerial camera is only about 1:8, depending on the atmosphere (Schwidefski and Ackermann, 1976, 78).

For CCDs the likelihood of the production of an electron is proportional to the number of photons. It is determined by the product of quantum efficiency (QE) and fill factor (FF), which can nowadays reach values around 0.5 (Dierickx, 1999). In the discussion below QE in fact always denotes the product QE*FF.

A CCD features a constant base signal from detector and amplifier noise and a strictly linear range which reaches close to the maximum number of charge carriers. This number depends mostly on the size of the pixel and determines the radiometric dynamics. For current pixel sizes of, for example, 6.5 μm, a linear range of more than 3 logarithmic units (12 bits) is obtained. Above the saturation level, normal CCDs show cross talk between other pixels (spilling or blooming). To prevent this, the CCD design has to include a so-called anti-blooming gate.

Granularity is given by the pixel size. Aliasing will occur from the regular arrangement of the pixels, as soon as object structures fall below the double pixel distance (Nyquist limit).

2.9.2 Sensitivity

The sensitivity of film is approximately proportional to the third power of the grain diameter (Finsterwalder and Hofmann, 1968, 74), proportional to the quantum efficiency of the grains and inversely proportional to the number of grains per equivalent pixel. Coarse-grained film has lower radiometric dynamics and worse spatial resolution, however, caused by the smaller number of grains per equivalent pixel. So for high image quality a film with medium sensitivity has to be chosen.

For CCDs the sensitivity is proportional to fill factor, proportional to quantum efficiency and inversely proportional to the maximum number of electrons per pixel.

The absolute sensitivity is higher for CCDs than film with the same pixel size, due to the high quantum efficiency (1 photon per electron compared to 3–20 photons per grain). The practical consequence is that the pixel size of the CCD is reduced (for example., 6.5 μm for CCDs compared to 15 μm for film) in order to reach a similar sensitivity to that of film. Thus, through the use of a substantially smaller focal plane (approximately 80 × 80 mm compared to 230 × 230 mm), a CCD camera can more compact.

2.9.3 Noise

CCDs exhibit noise accumulating with time, even under dark conditions. This is independent of the incoming light signal and can be subtracted. It sets an upper boundary for the exposure time of normal CCDs in the range of a few minutes, which is, however, irrelevant to photogrammetry. Film shows no such dark noise.

Furthermore, CCDs display so-called shot noise, which is signal-dependent and is caused by statistical variations in the number of incoming photons:

$$N_{\text{noise\_electrons}} = \sqrt{N_{\text{electrons}}}$$

For films, we have to face discretization noise, given for low exposure by the number of activated grains within an equivalent pixel with total number of grains N_{total}. Therefore it is comparable to the noise of a CCD pixel:

$$N_{\text{noise\_grains}} = \sqrt{\frac{N_{\text{black\_grains}}\ N_{\text{white\_grains}}}{N_{\text{total}}}} \approx \sqrt{N_{\text{black\_grains}}} \quad \text{(for low exposures)}$$

2.9.4 Signal to Noise Ratio (SNR)

The signal to noise ratio (SNR) is defined as the relationship between useful signal and noise signal:

$$\text{SNR} = \frac{N_{\text{photons}}}{N_{\text{noise\_photons}}}$$

The SNR of a CCD is proportional to the square root of the incoming photons N per equivalent pixel with a quantum efficiency QE:

$$\text{SNR} = \sqrt{\text{QE}\,N}$$

Thus the highest obtainable SNR is proportional to the square root of the pixel surface.

For a hypothetical one-photon grain the SNR is calculated as follows (Dierickx, 1999):

$$\begin{aligned}
\text{SNR} &= \sqrt{\text{QE}\,N}\ \frac{\sqrt{\alpha}}{\sqrt{\frac{1-\exp(-\alpha)}{\exp(-\alpha)}}} \\
\text{SNR} &\approx \sqrt{\text{QE}\,N} && \text{(for low exposures, } \alpha \text{ small)} \\
\text{SNR} &\approx \sqrt{\text{QE}\,N}\sqrt{\alpha\ \exp(-\alpha)} && \text{(for high exposures, } \alpha \text{ large)}
\end{aligned}$$

where $\alpha \equiv \frac{\text{QE}\,N}{N_{\text{total}}}$ and N_{total} is the number of grains per equivalent pixel. The corresponding formula for a three-photon grain is more complex.

In order to make a direct comparison of the signal dependent SNR, a CCD pixel with 10,000 electrons is shown in Fig. 2.9-2 together with an equivalent pixel with 10,000 one-photon grains and with 10,000 three-photon grains. The x axis is the

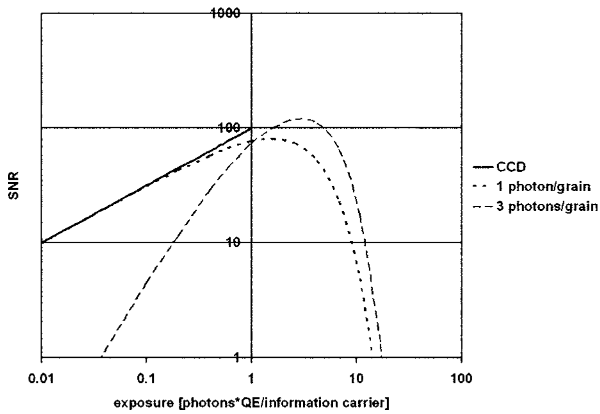

Fig. 2.9-2 Signal to noise ratio (SNR) as a function of the normalized exposure for an ideal CCD and two different models for film material; the maximum number of information carriers in each case is 10,000

normalized exposure (number of photons * quantum efficiency per total number of grains or electrons).

The comparison shows that for low exposures the ideal CCD and the one-photon grain behave identically and increase with the square root law up to saturation. Above saturation the SNR of the one-photon grain drops rapidly, approximately like that of the three-photon grain, and vanishes at tenfold overexposure within the noise. It can be seen again that, for film, a normalized exposure of one does not correspond to a complete activation.

While the one-photon grain has a good SNR also at low exposures, the three-photon grain can be used only from a tenth of the normalized exposure onwards.

2.9.5 Dynamic Range

The achievable dynamics are defined by the ratio of maximum signal to noise signal in the dark. This is bigger than the SNR because the dark signal does not contain any signal dependent noise.

For the comparison between film and CCD the definition should be refined as follows: the dynamics is the exposure range between the lower and upper point where the SNR SNR= 1.

From Fig. 2.9-2 the dynamics evaluate to:

Object	Dynamics
CCD	Maximum number of load carriers per pixel
One-photon grain	Tenfold number of grains per equivalent pixel
Three-photon grain	Multiple of the square root of the number of grains per equivalent pixel

In CMOS technology detectors with a logarithmic characteristic curve were developed to increase the dynamics.

To increase the dynamics in film emulsions, however, grains of different sizes can be mixed. Furthermore, the number of grains per unit area of the surface can be increased, though this lowers the sensitivity owing to smaller grains.

2.9.6 MTF

The MTF is determined by the distance between the information carriers. As can be seen in Fig. 2.9-3, film with a granularity in the range of 1 μm has an advantage over a CCD with 10 μm pixel size, even if one considers an equivalent film pixel of 10 μm.

The film MTF is modeled here by a Gaussian function:
$\mathrm{MTF} = \exp(-2\,(\text{resolution} \cdot 2\sigma)^2)$, where 2σ is the equivalent pixel size.

The CCD MTF is shaped like a $\frac{|\sin(\text{resolution} \cdot 2\pi\sigma)|}{\text{resolution} \cdot 2\pi\sigma}$ curve with a pixel distance of 2σ. The useful resolution is limited to the Nyquist frequency by aliasing between regular CCD structures. The theoretical resolution of the film is limited by both the MTF of the lens system and the shot noise, which increases drastically for higher resolutions.

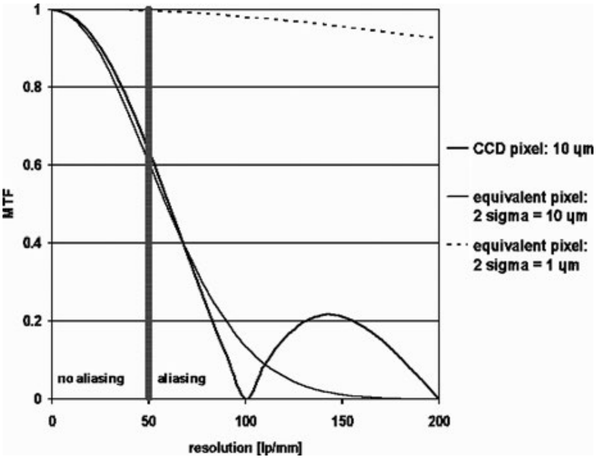

Fig. 2.9-3 MTF for 10 μm CCD pixel in comparison with a 10 μm equivalent film pixel and a diffraction-limited 1 μm grain; the *gray bar* denotes the position of the Nyquist frequency for a pixel distance of 10 μm

2.9.7 MTF · Snr

From the above it seems reasonable to consider the product of MTF as a function of the resolution and maximum SNR for a structure of the size of a line pair. The maximum obtainable SNR increases, for film as well as for CCDs, with the square

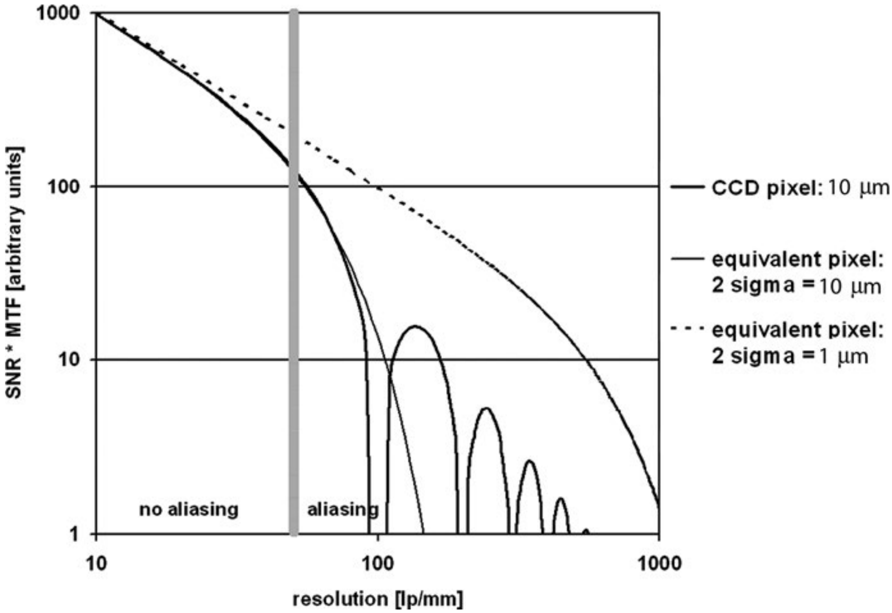

Fig. 2.9-4 SNR·* MTF for a 10 µm CCD pixel in comparison to a 10 µm equivalent film pixel and a diffraction-limited 1 µm grain with ideal illumination; the *gray bar* denotes the position of the Nyquist frequency for a pixel distance of 10 µm

root of the incoming photons, which are proportional to the area of the surface, i.e. inversely proportional to the square of the resolution. Hence, the SNR is inversely proportional to the resolution in this case.

As can be seen in Fig. 2.9-4, film is also better in this case, because it shows no aliasing and, for statistical reasons, it can reach double the Nyquist frequency, even for the same equivalent pixel size, while the CCD is limited to the Nyquist frequency.

2.9.8 Stability of Calibration

The geometric position and stability of the CCD can be fixed by appropriate methods of construction such that the images are reproducible, subject to the same operating conditions, within fractions of a pixel.

During the process of film development, i.e. the extraction of the unexposed silver halide crystals, a persistent shrinking of up to 69 µm across the film width of 230 mm occurs. This is partially compensated by the lower temperature and humidity during image acquisition (a 10% increase in humidity or a 5°C increase in temperature causes an expansion of 23 µm across the film width). This dimensional change can be measured using the fiducial marks exposed on the image and then taken into consideration.

Film, however, does not show radiometric stability. Apart from manufacturing tolerances in the emulsion, the sensitivity can be influenced, by a factor of 10, by the type of developer and the developing time by a factor of 10 (Schwidefski and Ackermann, 1976, 93). Furthermore, the colour sensivity of colour films changes with storage conditions. A reliable radiometric calibration can therefore be obtained only within a specific block of aerial imagery.

On the other hand, solid-state detectors can be calibrated well in the VISNIR range and are radiometrically stable for years. A prerequisite for this is a good thermal stabilisation of the focal plane to keep the thermal noise constant.

2.9.9 Spectral Range

Several types of film emulsions have been developed over time for different applications. Black-and-white film types include ortho film (blue-green-sensitive), now obsolete, pan film (blue-green-red) and infrared film, which is sensitive in the near infrared (blue-green-red-NIR). Colour film types include colour RGB film and the colour infrared film used in vegetation analysis (false colour IR film, FCIR). In an FCIR image the colours are shifted (green to blue, red to green and NIR to red). Finally, there are special emulsions for certain wavelengths, which have not been used extensively. To reduce the spectral bandwidth of the film, edge filters are available which are transparent beyond a certain wavelength. For example, a yellow haze filter can decrease atmospheric effects which occur especially in blue light.

Solid-state detectors have a spectral sensitivity that is determined to a great extent by the semiconductor material. The sensitivity of the widespread silicon CCD is limited in the long wavelength range by the band gap of silicon at 1,050 nm. Unfortunately, no semiconductor material yet known is suitable for the short wave infrared (SWIR) in terms of the necessary number of pixels and read-out rate for a high resolution airborne imaging camera. The sensitivity boundary of conventional CCDs in the blue at 400 nm can be lowered by special coatings down to 170 nm, as is done in laboratory spectrometers. Owing to the high sensitivity of CCDs, both broad-band filters with overlapping spectral bands and narrow-band interference filters can be used. The latter are more suitable for remote sensing. For film, however, the number of colour layers is limited to three, whereas additional channels can be used in the CCD technology.

For frame sensors, broad band colour filters are usually deposited directly on the chip surface in a square 2 by 2 pattern (for example, the RGGB Bayer pattern). In this way the actual geometric resolution decreases in both directions by a factor of two and the number of channels is limited to four! Alternatively, one can use separate a CCD sensor for each channel, which requires either separate lenses for each band or a telecentric lens with large rear focal length and a dichroitic beam splitter. For line sensors it is possible to put a series of stereo channels in full resolution in the focal plane following the multiple-line principle of Hofmann. With a telecentric lens and a dichroitic beam splitter, the spectral channels can be spatially coregistered.

2.9.10 Summary

For statistical reasons CCDs feature a higher dynamic range and a better sensitivity than film. This could be changed only by the development of a one-photon grain film.

Owing to the small grain size and an adjustable equivalent pixel size, film can deliver a higher geometric resolution, which, however, strongly reduces radiometric dynamics. For film also no aliasing occurs for small object structures. Film is more versatile at high resolutions, therefore, but the overall imaging quality is not better. Geometric stability is controllable in both film and CCD.

The big advantage of CCDs is that signal-dependent noise is independent of the maximum possible dynamic range. Thus faint signals can still be resolved well and, hence, CCD is more tolerant of underexposure.

Film is suited, owing to its non-linear characteristic curve, to the logarithmic sensitivity of the human eye, which makes it useful for direct visual interpretation. Modern image processing systems, however, allow the arbitrary stretching of the characteristic curve of digital data from CCDs. Furthermore, film offers the possibility of relatively long-lasting, compact archiving independent of the processing system, something which still has to be developed for digital data. A serious disadvantage of film is the lack of radiometric stability of the photo-chemical process, which prevents radiometric calibration.

The good linearity and radiometric stability of CCDs permits a calibration of the camera to absolute radiances and thus allows reproduceable measurements, which are also suitable for remote sensing. This makes it possible to calculate true ground reflectances by correcting for the effects of the atmosphere and for reflection dependent on view angle.

2.10 Sensor Orientation

2.10.1 Georeferencing of Sensor Data

The determination of exterior orientation the location and attitude of the sensor at the instant of exposure is a central topic for the acquisition of sensor data. It is unimportant whether the system is an imaging or non-imaging one, or whether it is area- or line-based. The relationship between the internal sensor coordinate system and the object coordinate system – often the national coordinate system – is important for all sensors as a precondition for data acquisition. The relationship between the sensor and the object space is called georeferencing. There is a basic difference between direct and indirect geo-referencing. The optimal method of orientation depends upon the required accuracy, the financial conditions and the time available. Taking this into account, a combination of direct and indirect methods can also be chosen. Called integrated sensor orientation, this also facilitates an efficient calibration of the whole sensor system as well as verification in the project area.

2.10.1.1 Relationship Between Sensor and Object Space

The mathematic model used in photogrammetry is usually based on the central perspective condition, simplifying the projection as linear rays. In most cases the bundle of rays in the sensor space is expected to be identical to the bundle of rays in the object space. Different positions of the entrance node and the exit node do not influence this relationship. This means that the object point P, the projection centre O and the corresponding image point P' are located on a straight line (Fig. 2.10-1). A perfectly flat focal plane is expected.

The geometric relationship between image point, object point and projection centre is the same whether the focal plane is treated as negative, as occurs during imaging, or as positive, the usual way to view the image. The relationship between the image point and the object point can be expressed by the collinearity condition (Fig. 2.10-2), which means that image point, projection centre and object point are located on a straight line.

The projection centre is the origin of the three-dimensional image coordinate system with the components $\mathbf{x}'(x', y', -f)$ and f as the calibrated focal length (Fig. 2.10-3). The image coordinate system is usually rotated by the attitudes ω, ϕ, κ with respect to the object coordinate system. The image coordinates in the object coordinate system are named $\mathbf{u}(u, v, w)$.

The object coordinate vector $\mathbf{X}(X, Y, Z)$ is identical to the position of the projection centre $\mathbf{O}(X_0, Y_0, Z_0)$ plus the sensor coordinate vector $\mathbf{p}$ as $\mathbf{u}(u, v, w)$ multiplied by a scale factor λ.

$$\mathbf{X} = \mathbf{X}_0 + \mathbf{p} \cdot \lambda \tag{2.10-1}$$

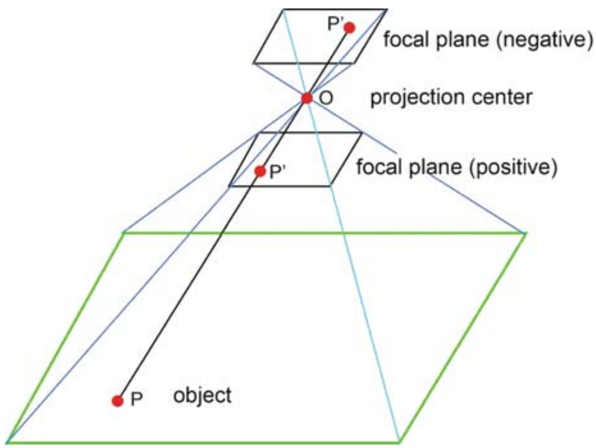

Fig. 2.10-1 Imaging with central perspective

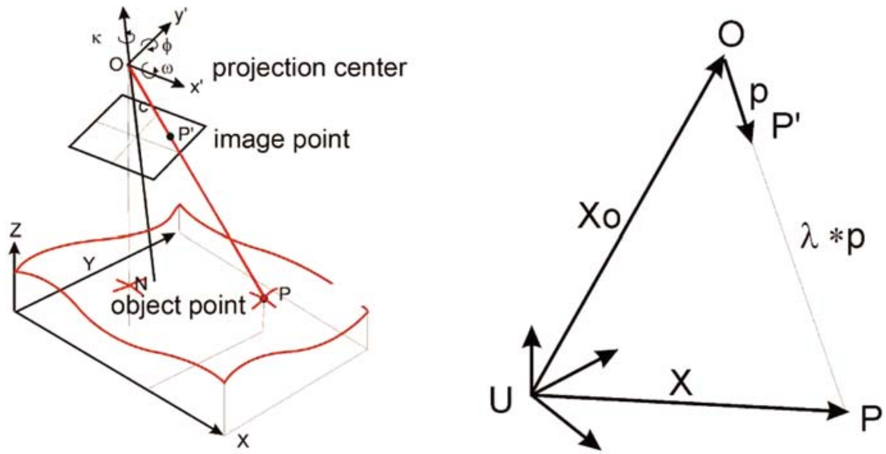

Fig. 2.10-2 Basic relationship of the collinearity condition

Fig. 2.10-3 Image coordinate system

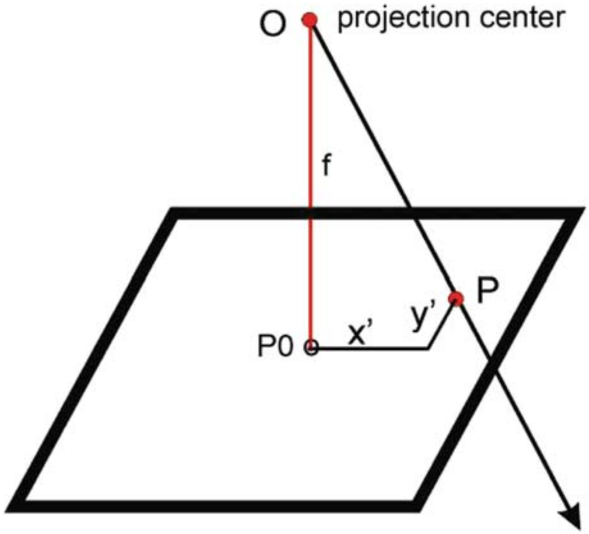

Only the components x' and y' of the coordinate vector $\mathbf{p}$ can be measured and not (u,v,w); this requires a transformation of the image coordinates with the rotations $\mathbf{R}(\omega,\phi,\kappa)$.

$$\mathbf{x}' = \mathbf{R} \cdot \mathbf{u} \qquad (2.10\text{-}2)$$

The rotation is performed by the rotation matrix **R**, determined by multiplication of the individual rotation matrices.

$$\mathbf{R}(\omega)=\begin{bmatrix}1 & 0 & 0\\ 0 & \cos\omega & -\sin\omega\\ 0 & \sin\omega & \cos\omega\end{bmatrix},\mathbf{R}(\phi)=\begin{bmatrix}\cos\phi & 0 & \sin\phi\\ 0 & 1 & 0\\ -\sin\phi & 0 & \cos\phi\end{bmatrix},$$
$$\mathbf{R}(\kappa)=\begin{bmatrix}\cos\kappa & -\sin\kappa & 0\\ \sin\kappa & \cos\kappa & 0\\ 0 & 0 & 1\end{bmatrix} \tag{2.10-3}$$

Usually the rotation matrix **R** is handled with rotated axes. The individual rotation matrices have to be multiplied corresponding to the sequence of rotations. Usually the sequences ω,ϕ,κ and ϕ,ω,κ are used. Equation (2.10-4) is based on rotated axes with the sequence ω,ϕ,κ:

$$\mathbf{R}=\mathbf{R}(\omega)\cdot\mathbf{R}(\phi)\cdot\mathbf{R}(\kappa)=$$
$$\begin{bmatrix}\cos\phi\cos\kappa & -\cos\phi\sin\kappa & \sin\phi\\ \cos\omega\sin\kappa+\sin\omega\sin\phi\cos\kappa & \cos\omega\cos\kappa-\sin\omega\sin\phi\sin\kappa & -\sin\phi\cos\phi\\ \sin\omega\sin\kappa-\cos\omega\sin\phi\cos\kappa & \sin\omega\cos\kappa+\cos\omega\sin\phi\sin\kappa & \cos\omega\cos\phi\end{bmatrix} \tag{2.10-4}$$

The relationship between the object coordinates and the image coordinates (2.10-1) with the rotation matrix inserted and inverted for the image coordinates leads to the collinearity equations if the unknown scale factor λ is expressed by the relationship for the focal length.

$$x'=\frac{a_{11}\,(X-X_0)+a_{21}\,(Y-Y_0)+a_{31}\,(Z-Z_0)}{a_{13}\,(X-X_0)+a_{23}\,(Y-Y_0)+a_{33}\,(Z-Z_0)}$$
$$y'=\frac{a_{12}\,(X-X_0)+a_{22}\,(Y-Y_0)+a_{32}\,(Z-Z_0)}{a_{13}\,(X-X_0)+a_{23}\,(Y-Y_0)+a_{33}\,(Z-Z_0)} \tag{2.10-5}$$

The collinearity equations define the relationship between the image coordinates and the object coordinates with a_{nm} as rotation matrix coefficients. It is valid for area sensors as well as for line sensors. In the line sensors the y' coordinates do not exceed 0.5 pixels if a geometric deviation for non-linear sensor lines is included as a correction.

2.10.1.2 Self-calibration with Additional Parameters

The mathematic model of the perspective relationship is a good approximation, but not a sufficient description of the real geometric situation. There are different sources of deviation from this model and no exact prediction is possible. Usually the accuracy of traditional analogue film cameras is limited by imperfect flatness of the film during exposure as well as systematic film deformations. This is not the case for CCD cameras. In both cases there is an influence of the optical system on the image geometry. We may have a radial symmetric distortion and also tangential distortion caused by lenses that are not centric. The imaging system may be influenced by air pressure, temperature changes and temperature gradients within the optics. Analogue cameras in particular have different conditions for each photo flight. The systematic deviation of the real image geometry from the perspective model is named systematic image error, even if it is caused by an imprecise mathematical model. Such systematic image errors can be estimated, at least partially, from bundle adjustment with self-calibration by additional parameters. By a combination of additional parameters nearly any type of deviation from the perspective model, except local ones, can be adjusted based on over-determination of the block adjustment.

Different sets of additional parameters are in use. The Ebner parameters (Gotthard, 1975) are based on systematic image errors in a grid of nine points by polynomials. This leads to the following set of formulae:

$$\begin{aligned} \Delta x &= P1 \cdot y' + P2 \cdot x' \cdot y' + P3 \cdot y'^2 + P4 \cdot x'^2 \cdot y' + P5 \cdot x' \cdot y'^2 \\ \Delta y &= P6 \cdot y' + P7 \cdot x'^2 + P8 \cdot x' \cdot y' + P9 \cdot x'^2 \cdot y' + P10 \cdot x' \cdot y'^2 \end{aligned} \tag{2.10-6}$$

Pn are the unknown coefficients of the additional parameters. A similar parameter set for a grid of 25 image points has been developed by Grün (1978). Such polynomials are not easy to analyse. For example, the often dominant radial symmetric distortion has to be compensated by a group of parameters. Furthermore, the parameters are correlated if the image points are not exactly located at the raster positions used for the formulae. Jacobsen (1982) developed a set of parameters describing the most important physical influences directly. This set also requires some general parameters, to compensate effects not covered by the physically justified ones:

$$\begin{aligned} \Delta x =\ & P1 \cdot y' + P2 \cdot x' + P3 \cdot x' \cdot \cos 2\beta + P4 \cdot x' \cdot \sin 2\beta + P5 \cdot x' \cdot \cos\beta \\ & + P6 \cdot x \cdot \sin\beta - P7 \cdot y' \cdot r \cdot \cos\beta - P8 \cdot y' \cdot r \cdot \sin\beta + P9 \cdot x'(r - C1) \\ & + P10 \cdot x' \cdot \sin(r \cdot C2) + P11 \cdot x' \cdot \sin(r \cdot C3) + P12 \cdot x' \cdot \sin 4\beta \\ \Delta y =\ & P1 \cdot x' - P2 \cdot y' + P3 \cdot y' \cdot \cos 2\beta + P4 \cdot y' \sin 2\beta + P5 \cdot y' \cdot \cos\beta \\ & + P6 \cdot y \cdot \sin\beta - P7 \cdot x' \cdot r \cdot \cos\beta - P8 \cdot x' \cdot r \cdot \sin\beta + P9 \cdot y'(r - C1) \\ & + P10 \cdot y' \cdot \sin(r \cdot C2) + P11 \cdot y' \cdot \sin(r \cdot C3) + P12 \cdot y' \cdot \sin 4\beta \end{aligned} \tag{2.10-7}$$

β describes the angle of the image vector with respect to the x' -axis. $C1 - C3$ are constant values depending upon the sensor size. $P1$ expresses the angular affinity, $P2$ the affine deformation, $P7$ and $P8$ the tangential distortion, and $P9$–$P11$ the radial symmetric distortion. Both sets of additional parameters can be used for area sensors, but must be changed for line sensors, which require different additional parameters. The most important parameter for the radial symmetric distortion is based on the third power of the image radius. For line sensors it is reduced to:

$\Delta x = P9 \cdot \left|(x' - C)\right|^3$. The constant value C describes the zero crossing of the distortion, which is required to avoid a correlation with the focal length. The parameter $P1$ in (2.10-7) describes the deviation of the line with respect to the direction perpendicular to the flight direction, while $P2$ in (2.10-7) is a scale factor for speed and time. It is also possible to include special parameters for images based on a connection of sub-scenes (Jacobsen, 1998) or other special geometric sensor problems. An alternative set of physically justified parameters has been developed by Brown (1971) for close-range images.

Self-calibration with additional parameters leads to considerable improvements of the image orientation and takes into consideration the real sensor geometry. Digital sensors have more stable inner geometry than film sensors, making a system calibration over a test field simpler and allowing the use of calibration results for a priori improvement of other blocks.

2.10.1.3 Indirect Georeferencing

Traditionally the image orientation of area sensors is determined indirectly. Using ground control points (points with known object and image coordinates), sensor orientation is computed by resection for single images and by bundle block adjustment for more than one image. The mathematical model is perspective geometry represented by the collinearity equation. For the 6 unknowns of a single image ($X_0, Y_0, Z_0, \omega, \phi, \kappa$) at least 3 control points are required – x' and y' of 3 image points provide 6 observations, the required minimum for 6 unknowns. Usually we have a block of images with endlap of 60% and sufficient sidelap, in which case the images can be connected by tie points (object points with corresponding image coordinates in at least 2 images). So by bundle block adjustment the image orientations and the object coordinates of tie points can be estimated based on a minimum of ground control points. To achieve an orientation accuracy of the same order as for single models (combination of 2 images with at least 60% overlap), full control points (with X, Y and Z object coordinates) are required in the boundary area of the block spaced at every 4–6 base lengths. The base length b is the distance between two neighbouring projection centres in the same flight line. Additional vertical control points (with known Z coordinates only) are required in sidelap areas approximately every 4 base lengths (Fig. 2.10-4). A larger spacing between control points leads to a lower absolute accuracy, but does not influence the relative accuracy.

An insufficiency and/or unfavourable distribution of vertical control points may cause instability in the geometry of the block. Traditional bundle block adjustment with ground control points is operational, but the determination of ground control points, including the manual measurement of their locations in the images, is time consuming. For this reason additional observations have made for a considerable time in order to reduce the number of ground control points. But only with the advent of relative kinematic GPS positioning did this become operational. The relative positions of the projection centre coordinates can be determined by GNSS, usually as a GPS solution, with higher accuracy, allowing a drastic reduction in the

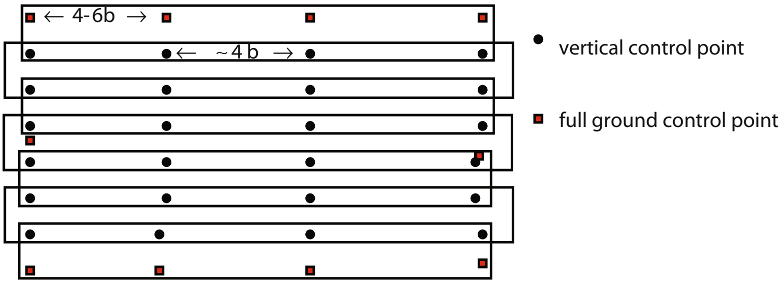

Fig. 2.10-4 Required control point distribution for a usual block with 60% endlap and 20–40% sidelap

number of control points required. The hybrid method of combined adjustment uses GPS coordinates of the projection centres as additional observations to the image coordinates and the few required ground control points.

Kinematic GPS positioning may be influenced by ambiguity problems, causing systematic positional errors, mainly shifts, and sometimes also time-dependent drift problems. These systematic errors may be different for the individual flight lines, caused by cycle slips during the turn from one flight line to the next. Additional shifts, and sometimes also drift parameters, have to be added to the combined block adjustment, requiring additional crossing flight lines, called cross strips (Fig. 2.10-5), or lines of control points at the ends of the flight lines. With cross strips, control points are required only in the corners of the block if the length of

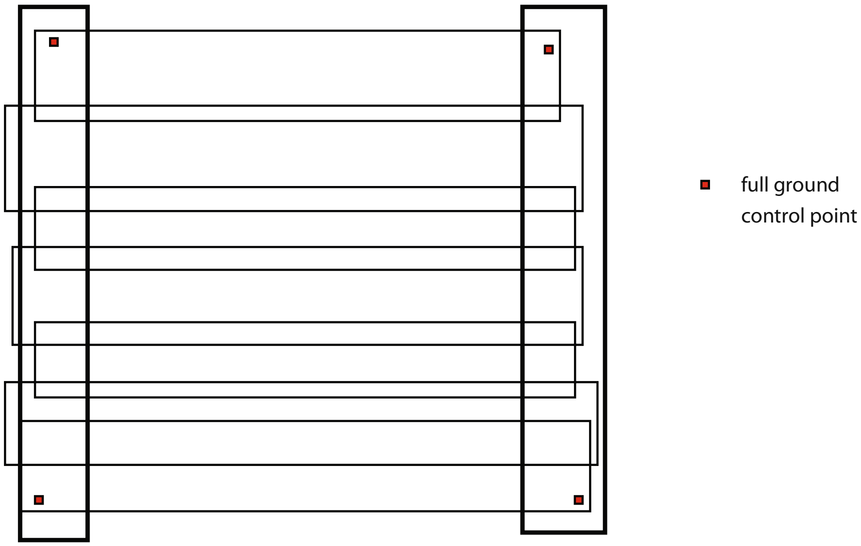

Fig. 2.10-5 Required number and distribution of control points for combined block adjustment with GPS coordinates of the projection centres, supported by crossing flight lines (cross strips)

the flight lines does not exceed 30 images. Of course, under operational conditions and for reasons of reliability, double control points (located close together), rather than single control points, should be used in the corners. For very long flight lines control points every 30 base lengths are required at the block boundaries. With such a configuration the cost of control point determination is minimized.

2.10.1.4 Orientation of Line-Scanner Images

Each perspective image has a unique geometry for the whole area it covers, whereas line scanners have a different exterior orientation for every line. But the exterior orientation does not change suddenly: it changes continuously and is differentiable. In the extreme case of satellite images, we have no change of the attitudes in relationship to the orbit. For aerial applications, neighbouring lines at least can be grouped together, allowing a functional model for the change of the orientation parameters. If the sensor orientation is determined by a combination of kinematic GPS positioning with inertial data, the exterior orientation for any line is given and in theory no block adjustment is required. If stereo line-scanner images are used for manual measurement, y-parallaxes may be present, disturbing the stereoscopic impression (Gervaix, 2002). This problem can be solved by aerial triangulation of line-scanner images.

Line-scanner images can also be oriented by means of bundle adjustment. Of course it is not possible to determine the orientation of each line separately; they have to be joined together in groups, requiring a functional model of the change of the orientation. The orientation of the group centre line will be computed. These centre lines are named orientation fixes (Müller, 1991). The adjustment of the line-scanner images is different to the adjustment of perspective area images since the effect of the roll and pitch angles with respect to the ground coordinate system is different. The effect of approximations is negligible if they are determined by the combination of GPS with inertial data and only a small improvement, especially for the elimination of the y-parallaxes, is achieved. Two- and three-line sensors such as the ADS40 or the HRSC enhance the stability of the orientation since the exterior orientation is basically the same for all lines taken at the same instant.

Based on the orientation fixes, the exterior orientation of line-scanner images can be determined by a modified bundle solution with tie and control points. The geometric relationship shown in Fig. 2.10-6 is valid for all orientation parameters with the exception of the different view directions. Without control points the datum (shift in X, Y, Z) and drift cannot be computed and the bundle block adjustment is limited to a relative improvement, reducing the y-parallaxes and facilitating manual, stereoscopic data acquisition with line-scanner images. Only a few applications require an absolute improvement of the orientation from combined GPS and inertial data. Of course, control points are required if no GPS and inertial data are available. In theory image orientation from three-line-scanners can be determined, without additional orientation information, with an accuracy similar to perspective area images. For single-line-scanner images, only approximations depending upon

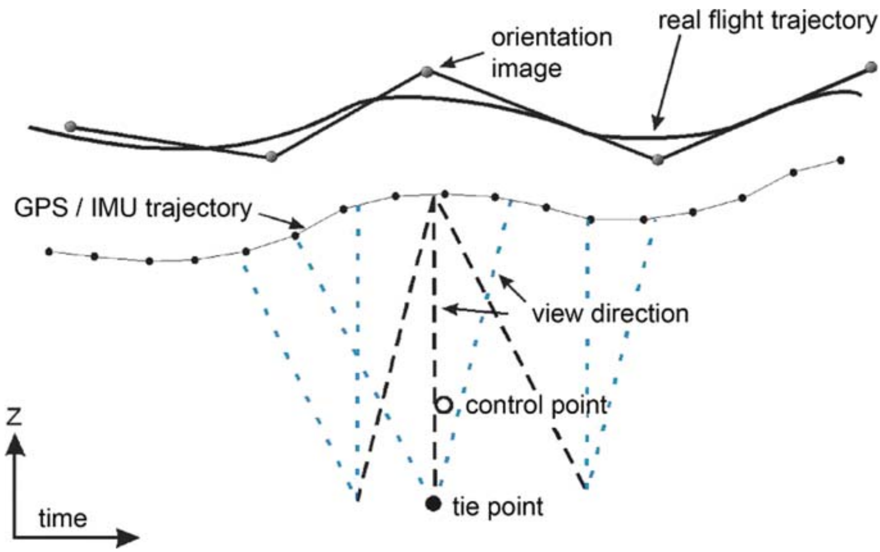

Fig. 2.10-6 Geometric situation for line- scanner bundle orientation

the changes of the exterior orientation can be computed. For ADS40 scenes generated by combined adjustment of the GPS and inertial information together with tie and control points, an object point accuracy can be reached in the range of one to two thirds of ground sampling distance for the horizontal component and around the ground sampling distance for the vertical component.

2.10.1.5 Direct Georeferencing

The trend in photogrammetric data acquisition from classical topographic mapping to applications that are close to online requires a faster and more efficient orientation process. Indirect georeferencing of sensor data has some limits for close to online applications. The orientation process is a bottleneck in the whole process chain, since it has to be completed before the next step can ensue. For time critical applications, therefore, the time required for the indirect orientation is unacceptable. Furthermore, for block adjustment a more or less regular location of the images with sufficient overlap is required, causing problems for small and irregular projects, especially if gaps between images cannot be avoided. Traditional orientation, moreover, cannot be used unchanged for non-imaging systems and new sensor types such as line scanner, laser scanner or synthetic aperture radar. Such systems require a direct determination of all orientation elements. An integrated system for the determination of positions and attitudes is available with the combination of GNSS and inertial sensors. This separates the orientation process from the data capture and enables the determination of the orientation elements for any instant. The computation of the orientation based on GNSS and inertial systems is potentially faster than the process of indirect georeferencing with control points. In addition, no special block configuration is required, the procedure can be used for any type of sensor and isolated areas can be covered.

2.10.2 Brief Review of GVP Concepts GPS

The NAVSTAR Global Positioning System (GPS) was originally developed by the US Department of Defense as a worldwide satellite-based radio navigation system for dual-use: to enhance the effectiveness of military forces and – rapidly growing – for civilian applications. It is made up of a network of GPS satellites continuously orbiting the Earth. The satellite receivers of all users define the user segment of the system. Each receiver picks up the signals from the GPS satellites and processes the results to determine three-dimensional information on current position, velocity and (when using special multi-antenna GPS receivers or a set-up of several receivers) attitude. All this is obtained with high absolute and consistent accuracy, anywhere in the world,[1] day and night, in any weather conditions.

The completely installed GPS space segment, which has been fully operational since July 1995, consists of 24 active satellites in six different orbit planes, with four satellites in each. The actual number of satellites is variable, depending on the status of individual systems. The radius of the almost circular orbits is about 26,500 km from the centre of the Earth. The inclination of each orbit plane is 55°. With a revolution time of 12 h (sideral time) and the above inclination, between 6 and 11 satellites with an elevation angle above 5° are typically visible and can be used for navigation on Earth. Nonetheless, the system providers guarantee the availability of only four satellites. The GPS satellites continuously transmit two low-power radio signals in the L-band. These carrier frequencies are L1, 1,575.42 MHz, and L2, 1,227.60 MHz. The frequencies are obtained as multiples of the fundamental GPS clock rate of 10.23 MHz. Two different binary codes are superimposed on the carrier, the less accurate C/A-code (on L1 band) and the precise P-code (L1 and L2 bands). The Y-code is used in place of the P-code whenever the antispoofing (A/S) mode is activated. This prevents unauthorized users from accessing the P/Y-code signal. In addition to A/S, so-called selective availability (S/A) is used by the US Department of Defense to degrade real-time GPS navigation performance. S/A is accomplished by manipulating the satellite message orbit data and/or the GPS fundamental clock frequency (dither). The GPS clocks are overlaid with short- and long-term modulations. This S/A signal degradation was stopped on May 1, 2000. The broadcast message, including information on the satellites' health and ephemerises, is modulated on the carrier waves as well.

The basic GPS observation types are pseudo ranges and carrier phase measurements. The corresponding observation equations are well known and given in (2.10-8) and (2.10-9), following, for example, Hofmann-Wellenhof et al. (2001) and Wells (1987):

---

[1]Due to the satellites' inclination, problems with satellite coverage can occur in the polar regions of the Earth.

$$p_R^S = \rho_R^S + c \cdot (dt - dT) + d_\rho + d_{\text{ion}} + d_{\text{trop}} + \varepsilon_p \tag{2.10-8}$$

$$\Phi_R^S = \rho_R^S + c \cdot (dt - dT) + \lambda N + d_\rho + d_{\text{ion}} + d_{\text{trop}} + \varepsilon_\Phi \tag{2.10-9}$$

The distance p_R^S from the receiver R to the satellite S is obtained from the measurement of the transmission time of code signals. It is calculated from the product $p_R^S = c \cdot (t_i^R - T_i^S)$, computed from the speed of light c, the satellite clock T_i^S and the receiver clock t_i^R . As can be seen from this equation, the difference between the receiver time (receiving of signal) and satellite time (sending of signal) is essential for the determination of the travel distance. Both clocks (mainly the receiver clock) are influenced by errors and the travel time of the signal is not truly identical with the speed of light in a vacuum. Thus the obtained distance p_R^S is called pseudo range. In order to compensate for these clock errors one additional observation is necessary. In summary four simultaneous pseudo range observations are necessary to solve for the three-dimensional position of the user including the one additional receiver clock offset. This so-called single receiver approach or navigation solution is mainly used in real-time absolute positioning, where less accurate positions are accepted. The positional degradation is due to uncompensated modelling errors in satellite position d_ρ, ionosphere and troposphere $d_{\text{ion},}$ d_{trop} and satellite and receiver clocks dt, dT. In order to achieve better accuracy, these error sources have to be modelled correctly. Alternatively, differential approaches for the processing of observations are possible, whereby the error sources mentioned above are reduced or even eliminated significantly.

The second main observation besides pseudo range is the so called carrier phase observation. This observation is obtained from the phase shift between received satellite signal and the reference signal generated by the receiver. In practice, the continuous carrier phase measurement consists of a measured fractional phase part, an integer count of numbers of full cycles measured by the receiver from the initial to the current epoch, and finally an unknown integer number of cycles at the first measurement epoch. The unambiguous measurement of signal phase is only possible within one cycle of the wavelength (L1: $\lambda_1 = 19.05$ cm, L2: $\lambda_2 = 24.45$ cm). This fraction of a cycle is measured with an accuracy of about 1–2 mm. The integer number of full cycles N between receiver and satellite at the initial epoch is initially unknown and is named phase ambiguity or simply ambiguity. It is different for each of the observed satellites but remains constant as long as the receiver maintains continuous lock of signals throughout the whole measurement interval, i.e. as long as no signal loss of lock or cycle slip occurs. As already discussed for the pseudo range observations, different error sources affect the quality of phase observations and have to be modelled or alternatively corrected by using differential processing approaches. Again, this will effectively increase the accuracy in positioning. The correct determination of phase ambiguities is essential for the final accuracy of positions based on phase observations. Different approaches to solve for the correct ambiguities are available, which are outside the scope of this publication. The estimation of ambiguities during motion has a large impact on kinematic applications. If a so-called on the fly (OTF) algorithm is applied, static initialisation periods before the survey become redundant. Static initialisation was formerly necessary to solve for the correct ambiguity numbers. With the availability of OTF algorithms, kinematic GPS surveys are performed in a much more efficient way.

As already mentioned, the use of differential GPS techniques (DGPS), i.e. the step from absolute to relative positioning, increases the accuracy even without exact modelling of the observational errors. This is based on the fact that errors are of similar size and influence on two neighbouring GPS stations. Through linear combinations of the observations at both receiver stations, the effect of unmodelled errors can be almost eliminated. Nevertheless, two prerequisites have to be fulfilled: one of the two receivers must be installed on a point with known coordinates (so-called reference receiver); and this receiver and the other (so-called rover) receiver must observe simultaneously. With the known position of the reference receiver, the effect of unmodelled errors is estimated from the difference between the results derived from the GPS observations and the known coordinates. The differences are then used to correct for the remaining modelling errors at the rover. Now the roving station is positioned relative to the reference station, and not absolutely, as was the case for the earlier single point solution.

Within differential GPS approaches, no raw pseudo range or phase observations are processed. The concepts are based on the use of linear combinations of the original fundamental L1 and L2 observations. Such combinations are possible between satellites, between receivers and between epochs. Depending on the number of differences formed, one has to distinguish between single and multiple differences. For a pair of stations (rover and reference station) simultaneously observing the same satellite, the between-receivers single difference is obtained. This difference eliminates the influence of satellite clock errors $\mathrm{d}t$ and removes to a great extent the effect of orbit errors and atmospheric effects, but only if the baseline distance between both receivers is sufficiently short. The receiver satellite double difference, i.e. the difference of two single differences with two different satellites, additionally eliminates the receiver clock error $\mathrm{d}T$. However, some terms remain within the observation equations describing minor and uneliminated effects of atmosphere. The influence of these effects is dependent on the effective baseline length between the two receivers. Assuming identical atmospheric conditions at both receiver stations, all atmospheric effects will be cancelled. The double-differenced phase observation is the main observation for high accuracy GPS applications.

Relative GPS positioning relies on the availability of a certain number of reference stations. In the ideal case, these stations should be part of a permanent network built up from reference stations almost evenly distributed in a certain area. The data from GPS reference stations is then used for the differential correction of the individual rover stations. For example, the Working Committee of the Surveying Authorities of the States of the Federal Republic of Germany (Arbeitsgemeinschaft deutscher Vermessungsverwaltungen) has installed an area-wide, stationary permanent GPS reference station network, which covers the whole of Germany. This service is called SAPOS [Satellite positioning service of German Land Survey (SAPOS, 2004)]. The permanent stations continuously provide differential corrections, which are transferred to the users via real-time radio communication or data transfer for later post-processing. As mentioned above, the accuracy of differential corrections is dependent on the baseline length, i.e. the distance to the roving station to be positioned. In order to minimize these distance-dependent effects, a set of several permanent reference stations can be used to form a combined differential correction which is optimized for the rover station itself. Such approaches, relying on multiple reference stations to obtain optimal differential corrections are named virtual reference station or area-weighted correction polynomials. This enables positioning accuracy within the cm range even for baseline lengths >30 km. Similar permanent network station concepts are available in many other countries.

In addition to such land-based permanent networks, satellite-based correction services are available and in use. Within so called satellite-based augmentation systems (SBAS), GPS differential corrections are provided to the users on Earth via satellite. Based on a network of monitor stations, the signals of GPS satellites are permanently monitored and analysed. From this, corrections on orbit and clock errors and the influence of ionosphere are obtained. These corrections are uploaded to geostationary satellites, which then transmit this information to the users. Since the transmitted correction signal is of a similar structure to the original GPS signals, the geostationary satellites may also serve as additional GPS satellites. Currently three different SBAS systems are in use or under development. The WAAS wide area augmentation system for North America, the European geostationary navigation overlay system EGNOS, its European counterpart, and the multi-functional satellite augmentation system MSAS, which is designed mainly for the use in Japan and the rest of Asia. Since all these satellite-based augmentation systems provide their information in a form compatible with the GPS signals, no additional radio receiver equipment is necessary to use this service.

The accuracy of GPS positioning is dependent mainly on the processed GPS observation type (pseudo range or phase observation) and the data processing concept (absolute/differential, static/kinematic, real-time/post-processing). Furthermore, the individual measurement set-up (baseline length for differential processing) and the satellite configuration influence the positioning accuracy. This includes multipath, receiver noise and variations of the antenna phase centre. In land-based and airborne applications, cycle slips and signal loss of lock are possible due to shading effects caused by buildings or the aircraft's wings during turns. All this has to be considered when GPS accuracy is discussed. Nevertheless, the accuracy numbers in Table 2.10-1 have to be construed to be for guidance only, and may be different for individual measurement scenarios.

Thus far the explanation of global navigation satellite systems (GNSS) has covered only the US NAVSTAR GPS. Besides this, two alternative GNSS are already available or in installation. The first one is the Russian GLONASS, which became fully operational at the end of the 1990s. Its positioning accuracy is comparable to GPS without S/A. In principle GLONASS and GPS are quite similar, but some

Table 2.10-1 Accuracy in GPS positioning

GPS observations and processing approach	Accuracy
Single point GPS positioning/absolute positioning	
Positioning accuracy C/A-Code (with S/A)	100 m
Positioning accuracy C/A-Code (no S/A)	10 m
Positioning accuracy Y-Code (military)	4 m
Differential GPS/relative positioning	
Positioning accuracy pseudo range observation	1–5 m
Positioning accuracy carrier phase observation	50 cm

differences are significant: most noticeable is that GLONASS has neither the degradation of precision nor the encryption of GPS. The accuracy and availability of GLONASS have declined due to lack of maintenance in the past. Nevertheless, modernisation and replacement of failing satellites by next-generation GLONASS satellites with longer life expectancies are in progress. So far, GLONASS has not become accepted by civilian users, but after the modernisation process it should also be offered as a commercial system. The main goal of Russian policy is to make GLONASS performance comparable to GPS by 2010 and to bring it to the mass-market.

The other GNSS is the European Galileo system, which is currently in its final installation phase. While the Russian GLONASS was originally designed mainly as a military system, similarly to GPS, the Galileo system is intended as a civilian system under the leadership of the European Union EU and the European Space Agency ESA. Thus the system is not under military control, which guarantees functionality and accessibility independent of any military activities. Furthermore, Galileo offers an additional integrity signal which provides information on the actual positioning accuracy to the user. In principle the technical design of Galileo is very similar to GPS. Nevertheless, owing to the use of a higher number of satellites (30 satellites nominally in three different orbits with an inclination of 56°) and four carrier waves for signal propagation, higher positioning accuracies are expected. Until 2005 the Galileo installation process was in its development and validation phase. The first prototype Galileo satellite was launched in December 2005 and the launch of the second was scheduled for early 2007. The system is expected to be able to offer an operational service from 2008 onwards.

Spurred by the development of the new European Galileo GNSS, major modernisation and improvements are also planned for the GPS constellation, i.e. a new civilian signal on L2 carrier wave and a new civil-only signal on a third carrier wave L5 to be broadcast at 1,176.45 MHz. All this is being done to compete with Galileo. Nevertheless, if all three GNSS are seen as complementary rather than competing systems, all this modification and modernisation will finally lead to a more consistent and accurate combined GNSS with higher integrity, reliability and accessibility.

2.10.3 Basics of Inertial Navigation

Inertial guidance systems or inertial navigation systems (from the Latin "inertia") were originally developed for the navigation of aircraft or ships. Inertial navigation may be defined as the real-time determination of the trajectory of a moving vehicle using sensors that react on the basis of Newton's laws of motion. In general these laws describe the dynamics of a body in an inertial reference system. If no external forces are applied, the body will remain at rest or in uniform rectilinear motion. If external forces are applied, the acceleration is directly proportional to the acting forces. From the measurement of such accelerations the velocity and position of a vehicle are finally obtained in two integration steps. The principle of inertial navigation is the two-fold integration of acceleration with respect to time. Depending on the degrees of freedom, a set of three accelerometers is normally used to measure the linear accelerations in three dimensions. This allows for the three-dimensional positioning of the vehicle. Nevertheless, using three accelerometers on their own on a vehicle is inadequate for three-dimensional inertial navigation, since the accelerometers are not aligned with the axes of the reference coordinate frame (i.e. inertial or earth-related frame). Thus the continuous orientation of the vehicle with respect of the reference frames has to be provided by measurements using gyroscopes. From their integrated angular rate measurements three directions are obtained to orient fully the accelerometer triad in three-dimensional space. First attempts to estimate the travelled distance from measurements of linear accelerations (so called dead reckoning) were done in the 1920s, mainly in Germany. The first operational inertial navigation systems were used in military applications and later civilian use also became accepted.

In general, an inertial navigation system comprises the inertial measurement unit itself (i.e. the set of three gyros and three accelerometers), a platform for the mounting of the sensors and finally an appropriate computer algorithm transforming the IMU measurements into relevant navigational information. Different system designs have been developed, depending on the configuration of accelerometers and gyros: stabilized platform systems or strap-down systems. In stabilized platform systems the sensors are fixed on a space-stabilized platform which decouples the sensors from the angular movements of the vehicle. Thus, the sensitive axes remain with their orientations fixed relative to a space-stabilized or a local level coordinate frame. Within the local level installation the platform physically provides the actual local level frame. The vertical sensor axis is in the plumb line direction and the other two components measure in the horizontal plane. From this, the changes in horizontal position are directly obtained from the integration of horizontal accelerometer measurements and the change in vertical position, from the vertical axis accelerometer. This minimizes the amount of processing time. On the other hand the mechanical attainment of stabilized platform systems is quite complex and therefore expensive. Thus stabilized platform systems are typically used only for highest accuracy demands. Due to their mechanical complexity the systems have to be handled with great care and high mechanical wear is possible. Alternatively, strap-down inertial navigation systems are more favourable for use in small and flexible environments. In contrast to the stabilized platform approach, the sensors are rigidly fixed ("strapped down") to the vehicle's axes and follow the full motion of the vehicle. This obviates the use of complex mechanics and therefore the production of these systems is less demanding and less expensive. Nevertheless, the computational effort is slightly higher because now the horizontal platform has to be accomplished analytically. Furthermore, the sensors are subjected to the entire range of dynamics of the vehicle, which degrades their maximum performance.

With the advent of smaller and less expensive gyros and accelerometers, strap-down technology is the favoured approach for medium to less accurate inertial navigation applications. This trend will be much more evident as new developments emerge, especially in the design of gyros. With the use of micro-electro mechanical system (MEMS) technologies, considerable potential for miniaturisation and cost decrease is apparent. Even though these MEMS-based sensors are of somewhat reduced accuracy, continuous improvement in design and manufacturing processes may finally lead to the replacement of mechanically or optically based inertial sensors, even for navigation purposes.

Another approach to classification of inertial navigation systems besides their individual system design relies on the potential accuracy of their positioning and attitude measurements. The systems are classified into three different accuracy groups according to the positioning error after 1 h of unaided navigation (Table 2.10-2): high accuracy or strategic grade systems with positional error well below 1 nautical mile[2] (nmi) (up to 0.1–0.2 nmi/h or better) after 1 h of unaided navigation, medium accuracy or navigation grade systems with positional error in the range of 1 nmi/h (0.5–2 nmi/h); and low accuracy or tactical grade systems with positional error substantially more than 2 nmi/h (in many cases up to several tens of nautical miles). The attitude accuracy in Table 2.10-2 is valid for the performance

Table 2.10-2 Accuracy of INS positions and attitude determination (Schwarz et al., 1994)

	System accuracy (RMS)		
Error budget	High (strategic-grade)	Medium (navigation-grade)	Low (tactical-grade)
Position			
1 h	0.3–0.5 km	1–3 km	200–300 km
1 min	0.3–0.5 m	0.5–3.0 m	30–50 m
1 s	0.01–0.02 m	0.03–0.10 m	0.3–0.5 m
Attitude			
1 h	10"–30" (0.003°–0.008°)	1′–3′ (0.016°–0.050°)	1°–3°
1 min	1"–2" (0.0003°–0.0006°)	15"–20" (0.004°–0.006°)	0.2°–0.3°
1 s	0.1"–0.2" (0.00003°–0.00006°)	1"–2" (0.0003°–0.0006°)	0.01°–0.03°

[2] 1 nautical mile (nmi) = 1,852 m

of the roll and pitch angles; for the heading angle the performance is worse by a factor of about 3–5. Since positioning and attitude data is obtained from integration processes, the absolute system accuracy is time dependent owing to the strong systematic error propagation. Within the table the corresponding accuracy is given for the 1 s and 1 min time interval as well. Depending on the individual performance of sensors, even larger errors are possible. The overall accuracy is influenced mainly by the gyro performance, which is characterised by the gyro's specific gyro drift value (given in [deg/h]). On the other hand, the accelerometer offset (given in [μg]) describes the accelerometer performance. The corresponding sensor accuracies for the three system performance classes are given as follows (guidance values only): 0.0001 deg/h and 1 μg (strategic grade), 0.015 deg/h and 50–100 μg (navigation grade), 1–10 deg/h and 100–1,000 μg (tactical grade) (El-Sheimy, 2003).

With the use of appropriate external update information the time dependent error behaviour is reduced significantly or almost eliminated. In the ideal case consistent absolute accuracies in the range of the 1 s interval are possible for high to medium accuracy inertial navigation systems as long as sufficient update information is available (Schwarz, 1995). Owing to the lower quality specifications for sensor bias stabilisation and sensor noise this 1 s performance cannot be obtained for the tactical grade systems, even with high quality updates.

As mentioned in the first paragraph of this section, Newton's laws underlie the basics of inertial navigation. If no external forces are applied, the body will remain at rest or in uniform rectilinear motion. If external forces are applied, the acceleration is directly proportional to the acting forces. The acting force **f** is obtained from the product of mass **m** and acceleration **a**, as given in (2.10-10). The acceleration is directly portional to the force assuming constant mass of the body.

$$\mathbf{f} = \mathbf{m} \cdot \mathbf{a} \tag{2.10-10}$$

It is interesting to see that acceleration as a unit of length is not obtained from a scale of length but from the measurement of inertial forces acting on the accelerated mass.[3] All this has to be performed in an inertial coordinate frame, which is defined as the system in which Newton's laws hold.

Based on this, differential equations describing the interrelationship between body acceleration $\mathbf{a}(t)$, body velocity $\mathbf{v}(t)$ and position $\mathbf{r}(t)$ are given as follows:

$$\begin{aligned} \mathbf{v} &= \frac{\mathrm{d}\mathbf{r}}{\mathrm{d}t} = \dot{\mathbf{r}} \\ \mathbf{a} &= \frac{\mathrm{d}\mathbf{v}}{\mathrm{d}t} = \dot{\mathbf{v}} = \frac{\mathrm{d}^2\mathbf{r}}{\mathrm{d}t^2} = \ddot{\mathbf{r}}. \end{aligned} \tag{2.10-11}$$

[3]The inertial coordinate frame satisfies Newton's laws only within the bounds of the given measurement accuracy of the sensors used. Thus, such a frame is named a *quasi*-inertial frame or operational inertial frame.

Assuming a *quasi*-continuous measurement of accelerations $\mathbf{a}(t)$ the instantaneous velocity of a body after a certain interval of time $t - t_0$ is obtained from

$$\mathbf{v} = \int_{t_0}^{t} \mathbf{a} \cdot \mathrm{d}t + \mathbf{v}_0 \tag{2.10-12}$$

with instantaneous position

$$\mathbf{r} = \int_{t_0}^{t} \mathbf{v} \cdot \mathrm{d}t + \mathbf{r}_0 = \int_{t_0}^{t} \left(\int_{t_0}^{t} \mathbf{a} \cdot \mathrm{d}t \right) \cdot \mathrm{d}t + \mathbf{v}_0 \cdot (t - t_0) + \mathbf{r}_0. \tag{2.10-13}$$

If the integration process starts with zero velocity $\mathbf{v}(t_0) = 0$, Equation (2.10-13) is reduced to

$$\mathbf{r} = \int_{t_0}^{t} \left(\int_{t_0}^{t} \mathbf{a} \cdot \mathrm{d}t \right) \cdot \mathrm{d}t + \mathbf{r}_0. \tag{2.10-14}$$

Typically, navigation is done in the Earth's gravity field, where additional accelerations occur and act independently on the mass being accelerated. Thus, the effect of such gravitational accelerations also has to be considered in the integration process. The modified second order differential equation valid for a moving object in the Earth's gravity field is given by

$$\ddot{\mathbf{r}}^i = \mathbf{f}^i + \mathbf{g}^i, \tag{2.10-15}$$

where $\mathbf{r}^i$ is the object position, $\mathbf{f}^i$ is the sensed linear acceleration (specific force) and $\mathbf{g}^i$ describes the gravity acceleration. All magnitudes are given in the inertial coordinate frame (i-frame). The second order differential equation is transformed to a set of first order equations:

$$\begin{aligned} \dot{\mathbf{r}}^i &= \mathbf{v}^i \\ \dot{\mathbf{v}}^i &= \mathbf{f}^i + \mathbf{g}^i. \end{aligned} \tag{2.10-16}$$

Since all linear accelerations $\mathbf{f}^i$ are originally sensed in system specific body b-frame, which is defined by the axes of the sensors, and not equal to the inertial coordinate frame, an orthogonal transformation matrix $\mathbf{R}_b^i$ is necessary to transform the measurements from the body b to the inertial frame i:

$$\mathbf{f}^i = \mathbf{R}_b^i \cdot \mathbf{f}^b. \tag{2.10-17}$$

$\mathbf{R}_b^i$ is obtained from

$$\dot{\mathbf{R}}_b^i = \mathbf{R}_b^i \cdot \Omega_{ib}^b, \tag{2.10-18}$$

where the skew-symmetric matrix Ω_{ib}^b is formed from the measurements of the angular rates ω_{ib}^b , given in the b-frame with respect to the i-frame. Similar to

(2.10-17), the matrix $\mathbf{R}_e^i$ is used to transform the gravity vector $\mathbf{g}^e$, typically given with respect to the earth-related *e*-system, to the inertial *i*-frame.

$$\mathbf{g}^i = \mathbf{R}_e^i \cdot \mathbf{g}^e \qquad (2.10\text{-}19)$$

Now all magnitudes in (2.10-16) are given and the motion equations for an object in the inertial frame *i* are described as follows:

$$\dot{\mathbf{x}}^i = \begin{bmatrix} \dot{\mathbf{r}}^i \\ \dot{\mathbf{v}}^i \\ \dot{\mathbf{R}}_b^i \end{bmatrix} = \begin{bmatrix} \mathbf{v}^i \\ \mathbf{R}_b^i \cdot \mathbf{f}^b + \mathbf{R}_e^i \cdot \mathbf{g}^e \\ \mathbf{R}_b^i \cdot \Omega_{ib}^b \end{bmatrix} \qquad (2.10\text{-}20)$$

From (2.10-20) the navigational information (position, velocity and attitude) is determined with respect to the inertial *i*-frame.

In regular applications, however, the inertial frame is a somewhat abstract coordinate frame. Navigation information, therefore, is determined in earth-related coordinates. Thus the resulting navigation states $\mathbf{r}^i$,$\mathbf{v}^i$,$\mathbf{R}_b^i$ have to be transformed to such an earth-related coordinate frame. For the navigation of a vehicle on Earth a local level topocentric navigation frame *l* is commonly used. Alternatively, navigation in a geocentric earth-fixed coordinate frame *e* is possible as well. If the navigation process is conducted in such a frame, the rotation of the Earth with respect to the previously used inertial frame is also taken into account. Without going into details here, the navigation equations for a moving body with respect to the earth-centred, earth-fixed *e* – frame are obtained as follows (Wei and Schwarz, 1990):

$$\dot{\mathbf{x}}^e = \begin{bmatrix} \dot{\mathbf{r}}^e \\ \dot{\mathbf{v}}^e \\ \dot{\mathbf{R}}_b^e \end{bmatrix} = \begin{bmatrix} \mathbf{v}^e \\ \mathbf{R}_b^e \cdot \mathbf{f}^b - 2 \cdot \Omega_{ie}^e \cdot \mathbf{v}^e + \mathbf{g}^e \\ \mathbf{R}_b^e \cdot (\Omega_{ib}^b + \Omega_{ie}^b) \end{bmatrix} \qquad (2.10\text{-}21)$$

where Ω_{ie}^b is the skew-symmetric matrix formed from the components of the Earth rotation vector ω_{ie}^b , which is transformed via $\mathbf{R}_e^b = \left(\mathbf{R}_b^e\right)^T$ from the *e* – frame to the sensor-specific body frame *b*. The term $2 \cdot \Omega_{ie}^e \cdot \mathbf{v}^e$ corrects for the coriolis force, which is dependent on the instantaneous speed of the vehicle on the rotating Earth. The correction for gravity depends on the instantaneous position and is obtained from appropriate gravity models. The navigation angles obtained from

$$\mathbf{R}_b^n = \mathbf{R}_e^n \cdot \mathbf{R}_b^e \qquad (2.10\text{-}22)$$

always relate the body frame to the local topocentric navigation frame *n*. The vertical axis of the *n* – frame always coincides with the local plumb line. Changes in the local plumb line directions have to be considered if one transfers the navigation angles to another, ellipsoid-related, local topocentric frame *l*. The matrix $\mathbf{R}_e^n$ is a function of the instantaneous position given in geographic coordinates (Λ,Φ) .[4] From $\mathbf{R}_b^n$ the navigation angles (r roll, p pitch, y yaw) are finally obtained. In the case where attitude information from inertial navigation is used in photogrammetric sensor orientation, the different definition of photogrammetric angles (i.e. ω,ϕ,κ) has to be considered. This results in additional transformation steps. The transformation of navigation angles, the role of the Geoid and the influence of deflections of the vertical are addressed in more detail in Section 4.9.2.

In order to solve the navigation equations in (2.10-21), initial values for the position $\mathbf{r}^e(t_0)$, velocity $\mathbf{v}^e(t_0)$ and attitude information $\mathbf{R}_b^e(t_0)$ have to be provided. The initial values for position and velocity are typically obtained from a static initialisation on a known coordinated reference point or alternatively from GPS surveys. In such stationary cases the vehicle has zero velocity with respect to the Earth. The determination of the initial orientation of the system is more complex. As already mentioned during discussion of stabilized platform systems versus strap-down system design, the initial orientation in strap-down navigation has to be accomplished strictly analytically. Thus a static alignment is performed where the components of the gravity vector are sensed in the three accelerometer axes. If the system is tilted from the horizontal, two levelling angles are obtained analytically from the rotation to achieve zero acceleration measurements in the now levelled two accelerometers. The heading alignment is then performed in the second step. Based on the measurement of the Earth angular rate vector, the yaw angle is estimated analytically from the rotation to obtain zero angular rate measurements within one of the two already levelled angular rate sensors (so called gyro compassing). This zero angular rate axis is then pointing towards the direction east, because the Earth angular rate vector consists only of a north and vertical direction component. The whole static alignment is typically performed as a two-step procedure – the so-called course alignment first followed by a fine alignment afterwards. In the first step the pure sensor signals are used for the rough alignment only, whereas in the refinement step sensor errors are also estimated and taken into account besides orientation errors.

It has to be mentioned that the Earth angular rate signal is relatively weak compared to the accuracy and noise of most of the gyros in current use. Thus gyro compassing is not possible for medium or lower accuracy inertial navigation systems. The noise of the gyro measurements prevents convergence of yaw angle determination. In such cases, the static alignment process is replaced by so-called in-motion alignment techniques. Here external information on vehicle position and velocity (typically provided by GPS) is used to obtain the initial orientation of the inertial navigation system. This approach is based on the coupling of INS orientation errors with INS velocity errors, which are observable from the external GPS

[4]The local topocentric coordinate frame and the navigation coordinate frame are both tangential frames but differ in their axis directions. From the geodetic point of view, the local topocentric frame is defined as an east–north–vertical (up) right-handed system, whereas the navigation frame is a north–east–vertical (down) right-handed system. The relationship between these frames is given as follows:
$\mathbf{R}_b^n = \mathbf{R}_l^n(\pi,0,-\frac{\pi}{2}) \cdot \mathbf{R}_b^l$

velocity measurements. Such a kinematic approach to system alignment is quite often used in integrated GPS/inertial systems (i.e. in airborne environments). Thus it is also named in-air or in-motion alignment.

As was already shown in Table 2.10-2, the accuracy of INS positioning, velocity and attitude determination is not constant but dependent on time. This is mainly due to the individual sensor errors, which affect the integration processes to obtain position and attitude from observed linear accelerations and angular rates. Additional errors in the initial starting values, sub-optimal software used for processing (i.e. incorrectly modelled gravity anomalies) and technical imperfections of the inertial sensors themselves are the main sources of the accumulating error budget. The sensor errors are mainly due to offset errors (gyro drift, non-zero bias accelerometers), scale factor errors, sensor noise, non-orthogonalities of sensor axes and acceleration dependent effects. All this has to be considered in an appropriate error model for accelerometers and gyros. The navigation equations (2.10-21) are supplemented by sensor-dependent magnitudes, as can be seen from (2.10-23). With the availability of sufficient update information these error terms are estimated within the navigation process.

$$\dot{\mathbf{x}}^e = \begin{bmatrix} \dot{\mathbf{r}}^e \\ \dot{\mathbf{v}}^e \\ \dot{\mathbf{R}}_b^e \\ \delta\dot{\omega}_{ib}^b \\ \delta\dot{\mathbf{f}}^b \end{bmatrix} = \begin{bmatrix} \mathbf{v}^e \\ \mathbf{R}_b^e \cdot (\mathbf{f}^b + \delta\mathbf{f}^b) - 2 \cdot \Omega_{ie}^e \cdot \mathbf{v}^e + \mathbf{g}^e \\ \mathbf{R}_b^e \cdot (\Omega_{ib}^b + \delta\Omega_{ib}^b + \Omega_{ie}^b) \\ -\mathbf{I}_\alpha \delta\omega_{ib}^b \\ -\mathbf{I}_\beta \delta\mathbf{f}^b \end{bmatrix} \tag{2.10-23}$$

In the extended model given above, the accelerometer bias $\delta\mathbf{f}^b$ and gyro drift terms $\delta\omega_{ib}^b$ are modelled as time-variant quantities (first-order Gauss-Markov process; $\mathbf{I}_{\alpha,\beta}$ are diagonal matrices containing the reciprocal process correlation times). The equation system in (2.10-23) now comprises 15 different states. The six sensor-related error states are independent of the coordinate frame used for the navigation process. They are modified according to the instantaneous error behaviour of the sensors. Although the error model is now modified and extended, the true error behaviour is still not modelled perfectly. This again will induce errors in all navigation steps. Their influences are only known approximately and have to be controlled via additional update information. In traditional inertial navigation this error control is done in static periods, where the integrated vehicle velocity from inertial measurements is compared to zero (so-called zero-velocity update point, ZUPT). If the vehicle position is known too, the inertially obtained position is also compared to this reference value (coordinate update point, CUPT). Due to the coupling between error states, these updates are sufficient to control the inertial error behaviour. With the advent of GPS, nearly continuous, high-performance position and velocity information became available. In almost all cases GPS is integrated with inertial navigation systems to take advantage of this update data. In addition, GPS and INS are of almost complementary system behaviour: GPS offers high long-term accuracy but has shortcomings due to short-term noise and limited frequency, whereas inertial navigation provides very frequent data with high short-term accuracy. Within integrated GPS/inertial systems the absolute positioning accuracy is mainly dependent on the performance of GPS positioning. On the other hand, the accuracy in integrated attitude determination is mainly due to the specific gyro noise. Within integrated inertial/GPS systems continuous positioning is possible even if the GPS signals are blocked owing to shadowing.

2.10.4 Concepts of Inertial/GPS Integration

The integration of inertial/GPS systems can be done via software- or hardware-based approaches. If one focuses on the former, the data from GPS and inertial measurements are combined via decentralized filtering. Within this concept two or more filters, separate but working in parallel, interact at certain times. In the case of an integrated inertial/GPS system, two separate filters are implemented. Firstly, the GPS measurements are filtered, but the second filter is the so-called master filter. This filter does more than process IMU data to obtain the position, velocity and attitude information. Furthermore, the output from the local GPS filter is used as pseudo-observations within the master filter to update its error states. In principle, the differences between GPS and inertial positions and velocities are used to estimate the error budget of inertial data processing. Since the errors in positioning are continuously coupled with the vehicle's attitude, GPS positioning and velocity update are sufficient to control fully the error behaviour of inertial attitude determination as well. The errors of inertial attitudes and IMU sensor errors are estimated from GPS position and velocity. This is possible because vehicle position always relies on the relationship between the inertial measurement frame (as defined by the IMU sensor axes) and the Earth-related navigation coordinate frame. Since this orientation information is obtained from the IMU angular rate measurements, the influence of IMU attitude on positioning and velocity is obvious.

The optimal estimation of system error states is typically done via Kalman filtering. This filter is based on the set of differential equations given in (2.10-23). Kalman filtering has been used for the recursive estimation of time-discrete linear processes, primarily in navigation applications, since around 1960, mainly for the following reasons (Brown and Hwang, 1992).

Kalman filtering facilitates real-time processing of measurements. The errors in navigation are controlled by appropriate update information in real time.

Secondly, the dynamics of the system become a linear model of the errors, i.e. the linearisation of the system dynamics is done with sufficient accuracy.

Thirdly, in navigation, multi-sensor system configurations are regularly used, so different types of input and output data have to be considered. Since all of this data has its specific accuracy behaviour, such a filter constellation is ideal for two-way updates.

Fourthly, the final output is obtained with the best estimated accuracy, based on an optimal combination of input values in the filter.

Detailed information on the generic Kalman filter equations can be obtained from the literature, for example, Grewal and Andrews (1993), Brown and Hwang (1992) or Gelb (1974). In navigation the time-discrete formulation of the algorithm is of relevance.

The update in Kalman filtering is possible in two different ways: In the feed-forward configuration, the navigation errors and system states are estimated and used for the correction of the integrated navigation information afterwards. Alternatively, within so-called feedback or closed-loop error control, the IMU sensors are continuously calibrated ranther than the output navigation information. After each update cycle the estimated error states are fed back into the navigation process of inertial data processing. In this case the inertial raw measurements (linear acceleration and angular rate) themselves are improved.

Filtering always provides the best estimated trajectory information at a certain point of time t_i, which already includes all previous measurements at epochs $t_k \leq t_i$. Smoothing is done, on the other hand, the opposite way, i.e. in the negative time direction. Here all future observations are used to estimate the states at the current time epoch t_i. Obviously, filter processes have real-time capability, which is an indispensable requirement for navigation applications. Smoothing is only performed during post-processing. The combination of filtering and smoothing in a post-processing approach increases the accuracy of the estimation of system errors. Such an approach is recommended for high precision trajectory determination. Highly precise navigation data, for example, is required for the direct georeferencing of airborne sensors.

Chapter 3
The Imaged Object and the Atmosphere

3.1 Radiation in Front of the Sensor

The object that has to be surveyed is generally illuminated by the sun (Fig. 3.1-1). In order to determine the impact of atmospheric effects on spectral radiance in front of the sensor, the spectral radiation at the top of the atmosphere has to be known. The data set can be found in various tables, for instance Neckel and Labs (1984) and is visualised by curve A (extraterrestrial irradiance) in Fig. 3.1-2. During travel through the atmosphere to the Earth's surface, solar radiation suffers weakening due to scattering and absorption. Scattering by the air molecules, also called Rayleigh scattering, depends strongly on wavelength: it is, approximately, inversely proportional to the fourth power of the wavelength of radiation. This means that the shorter wavelengths of the solar spectrum (for instance the blue light, ~0.45 μm) are scattered much more than the longer wavelengths (for instance, red light, ~0.65 μm). This is demonstrated by curve B in Fig. 3.1-2. In the near infrared domain, for wavelengths longer than about 1 μm, Rayleigh scattering can be neglected for practical

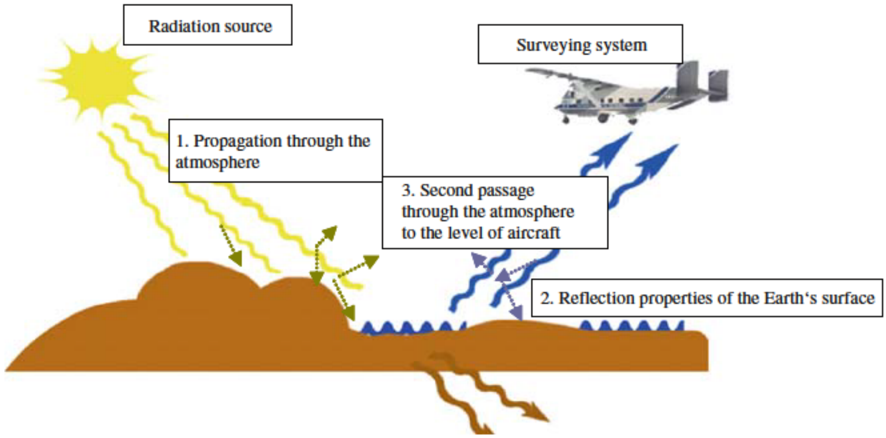

Fig. 3.1-1 Atmospheric impact on the images of airborne sensors [source: Hydrolab (2004)]

R. Sandau (ed.), *Digital Airborne Camera*, DOI 10.1007/978-1-4020-8878-0_3,

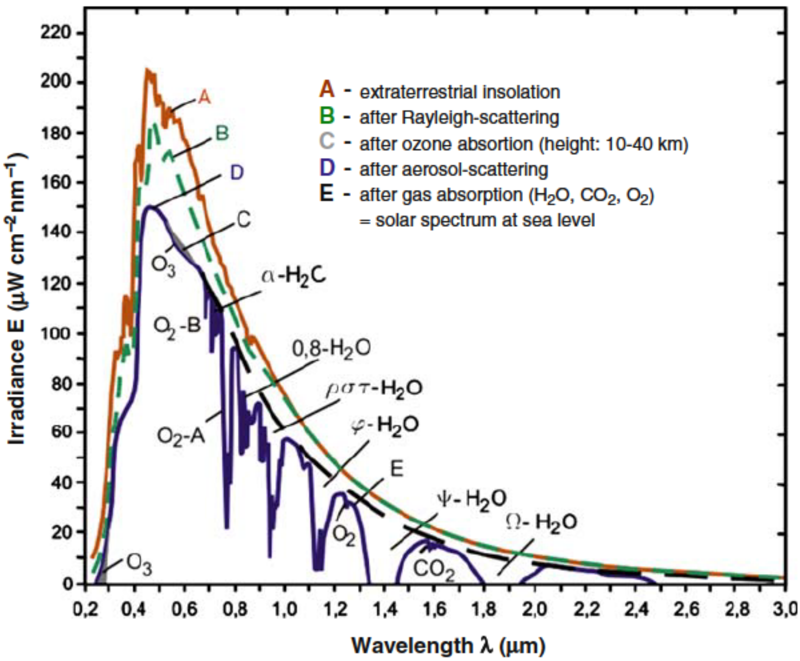

Fig. 3.1-2 Spectral distribution of incoming solar energy at the *top* of the atmosphere and at sea level (*y*-axis: irradiance *E*; *x*-axis: wavelength λ)

purposes. Besides the air molecules, the atmospheric aerosol (dust, fine particles) also contributes to the scattering of sunlight. The aerosol consists of particles of very different sizes and composition. Scattering by the aerosol differs, depending on its concentration and optical properties. Some types of aerosol, particularly urban aerosol, can also absorb the sunlight. Normally, the aerosol concentration is unknown at a specific place. Therefore either the impact of the aerosol on the light propagation is estimated by using appropriate models or the aerosol concentration in the boundary layer is approximated by using the horizontal visibility, which is often known and may be defined as the range within which the outline of a visibility marker can be recognised. It exhibits a measure of turbidity and is inversely proportional to the extinction coefficient (Equation 3.1-1).

Furthermore, from Fig. 3.1-2 it can be seen that different gases absorb solar radiation. Bands of atmospheric water vapour play a significant role. Indeed, they are so strong that at short wavelengths no solar radiation can reach the Earth's surface (χ- and Ω-band water vapour in Fig. 3.1-2). The water vapour concentration in the atmosphere is highly variable in time and space.

The extinction law (Lambert-Bouguer-law) describes the attenuation dL_λ of the monochromatic radiance L_λ along the path dz:

$$dL_\lambda = -\beta_{E\lambda} L_\lambda dz, \tag{3.1-1}$$

where $\beta_{E\lambda}$ is the extinction coefficient.

Integrating this equation results in:

$$L_\lambda(z) = L_{\lambda 0} e^{-\int \beta_{E\lambda} \mathrm{d}z};$$

$$\text{where } \tau \text{ (the opticaldepth)} = \int \beta_{E\lambda} \mathrm{d}z; \quad \text{then}$$

$$L_\lambda(z) = L_{\lambda 0} e^{-\tau};\ e^{-\tau} = T$$

where T is the transmissivity of the atmosphere. If the radiance penetrates the atmosphere completely unaffected, T equals 1. If no radiation can transmit the atmosphere, T will be exactly zero. Transmissivity always refers to perpendicular penetration. For an oblique path s through the atmosphere, we obtain (Fig. 1.3-4):

The exponent of the transmission is referred to as the relative optical air mass. In Fig. 3.1-3, a horizontal coplanar atmosphere has been assumed for simplicity; the curvature of the Earth and refraction are neglected. From this it follows that the exponent 1/cos θ is accurate only up to $\theta = 60°$. For larger zenith angles $\theta > 60°$, the curvature of the Earth and refraction have to be taken into account. Formulae and tables exist for the different constituents of the air (Iqbal, 1983).

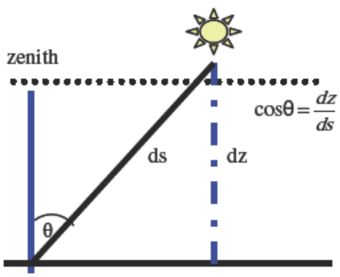

$$dL_\lambda = -\beta_{E\lambda} L_\lambda ds; \quad L_\lambda = L_{\lambda 0} e^{-\frac{\tau}{\cos\theta}} = L_{\lambda 0} T^{1/\cos\theta}$$

Fig. 3.1-3 Dependence of the extinction on the solar zenith distance θ for a homogeneous coplanar atmosphere

Figure 3.1-4 depicts the direct insolation penetrating to the Earth's surface for a pure Rayleigh atmosphere (free of aerosols) without absorbing properties.

The curve $m_l = 0$ characterises the extraterrestrial insolation and corresponds to the curve A in Fig. 3.1-2 (except for the finer details neglected in Fig. 3.1-4).

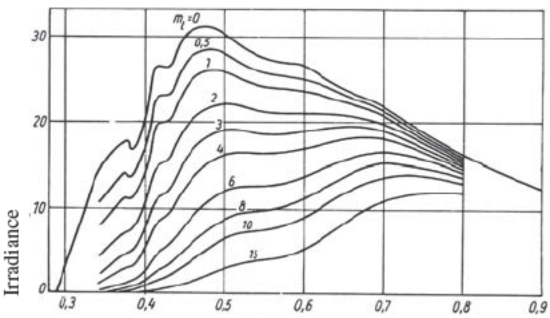

Fig. 3.1-4 Spectral distribution of the solar direct energy at the Earth's surface plotted against the relative optical air mass m_l [after Foitzik and Hinzpeter (1958)]

Figure 3.1-4 reveals that the ultraviolet and blue parts of the sunlight are removed from the solar spectrum to a great extent owing to scattering by air molecules when zenith distances are large. In contrast, the infrared parts of the sunlight are almost completely unattenuated at the Earth's surface even for $\theta \approx 84°$ (this means that $m_l \approx 15$). Thus the maximum solar energy at the Earth's surface shifts from the blue-green spectral range to the red domain.

The radiation scattered by air molecules and aerosols is partly backscattered into the upper atmosphere (dotted arrows in Fig. 3.1-1) and escapes into space. Part of this backscattered radiation hits the sensor in the aircraft or satellite (Fig. 3.2-1) and is termed path radiance. The part scattered into the lower atmosphere is called diffuse sky radiation and reaches the Earth's surface or the target to be detected. Thus the incoming radiation at the target on the Earth's surface consists of the direct solar radiation and the diffuse sky radiation. A rough rule of thumb is that under cloudless conditions the diffuse sky radiation amounts to 18% of the total incoming radiation. The direct solar radiation attenuated by penetrating the atmosphere and the diffuse sky radiation strike the Earth's surface (Fig. 3.1-1) and there are reflected according to the optical properties of the particular surface. This reflected radiation – after a second passage through the atmosphere to the sensor – generates the required image of the target. Different surfaces reflect very differently in the various spectral ranges. Some reference values for the spectral albedo are listed in Table 3.1-1. The spectral albedo is the ratio of the reflected irradiance [W/m^2] to the incoming irradiance [W/m^2] in the spectral domain under consideration.

Table 3.1-1 Reference values of the spectral albedo of different surfaces

Spectral domain	Bare soil (dry clay)	Vegetation (grass)	Snow (dry)	Bare soil (dry clay)
Blue	0.169	0.007	0.89	0.026
Green	0.268	0.051	0.906	0.049
Red	0.329	0.040	0.91	0.041
Near infrared	0.418	0.654	0.89	0.000

3.2 Radiation at the Sensor

The different radiation components striking the sensor are depicted in Fig. 3.2-1, assuming a flat area. On the target detected at time*t* comes the direct radiation (E_{dr}) and diffuse radiation (E_{di}). The direct radiation is the solar radiation incident on the surface after one passage through the atmosphere. As mentioned above, the diffuse sky radiation emerges from the scattering processes caused by the air molecules and aerosols. It is sunlight deflected by scattering from the primary direction and comes now to the surface target from all directions of the hemisphere. These components (E_{dr} + E_{di}) are reflected according to the reflectance $\rho_{\Delta\lambda}$ and reach the sensor after a second passage through the atmosphere (ray 2 in Fig. 3.2-1). During their second

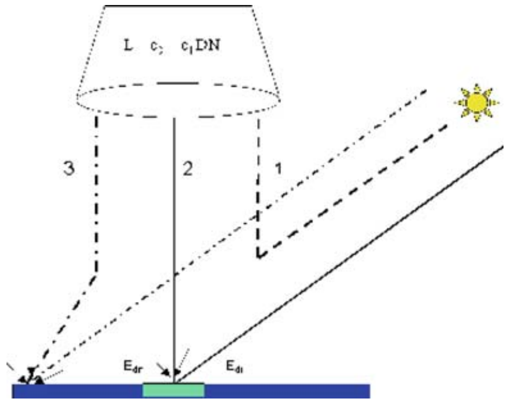

Fig. 3.2-1 Schematic diagram of the solar radiation components arriving at the sensor above a flat terrain [source: Rese (2004)]

pass through the atmosphere E_{dr} and E_{di} are impaired according to the transmission function $T_{\Delta\lambda,\,\Delta H}$ (ΔH indicates the altitude of the sensor above the Earth's surface). The components (E_{dr} + E_{di}) include the required information about the surface target.

$$L_{\Delta\lambda,\text{ at the sensor}} = (E_{dr} + E_{di})_{\Delta\lambda}\,\rho_{\Delta\lambda} T_{\Delta\lambda,\,\Delta H} + L_{\Delta\lambda 0} + L_N$$

In addition to these components carrying the information about the target, other radiation components arrive at the sensor at the time *t*. These are the so-called path radiance $L_{\Delta\lambda 0}$ (ray 1 in Fig. 3.2-1) and the radiation L_N reflected by the adjacent pixels (ray 3 in Fig. 3.2-1, also known as adjacency effect or blurring effect). The components 1($L_{\Delta\lambda 0}$) and 3 (L_N) blur the image. They emerge also from the scattering process. Due to scattering $L_{\Delta\lambda 0}$ is directed to the sensor without ever having reached the surface. L_N, as a part of the radiation reflected by the adjacent pixels, can be incident at the sensor at the time *t* owing to scattering, too (ray 3 in Fig. 3.2-1). The contributions of these unwanted components to the required signal are much stronger in the blue spectral region than in the near infrared, because the scattering by the air molecules depends very strongly on the wavelength. In addition the content and the size distribution of the aerosols play a role.

In Tables 3.2-1, 3.2-2, 3.2-3 and 3.2-4 the contributions of the path radiance ($L_{\Delta\lambda 0}$) and the total radiance in front of the sensor $L_{\Delta\lambda,\text{ in front of the sensor}}$ are listed

Table 3.2-1 Radiances in front of the sensor and path radiance above different surfaces; values are for the blue spectral channel (430−490 nm) and the conditions mentioned in the text

Flight altitude [km]	Path radiance $L_{\Delta\lambda 0}$ [μW/(cm^{2}sr)]	Water $L\Delta\lambda$, in front of the sensor [μW/(cm^2 sr)]	Vegetation $L\Delta\lambda$, in front of the sensor [μW/(cm^2 sr)]	Snow $L\Delta\lambda$, in front of the sensor [μW/(cm^2 sr)]
1	55	124	73.6	2,967
3	140	209	154	2,929
5	190	255	208	2,921

Table 3.2-2 Path radiance as percentage of the total radiance in front of the sensor in the blue spectral domain (430–490 nm)

Flight altitude [km]	Water [%]	Vegetation [%]	Snow [%]
1	44	75	1.9
3	67	91	4.8
5	75	92	6.5

Table 3.2-3 Radiances in front of the sensor and path radiance in the near infrared spectral channel (820–870 nm) above different surfaces

Flight altitude [km]	Path radiance $L_{\Delta\lambda 0}$ [μW/(cm^2 sr)]	Water $L\Delta\lambda$, in front of the sensor [μW/(cm^2 sr)]	Vegetation $L\Delta\lambda$, in front of the sensor [μW/(cm^2 sr)]	Snow $L\Delta\lambda$, in front of the sensor [μW/(cm^2 sr)]
1	9.9	9.9	1,179.3	1,627
3	21	21	1,150	1,582
5	25.4	25.4	1,143	1,571

Table 3.2-4 Path radiance as percentage of the total radiance in front of the sensor in the near infrared spectral domain (820–870 nm)

Flight altitude [km]	Water [%]	Vegetation [%]	Snow [%]
1	100	0.84	0.61
3	100	1.83	1.3
5	100	2.2	1.6

for a mid-latitude summer atmosphere with low aerosol content. The values are given for different flight altitudes. For the calculation of $L_{\Delta\lambda,\text{ in front of the sensor}}$, the albedo from Table 3.2-1 has been used.

The impact of the adjacency effect depends on the aerosol concentration and very strongly on the heterogeneity of the scene and the spatial resolution. It will not be discussed here in greater detail. If we use calibrated digital cameras both disturbing effects can be partly corrected by the application of appropriate software.

In addition to these effects the object itself is blurred owing to scattering of the light in the atmosphere, so a point spread function (PSF) has to be attributed to the atmosphere. Figure 3.2-2 demonstrates this schematically. A ray starting from point A is imaged in the image plane at point a under the assumption of ideal optics. If the ray is scattered at point S, however, and therefore detected in point b, it will appear to be started in point B. The illumination of the object at point A is moved to the location B outside the object A; thus the object is blurred in the image plane. The PSF of the atmosphere can be approximated using a 2D Gaussian distribution:

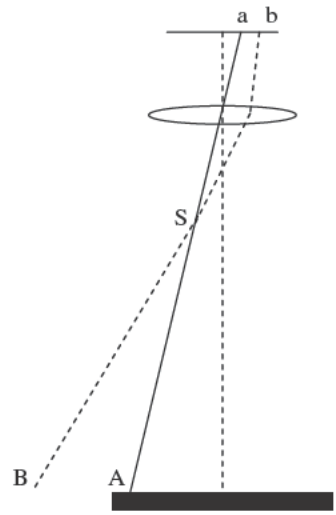

Fig. 3.2-2 Point spread function (PSF)

$$h(x,y) = \frac{1}{2\pi\sigma_{\text{atm}}^2} e^{-\frac{x^2+y^2}{2\sigma_{\text{atm}}^2}}$$

Here, x and y are the coordinates in the imaging plane. The root mean square deviation σ_{atm} describing the width of the PSF depends on atmospheric parameters such as water vapour content, aerosol content, temperature and wind speed. The atmospheric processes that impact σ_{atm} and are roughly described by the parameters mentioned above are the atmospheric scattering and the multiple reflections between the surface and the air molecules and the aerosols respectively, as well as turbulence effects.

The value of σ_{atm}^2 can be determined experimentally by flying with an airborne camera at different altitudes above a test site. The very first approaches have now been developed to calculate the components of σ_{atm}^2 theoretically for special cases.

3.3 Contrast of a Scene at the Sensor

In the two sections above it has been demonstrated that atmospheric scattering impairs the contrast of the scene. Generally the contrast C of a scene is defined by:

$$C = \frac{\rho_{\max} - \rho_{\min}}{\rho_{\max} + \rho_{\min}},$$

which means that the scene contrast is zero above a homogeneous surface. Taking into consideration the atmosphere we obtain for the contrast C' of a scene:

$$C' = \frac{r_{\max} - r_{\min}}{r_{\max} + r_{\min} + \frac{2E_A}{E_S T}}, \tag{3.3-1}$$

where E_A is the path radiance, multiplied by π, and E_S is the global irradiance. A schematic diagram is given in Fig. 3.3-1.

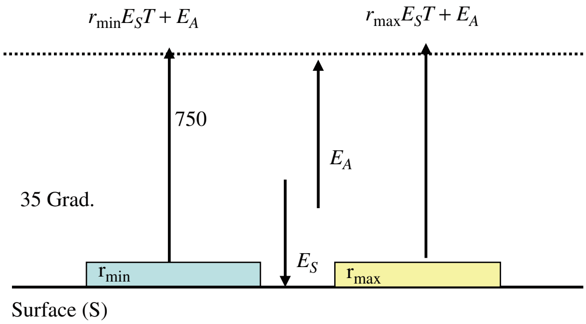

Fig. 3.3-1 Schematic diagram for deriving the scene contrast C' (taking into account the atmosphere) after: http://www rss.chalmers.se/gem/Education/RSES-2002/Imaging_systems.pdf

Figure 3.3-2 gives an idea about the values determining the scene contrast C' ((3.3-1) and Fig. 3.3-1). The ordinate on the left hand side gives the values of the path radiance arriving at the airborne sensor, whereas the transmission scale is shown on the right hand side. On the x-axis is the flight altitude. The calculations were done with the radiation transfer code MODTRAN4 for a model atmosphere at midday in summer for 48°N and 15°E. A rural aerosol is assumed as well as a horizontal visibility of 23 km. These assumptions characterise a very clean atmosphere. The results are given for the blue spectral range (430–490 nm) and the near infrared spectral domain (820–870 nm).

Figure 3.3-2 demonstrates again the strong impact of scattering by the air molecules, because a very slight aerosol concentration was selected in the model. The global irradiance E_S at the surface comprises the direct solar irradiance and the diffuse sky irradiance. The value depends on the sun's position and the atmospheric conditions (aerosol, water vapour). Clouds are generally neglected in this chapter.

For the model atmosphere mentioned above, Fig. 3.3-3 depicts the altitude-dependent curve of the contrast, taking into consideration the effect of the atmosphere. The contrast C' is again shown for the blue and near infrared spectral regions. The albedo used was taken from Table 3.1-1 for bare soil and vegetation.

3.4 Bi-directional Reflectance Distribution Function BRDF

Up to this point in the calculations, the spectral albedo has been used, given by the ratio of two irradiances. Irradiances always refer to the radiation incident from the atmosphere (hemisphere) or reflected into the atmosphere (hemisphere). This approach assumes that the surface reflects isotropically. Such a surface, with a reflectance that does not depend on the viewing angle, is called a Lambertian surface. Natural surfaces are not generally Lambertian: the reflected radiation of natural surfaces for a fixed sun position depends on the direction from which the surface is viewed (Fig. 3.4-1). The dotted arrow indicates the viewing direction; the sun has a fixed zenith distance of 35°.

If the directed effect of the reflection is to be taken into account instead of the albedo, we use the bi-directional reflectance distribution function (BRDF)

$$\mathrm{BRDF}(\lambda,\theta_S,\phi_s,\theta_v,\phi_v) = \frac{L_v(\lambda,\theta_S,\phi_s,\theta_v,\phi_v)}{E(\lambda,\theta_S,\phi_s)}[\mathrm{sr}^{-1}]. \qquad (3.4\text{-}1)$$

In (3.4-1) the symbols have following meaning: L_v is the reflected radiance per unit of area, wavelength interval and solid angle [W/(m^2 μm sr)], E – the incoming irradiance per unit of area and wavelength intervall [W/(m^{2}μm)], λ – the wavelength, θ – the zenith distance, ϕ – the azimuth, S – the sun and v – the viewer.

The theory and phenomenon of the BRDF are not described here. The reader is refered to the literature (Schönermark et al., 2004). It is emphasised, however, that it is essential to take into account BRDF effects when aerial photographs, acquired during different positions of the sun and/or different flight directions, are to be mosaicked together to form a large image. For digital aerial photographs, simple BRDF correction algorithms have proved to be very useful.

The difficulty is that the atmosphere, depending on the spectral region, the aerosol concentration and the flight altitude, modifies or masks the BRDF effect of the surface. This phenomenon is discussed using Fig. 3.4-2.

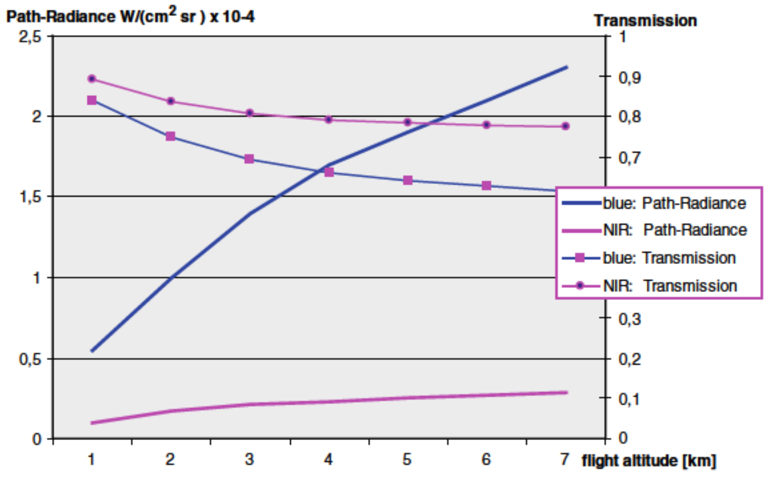

Fig. 3.3-2 Model calculations of the path radiance and the transmission, according to the flight altitude, for the *blue* and the near infrared spectral domain

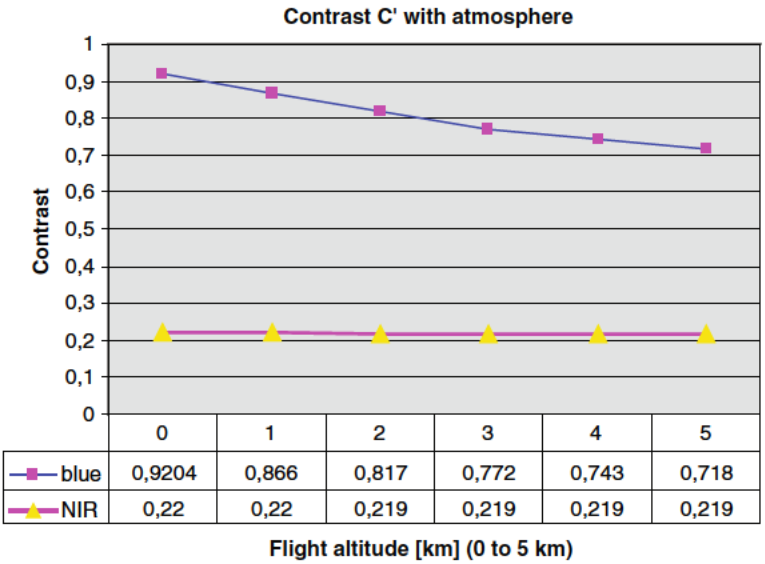

Fig. 3.3-3 Impact of atmospheric effects on scene contrast for bare soil and vegetation (see Fig. 3.3-1)

Fig. 3.4-1 Effects of bi-directional reflectance of grass [source: RSL (2004)]

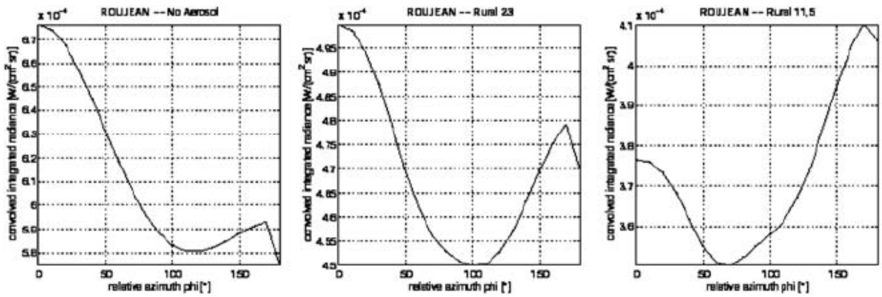

Fig. 3.4-2 Simulation of the radiance measured at a flight altitude of 2.5 km above the ground with the following parameters: midday on 21 July, above an alfalfa field, spectral region 775–825 nm (Rössig, 2004)

For the calculations, discrete BRDF values measured in the near infrared spectral region have been approximated (fitted to a function) by using a model (Roujean model). With this model and the radiation transfer code MODTRAN4, the radiances expected at the sensor (ADS40 in this case) have been calculated. In Fig. 3.4-2, the relative azimuth is marked on the *x*-axis: the values from 0° to 90° symbolise the backscattering region (the area which describes the scattering back to the sun) and the values from 90° to 180° characterise the forward scattering. The graph on the left-hand side of Fig. 3.4-2 depicts the results for an atmosphere free of aerosols. Owing to the fact that the scattering caused by the air molecules does not have a noticeable effect in the near infrared spectral domain, the graph describes the reflected radiation above the surface, i.e. the typical distribution of the reflectance directly above the vegetation selected for this study. In the middle image the calculations depicted are performed under the asumption that rural aerosols exist in the atmosphere that result in a horizontal visibility of 23 km. It is seen that owing to the scattering properties of the aerosols the backscattering decreases and the forward scattering increases. This effect becomes more pronounced with increasing aerosol content, as confirmed by modelling an atmosphere with a horizontal visibility of only 11.5 km (right-hand graph).

Chapter 4
Structure of a Digital Airborne Camera

4.1 Introduction

Based on the preceding remarks it can be said that in front of the lens there is a radiation mix consisting of scattered radiation and information reflected by portions of the scene. The scene can be regarded as a direct image of reality, even if there are limitations regarding the geometric representation, taking into account MTF (modulation transfer function) and radiometric representation (noise, sky light), or also as an indirect image, because it can be represented as a Fourier transform extending over the entire area being observed (the reflected radiation can be interpreted as the sum of many two-dimensional spatial frequencies). Whichever way it is perceived, the aggregate system of object, atmosphere and airborne camera with its wide variety of optical, mechanical and electronic components (all components are by and large linear component systems) can be described as an aggregate linear system and the complex relationships reduced to simple computational operations in Fourier space (multiplication instead of convolution.

In the this section, we consider the digital airborne camera and its various components as a system, irrespective of any specific design. The principles on which the components' operation is based and the parameters contributing to the quality of the overall system are discussed. This includes sections on the camera equation (for example, spectral characteristics), on the system MTF and on system noise.

Figure 4.1-1 shows a block diagram of a digital airborne camera. Radiation arriving at the lens needs to be broken down into its spectral components with a minimum of loss, sampled and stored in the form of compressed digital data for further processing. The degradation which the image and the radiation undergo even before they enter the optical system was described in quantitative terms using the parameters PSF (Point Spread Function) and MTF in Fourier space and noise σ^{phot} in Chapter 2 and 3.

With reference to all components of the aggregate system comprising object, atmosphere and airborne camera, the camera equation below, which describes the

R. Sandau (ed.), *Digital Airborne Camera*, DOI 10.1007/978-1-4020-8878-0_4,

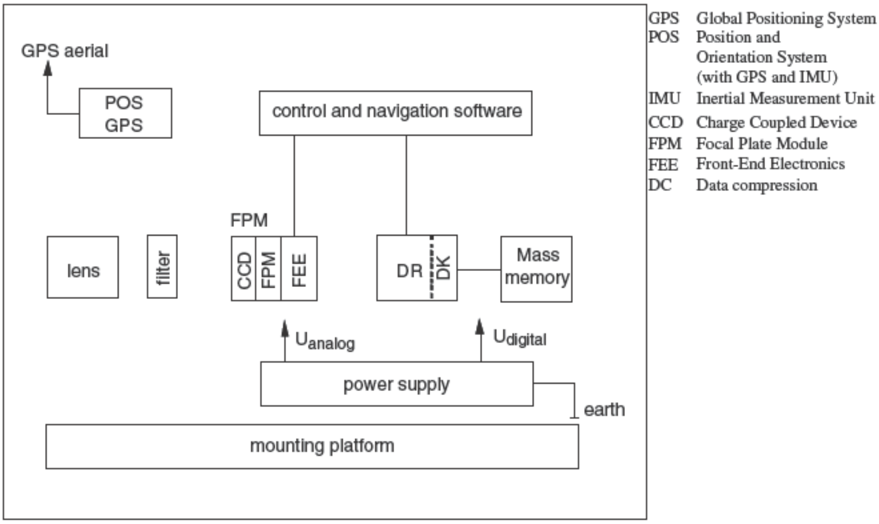

Fig. 4.1-1 Block diagram of a digital airborne camera

signal S_i at the optoelectronic converter element i, follows (2.2-8), (2.2-9), (2.2-10), (2.2-11), (2.2-12), (2.2-13), (2.2-14) and (2.2-15)

$$S_i = I_K \int_{t_{\text{int}}} \int_{\Delta\lambda} \left[R_{\text{CCD}}(\lambda) \cdot T_{\text{Opt}}(\lambda) \cdot L_i(\lambda) \mathrm{d}\lambda + \text{DS} \right] \mathrm{d}t \qquad (4.1\text{-}1)$$

where I_K is a constant dependent on the camera (focal length << flight altitude)

$$I_K = \frac{\pi}{4} \frac{A_{\text{d}} \cdot \cos^x(\vartheta_i)}{K \cdot (\frac{f}{D})^2}, \qquad (4.1\text{-}2)$$

where

t_{int}	is the integration time
$\Delta\lambda$	current wavelength range
R_{CCD}	CCD's spectral responsivity
T_{Opt}	spectral transmittance of lens and filter
L_i	spectral radiation flow in front of the lens
DS	dark signal generation rate
x	lens-dependent exponent of the "cos^4 law", $2 < x < 4$
ϑ_i	visor angle of the pixel i
f/D	f-number
K	conversion factor of the CCD
A_{d}	detector area
f	focal length.

In practical work, fixed integration times and values averaged in the observed wavelength range are used, i.e.,

$$R_{\mathrm{CCD}}(\lambda) \cdot T_{\mathrm{Opt}}(\lambda) \cdot L(\lambda) \approx R'_{\mathrm{CCD}} \cdot T'_{\mathrm{Opt}} \cdot L' \qquad (4.1\text{-}3)$$

from which (4.1-1) simplifies to the convenient equation

$$S_i = (I_K \cdot R'_{\mathrm{CCD}} \cdot T'_{\mathrm{Opt}} \cdot L' + \mathrm{DS})t_{\mathrm{int}} \qquad (4.1\text{-}4)$$

The signal S_i at the detector element i is a function of the radiation quantity *L'* in front of the lens and of a dark signal DS dependent on the detector. *L'* consists of the light reflected from the object and from sky light which diminishes contrast (see Chapter 3). The temperature-dependent dark signal DS consists of the mean value and a DSNU value (dark signal non-uniformity) and has to be subtracted; this is a systemic error term dependent on the structural components. Hence, it is determined when the camera is calibrated and stored in the correction value memory (see Sections 4.4, 4.6 and 5.2).

With every airborne camera, the aim is to achieve the best possible signal/noise ratio (SNR) in order to be able, at all processing stages, to work with data that are as close as possible to the information they contain. There are many components in the signal chain that affect noise in the digital airborne camera. If we restrict ourselves to making a rough breakdown of the noise components, the SNR can be described with

$$\sigma_{\mathrm{Camera}} = \frac{n_s}{\sqrt{\sigma_s^2 + \sigma_{\mathrm{fp}}^2 + \sigma_{\mathrm{rms}}^2}}, \qquad (4.1\text{-}5)$$

where n_s is the number of electrons collected in the CCD generated by the signal S_i, σ_s^2 the variance of the signal electrons n_s, σ_{fp}^2 the variance of the local responsivity differences (fixed pattern noise) and σ_{rms}^2 is the variance of the time-dependent noise of all other components involved.

The number of signal electrons is proportional to the number of photons impinging in the spectral band in question. Hence, the noise of the signal electrons also follows the Poisson distribution (see Section 2.6), i.e.,

$$\sigma_s = \sqrt{n_s}.$$

For instance, the time-dependent noise of the CCD and of the analogue data channel (rms noise) contains

- dark signal noise (Poisson distribution)
- noise of the reset and amplifier circuits ("kTC noise")
- charge transfer noise
- other noise components (1/*f* noise, thermal noise)
- noise response of the A-D converter.

This point is discussed in greater detail in Sections 4.4 and 4.6.

The causes of the fixed pattern noise σ_{fp} are the responsivity differences (Photo Response Non-Uniformity, PRNU) of the individual detector elements and the drop in light intensity towards the edge of the focal plane of a (wide-angle) lens ($\cos^4$ law).

Figure 4.1-2 shows the typical curve of the output signal of a CCD line (individual line or line of a matrix) with approximately 5,200 elements, the centre element of which is situated on the focal plate in the vicinity of the optical axis of a wide-angle lens.

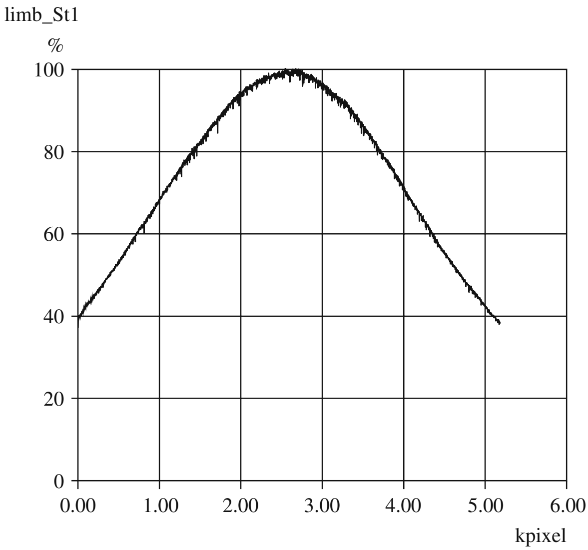

Fig. 4.1-2 *Typical curve* of an output signal of a CCD line in the focal plane of a wide-angle lens given a homogeneous intensity distribution of illumination

The curve in Fig. 4.1-2 represents the two portions of fixed pattern noise σ_{fp}, the $\cos^4$ drop in light intensity towards the edges of the focal plane behind a wide-angle lens and the photo response non-uniformity of the CCD elements. Both portions are actually systemic errors, but they can be regarded simply as noise if they are not recognized and corrected. If we consider a selected CCD element (for example, an element near the optical axis) and ignore σ_{fp} for this selected element, we obtain the SNR curve shown in Fig. 4.1-3 for this CCD element, given a saturation capacity of 500,000 electrons and a σ_{rms} of 200 electrons.

For saturation charges of 100,000–500,000 e^-, we obtain SNR values from 267 to 680, which correspond to 8 and 9 bits, respectively. But let us return to the real conditions as shown in Fig. 4.1-2. The light intensity drop to 40% (this corresponds to an FOV $\approx$ 100°) must be corrected. In signal processing in the case of digital cameras, this is normally done by electronic means (see Section 4.5).

When does the effect of PRNU have to be corrected, and how precisely? In CCD data sheets, PRNU is usually specified in percent of the output signal below saturation in the linear part of the characteristic curve. The fixed pattern noise of the responsivities of the CCD elements generated by PRNU, which changes into

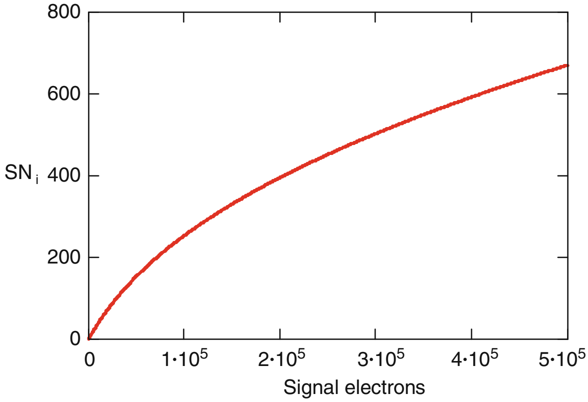

Fig. 4.1-3 Modulation-dependent SNR of a CCD element with a saturation capacity of $n_s = 500{,}000\ e^-$ and $\sigma_{rms} = 200\ e^-$

a time-dependent noise as a result of charge transfer, can be expressed by

$$\begin{aligned}\sigma_{fp} &= \frac{\text{PRNU}}{100\%} \cdot n_s \\ &= \frac{\text{PRNU}}{100\%} \sigma_s^2.\end{aligned} \tag{4.1-6}$$

Depending on the actual PRNU of the CCD signals, we derive from (4.1-5)

$$\text{SNR} = \frac{\sigma_s}{\sqrt{1 + \left[\frac{\text{PRNU}}{100\%}\sigma_s\right]^2 + \left[\frac{\sigma_{rms}}{\sigma_s}\right]^2}} \tag{4.1-7}$$

where it is assumed that a correction has already been made for the light intensity drop. Figure 4.1-4 shows the best possible SNR given full modulation, again assuming a saturation charge of 500,000 e$^-$ and $\sigma_{rms} = 200\ e^-$. The SNR is determined by the photon noise of input radiation and σ_{rms} up to a PRNU of 0.02%.

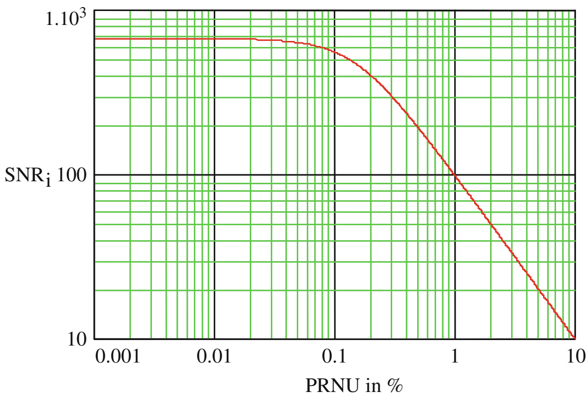

Fig. 4.1-4 SNR as a function of PRNU for $n_s = 500{,}000\ e^-$ and $\sigma_{rms} = 200\ e^-$

The influence of PRNU dominates from a PRNU of 0.1%. Since the PRNU values of CCD components are currently in the range of a few percent, a pixel-by-pixel PRNU correction is required, which can be carried out, for instance, along with the correction of the light intensity drop towards the edge of the focal plane. The signals corrected in this manner ensure good SNR values over the entire dynamic range DR of the camera

$$\mathrm{DR} = \frac{s_{\max} - \mathrm{DS} \cdot t_{\mathrm{int}}}{\sigma_{\mathrm{rms}}}. \tag{4.1-8}$$

Figure 4.1-5 shows an image covering a dynamic range of about 12 bits. Noise cannot be recognized in the dark part of the image or in the bright one.

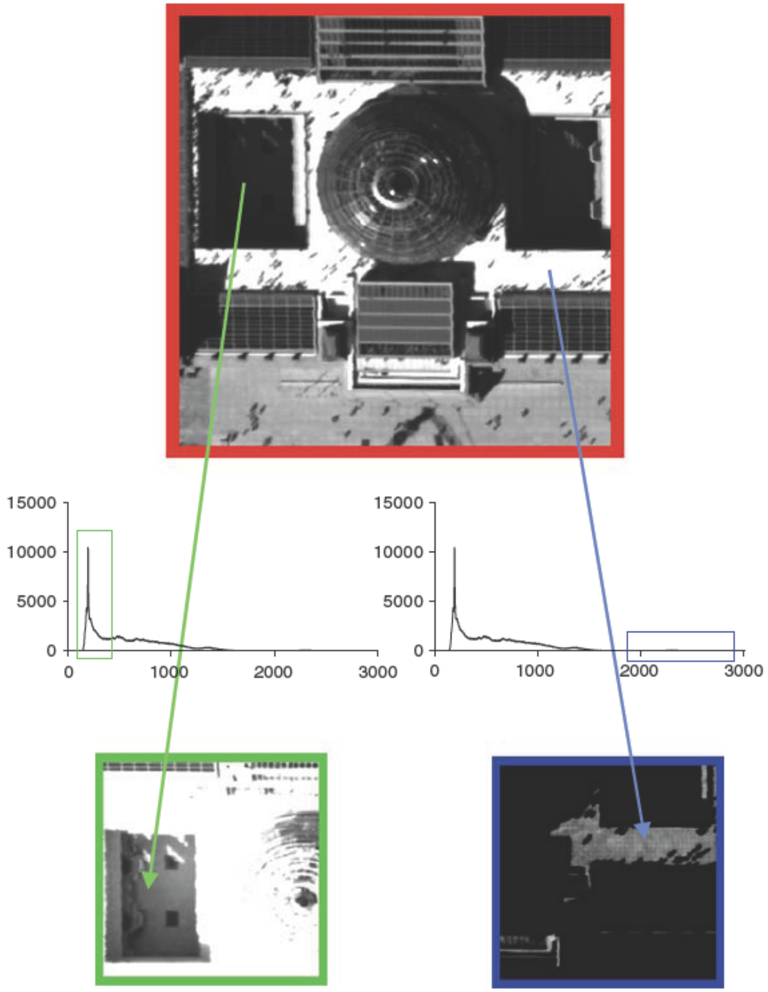

Fig. 4.1-5 Berlin's parliament building (Reichstag) with scene dynamics of approximately 12 bits

The quality of the spatial resolution of a camera or sensor system can best be described using the contrast transfer function MTF, through which the links between the various influencing factors are converted into simple multiplications in frequency domain using the mathematical operation of convolution. This procedure must be based on linear sub-systems. The rationale, derivations and mathematical tools for working with MTF are provided in Sections 2.3, 2.4 and 2.5. Thus, the expression for MTF of the camera in the direction of flight is

$$\mathrm{MTF}_{\mathrm{camera,x}} = \mathrm{MTF}_{\mathrm{optics}} \cdot \mathrm{MTF}_{D} \cdot \mathrm{MTF}_{\mathrm{electronics}} \cdot \mathrm{MTF}_{\mathrm{LM}} \cdot \mathrm{MTF}_{\mathrm{PF}}, \qquad (4.1\text{-}9)$$

where D = detector, LM = linear motion and PF = platform. As can be seen here, the wide variety of components influencing the spatial resolution in the direction of flight has been compiled into a simple multiplication equation.

4.1.1 Example

To illustrate the relationships, let us examine a simplified camera system in which the MTF terms of the electronic and platform influences can be neglected, i.e., they assume the constant value of 1.

$\mathrm{MTF}_{\mathrm{optics}}$ describes three components:

- Diffraction at the exit pupil (diffraction, see Section 2.4),
- Optical aberration (aberration, see Section 4.2.11) and
- Focus deviation,

the MTF components of which are multiplicatively connected to $\mathrm{MTF}_{\mathrm{optics}}$.

To simplify matters, let us consider the lens to have been ideally corrected and exactly focused (MTF in each case is 1). Then the diffraction terms remain, which, given a circular entrance pupil, produce an Airy disc with an f#-dependent diameter (see Sections 2.4 and 4.2.13). In Fig. 4.1-6, $\mathrm{MTF}_{\mathrm{optics}}$ is plotted for f# = 1.2.

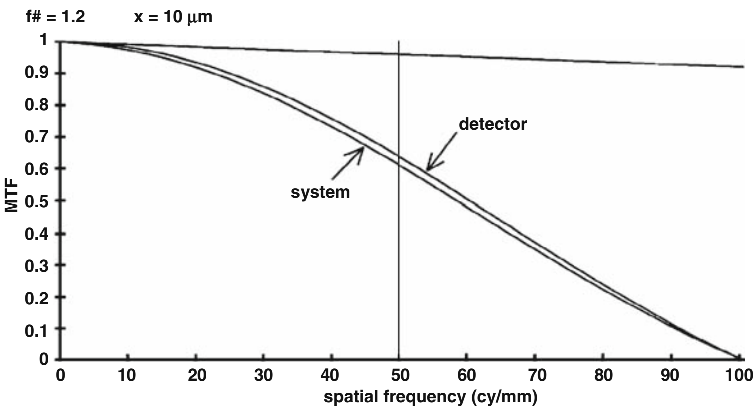

Fig. 4.1-6 MTF curve of an optical system with limited diffraction at f# = 1.2 of a detector at $x = 10\ \mu\mathrm{m}$ and the resulting MTF for the camera

MTF_D of the detector in the direction of flight is described by the function

$$MTF_D = \frac{\sin(\pi \sigma_x f_x)}{\pi \sigma_x f_x} \tag{4.1-10}$$

where σ_x is the expansion of the (rectangular) detector element and f_x the spatial frequencies (see Section 2.5). Figure 4.1-6 shows the associated MTF for $\sigma_x = 10\ \mu\text{m}$.

The linear motion taking place during the integration time t_{int} causes the term MTF_{LM} in (4.1-10), described by

$$MTF_{LM} = \frac{\sin(\pi - \Delta x \cdot f_x)}{\pi \cdot \Delta x \cdot f_x} \tag{4.1-11}$$

where $\Delta x = v.\ t_{\text{int}}$ is the path covered by the projection of the detector element on the earth's surface during the integration time. If Δx remains smaller than 10% of the GSD, the influence of linear motion can often be neglected. This situation is described in Section 4.10 and illustrated in Fig. 4.10-4. On the other hand, if the entire dwell time t_{dwell} is consumed by the integration time, i.e., $\Delta x = \text{GSD}$, then MTF_{LM} of the linear motion changes to MTF_D of the detector and the system MTF is downgraded in a manner that can no longer be neglected (see Section 4.10, Fig. 4.10-5). Figure 4.1-6 shows the MTF_{camera} according to (4.1-9) if the influences of the electronic array, the platform motion and the linear motion can be neglected (on account of $\Delta x < 0.2$ GSD) and a distortion-free, focused lens with f# = 1.2 and detectors with $\sigma = 10\ \mu\text{m}$ are used. MTF_{camera} is then the product of the component systems MTF_{optics} and MTF_D.

Points of reference for the magnitudes listed in (4.1-2), (4.1-3), (4.1-4), (4.1-5), (4.1-6), (4.1-7), (4.1-8) and (4.1-9) are provided in the following sections.

In the process of calibration, system parameters for a finished camera system are determined, camera-specific defects are recorded and the relevant information is used to correct the systemic, geometric and radiometric data generated by the camera (see Chapter 5).

Another component of a digital airborne camera, which is not be covered in detail in the following sections, is the power supply. It is one of the factors that play an essential role in determining the quality of data delivered at the output of the digital airborne camera for processing. The voltages provided by the power supply system for the analogue and digital signal-processing components must be stable and without cross-talk. An instrument earth concept tailored to the camera and the instrument earth system within the signal processing components have a major influence on data quality. The power supply system, like all other hardware components, must meet the safety requirements (shock resistance/crash, electromagnetic compatibility) and operating and storage conditions (temperature, moisture, etc.). The requirements the airborne camera must meet with regard to operating conditions (air pressure and temperature) are shown in Fig. 7.2-2.

4.2 Optics and Mechanics

The task of a photogrammetric system is to photograph a 3D scene on the Earth using analogue optics and then reconstruct it, in either analogue or digital form. To satisfy the high quality requirements of aerial photogrammetry, it is important to undertake the processes of both acquisition and reconstruction with minimum loss of information. How this objective can be achieved for the acquisition process is described below by considering optical imaging in terms of information transfer. We restrict ourselves to the imaging of one-dimensional objects to simplify the notation, as the transition to two-dimensional objects is straightforward.

An object of size D_{OBJ} in the object space, in our case part of a landscape, is imaged on a receiver through the lens, on either film or an electronic sensor. The resulting image of size D_{IMA} is therefore reduced by the factor $V_{\mathrm{OBJ}} = (D_{\mathrm{IMA}}/D_{\mathrm{OBJ}})$. As the object domain is a three-dimensional space, but the receiver can only acquire in two dimensions at the focal plane, there is already an initial, unavoidable loss of information. To keep this loss within limits, a ground scene is recorded several times using sensor arrays looking in different directions. This configuration results in the stereo operation of the aerial camera, with all its advantages and also its complications.

If we now consider the optical system in more detail, we will show that further, unavoidable losses of information occur, on the one hand due to the geometry of the optics, and on the other hand due to the wave nature of light. We will also show that the maximum amount of information can be transferred only through intense technical efforts.

4.2.1 Effect of Geometry

Every optical system, even a simple lens, is described by so-called “pupils”. This term refers to the locations through which all light beams from the object space pass. In the case of our eye, the pupil is the iris; in the case of a lens, as in Fig. 4.2-1, it is the aperture, called the “stop”.

The aperture is imaged at the so-called “entrance pupil” EP by the lens group on the object side (left from the STOP) and at the “exit pupil” AP by the lens group on the opposite, image side (right from the STOP). As a consequence the exit pupil is an image of the entrance pupil and its size is defined by the “pupil magnification”, which in turn depends on the lens data. In the case of a simple lens, EP, STOP and AP are in the same place and thus identical.

We can see that every optical system performs two tasks, resulting specifically in the object OBJ being imaged at the sensor IMA and, at the same time, the EP at the AP. The two images have different magnifications that are, however, dependent on each other.

If s is the distance between object OBJ and EP, and s’ the related distance between AP and IMA, then by using simple ray constructions the following relationship is obtained for the object magnification using the pupil magnification:

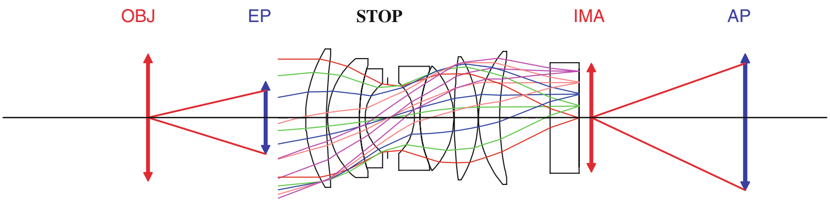

Inv = (Y$_{Obj}$ * Y$_{EP}$)/s = Y$_{Obj}$ * NA

Inv = (Y$_{IMA}$ * Y$_{AP}$) / s' = Y$_{IMA}$ * NA'

? W = S* * p * [Y$_{Obj}$ * NA] ^{2} = S* * p * Inv ^{2} ➔ Energy conservation, S* = radiance

Resolution dy = ?/NA ➔ Diffraction; Note: spatial frequency 1/ y ~ NA

Space-Bandwidth-Product ➔ = [Y$_{Obj}$ /dy] ^{2} = [Y $_{Obj}$ * N/?] ^{2} = [Inv / ?] ^{2}

Number of resolvable points N ~ ? W ➔ 1. & 2. Law of Thermodynamics

Fig. 4.2-1 The physics of optical systems

$$V_{OBJ} = (Y_{IMA}/Y_{OBI}) = (Y_{EP}/Y_{AP}) * (s'/s) = 1/V_{Pupil} * (s'/s) \qquad (4.2\text{-}1)$$

This relationship must have a physical justification! Do we therefore need to consider pupils with the same rigour as the object and the image? To address this question, we consider a point object. We assume the object emits light over a wide angular range and that part of this light fills the EP of the lens. The sine of the aperture angle, as seen from the point object OBJ and defined as the ratio of the EP radius $D_{EP}/2$ and the distance s is called the object side "numerical aperture" NA. The product with the object field diameter D_{OBJ} yields the quantity Inv = $(Y_{OBJ} Y_{EP})$/s, which can be defined in the same manner for the image side as Inv' = $(Y_{IMA} Y_{AP})$/s'. Using simple geometric constructions it can be shown that the two parameters are the same, hence the name "geometric invariant".

The invariant also describes an optical system in a physical manner: if it is squared and multiplied by the object radiance S, it is possible to determine the amount of power ΔW incident on the EP from the radiation emitted and directed in its entirety to the sensor, if material absorption is ignored.

$$\Delta W = S^* \pi/4^* [D^*_{OBJ} \mathrm{NA}]^2 \sim \mathrm{Inv}^2$$

The invariant is therefore necessary to ensure the conservation of energy. An optical system therefore fulfils the first law of thermodynamics. But does it also meet the second law, the conservation of the entropy, that is the information content in a stochastic system?

4.2.2 The Effect of the Wave Nature of Light

If we wish to address the transfer of information from the object to the sensor, we must take into account the wave nature of light as the information carrier. Every physical wave, even waves on water, is diffracted at fixed objects and also at holes such as optical apertures. All points on the obstacle on which the light is incident re-emit spherical waves of light that interfere with each other and combine to form the new, the "diffracted" wave front. Due to interference caused by the obstacle, the shape of the diffracted wave front is different to that of the incident wave.

In the case of an optical system, it is necessary to consider diffraction effects at the pupils. From physics we know that the diffraction of a plane wave at a circular aperture such as the EP results in intensity maxima and minima that appear at an observation angle $\delta\omega = m \cdot 1.22 \cdot \lambda/D_{\mathrm{EP}}$, where m is the diffraction order and λ the wavelength of the light. The first intensity minima is at $m = \pm 1$. If for the time being we ignore the irrelevant factor 1.22, which is due to geometric effects at circular apertures, and multiply the angular spread by s, then for the object resolution we obtain $\delta y = \mathrm{s} \cdot \delta\omega = \lambda \cdot \mathrm{NA}$, which is classically considered as the distance between two object points that can still be considered separate. The number of object points resolvable by the optics in both dimensions is therefore

$$N = [2 \cdot Y_{\mathrm{Obj}}/\delta y]^2 \sim [\mathrm{Inv}/\lambda]^2 \tag{4.2-2}$$

i.e. it is characterised by the ratio of the geometric parameter Inv to the wavelength of the light, the information carrier.

4.2.3 Space-Bandwidth Product

The reciprocal of the resolution $1/\delta y$ that appears in the definition of N has the dimension of a spatial frequency lp/mm, which is why the variable N is also termed the "space-frequency" product or more commonly the "space-bandwidth" product. Its finite value expresses the fact that every optical system can only transfer a finite amount of information, that is of resolved image points. To transfer as much optical information as possible, therefore, it is necessary either to use light with a very short wavelength and/or to take "fast" optical systems, i.e. with a high NA. For this reason modern photolithography for the manufacture of computer chips with structures in the sub-micrometre range uses extremely short wavelength light, i.e. "deep UV", or even X-rays, together with optics with an NA near the maximum value of 1. These highly complex systems are masterpieces of engineering and have now reached the limits of technical feasibility.

It is very interesting to see that N, due its dependence on Inv, also depends on the amount of energy acquired, i.e. the suspected relationship between energy acquired and information acquired, which is from the first and second laws of thermodynamics, is evident. This is not really surprising, since the principles of optics stem from thermodynamics. Ernst Abbe, often considered the founder of modern optics, identified and reported the relationship between optics and thermodynamics in the middle of the nineteenth century, based on how the latter was taught by Clausius and Helmholtz in Berlin. “Space-bandwidth” products are also known in electronics in a similar form as “time-frequency” products, as they characterise every linear transmission system. They are also to be found even in modern quantum mechanics in the form of “uncertainty principles”.

We will now estimate N for two examples from aerial photogrammetry. In the case of the ADS40 (see Section 7), 24,000 pixels were positioned in the swath direction, that is perpendicular to the aircraft’s heading. The optical “space-bandwidth” product in this direction must therefore be the same or greater than 24,000. This already rather high figure is surpassed by high performance lenses, for example for the Leica RC30 film camera. These lenses are specified to have a spatial resolution of 125 lp/mm across the entire image area of a 9-inch square of film: this figure corresponds to a resolvable pixel size of 0.004 mm. As a result, 57,000 image points are obtained in one dimension or a total of $3.2 \cdot 10^9$ pixels on the film area, measured after the wet development process that degrades the resolution by a good 50%. This remarkably large figure is further increased by a factor of 100–1,000 if the spectral resolution of the optics and film are also taken into account.

4.2.4 Principal Rays

Before we describe the imaging process in more detail, we define the principal ray in a light bundle starting from an object point in the direction of the optics. The term principal or often *chief* ray is used for the ray that hits the centre of the EP, that is, at the intersection between the optical axis and the EP plane. This ray characterises the centre of gravity of the intensity distribution in the light bundle, at least in well-corrected optical systems. Therefore it will always be possible to find the physically relevant intensity maximum anywhere between the object and the sensor by following the chief ray. This aspect is important if, as is shown below, one wants to calculate back to the 3-D object domain from the acquired 2-D sensor data.

4.2.5 Physical Imaging Model

The above explanations enable us to describe physically and model mathematically the imaging process. In a first step the EP is illuminated by the radiation emitted by the object. For this purpose the light wave emitted by an object point is considered. This wave arrives at the EP as a plane wave if the object is at a large distance from the optics, or as a spherical wave if the object is closer. The wave front, however, may already be distorted by the atmosphere.

The wave front in the EP is transferred to the AP by the optical system. Again the physical mechanism is wave propagation, but corrupted by diffraction at the aperture of each single lens. Thus we can conclude that when arriving at the AP, not only has the diameter of the wave front changed as expressed by the pupil magnification, but so has its shape owing to aberrations. These aberrations may be due to incomplete optical design, manufacturing faults on the lens surfaces, inhomogeneities in the glass, or even decentring of the mechanical lens holders. The wave front in the AP, aberrated in this manner, propagates onwards in free space to the image plane. At the sensor, the incident light amplitudes from all object points that are in phase interfere coherently, i.e. are added together. The intensity of the aerial image, that we finally observe, is obtained by squaring the amplitude distribution, which is done in reality by our eye or by the sensors, both of which are phase-invariant.

The intensity distribution in the image plane should be similar to the spatial object structure, although degradations due to the aberrations and diffraction effects must be accepted. The intensity distribution can also be multiplied by the sensor sensitivity function to obtain the definitive sensor signals (film grey-scale values or electrical signals).

The physics of the entire imaging process is therefore completely described by diffraction phenomena. Whenever we design an optical system, we should model the imaging process quantitatively. To reduce the complexity, diffraction effects are considered only for the two prominent, free-space light propagations, from the object to the EP and from the AP to the sensor. The complicated light transfer from the EP to the AP is approached by ray trace calculations, an approximation which fits rather well in most cases.

The diffraction mathematics can be described to a good approximation using a 2-D Fourier or Fresnel transformation of the complex optical wave front, if the aberrations caused by the optical system are reasonably small.

In the ideal case of an aberration-free system, the maximum image intensity for an object point is where the principal ray intersects with the sensor plane. In turn this would allow us to calculate the entire imaging process using only "principal ray optics", which would significantly reduce the complexity. This situation then also applies to the *inverse process*: from the knowledge of the position of an image point on the sensor, we could calculate back to the object using its principal ray if we know the positions of the pupils. As the energy is centred on the principal ray, this reverse transformation is physically legitimate.

In summary, it can be seen that stringent requirements are placed on the optics not only in terms of the image quality, but also so that the optical system can be modelled in simplified mathematical form for the reconstruction of the object structure from the image data.

4.2.6 Data Transfer Rate of High Performance Optical System

Now that we have outlined the physics of the imaging mechanism, we must estimate the performance of the lens as an information processor. For this purpose we consider the 2-D Fourier transformation of the wave front from the AP to the sensor plane. A 2-D Fourier transformation is equivalent to a 2-D correlation, the most

Fig. 4.2-2 Modern aerial photography lens UAGS for the Leica RC30 with square mounting frame for 9-inch film; note the circular appearance of the AP in the *middle* of the lens despite the large viewing angle

frequently used mathematical operation in image processing. In the case of large format lenses such as the UAGS on the RC30 aerial camera (Fig. 4.2-2), this operation requires approximately 1 nsec, which corresponds to the propagation time of the light from the AP to the image plane around 30 cm away. If this operation takes place simultaneously for the aforementioned $3.2 * 10^{12}$ spatial and spectral pixelsPixel, we are performing the complex mathematical operation at a data rate of $3.2 * 10^{21}$ pixels/s, which illustrates the enormous potential of optical parallel processors. This is a data rate that would be completely beyond any electronic digital system. The problem for the optics is the electronics, which are required by optical scientists to write in and read out the information.

4.2.7 Camera Constant and "Pinhole" Model

Every optical imaging model can be inverted and provides a physically justifiable formulation if we extend the "principal ray" for a pixel from the EP into the object domain to determine the unknown object point. In this way we reduce the entire optical system to a simple "hole" in the EP, the "pinhole". The direction of the principal ray is obtained if the location of the image on the sensor is transferred to a plane at a distance c from the EP and the ray is drawn from that plane to the EP. The distance c is called the camera constant and is approximately equal to the focal length for lenses focussed at "infinity". This constant must be determined carefully using special calibration measurements. It can vary slightly from pixel to pixel owing to distortions, vignetting and aberration effects and therefore must be capable of being derived from the acceptance certificates for every field angle. In Fig. 4.2-3 we show its position for a large field angle on a super-wide angle lens.

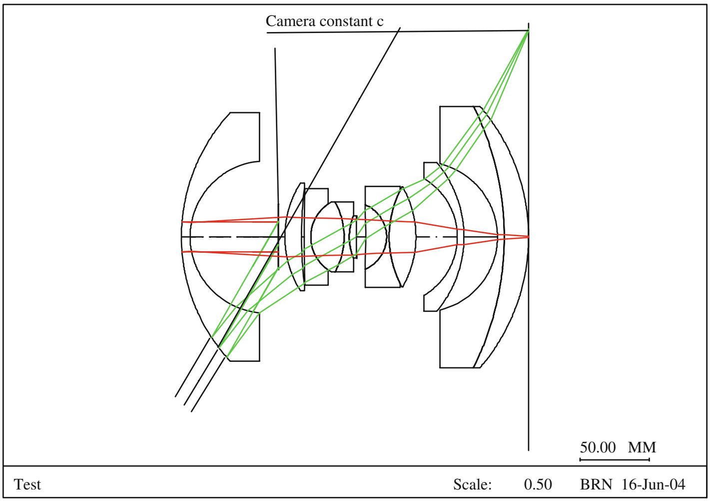

Fig. 4.2-3 Camera constant for a wide-angle lens with 120° field of view

4.2.8 Pupil Characteristics

Finally, a few key characteristics of the optics related to pupils will be mentioned: the perspective, the colour fidelity and the radiometric balance in the field of view.

4.2.8.1 Perspective

An image point focussed as sharply as possible on the sensor clearly corresponds to a point in the object domain. Object points in front of or behind this point are then imaged sharply in front of or behind this image point. As their light bundles come from the same AP, they are incident on the sensor at different points as a function of the directions of their principal rays and give an impression of perspective. The nature of the photographic perspective can be affected significantly by the position of the pupil. In Fig. 4.2-3 above, the two pupils are inside the system and a "natural" central perspective is obtained.

With certain digital cameras the situation is different. In this case the AP is consciously positioned towards "infinity" such that all principal rays are incident on the sensor at right angles. These "telecentric" optics are common in measuring instruments where a slight lack of image sharpness can be tolerated if the object depth varies slightly, but a change in the image position cannot be tolerated. The perspective is then parallel rather than central.

4.2.8.2 Spectral Imaging

In the example of the ADS40 digital airborne cameraAerial camera system described in Section 7 below, however, the main reason for the telecentric ray path is a cascade of interferometric beam splitters and colour filters in front of the sensor plane. The colour filters comprise approximately 100 thin, vapour-deposited coatings to achieve the steep spectral band pass required by the specifications. If the AP were located at a "finite" position, the light bundle for each pixel would be incident on the colour filters at a different angle. As the response of the filter coatings varies with the angle of incidence, this geometry would offset the position of the spectral edge. The resulting colour shift could be corrected by software, but this processing would be a hazardous and also unnecessary manipulation of the raw data. As the use of modern digital cameras for quantitative "remote sensing" measurements is increases, a pixel-dependent spectral offset represents a significant loss of information and is therefore unacceptable. With an AP at "infinity", all beams are incident on the filter coatings at right angles, with the result that all pixels are subject to the same spectral conditions and no correction is necessary.

Film lenses, on the other hand, do not need to be telecentric, as the colour separation takes place within the film material. This situation favours the classical, highly symmetrical lenses that are easier to correct "by design".

4.2.8.3 Radiometric Image Homogeneity

It is shown below that, for simple optics, the so-called $\cos^4$ law applies: this defines the reduction in light intensity from the centre of the image to the edge. For a lens with a maximum field angle of 45°, this would result in a reduction in the brightness at the edge of the image to $\cos^4(45°) = 0.25$ of the value in the centre. Such a reduction is unacceptable in practice as it would excessively limit the dynamic range of the film. The optics designer attempts, therefore, with considerable effort, to design the positions and sizes of the pupils such that the intensity drop across the field is largely mitigated. It can be seen that this effort has been successful by walking around a Leica UAGS lens and always seeing cat-like circular pupils independent of the viewing angle. This situation can be seen in Fig. 4.2-2. Instead of a $\cos^4$ dependency, an edge reduction function of approximately $\cos^{1.2}(45°) = 0.66$ is achieved, a significant improvement. In Fig. 4.2-4a, b we show both lens types,

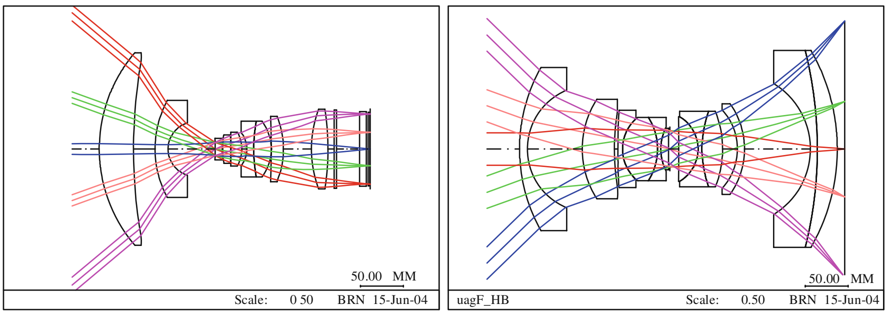

(a) **(b)**

Fig. 4.2-4 (**a**) Telecentric lens (AP at infinity) (**b**) Lens with AP at finite distance on the left a telecentric system for digital cameras and on the right a UAG-F for the Leica RC10 aerial camera with finite pupil position.

4.2.9 Design and Manufacturing Aspects

Typical specifications for large-format photogrammetric lenses are

- Field of view ±3060°
- Spatial resolution 120150 lp/mm
- Spectral range 420–900 nm
- F number ≤ 4
- Homogeneous distribution of brightness across the image
- Thermally and pressure stabilised
- Film camera: geometric distortion $\leq \pm 2$ μm across the entire 23 cm image field (for example, RC30)
- Digital camera: image-side telecentric ray path, i.e. AP at infinity (for example, ADS40)

High performance optical systems comprise 12–14 lenses. To meet these demanding specifications, comprehensive design work in the "optics design office" is required. In parallel, special computer programs are used to simulate all possible manufacturing errors so that the allowable manufacturing tolerances can be specified to the optics factory. The effects of environmental fluctuations such as temperature and air pressure on optical quality are also investigated.

A good design is always robust in relation to the tolerances. The glass used is most important. Here personal contact and mutual trust with large manufacturers such as Schott and Ohara are very important. The glass for each individual lens arrives at the optics factory as an optically tested glass block and all key optical data, such as the refractive index for several wavelengths and the homogeneity, is also supplied in the form of a test report. Once all the raw glass has arrived, the "original design" is optimised again and the thickness of the glass lenses recalculated. With this updated data the manufacture of the lenses is begun in the optics factory and all measured lens thickness data is reported back to the design office together with measurements of the surface forms. The air spacing between lenses or lens groups is then optimised once again; the measurement data that is by now available on the mechanical holders for the lenses or lens groups is also used in this optimisation. Sometimes a surface radius of a "final lens" is left open as a "last-ditch" hope, should the manufacturing tolerances absorb the budget available.

Typical manufacturing tolerances are 0.010 mm for lens thickness, 0.005 mm for air spacings and a few angular seconds for the decentring angles. These tolerances require extremely well controlled production processes, an aspect that is dependent on the quality of the tools and instruments. For systems at the limits of feasibility, the psychological factor plays a major role. The strong identification of the manufacturing team with the lens system as a unique personal achievement can often be observed.

The finished lens system is measured in the laboratory after production. During this process the MTF, the resolution and the distortion are checked and logged. Often it is necessary to change the two air spacings again before all acceptance conditions are definitively met.

4.2.10 Summary of the Geometric Properties of an Image

In this section, we discuss the common relationships of paraxial optics and their application to the conditions of aerial photography.

4.2.10.1 Focal Length and Depth of Focus

A fundamental quantity in any optical system is the focal length f and/or its reciprocal optical refractive power. The focal length indicates the focal point of an incident light beam from infinity relative to the lens. The shorter the focal length of a lens, the greater is its optical power to bring the light into the focal point. The choice of the focal length depends on the image size and the field angle. The lens formula dating back to the Renaissance can be written with the aid of this quantity (see (4.2-3) and Fig. 4.2-9):

$$\frac{1}{f} = \frac{1}{g} + \frac{1}{b} \tag{4.2-3}$$

where f is the focal length, g the subject distance (here the flight altitude h_g) and b the image distance (in this case, the position of the focal plane).

In the case of imaging from infinity, the image distance becomes the focal length

$$f/h_g \to \infty = b.$$

But what happens at "normal" flight altitudes? After transposition of (4.2-3), the position of the best image distance b (this corresponds to the normal position of the focal plane) is

$$b = \frac{f \cdot h_g}{h_g - f} \tag{4.2-4}$$

For a given focal length, the image distance, i.e., the plane of the sharpest image, depends on the flight altitude. Hence, the airborne lens, the sharpness of which is not so easy to adjust during flight, has to be designed such that sufficient image sharpness is ensured in a defined image distance range. The required tolerance range for the depth of focus, which is dependent on the range of flight altitudes, can be determined for the selected focal lengths as shown in Fig. 4.2-5.

Moreover, the image distance is a function of temperature, because the lens properties change as a result of volume expansion. Air gaps also vary with temperature.

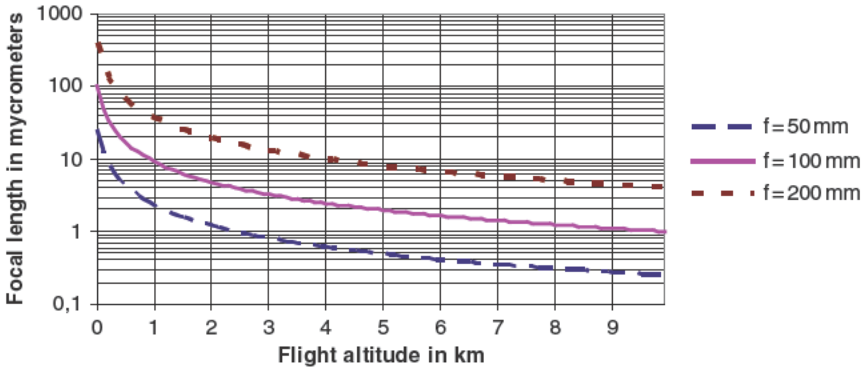

Fig. 4.2-5 Change of image distance to optimise the position of the focal plane for a lens depends on the flight altitude for the selected focal lengths

In particular, the coefficients of expansion of lens mounts and casing components have a decisive influence. The influence of temperature depends on the lens design and can be largely compensated through the use of combinations of materials with different coefficients of expansion. Many aerial photography lenses are athermal (Fig. 4.2-6 is an example).

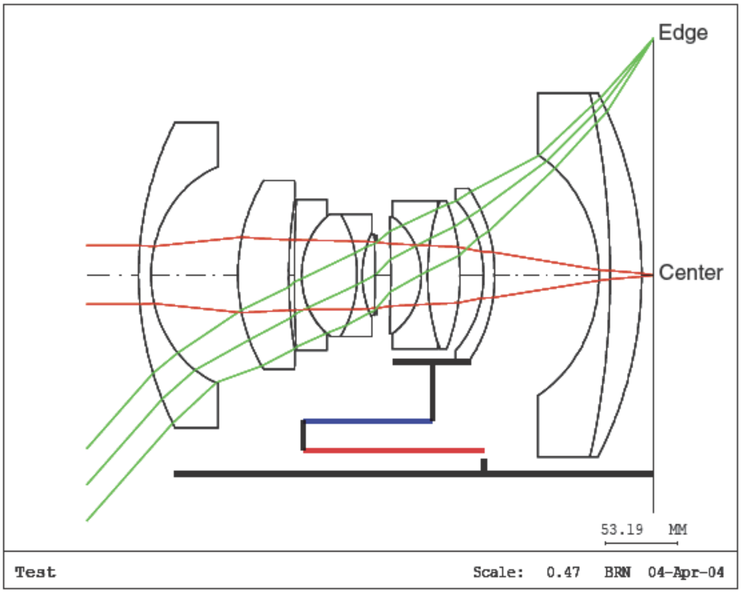

Fig. 4.2-6 Athermalisation: The lens array shown here is shifted along the optical axis relative to the mount cylinder. The amount of shift required per degree Centigrade is adjusted by making use of the length ratio of two shifting materials (such as aluminium and invar), an old trick used by watchmakers

Fig. 4.2-7 Dependence of air pressure on flight altitude

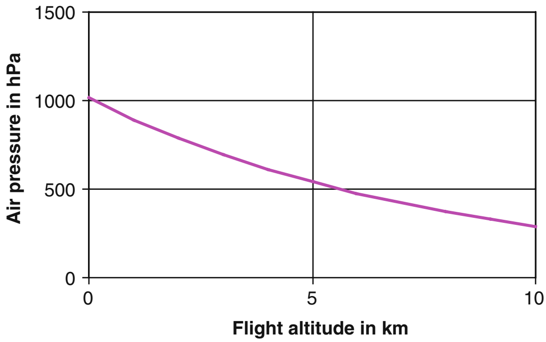

The influence of air pressure P_{Air} must also be compensated. Air pressure, and hence the index of refraction of air, diminishes with increasing flight altitude. Figure 4.2-7 shows the dependence of atmospheric air pressure on the flight altitude, the pressure diminishing exponentially with flight altitude according to

$$P(H) = 1013\,hPa \cdot e^{-\frac{H}{7.99\text{km}}} \tag{4.2-5}$$

The relative change in the index of refraction depends on air pressure at selected temperatures and is shown in Fig. 4.2-8.

The influences of temperature and air pressure on the depth of focus of the system as a whole, however, depend to a large extent on the actual construction, the materials used and the lens design. This point was already made with respect to the athermal design of the lens. It is not possible to give a general formula, such as the one for the variation of subject distance as a function of flight altitude. But we shall make a mental note of the fact that the image distance is a function of the flight altitude H, temperature T and of the altitude-dependent air pressure P:

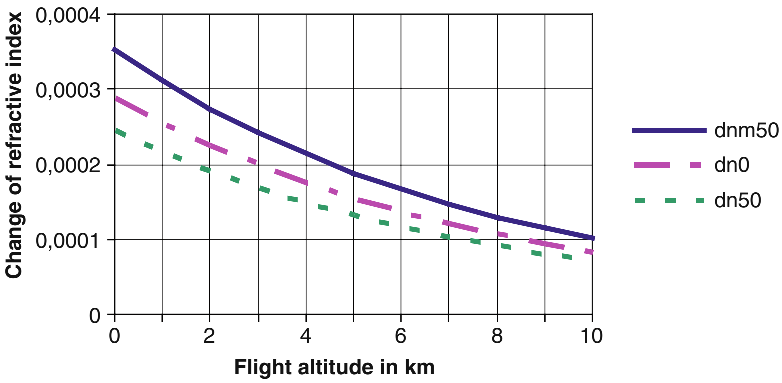

Fig. 4.2-8 Relative variation of the index of refraction of air depending on flight altitude for the temperatures –50, 0 and 50°C (altitude-dependent air pressure)

$$b = f(H, T, P) \tag{4.2-6}$$

Thus the lens must be sufficiently robust to withstand all these influences in order to produce a sufficiently sharp image under real or hypothetical conditions. A modern treatment of the thermal problem, especially the quantitative treatment of non-stationary thermal conditions, can be found in Leica (2003).

4.2.10.2 Transmitting Power and *f*-Number

Photogrammetric lenses often bear cryptic designations such as 15/4 UAGS or 30/4 NATS in the case of Leica. Whereas the first number, here 15, indicates the focal length in cm, the second number is the *f*-number, which is a measure of the transmitting power of a lens, i.e., the light taken up by the objective lens. As shown earlier on, the numerical aperture NA or NA' forms part of this parameter. The *f*-number is defined as:

$$f\# = 1/(2 \cdot \mathrm{NA}') = s'/(2 \cdot Y_{\mathrm{AP}}) \tag{4.2-7}$$

If an image is set to infinity, $f\#$ becomes $f/(2 \cdot Y_{\mathrm{EP}}) = f/A$, where A is the diameter of EP (the entrance pupil). The smaller the *f*-number, the "faster" the optical system, i.e., the greater its transmitting power. The opinion often voiced that the *f*-number is calculated from the ratio of focal length to diameter of the first lens is correct only if the EP is situated in the front lens. This normally holds for normal photographic lenses, but not for photogrammetric lenses. The aperture ratio is also commonly used as the reciprocal value of the *f*-number. For example, if $f = 100$ mm and $A = 25$ mm, then

$$A : f = 1 : 4 \quad \text{or}$$

$$\frac{f}{A} = \frac{100\ \text{mm}}{25\ \text{mm}} = 4.$$

4.2.10.3 Angles on the Lens and Image Sides

Some characteristic optical operating parameters are dealt with below. But first, let us consider Fig. 4.2-9, which shows the ideal case of an individual lens in which both pupils coincide in the centre of the lens. Let the lens be set to "infinity", such that the distance between the image plane and the centre of the lens is the focal length f and let a circular object field with diameter D be imaged on the image array with diameter d. The rays drawn in the figure are the principal rays with which we are familiar.

The intercept theorem applies

$$\frac{f}{h_g} = \frac{d}{D}. \tag{4.2-8}$$

The ratio f/h_g corresponds to the image scale.

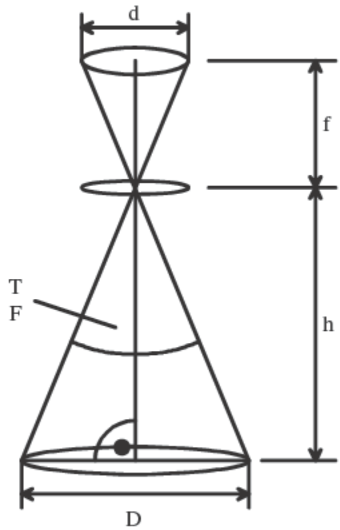

Fig. 4.2-9 Representation of some lens parameters

The peripheral rays limiting the diameter of the object field span the total field of view TFOV:

$$\mathrm{TFOV} = 2\arctan\left(\frac{D/2}{h_g}\right) \tag{4.2-9}$$

Accordingly, the following applies on the image side:

$$\mathrm{TFOV} = 2\arctan\left(\frac{d/2}{f}\right) \tag{4.2-10}$$

But, as a rule, circular films are not used. Indeed, rectangular image formats are used even with solid-state detectors (for example, CCD matrices) in the image plane, i.e., in the focal plane. Figure 4.2-10 shows the conditions in a square image format utilising the maximum image diameter.

According to the Pythagorean Theorem

$$d^2 = (2a)^2 + b^2 \tag{4.2-11}$$

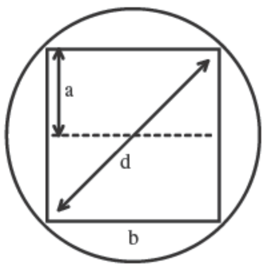

Fig. 4.2-10 Graphic illustrating fields of view

In the case of a square image $d^2 = 2b^2$.

Thus, the square image is $b \times b$, where $b = \sqrt{\frac{d^2}{2}}$.

4.2.10.4 Example

The image diameter for the image array of a 4096 × 4096 matrix with a pixel pitch of 9 μm must be

$$d = \sqrt{2b^2} = \sqrt{2718 \text{ mm}^2} \approx 52 \text{ mm}$$

The field of view (FOV) defined by a line of a matrix or of a line detector of length l is

$$\text{FOV} = 2 \arctan\left(\frac{l/2}{f}\right) \tag{4.2-12}$$

Figure 4.2-11 shows how the field of view FOV varies with the focal length. The line is assumed to have a constant length of $l = 78$ mm corresponding to a CCD line with 12,000 elements and an element spacing $x = 6.5$ μm.

The stereo angle γ of a CCD line camera is dependent on the distance a of the stereo lines from the "nadir line", i.e., the line in the centre of the image directed downwards (Fig. 4.2-12).

$$\gamma_z = \arctan\left(\frac{a}{f}\right)\sqrt{a^2 + b^2}. \tag{4.2-13}$$

γ_z can be regarded more generally as the angle of convergence of two parallel lines (Fig. 4.2-12). It can cause interference even in the case of closely packed lines. In the case of CCD lines arranged side by side with filters for red, green and blue,

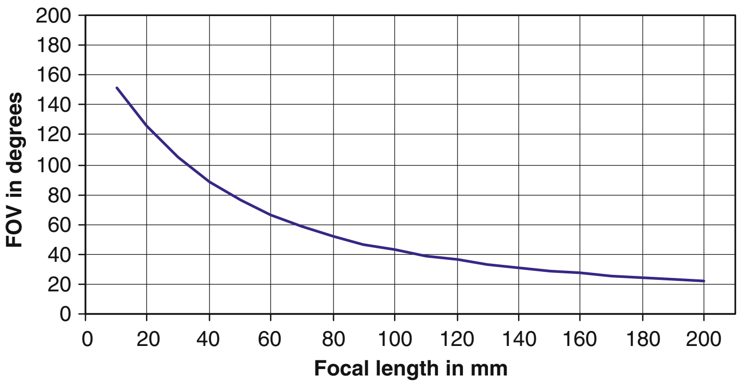

Fig. 4.2-11 Field of view depends on the focal length f of the lens (cross-track detector dimension is 78 mm □ 12,000 elements ($\sigma = 6.5$ μm)

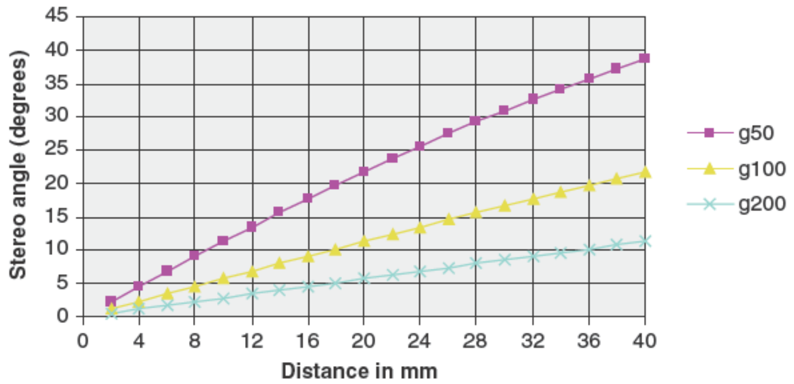

Fig. 4.2-12 The angle of convergence as a function of the spacing of the CCD lines for the focal lengths 50, 100 and 200 mm

interference fringes would form at steep edges if they would not be irradiated from a common IFOV using special measures (see Chapter 7).

In the matrix camera, the angle of convergence γ_M is a function of the overlap o and hence variable:

$$\gamma_M = \arctan \frac{s(1-o)}{f} \tag{4.2-14}$$

In (4.2-12), s is the format width of the matrix in the direction of flight and f is the focal length of the lens.

Figure 4.2-13 shows the range of γ_M for a camera with a 4 k × 4 k matrix and a pixel spacing of 9 μm for focal lengths of 15, 25 and 35 mm.

The two stereo angles of a three-line stereo camera need not be identical, i.e., the distances chosen for the two stereo lines to the nadir line can differ. The required

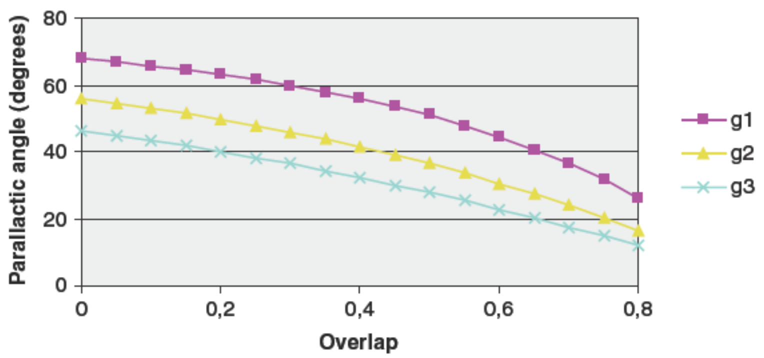

Fig. 4.2-13 Range of angles of convergence of a matrix camera as a function of the overlap o for focal lengths 15, 25 and 35 mm

total field of view, TFOV, of the lens then depends on the larger stereo angle. The following equation is used to calculate the TFOV from the known FOV and $\gamma_{\max}$

$$\mathrm{TFOV} = 2 \arctan \left[\tan^2 \frac{\mathrm{FOV}}{2} + \tan^2 \gamma_{\max} \right]^{\frac{1}{2}} \tag{4.2-15}$$

Thus, the image array diameter is

$$d = 2 \cdot \sqrt{\left(\frac{l}{2}\right)^2 + a_{\max}^2} \tag{4.2-16}$$

or also

$$d = 2 \cdot f \cdot \tan \frac{\mathrm{TFOV}}{2} \tag{4.2-17}$$

Thus the following applies to the instantaneous field of view (IFOV)

$$\mathrm{IFOV} = 2 \cdot \arctan \frac{x}{2f} \tag{4.2-18}$$

where x is the side length of the CCD element. For the sake of simplicity, we regard pixels as being square, where the side length and the distance between pixel centres must be equal. Given today's level of engineering, the intermediate spaces required for separating the optically active areas of the CCD elements are negligibly small. The microlenses placed in the optically active areas collect the light also from these areas to provide a fill factor of virtually 1 for the optically active areas of CCD elements within a CCD line or a CCD matrix (Fig. 4.2-14). This method is not devoid of risks, since it also brings unwanted light outside the ground pixel on to the sensor pixel.

Fig. 4.2-14 Example of a pixel array of a CCD line

Angles are expressed in degrees and milliradians here in line with the dimensions used in digital camera technology for FOV and IFOV. These units are readily convertible, however: 1 radian ≈ 57.3°.

4.2.10.5 Swath Width and Base Length

The following applies to the swath width S covered by the field of view

$$S = l \cdot \frac{h_g}{f} \tag{4.2-19}$$

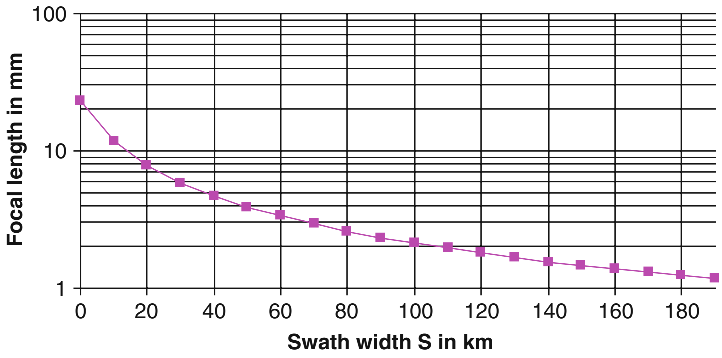

Fig. 4.2-15 Swath width S as a function of the focal length at the given constant flight altitude $h_g = 3$ km; the cross-track detector dimension is 78 mm (12,000 pixels @ $\sigma = 6.5$ µm)

Figure 4.2-15 illustrates the swath width, which is a function of the focal length f, for a flight altitude of $h_g = 3{,}000$ m.

For a given line length l and focal length f, the swath width-to-altitude ratio instantly tells us the swath width associated with a given flight altitude

$$\frac{S}{h_g} = \frac{l}{f}. \tag{4.2-20}$$

The stereo base length B, i.e., the distance a of the CCD lines (see Fig. 4.2-10) projected on to the ground, is expressed by

$$B = a \cdot \frac{h_g}{f} \tag{4.2-21}$$

For a given line spacing a and focal length f, the base length-to-altitude ratio instantly tells us the base length associated with a given flight altitude.

$$\frac{B}{h_g} = \frac{a}{f} \tag{4.2-22}$$

4.2.10.6 Ground Pixel Size and GSD

The size of the projection of a CCD element on the ground is dependent on the focal length and the flight altitude (Fig. 4.2-16):

$$X = x \cdot \frac{h_g}{f} \tag{4.2-23}$$

The GSD is the sampling distance on the ground, if we imagine the pixel centre point as the sampling point. If the sampling points in the direction of flight are selected such that there are no gaps between the lines, then $GSD_x = GSD_y = X$.

The GSD selected in direction x can differ from that in direction y. Rectangular ground pixels in which $GSD_x > GSD_y$ are obtained when the integration time in

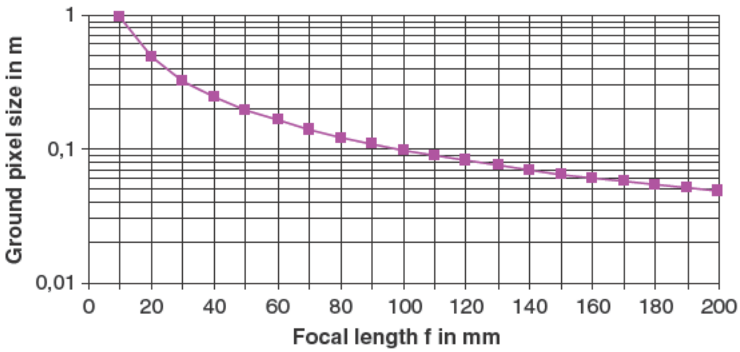

Fig. 4.2-16 GSD as a function of the focal length for a flight altitude of 3 km above the ground

the direction of flight is longer than the time it takes to fly over a pixel extension x (t_{dwell}). It was shown in Section 2.5 that to obtain higher ground resolution, the GSD can also be smaller in both directions than the pixel size.

4.2.11 Aberrations and Precision of Registration

In designing an optical system, the aim is to ensure the required image sharpness and correct image position over the entire image plane and for the entire spectral range. Many lenses are needed to achieve this in the case of a large image array, large numerical aperture and wide spectral range. The paradox of an objective lens system comprising multiple lenses is that each individual lens has to produce an inadequate image so that the image produced by the collective array meets the specifications. Despite the use of modern computer programs, the experience of a designer is still indispensable. The critical issue is not only to minimise the spot diameter, but to take into account the spot's fine structure, which is typically classified into five monochromatic aberrations (Fig. 4.2-17) and two chromatic aberrations (Fig. 4.2-18).

Aberration	Object	Image
Spherical aberration		
Astigmatism		or
Coma		
Distortion		or

Fig. 4.2-17 Types of monochromatic aberration

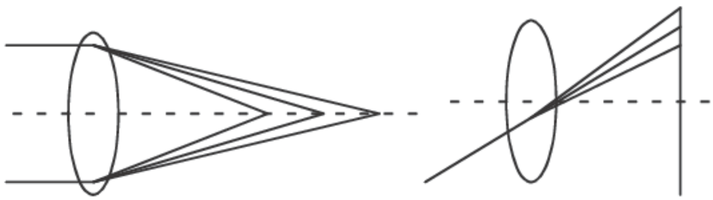

Fig. 4.2-18 Types of chromatic aberration: (a) longitudinal, (b) lateral

These aberrations of a higher order exist in practice, as combinations of the two illustrated above and also as colour combinations. It is important to correct such aberrations, since they can diminish the quality disproportionately if objects are out of focus. The effect of colour coma on the visual system is extremely annoying.

Aberrations are reduced to a minimum by shaping the lenses in an appropriate manner and choosing appropriate types of glass. Differences in dispersion between various types of glass are used to make corrections in colour, or achromatisation. It is possible to correct chromatic aberration using the cement radii of cemented lenses, because as glass/glass combinations their refractive power is weaker than that of a glass/air transition, so the varying dispersions can exert a stronger influence.

Peripheral lenses, i.e., lenses distant from the pupil, are often used to correct distortion, which is defined as a deviation from the ideal attitude Y_r, which is the radial distance from the optical axis in the image plane where φ_r is the field angle:

$$Y_r = f \cdot \tan \varphi_r \quad + \quad \text{distortion} \tag{4.2-24}$$

In film-based cameras, film distortions cannot be corrected, so that a high measure of distortion correction was required when developing lenses. In digital cameras, by contrast, distortions can be corrected by software if the precise distortion value is known through geometric calibration. Relative distortions up to 5% can be compensated through computation. Nor does it matter if the distortions are pillow- or barrel-shaped. This facilitates the design of lenses for digital airborne cameras.

The correction data, measured when the camera is calibrated, stored on the camera computer and used in rectifying image products, must retain its validity under all external conditions such as flight altitude, air pressure and temperature. Any error influences must be compensated by the design of the lens and of the "lens filter focal plane" system in a manner compliant with the required precision of registration (for example, deviations from reference values $\leq$ pixel/5).

Table 4.2-1 summarizes the quantities defined and discussed in this section.

Table 4.2-1 List of key geometric characteristics of an airborne lens for digital airborne cameras with focal length f: detector extent l_y in the cross-flight direction, size of a square detector element x and line distance a in the case of a line camera; and detector extent s in the direction of flight and overlap o in the case of the matrix camera

FOV	$2 \cdot \arctan\left(\frac{l_y/2}{f}\right)$
IFOV	$2 \cdot \arctan\left(\frac{x/2}{f}\right)$
Swath width S	$l_y \cdot \frac{h_g}{f}$
Pixel size on the ground X	$x \cdot \frac{h_g}{f}$
Stereo angle γ_z	$\arctan\left(\frac{a}{f}\right)$
Stereo angle γ_M	$\arctan\left(\frac{s(1-o)}{f}\right)$
Base length B	$a \cdot \frac{h_g}{f}$
Swath width to altitude ratio S/H	$\frac{l_y}{f}$
Base length to altitude ratio B/H_z	$\frac{a}{f}$
Base length to altitude ratio B/H_M	$\frac{s(1-o)}{f}$
Total field of view TFOV	$2 \cdot \arctan\left(\frac{d/2}{f}\right)$
Image array diameter d	$2 \cdot f \cdot \tan\frac{\mathrm{TFOV}}{2}$

4.2.12 Radiometric Characteristics

The radiometric characteristics of a lens include the spectral transmittance as a function of the wavelength and the field angle, the suppression of stray light and the depolarisation of light.

4.2.12.1 Spectral Transmittance

The spectral transmittance of the lens depends on the absorption behaviour of the glass materials and on the reflectivity of the glass surfaces. In general the bulk absorption is not critical for glass in the visible and near infrared spectral range with wavelengths below 1,000 nm, except for the blue spectral range with wavelengths below 450 nm (Fig. 4.2-19). In this range the lead-free glass now produced by all major manufacturers has more absorption than the old types of glass containing lead. This can cause serious problems for objectives with many lens elements.

The manufacturers therefore attempt to keep the transmission loss in limits using special antireflection (AR) coatings on the surfaces of the glass elements. For this

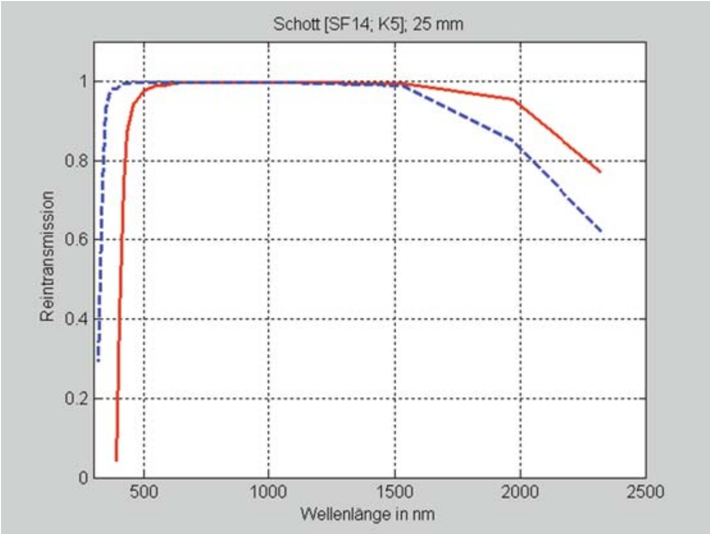

Fig. 4.2-19 Spectral transmission of Schott glass SF14 and K5 with a thickness of 25 mm

purpose we first consider the normal incidence of light on an uncoated glass surface. In air it reflects $R = [(n\text{-}1)/(n{+}1)]^2 = 4\%$, if we select $n = 1.5$. For a lens with 22 glass-air transitions the total transmission would be reduced from 1 to $0.96^{22} = 0.40$, that is less than half of the incident light is lost. It is therefore necessary to develop coatings with a reflectance of <1% over the entire spectral range and for a wide angular range. These requirements are contradictory, making it necessary to deposit in a vacuum a large number of coatings (up to 50) on each lens surface. Each coating is only a few tens of nm thick, which requires expensive, fully automated vacuum equipment, extensive experience and, above all, considerable psychological strength on the part of the operators if the 49th coating exceeds the tolerance!

The transmission measured on a large lens is shown in Fig. 4.2-20. It can be seen that at an average transmission of 0.8 for 22 glass-air transitions, an AR factor of 1% has been achieved over a wide range of the spectrum and that, even in the blue range, very good values were measured despite the material problems mentioned. The consistency of the transmission over the field angle range from 0° to 35° is to be assessed as high overall, as it allows the full dynamic range of the electronic sensors to be used.

4.2.13 Ideal Optical Transfer Function

From the consideration of the physics of optical systems that led to the term "spatial bandwidth" product, we know that every optical system necessarily acts as a "spatial filter", that is, it can only transmit an object of a specific size with a finite spatial

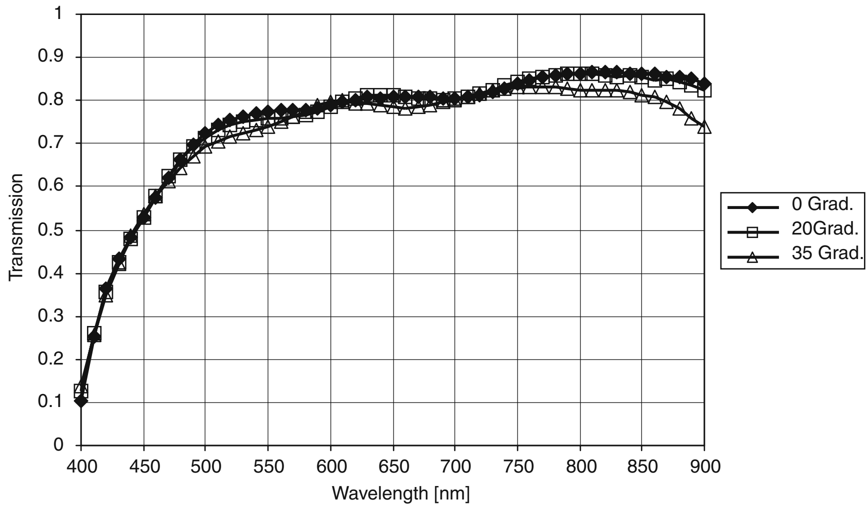

Fig. 4.2-20 Measured transmission values on a 14-element lens system with 22 glass-air transitions (ADS40) in the range between 400 and 900 nm for different field angles 0°, 20° and 35°. The high transmission figures, consistent particularly over the field angle, can only be obtained with extremely complex lens coating processes [Swissoptic AG, 2005]

bandwidth. This means that finer object details can only be transmitted with reduced contrast. There is a spatial frequency at which the contrast transmitted is so small that it is lost in the noise on the film or in the electronics. If a test image with known initial contrast is chosen as the object, this cut-off frequency is also given as a spatial "resolution" for this initial contrast.

Well corrected optical systems can be described as "linear" light intensity transfer systems and can therefore be characterised by a transfer function similar to electronics: this is called the OTF (Optical Transfer Function). The spatial intensity spectrum of our object, e.g. a city landscape, is then multiplied by the OTF for the optical system, resulting in the spectrum present at the sensor's position. As the OTF has a cut-off frequency, the aerial image spectrum at the sensor, prior to its recording by the film or the CCDs, is already reduced in resolution and contrast. In principle, therefore, we lose information during imaging. The Fourier transform of the OTF is also called the "incoherent" point spread function that defines how blurred an object point appears on the sensor.

In the case of diffraction-limited imaging it is found that

$$\mathrm{OTF}_{\mathrm{dl}}(k_x,k_y) = \begin{cases} \frac{2}{\pi}\left[\arccos\left(\lambda\frac{f}{D}k\right) - \lambda\frac{f}{D}k\sqrt{1-\left(\lambda\frac{f}{D}k\right)^2}\right] & \cdots \text{ for } \quad \lambda\frac{f}{D}k \le 1 \\ 0 \cdots \text{ otherwise} \end{cases} . \tag{4.2-24}$$

The diffraction at the edge of a circular aperture of a lens results in a diffraction pattern with an intensity described by the radially symmetrical Airy function

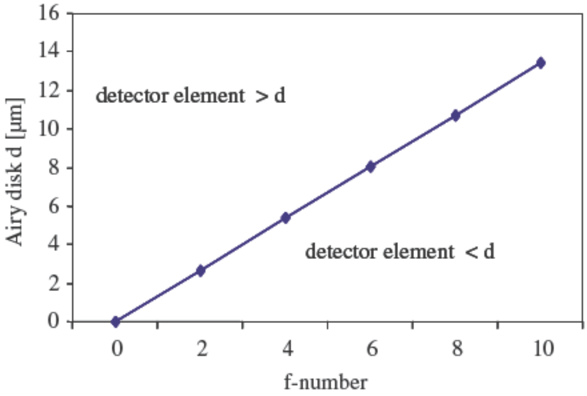

Fig. 4.2-21 Diameter d of the diffraction disc for a diffraction limited lens $d = f\left(\frac{f}{D}\right)$, centre wavelength $\lambda = 550$ nm

(see also Section 2.4 above). The diameter d of the first minimum depends on the numerical aperture of the lens. It is found that $d = 2.44 * f * \lambda/D$, where λ is the centre wavelength. Figure 4.2-21 shows the dependency of the diameter d on the stop number $f\# = f/D$ for a centre wavelength $\lambda = 550$ nm.

The area above the graphed line in Fig. 4.2-21 is the area in which the detector dimensions are larger than the Airy disc diameter d. Then the term "detector limited" system is used, since the geometric resolution of the camera is defined by the detector. If the detector element is smaller than the diameter of the Airy disc, the lens limits the resolution (optics-limited system).

The spatial frequency k is given by

$$k = \sqrt{k_x^2 + k_y^2} \tag{4.2-25}$$

with

$$\Theta = \arctan\left(\frac{k_y}{k_x}\right) \tag{4.2-26}$$

And the direction of the plane wave is given by

$$\exp\left[i2\pi(k_x x + k_y y)\right]. \tag{4.2-27}$$

Figure 4.2-22 shows the graph of OTF_B.

From Equation (4.2-25) it can be seen that at

$$\lambda\frac{f}{D}k = 1 \tag{4.2-28}$$

an exact band cut-off occurs. Spatial frequencies higher than

$$k_{\max} = \frac{D}{\lambda_{\min} \cdot f}, \tag{4.2-29}$$

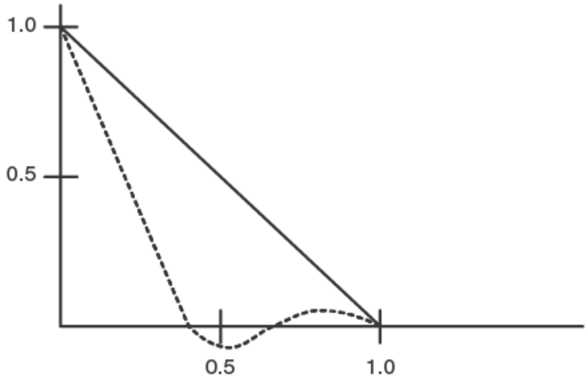

Fig. 4.2-22 OTF for a diffraction-limited lens (*solid line*) and a defocused lens (*dotted line*)

where λ_{min} is the minimum wavelength incident on the detector, cannot pass through the lens.

4.2.14 Real Optical Transfer Function

If real systems are described by their OTFs, it can occur that the function becomes mathematically complex, comprising an amplitude term and a phase term. This is the case, for example, if the incoherent point image has an asymmetrical spatial distribution, which could be due to lens centring errors. Then the OTF as the Fourier transform of the image point becomes complex. While the phase term PTF (Phase Transfer Function) will then keep the optics designer very busy, since it is a source of information on the inner configuration of the optics, the amplitude term, called the MTF (Modulation Transfer Function) is in most cases adequate as a description of the quality of the lens and is therefore often taken by the optics factory as the acceptance criterion for compliance with the specifications.

To determine the OTF, a test image, comprising black and white bars of variable width and spacing and known contrast, is imaged through the lens on a sensor, for example on film, and the observed contrast measured. The spatial frequency $k = 1/x$ given in lp/mm, corresponds to the spacing between the test bars. If the object is enlarged by the optical imaging, the frequency must be reduced correspondingly. In Fig. 4.2-23 a two-dimensional bar code is used as the test image; this image has a wide spatial spectrum. In the figure at the top both the bar code with contrast equal to 1 and its observed image, that is, the measured data, are shown. It can be seen that wider code bars are imaged with significantly higher contrast than narrower bars. The contrast ratio is shown in the figure at the bottom as a function of the frequency of the bar code, that is, the required MTF. At the same time the PTF is also given, which is equal to zero, as can also be seen from the symmetry of the bar code images. A PTF not equal to zero would, for example, be

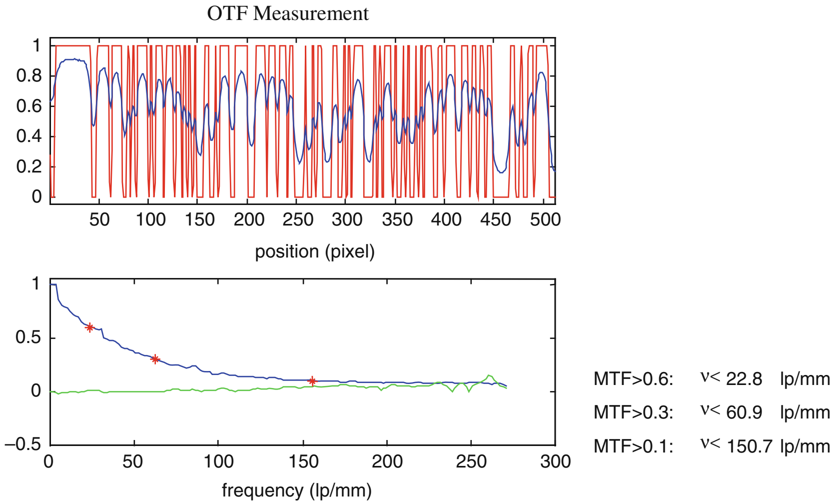

Fig. 4.2-23 Polychromatic OTF for a test lens: the graph at the *top* show the test pattern, a bar code image and the related detected image. The loss of contrast as a function of the width of the code bar can be seen. In the *lower graph*, this situation is plotted as a as a function of the spatial frequency, for both the MTF and the PTF

indicative of possible internal decentring of lens groups, which clearly is not the case here.

The OTF for a real lens cannot exceed the ideal OTF of purely diffraction-limited imaging. If the OTF is less than this ideal, the reduction is, e.g., due to residual aberrations in the design, as well as manufacturing tolerances. Diffraction-limited imaging is unaffordable for lenses as complex as those for aerial cameras, but it is also not necessary.

To design the optics MTF optimally, it is necessary to consider the entire information transfer chain. At this point we will limit ourselves to the case where the pixel layout on the detector is the limiting factor. If x is the pixel spacing and, for simplicity, also the pixel width, then $k_{\mathrm{pix}} = 1/(2x)$ is the related cut-off frequency (Nyquist frequency), so for $x = 3.25\ \mu\mathrm{m}$ we have $k_{\mathrm{pix}} = 153$ lp/mm. It is therefore unnecessary to develop a lens with higher resolution if the sensor is the limiting factor. The lens must therefore transmit information at spatial frequencies below the Nyquist frequency with the maximum possible contrast, but after this the contrast ideally should be reduced to zero.

There are two reasons for this. The high contrast in the low to medium frequency range is necessary since, during airborne use, the atmosphere also acts as a "low pass filter" owing to turbulence and other refractive effects and therefore prevents the optics "seeing" high resolution details on the ground. Nor should the contrast on coarser details be reduced by the optical system. Good lenses perform well in terms of contrast transfer at half the Nyquist frequency.

The second requirement, to keep the OTF as low as possible for frequencies above the Nyquist frequency, is justified by the so-called "aliasing effect". If details on the ground with frequencies above the Nyquist frequency are transmitted with good contrast, sensor undersampling will cause Moiré-like artefacts that will seriously degrade the image and can only be eliminated with extensive effort.

All the above results in an awkward situation for the optical system: the OTF cannot be engineered such that it is equal to one up to the Nyquist frequency and zero after it. It is therefore necessary also to optimise the OTF beyond the Nyquist frequency, but the contrast at frequencies above the Nyquist frequency must then be reduced using measures such as a slight defocus, double-refracting filters or other manipulations.

4.2.15 Field Dependency of the Optical Transfer Function

An important quality criterion for the imaging optics is the consistency of the polychromatic MTF over the field of view, that is, measured over the entire area of the sensor. It is now generally accepted that special averages must be computed for this figure; though the definition of the averages varies depending on whether the optical system is assessed for a two-dimensional array or a linear array.

4.2.15.1 Area Weighting

In the case of two-dimensional sensors such as film or a sensor array, the sensor area is divided into annular zones and the weighting is calculated from the ratio of the annular zone area to the total area. For example, a lens has a focal length of $f = 62.5$ mm and is used for field angles up to +/− 35°, corresponding to a maximum radius in the image of $f\,\tan(35°) = 43.7$ mm. The sensor is a square film with a half-diagonal of 50 mm. If the field of view is divided into 5° steps, eight field angles and, accordingly, eight image radii are obtained. Contiguous annular zones are now placed around these radius values and the area ratio calculated relative to the square film format. This situation is shown in Fig. 4.2-24 below: it can be seen that the centre of the image and the edge of the image have relatively low area weighting, while the image zones at 25° and 30° make major contributions. This weighting makes sense only if the measured image quality of the optical system is rotationally symmetrical.

In practice area-weighted averages are used for various quality criteria, such as the resolution, called AWAR (Area Weighted Average Resolution). For a high-performance lens an AWAR value of 120 lp/mm is appropriate. These figures are determined by imaging so-called "test codes", that is, standardised bar code patterns of variable frequency, in the annular zones and determining the local resolution. The code figures are arranged in the radial and azimuthal directions, as an optical system with astigmatism would produce different resolutions in the two directions.

0	0.0047
5.0	0.0383
10.0	0.0789
15.0	0.1247
20.0	0.1791
25.0	0.2469
30.0	0.2398
35.0	0.0875

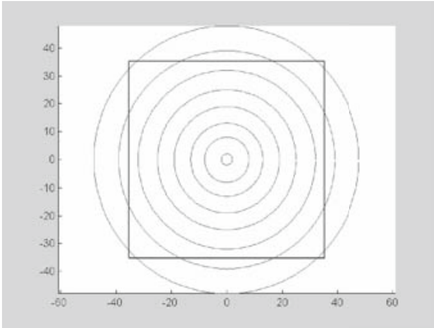

Fig. 4.2-24 Area weightings for a lens with a maximum field angle of 35° for eight annular zones within a square sensor area of 50 mm half-diagonal

Similarly defined quality variables are AWAF and AWAM figures, where *F* and *M* denote frequency and modulation respectively. For AWAF the frequencies at which the MTF has a specific value, for example 0.4, are determined; this figure is then stated as AWAF (0.4) = 70 lp/mm. For AWAM an average of the MTF values at a specific frequency is formed, for example, AWAM (65 lp/mm) = 0.42.

4.2.15.2 Equal Weighting

Referring to the radial symmetry, however, makes no sense for line sensors in push broom mode, such as the ADC40. In this case several rows of CCDs are arranged in the focal plane of the lens, perpendicular to the aircraft's headin. The polychromatic MTF figures or the resolution figures are determined in the direction of the aircraft's heading and perpendicular to the aircraft's heading instead of radially and in azimuth. Area weighting is then not required, as each sensor pixel is evaluated with unit weighting in both directions. Instead of AWAR, AWAM and AWAF, EWAR, EWAM and EWAF are used where the letter *E* stands for "equally". It is clear that the *E* weightings are much sharper than the *A* weightings, as they include the centre of the image and the edge of the image in their entirety.

Realistic measurements on an ADS40 test lens with focal length $f = 62.7$ mm are given in Table 4.2-2. The first column contains the field angle between 0° and 35°, and the seven columns to the right, the defocus, i.e. the distance between the sensor and a mechanical support, varying between 2.100 and 1.980 mm. For each field angle the "test codes" were exposed on film and visually evaluated after the film was developed. The frequency of the just resolvable test image is given for both orthogonal directions. *R* denotes radial, i.e. the code bars point in the radial direction, while *T* for tangential means that the code lines point in the azimuthal direction. Finally, *M* stands for the geometric mean of *R* and *T*.

Table 4.2-2 Measured resolution values for different field angles and defocus settings as well as averaged values AWAR and EWAR (data form an ADS40 with $f = 62.7$ mm) EWAR

w_deg EE*	2.100*	2.080*	2.060*	2.040*	2.020*	2.000*	1.980*
0.0 *R**	128.0*	144.0*	144.0*	144.0*	128.0*	128.0*	102.0∗
0.0 *T**	128.0*	144.0*	144.0*	144.0*	144.0*	128.0*	114.0∗
5.0 *R**	128.0*	143.0*	128.0*	128.0*	143.0*	128.0*	114.0∗
5.0 *T**	127.0*	127.0*	127.0*	143.0*	143.0*	127.0*	113.0∗
10.0 *R**	126.0*	141.0*	159.0*	126.0*	126.0*	112.0*	112.0∗
10.0 *T**	111.0*	139.0*	139.0*	139.0*	124.0*	111.0*	124.0∗
15.0 *R**	124.0*	139.0*	139.0*	139.0*	124.0*	124.0*	98.0∗
15.0 *T**	119.0*	134.0*	134.0*	119.0*	119.0*	119.0*	106.0∗
20.0 *R**	107.0*	120.0*	135.0*	135.0*	135.0*	135.0*	107.0∗
20.0 *T**	101.0*	101.0*	113.0*	113.0*	113.0*	113.0*	90.0∗
25.0 *R**	92.0*	116.0*	146.0*	146.0*	139.0*	116.0*	103.0∗
25.0 *T**	105.0*	105.0*	118.0*	118.0*	118.0*	118.0*	94.0∗
30.0 *R**	78.0*	111.0*	140.0*	140.0*	140.0*	124.0*	111.0∗
30.0 *T**	108.0*	108.0*	108.0*	121.0*	121.0*	108.0*	108.0∗
35.0 *R**	53.0*	66.0*	93.0*	132.0*	148.0*	148.0*	118.0∗
35.0 *T**	86.0*	96.0*	108.0*	136.0*	128.0*	136.0*	121.0
AWAR							
*R**	96.1*	117.1*	137.4*	138.2*	136.5*	125.3*	107.5
*T**	106.5*	111.5*	118.0*	122.3*	120.4*	116.2*	103.7
*M**	101.2*	114.3*	127.3*	130.0*	128.2*	120.7*	105.6
DoF(>100 lp/mm)*	0.120						
EWAR							
*R**	104.5*	122.5*	135.5*	136.3*	135.4*	126.9*	108.1
*T**	110.6*	119.3*	123.9*	129.1*	126.3*	120.0*	108.8
*M**	107.5*	120.9*	129.6*	132.6*	130.7*	123.4*	108.4
DoF(>100 lp/mm)*	0.120						

4.2.15.3 Conclusions

It can be seen from the measurements above that over the entire image field of ±35° the resolution is very high and above all very homogenous. The AWAR and EWAR figures are almost the same, so the lens can be used equally well for two-dimensional arrays and line sensors. Final inspection in the optics factory will "stake" the lens at a system dimension of 2.040 mm, that is, mechanically position the sensors at the distance where the AWAR figures are highest.

If AWAR figures >100 lp/mm are taken as minimum values for acceptable image quality, a "useable" depth of focus DoF of $\Delta z_{IMA} = 0.120$ mm results. This focus range is much larger than the value for an equivalent diffraction-limited lens $\Delta z_{DIFF} = \pm\, 2\lambda\, (F\#)^2 = \pm 0.016$ mm ($\Delta z_{DIFF} = 0.032$ mm), when using $\lambda = 0.5\ \mu$m for the wavelength and $F\# = 4$.

The design included such a large depth of field for two reasons. Firstly, it corresponds to $\Delta z_{OBJ} = f^2/\Delta z_{IMA} = 33$ m in object space, meaning that the lens can be operated without refocusing for object distances from 33 m to infinity. Secondly, and more importantly, we took into account the robustness of the lens under changing environmental conditions. In the case of temperature changes, for example between a warm lens and a variable cold environment, thermal gradients of the glass parameters appear in the radial direction, especially for the large lens elements. Consequently, the refractive index of the lens changes radially with time and temperature, leading to a variable defocus between image centre (still warm) and image edge (already cold). Thus we obtain an image curvature aberration that varies through time. But since the useable DoF is designed to be large enough, no serious degradation of the image quality occurs. The lens can be operated even under severe conditions without degradation of image quality and, more importantly, image magnification.

In conclusion we found that a lens can be effectively assessed by studying the relationship between its EWAR and DoF values.

4.3 Filter

Filters are required to adapt the airborne camera to the task and conditions, taking into account properties specific to the camera (lens, CCD line). They can be distinguished by their action (graded light filers, edge filters) and operating principles (absorption filters, interference filters). At this point, we do not discuss polarisation filters, which operate on a different principle.

As a rule, graded light filters are spectrally neutral grey filters of the absorption type, which are used as anti-vignetting filters in aerial film cameras. The angle-dependent edge intensity drop is compensated by transmittance that increases from the centre to the edge. To save costs, this component can be dispensed with in digital airborne cameras, because correction can be made to the data electronically without signal loss and without exerting a negative influence on the signal-to-noise ratio.

We concentrate here on the properties of colour filters (band pass filters), which are required for true-colour reconstruction of recorded image strips as well as for measurement of reflected intensities as required in remote sensing for the thematic interpretation of data from recorded areas. Band-pass filters are required for the applications mentioned before; they can be in the form of absorption filters or interference filters. Figure 4.3-1 and the table below it provide definitions of some terms used in describing filters

4.3.1 Absorption Filters

Absorption filters can be produced with coloured glass or with organic substances deposited directly on to the CCD. The organic substances that are directly deposited by CCD are clearly suitable for true-colour reconstruction. Long-term stability of the filter properties under the challenging storage and service conditions with regard to temperature and humidity should be checked on an individual basis. As a rule, coloured glass filters are used. Band-pass filters can be composed of a number of

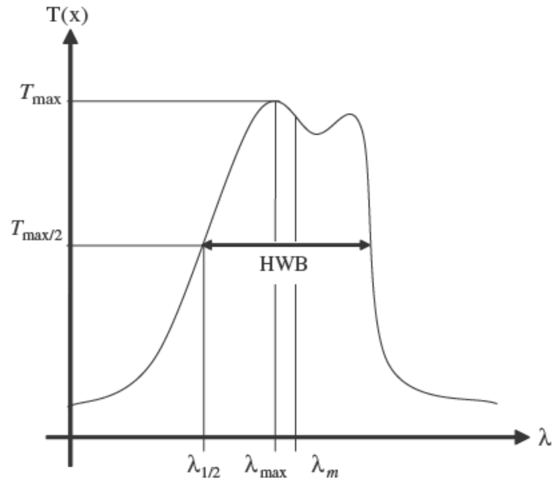

Fig. 4.3-1 Illustration of some filter characteristics (Oriel, 1987)

Transmission, T	Spectral transmission ratio: ratio of transmitted radiation flow to total incident spectral radiation flow in %
Effective index of refraction, n^*	The apparent index of refraction of an interference filter, which is a product of the combination of the refraction indices of the substrate, the finish and the epoxy
Full-width half-maximum (FWHM)	Portion of the transmission range at half of the maximum transmission ratio
Transmission width	Wavelength range between the blocking edge and the transmission edge; the position of the edges must be defined; HWB is the 50% transmission width
Edge slope	Slope of the transmission curve in percent $= 100\frac{(\lambda_{80}-\lambda_5)}{\lambda_5}\%$
Blocking range	Range outside the pass band in which the radiation is suppressed
Blocking ratio	Ratio of maximum transmission outside the pass band to the maximum transmission value T_{max}
Transmission edge	Describes the transition from the short-wave blocking range to the transmission range; usually defined as the wavelength at which transmission has reached 5% of T_{max}
Blocking edge	Describes the transition from short-wave transmission range to the blocking range; usually defined as the wavelength at which transmission has dropped to 5% of T_{max}
Peak wavelength λ_{max}	Wavelength at maximum transmission in the pass band
Centre wavelength, λ_m	Wavelength of the centre of HWB, not always identical with λ_m
Short pass filter	Filter that allows short wavelengths to pass through it, blocks long wavelengths and has a steep curve in the transition range
Long pass filter	Filter that blocks short wavelengths, allows long wavelengths to pass through and has a steep curve in the transition range

different colour filter glasses, which determine the rising and falling edges with regard to the blocking edge, the transmission edge, the centre wavelength, the edge steepness, HWB and the transmission T. Examples of such curves are shown in Figs. 4.3-2 and 4.3-3. The characteristic feature of glass filters is that steep falling

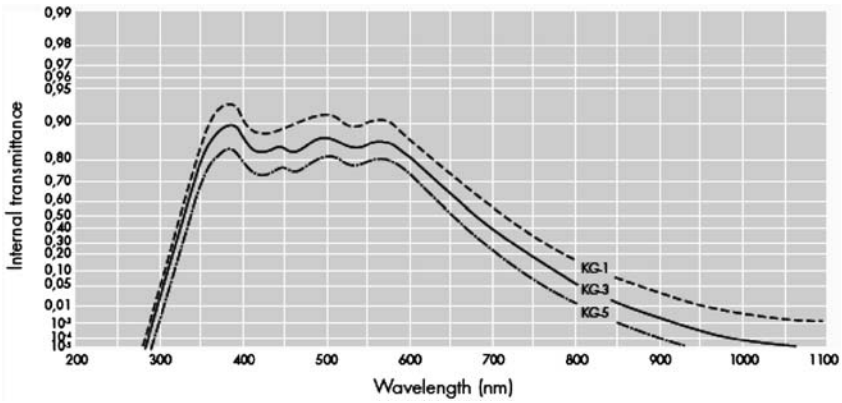

Fig. 4.3-2 Transmission curves for coloured glass with band-pass charactristics (Oriel, 2004)

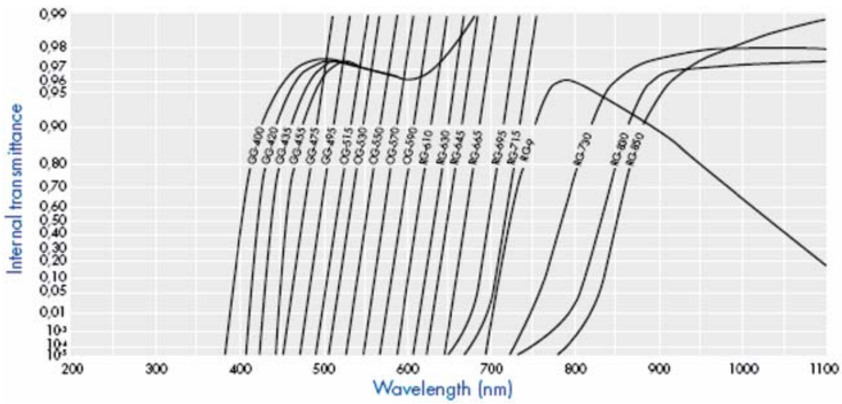

Fig. 4.3-3 Transmission curves for coloured glass, showing blocking edge gradations (Oriel, 2004)

edges are difficult to achieve. The gradation of the rising flanks is also very coarse for remote sensing applications. Glass filter combinations, however, produce very good results in true-colour reconstruction. It should also be noted that spectral transmission consists of two components

$$T(\lambda) = P(\lambda) \cdot T_g(\lambda), \qquad (4.3\text{-}1)$$

where $T_g(\lambda)$is the spectral transmission of the glass itself and $P(\lambda)$ is an almost constant factor which describes the losses at the two air-glass transitions and which, by means of appropriate surface coating, can be set approximately equal to 1.

Tilting does not affect spectral properties, but it extends the optical paths and hence reduces transmission. Temperature has little influence. An increase in temperature shifts the edges towards longer wavelengths. The shift is reversible and, depending on the glass filter, lies in the range> $\lambda/\Delta T \cong 0.02 - 0.25\,\text{nm/K}$in the temperature range 10–90°C.

4.3.2 Interference Filters

These filters are made using vapour-deposition by combining multiple thin layers of dielectric material with different indices of refraction. This is done in such a way that specific interferences are generated in transmitted light to obtain specific band-pass filters. It is also possible to define the transmission curve: steep rising and falling edges can be placed on the selected wavelengths. These are the filters of choice to meet tight tolerance parameters.

The central wavelength shifts linearly towards longer wavelengths with increasing temperature. The shift factor depends on the original central wavelength and varies between 0.016 and 0.03 nm/K in a temperature range of −50 to +70°C (Oriel, 2004).

Owing to the structure of the interference filters, there is a shift of the wavelengths to shorter wavelengths with increasing angles of incidence. In the case of small angles, this effect can be used to adjust a filter to a selected central wavelength, as shown by Equation (4.3-2). In the case of small angles of incidence, there is no distortion of the pass band or reduction of maximum transmission. Using

$$\lambda_\alpha = \lambda_0\sqrt{1-(\frac{n_e}{n^*})^2\sin^2\alpha}, \tag{4.3-2}$$

the shift of the central wavelength can be determined for $\alpha < 10°$.In this equation,$\lambda_\alpha$is the central wavelength at angle of incidence α;λ_0, the central wavelength, normal incidence; n_e, the index of refraction of the surrounding medium ($n_e = 1.0$ for air); n^*, the effective index of refraction of the filter; and α, the angle of incidence of light.

Since interference filters are hygroscopic, they must be protected from moisture. Interference filters should be chosen if narrow-band filters with defined steep edges are required for remote sensing applications.

4.4 Opto-Electronic Converters

Electronic images are formed through illumination and by converting radiation intensities into electrical signals. Semiconductor image sensors, i.e., CCD and CMOS components made of crystalline silicon in matrix or line arrays, are normally used as opto-electronic converters. In general, the advantages of crystalline silicon image sensors include the excellent electrical properties of this material and good control of the technologies involved. Both technologies are based on the (inner) photoelectric effect in which light impinging on a material excites electrons.

The CCD is photosensitive, fast and has a large dynamic range. It is relatively expensive, however, and its manufacture is complicated. Additional components are required for its drive and for eliminating undesirable effects such as smearing and blooming. Since CCD sensors require more space and consume more power, they are better suited to environments in which the emphasis is on high image quality rather than compactness and portability. They are particularly well suited for use in astrophotography, research and industry. CCD-based line sensors are used mainly in scanners.

CMOS sensors are economical with energy and can be made using efficient standard processes. Since image-processing electronic elements can be integrated on chips, they are compact in size. Blooming and smearing effects are prevented through individual pixel drive. This direct pixel drive through pixel match enables individual image sections to be read out at a high image repeat rate (windowing). Moreover, the CMOS sensor is designed for a greater temperature range than the CCD. Recent technological advances have made it possible to mass-produce CMOS chips at low prices. In view of ongoing development, CMOS technology can be expected sooner or later to catch up with CCD in terms of the image quality and, in view of its other advantages, crowd it out. But currently, the CCD sensor is the proven technology in terms of image sensing and it provides better image quality at high resolutions.

A distinction is made between digital cameras with area array CCD sensors (matrices) and those with linear CCD sensors. Depending on the application (moving or non-moving images, required resolution, etc.), lines or matrices are preferred.

Linear CCD sensors have proved themselves in scanner technology and, as a rule, they allow a markedly higher resolution at lower cost. CCD lines are arranged in the image plane of an object especially for CCD image acquisition from aircraft or satellites, making it possible to acquire all pixels of an image line oriented at right angles to the direction of flight. Through the sensor carrier's own motion, a ground strip is imaged line by line at an appropriate imaging frequency, hence the term pushbroom scanning. 24,000-pixel line CCDs consisting of staggered $2 \times 12{,}000$ pixel CCD lines (offset by ½ pixel) have been developed specifically for the ADS40 airborne camera.

4.4.1 Operating Principle

Since detailed descriptions of operating principles and physical aspects of semiconductor CCDs have already been published in the literature, only brief summaries are given here.

An image is a two-dimensional sample of light intensity of different colours. Light impinging on a photocell or a pixel of a (CCD) sensor produces an electrical charge in the form of free electrons (internal photoeffect) and, owing to the temporary absence of electrons in the crystal, positively charged holes. The number of electrons increases in proportion to light intensity, i.e., to the number of photons (light quanta). The free electrons are then collected in the silicon substrate potential sink while the holes move out of the silicon substrate. The potential sinks can trap only a certain maximum number of charges, which in the end determines the dynamics of the CCD sensor. The colour of the light – the energy of the photon plays only an indirect role. The optical properties (spectral transmission) of the electrode material determine the quantum yield (photo responsivity) at different wavelengths.

In its simplest form, the CCD is a linear array of tightly packed MOS diodes, the bias voltage of which is set such that there is a marked depletion of majority charge carriers on the surface. Basically the same process takes place in each MOS diode – the principle is shown in Fig. 4.4-1. Incident ultraviolet, visible or infrared light penetrates a very thin transparent electrode (1) and the translucent oxide layer (2) and then impinges on the semiconductor material (3). When a voltage is applied

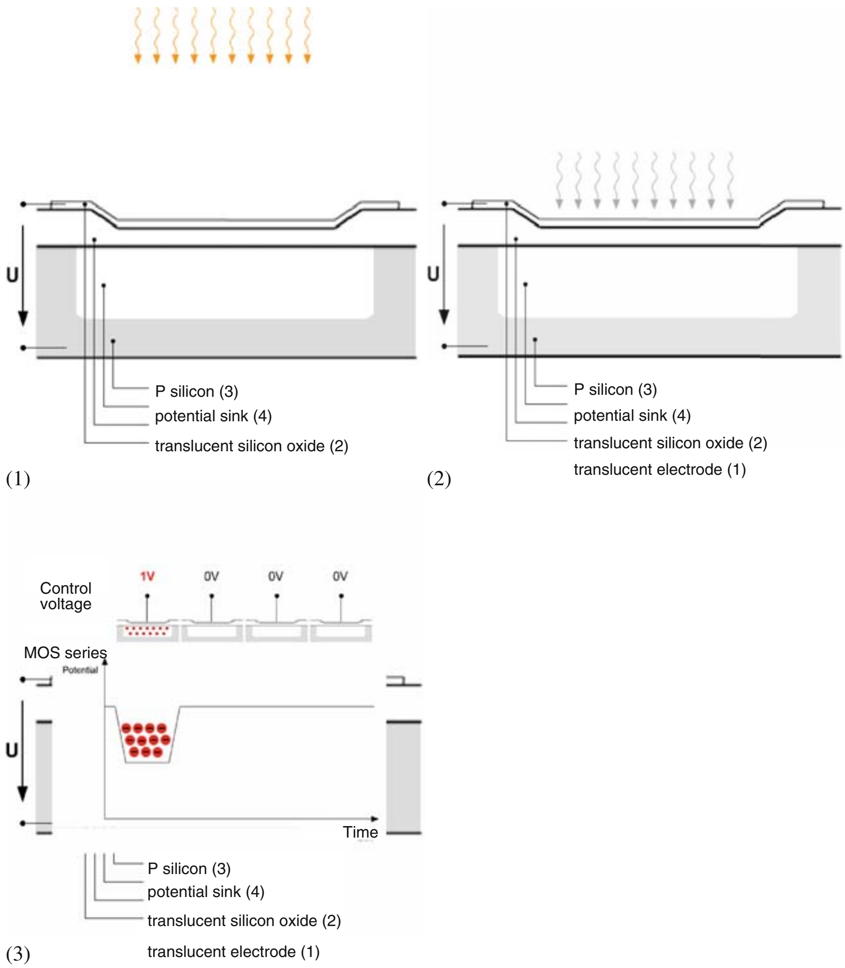

Fig. 4.4-1 Generation of charge carriers in silicon by incident light

to the electrode, a potential sink (4) is formed in specially doped silicon. More charge carriers are formed in this potential sink (charge-carrier-free zone) by the energy of the light quanta.

The image-dependent charges collected in the MOS diodes (pixels), rather as if in a pot, need to be read out before they can be processed. This takes place in two phases, which are different, but share a similar operating principle. In the first phase, all pixels of a line are shifted in a *parallel* arrangement to a readout register of the same length; in the second phase, they are shifted in this shift register in a *series* arrangement to the output.

The operating principle of the readout register is shown in Fig. 4.4-2. The charge is transferred from one cell to the next by changing the voltage level of adjoining cells. In principle, this operation takes place in three potential phases. The cells are isolated at the highest potential (0 V); at the second-highest (2 V), the charge carriers can move to the next cell; at middle potential (1 V), the charge carriers are collected in a trough, which is isolated from the adjoining cells.

The charges obtained by photoelectric means still need to be converted into voltage magnitudes that can be evaluated. The signal generated in the voltage converter must correspond as closely as possible to the original charge sample. For this reason,

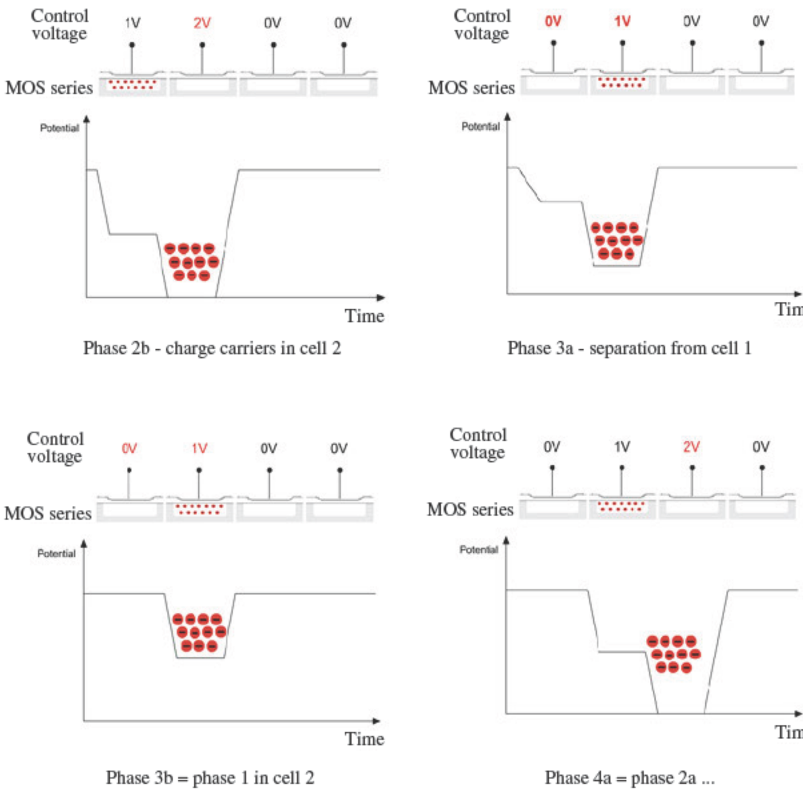

Fig. 4.4-2 Illustration of the charge transfer principle in a CCD

source follower circuits are used as charge-voltage transformers to ensure this linearity. Longer readout registers (>500 pixels) are frequently split for reading out in opposite directions from the centre and arranging output amplifiers at either end of such a split readout register.

Figure 4.4-3 shows a typical output stage. It is part of a typical Kodac CCD line array as shown in Fig. 4.4-7. The principle of the output stage is briefly explained as follows. The reset clock ϕ_R is “ON” to reset the *N*-doped side of the floating diffusion diode to a positive potential by means of transistor $Q1$. As soon as reset is switched to “OFF”, this side of the diode floats and the output signal charge can become effective by pushing the charge into the floating diffusion point using push clocks ϕ_1 and ϕ_2. This generates a voltage that can be evaluated and thus the output signal has reached its new value. In the next phase, the floating diffusion point is reset again and the process starts anew. The level that is produced at reset is termed reset level (typically 6–9 V; see also the clock diagram in Fig. 4.4-4) and is superimposed by a characteristic reset noise, part of the CCD noise, which is explained in Section 4.4.3.

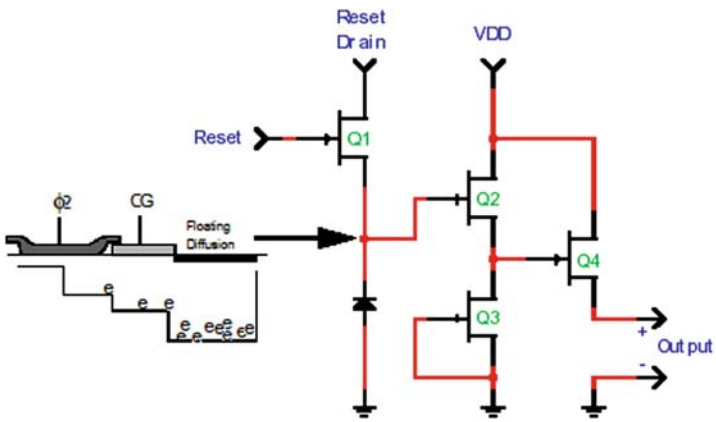

Fig. 4.4-3 Typical CCD output stage (Kodak, 1994)

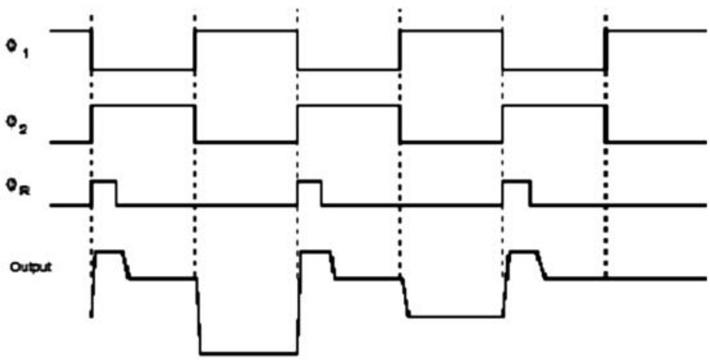

Fig. 4.4-4 Clock diagram of a CCD output stage (Kodak, 1994)

4.4.2 CCD Architectures

For a better general understanding, let us first review the various types of CCD sensors and their practical significance in imaging.

Line sensors consist of a single row of adjoining CCD cells (pixels). They sample the image line by line while either the object, such as a conveyor belt or CCD scanner, is in motion. For colour images, the red, green and blue colour portions must be acquired in three different exposure phases. Very high resolution is obtained with line sensors.

Trilinear line sensors consist of three parallel sensor lines, each of which carries a red, a green and a blue colour filter on its top side. This enables a colour image to be captured in a single scanning operation. The filters are mounted on the chip by the CCD manufacturer or subsequently on the cover glass according to the customer's specific requirements. Trilinear line sensors provide the maximum resolution and colour reproduction quality.

TDI line sensors can be regarded as a cross between line sensors and area array sensors. Unlike linear sensors, they have not one but several photosensitive lines arranged side by side. The shifting of the image data from one line to the next is synchronised with the motion of the object being scanned (or of the scanner, for example, a satellite) and the data are analogously cumulated. This gives TDI sensors advantages over conventional line sensors, which include reduced noise and, above all, higher responsivity. This is important in applications with fast-moving objects requiring exposure times that are too short for normal line sensors, since, owing to the fact that the lines are superimposed, exposure times of TDI sensors are effectively longer than those of linear sensors.

Area array sensors (matrices) capture all image pixels simultaneously, enabling moving objects to be photographed at (virtually) any shutter speed. They are optionally fitted with a colour filter matrix (Bayer mosaic) enabling a colour image to be captured in one step. The disadvantage here is that the resolution is diminished.

Interline and frame transfer CCDs use two separate surfaces for recording images and for transferring the charge. In this way, the readout operation and exposure of the next image can take place simultaneously. They are used primarily in digital and video cameras for recording moving objects and for full videos.

Full-frame transfer sensors use almost their entire surface for light conversion, thereby providing a better optical resolution than interline or frame transfer CCDs.

X3 image sensors (presented for the first time in 2002) represent an entirely new CCD technology, which makes it possible to make full use of the entire complement of pixels for colour images. X3 is based on the fact that that the depth to which light penetrates silicon depends on its wavelength. X3 has three superimposed layers with colour receptors embedded in silicon, so that the entire set of colour data can be recorded on each pixel. In this way, the colour resolution is virtually three times that of a conventional area sensor.

Driven by numerous special applications, a wide variety of line and matrix sensor architectures has come into being. The maximum number of pixels in the case of line sensors lies between 10 k and 20 k (unstaggered) and, in the case of matrix sensors, 10 k × 10 k. Since the technological complexity increases at an enormous rate, it is extremely difficult to manufacture larger sensors as monolithic units.

4.4.2.1 Lines

As already mentioned, line sensors usually consist of a single photosensitive line (except in the case of TDI). The horizontal shift register is situated beneath the line. A charge barrier prevents charges from flowing out into the shift register prematurely during the integration process. The principle is illustrated in Fig. 4.4-5.

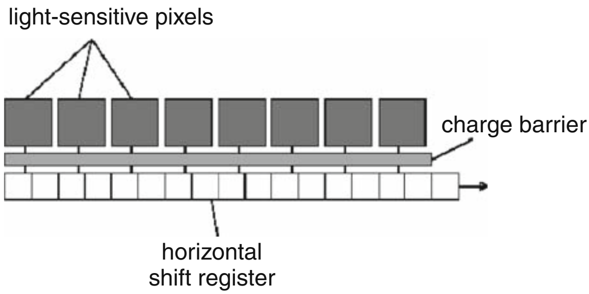

Fig. 4.4-5 Principle of the line sensor (Engelmann and Ahner, 2004)

The enormously high data rate is a key problem with larger CCD sensors. For instance, a line sensor 12,000 pixels long is to be read out at 2,000 lines per second. This corresponds to a frequency of 24 MHz if only one output is used (Fig. 4.4-7), which is close to the physical limits. Various methods are used to solve this problem: in the simplest case, one horizontal readout register can be placed above and one below the line (Fig. 4.4-6). If the pixels are numbered consecutively from 1 to x, the odd pixels (1, 3, 5, 7. . .) are read out downwards, the even ones (2, 4, 6, 8. . .) upwards. In this way the readout frequency is halved. This is referred to as the interleaved mode. The two data streams are processed separately and sorted only after undergoing analogue-digital conversion.

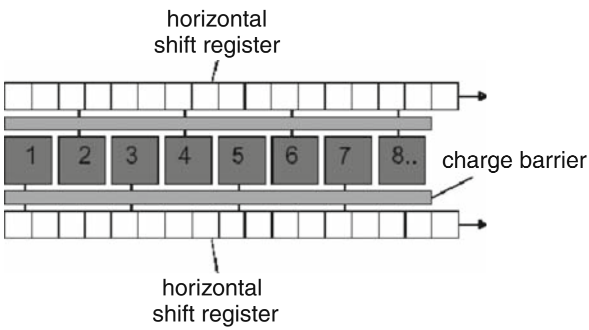

Fig. 4.4-6 Line sensor with interleaved pixels (Engelmann and Ahner, 2004)

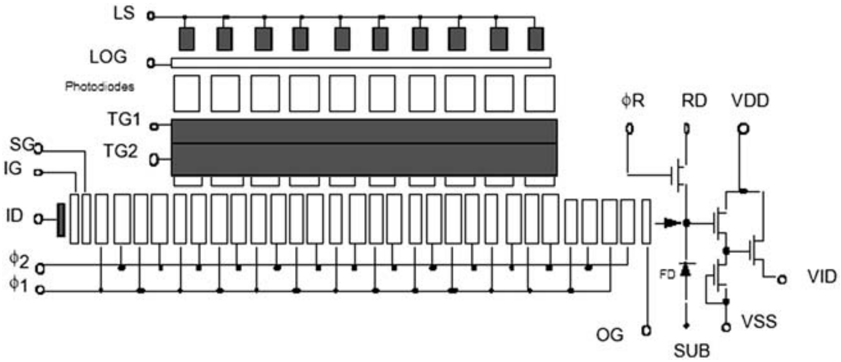

Fig. 4.4-7 Block diagram of a line sensor made by Kodak (IAI FZK, 2004)

The rate can be increased further by dividing the two readout registers into two halves that can be read out in opposite directions (in this way the frequency is halved again) or by subdividing the line into several smaller segments, which are then read out simultaneously and separately (this method is termed multi-tapping).

4.4.2.2 Matrices

The essential operating principles of the various matrix architectures mentioned in the foregoing are briefly described below (Engelmann and Ahner, 2004).

Interline Transfer Matrices

This sensor type is the prototype of the CCD matrix and is no doubt the most common sensor type worldwide. It is used in almost all commercial cameras and provides very good results even in professional image processing. In the interline transfer sensor, there are columns with vertical shift registers between the photosensitive pixels, which virtually constitute parallel readout memories for each pixel (Fig. 4.4-8). These registers are protected from incoming light rays by metal masks.

When the exposure time expires, the image is written at high speed in vertical registers which are provided as intermediate memories. Then, while these vertical registers are being read out, the pixels are already collecting photons of the next image, so neither a shutter nor a synchroniser is required.

The entire sensor is now read out line by line by transferring the charges of all vertical shift registers step by step, according to the bucket chain principle, downwards to the horizontal readout register. The charges are now read out according to the line architecture described in Section 4.4.2.1 and, depending on the application, processed into an analogue or digital signal. In this way, the entire sensor is read out line by line.

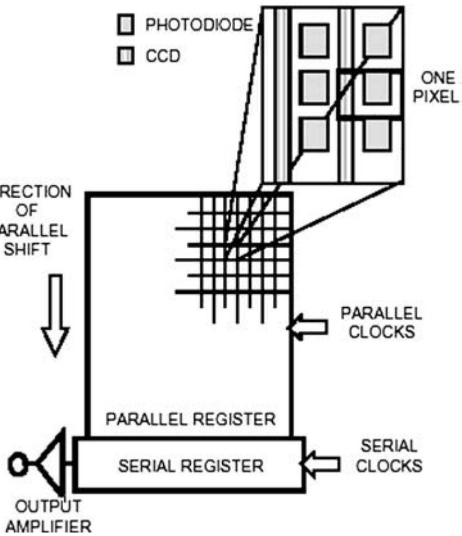

Fig. 4.4-8 Interline transfer CCD principle according (IAI FZK, 2004)

Frame-Transfer Matrices

The architecture of frame-transfer CCDs is similar to that of full frame CCDs. Frame-transfer matrices have a huge parallel shift register, which is divided into two areas of equal size. These areas are referred to as image array and storage array. The image array consists of a photosensitive photo diode register that serves as an image plane and collects the incoming photons on the CCD surface. After the image data have been collected and converted into electrical charges, the charges are immediately shifted to the storage array, which is normally non-photosensitive, to be read out by a serial shift register there (line architecture). The transfer time from the image array to the storage array depends on the size of the storage array. Matrices of this type operate in either full-frame or frame-transfer mode. By using mechanical shutters, a frame transfer CCD can be used to record two images in very quick succession, a feature that is occasionally used in fluorescence microscopy.

As can be seen in Fig. 4.4-9, the storage array must be covered to prevent interaction with the incoming photons. The image array collects new photons for the next image while the storage array is being read out. The ability also to do without a shutter or synchronisation is an advantage of this architecture, which makes it possible to increase the readout speed and increase the image rate.

In some cases, frame-transfer CCDs have problems with image smear effects, which are caused by simultaneous imaging and storage. Smear effects are limited to the time the matrix requires to shift the recorded image to the storage array. Generally, matrices of this type are more expensive than interline matrices, because it takes twice as much silicon to make them. The essential difference between frame transfer and interline transfer sensors is that the latter have no separate vertical

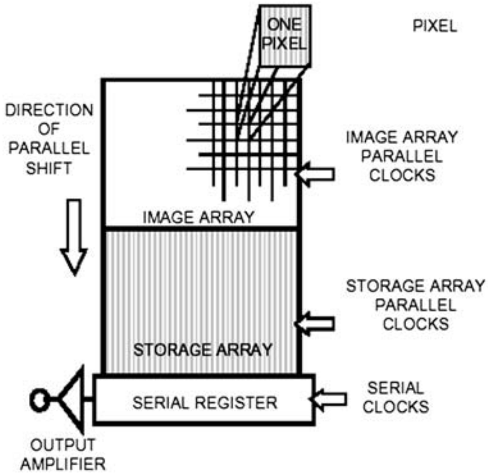

Fig. 4.4-9 Frame-transfer CCD principle (IAI FZK, 2004)

readout registers. Instead, the photosensitive pixels are themselves used as vertical readout registers, so there are no "blind spots" in the pixel field.

Full-Frame-Transfer CCD Matrices

Full-frame CCDs have very large pixel fields, which can provide images with the highest resolution currently possible. Owing to its simple structure, reliability and simple production technique, this CCD architecture is in widespread use. The fact that there are no blind spots in the pixel field is important (Fig. 4.4-11). The pixels cover the entire area on to which light impinges during the exposure phase (Fig. 4.4-10). The data are read out first line by line in parallel and then in serial manner.

The principal advantage of this matrix is its 100% light efficiency relative to the surface. To simplify storage and image processing operations, the resolution of many full-frame CCDs is to the power of two (512 × 512 or 1024 × 1024). To

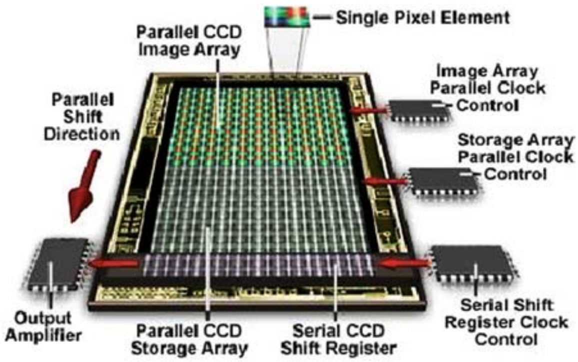

Fig. 4.4-10 Frame-transfer CCD architecture (Engelmann and Ahner, 2004)

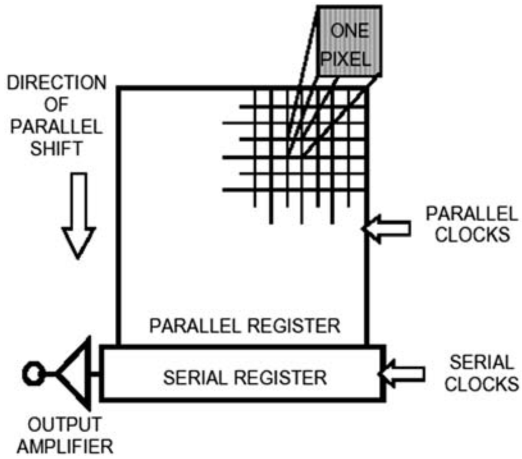

Fig. 4.4-11 Full-frame transfer CCD principle (IAI FZK, 2004)

prevent image distortion, they have square dimensions, up to 20 megapixels, and a pixel size of 7–24 μm.

Since the pixel field is used for both the exposure and readout, it is necessary to have a mechanical shutter or some other form of synchronisation to prevent smearing when photographing. These smearing effects are always produced when photodiodes are being continuously exposed, i.e., they are exposed or overexposed during readout as well.

The maximum readout speed is limited by the bandwidth of the output amplifier and by the speed of the peripheral processing electronic array (see Section 4.5). But it can be markedly increased if the image is divided into smaller sub-images of equal size, which are then read out simultaneously. In a subsequent operation, a video processor reassembles the image digitally. Both the front – and the rear-side exposures have been implemented with full-frame CCDs.

In the case of rear-side exposure, the incoming photons are converted into electrical charges more effectively than in the case of front-side ones, because the light coming from the rear does not have to cross the gate covered by the photosensitive photodiodes.

The disadvantage of full-frame cameras is that they can only provide individual time-delayed images and not a continuous video stream, because the shutter has to be shut repeatedly during readout. This predestines this type of CCD for scientific and medical applications, where little light is available and higher resolutions are required, such as astronomy.

TDI/CCD Lines

Time delayed integration (TDI) is a technology in which electrical charges of parallel CCD lines are pushed at right angles to the line in synchronisation with the motion of the object to be scanned (comparable to the vertical shift registers of an

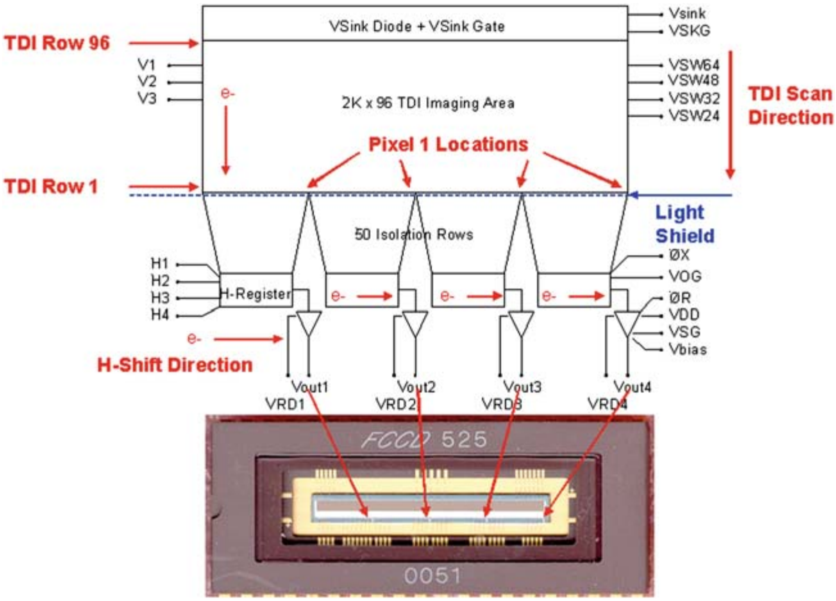

Fig. 4.4-12 TDI-CCD principle illustration based on CCD525 from Fairchild (Fairchild, 2004)

area array sensor). In this way, the same section of the object (despite its motion) is photographed over a number of lines (TDI stages) on the same pixel, so that the integration time is multiplied by the number of stages. The principle is illustrated in Fig. 4.4-12.

Or with other words: unlike linear sensors, TDI sensors have several photosensitive lines arranged side by side (a markedly asymmetrical matrix, at it were), the image data being pushed from one line to the next in synchronisation with the motion of the object to be scanned and read out according to a defined number of TDI stages, which in many cases is even selectable. The readout registers are subdivided (multi-tapping, see Section 4.4.2.1) to ensure very fast readout.

The advantages of TDI sensors over conventional line sensors include not only a noise reduction of N (N = number of TDI stages), but, even more importantly, increased responsivity (directly proportional to N). The latter is particularly beneficial, for instance, to applications involving fast-moving objects, when the integration times are too short for normal linear sensors.

Interlaced or Progressive Scan as Matrix Readout Mode

For the sake of completeness, readout methods commonly used in video technology of interlaced or frame-transfer CCD are briefly reviewed to show how flexible these sensors are and that the image composition is adaptable to a wide variety of (video) requirements.

On the one hand, there are sensors that operate exclusively with interlaced technology (field method). This method, in which each video image is composed of two fields, was originally used in television technology. The speed at which this happens is determined by the video standard. In Europe, the so called CCIR standard is normally applied. Under the CCIR standard, 25 whole images per second are produced from 50 fields. In the USA, the RS170 and the EIA standards, under which 30 whole images are produced per second from 60 fields, are commonly used. These standards are used almost exclusively in television and video devices that are currently in general use.

There are different ways of producing fields in a sensor. In the field integration mode, the two fields prescribed under the CCIR or RS170 video standard are recorded on the sensor at completely different time points. In each field, the charges are shifted from two superimposed pixels into a cell of the vertical shift register, i.e., they are in effect added up. As a result, the brightness is almost doubled. The position of the two pixels changes from field to field with a pixel offset in the vertical direction. The problem that arises as a result is that if an object is in motion, it is photographed at two different time points. If the fields are merged into a full image, the so-called comb effect is produced.

In the frame integrated mode, the two fields are also photographed at different time points, but in contrast to field integration mode, the integration times overlap. For each field, only the charges of one pixel are shifted to a cell of the vertical shift register. The position of the pixel changes from field to field with one pixel offset in the vertical direction, which means that the integration sections intersect each other over a certain length of time. Hence, a "standing" image can be generated by using a flash which is triggered precisely at the overlap. Sensors using the progressive scan technology produce an image consisting of a complete, full image, rather than of two fields. Typical image formats are VGA resolution (640 × 480 pixels) or super-VGA resolution (1,280 × 1,024 pixels), where the video signal is usually put out in the non-interlaced format. Normal television and video devices cannot handle this format, but it offers enormous advantages for image processing (compatible with PC technology). It is no longer necessary to trigger a flash at the right instant, since all pixels of the sensor are exposed simultaneously.

The two-channel progressive scan is an enhancement in which the CCD sensor operates with two horizontal shift registers. In this way, the sensor contents can be read out simultaneously via two video channels. To do this, all odd lines are read out via video channel 1 and all even lines of a full picture, via video channel 2. In the next full image, all even lines are transferred via video channel 1 and all odd lines, via video channel 2, etc. As a result, the sensor can now operate at double speed (for example, 50 or 60 full images per second), and, moreover, a normal interlaced signal, which is compatible with the normal video standard, is applied at each video channel.

4.4.3 Properties and Parameters

A multitude of physical quantities is required for defining and assessing CCD sensors and cameras. The principal ones are described below.

4.4.3.1 Signal-to-Noise Ratio

The signal-to-noise ratio (SNR) in a CCD sensor or in a CCD camera can be expressed in simplified form as a ratio of signal electrons to noise electrons:

$$\mathrm{SNR} = n_{\mathrm{signal}}/n_{\mathrm{noise}}. \tag{4.4-1}$$

where SNR is the signal-to-noise ratio, n_{signal} the number of signal electrons and n_{noise} the number of noise electrons. The number of signal electrons, which depends on the luminance or on the impinging photons, can be stated as follows:

$$n_{\mathrm{signal}} = (\Phi/h \cdot \nu) \cdot t \cdot \mathrm{AP} \cdot \eta. \tag{4.4-2}$$

where Φ is the intensity in [W/m^2], $h \cdot \nu$ the photon energy [Ws], t the exposure time [s], AP the pixel area [m^2] and η the quantum efficiency.

4.4.3.2 Noise Sources

Noise is defined as a signal of limited power,the random (statistical) properties of which are known. A distinction is made between noise sources in time and space. Noise in time can be minimised, but not eliminated. Noise in time typical of CCDs includes shot noise, reset noise, output amplifier noise and dark current noise. By contrast, spatially determined noise can be eliminated to a large extent through suitable correction algorithms, characteristic ones being PRNU and DSNU.

Fundamentally, noise electrons in CCD images are generated by three processes, which are connected with the release (photogeneration and thermogeneration) and the readout process of electrons:

Photon noise is equal to the square root of the number of signal electrons (in accordance with the laws of Poisson distribution in photogeneration). CCD noise is the term used for noise electrons (n_{CCD}) generated in CCD channels (transfer, dark current, fixed pattern noise, ...), statistically distributed around a mean (rms). Amplifier noise refers to electrons (n_{AMP}) generated in the output amplifier.

Since none of the three sources is correlated with each other, the following holds:

$$n_{\mathrm{noise}} = \sqrt{}\{\sqrt{}[\Phi/h \cdot \nu) \cdot t \cdot A \cdot \eta] + n_{\mathrm{CCD}}^2 + n_{\mathrm{AMP}}^2\}. \tag{4.4-3}$$

where n_{CCD} is the noise electrons in the CCD and n_{AMP} the noise electrons in the output amplifier.

If (4.4-2) and (4.4-3) are inserted in (4.4-1), then:

$$\mathrm{SNR} = (\Phi/h \cdot v) \cdot t \cdot A \cdot \eta / \sqrt{\{\sqrt{[(\Phi/h \cdot v) \cdot t \cdot A \cdot \eta]} + n^2_{\mathrm{CCD}} + n^2_{\mathrm{AMP}}\}}. \quad (4.4\text{-}4)$$

If a high light modulation occurs in the CCD, then photon noise dominates. This can be expressed in simplified terms:

$$\mathrm{SNR} \approx \sqrt{(\Phi/h \cdot v) \cdot t \cdot A \cdot \eta} \approx \sqrt{n_{\mathrm{signal}}}$$

or *S/N* is directly proportional to the square toot of quantum efficiency,

$$\mathrm{SNR} \sim \sqrt{\eta}. \quad (4.4\text{-}5)$$

For low modulation, the noise of the CCD and of the readout amplifier dominates:

$$\mathrm{SNR} \sim \eta / \sqrt{(n^2_{\mathrm{CCD}} + n^2_{\mathrm{AMP}})}. \quad (4.4\text{-}6)$$

For high modulation in the CCD, therefore, the signal-to-noise ratio is proportional to the square root of quantum efficiency. For small signals, the ratio is directly proportional to quantum efficiency and is determined primarily by noise in the CCD and in the output amplifier.

For example, if the CCD noise n_{CCD} is 8e⁻ (rms), and the amplifier noise n_{AMP} is 6e⁻ (rms), then $n_{\mathrm{GES}} = \sqrt{(n^2{}_{\mathrm{CCD}} + n^2{}_{\mathrm{AMP}})} = \sqrt{(82 + 62)}\mathrm{e}^- = 10\mathrm{e}^-$ (rms).

The magnitudes of individual components of CCD-specific noise merit further discussion. Shot noise, which is thermally generated and not correctable, has a Poisson distribution:

$$\sigma_{\mathrm{shot}} = \sqrt{Q} \quad (4.4\text{-}7)$$

where Q is the generated charge quantity [e⁻].

Reset noise is generated in the channel resistance of the reset FET of the CCD output amplifier, commonly also referred to as kTC noise on account of (4.4-9). Since the reset noise is constant over the clock period of a pixel, it can be corrected. The method used for this purpose is termed correlated double sampling (CDS) (see Section 4.5).

$$\sigma_{\mathrm{reset}} = \sqrt{4kTBR} \qquad \text{in [V]} \quad (4.4\text{-}8)$$

or

$$\sigma_{\mathrm{reset}} = \sqrt{4kTC/e} \qquad \text{in [e}^-\text{]}. \quad (4.4\text{-}9)$$

where k is the Boltzmann constant [J/K],

T temperature [K]. B noise power bandwidth [Hz],
R = effective channel resistance [Ω]
C = node capacity [F] and e electron charge [1.6 10–19 C].

Output amplifier noise is subdivided into white noise, also known as Johnson noise, and flicker noise, also termed 1/*f* noise. White noise is generated thermally through channel resistances of the output FET (source follower):

$$\sigma_{\text{white}} = \sqrt{4\text{kTBR}_{\text{out}}} \qquad \text{in [V]} \tag{4.4-10}$$

or

$$\sigma_{\text{white}} = \sqrt{4\text{kTBR}_{\text{out}}}/\text{CVF} \cdot \text{V} \qquad \text{in [e}^{-}\text{]} \tag{4.4-11}$$

where CVF is the conversion gain factor [μV/e^{-}] and *V* the amplification of the output amplifier.

Flicker noise is inversely proportional to frequency. The frequency at which the amplifier is determined only by white noise is referred to as 1/*f* corner frequency. In general, white noise increases and flicker noise diminishes with increasing amplifier (chip) area; for this reason, in designing an amplifier, the aim is to achieve an optimum between geometry and typical operating frequency. Figures 4.4-13 and 4.4-14 illustrate the typical noise curves of CCD output amplifiers.

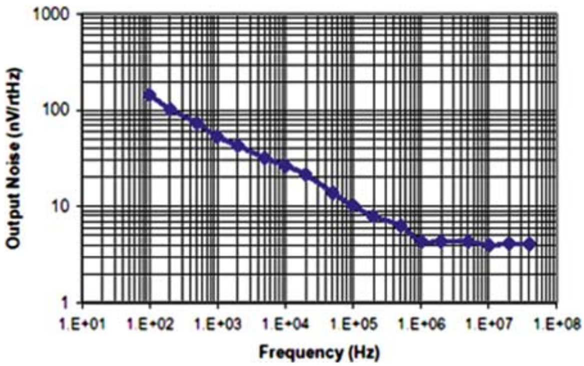

Fig. 4.4-13 1/*f* noise of the output stage of a Kodak CCD line (Kodak, 2001b)

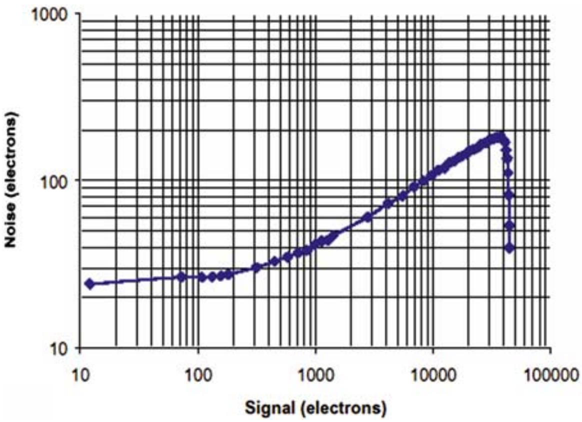

Fig. 4.4-14 Output amplifier noise of a Kodak CCD line at 28 MHz (Kodak, 2001b)

Various clocks are required for reading out the signal from the CCD, some of which have a very high frequency (horizontal and reset clocks). Their generation and the current pulses produced by the relatively high capacitive loads of the CCD registers (…pF to …nF, depending on the dimensioning), can result in considerable interference with the output signal. This noise, called clocking noise, can be reduced only through a precise design and good filtering of the power supply.

Dark current noise is the result of defects or faults in portions of silicon low-charge chips or at transitions to silicon dioxide. Additional electrons, which add up to form the signal, are generated stochastically here in the mid-band between the conduction band and the valence band. This is a thermal process which can be prevented only by cooling the CCD sensor.

A distinction is made between surface dark current, which accounts for the largest portion of the dark current and which is generated through defects in the semiconductor and in the manufacturing process on the surface of silicon dioxide, and bulk dark current, which is generated inside silicon dioxide by the defects.

Dark current is affected by two typical noise magnitudes, namely dark current non-uniformity and dark current shot noise. Whereas DSNU as spatial noise is correctable, shot noise is not. Just as in the case of photon shot noise, dark current noise has a Poisson distribution:

$$\sigma_{\text{dark}} = \sqrt{D} \qquad \text{in } [\mathrm{e}^-] \tag{4.4-12}$$

where D is the generated dark current [e^-].

4.4.3.3 Dark Signal (or Dark Current)

The mean noise level (or noise floor) is relatively constant and can therefore be corrected to a large extent. Depending on the requirement, a distinction is made between the sole dark current correction and the additional correction of the dark signal deviations between the pixels, the DSNU (see next section). In principle, each CCD line or matrix has, at the start of its readout register, several representative dark current pixels, which should be used as points of reference for the correction. Hence, the signal level of the dark current pixels represents the bottom threshold of the available dynamic range. Figure 4.4-15 shows the typical dark current image of an uncooled CCD matrix: the "bright" side characterises increased temperature caused, for example, by the output amplifier(s).

Dark current is essentially dependent on the exposure time or integration time and on chip temperature. It can be markedly minimised through cooling. The general rule is that the dark current is halved every time the sensor is cooled by approximately 7 K (see Fig. 4.4-16). Depending on the manufacturer, the physical specifications are given in [pA/Pixel] or [pA/cm^2], or also in [e^-/pixel · ms], but most commonly in [μV/ms].

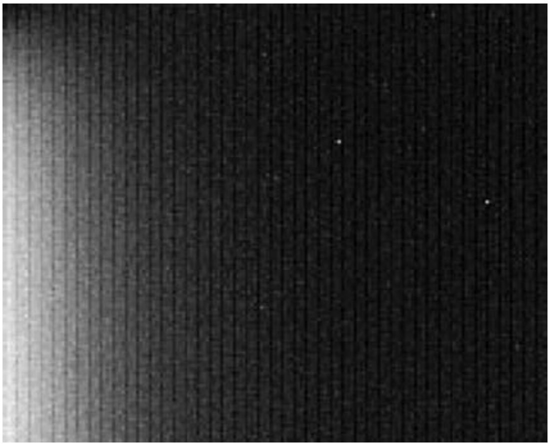

Fig. 4.4-15 Dark current image of a CCD matrix

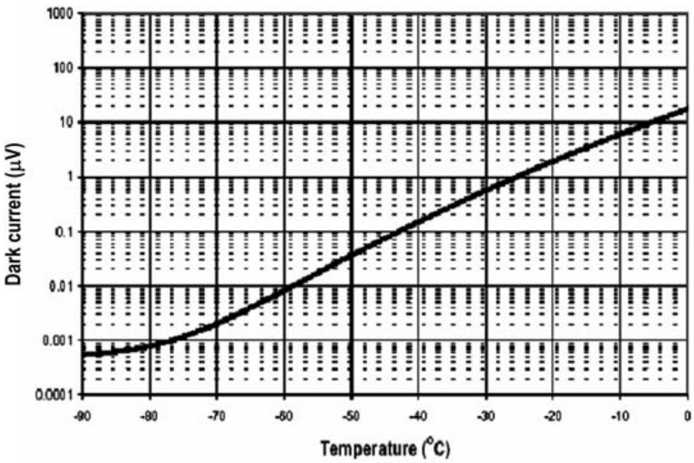

Fig. 4.4-16 Dark current in relation to the temperature of a (cooled) CCD matrix

4.4.3.4 Dark-Signal Non-Uniformity (DSNU)

DSNU expresses the non-uniformity of pixels of a CCD sensor in absolute darkness and is a specification of dark current. Absolute uniformity of all pixels would be ideal, but minute differences between wafers caused through manufacture, defects and, above all, chip temperature affect uniformity. Dark current and DSNU can be minimized through tempering (cooling). Dark current and DSNU also diminish with increasing readout frequency or shorter integration time t_{INT}. The value is usually given in [μV/ms] with respect to a certain integration time.

The use of a correction depends on the particular application and is normally required only at very high signal resolutions or very long integration times and/or when sensors are not cooled. Since the signal level swing of DSNU in terms of the dynamic scope of the CCD is very small, a correction is normally made digitally by subtracting the pixel values of a stored dark current image from the pixel values of acquired images.

4.4.3.5 Photo Response Non-Uniformity (PRNU)

Often also referred to as *vignetting* or *fixed pattern noise*, PRNU expresses the non-uniformity or the deviation from uniformity of photo responsivity of the pixels of a CCD sensor under uniform exposure conditions (flat field). Absolute equality of all pixels would be ideal here, but unfortunately not all pixels on a CCD chip have uniform responsivity. In extreme cases, i.e., at very low pixel responsivity, we speak of "dead" pixels. Minimal differences across a wafer arising from the manufacturing process, defects and differences in amplification are the cause of this non-uniformity. It is important to differentiate between non-uniformity when there is illumination (PRNU) and when there is darkness (DSNU). PRNU is expressed in [%] relative to saturation voltage U_{SAT}.

A pixel-related correction is required in any case in signal processing for signal resolutions >6 bits; depending on the requirements, it must be made multiplicatively (since an amplification fault is involved), in analogue fashion (MDAC) or digitally. Correction images or correction factors are produced by averaging several images of all photosensitive pixels at about 50% U_{SAT} at absolutely uniform illumination (flat field) and stored as a correction matrix. It should be borne in mind that in this manner the PRNU is eliminated to a very large extent, but shot noise is increased by a factor of $\sqrt{2}$ (this also holds for DSNU correction).

4.4.3.6 Dynamic Range (DR)

The ratio of the maximum output signal (saturation limit of a pixel) to its photo responsivity is known as the dynamic range. A CCD's photo responsivity is limited by dark current noise. As mentioned earlier, the dynamics of a CCD sensor can be improved by cooling. The DR is expressed in [dB] and is one of the basic parameters for assessing a sensor's range of applications.

$$\mathrm{DR} = 20 \quad \log \quad (\mathrm{USAT}/\mathrm{UDARK}_{\mathrm{rms}}) \tag{4.4-13}$$

or also

$$\mathrm{DR} = 20 \quad \log \quad (\mathrm{QSAT}/\mathrm{QDARK}) \tag{4.4-14}$$

where USAT is the saturation voltage [V], UDARKrms the dark current voltage (rms) [V], QSAT (= FW) the full well charge quantity [e$^-$] and QDARK (= D) the generated dark current [e$^-$].

4.4.3.7 Noise Measurement (Photon Transfer Curve, PTC)

Generating a photon transfer curve is an expedient way of characterising CCD sensors or CCD cameras. Apart from basic noise measurement, the photon transfer curve also provides the full well and the transfer in electrons per A-D converter state [e^-/LSB]. In this way, the dynamic range can be calculated. Each dot on the PTC represents a pixel group, illuminated by a flat field, with varying exposure time because, although the integration time is constant, the time of light incidence on to the sensor varies. In this manner the dark current can be subtracted as a constant error. The noise (standard deviation) is now plotted for each pixel group with reference to the mean signal value. The result is a curve comprising three basic sections: the first section (flat) shows the noise floor level, i.e., minimum system noise; the second (rising) section shows the typical operating range of the sensor system; and the third section shows the limit by pattern noise (correctable).

Figure 4.4-17 shows, for example, that (similar to the calculation in (4.4-14)) this system provides the following dynamic range:

$$\mathrm{DR} = 20 \quad \log \quad (\mathrm{FW}/D) = 40{,}000/25 = 64\ \mathrm{dB} \tag{4.4-15}$$

where FW is full well [e^-] and D noise floor or dark current [e^-].

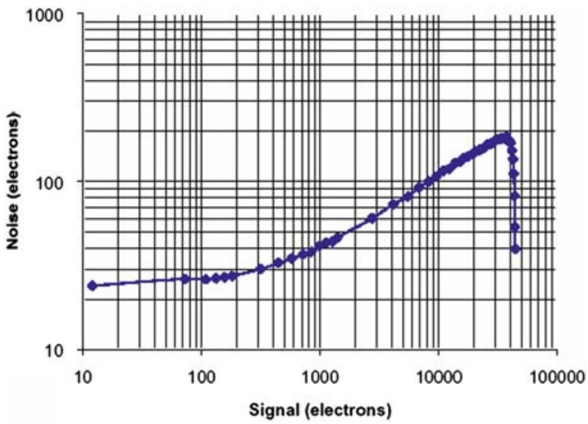

Fig. 4.4-17 PTC of a Kodak full-frame matrix, including board at 28 MHz (Kodak, 2001b)

4.4.3.8 Blooming and Antiblooming; Smear and Transfer Efficiency

All stored data should be read out in its entirety, so that no data belonging to the last image acquired remains after reading out a CCD. But even a CCD is not an ideal component. Blooming, transfer inefficiency and smear effects impair the charge transfer and/or the image quality.

The capacity of a pixel is determined by its size. There is a linear relationship between the number of electrons generated and the incident light. When a pixel approaches its saturation limit (filled with electrons), this linear relationship collapses. The pixel's reaction to additional light drops as a result and finally almost disappears. The point at which the reaction to incident light is no longer linear is also referred to as linear full well and it plays a major role in the dynamics of a CCD. When a pixel is saturated, charges jump over to adjacent pixels, which also become saturated as a result and signal high degrees of brightness. When the entire image array is saturated, frequently in the event of prolonged and intense irradiation, the output node can also be saturated. In most cases this leads to a collapse of the entire system. Various precautions should be taken to prevent such blooming.

A horizontal antiblooming gate is installed beside a pixel. Given an appropriate drive, electrons move over to the antiblooming drain created by the gate rather than to the adjacent pixel. The advantage of this solution is its simple construction and its efficiency. The disadvantage is that it occupies space at the expense of a photosensitive element of the CCD.

Clocked antiblooming uses the fact that overflowing electrons can combine with positive "holes" before they reach adjacent pixels. This supply of holes is constantly replenished through clocking (for example, in horizontal fly-back, HSYNC). The advantage of this arrangement is that no photosensitive space is wasted. Its drawback is the complex drive with three clock levels and reduced full-well capacity. With this method, blooming can be prevented up to a 50- to 100-fold overexposure.

Just as in the case of horizontal antiblooming, a vertical antiblooming structure is constructed beneath the photo diodes with the aid of an additional device. Vertical antiblooming structures can be built for all CCD types, but they are relatively complex and difficult to optimise.

There are several disadvantages of antiblooming precautions. The structure is complex and optimisation of CCDs is difficult. The trapping of electrons brought about by recombining electrons with "holes" can produce a severe, level-dependent deterioration of PRNU. And the effective depth of silicon responsible for the generation of electrons is reduced. This results in diminished red and infrared responsivity.

There are counterbalancing advantages, however. Excessive diffusion (diffusion MTF) is prevented, i.e., the MTF is improved. The generation of dark current is minimised. High efficiency can be achieved at up to 104-fold overexposure. And the antiblooming structures are compactly situated beneath a photo diode and do not take up any photosensitive space.

Charge transfer efficiency is the measure of the amount of charges successfully shifted in a complete shifting operation in a shift register (two to four phases, depending on the CCD). The effect produced by electrons lost during charge transfer is referred to as charge transfer inefficiency, CTI. CTE and CTI are fractions of the actual charge, for instance 10^{-4}; The mathematical relation is simple:

$$\mathrm{CTE} = 1 - \mathrm{CTI} \tag{4.4-16}$$

When charges are transferred from a pixel to the shift register, CTI is expressed as lag.

4.4.3.9 Smear

A smear is a faulty signal, which runs from top to bottom (vertically) in a bright section of an image (see Fig. 4.4-18). Its causes in common types of CCD vary:

Frame Transfer CCD

In frame transfer CCDs, smear is produced by incident light, while the generated image is pushed from the exposure zone to the storage zone (frame shift).

Interline Transfer CCD

In interline transfer CCDs, smear is caused by scatter photons that enter the covered shift register instead of being collected in photo diodes.

A white rectangle (100% modulation) whose height is 10% of the complete image is chosen against a black background (0% modulation) in Fig. 4.4-18 to show the principle of smear.

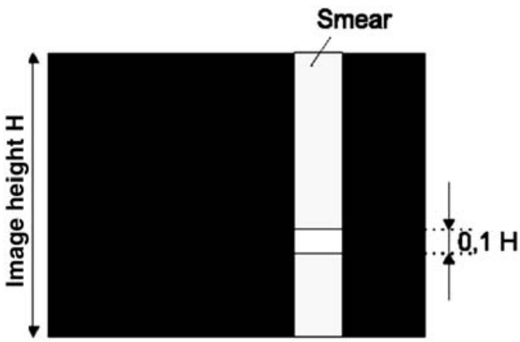

Fig. 4.4-18 Illustration of the smear effect principle in CCD matrices

4.4.3.10 Quantum Efficiency, Sensitivity, Responsivity

A sensor's sensitivity is defined as the intensity of the signal that is produced in the sensor if a certain amount of optical energy is introduced. Depending on the approach used, in physical terms it is expressed in [A/W], [Lux], [V/μJ/cm^2] or [e$^-$/μJ/cm^2]. As mentioned earlier, light or photons are converted in accordance with the natural laws governing the inner photoelectric effect. In simplified terms, an electron can be said to become "mobile" as a result of a photon arriving in the conduction band if the photon's energy Eph is equal to or greater than the energy of the band gap (valency and conduction band) Eg and of the material (silicon). Hence, photon energy is:

$$\text{Eph} \geq \text{Eg} \quad \text{and} \quad \text{Eph} = h\,v = h\,c/\lambda \tag{4.4-17}$$

Fig. 4.4-19 Responsivity of the full-frame matrix KAF-6303E from Kodak (Kodak, 2001a)

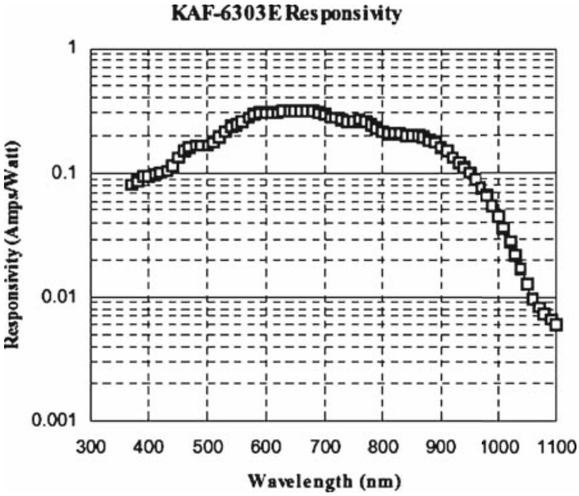

where $h^*\nu$ = photon energy [Ws], ν = frequency [s-1], h = Planck's constant [6.63 10^{-34} Ws^2], c = speed of light [$3 \cdot 10^8$ m/s] and λ = wavelength [m].

Sensitivity S, responsivity R or quantum efficiency η must be expressed in relation to the wavelength in order to make a precise assessment of an imaging sensor. An example is shown in Fig. 4.4-19. Quantum efficiency η of the pixel and the charge-to-voltage conversion factor of the CCD output amplifier are the basis for calculating responsivity:

$$R(\lambda) = \mathrm{e} \cdot \eta \cdot \lambda/\mathrm{hc} \quad \text{in [A/W]} \tag{4.4-18}$$

or

$$R(\lambda) = \mathrm{AP} \cdot \mathrm{e} \cdot \eta \cdot \lambda/\mathrm{hc} \quad \text{in } [\mathrm{e}^-/\mu\mathrm{J/cm}^2] \tag{4.4-19}$$

or

$$R(\lambda) = \mathrm{CVF} \cdot \mathrm{e} \cdot \eta \cdot \lambda/\mathrm{hc} \quad \text{in } [\mathrm{V}/\mu\mathrm{J/cm}^2] \tag{4.4-20}$$

where AP = pixel area [m^2], e = electron charge [$1.6 \cdot 10^{-19}$ C] and CVF = conversion gain factor [$\mu V/e^-$].

The relationship between the saturation electron number FW (full well), conversion factor CVF and saturation voltage is expressed by

$$\mathrm{FW} = \mathrm{USAT/CVF} \tag{4.4-21}$$

where FW = full well [e^-], USAT = saturation voltage [V] and CVF = conversion gain factor [$\mu V/e^-$]

Quantum efficiency is calculated from the sensitivity (responsiveness):

$$\eta = S \cdot h/\mathrm{e} \cdot c/\lambda \tag{4.4-22}$$

where S = sensitivity [A/W], η = quantum efficiency, h = Planck's constant [$6.63 \cdot 10^{-34}$ Ws^2], c = speed of light [$3 \cdot 10^8$ m/s], e = electron charge [$1.6 \cdot 10^{-19}c$] and λ = wavelength [m].

Since the wavelength is expressed in [μm], it follows from (4.4-22) that:

$$\eta = 1.24 \cdot S \cdot \lambda. \tag{4.4-23}$$

A typical example of the curve of quantum efficiency in relation to the wavelength is shown in Fig. 4.4-20. Quantum efficiency can be influenced by a number of physical magnitudes such as:

- the absorption coefficient, which indicates how deeply a photon must penetrate to generate an electron,
- recombination lifetime, i.e., the "lifetime" of the electron generated by a photon before it recombines,
- diffusion length, which indicates the mean wavelength after which an electron recombines,
- cover materials (such as silicon dioxide) overlaying the photo-responsive silicon.

In many cameras or CCDs, sensitivity is indicated in lux. But in most cases this unit is not suitable for scientific work. A meaningful lux value depends too much on various conditions such as:

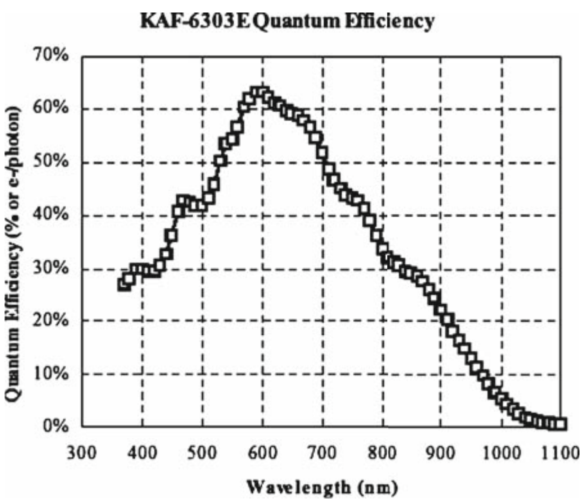

Fig. 4.4-20 Quantum efficiency of full-frame matrix KAF-6303E from Kodak (Kodak, 2001a)

- spectral distribution of illumination
- spectral responsivity of the imaging sensor
- the image, objective
- the achievable modulation
- measuring array used.

Luminance E expressed in lux can be converted into photon flux using the spectral brightness sensitivity of the eye. If a certain amount of radiation is evaluated physiologically, then this depends decisively on the spectral curve. If green light at a wavelength of 555 nm (maximum eye sensitivity) is projected on to an area of 1 m^2, this is perceived as a luminance of 680 lux. But in red (750 nm) this intensity is perceived as only 0.1 lux!

This relationship is expressed in terms of the radiation equivalent K:

$$K = 680\,\mathrm{Lux} \cdot \mathrm{m}^2/\mathrm{W} \quad \text{(at 555nm)} \tag{4.4-24}$$

$$E = K \cdot V(\lambda) \cdot \Phi \quad \text{in [Lux]} \tag{4.4-25}$$

where E = luminescence [lux], Φ = intensity [W/m^2], V(λ) = brightness sensitivity of the eye and K = radiation equivalent [lux $\cdot$ m^2/W].

The intensity Φ of light is determined by the number n of photons impinging on area A with the energy Eph = $h \cdot \nu$ in a time interval t_{int}:

$$\Phi = n \cdot h \cdot \nu / A \cdot t_{\mathrm{int}} = n \cdot h \cdot c/\mathrm{AP} \cdot \lambda \cdot t_{\mathrm{int}} \quad \mathrm{in[W/m^2]} \tag{4.4-26}$$

where λ = wavelength [m], AP = pixel area [m^2], t_{int} = time interval [s], h = Planck's constant [Ws^2], $h \cdot \nu$ = photon energy [Ws] = Eph, and c = speed of light [m/s].

The photon number is obtained again by inserting (4.4-24) and (4.4-25) in (4.4-26):

$$n = [A \cdot \lambda \cdot t_{\mathrm{int}}/h \cdot c \cdot \mathrm{K} \cdot \mathrm{V}(\lambda)] \cdot E \tag{4.4-27}$$

where n = photon number.

4.4.3.11 Shutter

A shutter is provided in an imaging system to be able to start or stop an exposure at will. The electronic shutter, which of course has advantages over the mechanical shutter, is a feature of all matrix CCDs and especially of interline transfer systems.

4.4.3.12 Modulation Transfer Function (MTF)

The quality of an image depends on the resolution (definition) and contrast of the entire transfer system. Both quantities are taken into account in the modulation transfer function (MTF), which describes the attenuation of spatial frequencies of an image by the components of the capture system, i.e. the lens and the CCD sensor in the case of CCD cameras.

The quality of modulation reproduction diminishes more and more for finer structures and drops to zero for a certain (high) number of line pairs per millimetre. The highest spatial frequency is not essential for the perceived definition, but rather the highest possible contrast reproduction over the entire spatial frequency range, up to the highest spatial frequency appropriate for the application.

The relationship between vertical and horizontal line pairs per unit length (generally 1p/mm, but also lp/pixel) and their reproduced contrast is usually represented for evaluation. High contrast means good separation of bright and dark lines, whereas poor contrast means structures that are poorly or hardly defined. The requirements that objectives have to meet vary according to sensor dimensions and pixel size.

To produce high-definition images, for instance, with CCDs with a pixel size of 6 μm (in the case of 1/3" cameras), a resolution of 80 lp/mm at the edge of the objective and the highest possible contrast are required in order to make full use of the sensor resolution. In the case of 4.5 μm (1/3" cameras), the resolution required is 104 lp/mm.

The Siemens star, consisting of purely black and white structures, is commonly used for assessing the optical quality of the MTF of such camera systems. Here, the fineness of the structure increases from the outer edges to the centre of the star. This makes it possible precisely to analyse the individual circle radii after determining the exact centre of the star. The greater the deviation from an ideal rectangular function, the worse the system's transfer. Figure 4.4-21 shows a photograph of the Siemens star taken with a simple, inexpensive CCD camera. The diminished resolution is

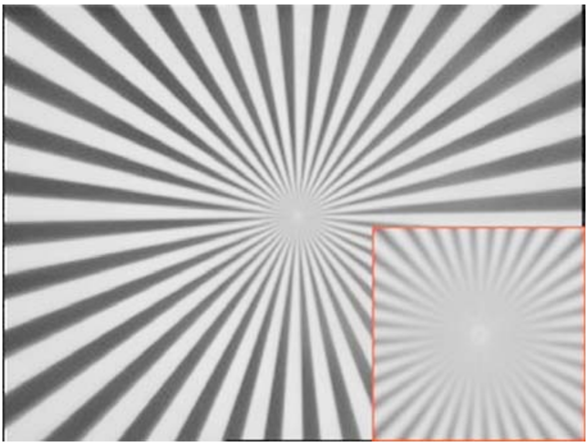

Fig. 4.4-21 Siemens star, photographed with an inexpensive camera (IAI FZK, 2004)

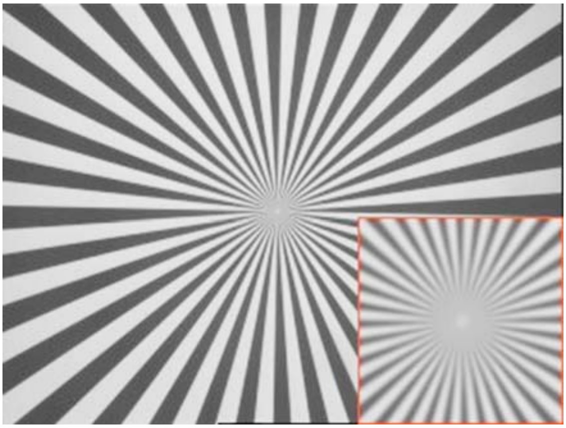

Fig. 4.4-22 Siemens star, photographed with a high-quality CCD camera (IAI FZK, 2004)

distinctly visible, especially in the centre of the star (magnification shown at bottom right).

The same test pattern was photographed with a high-quality CCD camera (Fig. 4.4-22). The contrast of the entire photograph is better and the resolution of the very fine structures in the centre is also markedly higher.

The resolution of the two images photographed, and hence the quality of the two imaging systems, can be calculated with the aid of suitable software. The curve of the calculated MTF is shown in Fig. 4.4-23. The contrast of System 1 (Fig. 4.4-21) diminishes faster with increasing frequency than that of System 2 (Fig. 4.4-22). Hence, System 2 has a better overall transfer behaviour.

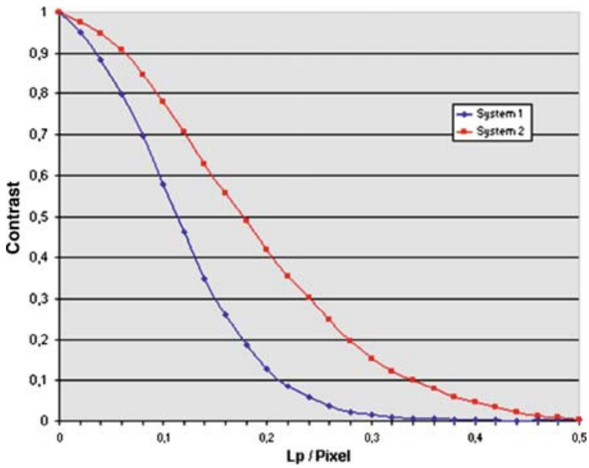

Fig. 4.4-23 The MTF shows the difference between Systems 1 and 2 (IAI FZK, 2004)

4.5 Focal Plane Module

4.5.1 Basic Structure of a Focal Plane Module

In optoelectronic cameras for aerial photography, the focal plane replaces the film holder plane. The basic structure of a focal plane can consist of completely assembled and housed CCD components. Another option is to use bare chips pre-tested by the manufacturer, which are then mounted on a carrier using hybrid technology. Both methods are used in practice. For smaller series, it is better to use pre-assembled CCD components, as they allow relatively uncomplicated modifications to the focal plane array.

Some requirements for focal planes are different from those for film planes, whereas the following ones are the same.

Mechanical aspects: The CCD components are mounted on a carrier design for long-term mechanical stability, the focal plane base. The plane formed by the pixels of the CCD elements on the focal plane is aligned vertically with the optical axis of the lens at the distance determined by the focal length. The connection between the lens and the focal plane must be mechanically strong, reproducible and free of constraining forces.

A proven option is to use a combination of opposing prisms and spheres of hardened steel as connecting elements. For example, the prisms can be aligned at the lens mount, offset by 120° each with a certain radius relative to the optical axis of the lens, and the spheres connected to the focal plane base plate at the opposite points. In order to create a focussed image, the distance of the focal plane from the lens – depending on its properties – may only have a low tolerance. This focal distance is the sum of various individual tolerances like those which must be observed when using film material.

The following requirements of a focal plane are not the same as those for a film plane:

Thermal stabilisation of the CCD rows: As explained in Section 4.4.3, the temperature of the focal plane must be stabilised in order to attain good radiometric resolution. For most applications, 20°C is sufficient. The CCD components of the focal plane have thermal power losses when in operating status, which cause them to heat up and therefore must be dissipated. As digital cameras for aerial photography must also function at ambient temperatures above 20°C, active thermal stabilisation is required, generally via Peltier elements.

The thermal power losses which occur can vary greatly, depending on the number, layout and properties of the CCD elements on the focal plane. 10–20 W are typical values. The CCD components discharge the thermal power loss into the ceramics of the base, from which it is routed to the heatsink via highly efficient heat conductors (e.g. heat pipes).

In order to prevent shifting of the modules on the focal plane at different working temperatures, the base must have the same expansion coefficient as the CCD components, and, for electrical reasons, it must be an isolator. This principle applies regardless of whether the CCD components are combined to form a focal plane as silicon chips or as housed assemblies. Only materials which meet these requirements, therefore, can be used for base plates. Ceramics, in particular, are suitable. High quality bases can be made of aluminium nitrite ceramic. Beryllium oxide ceramic would be even better: this material has particularly high heat conductivity, but is extremely toxic, which means that few manufacturers can process it.

Deviations from flatness: **I**f the focal plane is comprised of CCD components in a housing, particular attention must be paid to the tolerances. These are, first and foremost, housing tolerances (housings can have errors in height and parallelism) and, secondly, CCD rows which are not straight, owing to errors in adhesion by the CCD manufacturer. Failure to pay attention to these possible sources of error can lead to the surface formed by the pixels on the focal plane varying greatly from a flat plane. Figure 4.5-1 (Perthometer measurement) shows examples of this.

The dotted lines in the diagram show the height progression of the row pixels measured relative to the underside of the housing. The maximum height difference is 80 μm. However, the required positioning precision for the focal plane had a total tolerance of only ±20 μm. The height adjustment necessary was achieved by grinding the respective AlN ceramic mounts of the rows used here. The continuous lines in Fig. 4.5-1 show the measurement results after corrective grinding.

Protection against dust and moisture: In contrast to film, which is moved across the image plane, the focal plane always remains in the picture plane of the lens. Unless special measures are taken, dirt gathers and leads to unacceptable deterioration in image quality after a certain period of use. Owing to the great differences in air pressure at different altitudes, hermetic sealing of the focal plane and the space between the focal plane and the lens presents problems due to the related mechanical deformation. A technically feasible solution is to filter and dehumidify the air such that aerosols ≥ 1 μm are filtered out and the humidity is limited by absorbers such that no condensation can form from water vapour.

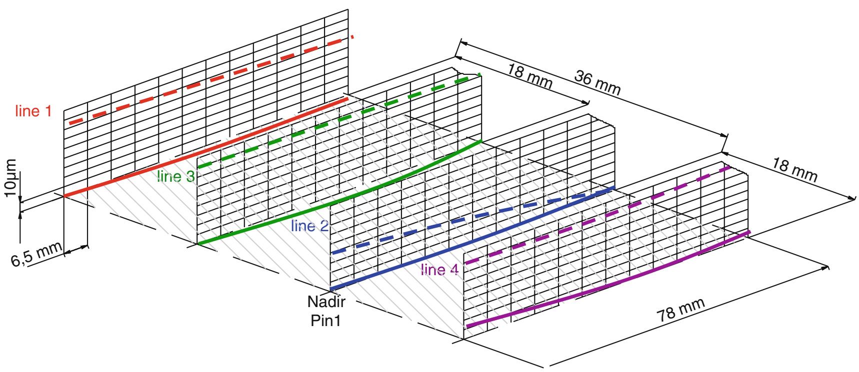

Fig. 4.5-1 Deviations of the CCD components before and after assembly on a common focal plane (Source: M. Greiner-Bär, DLR, Institute for Planetary Research, Berlin)

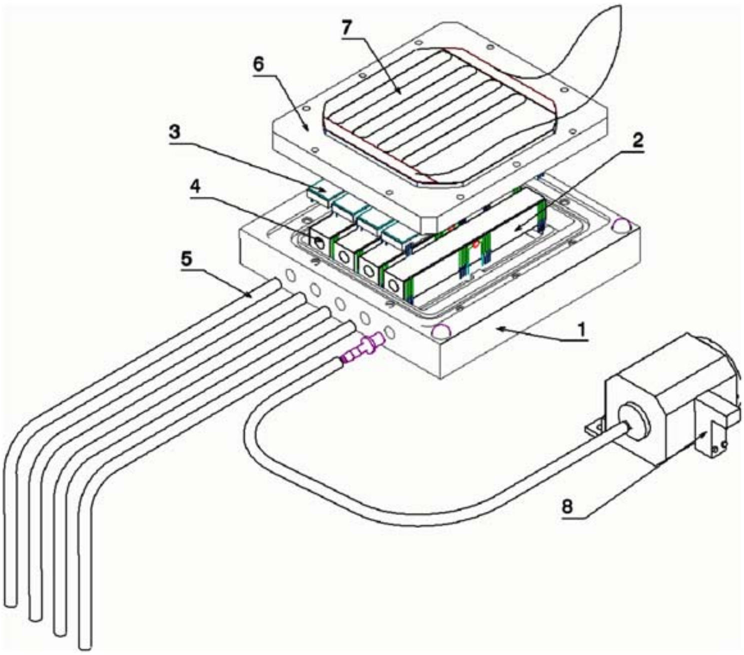

Fig. 4.5-2 Focal plane structure example (Source: U. Grote, DLR, Institute for Structural Mechanics, Braunschweig)

Figure 4.5-2 is an exploded view of the structure of a four-row focal plane used in practice in a digital camera for aerial photography. Base 1 consists of a mechanically robust aluminium oxide ceramic with low heat conductivity.

The four ceramic cuboids (2) are made of AlN ceramic and serve to hold the CCD rows (3). The four ceramic cuboids (2) are ground to size using optical technology methods such that the pixels in the CCD rows (3) form a plane with tight tolerances (see also Fig. 4.5-1). The holes (4) in the ceramic cuboids (2) hold heat pipes (5), which dissipate the thermal power loss of the CCD rows, to a heat exchanger (not shown here). The ceramic frame (6) with the integrated scattered light hood (7) provides the closure to the outside. The electromagnetic valve (8) opens during operation, thus connecting the inner focal plane chamber via a dust filter and water vapour absorber to the outside.

4.6 Up-Front Electronic Components

A Electronic components immediately adjoining the CCD sensor are sometimes referred to as up-front electronic systems. They include external wiring elements such as clock drivers and power supply, which are essential for the operation of

Fig. 4.6-1 Principle of front-end electronic components

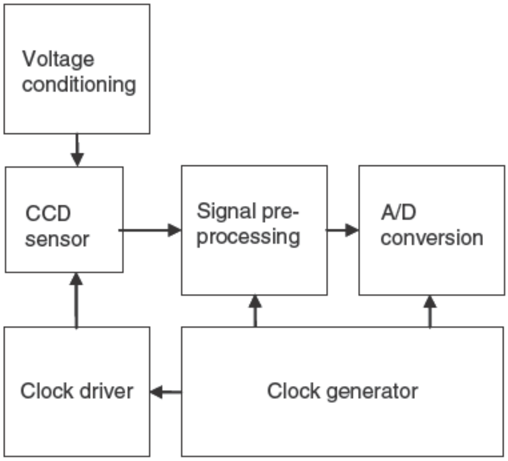

the sensor, and the sensor signal-processing components. An overview is shown in Fig. 4.6-1.

4.6.1 CCD Control

Depending on the complexity and type of a CCD component, several clock signals need to be generated to transfer the charges from the pixels to the output stage. The effort varies considerably, depending on the operating principle and technology of the sensors. An example of a clock scheme of a 3k × 2k matrix sensor KAF-6303LE from Kodak is shown in Fig. 4.6-2.

Each of the CCD clock signals requires specific low or high levels, which can vary enormously depending on the manufacturing technology, as shown in Table 4.6-1. Clock generation normally takes place in a programmable FPGA circuit (Xilinx, Actel, etc.), whereas, for converting levels from TTL/CMOS to corresponding levels of the CCD, clock drivers or level converters are required. Either special-purpose ICs from CCD manufacturers, which output all signals for a specific CCD, or general-purpose, standard ICs are available for this purpose. In some cases, even discrete solutions (transistors) can be used.

Certain CCD sensors can also be driven with a 5 V CMOS level, but this applies only to a limited selection of line sensors for flatbed scanners or standard industrial applications. Toshiba and Sony specialise in this field. To simplify the application, the level converters/clock drivers are integrated into these sensors, but in general they do not meet higher standards with regard to signal quality (noise, increased on-chip heat generation).

Like clock generation, the provision of individual voltages is a relatively involved process. For instance, five different operating voltages are needed for the KAF-6303LE matrix sensor (Table 4.6-2).

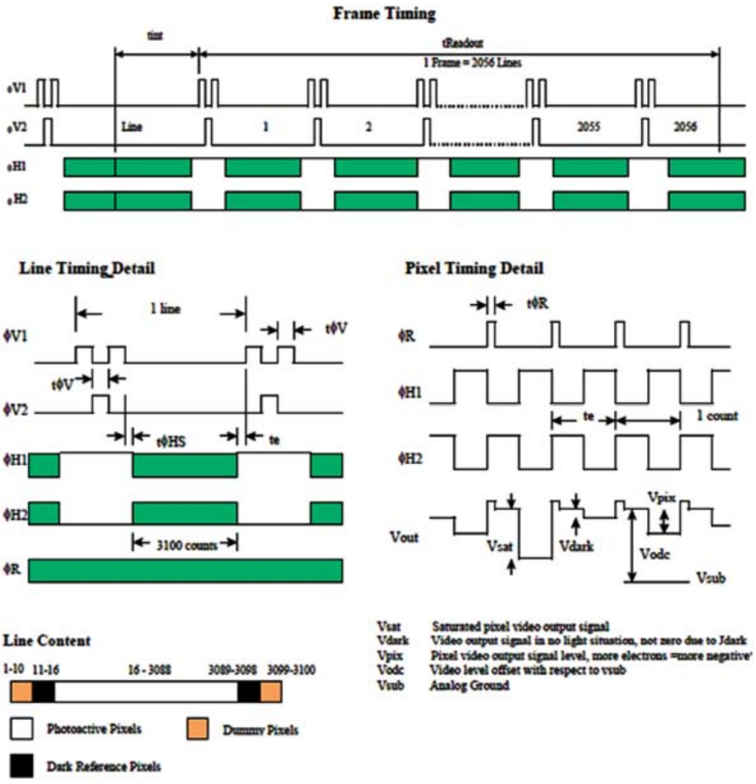

Fig. 4.6-2 Timing details for the KAF-6303LE sensor (Kodak, 1999)

Table 4.6-1 Relationships between levels of clock signals of the KAF-6303LE sensor (Kodak, 1999)

Description	Symbol	Level	Min.	Nom.	Max.	Units	Effective capacitance
Vertical CCD Clock – Phase 1	φ V1	Low	−10.5	−10.0	−9.5	V	820 nF (all φV1 pins)
		High	0.5	1.0	1.5	V	
Vertical CCD Clock – Phase 2	φV2	Low	−10.5	−10.0	−9.5	V	820 nF (all φV2 pins)
		High	0.5	1.0	1.5	V	
Horizontal CCD Clock – Phase 1	φH1	Low	−6.0	−4.0	−3.5	V	200 pF
		High	4.0	6.0	6.5	V	
Horizontal CCD Clock – Phase 2	φH2	Low	−6.0	−4.0	−3.5	V	200 pF
		High	4.0	6.0	6.5	V	
Reset Clock	φR	Low	−4.0	−3.0	−2	V	10 pF
		High	3.5	4.0	5.0	V	

Table 4.6-2 Operating voltages of the KAF-6303LE sensor (Kodak, 1999)

Description	Symbol	Minimum	Nominal	Maximum	Units	Maximum DC current (mA)
Reset drain	Vrd	10.5	11	11.5	V	0.01
Output amplifier return	Vss	1.5	2.0	2.5	V	0.45
Output amplifier supply	Vdd	14.5	15	15.5	V	Iout
Substrate	Vsub	0	0	0	V	0.01
Output gate	Vog	3.75	4.0	5.0	V	0.01
Guard ring	Vguard	8.0	10.0	12.0	V	0.01

4.6.2 Signal Pre-Processing

Signal pre-processing encompasses adaptation to the CCD output, filtration and pre-amplification of the signal and conversion of the clocked CCD signal into a brief DC voltage value, which can be sampled by an A-D converter. The principle is illustrated in Fig. 4.6-3.

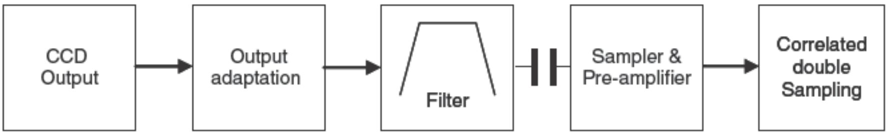

Fig. 4.6-3 Principle of the CCD signal-processing chain

As mentioned previously, the relatively low-impedance output stage of the CCD (see also Section 4.4.1) is provided by a video signal with a saturation level of 1–3 V, which is superimposed with a DC level (generally 5–10 V). This signal cannot be directly coupled to an A-D converter unless it is first "processed" in several steps.

Manufacturers often recommend a CCD output wiring, usually in the form of an emitter follower (Fig. 4.6-4). A wiring system can deviate from the manufacturer's design (for example, with operation amplifiers), but it is imperative to ensure that

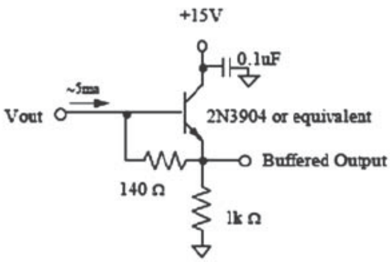

Fig. 4.6-4 Recommended output wiring of the KAF-6303LE sensor (Kodak, 1999)

the DC operating point and/or the maximum load of the CCD output stage is not exceeded.

Band-limiting filtration of the signal is advisable in any case before further signal processing stages in order to eliminate unnecessary noise components as early as possible.

If a pre-amplifier proves necessary, there should be a DC separation upstream of it, otherwise the large DC portion is amplified along with the AC or a pure AC amplification is used. Whether or not clamping is provided downstream of the AC coupling, for example, at the dark signal pixel level, depends on the subsequent processing to which the signal is subjected.

The overall quality of the signal processing is decisively influenced by the sampling of the video signal. There are several possibilities here, but correlated double sampling (CDS) has emerged as the basic principle. This sampling method is based on the difference between the level of floating diode and the video level of the CCD output. The timing of this sampling principle is shown in Fig. 4.6-5. This method has advantages. Firstly, one obtains the actual absolute value of the signal level without offset. Secondly, residual noise, i.e., the oscillations of the residual level from one pixel to the next, is suppressed, since only the current residual level that belongs to the video level is always used. The reset or floating diode level and the video level are correlated, hence correlated double sampling. Thirdly, further filtration is achieved through sampling with narrow sample pulses, which suppresses most of the low-frequency portions of the $1/f$ noise. The narrower the sampling pulses ϕ_C and ϕ_S and the closer they are pushed together, the better the noise suppression.

The two most commonly used CDS methods differ in the following respects: either (a) after an AC coupling, the clamping of the CCD signal is effected in each residual level, followed by a sampling of the video level, or (b) both floating diode and video levels are sampled separately with sample-and-hold circuits and then the difference signal is formed. In most cases, this difference signal is in turn sampled by a sample-and-hold circuit to be able to provide the subsequent A-D converter with the video signal processed in this manner for the entire pixel period.

Special-purpose circuits, which carry out the entire CCD signal-processing operation, are available from a number of manufacturers. This facilitates the application considerably. An example is the TH7982A made by Atmel (France), in which not

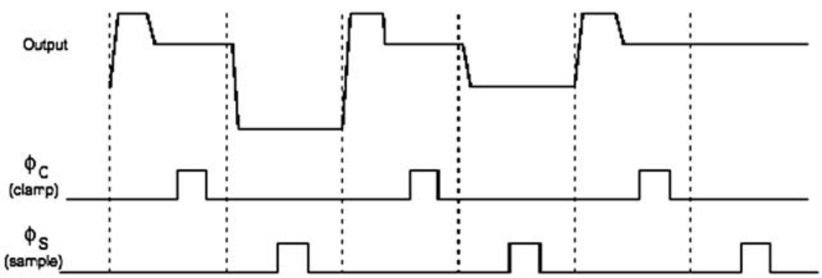

Fig. 4.6-5 Correlated double sampling principle

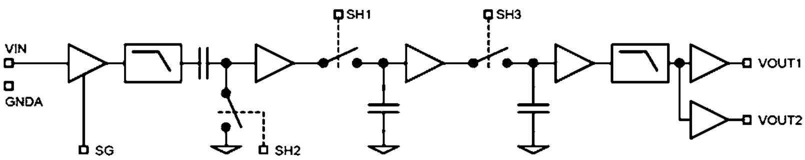

Fig. 4.6-6 Operating principle of the TH7892A CDS circuit (ATMEL, 2001)

only the CDS, but also the pre-amplifier, pixel corrector and the buffer for the A-D converter are integrated. The operating principle of the TH7982A is shown in Fig. 4.6-6.

For a better understanding, refer to the timing diagram shown in Fig. 4.6-7. The actual SH2 (floating diode) and SH1 (signal) CDS pulses are recognisable. For a kind of pipeline processing, a further sample pulse is added to them, which samples the difference signal of the pixel *n* formed by SH2 and SH1 while the floating diode signal of the pixel *n* + *1* is already being captured again by SH2. As an option, undesired pixels (for example, defects) can be suppressed by a defined fading out of the SH1 pulse, SH3 then samples the previously stored value again. Two output buffers of different configuration make it possible to adapt to different A-D converter types with a signal level of either Vout = ±1 V symmetrical to ground or with standard video level Vout = 1 V/50 Ω relative to ground (0 V).

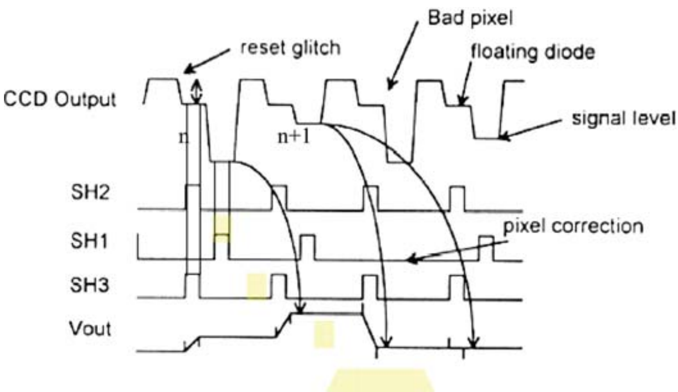

Fig. 4.6-7 Timing diagram of the TH7892A (ATMEL, 2001)

4.6.3 Analogue-Digital Conversion

The charges collected by the CCD are finally converted from the analogue signal range to a digital signal in the A-D conversion operation. The A-D converter appropriate for the application in question can be selected from the extensive range of commercially available converters. The selection parameters include sampling rate, resolution, linearity, input storage comparison, design and power drain.

The performance of an A-D converter is primarily restricted by quantization errors and technology. Some of the ways of assessing the quality of an A-D converter are briefly discussed. An A-D converter is a quantisizer, which translates analogue signals into discrete (digital) steps. Each step is represented by a binary value. Since an A-D converter is a quantisizer, it also exhibits a quantization error. Even an ideal A-D converter does this, since the digital value represents a certain analogue value that can deviate slightly from the input signal as soon as an analogue signal has been converted.

The quantization error is determined by the difference between a linear response function and the "staircase function" which is characteristic of A-D converters. The function of the quantization error has the shape of a sawtooth signal and oscillates between ±0.5 LSB once per LSB (LSB: least significant bit), since the data converter cannot recognise an analogue difference of <1 LSB (see Fig. 4.6-8). The effective quantization noise Q (rms) $= q/\sqrt{12}$ ($q =$ LSB measure) can be calculated on the basis of this sawtooth.

An A-D converter's signal-to-noise ratio is a measured quantity for broadband noise that is added to the analogue input signal (from the CCD and/or signal processing) during the conversion process. The theoretical SNR of an ideal A-D converter is calculated as follows:

$$\begin{aligned} \mathrm{SNR} &= U_{\mathrm{signal}}(\mathrm{rms})/Q(\mathrm{rms}) \\ &= (2^n/2 \cdot \sqrt{2})(1/\sqrt{12}) \\ &= 2^n \cdot \sqrt{3} \cdot \sqrt{2} \\ &= 1.225 \cdot 2^n. \end{aligned} \tag{4.6-1}$$

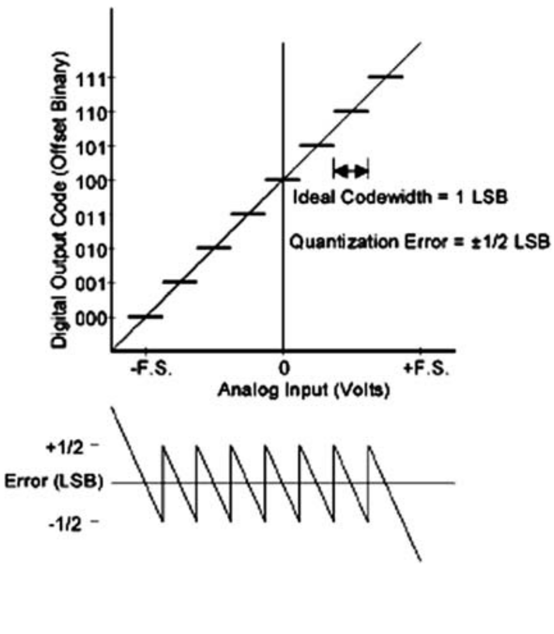

Fig. 4.6-8 Quantization errors in A-D converters (Coffey et al., 1999)

Thus

$$\begin{aligned} \mathrm{SNR_{dB}} &= 20 \cdot \log(1.225) + n \cdot \log(2) \\ &= 1.76 + 6.02 \cdot n \end{aligned} \tag{4.6-2}$$

Equation (4.6-2) describes the theoretically attainable signal-to-noise ratio (SNR) of an ideal A-D converter (quantization noise is the sole noise source of an n-bit A-D converter). Ideally, U_{Signal} relates to a full-scale sinusoidal signal: the effective value (root mean square) of the sinusoidal signal is obtained by dividing the peak-to-peak value by $2\sqrt{2}$.

Hence, based on (4.6-2), an SNR of 86 dB is almost ideal for a 14-bit A-D converter:

$$\mathrm{SNR_{dB}} = 1.76 + 6.02 \cdot 14$$

or

$$\mathrm{SNR} = 86\,\mathrm{dB}.$$

The actual parameters of an A-D converter and its wiring can best be determined with the aid of the Fast Fourier Transform (FFT). Using this method, all the system components involved are covered. Instead of the sampled CCD signal, a sinusoidal signal with extremely low noise and distortions is coupled, the converter is fully modulated and the FFT is determined on the basis of recorded digital values. The result is an FFT plot, such as the one shown in Fig. 4.6-9.

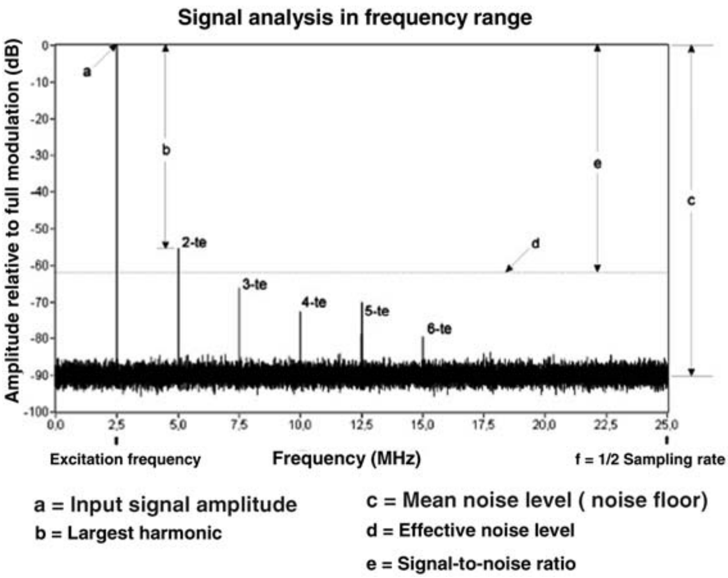

Fig. 4.6-9 FFT as a means of determining A-D converter parameters (Datel, 2003)

Apart from the signal-to-noise ratio, the FFT analysis provides additional technical data such as the total distortion factor (linearity) and spurious frequency spacing, which will not be covered in detail here. The possibility of determining the resulting number of bits of the actual resolution of the A-D converter is also interesting.

The SNR value of a system is calculated as a ratio of the effective value of excitation to the effective value of all noise components. Thus, by analogy with (4.6-1),

$$\mathrm{SNR} = U_{\mathrm{Signal}}(\mathrm{rms})/U_{\mathrm{Noise}}(\mathrm{rms}) \tag{4.6-3}$$

Or, in [dB],

$$\mathrm{SNR}_{\mathrm{dB}} = 20 \cdot \log\left\{U_{\mathrm{Signal}}(\mathrm{rms})/U_{\mathrm{Noise}}(\mathrm{rms})\right\} \tag{4.6-4}$$

The measured data acquisition time (start and end of acquisition), which is also termed windowing, is limited. This rectangular window function has an effect in the case of the FFT. The number N of FFT dots yields a correction factor for the y readings. In logarithmic terms this yields the shift $10 \cdot \log(N/2)$ in the case of windowing. If the measured data underlying the FFT calculation were acquired asynchronously, i.e., without a fixed phase and frequency correlation, then the measurement should be evaluated with another windowing function (for example, Hanning, Hamming, Blackmann-Harris et al.). In this way the error caused by the phase position of the periodic sinusoidally shaped excitation relative to the window is minimised.

Assuming coherent sampling with a rectangular windowing function, we obtain the following noise floor:

$$U_{\mathrm{Noise}}[\mathrm{dB}] = \text{effective noise level} + 10\log(N/2) \tag{4.6-5}$$

where $N =$ number of FFT dots and $N/2 =$ number of frequency positions.

Another important aspect for evaluating and/or selecting an A-D converter is the sampling rate. According to the sampling theorem, an original signal can be unequivocally restored only if the sampling rate fs of the converter is at least twice as high as the highest frequency fc occurring in the signal, i.e., $fs > 2fc$.

This holds true only, however, if the input signals are assumed to be sinusoidally shaped. When A-D converters are used for digitising CCD signals, this statement is compromised, since the input is not a sinusoid, but rather a quasi-discrete signal which changes its value at equal intervals. It suffices (theoretically) if the converter's sampling rate of say 10 Msamples/s is identical to the CCD's video frequency, in this case namely 10 Mpixels/s. The basic condition here is, of course, that the A-D converter has enough time to sample the quasi-stationary value (processed by CDS) of the video signal. An example of such timing is shown in Fig. 4.6-10. Apart from the CDS signals SHP and SHD, this timing shows the DATACLK signal. This is the control pulse for the A-D converter, which is synchronous and staggered in time, but with the frequency as the CCD video signal. It can be seen from the position

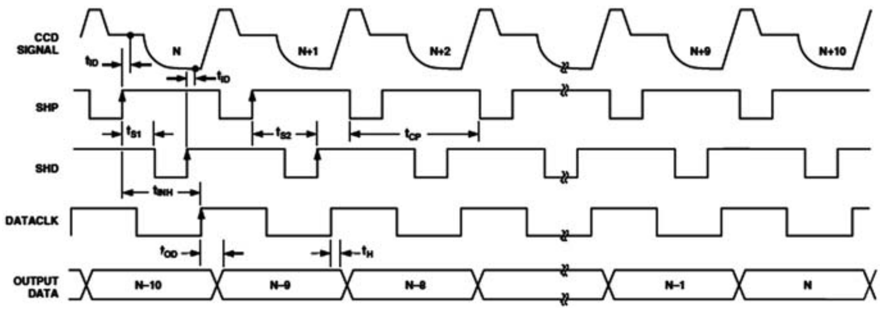

Fig. 4.6-10 Timing of the AD9824 CCD signal processor (Analog Devices, 2002)

of pixel *N* that the pixel is processed in a pipeline process of nine steps before it is available as a digital value at the output of the A-D converter.

Compared to TH7982A, the CCD signal processor AD9824 is a further functional integration stage of analogue CCD processing, which is currently the highest such stage available. Input MUX dark-signal clamping, CDS, pre-amplifier and an A-D converter are integrated on a single chip.

4.7 Digital Computer

The generation of digital data and its preliminary processing by calibration values in the front-end electronics was described in the previous section. This section deals with digital data processing in the camera and with the control and monitoring of the system as a whole. The key system components and their functions are reviewed to provide a general overview. Some aspects are then decribed in greater detail.

4.7.1 The Control Computer

From the technical point of view a control computer is a PC supplemented with camera-specific components (Fig. 4.7-1). It is a composite of various functional units controlled, monitored and coordinated by software. It consists of three functional units:

1. PC with the associated standard components such as graphics board and LAN
2. Image data channel
3. Add-on components such as camera-specific interfaces to external units, camera suspension, GPS/IMU system and modules for monitoring and controlling ambient conditions.

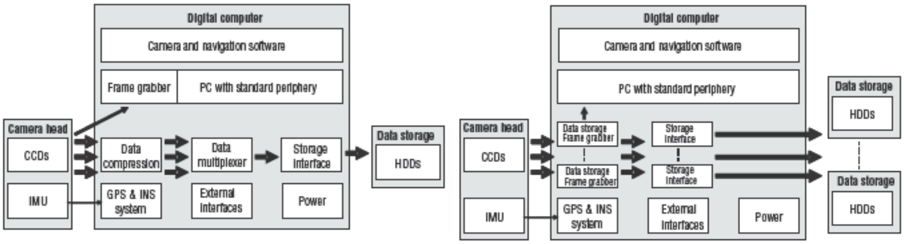

Fig. 4.7-1 System overview

4.7.1.1 Control and Monitoring PC and Software

The PC hardware contains components similar to those found in any office PC. They include the CPU and memory, mother-board with standard interfaces and system drives. These components constitute the basic framework of the computer and the platform for the control and monitoring software. Special hardware components such as touchscreen support are also part of this complement of basic equipment.

A framegrabber card is frequently used as an interface between the PC and the image data channel. The framegrabber generates and fades in image data recorded by CCD sensors or auxiliary cameras during flight. These images are processed in real time and used by the operator as orientation and navigational aids, for quality control and for monitoring the camera during operation.

Image data is processed and stored in real time in the image channel. The channel is designed specifically for this purpose, its operation is essentially autonomous, and the PC only initialises, monitors and controls it. In order not to impede performance during operation, therefore, the PC is not directly involved in data processing and storage, but only controls certain system processes.

There are various approaches to implementing a data channel. These range from framegrabbers with disc controllers, to several PCs in parallel connection (for example, one computer with storage system for each CCD), to data channels with memory management and data compression. Performance features such as data rate, data handling flexibility, redundancy, memory requirement, power consumption and service conditions should be estimated on a case-by-case basis and the advantages and disadvantages weighted accordingly (especially with regard to field application).

Before going into the key aspects of digital data processing, we shall first explain the supplementary camera-specific components and interfaces, which, depending on the integration depth of a camera system, perform important functions and open up interesting possibilities for application (Fig. 4.7-2).

The most important supplementary component of a digital camera is the GPS/IMU system (see Section 4.7.1.3). It supplies raw data for precise offline calculation of position and attitude and provides a solution for the same parameters in real time. If this data is processed in the camera system in real time, i.e., without significant delay, it can be used for stabilising the camera mount. Moreover, the position and attitude data can be used to determine parameters for controlling drift.

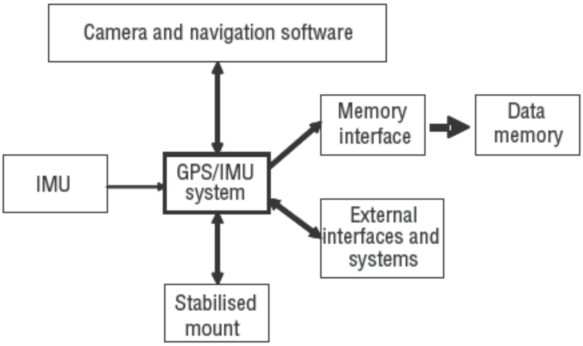

Fig. 4.7-2 Supplementary components and data flows

In this way, the camera in its mount can always be aligned relative to the direction of flight independently of the aircraft's heading. This data is also used by the sensor control and flight management software. If this position and attitude information is not available, at least a GPS receiver must be integrated for flight management.

The flight management and navigation system is indispensable from the operational viewpoint. It enables the pilot to perform efficient photo flights. It also manages the flight status and configures and monitors the camera system.

In most camera systems available today, the flight management and navigation system is an external supplementary component, rather than an integral part of the system. This is not important with respect to functionality, but it is significant from the operator's point of view. In an integrated design, camera monitoring, flight management and control of the subsystems are carried out from an integrated user interface. This obviates the need to install several screens and input units in aircraft where conditions are frequently cramped.

Another important supplementary component is the stabilised camera mount. It cushions the camera in the aircraft and actively compensates irregularities in the aircraft's motion (see Section 4.10). This reduces image smear. A stabilised mount also increases flight efficiency by reducing lateral overlaps with the adjacent strips and the full image width is always recorded thanks to automatic drift control.

Depending on the mount, it may be necessary to connect additional sensors to the main system. This is the case, for instance, when several sensors are supplied with data by one GPS/IMU system, when several sensors are controlled by one flight management and navigation system or when the data recording process has to be synchronised. The interfaces used for this purpose are serial interfaces such as RS232, LAN or glass fibre connections which transmit several data streams simultaneously.

4.7.1.2 The Image Data Channel

The image data channel is the camera-specific part of the control computer that processes the digital image data generated by the camera head. The data undergoes the following processing steps: buffering, compression, generation and insertion of additional data for subsequent processing and analysis, and formatting for efficient storage. All these steps must be carried out in real time, which means that data cannot be buffered for subsequent processing but must be processed the moment it occur. This is a peripheral condition, which is very challenging when developing a digital camera system and which requires the use of fast processors such as DSPs (digital signal processors) or even hardware solutions.

The implementation of the individual processing stages depends on the data rate and the required functionality. Individual camera systems support data compression. A hardware solution is required for this processing stage owing to the high data rates and complexity. The special-purpose hardware is supported by DSPs, which carry out data pre-processing operations as such sorting, normalising, or transforming with a lookup table, and which control compression. In this manner, various compression modes (lossless, lossy) can be selected or various quality criteria satisfied. Data compression is dealt with in Section 4.7.2.

The data rate may fluctuate somewhat at the data compression output, depending on the compression mode and image content. To prepare data for storage in an optimal manner and to support variable allocation of CCD line/matrix to the storage medium, a kind of cross-bar function is helpful in the system. This makes it possible to distribute a given number of data inputs (for example, data streams from CCD line/matrices) to any number of memory drives in such a manner that both the total data rate and the storage capacity can be utilised in an optimal manner. In addition, this intelligent memory management makes it possible to recognise transfer errors in real time and to correct them before the data is stored. There are cameras that do not have this functionality but instead use several memory systems, each of which contains only part of the flight data. With these cameras, the flight data have to be copied subsequently.

House-Keeping Data, HKD

The foregoing comments show that a digital camera system is very complex. It comprises many hardware and software components, processes data at very high speeds and executes algorithms in real time. For monitoring purposes and to diagnose errors, important system parameters are introduced as house-keeping data into the data stream during operation, continuously evaluated and stored for future analysis. These include temperature data, configuration data, hardware settings and controller parameters.

Interface to the Data Memory

The interface to the data memory is determined mainly by commercial storage media available on the market today. Since hard disks are most commonly used in digital cameras (see Section 4.7.3 on data memories), the comments here will be confined to this storage medium. HDDs can be divided into two categories. SCSI hard discs are used in servers. They are very reliable, perform fast and have SCSI or fibre channel interfaces. But they are more expensive than HDDs for office PCs, which use mainly IDE hard disks with an ATA interface (in series or parallel connection). The latter have a somewhat bigger memory capacity than the SCSI HDDs and are cheaper, but not as reliable.

One has to choose between these two categories of HDD when selecting an interface. The range of choices available is narrow if one considers system parameters such as maximum data rate and number of independent data streams. One should bear in mind that the SCSI interface is a bus system to which up to 15 drives can be connected. An ATA interface supports a maximum of two drives on one bus. Depending on the camera system, several data memories and bus systems must be implemented to ensure that images can be stored during operation. Consequently, the outlay for hermetisation increases and, in the case of several separate data memories, more space is required in the aircraft. From the operational point of view, a compact solution is desirable. It must be possible after a photo flight easily to remove the data memory from the aircraft. To meet this requirement, the bus system must be separable and yet robust enough for use in the air. Solutions with SCSI disks allow for simpler topologies and the reliability of the flight system is higher. IDE disks are an inexpensive solution for storing data in the office.

Standard disk controllers are used for driving all the bus/disk types mentioned above. A multitude of controller cards is commercially available from various suppliers. The cards differ from one another mainly in their data rates and functionality. First and foremost, controllers that are programmable or that provide RAID support and hence, depending on the RAID level, support redundant data recording, are of interest for use in a camera system.

4.7.1.3 GPS/IMU SystemIMU

Image data recorded during a flight becomes input data for subsequent processing. Various processing steps, which depend on the type of CCD (line/matrix) used in a camera, are required for producing the finished product. The principal difference between a line CCD and a matrix CCD is that in a line sensor each image line has its own exterior orientation, whereas in a matrix sensor the exterior orientation applies to the entire image. The orientation and position of the camera head need to be measured with a certain precision and the measured values recorded during flight, so that later on in the post-processing operation the images from a line sensor can be assembled into an image strip. To this end, an INS (internal navigation system) is used, which consists of an IMU (inertial measurement unit), a GPS receiver and a computer unit for processing the GPS and IMU data.

An INS operates as follows. An IMU consists of three gyros and three acceleration sensors. It measures the rates of rotation around the three axes and acceleration in the three directions, for instance at 200 Hz. The software of the INS computer integrates the delta values/increments and estimates the sensor error, attitude and position by means of Kalman filtering. The GPS data also flows into the calculation, by providing fixed points for linking the calculated solution, which would otherwise drift off over time as a result of sensor errors. These calculations are carried out during flight (in real time), as well as in the course of subsequent post-processing. In the latter case, a more precise, but more computer-intensive error model is used and the data are processed back and forth in time. Thus a more precise solution is obtained. Depending on the application, the precision required for the calculated orientation can be a few seconds of rotation (for instance, for direct georeferencing). This precision is determined mainly by the performance parameters of the IMU.

To achieve the measuring accuracy described above, the IMU must be integrated in the camera head in a very stable, permanent manner, so that there is no movement between them when in operation.

Various levels of integration are possible for the combination of the camera and the GPS/INS. In most cases, precautions are taken to ensure that the measured data from the GPS/INS can be synchronised with the image data of the camera. To this end, synchronisation pulses (for example, PPS from GPS) are measured in the time system of the camera and of the GPS/INS, and the time markers determined are stored. Events taking place between these time markers can be interpolated with sufficient accuracy. With this approach, the systems, with the exception of the synchronisation pulses, operate completely independently and data is stored on separate media. A higher level of integration enables the data of the GPS/INS to be stored along with the image data, so that the operator does not have to handle them separately. The operating system of the INS can also be integrated in various ways. Solutions are available that require several monitors and even fully integrated user interfaces in which various system components can be operated from the shell.

4.7.1.4 Power and Ambient Monitoring

Owing to the challenging requirements with respect to data rate and processing performance, components at the high end of PC/server performance are required for a camera system. These components are cost-effective, but since they are designed for the office environment, their usefulness in service on an aircraft is limited. There are special requirements in terms of the mechanical structure and especially the environmental specifications (for example, temperature range). The amount of power provided by the supply systems of small surveying aircraft is limited: this imposes limits on the camera system's power consumption. Often the aircraft battery is the sole source of on-board power for operations such as copying data or making system tests. In such situations, low power consumption is important. Power supply problems such as undervoltage, overvoltage or voltage interruptions can also occur in operating the camera during flight, disrupting reliable operation and making error analysis difficult. These problems can be accepted and the associated restrictions laid down. Or one can implement a monitoring system to capture all relevant ambient influences. Such a system is always active, maintaining the camera system's operational state through controlled heating, cooling or other actions. There are also systems available for monitoring the aircraft power supply system that perform the necessary protective functions and alert the operator when the operating conditions require correction.

4.7.1.5 Cabling and Integration

Just as in the case of ambient conditions, there are special requirements with respect to the electro-mechanical integration and installation of a camera system in an aircraft. Experience shows that plug-and-socket connectors and cabling are particularly critical with regard to reliability. It is thus preferable to have a high level of integration with few internal and external connections: robust plug-and-socket connectors and cables are essential for smooth operation. Standard connectors used in PC technology are not suitable.

4.7.2 *Data Compression*

Digital capture of image data has grown in popularity in recent years and is currently experiencing a boom in various fields of application. The breakthrough in the commercial sphere has been instrumental in making it possible to capture image data in digital form and to process it subsequently on a computer or transmit it via the internet. The data volumes are enormous. For efficient storage, transmission and handling, it is expedient to store data in as compact a manner as possible. Solutions are provided through data compression.

The aim of this section is to provide an outline of the mode of operation of the principal methods of compression and to establish a connection to their application in digital camera systems. A great deal of literature is available on this subject for readers interested in deepening their knowledge in this field beyond the scope of the information presented here.

The goal of data compression is to reduce the volume of data by eliminating redundant or less relevant portions of the data. The algorithms used for this purpose can be divided into two main categories: lossless and lossy. Lossless methods convert a data set into a form with less redundancy, a higher degree of compactness and a lower storage requirement. Through appropriate decompression, the original data set can be completely restored. Typically, such compression methods are used with text documents, program codes, etc. When dealing with this kind of data, it is essential that the original information can be restored at any time. Lossy methods are used when part of the original data set can be eliminated without this being noticeable in, or having a detrimental effect on, the restored data set. Lossy methods are used for compressing speech, music, photos and films. Data are evaluated following decompression by human perception through the senses of hearing or vision. Owing to the properties of these senses, smaller losses are not perceptible or are compensated. Hence, in the case of lossy data compression, the data, when decompressed, is no longer fully identical to the original data, but still similar enough that the observer does not notice any detrimental changes. The degree to which decompressed data may differ from the original depends to a large extent on the application in question; this has to be decided on a case-by-case basis. The compression factor in the case of lossless methods for digital airborne cameras is approximately two. In the case of lossy methods, it can be as high a five without creating significant artefacts or image distortions.

4.7.2.1 Lossless Data Compression

Lossless data compression removes redundancy from the data and codes it in a more compact form without loss of information. The following two methods from this family are commonly used.

Run-Length Encoding

In the case of run-length encoding, identical, consecutive symbols such as bytes are counted and replaced by a single symbol and the corresponding numerical value, indicating the number of times the symbol needs to be used to restore the original symbol series. Special characters in the data stream mark the places where such a symbol/number pair is used. This method can be especially useful for black/white drawings with homogeneous areas. It is not so well suited for compressing photos, because they contain diverse colour values and noise.

Huffman Coding

Lossless methods using statistical distribution of symbols such as bytes for optimal coding of a data set are better suited for photos. Symbols that occur frequently in a data set are replaced by a shorter code word, whereas symbols that occur seldom are replaced by a longer code word. Hence, encoding in this context means substituting a symbol by another, optimised bit sequence. As a result, less frequent symbols can be represented by longer bit sequences than the original ones. But the data set as whole is represented in a more compact manner, because frequently occurring symbols are represented in an abbreviated form. Since the encoding key is needed for decompression, it is stored along with the encoded data. The additional storage space needed for this purpose is much less than the space saved by encoding. A code tree that can be implemented easily and efficiently is used for decompression.

The original data must always be restored through lossless decompression methods. Thus decompression must be unequivocal.

4.7.2.2 Lossy Data Compression

Lossy methods are based on the assumption that a data set contains information that can be eliminated without this later being noticed by the observer or having a distorting effect. By virtue of its standardisation, JPEG is the most common method of compressing image data. JPEG works with image blocks of 8×8 pixels. These blocks are individually transformed into a frequency range with the aid of the discrete cosine transformation (DCT), then the calculated 8×8 frequency portions are quantified by dividing each of the 8×8 portions by a certain value that is specified in an 8×8 quantization table. Higher frequency portions are smoothed as a result of division with reduced precision. The quantified frequency portions are then processed separately as AC and DC values, compressed in a lossless manner by means of Huffmann coding, formatted and stored.

The quantisation table can be initialised using one's own values or those suggested in the JPEG standard. One should bear in mind that data are removed in the quantisation process, because the precision of the quotient that is stored is diminished. The value of the quantisation coefficient determines the amount of data that is lost. In this manner the quality loss of an image can be influenced.

Thus certain data, additional to image data, has to be stored for the decompression. This is similar to the lossless methods. In the decompression process, the data set undergoes the same stages of compression, but in the reverse order. Owing to quantization, however, the decompressed data set is no longer identical to the original data after decompression.

Owing to the block size of 8 × 8 pixels, visible artefacts can occur at block boundaries, or even within blocks in the case of JPEG at high compression rates. In practice, compression rates of five to a maximum of ten are used and visible artefacts are rare. The effects that can occur in a reconstructed image depending on the compression factor are shown in Fig. 4.7-3, where a reference image is used

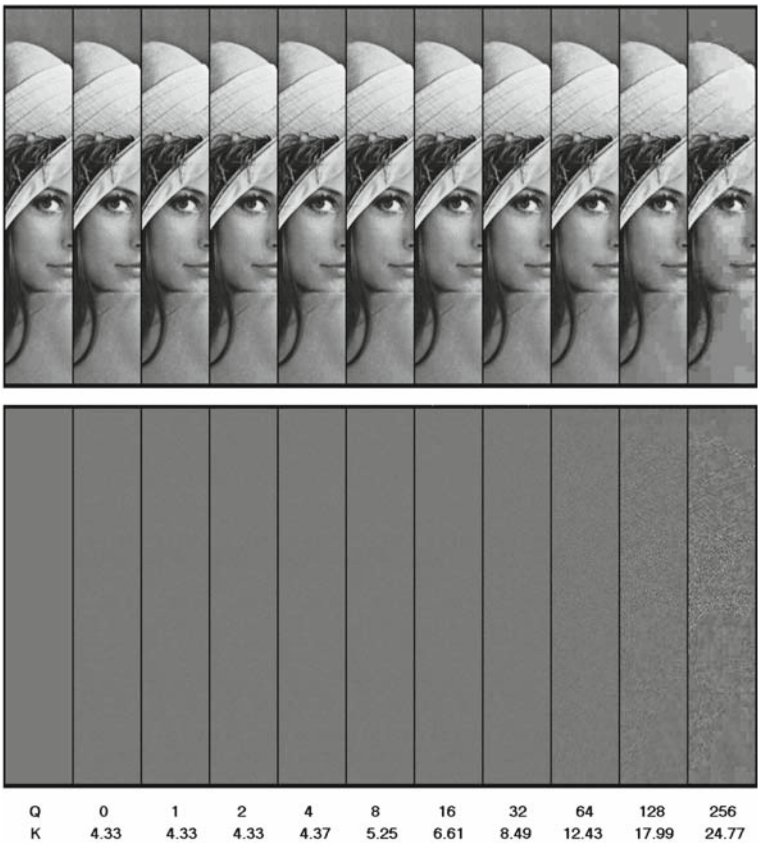

Fig. 4.7-3 Compression sequences (*top*); difference sequence (*bottom*) with offset 128 and the relevant quality factor Q or compression factor K

to illustrate the influence of the JPEG Q factor, which in conjunction with the image dynamics, produces the effective compression factor. The reference image with the smooth, fine structures (in this case for instance the eye lashes) contains all the complications that produce various effects with different compression methods. One can recognize that this complex image structure displays fault effects visible in a difference image only from a compression factor of about 12.5 and also in a reconstructed image from a compression factor of 18 (Sandau, 1998). The maximum compression rate used in photogrammetric applications is five. In this manner it is ensured that no geometric distortions occur when using the JPEG method.

4.7.2.3 Data Normalisation

Many compression methods such as JPEG are optimised and/or standardised for 8-bit data. Digital cameras, however, produce data with a resolution of at least 12 bits. Before this data can be compressed, many compression methods require that it be reduced to 8 bits (Fig. 4.7-4). To ensure an almost lossless normalisation, the minimum and maximum are determined from a data set. The minimum is subtracted from the data set as an offset and stored separately. The resulting data set gives the dynamic range. In practice, if the outliers (for instance hot spots caused by light reflection at mirror-like surfaces) are removed in the maximum formation process using a threshold, less than 10 bits dynamic range remains in most of the cases. Hence, the data can be readily reduced to 8 bits with the aid of a defined lookup table. If the lookup table can be modified, individual ranges can be given a higher or lower weighting in the transformation process, thereby minimising the application-specific normalisation losses. Following normalisation, the data is subjected to further processing using the selected compression method.

The order of operations is reversed when performing the reverse transformation, i.e., decompression, then reverse transformation with the aid of the lookup table, then addition of the offset.

To keep the normalisation losses low or to avoid them altogether, a sensible minimum and maximum should be selected and a suitable lookup table used. This method works almost free of loss if the correct parameters are used.

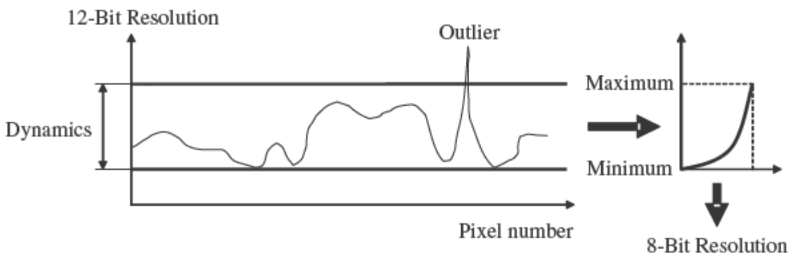

Fig. 4.7-4 Normalisation

4.7.2.4 Compression in Hardware

A digital camera can generate data at rates of 200 MB/s and higher. This determines the data compression rate necessary to reduce the data rate before storage. An additional requirement is that the continuous data stream has to be processed in real time in order to reduce the data storage and handling load.

If several compression units process the data stream simultaneously, the data throughput of each unit is reduced to less than 100 MB/s. But this is still to much to process with reasonable efficiency using software. A hardware solution is needed, based on compression chips or FPGAs and optimised to perform the required operations at very high speed. JPEG was standardised quite some time ago and, as a result, various manufacturers implemented it in their hardware and are offer it as a component for integration. The first solutions for newer compression methods such as JPEG 2000 are already commercially available. They do not quite meet all the requirements as yet, but no doubt will soon be able to reach the necessary data rates. Unlike JPEG, new methods process substantially larger data blocks (so called tiles) and offer more configuration options, albeit at a cost of increased complexity.

4.7.3 Data Memory/Data Storage

A memory capacity of several hundred GB to several TB and data rates of several hundred MB/s are the basic criteria for selecting data carriers. In most cases, commercial data carriers are used for reasons of cost. Two memory technologies available on the market for standard components today can meet these criteria: hard disk drives (HDD) and tape drives. Thanks to their higher reliability and easier integration, HDDs have achieved undisputed dominance in the market. The disadvantage of tape drives is that the drive and the data carrier are openly accessible, which puts them at high risk of damage through ambient influences such as dirt, dust, moisture and air pressure changes. Moreover, it is difficult to prepare data for storage on tapes in real time, because tape drives are designed for data streaming and require a constant input data rate. This calls for large intermediate buffers with the necessary memory management systems, which accumulate data before it is transferred block by block on to the tape at a high data rate. HDDs have this problem only to a limited extent. Their transfer efficiency on the data bus is somewhat lower owing to the smaller data blocks, but they have an internal memory which is enough to bridge the disk access time. This enables the data to be transferred at a variable data rate on to the disk without having to take special external measures. Other factor in favour of HDDs are that their data storage capacity and data rate are constantly increasing and that their cost-effectiveness is improving from generation to generation.

It is difficult to meet the environmental specifications with either technology. Flash disks would meet these specifications, but, owing to their small storage capacity and high costs, they are not suitable for storing the data from a digital airborne camera. Since commercial products do not provide an ideal solution, therefore, compromises need to be made. Hermetic HDDs housed in an airtight casing, which maintains the internal conditions specified for the operation of the HDDs even in the event a drop in ambient pressure, are the most common solution. Yet hermetic HDDs are difficult to cool, since the heat generated cannot be drawn off by a fan. For this reason the HDD needs to be thermally coupled with the pressure casing so that the dissipation can be controlled. The heat is then removed externally from the casing by convection, for example, by fans. A similar problem arises when the operating temperature has to be reached at freezing temperatures, in which case the HDD is heated with heating elements in order to achieve the required operating temperature as quickly as possible.

Precautions need to be taken also with respect to vibration and shock. Despite the fact that HDDs are quite robust, the data memory needs to be protected from continuous and peak loads through suitable cushioning to ensure reliable service on an aircraft.

All measures described in the foregoing are necessary to protect the memory medium from damage through ambient influences. It is also necessary to ensure that data is not lost in the event of a malfunction and that it can be readily reconstructed. Two basic configurations are possible for this purpose. The data could written in duplicate on two memory systems with HDDs. Alternatively, redundancy could be included with the data during storage and the data distributed over several hard disks such that the complete data set could be recovered from the contents of the other HDDs (this is the so-called RAID solution). One should bear in mind, however, that RAID solutions are available at various levels and not every level automatically guarantees higher data integrity.

We conclude with a note from the operational viewpoint. Power failures may occur during operation on an aircraft (for example, release of the safety switch). If this happens, it must be ensured that the recorded data remains usable or can be readily restored by closing open files and similar measures. The camera can be protected from power failures by supplying it with power from backup batteries to ensure that it can continue operating even during brief periods of mains failure. But this type of protection requires a relatively large additional volume and weight, which can be challenging, especially on small aircraft.

4.8 Flight Management System

The planning and execution of surveying flights is demanding for both the pilot and the camera operator, because flying hours are expensive and a great deal of organisational work is involved. Moreover, the time window available for flying over a specified area is small owing to the changing vegetation and other limiting factors. An automated camera system that is easy to operate simplifies this task and increases efficiency. This covers the entire processing chain, which extends from flight planning and flight execution to data evaluation and processing. Automated and optimised processing steps helps prevent errors caused by manual interaction.

In earlier times, flight plans were dawn up with the aid of maps, which was a time-consuming operation. Visual flight navigation was used and it was difficult to execute the flight lines in a precise manner in order to cover the required area properly. The lines flown had to be tediously plotted on a map when the flight report was drawn up following the flight mission. Thanks to GPS, high-performance receivers and related computer hardware and software, these operations are considerably easier today. Flight management systems (FMSs) for supporting navigation and determining position are the key to successful and cost-effective surveying flights. A modern FMS combines the advantages of a GPS-based surveying flight system with those of a sensor control system that is largely automated and that supports continuous data flow from planning to data processing (Fig. 4.8-1).

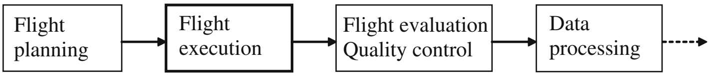

Fig. 4.8-1 Processing chain

This section deals mainly with sensor and FMS software. For the sake of clarity in delineating the functions and interfaces, we first deal with flight planning and flight evaluation. This will be followed by a more detailed description of sensor control and flight execution. Data processing is dealt with in Chapter 6.

4.8.1 Flight Planning

Flight planning is the first step in the processing chain and is normally done at the office. If planning errors are noticed when the aircraft is already in the air, however, plans may have to be corrected during flight. A plan lays down the flight lines required to cover the project area according to the specifications. It can also be used for optimising the flight course to provide the pilot with flight guidance support.

In practice, the task for a flight project may be formulated as follows: "Map the city centre area in colour using a ground resolution of 10 cm and a lateral overlap of 60%." When planning this flight, the outline of the specified area is scanned as a polygon on existing maps. In the case of paper maps, a digitiser is used for this purpose and, in the case of digital maps, it is done directly on the computer screen. Taking into account the sensor geometry and the specified boundary conditions such as coordinate system, overlap and preferred flight direction, the flight lines are optimised and, depending on the sensor type, the camera triggering or start and stop points plotted. If required, additional flight lines, individual images or waypoints needed for geometric stabilisation of the processed data, for a desired flight path or for other purposes can be added. The completed plan is exported as a file to be used for executing the flight. Modern planning software has an interactive graphical user interface, which instantly displays the result when parameters are changed. Moreover, high-performance flight planning software supports planning in various coordinate systems and over multiple map zones and enables a digital terrain model (DTM) to be used for flight plan optimisation. An integrated system and a continuous processing chain make it possible to establish the configuration of the map system even when plotting the flight plan.

4.8.2 Flight Evaluation

It is important to have quality control and clarity about the project status after each step in the process. For instance, after a flight, the user wants to have a comparison between the planned data and the flight data. Imaging material is passed on to the next processing step only after the operator has checked to see if all data has been captured as specified, i.e., the software must be able to evaluate flight plan data against the actual flight data. But to be able to make a detailed analysis after a flight, all requisite information, such as GPS positions, camera triggering or start and stop points, additional data generated by the operator (for example, clouds in the image), camera status and error messages, needs to be recorded by the FMS during the flight. After the flight, this data is transferred from the flight system to the office for evaluation.

4.8.3 Flight Execution

After flight planning, the next stage in the processing chain is flight execution, in which the flight plans are copied from the office to the flight system. As explained above, numerous factors impose constraints on the flight mission. In general, the execution of a flight involves a great deal of work and is very cost-intensive. A flight mission must therefore be carried out as efficiently as possible. This is facilitated by a camera system that is largely automated. Based on the flight plan data, it operates almost without user interaction, automatically recognizes errors and informs the operator about the status of the system. For a flight mission to be successful, it is necessary to have an optimised and correct flight plan.

During the flight, the flight management system (FMS) interprets the flight plan selected and performs the following principal tasks:

(1) Flight guidance along all lines of the flight plan, including quality control and autotracking of the project status
(2) Control and monitoring of sensors and external systems in accordance with the flight plan data.

At the start of the flight, the operator selects a flight plan and the next line to be flown. Based on the current position, the FMS computes an optimum flight path to the start of this line, taking into account the definable flight parameters. The current position required for this purpose is provided by the GPS. The coordinates of the start of the line are provided by the flight plan. The optimum flight path is displayed for the operator and the pilot. Most systems have display screens that are optimised to meet the requirements of the operator and the pilot. As a rule, the pilot flies along the proposed flight path. The proposed flight path is not binding, however, and there is a number of reasons for which the pilot may choose to deviate from the proposed flight path. If this occurs and a definable tolerance is exceeded, the system computes a new approach path based on the current position. After the aircraft reaches the start of the line, the FMS guides the aircraft along the line. Then the operator or the FMS selects the next line to be flown and the FMS again computes an optimum approach path.

In addition to providing flight guidance, the FMS controls the sensor systems along the flight line. Push-broom sensors are switched on at the start of a line and switched off again at the end. Area sensors are released in a defined cycle along the flight line. The FMS obtains the position from the flight plan and releases the shutter of the area array sensor as soon as the aircraft passes the photo centre. To ensure that a strip of images or a single image has been recorded with the required precision, the FMS captures the effective switch on and off positions or the release position and computes the deviations from the plan data. If the deviations exceed certain tolerances even before the release point, the imaging operation is not started and the operator informed accordingly. The FMS records such a flight line as not having been flown if the flight has not been repeated and the line flown successfully. The FMS records various data during the flight for subsequent flight analysis with the aid of the flight analysis software. This logged data comprises the GPS positions for switch on and off points or release points, angular data from the stabilised mount, various sensor settings, additional data generated by the operator such as "clouds along the flight line", etc. After completion or interruption of a flight, the recorded data can be exported and analysed using the flight analysis software. In this manner, the project status can be determined, quality control carried out and, if required, the flight plan for the next phase of the project revised.

The second task of the FMS is controlling and monitoring the sensors and external systems. Depending on the depth of integration, there are different solutions and tasks for the individual components. Two typical sensor system configurations are shown below (Figs. 4.8-2 and 4.8-3).

In the configuration shown in Fig. 4.8-2, the sensor system and the FMS operate almost independently of each other. The sensor is only started by the FMS and, at most, provided with the data required for operation. Since the sensor is configured, operated and monitored via a separate operating interface, the FMS and the sensor system have separate display screens, input units, etc. External components such

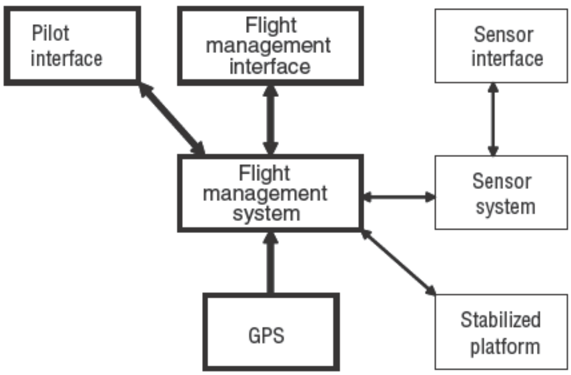

Fig. 4.8-2 Sensor system with an external FMS

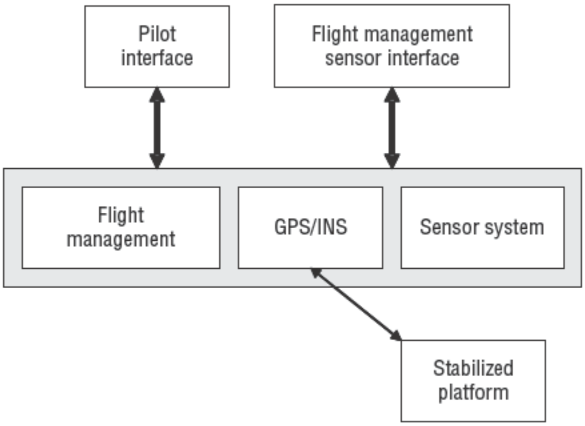

Fig. 4.8-3 Sensorsystem mit integriertem FMS

as a stabilised mount are controlled by the FMS in this arrangement. The FMS has only one ordinary interface to the sensor, which is an advantage. This solution is usually chosen when the sensor and the FMS are from different manufacturers. The main disadvantage is that different user interfaces are used to operate the FMS and the sensor, resulting in more space being required on the aircraft and diminished convenience in operating the systems.

If the FMS and the sensor control system are integrated with a single user interface (Fig. 4.8-3), it is more convenient to oversee and operate the system. If additional components such as the GPS/IMU are integrated, the system can be almost fully automated and can be operated from a single user interface. In this arrangement, the FMS, sensor control and operation of external components are integrated into a unit that is transparent to the user.

The processing chain can be further optimised by establishing the sensor configuration during the flight planning stage. This data, along with the flight plan, can be read into the flight computer, such that the sensor is configured automatically during flight without user interaction. This solution is particularly helpful in the case of complex sensor systems with numerous parameter options and it operates well in the case of an integrated solution.

Taking into account the influence of the wind on the flight path, automatic sensor integration, time control and other additional features provide the pilot and the operator with additional support. These features increase the efficiency and reduce operator errors.

4.8.4 Operator and Pilot Interface

Using the operator interface, the operator controls and monitors the flight over a project area and – if the system is integrated – the functions of the sensors and additional components. Depending on the solution chosen, a keyboard, individual control buttons or a touch-sensitive display screen is provided as an input unit. A small separate display screen is usually provided to support the pilot with graphic and numeric navigation data to enable him to follow the flight pattern laid down in the plan. Deviations from the target course are displayed and the optimum flight path suggested. In the case of an integrated system, it is even possible to control the entire system via the pilot interface. This enables the pilot to carry out the flight mission on his own. To meet the different data requirements of the camera operator and the pilot, it is advisable to have the screen content and the information tailored to their particular requirements and displayed independently on the operator and pilot interfaces. Only few systems support this, however, and most systems provide the operator and the pilot with the same information, which makes it necessary for them to coordinate their work during the flight accordingly.

To conclude this section, two views of the Leica FCMS are shown below (Figs. 4.8-4 and 4.8-5). These show what an integrated user interface can look like and the options available.

4.8.5 Operator Concept

The FCMS is operated via a touch-sensitive screen. A keyboard is not required. Whenever possible, graphic elements are used and text is used only if necessary. Ten context-sensitive pictogram fields are available as control elements.

In the navigation view (Fig. 4.8-4), the control fields down the left-hand side are as follows (top to bottom): general project information; sensor status; image class; mass memory status; and GPS status. The control fields down the right-hand side are as follows (top to bottom): flight altitude; bearing; line status; and flight speed

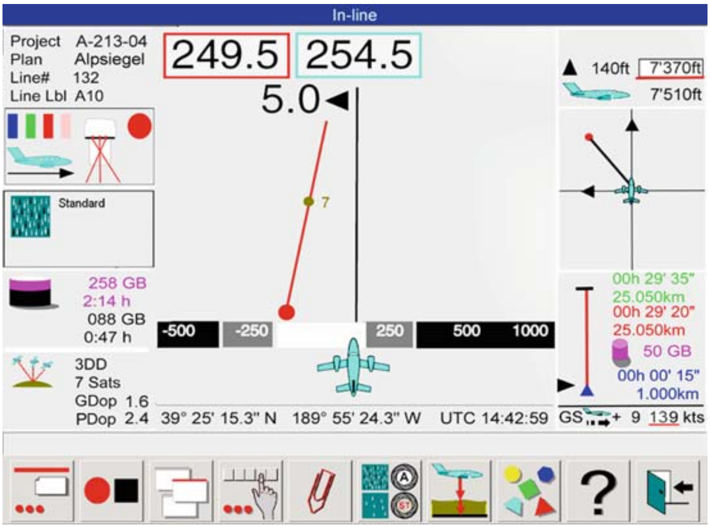

Fig. 4.8-4 Navigation view "on the line" in the Leica FCMS

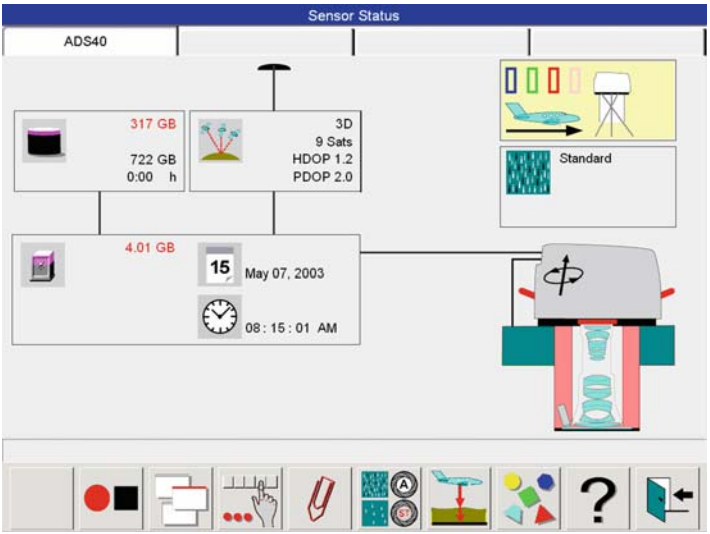

Fig. 4.8-5 Sensor status as seen on the Leica FCMS

over ground. The information in the centre of the image comprises: graphics display for navigating along the flight line, position and UTC time. The bottom part of the view consists of a status line and pictogram fields for user commands.

In the sensor status view (Fig. 4.8-5), the control fields down the left-hand side are as follows (top to bottom): mass memory status; GPS status; computer memory status; time information; and date. The control fields down the right-hand side are as follows (top to bottom): sensor status; image class; and hardware status of sensor head. The bottom part of the view consists of a status line and pictogram fields for user commands.

4.9 System for Measurement of Position and Attitude

4.9.1 GPS/IMU System in Operational Use

For the operational use of GPS/IMU systems for measuring positioning and attitude, the definition of system performance and requirements is elementary. As already indicated in the introductory part of Section 2.10, system choice depends on factors such as the following. Are the integrated GPS/IMU systems used as standalone components for the direct georeferencing of airborne sensors, or is the exterior orientation directly measured by GPS/IMU further refined in a process of aerial triangulation? As an extreme example, the GPS/IMU exterior orientations may be used only as initial approximations for the aerial triangulation. What are the final required accuracies for position and attitude? Are the GPS/IMU sensors used in very high dynamic or low dynamic environments? Is GPS update information available almost continuously or are there long sequences which have to be bridged because GPS data is not available? Such scenarios often occur in land applications owing to satellite blocking in built-up areas. Is alternative update information available besides GPS? Is there a need for real-time navigation? What reliability in navigation has to be guaranteed throughout the mission? All these factors lead to solutions that are application dependent, so within this context general recommendations are difficult.

The following discussion covers the influence of variations in the accuracy of the parameters of exterior orientation (for example, from GPS/IMU systems) on the determination of object points. As can be seen from Fig. 4.9-1, variations in exterior orientation certainly affect the performance. The results depicted in the figure are from simulations based on the following input values: stereo pair of images, standard 60% forward overlap, image format 23×23 cm^2, camera focal length 15 cm (wide-angle optics), flying height above ground 2,000 m, image scale 1:13,000. The true image coordinates of 12 homologous points within the stereo model are overlaid with random noise of standard deviation 2 μm. This noise represents the accuracy of standard image measurements. The resulting object coordinates are obtained from direct georeferencing based on the simulated exterior orientation elements. Finally, the coordinates of object points are compared to their reference values. Figure 4.9-1 shows how object point accuracy depends on variations in the quality of exterior orientation, whereas Fig. 4.9-2 is obtained from exterior orientations with fixed accuracy (i.e. position $\sigma_{X,Y,Z} = 0{,}1$ m, attitude $\sigma_{\omega,\phi,\kappa} = 0.005$) and depicts the influence of variations in flying height and image scale. Again the final accuracy of object point determination is illustrated. As in the case of the first simulation, the image coordinates are overlaid with 2 μm noise. All other parameters remain unchanged from the first simulation.

As expected, the quality of exterior orientation has a direct influence on the accuracy of point determination. In all cases the object point performance is linearly dependent on position and attitude accuracy as well as flying height and image

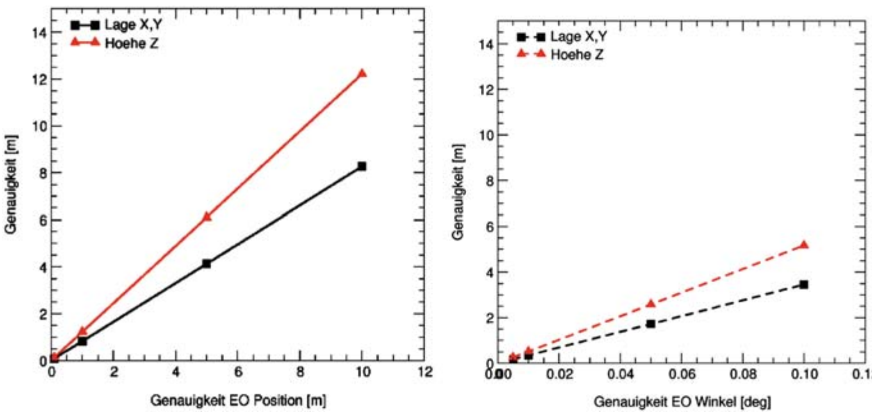

Fig. 4.9-1 Influence of variations in the accuracy of positioning (*left*) and attitude (*right*) on object point determination from direct georeferencing

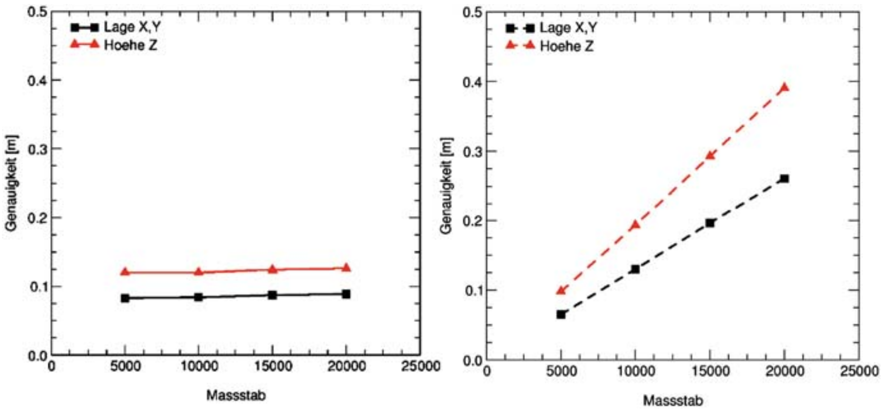

Fig. 4.9-2 Influence of variations in image scale and flying height on object point determination from direct georeferencing, assuming constant accuracy of positioning (*left*) and attitude (*right*)

scale. Assuming positional errors in exterior orientation of about $\sigma_{X,Y,Z} = 5\,\mathrm{m}$ in all components, the accuracy finally obtained in object space is around 5 m (mean). The performance in the height component is worse due to the specific geometry of image ray intersection. Similar behaviour can be seen if erroneous attitude information is assumed. With an orientation error of $\sigma_{\omega,\phi,\kappa} = 0.05°$ the resulting error in object space is about 1.7 and 2.6 m for horizontal and vertical components respectively. This error budget can also be estimated by using the well known equation $h_g \cdot \tan(\sigma_{\omega,\phi,\kappa})$, where h_g describes the flying height above ground. The overall influence caused by both position and attitude errors is derived from the two individual errors by means of the rules of error propagation.

If the accuracy of the attitude values remains constant ($\sigma_{\omega,\phi,\kappa} = 0.05°$), the performance in object space decreases linearly with increasing flying height, which corresponds to a decrease in image scale, assuming that the camera constant remains unchanged. On the other hand, the influence of positioning errors in exterior orientation is almost unaffected by flying height and image scale, but remains constant for the range of image scales covered. Only a very small decrease in accuracy is visible for smaller image scales. This is due to the overlaid noise in image coordinate measurements, which has slightly more influence in the case of smaller image scales acquired from higher flying heights: image space errors have more effect in object space if small scale imagery is considered. If one directly compares the influence of positioning and attitude errors on the overall error budget in object space (Fig. 4.9-2), the influence of attitude errors dominates for flying heights above approximately 1,000 m (corresponding image scale 1:6,500). Note that this threshold holds for the chosen simulation parameters only. For very large scale flights from low flying heights, the influence on positioning errors is the limiting factor in direct georeferencing. For small scale imagery from high altitudes, the attitude performance is the dominating factor with respect to the quality of direct georeferencing.

Depending on the desired applications, the main focus has to be on higher positioning performance or alternatively higher quality in attitude determination. This ultimately defines the quality requirements for GPS/IMU exterior orientations (see Fig. 4.9-1), as well as the approaches taken for GPS/IMU processing (i.e. real-time, post-processing, GPS processing [Table 2.10-1)].

For digital camera systems, the maximum tolerable error in object space is limited by the sensor's ground sampling distance (GSD). Assuming that the smallest object to be identified in the images has to be at least the size of one object pixel, the required accuracy of object point determination also has to be in the range of one object pixel or better. From this the following equation can be found:

$$h_g = c \cdot m_b = c \cdot \frac{\mathrm{GSD}}{\mathrm{pix}} = \frac{c}{\mathrm{pix}} \cdot \mathrm{GSD} = k \cdot \mathrm{GSD}. \tag{4.9-1}$$

The resulting flying height above ground h_g is a function of camera focal length c and sensor pixel size pix. The k factor is obtained from the quotient of these. Its reciprocal value $\frac{1}{k} = \frac{\mathrm{pix}}{c}$ is known as the instantaneous field of view (IFOV) of the sensor. Equation (4.9-1) also shows that in the case of digital imaging the GSD plays a similar role to image scale in data acquisition from the former analogue imagery.

Integrated GPS/IMU systems used for the direct orientation of airborne sensors are typically used in the following circumstances. The update information from GPS is available throughout the whole mission flight. If any satellite blockages and signal loss of lock are present, they appear mainly during flight turns. Sequences without any GPS update information are relatively short. Within the remaining parts of the trajectory, enough GPS data is available between two signal loss of lock events to resolve the integer phase ambiguities reliably. This is mandatory in the case where differential carrier phase processing is required and applied. Such considerations are of importance in the case of decentralized GPS/IMU data processing. Here raw GPS measurements (pseudo-range, doppler and phase observations) are not used for update, but already processed GPS position and velocity data (so-called pseudo-observations) are fed into the filter. This requires a minimum of four satellites to provide update information. Alternatively, if the GPS/IMU processing is performed within a centralized filtering approach, raw GPS observations are used as update information. Thus updates are possible even within periods where less than four satellites are available. Nevertheless, GPS/IMU systems used in airborne applications for direct sensor orientation are mostly based on the decentralized filter, owing to the higher flexibility of decentralized filters if additional components are integrated, i.e. updates from other sensors. This is different to centralized filters, where major parts of the algorithm have to be redesigned for changes in system configuration.

If such integrated GPS/IMU systems for measurement of position and attitude are used in dynamic environments, a certain bandwidth and sampling rate have to be achieved to describe the dynamics of the sensor's movement sufficiently. Since the high frequency parts of the dynamics are measured by the inertial sensors, the IMU specifications are of major concern. Within Fig. 4.9-3 two different spectra from inertial attitude determination are given for the same IMU chosen for this example, in both static and airborne kinematic environments. The inertial data were measured with 200 Hz frequency, thus frequencies up to 100 Hz are detectable. The influence of the different system dynamics is obvious. Notice the different scaling of the amplitude axis.

For the static environment almost no external vibrations are present. The frequencies visible in the first spectrum are mostly due to the sensor-specific measurement noise.[1] This situation is different for the same sensor if analysed in kinematic mode. The frequency plot is obtained from data from a small portion of a flight, where the aircraft was on a photogrammetric image strip. In contrast to the static spectrum, higher amplitudes and additional lower frequencies <15 Hz are present, representing the dynamics of this specific airborne environment. If the inertial sensor is rigidly fixed to the aircraft's body, this spectrum represents the movement of the aircraft. Quite often, however, the IMU is fixed on a stabilized platform close to the imaging sensor itself. In such cases the spectrum represents the dynamic environment of the sensor. The kinematic spectrum in Fig. 4.9-3 shows a dominant peak around 18 Hz. This reflects vibrations caused by the aircraft engines. In the higher part of the spectrum additional small frequency peaks are present, but with much lower amplitudes. Such frequencies are negligible as long their amplitudes are smaller than the pixel resolution of the sensor to be oriented. If one considers a digital camera with $10 \times 10\ \mu m^2$ pixel size in image space and a focal length of 10 cm, the resulting IFOV is about 0.1 mrad (corresponding to 0.006°). If such a camera is used in combination

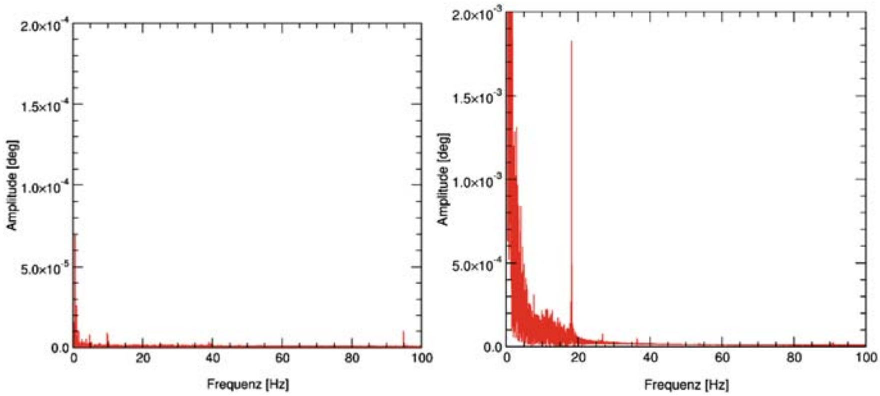

Fig. 4.9-3 Spectral analysis of IMU attitudes (pitch angle) in static environment (*left*) and during a photogrammetric flight (*right*)

[1]The sensor-specific noise is dependent on the performance of the gyros and accelerometers. For attitude sensors the performance of the IMU gyros is critical. The noise is given by the random walk coefficient denoted in $\left[{}^\circ/\sqrt{h}\right] \hat{=} 60 \cdot \left[{}^\circ/h/\sqrt{Hz}\right]$. If this random walk coefficient is multiplied by $\sqrt{t}$ the accuracy of attitude determination after a certain time interval $t[h]$ is estimated.

with an IMU, the inertial sensors have to be capable of resolving for those frequencies. For the example of the frequency plot in Fig. 4.9-3, only very low frequencies below 5 Hz have amplitudes higher than the assumed IFOV. All other frequencies are of negligible influence on the orientation determination of the sensor. In this specific case the use of a 50 Hz IMU would be perfectly adequate to cover the relevant spectrum of the sensor's movement. Please note that this holds only for this specific airborne dynamic environment, which was chosen to generate the frequency plots [see also Sujew et al. (2002)]. For flight configurations in different dynamic environments, the IMU has to resolve at higher sampling rates to cover all relevant frequency components. In all cases Nyquist's well known sampling theorem has to be considered. Besides this, the requirements in IMU specifications are becoming more stringent as the IFOV of the sensor to be oriented decreases.

Two commercial product families lead the market for integrated GPS/IMU systems used in operational applications for airborne direct georeferencing. The first system family, POS/AV, is provided by Applanix (Toronto, Canada), which is now part of the Trimble company. The second is the AEROcontrol product from IGI (Ingenieurgesellschaft für Interfaces) of Kreuztal, Germany. Both systems use the decentralized filtering approach. The accuracy potential of these high level systems is sufficient even for highly demanding applications in airborne direct georeferencing. The POS/AV-510 and AEROcontrol-IId systems are illustrated in Figs. 4.9-4 and 4.9-5 respectively. The performances of various systems are given

Fig. 4.9-4 POS/POSAV-510 system (© Applanix Corporation)

Fig. 4.9-5 AEROcontrol-IId system (© IGI mbh)

Table 4.9-1 System related accuracy for Applanix POS/AV and IGI AEROcontrol (accuracy given by the manufacturers)

	Applanix			IGI
	POS/POSAV-310	POS/POSAV-410	POS/POSAV-510	AEROcontrol-IId
Position [m]	0.05–0.3	0.05–0.3	0.05–0.3	<0.1 (X.Y) <0.2 (Z)
Velocity [m/s]	0.075	0.005	0.005	0.005
Roll/pitch angle [°]	0.015	0.008	0.005	0.004
Heading angle [°]	0.035	0.015	0.008	0.01
Drift [°/h]	0.5	0.5	0.1	0.1
Noise$\left[{}^\circ/\sqrt{h}\right]$	0.15	0.07	0.02	0.02

in Table 4.9-1. The accuracies given are obtained from post-processed differential GPS carrier phase processing.

The noise values (random-walk coefficient) specify the short term IMU performance. Both manufacturers use fibre-optic gyros (FOG) as primary components within the integrated GPS/IMU system. If one compares the different accuracies within the POS/AV product family, the positioning performance in all cases is similar. On the other hand the attitude performance relies entirely on the performance of the IMU gyros. This again verifies the assumption in Section 2.10.3 that positioning in GPS/IMU data integration is dependent mainly on the absolute accuracy of GPS.

The absolute positioning and attitude accuracies given by the manufacturers in Table 4.9-1 for POS/AV-510 DG and AEROcontrol-IId were evaluated and verified several times by independent tests. For such tests, the integrated GPS/IMU system is combined with an airborne photogrammetric camera and flown over a photogrammetric test site. This allows for an alternative determination of the exterior orientation parameters based on photogrammetric orientation techniques. Aerial triangulation estimates exterior orientations indirectly via bundle adjustment from tie point measurements and coordinates of known object points. These mathematically derived, photogrammetric orientation values for each individual camera station are then compared to the directly measured GPS/IMU positions and attitudes interpolated at the camera exposure times. Such an approach is the only way independently to evaluate the quality of directly measured GPS/IMU orientation values in airborne kinematic environments. Nevertheless, one has to bear in mind that the indirectly estimated orientations from aerial triangulation are the result of a mathematical process of parameter estimation. The estimates are optimal in the mathematical sense but do not necessarily represent the true physical orientation parameters of the sensor at the time of image registration. Thus, the overall performance of GPS/IMU exterior orientations is finally evaluated from check point analysis in object space. Here the coordinates of object points from direct georeferencing are compared to their pre-determined reference values. Such comprehensive comparison not only covers the performance of GPS/IMU orientation but also evaluates the quality of the camera used and the correctness of the overall system calibration parameters. Such performance tests are published, for example in Cramer (1999, 2003) and Heipke et al. (2001). In principle, direct georeferencing using integrated GPS/IMU systems such as POS/AV-510 or AEROcontrol-IId has been empirically verified as providing an object point quality with an accuracy factor only 1.5-2x below the performance of traditional aerial triangulation. Although this quality of object point determination is of somewhat lower accuracy, such performance is already sufficient for a large number of applications. It is interesting to note that not only is the performance of direct georeferencing limited by the GPS/IMU positions and attitudes, but, furthermore, the overall calibration of the whole sensor system, including the camera, is a major topic of concern and also a limiting factor. A suboptimal calibration will significantly decrease the accuracy of an application. Thus, overall system calibration and other more practically oriented topics in direct sensor orientation are considered in the ensuing discussion.

4.9.2 Integration of GPS/IMU Systems with Imaging Sensors

4.9.2.1 Overall System Calibration

A critical prerequisite for direct determination of exterior orientation parameters is the assumption of fixed relationships between all sensor components, i.e. three-dimensional translations and rotations. This requirement is especially stringent for the rotation components between IMU and camera coordinate frame. For example, if the IMU and the camera are separated by a spatial offset of 1 m, an undetermined 1 mm tilt between the two components will induce an orientation error of 0.05°. To achieve the highest performance, the rigid mounting of all sensor components on the same platform is essential. In most cases, the IMU is fixed as closely as possible to the imaging sensor. In the case of the newly designed digital airborne camera systems, the IMU is even installed inside the camera housing, very close to the focal plane itself. Mounting the IMU inside the camera body is also advantageous from a second point of view: due to the shock absorbers and the active camera mount, high frequency vibrations of the aircraft are almost fully absorbed and are no longer part of the data sensed by IMU. This is a positive influence on the subsequent inertial data processing (Skaloud, 1999).

The GPS/IMU positions and attitudes are related to sensor-specific coordinate frames. For example, the IMU-related body frame is defined by the physical directions of the inertial sensor axes. In addition, the different origins of the various sensors exhibit certain eccentricities. Therefore the results have to be reduced to one specific reference point, defined primarily in terms of the camera. The determination of the correct relationships, including offsets as well as rotations, between IMU, GPS and camera is the main task of boresight system calibration. As already pointed out, any remaining errors in the calibration parameters are of considerable influence in object space, due to the extrapolatory character of direct georeferencing.

The translation components between the different sensors (so-called lever arms) are typically determined by classical terrestrial surveys. This has to be done for each individual system installation. During this survey the phase centre of the GPS antenna, the centre of the IMU sensor axes and the camera perspective centre (located in object space) are used as reference points. The distance of the object side camera perspective centre from the camera focal plane is dependent on the optical system of the camera. Note that this distance is not identical to the generally used camera focal length parameter, which is provided by the manufacturer of the photogrammetric camera on demand. If a priori information on the lever arms are available, they are introduced in the GPS/IMU data processing.[2] Hence, the GPS/IMU positions finally obtained are already reduced to the physical perspective centre of the camera. The correct reduction of lever arms must also compensate for the movement of the stabilized platform. The rotations relative to the aircraft body also result in variations of the GPS lever arm components. The amount of such variations is minimized if the physical offset is as small as possible. Typically, the antenna is fixed directly above the camera on top of the aircraft's fuselage. Alternatively, the angles of the stabilized mount relative to the aircraft's body are recorded and used for the subsequent correction of the valid lever arm components at the time of exposure.

The determination of the physical misorientation between the IMU body frame axes and the camera coordinate frame is more complex, because the sensor axes are not directly observable in a terrestrial survey. The GPS/IMU attitude information is related to the IMU sensor axes, defined by the physical orientation of the IMU sensors (i.e. gyros). The image coordinate frame of the camera is defined by interior orientation. Owing to the practicalities of mechanical mounting, the IMU and camera frame are not physically aligned. This misalignment has to be determined and corrected. Nevertheless, as long as no relative rotations between the IMU and the camera coordinate frame occur, the misorientation will remain constant. The angles have to be determined via calibration: this process is called boresight angle calibration.

Boresight angle calibration is performed in different ways. For a certain number of images the GPS/IMU angles are compared to the photogrammetrically derived orientations and the misalignment estimated. Such calibration may be done over special calibration test fields. Some manufacturers of digital cameras provide a priori boresight values with their systems. Alternatively, the unknown boresight angles are modelled as one group of unknown parameters within aerial triangulation. If the directly measured GPS/IMU data is introduced as direct observations, the three misalignment angles are determined. This approach is called integrated sensor orientation and allows for the calibration of the misalignment as well. This can also be done from the mission data itself, even without ground control. Such a method is not only advantageous in terms of efficiency, but, in addition, the remaining systematic errors in the camera can be compensated by means of appropriate sets of

[2] Alternatively the lever arm between the IMU and the GPS antenna can be handled as unknown parameters during GPS/IMU Kalman filtering. Nevertheless, the remaining translation between IMU and camera perspective centre has to be known a priori.

self-calibration parameters. Self-calibration of photogrammetric sensors is gaining in importance again, when direct georeferencing is being performed. Any uncorrected systematic error in the camera or the whole sensor system including the GPS/IMU components, i.e. any difference between the true physical situation during image data acquisition and the assumed mathematical model applied for data processing, will induce errors in object space. It is important to see that not only each component but the whole sensor system has to be embraced within the overall system calibration process.

In integrated sensor orientation, the overall system calibration is determined and optimized for each individual mission area. This approach is favoured, therefore, for applications requiring high accuracy and reliability. As soon as remaining systematic effects are detected within the orientation process, they are compensated by applying the appropriate sets of additional parameters, together with a minimal number of ground control points if necessary. Comprehensive investigations on the use and potential of integrated sensor orientation can be found in Heipke et al. (2001). Some remarks on the stability of overall system calibrations over longer time periods are given, for example, in Cramer (2003).

For reasons of completeness, the correct time synchronisation between all the sensor components involved deserves mention. This has to be achieved within the integrated inertial – and GPS system components themselves as well as the camera.

4.9.2.2 Geodetic Aspects

If integrated GPS/IMU positioning and measurement systems are used in production, the choice of an appropriate coordinate frame is important. Since the goal is usually the acquisition of geospatial data, results are often related to a national projection system based on the national reference frame. Most national reference frames are based on conformal projections, for example transverse Mercator projection (UTM or Gauss-Krüger). The national mapping frame is there to flatten the Earth. Such flattening of a curved surface affects the geometric relationships and results in distortions (scale variations) in the horizontal coordinates and heights. Furthermore, these variations are dependent on the distance from the central meridian, which serves as one coordinate axis of the individual strip system. In the Gauss-Krüger projection, the central meridian is mapped at its true length. For height determination, the Geoid is used as the national height reference surface. The Geoid differs from the national reference surface (i.e. ellipsoid). These differences are known as geoidal undulations.

The photogrammetric model of central perspective is based on a Cartesian coordinate system (i.e. local topocentric frame), which differs from the mapping frame. The influences of Earth curvature and scale variations have therefore to be corrected. For Earth curvature the corrections are applied in image space or, alternatively, in object space. Conversely, different scales in height and horizontal components are not normally considered. In the case of indirect georeferencing these distortions affect mainly the estimated exterior orientation parameters. The mathematically determined perspective centres are shifted from their true physical locations, but the object coordinates finally obtained are almost unaffected. Nevertheless, in direct georeferencing one has to take these effects into account. In a similar way to sub-optimal system calibration, the effects of uncorrected coordinate distortions will significantly decrease the accuracy of object point determination. To solve for this, the camera focal length for each individual camera station can be adapted according to the local distortions, but this approach offers only an approximate solution. More rigorous is to conduct the processing in a Cartesian coordinate frame, where the mathematical conditions of central perspective hold, and to transform the results to the mapping frame afterwards [see for example Greening et al. (2000)]. A more thorough analysis of this problem is given by Ressl (2001) and results based on empirical data sets are published in Jacobsen (2003).

The Geoid mentioned above is also used as the vertical reference surface. Land surveyors typically use orthometric heights, which are directly related to the Geoid. The vertical information from integrated GPS/IMU systems, however, corresponds initially to the ellipsoidal reference frame (WGS84). Thus, ellipsoidal heights have to be transformed to heights above the Geoid. Depending on the level of accuracy required, Geoid models of different resolution and accuracy are available. If necessary, additional local adaptations are performed to obtain the correct height reference. Furthermore, the shape of the Geoid defines the direction of the gravity vector dependent on the actual position and the terrain variations. This plumb line also defines the vertical axis of the navigation coordinate frame, which is also germane to the determination of GPS/IMU orientation angles. Nevertheless, owing to gravity anomalies, the geoidal surface departs from the ellipsoid, so the plumb line does not coincide with the ellipsoidal normal. In some regions the slope of both references is almost linear, whereas in other regions (mostly in mountainous areas) non-linear variations occur. The deflection of the vertical impacts navigation angles and has to be considered in the transformation to the mapping coordinate frame. Uncompensated deflections of the vertical may induce errors up to 20″ (Greening et al., 2000). Variation over a certain region of interest is especially critical, though the constant part of these effects is already compensated within the calibration of the boresight angles.

4.9.2.3 Transformation of Rotation Angles

The discussion above clearly indicates the need for several transformations that have to be applied to the positioning and attitude data obtained. Proper attention must be paid to the correct transformation of rotation angles. The navigation angles originally obtained have to be transformed to the photogrammetric angles. The appropriate parameterisation has to be considered also. Typically, the orientation angles in photogrammetry are given as ω, ϕ, κ. As already depicted in (2.10-22), the navigation angles r, p, y (roll, pitch and yaw) are obtained from a transformation matrix, which relates the inertial body frame system to the local navigation frame n. If the sensor is moving, as is always the case for kinematic applications, the local navigation frame moves as well. Its origin is always defined by the actual position of the sensor. This has to be corrected and compensated to obtain the orientations compatible with subsequent photogrammetric processing.

If the photogrammetric process is carried out in a local topocentric coordinate frame, the following equation describes one possible way to obtain compatibility of navigation angles *r, p, y* and photogrammetric angles ω, ϕ, κ:

$$\mathbf{R}_{\mathrm{p}}^{\mathrm{l}}(\omega,\phi,\kappa) = \mathbf{R}_{\mathrm{n}}^{\mathrm{l}}(\pi,0,-\frac{\pi}{2}) \cdot \mathbf{R}_{\mathrm{e}}^{\mathrm{n}}(\Lambda_{\mathrm{t_i}},\Phi_{\mathrm{t_i}}) \cdot \mathbf{R}_{\mathrm{b}}^{\mathrm{n}}(\mathrm{r,p,y}) \cdot \mathbf{R}_{\mathrm{p}}^{\mathrm{b}}(\pi,0,0) \tag{4.9-1}$$

As one can see from (4.9-2), the relationship is obtained from an interlaced rotation sequence. The rotation matrix R_b^n contains the navigation angles, which are obtained from integrated GPS/IMU data. The matrix R_p^broughly aligns the axes of the camera-specific photo coordinate system *p* and the inertial body frame *b*. Within this rotation the boresight misalignment can also be included. Typically the axes of the camera coordinate system point forward (*x*-axis in the flight direction) and vertically upward (*z*-axis), with the *y*-axis completing the right-handed system by pointing to the left wing of the aircraft, for example. The inertial body frame, however, is normally defined as follows: *x*-axis pointing forward (in the flight direction), *z*-axis pointing downward, with the *y*-axis completing the right-handed frame (pointing to the right wing of the aircraft). The matrix R_n^e relates the moving navigational coordinate frame *n* to the earth-centred earth-fixed coordinate frame *e*. This transformation is dependent on the actual origin of the navigation frame. Thus the matrix is built up at the actual position at a distinct time epoch t_i. Within this context any deflections of the vertical must also be considered. The remaining matrices R_e^n and R_n^l describe the relationship to the photogrammetric coordinate frame. As already mentioned, this local topocentric coordinate frame is located at a fixed origin. Such a frame fulfils all photogrammetric requirements. Now theR_p^lmatrix, formed from the photogrammetric angles, is available. This transformation from photo to local topocentric frame yields the angles, though the different angle parameterisations that are possible have to be considered too. More details on the angle parameterisations typically used in photogrammetric applications are given in Bäumker and Heimes (2001).

Although the processing in cartesian coordinate frames has certain advantages, especially from the photogrammetric point of view, many applications have to be processed in the mapping coordinate frame LK directly, as already discussed. If such a mapping frame is required, the GPS/IMU orientations have to be transformed into this coordinate frame as well. This can be done with the following equation:

$$R_p^{\mathrm{LK}}(\omega,\phi,\kappa) = R_l^{\mathrm{LK}}(0,0,\gamma) \cdot R_n^l\left(\pi,0,-\frac{\pi}{2}\right) \cdot R_b^n(r,p,y) \cdot R_p^b(\pi,0,0) \tag{4.9-2}$$

The navigation coordinate frame always coincides with the gravity vector. Thus at any time instance a tangential plane to the Geoid is defined. This tangential plane is identical with the ellipsoidal tangential frame as long as the deflection of the vertical is neglected. Therefore, the GPS/IMU orientations are already related to the ellipsoid. The two matrices R_p^b and R_n^l again model the alignment of camera and IMU coordinate frame, and navigation and local topocentric coordinate frame, respectively. Because the heading from GPS/IMU is related to geographic north, which does not coincide with the north direction in the mapping frame, the matrix $R_p^{LK}(0{,}0{,}\gamma)$ compensates this influence of meridian convergence. γ, which describes the angular difference between mapping north and geographic north. Direct georeferencing in mapping coordinate frames is also discussed by Jacobsen (2002) and Kruck (2003).

4.10 Camera Mount

4.10.1 Rigid Mount

The original purpose of mounts for analogue airborne cameras was to provide a rigid mounting base. This is still the primary function with regard to airworthiness and air safety. The collective term "rigid mount" includes terms such as "rigid fixture" and "rigid support", which were previously used in some countries, as well as the more recent "rigid suspension with springs".

In general, today's camera mounts are compliant with the basic requirements for use on aircraft covered by the term "rigid mount". Whereas internal mechanical connections between the platform and the camera or sensor are the responsibility of the manufacturers, external connections between the mount and the aircraft are the responsibility of authorised aviation personnel, who are also responsible for carrying out the airworthiness approval test of the system as a whole. The most important function here is to ensure a safe attachment of the mount to the aircraft floor.

We define the terms roll, pitch and yaw to facilitate the discussion. Roll, which refers to motions at right angles to the flight axis over the wings, is the most active of the three axes in relation to the rates of rotation and attitude deviations. In the case of manual control, the roll axis is usually set to zero, which represents the mean value of the expected motions of $\pm 5°$. Pitch is related to the up and down motion of the aircraft's nose, which creates the smallest amount of disturbance, but in most cases it is associated with an offset resulting from the difference between the position of the longitudinal axis (nose up/down), which is dependent on flight speed, and the rigid aircraft floor. To bring this pitch also within the $\pm 5°$ range, this constant offset is achieved by a wedge-shaped adapter inserted beneath the mounting platform. Two disturbance components are involved in yaw: the aircraft motion around the vertical axis; and tacking against crosswind. The yaw can be as large as 30°; with this amount of disturbance, an aerial photo flight can no longer meet high quality requirements and it is no longer possible to achieve the required amount of lateral overlap.

4.10.2 Frequency Spectrum in Aircraft and MTF

Two important frequency spectra are relevant for mounting platforms on aircraft. Each aircraft has its natural resonances, which depend on the engine type, number

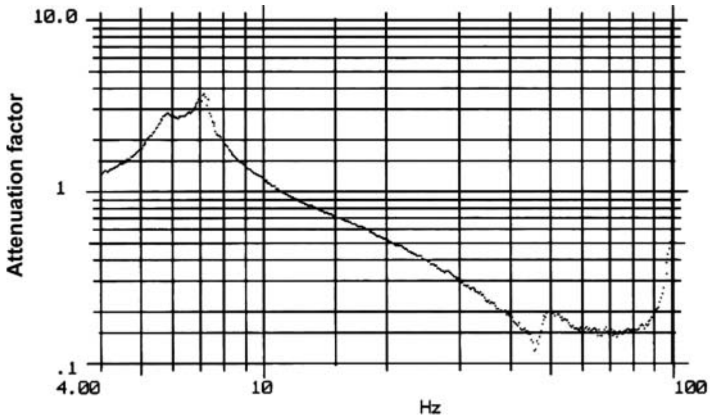

Fig. 4.10-1 Passive attenuation

of engines, speed and number of rotor blades. These narrow-band frequencies, most of which have high amplitudes, are in the range 20–120 Hz. These interfering frequencies are dampened through "passive attenuation", which is achieved through vibration absorbers installed under the mounting platform or under the camera and the sensor; they attenuate such vibration in the approximate range10–150 Hz. Passive attenuation also diminishes vertical impacts caused by flight turbulence. Figure 4.10-1, showing the ratio of the output to input signal, is a typical attenuation curve along one axis using passive attenuation.

The second frequency spectrum is the main reason why increasing use is being made of controlled camera mounts. In most aircraft, the mean angular velocities of flight motions during an aerial photography flight can be as high as 3°/s and can reach peaks of 10°/s. These disturbance frequencies, caused by turbulence and intentional flight manoeuvres, have a low-frequency spectrum. Frequency measurements in various aircraft lead to the conclusions that relevant rotary motions in an aircraft are mostly in the low-frequency range. The amplitude decreases with increasing frequency from about 1 Hz and by about 7 Hz it is reduced by a factor of 100 (Fig. 4.10-2).

The two components (vibrations and flight motions) of the remaining interferences involved when a camera mount is used are reactions to various events and must therefore be considered separately. Vibrations, in turn, also have two components, i.e., sinusoidal motion and random motion or jitter, all of which have a multiplicative effect on the platform $\mathrm{MTF_{PF}}$ in accordance with

$$\mathrm{MTF_{PF}} = \mathrm{MTF_{FB}} \cdot \mathrm{MTF}_J \cdot \mathrm{MTF_{sin}}. \tag{4.10-1}$$

The $\mathrm{MTF_{sin}}$, MTF_J and $\mathrm{MTF_{FB}}$ components are now examined separately to obtain the attenuation values that must be achieved with the platform.

Flight motions caused by external conditions during an aerial photography flight can be approximated through linear motion or motion of the projection of a detector

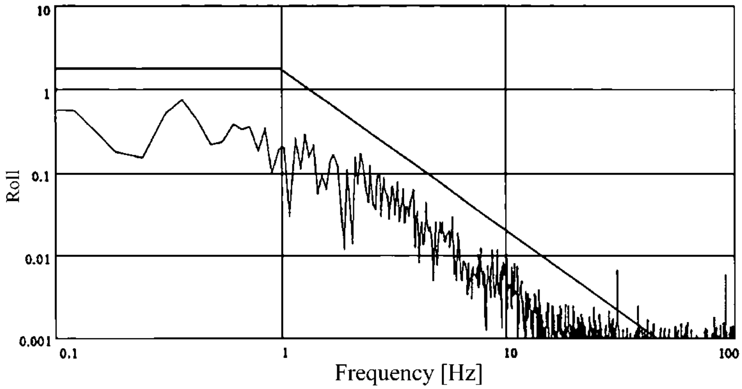

Fig. 4.10-2 Aerial photography flight frequency spectrum

element on the earth's surface by rotation about one of the three axes. As shown in Section 4.1, the MTF of linear motion is described by the sinc function. The following then applies to the motion of the ground track caused by the aircraft's roll or rotation about its longitudinal axis:

$$\begin{aligned} \mathrm{MTF}_{\mathrm{FB},y} &= \sin c(\pi \cdot a_{\mathrm{FB},y} \cdot f_y) \\ \mathrm{MTF}_{\mathrm{FB},y} &= \frac{\sin(\pi \cdot a_{\mathrm{FB},y} \cdot f_y)}{\pi \cdot a_{\mathrm{FB},y} \cdot f_y}. \end{aligned} \tag{4.10-2}$$

This applies analogously to the pitch in the flight direction x: yaw and translations (pushing motions) can influence the x and y directions. It should be noted here that the MTF influence brought about by normal flight motion during integration time t_{int} was taken into account in Section 4.1. Here we are considering additional disturbances that are reflected in the MTF components mentioned. In (4.10-2), $a_{\mathrm{FB},y}$ is the distance travelled by the projection of the detector pixel on the earth's surface at right angles to the line of flight in the dwell time t_{dwell} and f_y is the spatial frequency at right angles to the line of flight. As mentioned in Section 4.1, the MTF components attributable to the linear motion, which result in smearing of the ground pixel or IFOV by 20% of the GSD, are negligible.

Figure 4.10-3 shows the MTF curves for motion distances of $a_{\mathrm{FB}} = 0.2$ GSD (MTFa1), $a_{\mathrm{FB}} = 1$ GSD (MTFa2) and $a_{\mathrm{FB}} = 1.5$ GSD (MTFa3). MTFa2 corresponds to the detector MTF. At $a_{\mathrm{FB}} = 1.5$ GSD, MTF becomes negative and a phase reversal takes place (see also Sections 2.4 and 4.1). The spatial frequency normalised to the detector element distance y is plotted on the x axis in Fig. 4.10-3, in which $f_i = \frac{f_y}{f_{y,\max}}$ given $f_{y,\max} = \frac{1}{y}$, i.e., $f_i = 1$ corresponds to a spatial frequency of 155 lines/mm given a detector element distance of 6.5 μm.

Figure 4.10-4 shows that a linear motion over a distance $a = 0.2$ GSD has only a small influence on the total MTF. If we assume that the MTF of the detector has

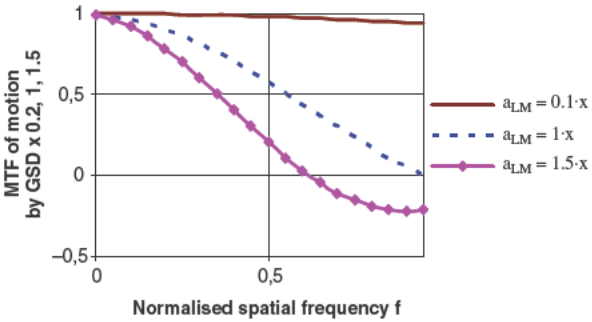

Fig. 4.10-3 MTF curves in the case of linear motion over distances of $a = 0.2$ GSD (MTFa1), $a = 1$ GSD (MTFa2) and $a = 1.5$ GSD (MTFa3)

Fig. 4.10-4 MTF curve of linear motion given $a = 0.2$ GSD (MTFa1) and the resulting MTF (MTF1) determined by multiplying by the detector MTF (MTFd)

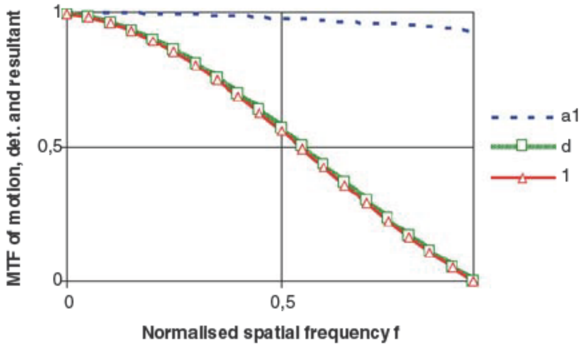

a substantial influence on the MTF of the camera, the degradation of MTFd is so small that at $a \leq 0.2$ GSD it can be neglected.

4.10.2.1 Example

For GSD of $x = y = 10$ cm, flight altitude $H = 1{,}000$ m, flight speed $v = 180$ km/h $= 50$ m/s, we obtain from (2.8-3)

$$t_{\text{dwell}} = \frac{x}{v} = 2\,\text{ms}$$

and from (4.2-16)

$$\text{IFOV} = 0.0057°.$$

The angular velocity Ω in the direction of roll for bridging a GSD is

$$\dot{\omega} = \frac{\text{IFOV}}{t_{\text{dwell}}} = 2.86°/\text{s}.$$

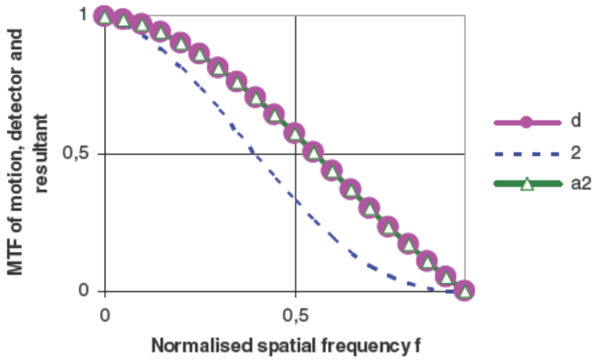

Fig. 4.10-5 MTF curve of linear motion where a = 1 GSD (MTFa2) and the resulting MTF (MTF2) determined by multiplying by the detector MTF (MTFd)

To prevent the motion distance from exceeding 20% of GSD, a controlled mount must be used to limit the influence of roll on the camera to <0.6°/s. The same applies analogously to φ and χ, the angular velocities in the pitch and yaw directions. Figure 4.10-5 shows that the MTF_{FB} curve for $a = 1$ GSD, which is congruent with the detector MTF, causes a more degraded overall MTF relative to the detector MTF, which can no longer be neglected when determining the camera MTF.

We turn to the MTF of jitter, MTF_J. If by using passive attenuation it is possible to decouple the resonance frequencies from the camera to a large extent, since these depend on the aircraft type and the engine components (engine speed, number of pistons, number of propellers, etc.), most of the remaining disturbances can be regarded as random motions or jitter, caused by a superimposition of several high-frequency disturbances, which can have random distributions. In this case, the central limit theorem of probability calculus (see Section 2.6) can be used to simplify the description of this complex situation. According to this theorem, a superimposition of a multitude of random distributions, which do not have to be normal distributions, transforms asymptotically into a normal distribution:

$$\mathrm{MTF}_J = \exp\left(-2\pi^2\sigma_J^2 f_J^2\right), \qquad (4.10\text{-}3)$$

where σ_J represents rms and f_j represents the spatial frequencies. Figure 4.10-6 shows the corresponding MTF curves for $\sigma = 0.1\,x$ and $\sigma = x$ (x is the detector element spacing) in comparison with the detector MTF. It can be seen from Fig. 4.10-7 that the degradation of the detector MTF by a jitter where $\sigma = 0.1\,x$ is so small that this influence be disregarded.

For example, if the spacing between the detector elements is $x = 10$ µm, the focal distance $f = 50$ mm, we obtain, according to (4.2-16)

$$\mathrm{IFOV} = 2\arctan\frac{x}{2f} = 0.2\ \mathrm{mrad}.$$

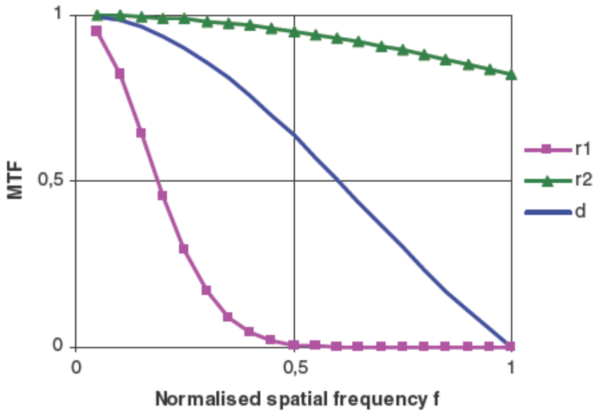

Fig. 4.10-6 MTF jitter curves at $\sigma = 0.1\,x$ (MTFr2) and $\sigma = x$ (MTFr1) in comparison to detector MTF (MTFd), where x is the detector element spacing

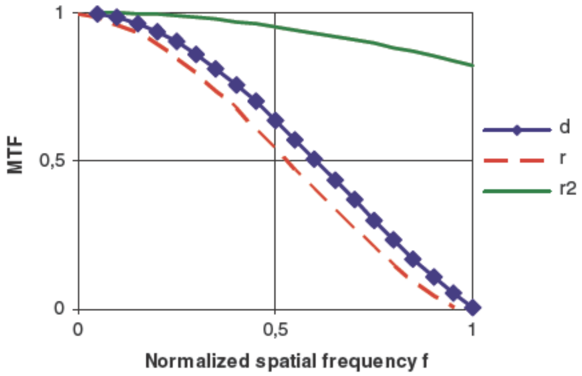

Fig. 4.10-7 MTF jitter curve where $\sigma = 0.1\,x$ (MTFr2) and the resulting MTF (MTFr) determined by multiplying by the detector MTF (MTFd)

Thus the random deflections or disturbance deflections remaining after the passive attenuation may not deflect the camera by more than 20 μrad (rms) or approximately 4 arcsec (rms) from the normal position.

A resonance peak that is still active on the platform after passive attenuation, which cannot be incorporated into the jitter term, is factored into the determination of the platform MTF and hence into that of the camera MTF via MTF_{sin}. The sinusoidal motions from resonances after passive attenuation have the following form

$$\Psi_{\sin} = a_s \cdot \sin(\omega t) \tag{4.10-4}$$

where a_s = amplitude and ω = angular frequency of the oscillation.

If the camera is subject to many sinusoidal motions during the integration time, then

$$t_{int} >> \frac{2\pi}{\omega} \tag{4.10-5}$$

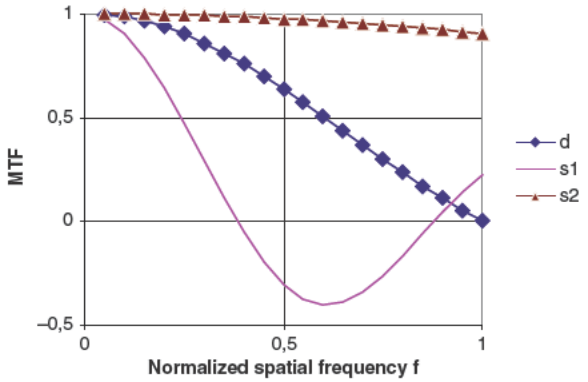

Fig. 4.10-8 MTF curves representing sinusoidal disturbance motion with the amplitudes $a_s = x$ (MTFs1) and $a_s = 0.1\ x$ (MTFs2) in comparison with the detector MTF (MTFd)

$\mathrm{MTF_{sin}}$ is described via the zero-order Bessel function $J_0(2a_s\pi f_{x,y})$, where $f_{x,y}$ represents the sinusoidal motion x or y. A Bessel function $J_0(x)$ can be calculated via an alternating series (Bronstein and Semendjajew, 1989), the computation of which can be truncated after the first members

$$\mathrm{MTF_{sin}} = J_0(2\pi a_s f_x). \tag{4.10-6}$$

Figure 4.10-8 shows the curves of Bessel functions for $a_s = x$ and $a_s = 0.1\ x$ (where x is the spacing between detector elements) in comparison with the detector MTF, where the normalised spatial frequencies are plotted on the x axis.

Note that here, too, MTF assumes negative values when $a_s = 1$. Figure 4.10-9 clearly shows that the degradation can often be disregarded for $a = 0.1\ x$. Hence, due to the influence of the platform, the resonance frequencies must be attenuated to the point where their influence limits the deflections of the pixel projection on the earth's surface to ±0.1 GSDGSD.

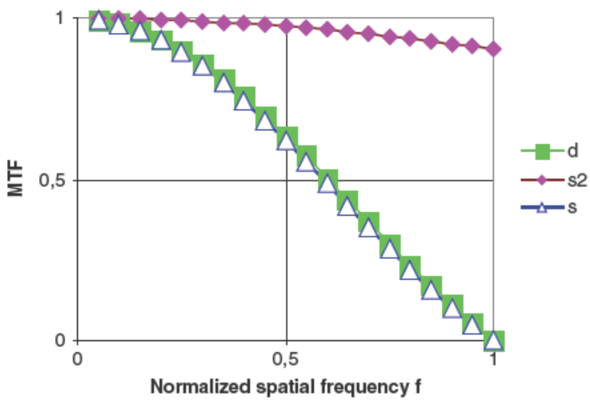

Fig. 4.10-9 MTF curve of $\mathrm{MTF_{sin}}$ for $a = 0.1\ x$ (MTFs2) and the resulting MTF (MTFs) determined by multiplying by the detector MTF (MTFd)

After these explanatory remarks, the $\mathrm{MTF_{PF}}$ can be transferred from (4.10-1) to

$$\begin{aligned}\mathrm{MTF}_{\mathrm{PF},x} &= \sin\mathrm{c}(\pi a_{\mathrm{FB},x} f_x) \cdot \exp\left(-2\pi^2\sigma_{J,x}^2 f_x^2\right) \cdot J_0(2\pi a_{s,x} \cdot f_x)\\ \mathrm{MTF}_{\mathrm{PF},y} &= \sin\mathrm{c}(\pi a_{\mathrm{FB},y} f_y) \cdot \exp\left(-2\pi^2\sigma_{J,y}^2 f_y^2\right) \cdot J_0(2\pi a_{s,y} \cdot f_y).\end{aligned} \tag{4.10-7}$$

Figure 4.10-10 shows that even if the limit values $a_{\mathrm{FB}} = 0.2\ x$, $a_s = 0.1\ x$ and $\sigma_J = 0.1\ x$ mentioned above are exhausted in all component MTFs, the detector MTF is not substantially degraded by multiplication by the component MTFs

$$\mathrm{MTF_{res}} = \mathrm{MTF_{PF}} \cdot \mathrm{MTF_D}$$

where $\mathrm{MTF_{res}}$ is the resulting MTF.

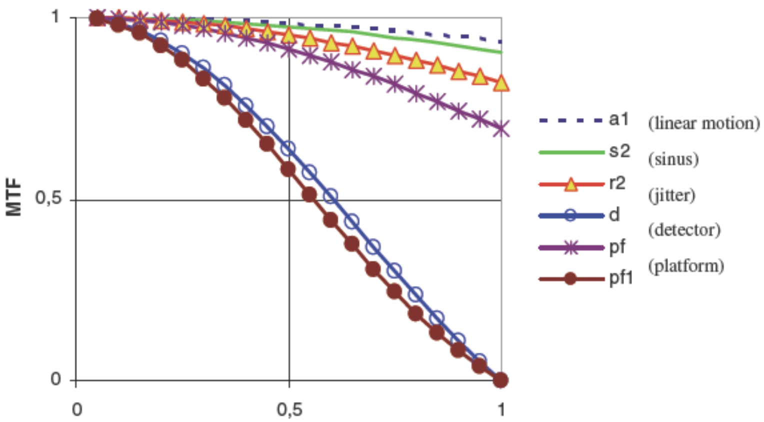

Fig. 4.10-10 MTF curves of the components using limit values $a_{\mathrm{FB}} = 0.2\ x$ for linear motion (MTFa1), $a_s = 0.1\ x$ for sinusoidal motion (MTFs2), $\sigma_J = 0.1\ x$ for jitter (MTFr2) and the MTFpf formed by multiplying all disturbance components. The resulting MTF (MTFpf1) is the multiplication of MTFpf by the detector MTF (MTFd)

4.10.3 Uncontrolled Camera Mount

The use of uncontrolled mounts is diminishing progressively, since they can no longer meet present-day standards with regard to economy, precision and comfort. Only the "rigid mount" and "passive attenuation" functions and the manual central position setting of uncontrolled platforms are controlled by the operator.

The disadvantages of uncontrolled mounts are their operator-intensive operation, long flying time as a result of the large amount of lateral overlap required, poor nadir position of the flight strip and inferior image quality due to image and/or pixel smearing. Figure 4.10-11 shows the effects that occur when only the "rigid mount" and "passive attenuation" functions are implemented. The image strip was produced using a line camera during a flight over Berlin with a GSD of 30 cm. The roll, pitch

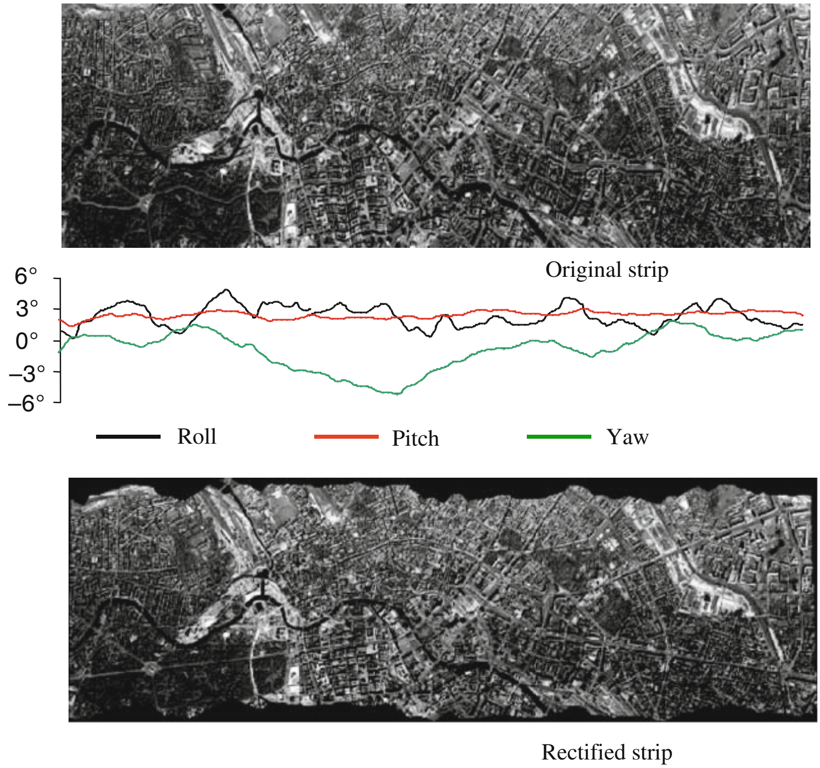

Fig. 4.10-11 Uncontrolled camera mount

and yaw were relatively severe. Image distortion could be rectified with the aid of data from a POS (position and orientation system). The high correlation between the roll values and the attitude variations in the distortion-corrected image can be clearly seen. Positional variations are significantly reduced by using a controlled mount, so that only small lateral overlaps of the flight strip are required.

4.10.4 Controlled Camera Mount

Controlled mounts with automatic image stabilisation and automatic attitude control meet two requirements. Image stabilisation has the same requirements and characteristics for both analogue and digital airborne cameras. The input values to the control loop are the angular velocities of the three axes, which are measured by gyros, and the objective is to keep the residual angular velocities as low as possible. It is expected that when a controlled mount is used, the residual angular velocity for the remaining maximum image smear remains below 0.3°/s.

Attitude control supports the control loop of the image stabilisation system. In analogue film cameras, the mount must be controlled in such a way that deviations from the nadir caused by roll and pitch and from the true track caused by yaw stay within the range of a few tenths of one degree.

The input values for attitude control often come from the two attitude sensors affected by inertia, which means that this control loop is strongly influenced by flight behaviour. A value of approximately 0.2° will not be achieved if directional corrections are made by "pushing" instead of rolling, if the mount is situated too far from the aircraft's axis of rotation and if there is a large amount of translation disturbance. External reference is required for control with regard to yaw, because the mounts cannot measure the values required for determining the difference between heading and true track. For this reason, external reference for yaw needs to be determined manually by the operator, or the input magnitude is transmitted from external devices by an interface.

Attitude control can be dramatically improved with a digital airborne camera, since it normally has an integrated POS, which can supply the mountwith attitude values for all three axes and improve the attitude control by at least a factor of 10. Image stabilisation is also improved, since the gyros provide much better interpolation values. It can be seen in Fig. 4.10-12 that the "frayed" edges that occur with uncontrolled platforms are absent in the corrected image strips (see Fig. 4.10-11).

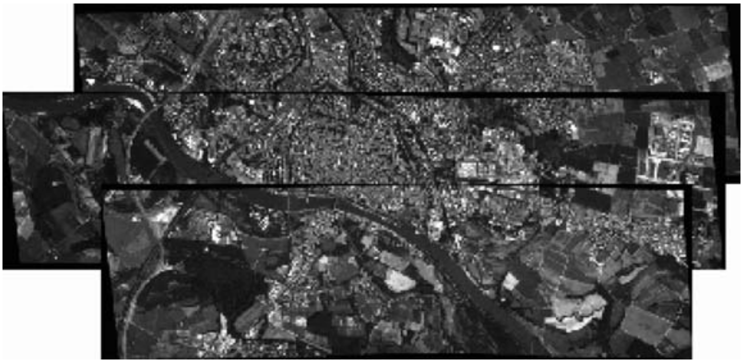

Fig. 4.10-12 Rectified strips made with a controlled mounting platform

Chapter 5
Calibration

Since the effective resolution of classical airborne cameras and even more so their radiometric performance were determined to a large extent by the film, these cameras were calibrated with regard only to image geometry and the limit of resolution of the lens. In the case of digital cameras, however, a complete calibration can be carried out at the system level, including effective resolution and spectral responsivity.

Depending on the application of the camera, a calibration of various parameters and quality standards is required, depending on not only users' requirements but also the guidelines of the certification authorities of the country concerned. Whereas in the past, certification was required only for geometric calibration to obtain an approval for a camera for surveying purposes, current requirements have been extended to include radiometric parameters. The type of certification is also undergoing changes. In the past, many countries relied on an accredited calibration laboratory or set up their own calibration office for this purpose. A camera's imaging geometry was determined by measuring its essential components (lens, fiducial marks, pressure plate).

Owing to the multitude of digital cameras and their complex internal structures, the classical procedure is seldom permitted anymore. The result is that in most cases the entire system is calibrated. This is done in a laboratory, or by using self-calibration after test flights in typical working conditions, or a combination of the two. The situation concerning certification of camera systems is similar. Increasingly, the requirement here is that the practical performance of a camera be demonstrated on a flight over a test field.

5.1 Geometric Calibration

The purpose of geometric camera calibration is to establish an unequivocal relationship between points on an image plane and the object space. Since in the case of an aerial photograph, the position of the projection centre on the object side is virtually invariable, a much more simplified model than in the close-range case can be used. It is only necessary to determine the position of the projection centre on the

R. Sandau (ed.), *Digital Airborne Camera*, DOI 10.1007/978-1-4020-8878-0_5,

object side and the relationship between the point position in the image space and the direction in the object space. For all other aerial image objects, this relationship is unequivocal.

The model currently used to describe this relationship is that of a pinhole camera, together with a method for correcting distortions in the image plane. But this is by no means the most efficient representation for today's digital evaluation, in which a tabulation of the imaging directions, or at least of distortion corrections, is more sensible for implementing optimum real-time transformations.

The development of classical airborne cameras and of the associated calibration technology was closely linked to the capabilities of the devices used for restitution. In designing mechanical and optical analogue devices for restitution, it was reasonable to implement the simplest possible model, namely that of the pinhole camera. Every deviation from this model necessitated costly auxiliary constructions. Consequently, great efforts were made to achieve an optimum geometric quality of the imaging array. This related to the planeness of both the imaging medium – initially photographic plates and then a combination of a perfectly plane pressure plate and plane film – and the lens, which, should have no worse defects than radially symmetric distortion. In the final generation of airborne cameras, this objective was achieved to perfection. Distortion was reduced to less than 2 μm and the pressure plates ensured that the same degree of precision was achieved with respect to the support plate of the film.

The calibration of a classical airborne camera comprises three parts, namely ensuring the quality of the plane position, determination of the position of 4–8 fiducial marks and the main part, which is the determination of the imaging geometry of the lens. This last requirement was usually limited to measuring the image diagonals with the aid of goniometers (Bormann, 1975).

The optical path is reversed when measuring the lens, i.e., a measuring piece (a pane of glass illuminated from behind) with a calibrated test pattern is used instead of a system consisting of a pressure plate and film. A telescope set to infinity is aimed at the patterns on the glass pane through the lens. The measured variable is the angle of the telescope when pointing at the pattern element in question. An example is shown in Fig. 5.1-1.

The horizontal goniometer – mechanically the simplest form of this device, in which the camera lens is in a horizontal position and the axis of rotation in the pupil on the object side in a vertical position – subsequently gave rise to vertical goniometer systems in which the lens is tested in its operating position to avoid deformations in the lens assembly. In addition, the type of measurement and its evaluation were increasingly automated and improved.

The result of the measurement of a classical aerial film camera consists of the camera constant and a radially symmetrical distortion. The camera constant is selected to minimise the residual distortion.

The principal image point defined by a vertical line from the projection centre on the image side to the image plane is designated as the reference point for image evaluation. In practice, this point is determined through autocollimation of a reflection from the surface of the measuring piece and is consequently usually referred

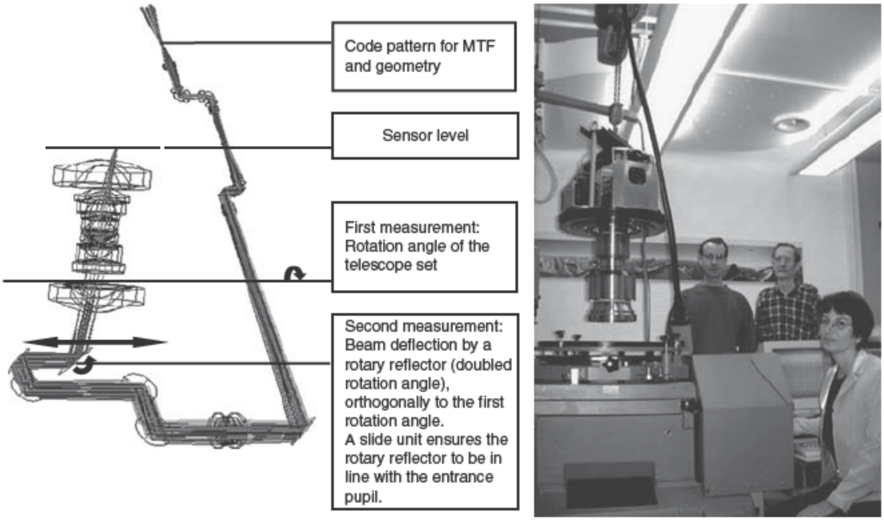

Fig. 5.1-1 Optical path of a vertical goniometer with a folded optical path for projecting code patterns on to the image plane of the camera (the illustration shows the Coded Vertical Goniometer (CVG), developed by Leica Geosystems). The basic device, known as the Electronic Vertical Goniometer (EVG) with a reverse optical path and without a rotary reflector slide unit was developed for calibrating classical aerial film cameras. The photo shows the CVG during insertion of the first prototype of the ADS40

to as the principal point of autocollimation (PPA). The position of the centre of the radially symmetric distortion can be used as another calibration parameter. It is often referred to as the principal point of symmetry (PPS), but it definitely does not have the properties of a principal point of central projection. Even though it is often used in software for photogrammetric workstations, its usefulness for "real" airborne cameras is questionable. Even in older lens designs with perceptible distortion, the adjustment of the system was so precise that the PPS did not deviate significantly from the PPA. In lenses of more recent design, it is virtually impossible to determine the PPS as there is no distortion. Its value is limited primarily to lenses not designed as measuring lenses, for example those supplied in some small- and medium-format digital airborne cameras.

Test field calibration can be used as a supplementary method or as an alternative to laboratory calibration. This is done with the aid of bundle adjustment, where a photogrammetric block of a test field with signalised and precisely surveyed control points is evaluated (Kölbl, 1972). Orientation determinations from the processing of recorded values from a GPS/ IMU system can be used as a primary or supplementary link to a master coordinate system. Apart from exterior camera orientation, which is of no interest in calibration, interior orientation can also be determined through this process. Given sufficient redundancy, extended models can be used for determining not only the principal point, camera constant and radially symmetric distortion, but also other lens and pressure plate defects. Several carefully developed sets of parameter sets are available, but perhaps the best known one is that proposed by D.C. Brown (Brown, 1976), a smaller variant of which is implemented in numerous photogrammetric software products.

The calibration method using parameter estimation in bundle adjustment can also be employed for “self-calibration” during production flight missions and for compensating systematic image deformations.

GPS/ IMU systems, which determine their orientation through combined processing of data from an IMU (internal measurement unit) and from a GPS receiver, can provide substantial support in the processing of aerial photographs. Since the relative positions of the IMU and the camera are known a priori, GPS/IMU results can provide substantial support for the bundle adjustment of a block or replace it altogether if the requirements are not too demanding. The determination of the relative positions of the IMU and the camera, which is often termed “boresighting”, is also done with the aid of bundle adjustment of images acquired in a special arrangement of flight lines.

Digital airborne cameras require a modified form of laboratory calibration. Since the image recorder cannot be simply replaced by a measuring piece, it advisable to calibrate the camera as a system consisting of an optical system and an image recorder. In this case, however, the use of a regular optical path, by projecting a test pattern into the camera by means of a collimator, gives rise to various options with respect to the measuring array, structure and type of the test pattern.

The classical method of measuring image diagonals can be used for area array sensors, but a biaxial measurement is also not only possible but advisable, since a correction field covering the entire area can be introduced without any problems, as the images are evaluated digitally in any case. In the case of line cameras, for which it is impractical to measure image diagonals, since each semi-diagonal intersects each line only once, a biaxial goniometer array is indispensable. Points along each sensor line are measured in this case.

A goniometer array with a moving camera has the advantage of a compact and solid goniometer array in the form of an azimuthal mounting fork like the one commonly used for telescopes or theodolites. The collimator is firmly positioned and can therefore be fitted with additional equipment without any problems. An example is shown in Fig. 5.1-2.

The moving collimator array has the advantage of avoiding deformations caused by the camera’s own weight. In particular, solutions are possible in which the camera can remain in its vertical operating position. The problem here is the protruding two-armed goniometer system, which has to swing the collimator round the lens. If additional devices are to be used on the collimator, the only option is to use the direct collimator optical path through a folded optical path over the axes of the goniometer in a manner similar to that used in the Coudé focus of telescopes.

The “natural” test pattern, a point light source at infinity, is of little use, since it can only be achieved through multiple measurements with small shifts with sub-pixel accuracy. Moreover, locating a line of a line sensor is a lengthy procedure. It is more expedient to use larger test patterns which cover several pixels and make it possible to determine a reference point based on the overall geometry of the test pattern image with sub-pixel accuracy.

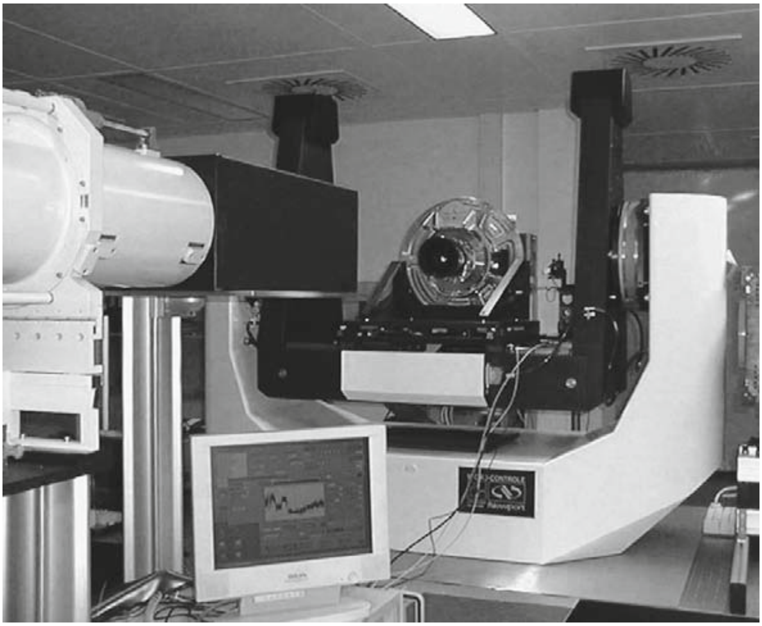

Fig. 5.1-2 Goniometer with moving camera and firmly positioned collimator (DLR, Institut für Optoelektronik, Berlin). The collimator can be seen in the foreground. In the background is the mouting fork, which can be used for complete small satellites, but here it carries only an early prototype of the ADS40 and a small test optical system

The simplest test pattern for area array sensors is a full circle covering several pixels. The centre of its image can be determined by fitting an ellipse with subpixel accuracy. But more elaborate, coded test patterns, which can also provide information about image quality, are also conceivable.

Coded test pattern that also enable the amounts of deviation to be determined along and at right angles to a line are suitable for line sensors (Fig. 5.1-3). The calibration value is obtained by adding the goniometer position and residual amounts of deviation (Fig. 5.1-4).

Multi-frame cameras, an image from which is formed by joining several component images, also have distinctive features. In principle this approach could be used to enlarge the swath width of line cameras, but, despite the fact that it has already been used with the MOMS-02 sensor, its application in commercial airborne cameras is currently limited to cameras with area array sensors. The individual cameras in such a system can be calibrated by the goniometer method without difficulty. A very large and distortion-free collimator would be required, however, to calibrate the entire group of individual cameras. Moreover, such camera groups are prone to minor maladjustment of the individual cameras relative to each other. It is therefore more satisfactory to calibrate only the individual cameras and to link them together for each set of photographed images of the photographed object only after image

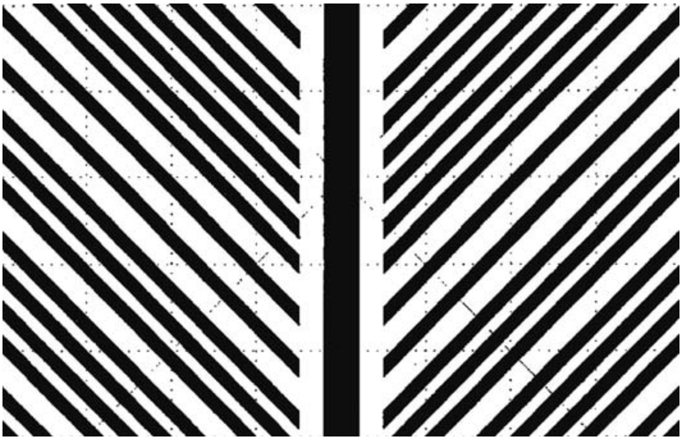

Fig. 5.1-3 Detail of the central area of a herringbone code for simultaneous determination of deviations of a *sensor line* in both coordinate directions. The position along the *sensor line* horizontally intersecting the code image defines the symmetrical code image as the *centre* and the irregular spacing of the code lines at right angles to it makes it possible unambiguously to determine the position. The *broad line* in the *centre* helps to locate the axis of symmetry of the code

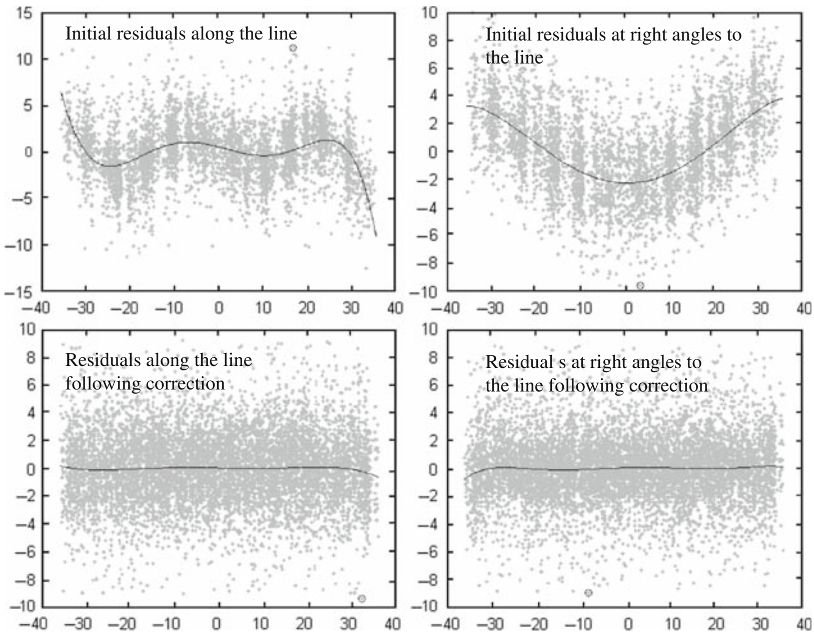

Fig. 5.1-4 Residuals in the image plane along the *line* of a line camera (ADS40) and modelling using polynomials of the 6th degree. Residuals [μm] are plotted according to their positions along the *line* [mm]. The *upper* two images show residuals at an early phase of the compensation process; the *lower* images show residuals after correction. The pixel size is 6.5 μm and the line length, 78 mm

acquisition, by correlating image elements in the overlap areas of the individual images.

The test field calibration method using bundle adjustment plays a much more important role in digital sensors than in classical aerial photography, with respect to both calibration and the certification of camera systems. Apart from calibrating component systems, aligning IMU systems or multi-frame arrays, etc., it is also used for composite systems. For line sensors in particular, it has been found that, owing to the relatively involved and trouble-prone laboratory calibration method with a biaxial goniometer, better results can be obtained with test field calibration than in the laboratory.

Sets of parameters for self-calibration, which have already been used for aerial film cameras, can be employed for digital cameras with area array sensors. In principle, they can also be employed for line cameras, but they do not fully describe a line camera with close-to-sensor optical components. It is advisable to model the residual distortions line by line.

5.2 Determination of Image Quality

The classical measure for determining image quality is the limit of the photographic resolution of the lens. Test patterns photographed under defined conditions of brightness and contrast are used for this purpose (Fig. 5.2-1). Hence, the finest resolved pattern provides the local resolution limit of the lens. AWAR (area weighted average resolution) is used to obtain a holistic description of the lens.

This measure is hardly suitable for calibrating a digital camera system, since spatial discretisation by the sensor cells exerts a strong influence on the limit of resolution and can lead to aliasing effects if the design of the optical system is not appropriate. This was discussed in Section 2.5. It is therefore advisable in the case of digital sensors to define the MTF in greater detail than solely by determining the limit of resolution.

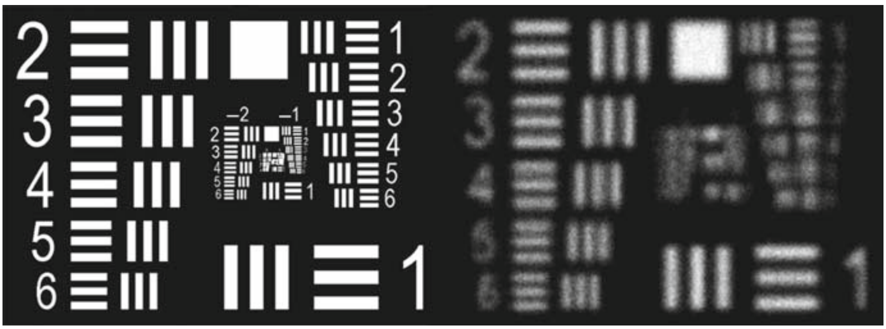

Fig. 5.2-1 A “NASA 1951” target, which is frequently used to determine the limits of resolution of lenses. The target is seen on the *left* in the photo and a simulated image on film, on the *right*

It should be stressed once again here that the objective of an optical system for digital sensors must be to limit its resolution in such a way that no aliasing occurs at the Nyquist frequency or beyond, rather than to achieve the maximum possible resolution.

Either a sequence of regular bar patterns of varying density or an irregular pattern that contains all spatial frequencies of interest can be used for determination of the MTF for area array sensors and line sensors along the line. It is more challenging to determine the MTF of a line sensor at right angles to the line (Fig. 5.2-2). Apart from the dynamic solution of scanning a test pattern, the static solution, in which a line slightly inclined vis-à-vis the sensor line is scanned, can be used.

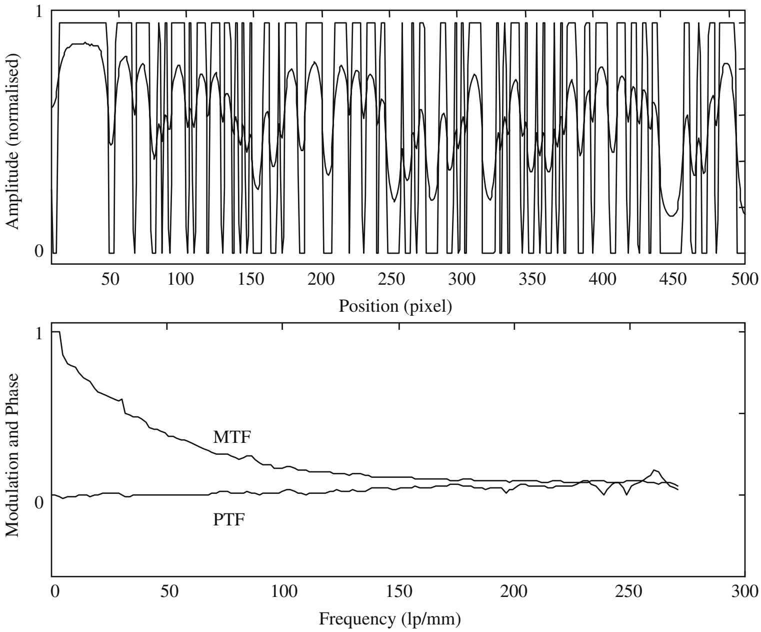

Fig. 5.2-2 MTF test pattern and the result of an evaluation. A low-resolution lens is used in this example to illustrate how the MTF can be determined from the image of a bar pattern. The *top* image shows the amplitude of a random bar pattern (*rectangular curve*) along with that of the image; the *bottom* one, the MTF and the PTF (phase transfer function). A code pattern with considerably more elements has to be used for high-resolution airborne cameras to be able to resolve the higher frequency ranges

5.3 Radiometric Calibration

The principal parameter of radiometric calibration is the spectral responsivity of the camera. Since this is a very stable parameter in digital cameras, it pays to invest much more in it than in the case of film-based cameras.

The individual cells of CCD and CMOS sensors show minor variations with respect to both the DS (dark signal) and the light responsivity PR (photo response).

Variations of these parameters are termed DSNU (dark signal non-uniformity) and PRNU (photo response non-uniformity). Moreover, the dark signal, which emanates from the sensor itself and from the unidirectional noise of the readout electronic system, is highly temperature-dependent and increases in proportion to the integration time of the sensor.

The compensation of DSNU and of the components of the global DS dependent on temperature and integration time takes place, when the highest level of quality is required, by subtracting a dark frame (a dark image with the same integration time), which is photographed almost simultaneously with the original image. Since this is impractical owing to an airborne camera's rapid image sequence, a one-off calibration of the DSNU and DS is carried out. In determining and compensating the current DS, it is expedient to integrate a number of "dark" (covered) cells in the sensor and to use these cells' signal level for determining the global correction variable.

Whilst global DS correction in real time can take place in the analogue section of the imaging process, i.e., before digitising the CCD signal, it is advisable to carry out DSNU and PRNU corrections only after the data has been digitised. The corrections can be made in real time while photographing or when accessing the image data. Preference should be given to real-time correction, since corrected images can be compressed without difficulty, whereas the distortion signatures in uncorrected images result in diminished compression or in an increased number of compression artefacts.

The relatively small number of CCD cells in line cameras makes for convenient storage of correction values in the camera system and hence for convenient real-time corrections (Fig. 5.3-1), followed by data compression, which is currently barely practicable in the case of large array cameras. Fast memories for real-time correction with at least 3 bytes per pixel (1 byte for DSNU and 2 bytes for PRNU) are impractical to implement for sensor sizes in the two-digit megapixel range.

Irrespective of whether the images are corrected in real time or subsequently on the ground, the camera system's DSNU and PRNU remain as variables to be calibrated. If global DS compensation is in place, the determination of the DSNU correction for a camera system is limited to a one-off determination of this dark signal, i.e., by imaging with a covered lens. To diminish noise, it is advisable to average several measurements. Taking a series of measurements at varying temperatures and integration times is advisable if the hardware is not provided with DS compensation.

It is advisable to determine the PRNU correction as a system correction, which compensates not only the image recorder's actual PRNU, but also the influences of the analogue part of the electronic system and in particular of the optical system. The principal part of the system PRNU of a wide-angle camera results from the light decrease of the lens, which varies as $\cos^4$ of the angle of incidence in the case of a thin lens, but today's lenses have a substantially flatter variation.

The system PRNU can be determined simultaneously for all spectral channels and the entire image area or line array. For this purpose there must be a calibrated, homogeneous and isotropic light source that illuminates the entire lens or

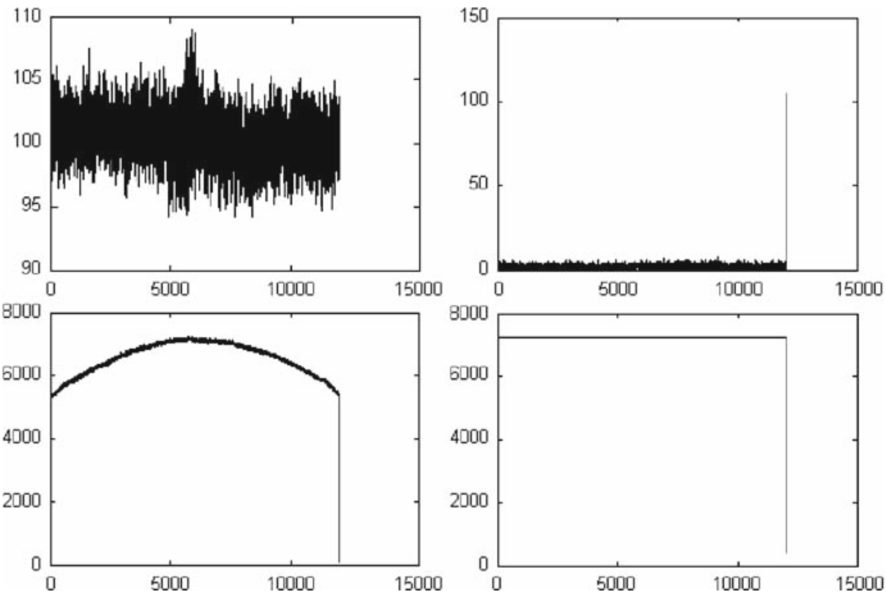

Fig. 5.3-1 DSNU and PRNU correction for one line of ADS40. 12,000 pixels are plotted along the *horizontal axis*, signal intensity in *grey* scale values is represented along the *vertical axis*. The *top left* graphic shows the dark signal of the *line*, which is regulated to a base value of 100 via dark pixels; the *top right* represents the residual noise after DS and DSNU correction, i.e., after subtracting the calibration values. The *bottom left* graphic shows the signal with the effects of PRNU and edge intensity drop of the Ulbricht sphere's optical system; the *bottom right* shows the final corrected signal obtained through inverse scaling using the calibration values

the lens array over the full aperture angle. The only feasible solution for large aperture angles is an Ulbrich sphere. This is a hollow sphere, which in the ideal case has a perfect isotropic and loss-free reflecting inner surface. Light is admitted into the sphere through a small opening and homogenised through multiple reflections from the inner surface. A second small opening in the sphere then acts as a perfect homogeneous and isotropic light source. In practice, however, spheres of this type have several shortcomings with regard to the coating, which is not isotropic, nor is its reflection loss-free. The size of the outlet opening has to be considerable to accommodate an aerial photography lens, let alone a lens assembly. Both inadequate reflectivity of the coating and the large outlet opening reduce the total brightness of the light source. All three influences affect the quality of the light source. Hardly any improvement can be achieved with coatings other than the usual coating with barium sulphate (reflectivity 94−98% in the visible and the near infrared spectral range), but the influence of the outlet opening can be reduced by increasing the size of the sphere. Since the size of the sphere is subject to practical limits, additional measures to improve the homogeneity are advisable. They include, in particular, distributing the light entering the sphere by arranging for it to come from several

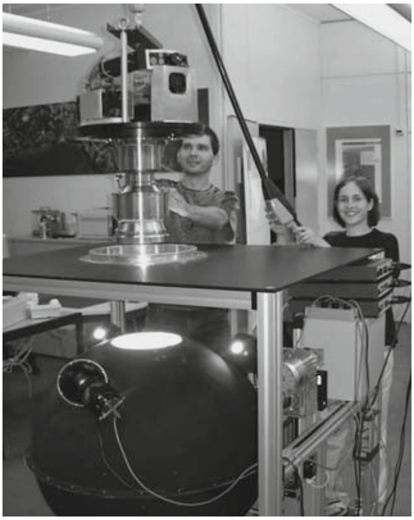

Fig. 5.3-2 Ulbricht sphere with three “satellite spheres”; hemisphere diameters: 90 cm and 15 cm, respectively; outlet opening: 25 cm; illumination: 3 × 150 W low-voltage halogen lamps (Leica Geosystems)

light sources and pre-homogenising the light, for example by means of “ satellite spheres” (Fig. 5.3-2).

Spectral calibration is carried out with the aid of a calibrated, tunable light source. Usually such a light source is provided in the form of a monochromator, i.e., it contains a broad-band light source (incandescent lamp) and a grid or prism spectrograph, with the aid of which a narrow spectral band is extracted. Such devices are quite expensive, but a wide range is commercially available for a variety of laboratory applications. Unfortunately, the total intensities that are available are hardly sufficient for direct calibration of an airborne camera with the aid of an Ulbricht sphere. Since the pixel-wise responsivity differences of camera channels are already known, however, it suffices spectrally to measure only small image areas in each case and interpolate between them. Using an adapted optical system construction, it is possible to achieve negligibly small spectral differences over the entire image area.

Moreover, the polarisation in the camera’s optical system is of interest for remote sensing applications, because it, along with the polarisation of light reflected from the ground, leads to disruptions in intensity. Since there is spectral variation of polarisation at thinly coated surfaces of the optical system, it is expedient to combine its acquisition with spectral measurement.

Another factor determining image quality is stray light reaching the sensor. Two types of this kind of light occur in every optical system. The first of these is double images caused by double or multiple reflections between optical surfaces in an optical path (surfaces of lenses, filters, cover glasses and perhaps beam splitter systems), and the second, stray light that is formed on mounts and other surfaces outside the actual optical path. These two stray light components are captured only in part when determining the MTF, because parts of the stray light can come from remote sources.

By splitting the system, especially the lens system, the parts can be measured individually using conventional methods. But the best instrument for determining stray light is the digital camera system itself. Owing to the direct availability of the images, the entire angular range of the incident light can be scanned in a relatively short time with the aid of a collimated light source. False images can be readily identified through image analysis.

Chapter 6
Data Processing and Archiving

At first glance, high-resolution airborne cameras produce frighteningly large quantities of data. On a good flight day, it is entirely possible to collect several hundred gigabytes of raw data. This is largely irrespective of the technology used. For sets of stereo images that can be triangulated, a line camera records each ground pixel three times. Using an array camera and the typical minimum forward overlap of 60%, a 2.5-fold amount of data compared to a sequence of non-overlapping images is produced; and in the case of larger forward overlaps to obtain smaller stereo angles, even greater quantities of data are created.

Although the amount of data does not differ from that of film aerial photographs scanned with the same ground pixel size, quality control and data archiving is more problematic in the case of digital cameras, because the images cannot simply be viewed on an illuminated table or archived directly like a film. In cameras that do not produce DSNU/PRNU-corrected and compressed data, such as all of today's large-format array cameras, it is advisable to carry out the correction and compression before archiving. High-capacity magnetic tape cassettes and hard disks can be used for data storage. The latter provide faster data access and are only slightly more expensive. For the sake of data security, data should be archived in duplicate, and data on data carriers approaching their storage time limit should be copied on to other carriers.

Video systems installed alongside the camera, which provide a direct view of the current cloud and shadow situation, can be used for immediate in-flight quality control. In addition, it is advisable to have a "quick-look" branch off the raw data stream, i.e., a sample thumbnail, for immediate display.

At the time of writing, the processing of image data can start only when the surveying flight mission is completed. With improving computer performance, however, it will be possible to carry out part of the processing in real time during the flight, perhaps even to produce orthorectified images, but it will be possible to achieve image products of the highest geometric and radiometric quality only when the entire block of imagery from the flight mission(s) is available and has been subjected to adjustment processes as a whole.

There is a slight difference in the processing workflow between line and array cameras, especially with respect to the initial processing steps. There is also a major

R. Sandau (ed.), *Digital Airborne Camera*, DOI 10.1007/978-1-4020-8878-0_6,

difference in the “sensor model”, the mathematical representation of the sensor, the basic functionality of which consists of transforming the coordinates between the image and the three-dimensional model or ground system. Although the classical sensor model of the aerial film camera can be used in the case of array cameras, including images composed from multi-frame systems, an expanded version is required for line cameras, because here a raw image strip consists of a sequence of single-line individual images with a common interior orientation, but with a varying exterior orientation.

The principle of the workflow used in processing imagery from today’s high-resolution airborne cameras is illustrated in Figs. 6-1, 6-2, 6-3 and 6-4. Combinations of the steps shown and modified sequences can be used too. The first phase, which includes the processing necessary to go from the images captured in the camera’s mass memory on board the aircraft to the raw data that enters the photogrammetric process, consists of three steps (Fig. 6-1):

1. The process begins with downloading data from the camera’s disk memory and setting up a project structure.
2. This step is imperative for line cameras and optional for array cameras: determination of a preliminary exterior orientation with GPS/IMU data from the aircraft and data from a GPS base station. If the project requirements are less stringent, this also provides the final exterior orientation.
3. For cameras without real-time corrections during imaging (such as today’s high-resolution area array cameras), it is necessary to perform DSNU and

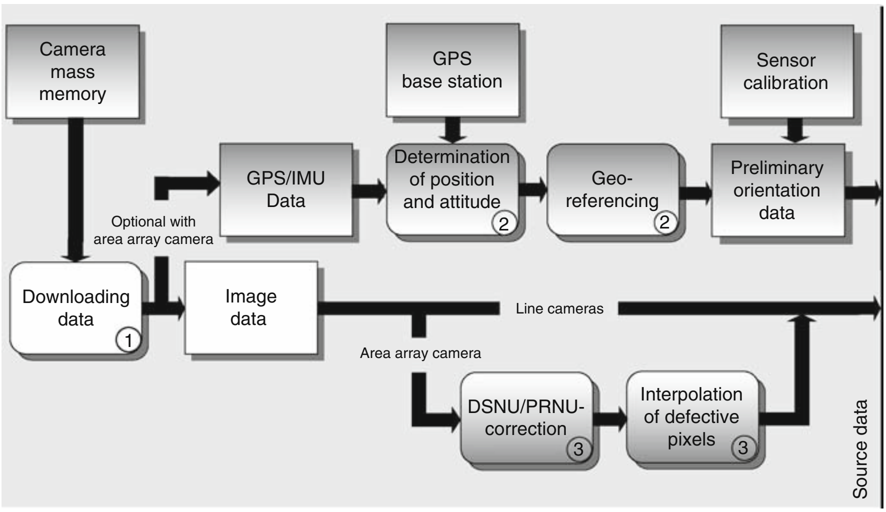

Fig. 6-1 Processing chain for digital airborne cameras: the first phase, from downloading the images captured in the camera’s mass memory on board the aircraft to the raw data the enters the photogrammetric process (described in Steps 1–3 in the text)

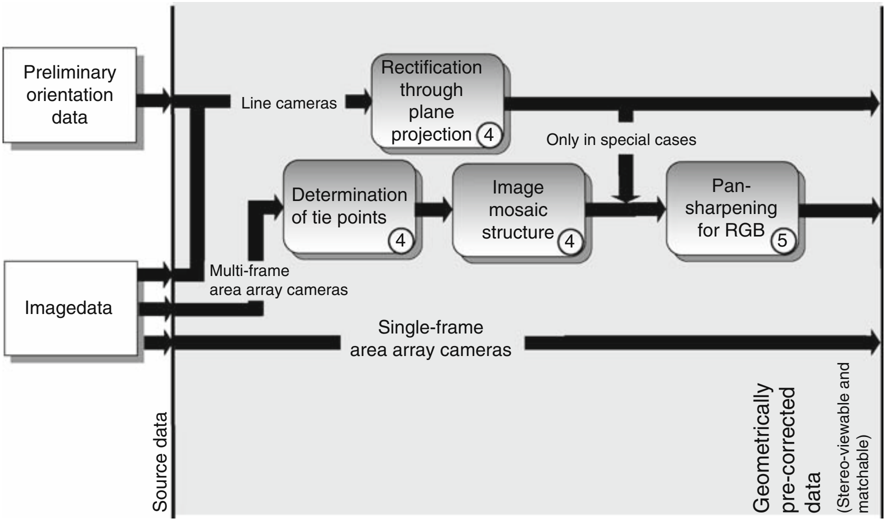

Fig. 6-2 Processing chain for digital airborne cameras: the second phase, geometric pre-processing of the raw data (described in Steps 4 and 5 in the text)

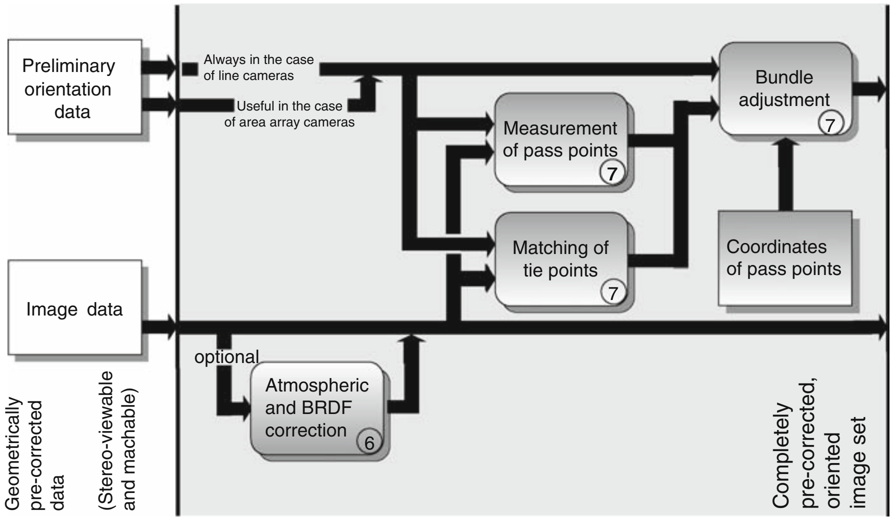

Fig. 6-3 Processing chain for digital airborne cameras: the third phase, final image pre-processing and triangulation to obtain final orientation data and coordinates of pass points for use in further photogrammetric operations (described in Steps 6 and 7 in the text)

PRNU correction of image data. For array cameras only, there is usually some interpolation of defective pixels.

4. The second phase includes geometric pre-processing of the raw data (Fig. 6-2). This involves two further steps:

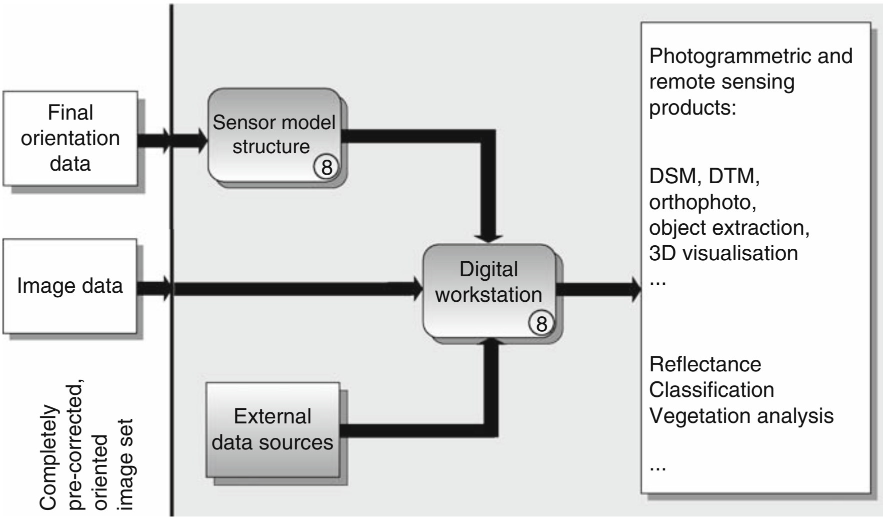

Fig. 6-4 Processing chain for digital airborne cameras: the fourth and final phase involves photogrammetric processing of the refined image data and the results of triangulation to produce the deliverables from the project (described in Step 8 in the text)

(a) In line cameras, images are corrected by projecting them on to a plane. For multi-frame cameras, it is necessary to create the composite image as a mosaic of the component images by locating homologous points in the overlap zones and correcting the images accordingly.
(b) If the camera generates colour images at reduced resolution compared to the panchromatic, a pan-sharpening process is performed on the colour images.

5. The third phase may involve some final image pre-processing but its main purpose is triangulation in order to obtain final orientation data and coordinates of pass points for use in further photogrammetric operations (Fig. 6-3). There are two steps:

(a) Optional for all camera types: Radiometric correction of images with respect to atmospheric and BRDF influences.
(b) Triangulation of a set of images comprising automatic determination and measurement of tie points and bundle adjustment. The result is precise exterior orientation of the projection centres of all images involved, optionally supplemented with interior orientation variables (self-calibration). Special characteristic for line cameras: since an estimation of the projection centres of all individual lines would be underdetermined, orientation is performed using selected flight path points, the spacing of which is selected such that an interpolation with the aid of the GPS/IMU result can be carried out between them.

6. The fourth and final phase involves photogrammetric processing of the refined image data and the results of triangulation to produce the deliverables from the project (Fig. 6-4):
7. Further processing steps up to the final product are similar to those used for scanned film aerial photographs, provided that the post-processing software provides a suitable sensor model.

The vertical bars at the ends of the component images are often also referred to as processing levels or data levels (for example, data product level 0, 1, . . .). There is no standard definitions of such data products, however. The data products of such interfaces can often be imported to other processing platforms for further processing.

With the greater dynamic range of digital imaging systems, which manifestly exceeds the 8 bits that can be acquired with film, it is advisable to design the entire processing chain for a greater bit depth. For reasons of processing speed, only 16-bit depth per image channel is appropriate for today's computer systems.

The situation is different with regard to end products. For reproduction in printed form or on screen, 8 bits per pixel per channel are usually sufficient and often specified. Here, the data volume can be further reduced by using common compression methods, especially JPEG. Compression ratios of 3:1 can be achieved without perceptible loss of image quality or changes in geometry (Tempelmann et al., 1995), and even substantially higher ratios are possible with colour images.

Chapter 7
Examples of Large-Scale Digital Airborne Cameras

In the preceding chapters, we have investigated and explained all known theories and technologies which need to be well understood in order to develop and produce digital cameras, and to market and maintain them on a worldwide scale. The reasons for the transition from analogue to digital airborne cameras are explained in Chapter 1, especially such aspects as

- areas of application in photogrammetry and remote sensing,
- complementarity of airborne and spaceborne sensor systems,
- matrix and line sensor concepts.

All the information given in Chapter 1 and the succeeding chapters leaves open the question of which basic concept (matrix or line sensor) and which implementation variant are to be used. This decision is to be according to the main application areas addressed and the available technologies. This chapter gives selected examples of different implementations. As explained in Section 1.5, this book focuses its attention on large format cameras. The three examples selected – ADS40/ADS80, DMC and UltraCam – are representative of the variations available on the market today. These cameras may be briefly as follows:

- The ADS40/ADS80 is a multiple-line sensor, which generates continuous image strips for all channels (pixel carpet type).
- The DMC generates high-resolution panchromatic images from four images with slightly divergent optical axes (butterfly type).
- In the UltraCam, the high resolution image is composed in patchwork manner from nine matrices acquired by four cameras (patchwork type)

All three cameras are being successfully marketed worldwide.

7.1 The ADS40 System: A Multiple-Line Sensor for Photogrammetry and Remote Sensing

7.1.1 Introduction

The realization of the project ADS40, which is considered the 1st generation, spanned a time period of 20 years the phases of which can be summarized in the following manner:

R. Sandau (ed.), *Digital Airborne Camera*, DOI 10.1007/978-1-4020-8878-0_7,

- Formulating a vision
- Pre-projects and feasibility studies
- Meetings with inventors, developers, scientists and component providers
- Observing and assessing the market
- Initiating the innovation process
- Formulating the business plan and the product requirements

The development of components and prototypes took place in the period from 1997 till 2001. The digital airborne sensor ADS40 was presented to the world mapping community on the occasion of the XIX ISPRS Congress in Amsterdam in July 2001. This sensor was developed jointly between DLR (German Aerospace Center) in Berlin and Leica Geosystems (previously LH Systems) in Switzerland. The airborne digital sensor ADS40 is part of the first commercially available digital large format airborne survey system. The optical performance characteristics based on a resolution of over 130 lp/mm and a FoV (Field of view) of 64° result in excellent area coverage performance similar to that of the known aerial film cameras, which produce aerial photographs in the format 23 × 23 cm (9″ × 9″). This ADS40 Airborne Digital Sensor System is an innovation in the world of photogrammetry, because it also fulfills the multispectral requirements in the field of remote sensing. The narrow bands of the filters, the linear sensitivity curve of the CCD lines and their absolute spectroradiometric calibration made the transition possible from a photographic sensor to a complete image measuring device. The data generated by the CCD lines is radiometrically corrected in real-time before it is stored on the mass memory. The line-perspective imagery with uniform illumination in flight direction allows for automatic reduction of disturbing illumination and reflectance effects. The tuning of geometric and radiometric resolution opens new possibilities in the field of research and development. Through the integration of a GNSS sensor and an inertial measuring unit (IMU) into the system exact geo-referencing and co-registration of individual multi-spectral bands is possible for the first time.

7.1.1.1 2nd Generation ADS40

In 2007 two additional sensor heads the SH51 and SH52 were added to the ADS40 System. An innovative, patented beamsplitter called Tetrachroid with dichroitic filters allows the co-registered data acquisition of high resolution imagery across all bands at equal GSD. The ADS40 is the only large format airborne digital camera that can make this claim. This eliminates the need for often time consuming processing steps such as pan-sharpening and the creation of virtual images, which are an integral part of multispectral image generation with large format digital array cameras. Digital imagery generated with the ADS second or third generation does therefore no longer show color fringes along edges.

7.1.1.2 3rd Generation ADS80

Technical improvements already introduced, tried and tested with the 2nd generation Sensor Head are maintained in the third generation. The thermal and pressure stabilized lens, the focal plate and the IMU, which with the help of a specially designed table has been brought into the optical axis of the sensor, are tightly integrated into a quasi-monolithic block that guarantees highest (geometric) stability. This extremely stable design allows support and exchange of various IMU types and the application of a simplified sensor model with significantly less local distortion parameters. Survey flights undertaken at two different altitudes and following a simple pattern can be used for system calibration through bundle block adjustment. Independent research by Passini and Jacobsen (2008) reveals that the geometrical accuracy and the use of pushbroom data in photogrammetry is at par if not better than that of digital frame cameras.

7.1.1.3 Advantages Which Speak for the Line Sensor Technology

The experience with line sensors in satellites which are circling the Earth and Mars has proven that data quantities can be kept to an optimal level whilst providing best stereo observation quality. Equally line sensor technology has proven that it is possible to produce sensors, which can capture multiple spectral ranges with high geometric and radiometric resolution. Furthermore the simple, exact geometry of a line sensor combined with the exact spatial trajectory and absolute orientation thereof given by the GNSS/IMU system provides distortion-free image strips. Geometric distortion caused by patching together surface array images from various cameras into one large virtual image is avoided.

Other advantages of line sensor cameras are:

- Same resolution at the instant of image capture in all bands
- Complete spectral separation in all bands
- Parallel line perspective images with superior color continuity in large mosaics
- Line sensors have no defective pixels
- The Base/Height ratio is superior to that of rectangular digital frame cameras
- No shutters are required, which in multi lens systems need accurate synchronization and can fail
- One high-quality, temperature and pressure controlled lens with a single focal plate maintains calibration permanently

7.1.1.4 Economic Aspects and Competitive Systems

Contrary to satellite-borne cameras the return on investment of airborne cameras for earth observation depends largely on flight management and flight economy because they are not financed by government organizations nor do survey companies have free access to the required airspace. For these reasons a large effort was also necessary to develop a reliable flight management and camera control system as well a flight planning and flight evaluation system. To compete favorably against the existing film based aerial cameras development priority was also given to the following:

- Area coverage performance equal to the film-based aerial cameras
- Savings in flight cost by capturing all spectral bands simultaneously with better radiometric resolution than film or surface array cameras
- Stereo viewable image strips with a choice of various stereo angles from the same flight
- Providing simultaneously new applications in airborne remote sensing
- Faster data processing based on the simple line sensor geometry

7.1.1.5 The Path to the Ideal Lens System for Airborne Digital Cameras

Choosing the line sensor concept for the CCD sensors provided many advantages:

- All CCD sensors can be placed on a single focal plate and all spectral bands can be captured through only one high quality lens system
- Line sensors can be used which provide a 2–3x wider swath than surface arrays
- Economical, defective-free CCD sensors could be used
- In flight direction all bands produce 100% overlapping image strips
- Image strips are homogeneously illuminated due to constant line viewing angles
- Better image quality because the extreme edges of the field of view of the optics are not used
- It is possible to use staggered CCD lines to increase the image resolution and decrease aliasing

For the optical designers the decision to use line sensors represented a major opportunity, to fulfill different further user demands. The narrow bands in the spectral range useful for the applications of remote sensing and the demand for a continuous spectral response (central wavelength and range) across the entire length of the CCD line led to the demand for a telecentric lens on the imaging side of the optics (see Fig. 7.1-1).

For photogrammetric applications the focal length and the place of registration of each pixel must remain stable on the focal plane, also under strongly changing

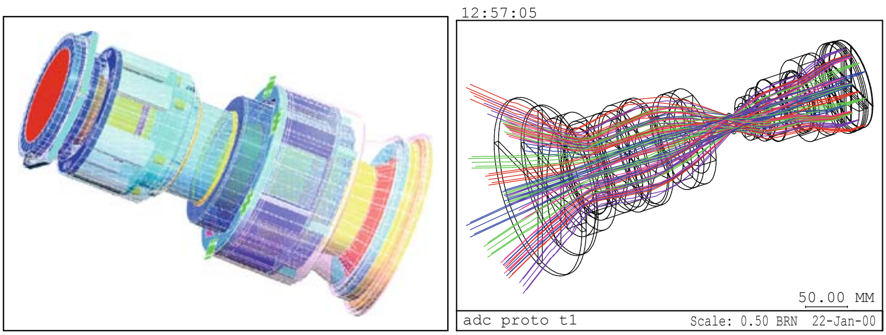

Fig. 7.1-1 Telecentric optics DO64 with passive temperature compensation

conditions of temperature and pressure during the flight. The ADS40 optics are stabilized by means of a unique mechanical compensation system that adjusts for variations in temperature.

The operating range for optics and electronics are shown in Fig. 7.1-2.

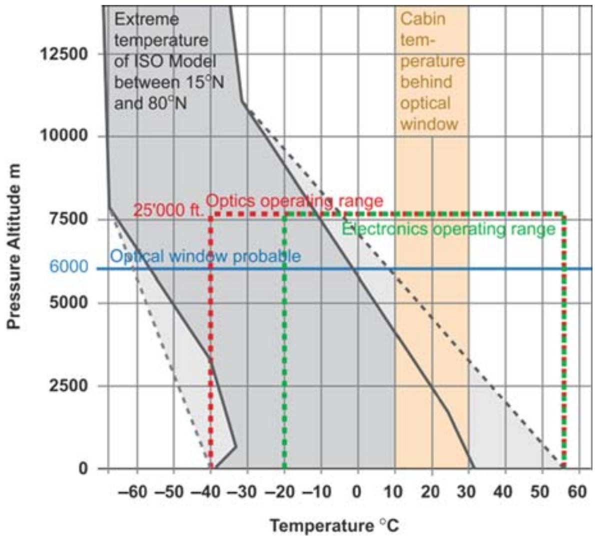

Fig. 7.1-2 Operating range for optics and electronics in the range of the atmosphere accessible to aircraft

7.1.1.6 The Definition of the Filters

The ADS40 and ADS80 have special, narrow-band filters for the spectral regions red, green, blue and near infrared (see Fig. 7.1-3). Thus the ADS40 sensor is a useful tool for remote sensing beyond traditional applications for photogrammetry. All methods and possibilities of image analysis, e.g. for automatic interpretation and classification of image content, can be applied to the ADS40 and ADS80 images.

The narrowness of the spectral bands and the steep flanks of the filters are ensured with interference filters. A special algorithm, developed by the University of Illmenau, Germany permits a conversion of the RGB and Pan images into a true color image.

A complete novelty compared to all line sensor cameras developed in former times is the development of special beam splitters the so-called Trichroids in the first generation of the ADS40 and the Tetrachroids in the 2nd generation ADS40 and 3rd generation ADS80. The location in the spectrum is realized by means of dichroitic filters. These differ from the classical beam splitters, which divide the entire irradiated energy onto several detectors. Instead dichroitic filters provide a spectral separation and allocation. The entire energy contained in the spectral channels is led with little loss at the reflection surfaces to the detectors. The Trichoid produces

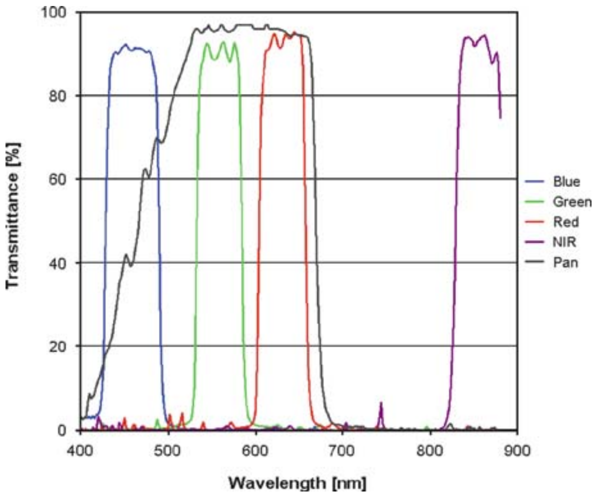

Fig. 7.1-3 Definition of the narrow band filters of the ADS40 and ADS80 Sensor

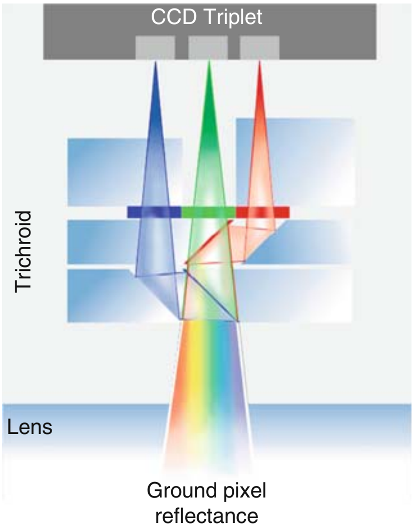

Fig. 7.1-4 Cross-section through the Trichroid energy beam splitter (1st Generation ADS40)

co-registered RGB multispectral channels (see Fig. 7.1-4) and the Tetrachroid even co-registered RGBN channels (see Fig. 7.1-5).

7.1.1.7 The Choices for the Focal Plate Module

As a CCD provider the company ATMEL (previously known as Thomson) was chosen, a company that also provides very similar CCD lines for the SPOT 5 satellites

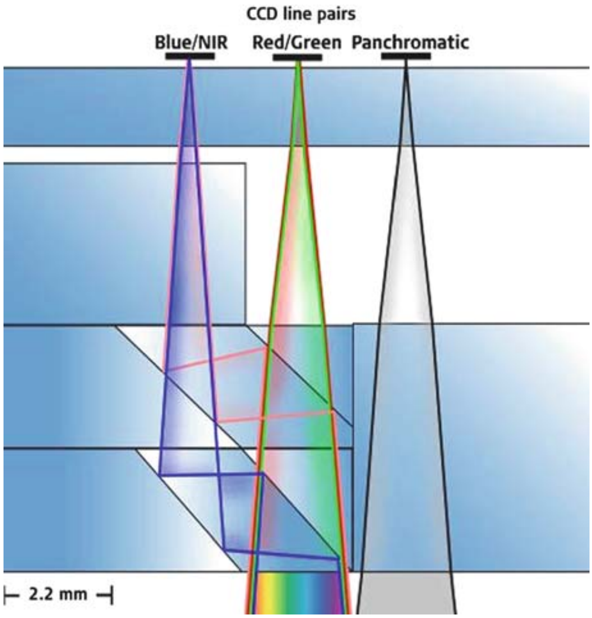

Fig. 7.1-5 Cross-section through the Tetrachroid energy beam splitter (2nd generation ADS40 and 3rd generation ADS80)

of CNES. The fact that ATMEL was capable of providing a triple CCD with staggered dual lines was a special challenge. This choice was made consciously with the intention to use similar algorithms as used in the SPOT 5 satellite to increase the image resolution by means of staggered lines. It will be possible to fully exploit this capability once better stabilized platforms become available.

In the case of the first generation sensor head it was possible to image the 3 color channels at the same viewing angle. This made it possible to design different focal plates of which the two of the four most demanded are pictured in Figs. 7.1-6 and 7.1-7, respectively.

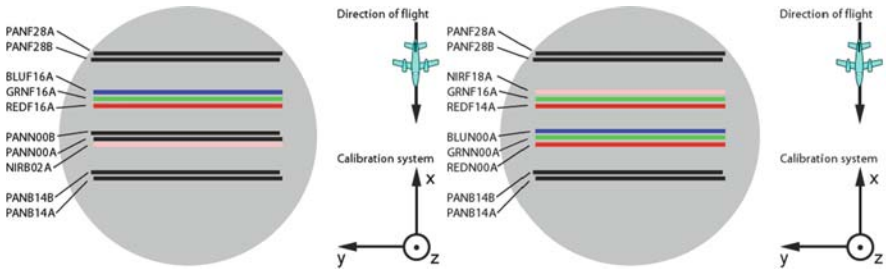

Fig. 7.1-6 The two most demanded types of first generation focal plates (location of lines on the focal plate is not to scale)

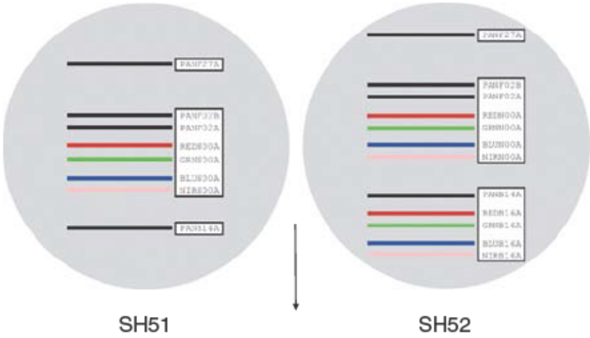

Fig. 7.1-7 The two focal plate types available in the 2nd generation ADS40 and in the SH81 and SH82 3rd generation ADS80 sensor heads (location of lines on the focal plate is not to scale)

Fig. 7.1-8 The first generation sensor head SH40 of the ADS40 System

By describing the focal plates of the sensor head the essential inner parts are given. For the exterior design (see Figs. 7.1-8 and 7.1-9) the following criteria had highest priority:

- Handling
- Safety
- Design (form and colors)

7.1.2 The Digital Control Unit

The request for a single, compact control unit, which contains all necessary elements such as power supply, digital computer with operating system, sensor

Fig. 7.1-9 The 2nd generation sensor head SH51 and/or SH52 of the ADS40 System and 3rd generation sensor head SH81 and/or SH82 of the ADS80 System

specific modules, GNSS receiver, inertial position and attitude processing unit and mass memory, has been fulfilled by the design of the Control Unit CU40 (see Fig. 7.1-10). This self developed unit fulfils many other requirements which are of large importance to the user.

This includes the following characteristics:

- Low weight,
- Low power consumption
- Small volume
- Few cables
- Robust in handling and reliable in use
- Fulfills the standards of electromagnetic susceptibility in the aircraft
- Remote control of all functions

To fulfill the requirement of geo-referenced image strips the Inertial Position and Attitude System with integrated GNSS receiver and IMU control system was integrated in the CU40. With this the operator is relieved of the handling of these two complex systems. By means of a single switch all modules are powered up. A system test checks every module for availability and functionality. The entire start-up process is overseen by an environmental controller, which reports to the user if any module is outside the required operating temperature range or cannot start-up

Fig. 7.1-10 The digital Control Unit CU40

for any other reason. Error warning show the operator if the start-up process was interrupted.

For decades airborne hyper spectral scanners were equipped with expensive, unreliable, large and heavy tape recording units. The high cost, weight and volume of the tape units of the 70's and 80's were no longer accepted for airborne use. In the middle of the 90's the breakthrough to small, light and power saving hard disks with more than 150 GB storage capacity reached the market. This eliminated one of the main obstacles to design a cost-effective airborne digital sensor. Also a 400 Mbit/s data channel including galvanic separation between emitter and receiver was available by applying glass fiber cable technology. Only a thin, light and very robust glass fiber cable connects the CU40 control unit with the sensor head. The connection of the mass memory MM40 (see Fig. 7.1-11) is established through reliable and robust multi-pin connector at one end of a slide system on top of the control unit CU40. Technological progress has made it possible to develop modern mass memory solutions with the following characteristics:

- Portable mass memories
- Exchangeable during flight
- Memory space for at least 4 h of uninterrupted data acquisition
- Reliable performance up to a flying height of 25,000 ft (7,600 m) without pressurized cabin.
- Resistant to vibrations and abrupt pressure and temperature changes

Large capacity flash disk technology has evolved into a viable alternative to hard disks.

Fig. 7.1-11 The 0.9 Terabyte Mass Memory MM40 of the ADS40

Fig. 7.1-12 Flash Disk MM80 (192 or 384 GB) of the ADS80

The advantages of flash disk technology are:

- reduction of volume and weight (one MM80 weighs 2.5 kg, see Fig. 7.1-12)
- no moving parts
- insensitive to pressure changes
- totally erasable

7.1.2.1 Control Unit CU80 and Mass Memory MM80 for the 3rd generation ADS80

Compared to earlier generations of the ADS, external and internal interfaces were reduced to achieve not only simpler integration, but also higher stability. The power supply to the CU and SH is controlled via a single, central switch. During data recording in-flight, the incoming data is moved away from the sensor head via the PCIe interface, the Standard Bus System and CPU RAM to the Mass Memory MM80. This includes image data, information related to the focal plate, additional statistical data from the sensor head, spatial and orientation data from the IPAS20 Position and Attitude System embedded in the CU80, performance data from the PAV30/80 stabilized mount and flight and system data generated by FCMS, which supervises and controls the survey flight. In the new Leica ADS80 FCMS is taking on a much more central role not only in integrating the individual components such as controlling the power supply to the MM80, flight parameters and sensor configuration. In addition, FCMS is now taking on the control over the image data, which are transferred via the Host Bus Adapter to the new MM80 with flash disk technology. The memory of the CPU RAM is used as a buffer to balance out delays when writing data onto the MM80. Latest PCIe technology supports the correction and intelligent management of errors, which contributes significantly to guarantee reliable data recording, management and storage.

The ability of the Leica ADS80 (see Fig. 7.1-13) to achieve ground resolution better than 5 cm at higher flying speeds requires as higher data throughput as well as a higher bandwidth for data storage. This is achieved by using several Flash Disks in one MM80 unit. Currently, the user can choose between MM80 units with 192 or 384 GB data storage capacity. The new CU80 offers space for two adjacent MM80 units, which can be configured either as joint volumes or as master and backup units. In addition, a single MM80 can also be used. The MM80 can be exchanged during flight, thereby offering unlimited data storage. In order to configure and optimize data storage performance and data redundancy, a RAID can be generated for data recording. Data is stored by lines with direct access and not by acquisition time, which allows the generation of continuous image strips much faster than before. Compared to earlier hard disk technology the use of flash disks leads not only to more reliability and performance, but also a weight reduction of some 25 kg at similar data storage capacity.

7.1.3 Sensor Management

The main characteristics of the user interface of the ADS40/ADS80 Airborne Digital Sensor are:

- Easy to use
- Central control interface for all functions of the sensor

Because the Inertial Position and Attitude System IPAS, which delivers information concerning navigation, drift and location has been totally integrated into the ADS40/80 the navigation sight used in aerial film cameras could be eliminated. In its place the Operator Interface (see Fig. 7.1-14) allows the user to control the system. It allows a comfortable in-flight operation without mouse and keyboard.

The touch sensitive LCD screen of high luminosity enables the realization of above mentioned requirements. A special Flight Control and Management Software

Fig. 7.1-13 Complete ADS80 System. From *left to right*: OI80 Operator Interface, CU80 Control Unit, SH81 Sensor Head, PAV80 Camera Mount

Fig. 7.1-14 The Operator Interface OI40/OI80

FCMS was developed, which allows the user intuitive access to all functions with little use of language elements. Clear pictograms guide the users which are located in many countries around the world. The FCMS software allows a complete configuration and control of the entire system.

An integrated video camera shows the area which is being over flown and allows an independent check if the planned flight line is being flown. This visual check also allows a simple quality control regarding the presence of clouds on the flight line.

7.1.4 The Flight Planning and Navigation Software

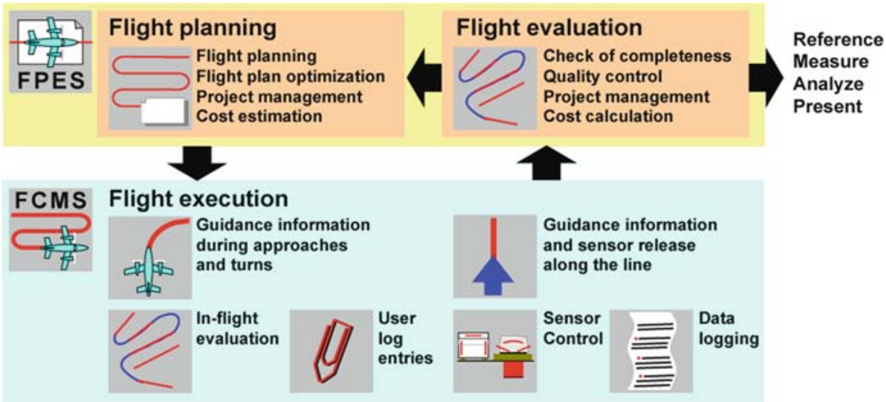

Fig. 7.1-15 Integrated workflow from flight planning to flight execution

The FCMS Flight & Sensor Control and Management System also include Flight Guidance and the Pilot and Operator Controller OC50 for FCMS, which is used for all Leica Sensors including Airborne Laser Scanners. The flight plan established with FPES can be introduced directly into the FCMS of the sensor and the survey flight will be executed directly from the Operator Interface OI40/80 or the OC50 (Figs. 7.1-15 and 7.1-16).

With the introduction of Leica's IPAS10 (Inertial Position & Attitude System) and the Leica FPES (Flight Planning & Evaluation Software) in 2006, the strategy of offering the user a complete workflow of sensor related software was achieved. The main benefit is a seamless data flow from flight planning to all photogrammetric applications for all Leica sensors. Training and support cost is thereby reduced when operating different types of Leica sensors.

Fig. 7.1-16 New FCMS (Flight & Sensor Control Management System) incl. Flight Guidance and the Pilot and Operator Controller OC50 for FCMS

The main tasks of FPES are that flight planning, proposals, flight reporting and invoicing can be made from the same tool. FPES blends with the FCMS (Flight & Sensor Control and Management System) and can be used on all types of geographic and grid coordinate systems. They allow efficient flight planning based on a DTM for all types of sensors including RC30, ADS40/80, ALS50/60 and other frame and line sensors as well as sensors operating in an ON/OFF mode. 4 models of the Leica IPAS10/20 are available for the ADS40/80 and the ALS50/60 and provide additional functionality like the PPP technology. The introduction of PPP algorithms/technology into the post-processing of GPS signal observations solves carrier-phase ambiguities without the need for a base station. This eliminates a logistics restriction associated with GNSS use with airborne sensors and eliminates the requirement of a DGPS reference station on a known point within 50 km of the operating sensor. This provides the user greater aircraft disposition flexibility when capturing imagery of very large and remote areas (forest, desert, plains etc.) and saves project preparation and operating costs.

7.1.5 The Position and Attitude Measurement System

The Inertial Position and Attitude System IPAS10/20 is completely integrated into the ADS40/80 system. The IMU is integrated in the sensor heads SH40, SH51/SH52 or SH81/82 where it is rigidly connected to the focal plate (Fig. 7.1-17).

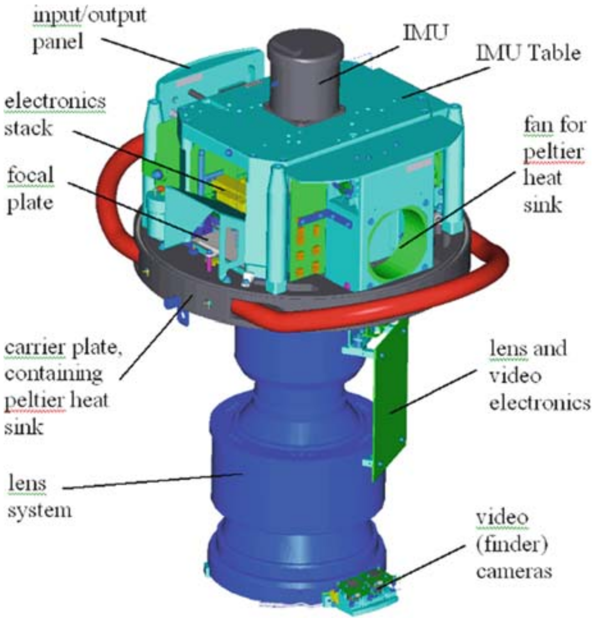

Fig. 7.1-17 View of the SH52/SH82 Sensor Head without housings

Table 7.1-1 List of 4 IMU's (Inertial Measurement Units) from 4 different manufacturers

		NUS4	DUS5	NUS5	CUS6
Absolute accuracy after post-processing (RMS)	Position	0.05–0.3 m	0.05–0.3 m	0.05–0.3 m	0.05–0.3 m
	Velocity	0.005 m/s	0.005 m/s	0.005 m/s	0.005 m/s
	Roll & Pitch	0.008 deg	0.005 deg	0.005 deg	0.0025 deg[1]
	Heading	0.015 deg	0.008 deg	0.008 deg	0.005 deg[1]
Relative accuracy	Angular random noise	≤0.05 deg/ sqrt(hour)	≤0.01 deg/ sqrt(h)	≤0.01 deg/ sqrt(h)	≤0.01 deg/ sqrt(h)
	Drift	≤0.5 deg/h	≤0.1 deg/h	<0.1 deg/h	<0.01 deg/h

This very rigid table allows the installation of the IMU exactly in the optical axis of the single telecentric lens of the ADS40/80 which makes the geo-referencing solution more accurate than in any other large format camera with multiple lenses. IMU's from 4 different manufacturers allows the users to adapt to international exportability restrictions. (Table 7.1-1)

The GNSS/IMU control processor boards are integrated into the Control Unit CU40/CU80. The operator controls the GNSS/IMU system. All functions of the IPAS10/20 System are controlled automatically by the FCMS software.

7.1.6 The Gyro Stabilized Mount for the ADS40

The PAV30 mount (Fig. 7.1-18) is worldwide one of the most used for the RC30 Aerial Camera System and is already installed in many aircraft around the world. For this purpose the PAV30 is equipped with its own inertial stabilization sensors. It was an obvious choice to use the PAV30 also for the ADS40. This required that the following additional requirements are also fulfilled:

- The total weight of the sensor head of the ADS40 plus and adapter had to be equal to the RC30
- Vibration damping had to be as good or better than for the RC30
- The PAV30 is required to accept the higher accuracy attitude data from the Inertial Measurement Unit (IMU), which results in an improved stabilization performance.
- The Inertial Position and Attitude System IPAS10/20 has to deliver a precise reference for the automatic drift control of the PAV30.

The lower weight of the sensor heads SH40, SH51 and SH52 is compensated by means of a mass compensator, which maintains the equal center of gravity and moment of inertia for the PAV30 as given by the RC30.

Fig. 7.1-18 Gyro-stabilized Camera mount PAV30

In 2009 the PAV80 has been designed for the ADS80 with the aim of eliminating some operational restrictions enforced on the ADS40 user by the PAV30.

The most important improvement of the PAV80 is its adaptability to the weight of the payload. Thus the mass compensator is unnecessary. This reduces the weight on board the aircraft by a further 39 kg.

7.1.7 The Radiometric und Geometric Calibration

Radiometric information plays a growing role in imaging data. Airborne digital sensors are now capable of providing high quality radiance information. Therefore laboratory calibration facilities with integrating spheres have been installed in various regions of the world to ensure the radiometric accuracy of the ADS40.

From the data processing software GPro 3.0 onwards, the radiometric calibration factors are used to calculate standardized images for photogrammetry. For remote sensing applications radiance calibrated images can easily be calculated, which are the basis for further data products like ground reflectance images

The geometric calibration process, which was used for the SH40, used a combined approach of self-calibration in bundle adjustment and a polynomial fit on the residuals of each sensor line. The polynomial fit was necessary, because the

"Brown" parameter set could not model the relative shift of more than three CCD lines (Brown, 1976). The situation changed with the SH51/52. The parameter set has now to cover nothing more than the basic opto-mechanical properties of the components. These are the principal distance, the radial-symmetric distortion and the position and the orientation of the individual CCD lines in the focal plane. A subset of these parameters should also be suitable for self-calibration on-the-job to compensate for effects like abnormal atmospheric refraction.

Estimation of ADS calibration parameters in ORIMA is always done relative to an existing input "calibration". ORIMA uses the ADS sensor model library to convert tie and control point measurements into "calibrated" focal plane coordinates. On the output side, ORIMA applies the effects of the estimated calibration parameters to the input calibration and writes out a new calibration data set.

Tie points for such a self-calibration are extracted from 88 scenes of a flight of a two-height double-cross ADS calibration block as shown in Fig. 7.1-19.

This method offers the great advantage that it is not a factory laboratory calibration and can be repeated by users anywhere in the world based on cross flights made in the users own environment and according to the national requirements.

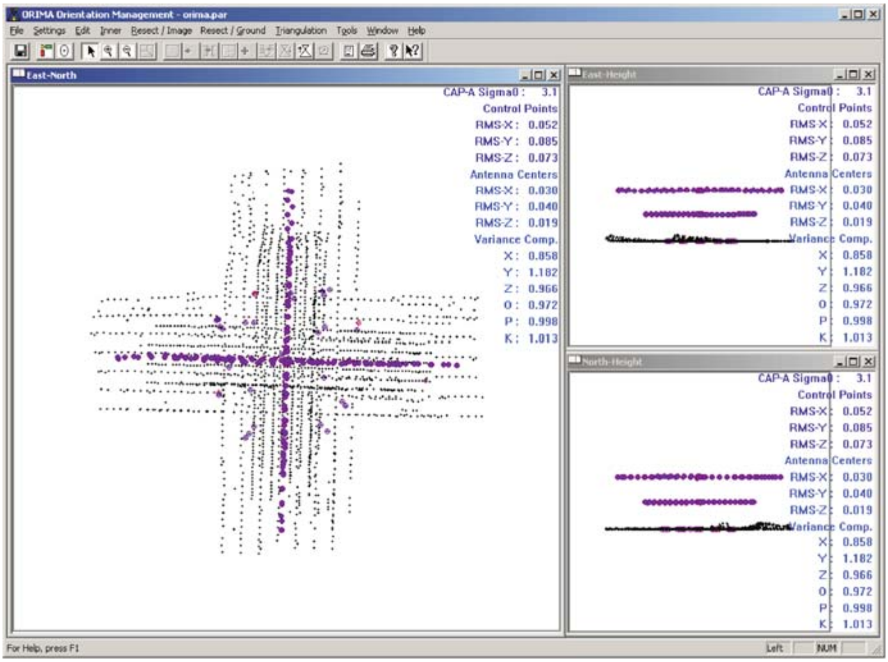

Fig. 7.1-19 Example of cross-flight self-calibration result with the ADS40

7.1.8 Data Processing

The digital sensor revolution happening right now will result in an information explosion. The processing and management of data acquired by digital sensors requires an enormous computational effort. The Aerial Digital Sensor ADS40 from Leica Geosystems AG generates large amounts of data of over 100 GB of raw data per hour if all the CCD lines are active. The ADS40 is a high performance digital sensor, capable of delivering photogrammetric accuracy with multi-spectral remote sensing quality imagery. The ADS40 is a three-line-scanner that captures imagery looking forwards, nadir and backwards from the aircraft. Every portion of the ground surface is imaged multiple times. With its simultaneous capture of data from three panchromatic and up to two times four multi-spectral bands, the ADS40/SH52 provides unparalleled qualities of image and position data. (Fig. 7.1-20) Digital workflow from flight planning through acquisition to product generation is one of the major advantages of the sensor.

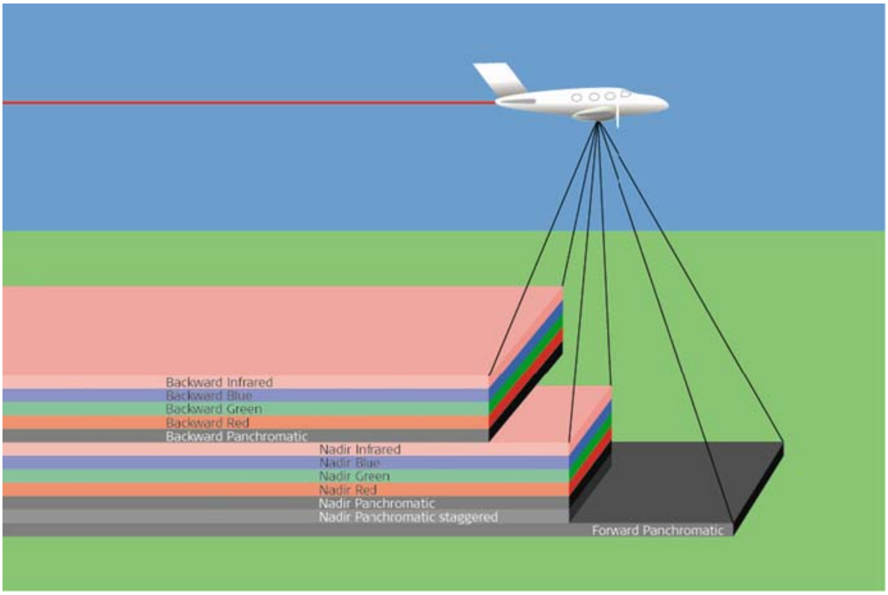

Fig. 7.1-20 Data collection scheme of 12 bands with 100% forward overlap in the SH52 and SH82

This data passes through different levels of processing before products are generated; the first step in the workflow is downloading the data and adding the geo-positioning information using data supplied by the Inertial Position and Attitude System IPAS10/20 and the IPAS Pro software. The geo-referenced images are then rectified to a plane to create stereo-viewable and geometrically corrected Level 1 images. The Level 1 images are also useful for the next process which is automatic point matching. Based on the accuracy requirements, the images are then triangulated using ORIMA, Leica's triangulation package. Finally, ortho-photo images using existing DTM or DTM generated from the triangulated images are created. Due to the large amount of data being processed this workflow could take an extended time. GPro and now XPro the 3rd generation are the ground processing software packages for the ADS40 and ADS80 that control the workflow as described. They provide full functionality to download, generate geo-referenced and ortho-rectified images from the recorded imagery and positioning data. They consist of highly optimized and threaded applications that are designed to handle large data sets (Fig. 7.1-21). In addition they also allow the user to perform various automated processes and data management tasks.

The 3rd generation data processing software XPro released in 2008.

Software solutions such as Leica XPro, which are specifically designed to post-process line sensor data, facilitate the generation of highly accurate image strips even in areas where no or little ground control data is available.

For a long time there was a perception in the market that the processing of push-broom data would require special and extensive knowledge and would differ hugely

Fig. 7.1-21 Overview of the ADS40 and ADS80 Data Processing Workflow

from the traditional frame based processing and analysis. Over the past years more and more software solutions came to the market, which were especially designed to process line sensor data. With the correct software, simple sensor design, the use of IMU's and innovative algorithms users today can process even the largest data sets much faster than what is possible with large format digital frame cameras. Leica XPro, for example, uses the power of the graphics card when visualizing large data sets. Simplified triangulation workflows in black box design in a distributed processing environment reduce the processing time significantly whilst maintaining data quality, and support the generation of orthophotos or stereo imagery "at the speed of flight".

The combination of highest image quality, multipurpose applications, highest productivity and simply delivering more information show clearly that the pushbroom principle is not only the preferred design in satellite based remote sensing, but more and more establishes itself as a standard in airborne digital imaging.

7.1.9 Images Acquired with the ADS40

Fig. 7.1-22 Vaihingen, Germany, Orthophoto 1:500, altitude 0.5 km, GSD 5 cm

Fig. 7.1-23 Balgach, Switzerland, Orthophoto for forest inventory 1:1500, altitude 1.5 km, GSD 15 cm

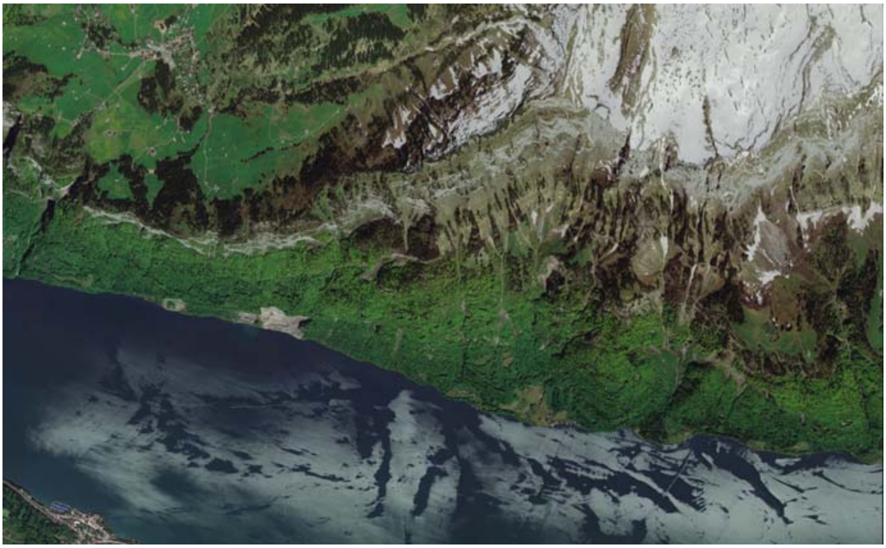

Fig. 7.1-24 Walensee, Switzerland, Orthophoto for alpine area mapping 1:5000, altitude 2.0-/3.6 km, GSD 20/36 cm

Fig. 7.1-25 Waldkirch, Switzerland, Orthophoto 1:2000, altitude 2.0 km, GSD 20 cm

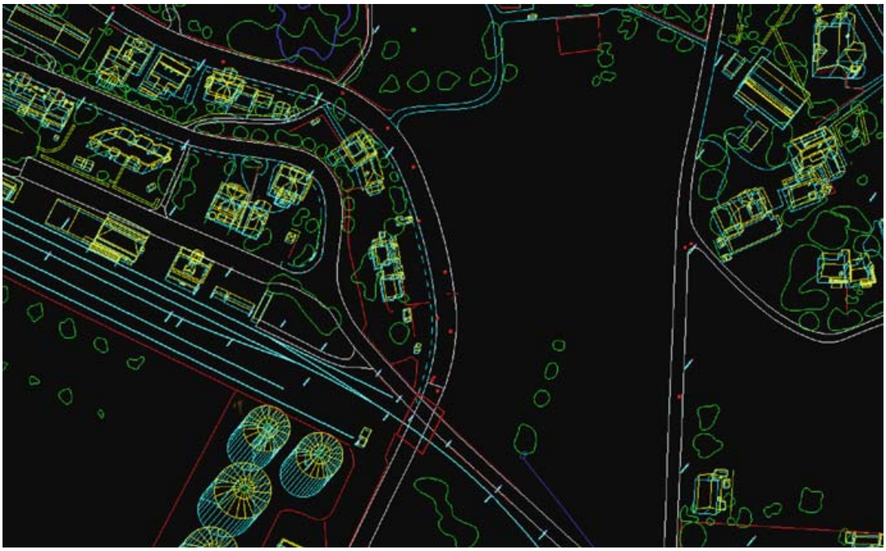

Fig. 7.1-26 Waldkirch, Switzerland, Vector map 1:2000, altitude 2.0 km, GSD 20 cm

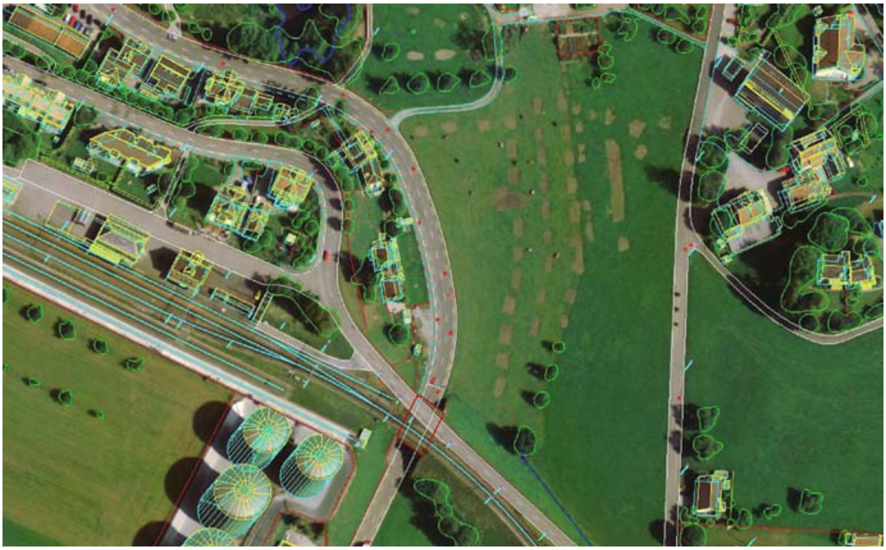

Fig. 7.1-27 Waldkirch, Switzerland, Orthophoto map 1:2000, altitude 2.0 km, GSD 20 cm

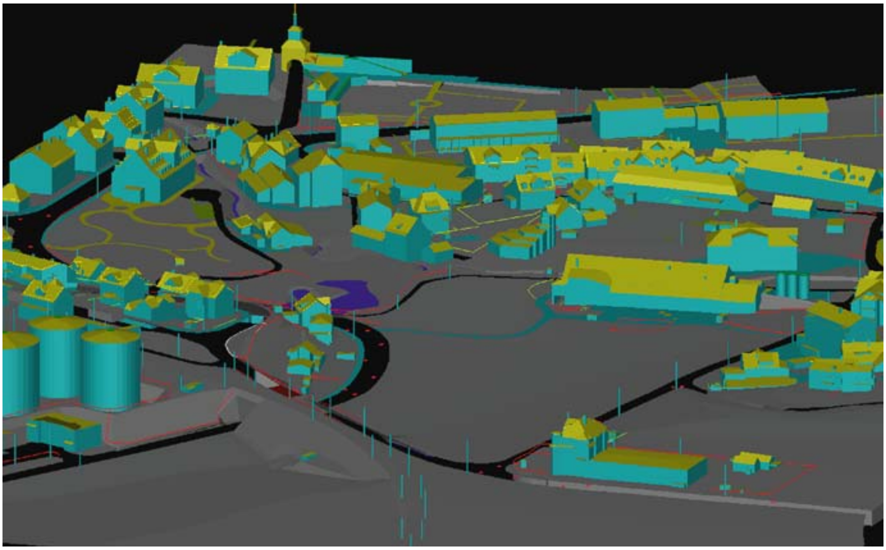

Fig. 7.1-28 Waldkirch, Switzerland, 3D perspective, altitude 2.0 km, GSD 20 cm

Fig. 7.1-29 Aalen, Germany, Image strip 1:35,000 for sensor calibration, altitude 1.2 km, GSD 12 cm

Fig. 7.1-30 Aalen, Germany, Overview map 1:2500 (zoom of 7.1-29), altitude 1.2 km, GSD 12 cm

Fig. 7.1-31 Aalen, Germany, Orthophoto 1:1000 (zoom of 7.1-29), altitude 1.2 km, GSD 12 cm

Fig. 7.1-32 Aalen, Germany, Orthophoto of the stadium 1:1000, altitude 1.2 km, GSD 12 cm

Fig. 7.1-33 Aalen, Germany, Orthophoto 1:1000, altitude 1.2 km, GSD 12 cm

Fig. 7.1-34 Eiderstedt, Germany, False-colour orthophoto for the update of biotopes 1:5000, altitude 2.0 km, GSD 20 cm

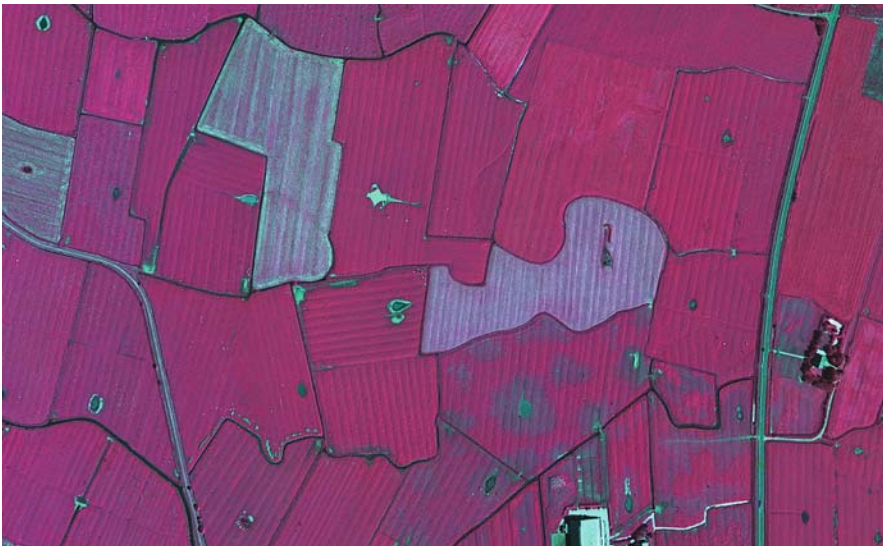

Fig. 7.1-35 Eiderstedt, Germany, False-colour orthophoto for the update of biotopes 1:2500, altitude 2.0 km, GSD 20 cm

Fig. 7.1-36 Eiderstedt, Germany, False-colour orthophoto for the update of biotopes 1:1000 (zoom of 7.1-35), altitude 2.0 km, GSD 20 cm

7.2 Intergraph DMC Digital Mapping Camera

The Intergraph Digital Mapping Camera (DMC) is a large format digital mapping camera, based on frame sensor technology. The workflow for mission planning and photo flights is very similar to analogue film cameras. Image post-processing is required for the raw image data. Aerial images from the DMC have a central perspective and the photogrammetric workflow is similar to that for scanned film images.

7.2.1 Introduction

The DMC (Fig. 7.2-1) is based on a CCD frame sensor design with central perspective and stable inner geometry. At the time the DMC was designed, it was the clear intention to develop a very versatile digital airborne camera to cover a wide range of applications from large scale mapping with 5 cm GSD from high-resolution imagery up to small-scale application with 1 m GSD for remote sensing.

Owing to its frame sensor design, the DMC does not require the sophisticated post-processing of line sensors necessary to rectify the raw image data. It is also not dependent on GPS/INS technology, although most of today's photo flight missions demand high-precision GPS and very often direct georeferencing capabilities as well. But not depending on constant IMU data for post-processing, gives the user

Fig. 7.2-1 DMC camera located in a T-AS gyro stabilized mount

one more degree of freedom and reduces technical risks affecting the success of the photo flight mission.

The design of the DMC has a frame sensor basis and allows the user to continue with the same workflow as for scanned film images, which means that analogue film cameras can be operated in parallel with the DMC for the same production line.

7.2.2 Lens Cone – Basic Design of the DMC

Since it is not (as yet) economically possible to install a single, large area, digital colour array CCD that could reach the format of a 230 × 230 mm film camera, the DMC solution is to incorporate several compact camera heads, each with its own lens and CCD sensor. The modules are then aimed at the scene at slightly displaced field angles. Four panchromatic modules in the centre of the frame are surrounded by four multispectral camera heads at the periphery of the frame. Figure 7.2-2 illustrates the ground coverage taken by the four panchromatic camera heads. The DMC employs four 7 k × 4 k large-area CCD chips, each with an f4 120 mm focal length

Fig. 7.2-2 Ground coverage of the DMC with four panchromatic camera heads

lens operating in the panchromatic (visual response) mode. The overall panchromatic resolution (over the ground) is 13,824 pixels across track and 7,680 pixels along track. The cross-track FoV is 69.3°, formed from two 7 k pixel dimensions, and the along-track FoV is 42°, formed from two 4 k pixel dimensions.

The multispectral array is made up of four f4 25 mm focal length lenses exposing four channels, R, G, B and NIR. The multispectral chips are of lower area resolution, each being 3 k × 2 k pixels.

All CCD sensors are Dalsa models with 12 μm square pixels (>12-bit dynamic range) and have a special architecture with four readout registers placed at the corners of the chip. This provides for high readout rates, such that an image repetition frequency of one image every 2.1 s can be achieved, an important feature to acquire aerial images for stereoscopic viewing at high forward overlap and high ground resolution.

7.2.3 Innovative Shutter Technology

An electromechanical inter-lens shutter system is employed on each camera, with precise synchronisation of all camera exposures to exclude geometric errors. These shutters are of a design customized for airborne operation, with few mechanical parts and very high reliability. There is no need for frequent shutter exchanges as is the case for other types of aerial camera.

All eights shutters are continuously monitored by microcontrollers and adjusted in real time for any kind of variance, to maintain a stable exposure cycle over time. The shutter speed is variable and can be selected in steps between 1/50 and 1/300 s.

7.2.4 CCD Sensor and Forward Motion Compensation

Forward image motion (FIM) is an important influence on image resolution in both analogue and area-array digital images, where, with poor light levels or low flying height, the image exposure time may be too long to avoid significant image blur (Graham et al., 1996). FIM is a function of a number of parameters:

$$\mathrm{FIM} = f^{*}V^{*}t/H$$

where f = focal length of lens, V = ground speed of aircraft, t = exposure time (i.e. shutter speed) and H = height of aircraft above mean ground level.

In terms of aerial films, the usual accepted limit of FIM is that it should not exceed 25 μm, but this is usually less in cameras with forward motion compensation (FMC). For the DMC, a shutter speed of 1/200 s at 150 knots (77.25 m/s) airspeed and 5 cm GSD would amount to an image blur of 8 pixels, i.e. 96 μm on the CCD sensor.

A fully electronic forward motion compensation (FMC) of the digital image is available by means of the time-delayed integration (TDI) mode during exposure. In

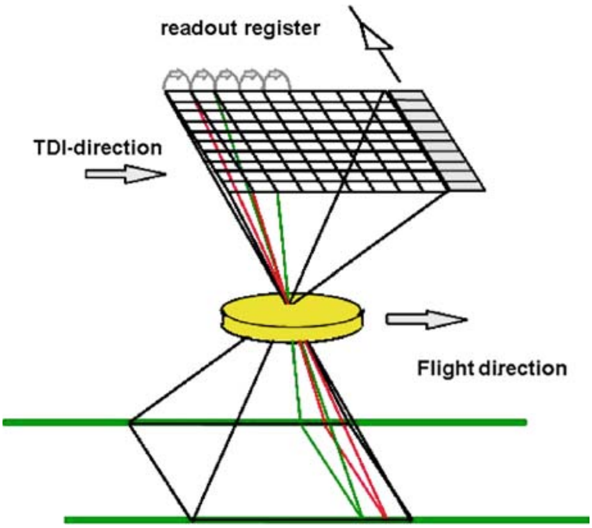

Fig. 7.2-3 Forward motion compensation by TDI

this way, compensation for image blur in low altitude and high resolution applications is assured (FMC has been standard for analogue aerial cameras since 1982). FMC is implemented on the DMC in a completely electronic way. In normal reading out of CCD pixels in an area-array imaging system, the charge contents of each CCD pixel are transported line-by-line to the readout registers (Fig. 7.2-3).

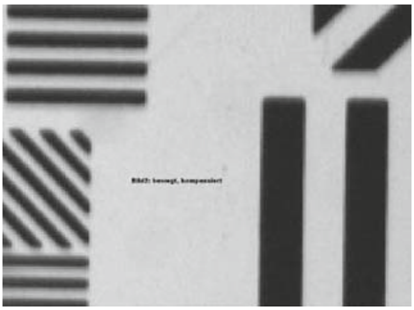

Fig. 7.2-4 Resolution target with FMC

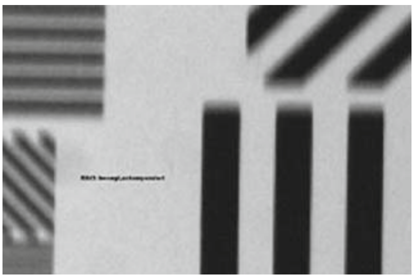

Fig. 7.2-5 Resolution target without TDI

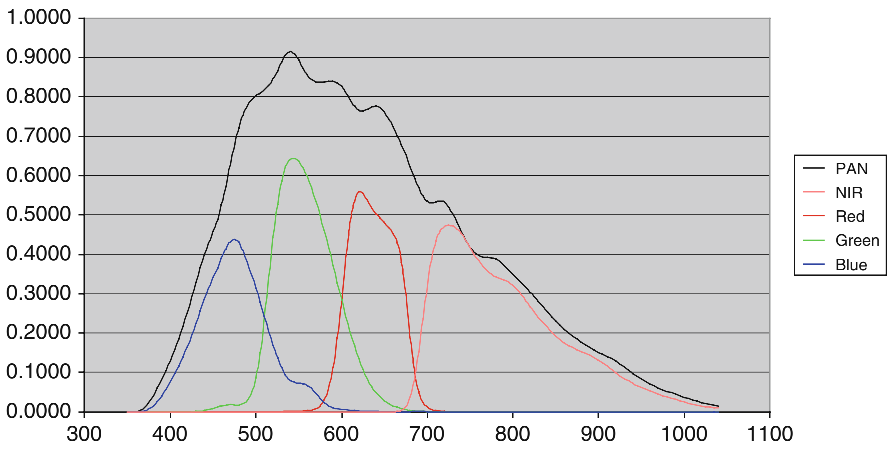

Fig. 7.2-6 DMC spectral sensitivity

7.2.5 DMC Radiometric Resolution

All of the DMC modules have a total CCD resolution of 12 bits, which enables better exposure sensitivity, allowing details to be recorded on the CCD even in bright or dark exposure conditions due to reflections, shadowing or clouds, thus increasing the number of flying days considered acceptable.

Each multispectral camera has its own colour filter. There is a slight overlap between the individual bands to achieve a better native colour impression. The colour filter sensitivity is as follows (Fig. 7.2-6):

Blue: 400–580 nm
Green: 500–650 nm
Red: 590–675 nm
NIR: 675–850 nm

7.2.6 DMC Airborne System Configuration

A typical DMC installation is shown in Fig. 7.2-7, which is almost identical to existing film camera installations. The DMC camera body has similar dimensions to the RMK TOP aerial film camera and is designed to fit into the existing gyro-stabilised mount T-AS. The sensor management system, with real-time controller hardware and pilot display, is used to control the camera system. An optional IMU can be integrated into the DMC, opening up the possibility of direct georeferencing and working without ground control or with a reduced set of ground control points (GCPs).

Raw image data is stored on a set of 3 FDS Flight Data Storage units. These are ruggedized storage systems with hardened pressurized enclosures, each of which

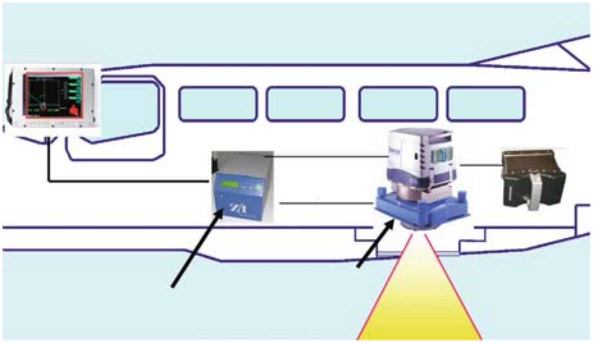

Fig. 7.2-7 DMC system installed in an aircraft

includes two 300 GB SCSI disk drives. A set of 3 FDS can store up to 4,400 images, where one FDS is connected to 2 panchromatic camera heads (each 7 k $\times$ 4 k) or to 4 multispectral camera heads (each 3 k $\times$ 2 k). The data interface is a high speed 1 Gb copper-based fibre-channel interface. The FDS is certified to be operated at up to 8,000 m altitude in an unpressurized environment. Special environmental tests following the RTCA/DO 160 aircraft standard guarantee high reliability and high data safety for the user.

In the aircraft, each FDS is installed in a special designed carrier ("FDS shoe") and can be easily removed without unplugging any cables or connectors. The "shoe" can be mounted to the aircraft seat rails for crash load safety.

For image data post-processing the FDS is either connected directly to the post-processing software servervia fibre-channel connection or hooked up to a field copy station for mobile data copy to removable hard disk drives or USB disk drives.

7.2.7 System Calibration and Photogrammetric Accuracy

The DMC is certified by USGS (United States Geological Service) to meet the US national mapping standards and accuracy. The basis for this high quality level is a robust mechanical and optical design and an intensive quality test program. Extensive environmental testing is part of the manufacturing process. Each camera system undergoes a laboratory calibration, where focal length, lens distortion and other characteristics are precisely measured. After this laboratory calibration, each camera system is subject to a burn-in flight to perform the platform calibration. Finally all calibration data are stored on a calibration CD and delivered with the system to the customer. The user can repeat at any time a verification flight to check platform calibration. The DMC is fully field serviceable and each component can be exchanged on-site.

The mapping accuracy of the DMC is:

$$\text{for X,Y} \qquad 5\,\mu\text{m}^{*}\text{photo scale, e.g.2.5cm@6 cm GSD}$$

$$\text{for Z0.05\% of flying height above terrain, e.g. 3 cm @ 6 cm GSD}$$

This high accuracy leads to the possibility of flying at higher altitudes compared to film cameras while meeting the same mapping requirements.

7.3 UltraCam, Digital Large Format Aerial Frame Camera System

7.3.1 Introduction

UltraCam is a large format digital aerial frame camera. The design is unique and based on a multi cone concept. The camera is produced by Vexcel Imaging GmbH, a wholly-owned subsidiary of Microsoft Corporation.[1] The first UltraCam was presented in May 2003 at the 2003 ASPRS Annual Conference in Anchorage, Alaska, in its initial implementation as the 85-megapixel UltraCam$_{D}$ system (Leberl et al., 2003). Three years later, at the 2006 ASPRS Annual Conference in Reno, Nevada, the 136-megapixel format UltraCamX was introduced.

Fig. 7.3-1 Large scale aerial image at 3 cm GSD. This 700 pixel by 500 pixel sub-area of an UltraCam image covers only 21 m by 15 m on the ground

The new UltraCamX was developed with the experience and success of the UltraCam$_{D}$ during the three previous years, undergirded by a rapid evolution of the digital sensor market and a transition to the fully digital photogrammetric workflow. A review of the period since the ISPRS Congress in 2000 in Amsterdam, when the first digital large format aerial cameras were presented, shows a rather slow initial acceptance of the new technology. It was not until 2004 that a significant number of digital large format aerial cameras was sold by the then three competing vendors, so

[1] Microsoft Corporation operates though Vexcel Imaging GmbH. The Austrian team is denoted as "Microsoft Photogrammetry". In this text, we will use both "Vexcel" and "Microsoft".

that worldwide count of systems in operation reached a significant number. Since 2004 digital cameras began to have a major impact on the global perspective of the photogrammetric all-digital workflow and value systems.

7.3.2 UltraCamX Produces the Largest Format Digital Frame Images

7.3.2.1 Overview of the UltraCamX

The UltraCamX camera system is the most recent implementation of the basic UltraCam imaging principle. It takes advantage of the most valuable developments of the industry in the technologies of sensors, data storage and data transfer as well as Vexcel's in-house experience and know-how. As will be reviewed later, some essential elements of the camera technology were special custom developments for the UltraCam.

The significant advantages of the UltraCamX include:

- large image format of 14,430 pixels cross-track and 9,420 pixels along-track
- image repeat rate based on a data rate of 3 gigabits per second
- excellent optical system with 100 mm focal length for the panchromatic camera heads and 33 mm for the multispectral camera heads, for an exact 1:3 pan-sharpening ratio
- image storage capacity of 4,700 frames for one single data storage unit
- almost unlimited image harvest due to exchangeable data storage units
- instant data download from the airplane by means of removable data storage units
- fast data transfer to the post-processing system using the new docking station.

The camera consists of the Sensor Unit, the onboard storage and data capture system, the operator's interface panel and two removable data storage units. This airborne configuration is shown in Fig. 7.3-2. It is complemented by an elaborate software system for mission planning and in-flight camera operation, the Camera Operating Software COS.

Of course, there is also an integral systems component in the office, be it a field office or the main home office. This addresses the processing of the acquired imagery into deliverable imagery, in the form of the Office Processing Center OPC.

7.3.2.2 The UltraCamX Sensor Unit

The UltraCamX Sensor Unit consists of eight independent camera cones, as shown in Fig. 7.3-3. Four of these contribute to the large format panchromatic image; the other four, to the multispectral image. The sensor head of the UltraCamX is equipped with 13 FTF5033 high performance CCD sensor units, each producing 16 megapixels of image information at a radiometric bandwidth of more than

Fig. 7.3-2 The UltraCamX digital aerial camera system with the Sensor Unit (*right*) and the airborne Computing Unit including two removable Data Units (*left*). The camera is operated in the air through the Interface Panel (*middle*)

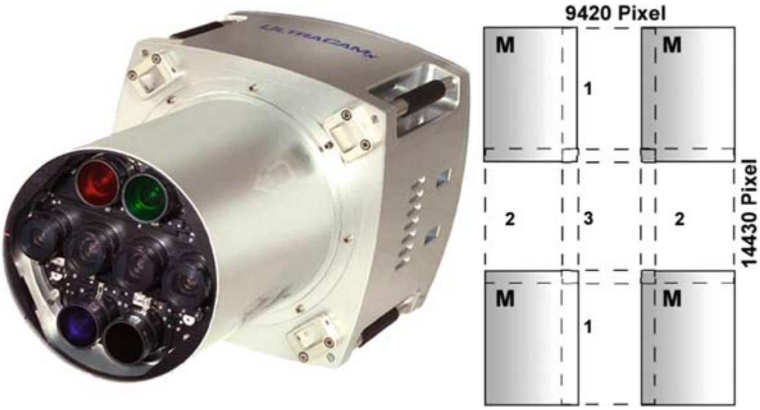

Fig. 7.3-3 The UltraCamX sensor head (*left*) consists of eight camera heads, four of them contributing to the large format panchromatic image. These four heads are equipped with nine CCD sensors in their four focal planes. The focal plane of the so called Master Cone (M) carries four CCDs (*right*)

12 bits. The CCD elements have a pixel size of 7.2 μm square. A single image trigger results in a readout of 13 * 16 * 2 = 416 MB, since each pixel is recorded on to 16 bits. The A/D converter uses a 14-bit approach.

Each camera cone is equipped with a high performance optical system designed by LINOS/Rodenstock specifically for the UltraCam. The focal length of the panchromatic camera is 100 mm, that of the multispectral camera is 33 mm. As mentioned previously, this set of two lens types supports a pan-sharpening ratio of 1:3.

The image format of 14,430 pixels cross-track by 9,420 pixels in the flight direction results in a high rate of productivity in the air. At a 25% side overlap between strips, the UltraCamX covers a strip width at more than one mile or 1,650 m at a pixel size on the ground of 6″. Table 7.3-1 summarizes the salient items of the UltraCamX specifications.

Table 7.3-1 Technical Data and Specifications of the UltraCamX Sensor Unit

Technical data for UltraCamX Sensor Unit	
Panchromatic channel	
Multi-cone multi-sensor concept	4 camera heads
Image size in pixel (cross-track * along-track)	14430 * 9420 pixel
Physical pixel size	7.2 μm
Physical image format (cross-track * along-track)	103.9 * 67.8 mm
Focal length	100 mm
Lens aperture	$f = 1/5.6$
Angle of view (cross-track/along-track)	55°/37°
Multispectral channel	
Four channels (red, green, blue, near infrared)	4 camera heads
Image size in pixel (cross-track * along-track)	4992 * 3328 pixel
Physical pixel size	7.2 μm
Physical image format (cross-track * along-track)	34.7 * 23.9 mm
Focal length	33 mm
Lens aperture	$f = 1/4$
General	
Shutter speed options	1/500–1/32 s
Forward motion compensation	TDI controlled, 50 pixels
Frame rate per second	1 frame in 1.35 s
A/DC bandwidth	14-bit (16,384 levels)
Radiometric resolution	>12 bits/channel

7.3.2.3 The UltraCam X Storage System

The data storage system of the UltraCamX improves the end-to-end workflow of the airborne mission over the previous UltraCam$_D$ arrangement and achieves an improvement in the working conditions of the crew. The system contains two independent Data Units for redundant image capture. The Data Units can capture up to 4,700 images, each consisting of 206 raw input megapixels, which are converted into deliverable images with 136 megapixels each and – most valuable for large-scale missions – can be exchanged for additional Data Units within a few minutes. Thus one can collect a virtually unlimited number of images during a single flight mission, simply by swapping data units in flight. Compared to the UltraCam$_D$, the UltraCamX Data Unit has a capacity that is four times larger, since the number of images per Data Unit has increased from 2,700 to 4,700, and the size of each image, from 86 megapixels to 136 megapixels.

The downloading of the acquired images is accomplished by simply disconnecting the Data Units from the camera system on completion of a flight mission and shipping the raw data to the field office or the home office where the post-processing takes place. A quality control step can be performed in the field, however, either airborne while still returning to the airport, or on the ground upon arrival at the airport, using a laptop computer.

The downloading of the image data is supported by a Docking Station (Fig. 7.3-4), which supports the complete data transfer of 4,000 images within 8 h through four parallel data transfer channels. This results in a 24-h cycle of flying, data download, copying and QC.

Fig. 7.3-4 UltraCamX on board Computing Unit (*left*) and Data Unit attached to the Docking Station (*right*). The download of image data to the post-processing station is supported by four parallel data streams

7.3.2.4 The UltraCam Software Components

The Camera Operating System COS and the Office Processing Center OPC are the two software components required to operate the camera and process the raw image data into a deliverable image product on completion of a flight mission. Figure 7.3-5 presents a typical view of the Graphical User Interface for the OPC software.

7.3.3 UltraCam Design Concept

The UltraCam large format frame camera is based on a unique design of the sensor head. It is composed of eight individual “cones” and 13 CCD sensor arrays. A cone in turn is built with an optical lens and one or more CCD arrays with the associated electronic components. Each CCD feeds into a separate data stream, resulting in

Fig. 7.3-5 COS GUI (*left*) enabling the on board quality control of each picture and OPC GUI (*right*) addressing an entire flight mission with many images

Fig. 7.3-6 Full set of 13 UltraCam CCD-sensor and electronics components. Nine units are used for the large-format panchromatic image; four units are responsible for the multispectral bands

13 parallel data tracks (Fig. 7.3-6). This type of parallel architecture supports fast image capture and data readout.

7.3.3.1 The Large-Format Panchromatic Sensor

Four camera heads and 9 CCD sensor arrays contribute to the large-format panchromatic image. Figure 7.3-7 illustrates the assembly of a large-format image from four separate exposures, each consisting of one or multiple CCD tiles. There are several advantages of this design:

- The Master Cone defines the image format and operates with one shutter exposure for the four CCDs.
- FMC is correctly implemented (the optical axes are parallel)
- Syntopic exposure enables large-scale urban missions.

Fig. 7.3-7 UltraCamX panchromatic camera heads. The Master Cone and three slave cones contribute nine CCD arrays to the full frame (*left*). Overlap areas between CCD tiles are used to control the stitching process to sub-pixel accuracy (0.1 pixel) (*right*)

The nine tiles must be "stitched" into a single, seamless image. Stitching is a core function of the OPC software and employs the overlaps between the individual tiles. The result of the stitching process is reported and documents the geometric quality of each frame. An accuracy level of 0.1 pixel can be achieved.

The four cones of the panchromatic part of UltraCam are aligned in parallel with the flight path. This enables a special exposure concept – the so-called "Syntopic Exposure". Each shutter is triggered after a short delay in such way that all four cones take the exposure at one and the same position as the aircraft moves forward.

7.3.3.2 The Four Band Multispectral Sensor

The UltraCamX is equipped with four individual sensor heads for visible light (red, green and blue) and near infrared light. Figure 7.3-8 presents the spectral sensitivities of the four channels. Whereas the panchromatic image is composed of 3 $\times$ 3 CCD tiles, the colour image bands consist of single CCD tiles. The final colour image is compiled from a combination of the panchromatic and the four colour channels. This process is denoted as "pan-sharpening" and has already been widely used in remote sensing applications.

Figure 7.3-9 summarizes the concept of the output of five separate channels, namely the panchromatic and four colour bands and a resulting pair of (a) colour and (b) false-colour infrared images.

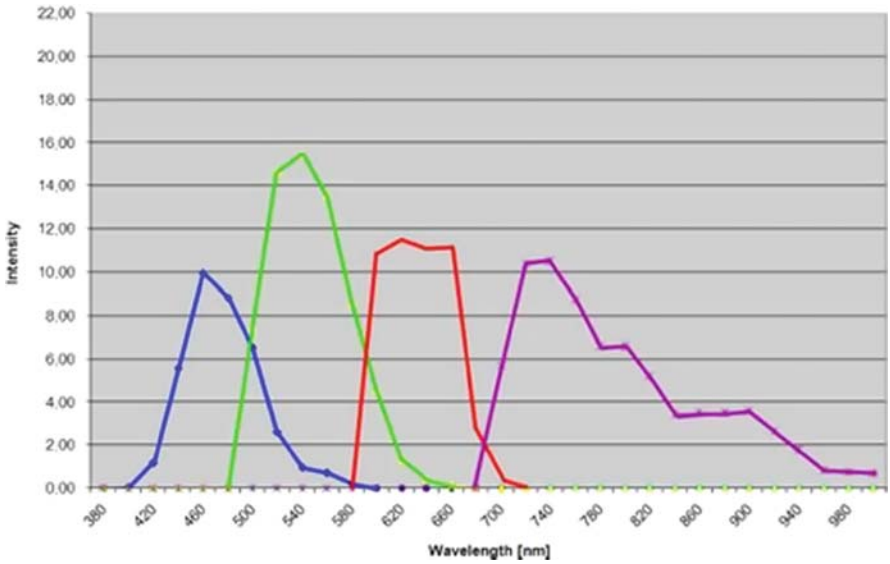

Fig. 7.3-8 UltraCamX multispectral cones. Volume filters are used to separate the four bands

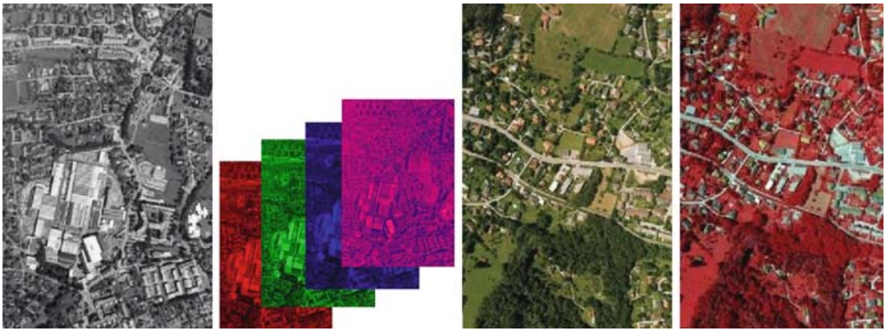

Fig. 7.3-9 Sample image data set with a panchromatic band and four colour bands, as well as the resulting pair of colour and false-colour infrared images

7.3.4 Geometric Calibration

7.3.4.1 The UltraCam Calibration Laboratory and Image Measurements

Vexcel's Calibration Laboratory has been in operation since July 2006 and represents a second-generation solution. It consists of a three-dimensional calibration target with 394 circular marks. These marks are surveyed to an accuracy of about ±0.1 mm in X and Y and ±0.2 mm in Z and have a well defined circular pattern. The entire structure is 8.4 m by 2.5 m at the rear wall and 2.4 m in depth. Rear wall, ceiling and floor carry 70 metal bars with 280 marks; four additional vertical bars in the center of the structure carry 16 marks; 98 marks are mounted on the rear wall. The mean distance between marks is about 30 cm (Fig. 7.3-10).

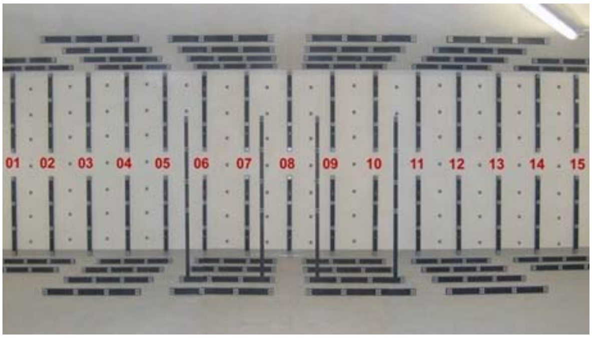

Fig. 7.3-10 The UltraCam calibration laboratory is equipped with a three dimensional target containing 394 marks. The entire volume is 8.4 m by 2.4 m by 2.5 m

During the data capture 84 images are taken from three different camera stations in such a way that the camera is tilted and rotated. In this set of 84 images almost 18,500 image positions of the surveyed marks can be recognized from the four panchromatic camera heads and about 17,500 image positions from each of the four color camera heads, as well.

Software is used to compute image positions of each mark in each image of the entire set of images, with sub-pixel accuracy. This results in a dense and complete coverage of coordinate measurements over the entire image format. Figure 7.3-11 shows the distribution of measured points in an image. One single calibration dataset consists of almost 90,000 measured image points.

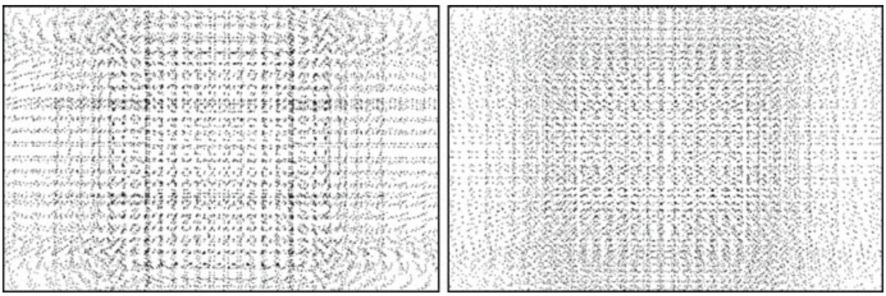

Fig. 7.3-11 The automatically detected image positions cover the entire frame of the camera. About 18,500 points are detected in the panchromatic channel (*left*) and 17,500 points are detected in each of the four colour bands (*right*). A single image trigger will therefore produce a total of about 90,000 points

7.3.4.2 Computing the Camera Parameters

The computation of the unknown camera parameters is based on the least squares bundle adjustment method of BINGO (Kruck, 1984). The specific design of the UltraCamX sensor head required some modifications to the software. It was most important to introduce the ability to estimate the positions of multiple CCD sensor arrays in one and the same focal plane of a camera head.

The unknown parameters which are estimated within the bundle adjustment procedure can be separated into three groups:

- The traditional camera parameters to define the bundle of rays (principal distance and coordinates of the principal point)
- The specific UltraCam parameters for each CCD position in the focal plane of each camera cone (shift, rotation, scale and perspective skew of each CCD)
- Traditional radial and tangential lens distortion parameters (for each lens cone).

When the correlation between these parameters is investigated, it is obvious that CCD scale parameters are correlated with the principal distance of each cone and CCD shift parameters are correlated with the principal point coordinates of each focal plane (Gruber and Ladstädter, 2006). It was therefore necessary to reduce the entire set of parameters in order to avoid such correlation. This was done in such a way that principal distance and principal coordinates of all eight cones of the UltraCamX were introduced as constant values. It is further noteworthy that there exists an additional correlation between the CCD rotation parameter and the angle kappa of the exterior orientation. This correlation could be resolved by removing one and only one CCD rotation parameter of the parameter set of each camera head (Kröpfl et al., 2004).

The resulting quality of the geometric laboratory calibration is documented by the $\sigma 0$ value of the bundle adjustment. This value was observed at a level of ± 0.4 to $\pm$ 0.5 μm for all calibrations of the panchromatic camera cones carried out in the new Calibration Laboratory (Fig. 7.3-12). This is a slight but significant improvement compared to the results achieved from the initial Calibration Laboratory, which was in use until mid 2006.

7.3.4.3 Post-Processing for Stitching and Additional Improvements

The results from the laboratory calibration are stored in a data set, which is used during the post-processing of each frame exposed by the camera. During this post-processing we apply parameters to describe dimensional changes of the camera body which may be caused by the change of environmental parameters during a flight mission (e.g. any thermal effect). Such thermal changes cause symmetric expansion or shrinking of the backplanes of the UltraCam cones. The CCDs mounted on the backplanes will therefore "drift away" from their calibrated positions when the temperature during flight deviates from the temperature at calibration

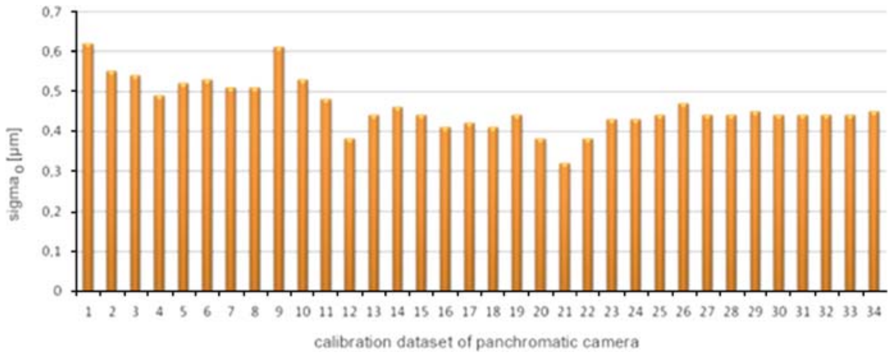

Fig. 7.3-12 A subset of 34 cameras was investigated and is illustrated. Results of the bundle adjustment after the estimation of camera parameters (panchromatic camera) are documented by the σ_0 values of the adjustment. They are in the range of ±0.4 to ±0.5 µm. Slightly larger values (±0.5 to ±0.6 µm) were observed from the initial Calibration Laboratory, which was in use until mid-2006

time. If this effect is neglected in the "stitching" process, systematic deformations will be visible in the images.

These self-calibration parameters are computed from the stitching scales 1 and 2 and the well known distances between the stitching zones. Sensor drifts can now be modelled and compensated. Finally, a second stitching procedure is performed using the modified calibration parameters. The stitching scales are expected to be close to 1.0 after the self-calibration has been applied. This self-calibration method has been introduced successfully into the post-processing software of the UltraCam digital camera system (Ladstädter, 2007).

7.3.5 Geometric Accuracy at the 1 µm Level

7.3.5.1 Aerial Triangulation by σ_0

The first step is the geometric laboratory calibration of each UltraCam. Then each camera's performance is verified by a flight mission over a well known test area. A flight pattern with high overlap (80% end-lap, 60% side-lap) and cross-strips is used, to offer a highly redundant data set suitable for investigating the interior geometry of the camera. Figure 7.3-13 presents a project overview.

The automatic tie point matching is done using Inpho's aerial triangulation software package MATCH-AT. The adjustment of the aerial triangulation is computed by BINGO, with cross-check and additional self-calibration options.

GPS/IMU systems were used to provide Earth observation parameters and did show excellent results (Kremer and Gruber, 2004).

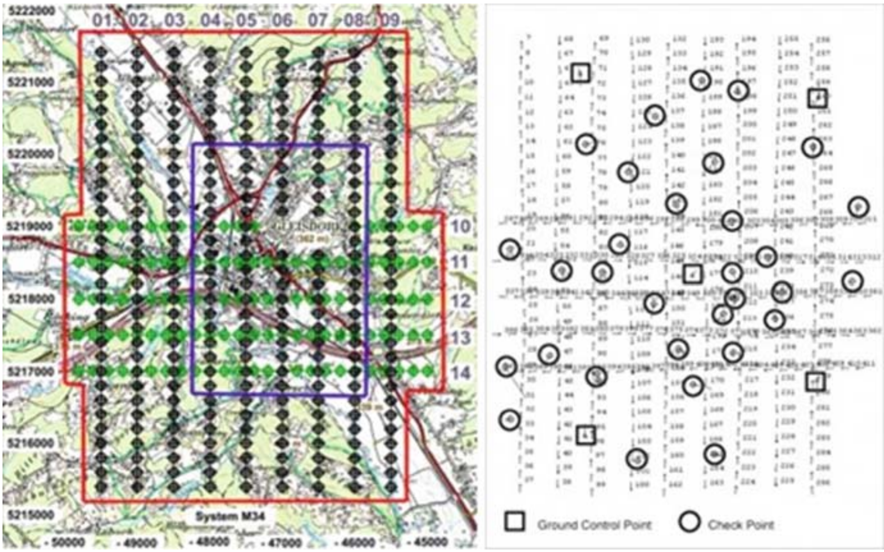

Fig. 7.3-13 Test area near Graz, Austria. Flight plan with 14 flight lines (404 images) and the AAT result after the UltraCamX photo mission (processing by MATCH-AT and BINGO software)

The σ_0 value reflects the quality level of image coordinate measurements of an aerial triangulation project. Such values are computed for each camera. Figure 7.3-14 provides the σ_0 values for 26 UltraCamX image datasets. These values are close to, or oftentimes smaller than ± 1 µm (Fig. 7.3-14), based on a large degree of redundancy from the high overlaps and added cross strips.

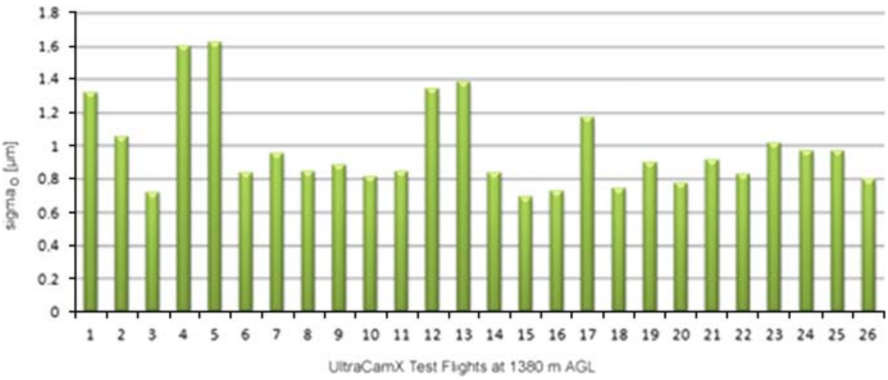

Fig. 7.3-14 Results of the automatic aerial triangulation from several UltraCamX testflights at 10 cm GSD (1,380 m AGL), with σ_0 values are in the range ± 0.7 to ± 1.6 µm. The average value of σ_0 is better than ± 1 µm

7.3.5.2 Aerial Triangulation by Check Points

Another widely accepted method to verify and assess the geometric performance of mapping cameras is the use of check points. We use the results from six individual flight missions and six individual cameras to analyze the geometric performance of these cameras. With an average of 199 check point measurements, deviations of ±38, ±46 and ±56 mm in X, Y and Z respectively were observed at the GSD of 10 cm. The vertical accuracy of this dataset corresponds to 0.04‰ of the flying height (cf. Fig. 7.3-15).

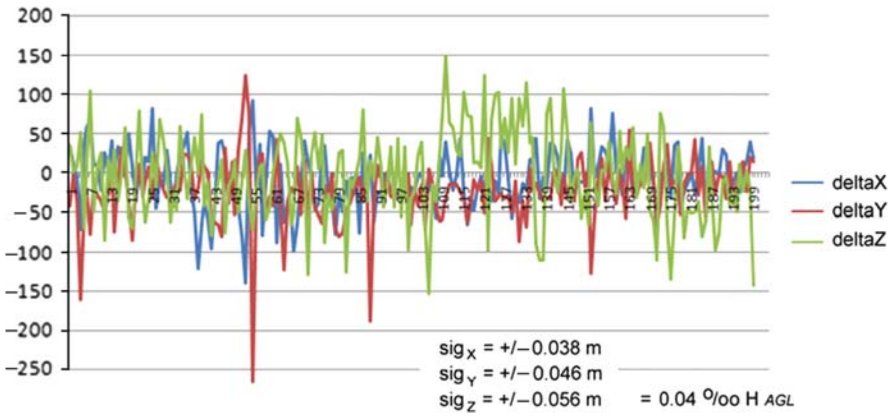

Fig. 7.3-15 Residuals of check points after the bundle adjustment. Results from six individual cameras and flight missions at 10 cm GSD were merged and 199 measurements from 35 checkpoints were analyzed

7.3.5.3 Geometric Improvement by Auto-Calibration

The end-to-end digital workflow of the UltraCam processing chain offers several auto-calibration options. One specific function is already implemented in the post-processing software to reduce the effects of thermal changes during a flight mission (cf. Fig. 7.3-16). In addition, we have observed positive effects when traditional radial symmetric distortion parameters are introduced into the bundle solution. Such parameters are well known in the community, almost every bundle solution offers them and almost any digital workstation is able to accept such parameters. The magnitude of these parameters is small (<0.5 pixel), but their effects are systematic and can therefore not be ignored. In addition to the widely known radial symmetric distortion parameters we have investigated the positive effect of camera-specific parameters. Figure 7.3-17 illustrates how the additional parameters are being used. These parameters are introduced in order to compensate for any asymmetric changes of the geometry of the camera. Again, the magnitude of these parameters is expected to be rather small but will play a role when high accuracy is needed. The remaining

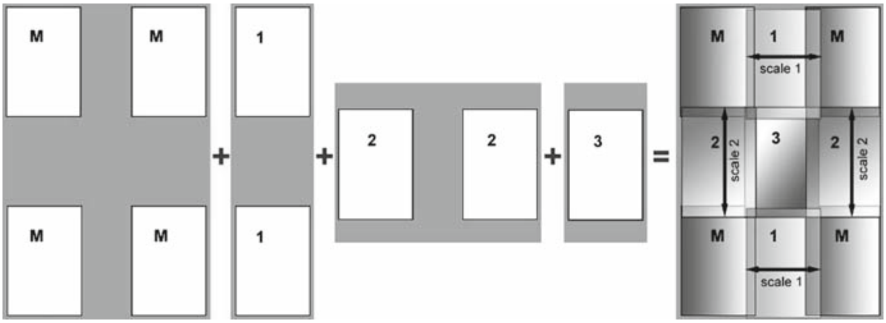

Fig. 7.3-16 Scheme of the UltraCam stitching concept, which is implemented in the image post-processing in order to transform the image information from the four camera heads into one single frame. The two scales shown on the *right* are computed during this step and compensate for any dimensional changes of the camera body

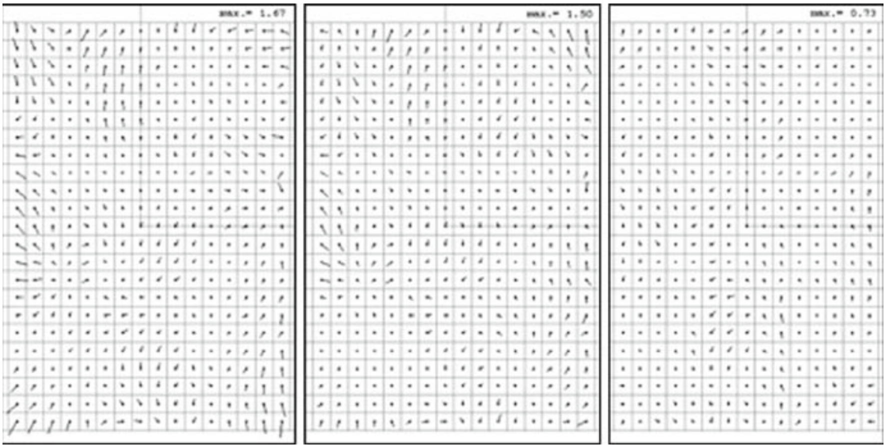

Fig. 7.3-17 Image residuals after the aerial triangulation without additional self-calibration parameters, showing a maximum of 1.67 µm (*left*). Applying radial symmetric distortion parameters (*middle*) and camera-specific parameters (*right*) reduces the remaining image distortions to the sub-micrometre level

residuals in the images have a maximum at ±1.67 µm when no additional self-calibration parameters are applied. When radial symmetric distortion parameters are applied, this value decreases to ±1.5 µm and, finally, when additional asymmetric parameters are also included, to a very accurate value ±0.73 µm.

With the application of automatic self-calibration, users are assured that systematic image errors are stable and do not change during the flight mission for a specific image block. This stability is a clear advantage of the digital camera over the film camera. The achievement of significant increases in accuracy by means of additional parameters testifies to the stability of the errors with time.

7.3.6 Radiometric Quality and Multispectral Capability

The UltraCamX exploits the radiometric quality of the high performance CCD sensor FTF5033 manufactured by DALSA and preserves this quality by means of in-house proprietary electronics circuits. No less than 13 bits of radiometric information can be extracted via the 14-bit analogue/digital converter. Such broad bandwidth allows the resolution of dark and bright areas in one and the same scene, for example from a city area on a bright sunny day with dark shadows in the streets and almost white roofs or other bright objects. The performance in dark image regions shows the full potential of the sensor and its sensitivity. Only ±6 DN @ 16 bit (= ±0.4 DN @ 12 bit) of noise could be detected in shadows.

Figure 7.3-18 shows frame 1,090 from a flight mission over the city of Graz, Austria on 27 March 2007, a clear sunny day. At a flying height of 900 m above ground level a ground sampling distance (GSD) of 6.5 cm was achieved. Two sub-areas of the panchromatic camera image containing very bright objects (umbrellas and welded roofs) as well as dark shadows were analyzed by computing the histogram. Levels of intensity from 350 DN to 7,800 DN @ 16 bit could be detected, yet image areas were not saturated. Such huge dynamic range of 7,450 DN corresponds to almost 77 dB or 12.9 bits.

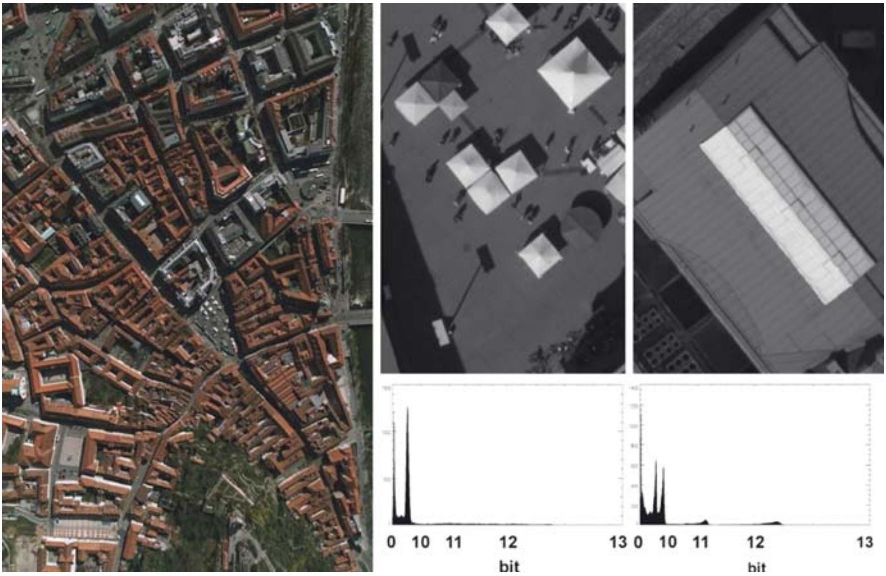

Fig. 7.3-18 Frame 1,090 of an UltraCamX on flight mission over the city of Graz. Two details of the image show a radiometric bandwidth of almost 13 bits. The darkest pixels are at a level of 350 DN and the brightest pixels are at a level of 7,800 DN in a 16-bit representation

The multispectral channels of the UltraCamX offer true colour (red, green and blue) as well as near infrared bands and therefore support multispectral classification, which benefits from a large radiometric range.

7.3.7 The Potential of Digital Frame Cameras

The driving force behind innovation in aerial photogrammetry for about 100 years was to minimize the number of photographs for a given project. The reason was simply cost, which was directly proportional to the number of images to be flown, which determined the film to be purchased, processed in a photo-laboratory, perhaps scanned into a digital format, triangulated and finally manually converted into information by photogrammetric procedures. The costs for aerial triangulation, DEM generation and orthophoto processing were a linear function of the number of images in a project. Cutting the number of flight lines in half meant a reduction in the cost of a project by the factor of four. The rapid acceptance of digital cameras is the result first of all of an increase in image quality and secondly of the economic advantages over the continued use of film cameras, simply because there is no longer a need to purchase film, develop it and scan it into pixel arrays. Higher image quality produces a better product, or supports a reduction of flight lines by flying at higher altitudes. This drives aerial photogrammetry away from film-based workflows and towards fully-digital approaches.

The third reason for acceptance, however, is the most important factor: the individual digital image does not produce any variable cost. Therefore the operation of a digital airbornee camera is feasible with only fixed annual costs, independent of the number of images being produced, be this 1,000 or 100,000 images per year. Only the costs for the fuel and fees in using the aerial camera platform are variable. The result is an opportunity to automate photogrammetric procedures that previously could not be efficiently automated. The many past failures to automate photogrammetric procedures can be attributed to, firstly, the limitations of film quality in the form of grain noise and a limited dynamic range; secondly, economy in the use of film, preventing the creation of sufficiently redundant image blocks properly to support automation. Having each terrain point on only two images for stereo does not represent sufficient support for robust automation, where perhaps five images are needed. Of course, producing a larger number of images only makes sense if subsequent processing efforts for those images are also independent of their number. Therefore automation is the prerequisite for a free choice of the number of images, and this free choice is a prerequisite for successful automation.

It is obvious that the future of modern photogrammetry lies in a fully automated workflow. Automated aerial triangulation may use a vast redundancy of 1,000 or more tie points in every image; the creation of a DEM may rely on 80–90% forward overlap and 30–80% sidelap to look in between vertical objects and match five images instead of a mere two; the orthophoto may be in the form of a 3D photo-texture placed on top of the 3D object surface, with classical orthorectification being nothing more than a special case of the more general "three-dimensional orthophoto". Finally, 3D vectors for GIS may be derived from land use classification and from image analysis, which may also support the classical processes of aerial triangulation, DEM generation and 3D orthophoto creation.

Digital large format airborne cameras help photogrammetry to "strike back", so to speak, after a period of retreat where airborne laser scanning took over the generation of point clouds for DEMs and GPS /IMU compromised the role of aerial triangulation. The lack of any variable cost for a digital image changes the rules of photogrammetric imaging and mission planning. This leads to automation opportunities that will invigorate photogrammetric innovation, offer alternatives to airborne laser scanning for the generation of point clouds and re-establish aerial triangulation as the central tool for precise image block formation for subsequent multi-image analyses. All this will also lead to opportunities to create new types of data and thus "content" for the ever-expanding information society.

It will be the "affordability due to automation" that will make the global 3D databases for "locational awareness on the Internet" a practical reality. Photogrammetry may gain in relevance by moving centre-stage in the world of high-bandwidth digital geospatial data creation and broadband Internet-based delivery.

7.3.8 Microsoft Photogrammetry

The acquisition of Vexcel Corporation, Boulder, Colorado and Vexcel Imaging GmbH, Graz, Austria, by Microsoft Corporation, Redmond, Washington raised questions, expectations and guesses in the photogrammetric community when it was announced in May 2006. The acquisition was driven by Microsoft's "Virtual Earth" initiative. The target of this program is to model in three dimensions the human habitat of the world – a few thousand cities and their neighbourhoods as well as rural areas between cities. Photogrammetry is the prime technology to do this job; the UltraCam is the preferred airborne sensor to build an automated 3D urban building modelling pipeline.

7.3.8.1 Aerial Missions

Aerial photo missions are carried out at a large scale (six-inch GSD) at end-laps of 80% and sidelaps of 60%. This results in a much larger set of aerial images than was previously typical in aerial photogrammetry. This highly redundant image data set, however, supports the automatic processes of aerial triangulation, digital elevation modelling and feature extraction. Redundancy also ensures the robustness of the process and the automatic detection of blunders, mismatches and outliers. Another important advantage of the large overlaps is the rigorous reduction of occlusions, a most helpful side effect when working in densely built up areas of city centres (Fig. 7.3-19).

7.3.8.2 Best Visuals for Non-Expert Users

Throughout the history of photogrammetry, geospatial data was produced by experts to be presented to and used by experts. Depending on the mapping scale a specific set of symbols had to be used to ensure that maps remained readable, details visible

Abbreviations

AC	Alternating Current
AWAF	Area Weighted Average Frequency
AWAM	Area Weighted Average MTF
AWAR	Area Weighted Average Resolution
CCD	Charge Coupled Device
CTE	Charge Transfer Effectivity
DB	Dynamic range
DC	Direct Current
DEM	Digital Elevation Model
DFT	Discrete Fourier Transform
DSNU	Dark Signal Non-Uniformity
EWAF	Equally Weighted Average Frequency
EWAM	Equally Weighted Average MTF
EWAR	Equally Weighted Average Resolution
FEE	Front End Electronics
FET	Field Effect Transistor
FFT	Fast Fourier Transform
FMC	Forward Motion Compensation
FOV	Field of View
FPM	Focal Plate Unit
GPS	Global Positioning System
GSD	Ground Sample Distance
IFOV	Instantaneous Field of View
IMU	Inertial Measurement Unit
INS	Inertial Navigation System
IR	Infrared
MS	Multispectral
MTF	Modulation Transfer Function
NIR	Near Infrared
OTF	Optical Transfer Function
PAN	Panchromatisch
POS	Position and Orientation System
PRNU	Photo Response Non-Uniformity

R. Sandau (ed.), *Digital Airborne Camera*, DOI 10.1007/978-1-4020-8878-0,

PSF	Point Spread Function
PTF	Phase Transfer Function
RGB	Red Green Blue
SNR	Signal to Noise Ratio
TDI	Time Delayed Integration
TFOV	Total Field of View

Bibliography

Ackermann, F. (1995): Digitale Photogrammetrie – Ein Paradigma-Sprung. ZPF, 3, 106–115

Ackermann, F., J. Bodechtel, F. Lanzl, D. Meissner, P. Seige, H. Winkenbach and J. Zilger (1991): MOMS-02/SPACELAB D-2: A high resolution multispectral/stereo scanner for the 2nd German Spacelab mission. SPIE, 1490, 94–101

Albertz, J. (1999): 90 Jahre Deutsche Gesellschaft für Photogrammetrie und Fernerkundung e. V. PFG, 5/1999, 293–349

Albertz, J. (2001): Einführung in die Fernerkundung – Grundlagen der Interpretation von Luft- und Satellitenbildern. 2. Aufl., Wissenschaftliche Buchgesellschaft, Darmstadt

Albertz, J. and W. Kreiling (1989): Photogrammetrisches Taschenbuch. 4. Aufl., Wichmann-Verlag, Karlsruhe

Analog Devices (2002): AD9824-Complete 14-Bit 30 MSPS CCD Signal Processor, Rev.0, © Analog Devices, Inc., 2002

ATMEL (2001): TH7982AVWB90NB Detail Specification Correlated Double Sampling for Space Applications, ATMEL Grenoble, 22.11.2001

Bähr, H.-P. and T. Vögtle (Hrsg.) (1998): Digitale Bildverarbeitung – Anwendungen in Photogrammetrie, Kartographie und Fernerkundung. 3. Aufl., Wichmann Verlag, Heidelberg, 373 S.

Bass, M., E. W. van Stryland, D. R. Williams and W. L. Wolfe (Eds.) (1995): Handbook of Optics. 2nd Ed., McGraw-Hill, New York

Bäumker, M. and F.-J. Heimes (2001): New calibration and computing method for direct georeferencing of image and scanner data using the positions and angular data of an hybrid inertial navigation system. In: Heipke, C., K. Jacobsen and H. Wegmann (Eds.): Integrated Sensor Orientation – Test Report and Workshop proceedings. 16 S.

Bormann, G. E. (1975): Measurement of Radial Lens Distortion with the Wild Horizontal Goniometer. ISP Commission I working group study

Brieß, K., W. Bärwald, F. Lura, S. Montenegro, D. Oertel, H. Studemund and G. Schlotzhauer (2001): The BIRD-Mission is completed for launch with the PSLV-C3 in 2001. In: H. P. Röser, R. Sandau and A. Valenzuela (Eds.): Small Satellites for Earth Observation III. Wissenschaft und Technik Verlag, Berlin

Bronstein, I. N. and K. A. Semendjajew (1989): Taschenbuch der Mathematik. 24 Aufl., Verlag Nauka, Moskau und BSB B. G. Teubner Verlagsgesellschaft, Leipzig

Brown, D. C. (1971): Close-range camera calibration. Photogrammetric Engineering, 37(8), 855–866

Brown, D. C. (1976): The Bundle Adjustment – Progress and Prospects. XIIIth Congress of the ISP, Commission III, Helsinki

Brown, R. and P. Hwang (1992): Introduction to Random Signals and Applied Kalman Filter ing. J. Wiley and Sons, New York, 502 S.

Coffey, K., J. Warta and A. Krämer (1999): Rauschverhalten hochauflösender AD-Wandler. Elektronik-Industrie, 11/1999

Cramer, M. (1999): Direct geocoding – is aerial triangulation obsolete? In: Fritsch, D. and R. Spiller (Eds.): Photogrammetric Week '99. Wichmann Verlag, Heidelberg, S. 59–70

Cramer, M. (2003): Erfahrungen mit der direkten Georeferenzierung. Zeitschrift für Photogrammetrie, Fernerkundung und Geoinformation PFG, 4/2003, 267–278

Cramer, M. (2004): www.ifp.uni-stuttgart.de/eurosdr/cramer-eurosdr-isprs.pdf

Datel (2003): Applikation zur Messdatenerfassung

Derenyi, E. E. (1970): An exploratory investigation concerning the relative orientation of continuous strip imagery – A thesis submitted in partial fulfilment of the requirements for the degree of Doctor of Philosophy in the Department of Surveying Engineering of the University of New Brunswick, March 1970

Dierickx, B. (1999): Electronic image sensors vs. film: beyond state-of-the-art. OEEPE Workshop on Automation in Digital Photogrammetric Production, 21–24 June 1999, Paris. http://www.fillfactory.com/htm/technology/pdf/oeepe99.pdf

Dimac (2004): www.dimacsystems.com

Ebner, H., D. Fritsch, W. Gillessen and C. Heipke (1987): Integration von Bildzuordnung und Objektrekonstruktion Innerhalb der Digitalen Photogrammetrie. BuL, 55, 194–203

Eckardt, A. (2002): Design und Verifikation der ersten digitalen kommerziellen Luftbildkamera (ADS). Dissertation, TU Berlin

El-Sheimy, N. (2003): Inertial techniques and INS /DGPS integration, lecture notes, ENGO 623 course, Department of Geomatics, The University of Calgary, Calgary, Canada

Engelmann, M. and N. Ahner (2004): CCD -Technik und Bildaufnahme. Vortrag im Rahmen der Vorlesung Elektronische Bauelemente an der TU Chemnitz

Fairchild (2004): Spezifikation der CCD525. Fairchild, USA

Falkner, E. (1994): Aerial Mapping, Methods and Application. CRC Press Inc., Florida

Finsterwalder, R. and W. Hofmann (1968): Photogrammetrie. 3. Aufl., De Gruyter, Berlin, 455 S.

Foitzik, L. and H. Hinzpeter (1958): Sonnenstrahlung und Lufttrübung. Akademische Verlagsgesellschaft, Wiesbaden

Fricker, P., R. Sandau and A. S. Walker (2000): Progress in the development of a high performance airborne digital sensor. Photogrammetric Record, 16 (96), 911–927

Fritsch, D. (1998): Photogrammetrie und GIS – eine Ehe mit Zukunft. Keynote Paper Intergraph's 1. Photogrammetrie-Forum 1998

Fritsch, D. and D. Stallmann (2000): Rigorous Photogrammetric Processing of High Resolution Satellite Imagery. International Archives of ISPRS, XXXIII(B1), 313–321, Amsterdam

Gelb, A. (1974): Applied Optimal Estimation. MIT Press, Cambridge, Massachusetts, US, 374 S.

GeoMat (2004): Geographische Materialien, 26, 173–182

Gervaix, F. (2002): Aerotriangulation : auch für den ADS-40 Luftbildsensor? PFG, 2, 85–91

Göhring, D. (2002): Digitalkameratechnologien – Eine vergleichende Betrachtung, CCD kontra CMOS , 12.08.2002. Technische Informatik, Humboldt Universität zu Berlin

Goodman, J. W. (1985): Statistical Optics. J. Wiley and Sons, New York

Gotthard, E. (1975): Zusatzglieder bei der Aerotrangulation. In: BuL 43, 218–221

Graham, R. W., W. S. Warner and R. E. Read (1996): Small Format Aerial Photography. Whittles Publishing, Scotland

Greening, T., W. Schickler and A. Thorpe (2000): The proper use of directly observed orientation data: Aerial triangulation is not obsolete. In: Proceedings ASPRS annual conference, on CD-Rom, 12 S., Washington DC, May 22–26

Grewal, M. and A. Andrews (1993): Kalman Filter ing: Theory and Practice. Prentice Hall, New Jersey, USA, 382 S.

Gruber, M. and R. Ladstädter (2006): Geometric issues of the digital large format aerial camera UltraCamD. International Calibration and Orientation Workshop EuroCOW 2006 Proceedings, 25–27 Jänner 2006, Castelldefels, Spanien.

Gruber, M. and U. Manshold (2008): UltraCamX-Large Format Digital Aerial Camera, DGPF Conference, Oldenburg, April 23-25th, 2008, Presentation

Grün, A. (1978): Accuracy, reliability and statistics in close range photogrammetry. Inter-Kongress Symposium, Com. 5, Stockholm, Schweden

Grün, A. and E. Baltsavias (1986): High Precision Image Matching for Digital Terrain Model Generation. International Archives of Photogrammetry and Remote Sensing, XXVI, III/1, 284–296, Commission III. Rovaniemi

Gruen, A. and L. Zhang (2003): Sensor modeling for aerial triangulation with Three-Line-Scanner (TLS) imagery. Photogrammetrie, Fernerkundung, Geoinformation (PFG), 2, 85–98

Heipke, C., K. Jacobsen and H. Wegmann (Eds.) (2001): Integrated sensor orientation – test report and workshop proceedings, OEEPE official publication No. 43, 297 S., verfügbar unter http://www.oeepe.org/ (Zugriff August 2004)

Hildebrandt, G. (1996): Fernerkundung und Luftbildmessung. Herbert Wichmann Verlag, Heidelberg

Hofmann, O. (1982): Dynamische Photogrammetrie. BuL, 3, 3–19

Hofmann, O. (1988): Photogrammetrisches Verfahren für Fluggeräte und Raumflugkörper zur digitalen Geländedarstellung. Patent DE 294087122, angemeldet 1979, erteilt 1983

Hofmann-Wellenhof, B., H. Lichtenegger and J. Collins (2001): Global Positioning System: Theory and Practice. Springer-Verlag, Wien, 382 S.

Holst, G. C. (1998a): Sampling, Aliasing , and Data Fidelity. SPIE Optical Engineering Press, Washington

Holst, G. C. (1998b): Testing and Evaluation of Infrared Imaging Systems. SPIE Optical Engineering Press, Washington

Holst, G. C. (1996): CCD arrays, Cameras and Displays. SPIE Optical Engineering Press, Bellingham, Washington

Hydrolab (2004): http://hydrolab.arsusda.gov/rsbasics/noise.php

IAI FZK (2004): Bestimmung der Auflösung von Bilderfassungskomponenten © 2004 – Institut für Angewandte Informatik; Forschungszentrum Karlsruhe (http://www.iai.fzk.de/projekte/mikrologistik/bildverarbeitung/module/aufloesung/index.html)

Intergraph (2008): http://img.en25.com/web/Intergraph/DMC.pdf

Iqbal, M. (1983): An Introduction to Solar Radiation . Academic Press, New York

Jacobsen, K. (1982): Programmgesteuerte Auswahl zusätzlicher Parameter. In: BuL 1982, 213–217

Jacobsen, K. (1998): Geometric Potential of IRS-1C PAN-Cameras. ISPRS Com I Symposium, Bangalore, India

Jacobsen, K. (2002): Calibration aspects in direct georeferencing of frame imagery. ISPRS Commission I/Pecora 15 conference proceedings, IAPRS (34), Part 1 Com 1, 82–89, Denver, 2002

Jacobsen, K. (2003): System calibration for direct and integrated sensor orientation. In: Proceedings ISPRS WG I/5 workshop on theory, technology and realities of inertial/ GPS sensor orientation, on CD-Rom, 6 S., Castelldefels, 2003

Jahn, H. and R. Reulke (1995): Systemtheoretische Grundlagen Optoelektronischer Sensoren. Akademie Verlag, Berlin

Johnson, J. (1985): Analysis of Image Forming Systems. In: Proceedings of the Image Intensifier Symposium, 249–273. Warfare Electrical Engineering Department, US Army Engineering Research and Development Laboratories, Ft. Belvois, VA. Nachdruck dieses Artikels im Selected Papers on Infrared Design, R. B. Johnson and W. L. Wolfe (eds.): SPIE Proceedings 513, 761–781

Kodak (1994): Solid State Image Sensors_Kodak-Grundlagen_DS00-001, Rev. 0, 08.12.1994

Kodak (1999): KAF- 6303LE 3072 (H) x 2048 (V) Pixel Enhanced Response Full- Frame CCD Image Sensor, Rev. A, 25.09.1999

Kodak (2001a): ConversionOfLightToElectronicCharge_Kodak_MTD-PS0217; Rev. 1, 29.05.2001

Kodak (2001b): Image Sensor Noise Sources, Application Note Kodak MTD/PS-0233, Rev. 1, 01.08.2001

Kodak (2004): www.kodak.com/global/en/service/manuals/GLB_en_urg_00088_manual/urg 00088toc.jhtml

Kölbl, O. (1972): Selbstkalibrierung von Aufnahmekammern. Bildmessung und Luftbildwesen, 40(1), S. 31 ff.

Konecny, G. (2003): Geoinformation: Remote Sensing, Photogrammetry and Geographic Information Systems. Taylor and Francis, London and New York

Kramer, H. J. (2002): Observation of the Earth and its Environment: Survey of Missions and Sensors. 4. Aufl., Springer Verlag, Berlin/New York

Kraus, K. (1988): Fernerkundung, Band 1 (Physikalische Grundlagen und Aufnahmetechnik). Dümmler, Bonn

Kraus, K. (1990): Fernerkundung, Band 2 (Auswertung photographischer und digitaler Bilder). Dümmler, Bonn

Kremer, J. and M. Gruber (2004): Operation of the UltraCamD together with CCNS4/Aerocontrol – first experiences and results. The International Archives of Photogrammetry and Remote Sensing, XXXV/1, 172 ff., July 2004, Istanbul, Turkey

Kröpfl, M., E. Kruck and M. Gruber (2004): Geometric calibration of the digital large format aerial camera Ultracam. The International Archives of Photogrammetry and Remote Sensing, XXXV/1, 42 ff., July 2004, Istanbul, Turkey

Kruck, E. (1984): BINGO: Ein Bündelprogramm zur Simultanausgleichung für Ingenieuranwendungen – Möglichkeiten und praktische Ergebnisse. Intenational Archive for Photogrammetry and Remote Sensing, Rio de Janairo 1984

Kruck, E. (2003): Rotations of space and coordinate transformations. In: Proceedings ISPRS WG I/5 workshop on theory, technology and realities of inertial/ GPS sensor orientation, on CD-Rom, 5 S., Castelldefels, 2003

Ladstädter, R. (2007): Softwaregestützte Kompensation temperaturabhängiger Bild-Deformationen für die Vexcel UltraCam. Vorträge Dreiländertagung SGPBF. DGPF und OVG, Basel, Vol. 16, pp. 609–616

Leberl, F., R. Perko, M. Gruber and M. Ponticelli (2003): The UltraCam Large Format Aerial Digital Camera System. In: Proceedings of the American Society For Photogrammetry & Remote Sensing, 5–9 May, 2003, Anchorage

Leica (2003): http://www.leica-geosystems.com/ctc/heat_conduction

Leica (2004): http://www.gis.leica-geosystems.com/products/ads40/default.asp

McCluney, R. (1994): Introduction to Radiometry and Photometry. Artech House, Boston/London

McGlone, J. C., E. M. Mikhail and J. Bethel (Eds.) (2004): Manual of Photogrammetry . 5. Aufl., Bethesda: ASPRS, 1151 S.

Möller, M. (2003): Urbanes Umweltmonitoring mit digitalen Flugzeugscannerdaten. Herbert Wichmann Verlag, Heidelberg

Müller, F. (1991): Photogrammetrische Punktbestimmung mit Bildern digitaler Dreizeilenkameras. DGK C372

Murai, S. (1998): GIS Work Book, Fundamental Course (1996) and Technical Course (1997). Japan Association of Surveyors, Tokio

Neckel, H. and D. Labs (1984): The Solar radiation between 3300 and 12500. Solar Physics, 90, 205–250

Oertel, D., K. Briess, W. Halle, M. Neidhardt, E. Lorenz, R. Sandau, F. Schrandt, W. Skrbek, H. Venus, I. Walter, B. Zender and B. Zhukov (2003): Airborne forest fire mapping with an adaptive infrared sensor. International Journal of Remote Sensing, 24(18), 3663–3682

Oriel (1987): Optische Filter . L.O.T.-Oriel GmbH, Langenberg

Oriel (2004): http://www.lot-oriel.com/pdf/all/filter_glas_ch.pdf

Passini, R. and K. Jacobsen (2008): Accuracy analysis of large size digital aerial cameras. International Archives of Photogrammetry and Remote Sensing, XXXVII(B1), S. 507–514, Peking

PCO (2004): PCO-Veröffentlichungen (www.pco.de/download/)

Petrie, G. and A. S. Walker (2007): Airborne digital imaging technology: a new overview. The Photogrammetric Record, 22(119), 203–225

Pomierski, T., D. Kollhoff, E. Stefanov and K.-H. Franke (1998): Realisierung von True Color für ADC. GBS GmbH, Ilmenau

Ratches, J. A., W. R. Lawson, L. P. Obert, R. J. Bergemann, T. W. Cassidy and J. M. Swenson (1975): Night Vision Laboratory Static Performance Model for Thermal Viewing Systems. ECOM-Report ECOM-7043, p. 56, Fort Monmouth, NJ

Rese (2004): http://www.rese.ch/atcor/atcor3/atcor2_method.html

Ressl, C. (2001): Direkte Georeferenzierung von Luftbildern in konformen Kartenabbildungen. Öster. Zeitschrift für Vermessung und Geoinformation VGI 2/2001, 89, 72–82

Röser, H.-P., A. Eckardt, M. von Schönermark, R. Sandau and P. Fricker (2000): New potential and applications of ADS40. International Archives of Photogrammetry and Remote Sensing, XXXIII(B1), 251–257

Rössig, R. (2004): Berechnung von Look-up-Tafeln zur Atmosphärenkorrektur radiometrisch geeichter digitaler Luftbildaufnahmen. Diplomarbeit, Institut für Raumfahrtsysteme der Universität Stuttgart, Januar 2004

RSES (2002): http://www rss.chalmers.se/gem/Education/RSES-2002/Imaging_systems.pdf

RSL (2004): http://www.geo.unizh.ch/rsl/research

Sandau, R. (1998): Weitwinkel-Stereoscanner WAOSS für die Mission Mars 96. Verlag Dr. Hänsel-Hohenhausen, Egelsbach/Frankfurt a. M./Washington

Sandau, R. (2000): Design principles of the LH systems ADS40 airborne digital sensor. International Archives of Photogrammetry and Remote Sensing, XXXIII(B5), 258–265

Sandau, R. (2004): High resolution mapping with small satellites. International Archives of Photogrammetry and Remote Sensing, XXXV(B1), 108–113

Sandau, R. and A. Eckardt (1996): The stereo camera family WAOSS/WAAC for spaceborne/airborne applications. International Archives of Photogrammetry and Remote Sensing, XXXI(B1), 170–175

SAPOS (2004): www.sapos.de, Zugriff August, 2004

Schönermark, M. V., B. Geiger and H.-P. Röser (Eds.) (2004): Reflection Properties of Vegetation and Soil with a BRDF Data base. Berlin, ISBN 3-89685-565-4

Schott (1998): Schott Glass Technologies Inc.: Filter ′98, Optical Filters www.schottglasstech.com

Schowengerdt, R. A. (1997): Remote sensing . Models and Methods for Image Processing. 2. Aufl., Academic Press, San Diego, 522 pp.

Schwarz, K.-P. (1995): Integrated airborne navigation systems. In: D. Fritsch/D. Hobbie (Eds.): Photogrammetric Week ’95. Wichmann Verlag, Heidelberg, pp. 139–153

Schwarz, K.-P., M. Chapman, E. Cannon, P. Gong and D. Cosandier (1994): A precise positioning/attitude system in support of airborne remote sensing. In: Proceedings ISPRS Commission II, Ottawa, Canada, 191–201

Schwidefski, K. and F. Ackermann (1976): Photogrammetrie: Grundlagen, Verfahren, Anwendungen. 7. Auflage., Teubner, Stuttgart, 384 S.

Skaloud, J. (1999): Optimizing georeferencing of airborne survey systems by INS /DGPS , UCGE report 20126, Ph.D. thesis, University of Calgary, Canada, 160 S., digital verfügbar unter http://www.geomatics.ucalgary.ca (Zugriff August, 2004)

Starlabo (2004): www.starlabo.co.jp

Sujew, S., F. Scholten, F. Wewel and R. Pischel (2002): GPS / INS -Systeme im Einsatz mit der HRSC – Vergleich der Systeme Applanix POS /AV-510 und IGI AEROcontrol-IId. Zeitschrift für Photogrammetrie, Fernerkundung und Geoinformation PFG, 5/2002, 333–340

Swissoptic, A. G. (2005): www.swissoptic.com

Tempelmann, U., Z. Nwosu and R. M. Zumbrunn (1995): Investigation into the geometric consequences of processing substantially compressed images. In: McKeown, D. M. and I. J. Dowman (Eds.): Integrating Photogrammetric Techniques with Scene Analysis and Machine Vision II. Proceedings of the SPIE, 2486, 48–58

Thom, Ch. and I. Jurvillier (1997): Current status of the digital aerial camera IGN. In: D. Fritsch/D. Hobby (Eds.): Photogrammetric Week '97, Wichmann Verlag, Heidelberg, pp. 75–82

Triebfürst, B., D. Saupe and H. Saurer (1997): Kompression und Generalisierung von Fernerkundungsdaten in einem GIS mit einem optimierten Wavelet-Kodierer. In: Angewandte Geographische Informationsverarbeitung IX, 2.–4. Juli 1997, Salzburger Geographische Materialien, 26, 173–182

Voiß, S. and K. Schinzel (2002): Präsentation Flash-Anwendungen. TU Ilmenau, Germany

Wehrli (2004): www.wehrliassoc.com

Wei, M. and K.-P. Schwarz (1990): A strap-down inertial algorithm using an earth-fixed cartesian frame. Navigation, Navigation 37(2), 153–167

Wells, D. E. (Ed.) (1987): Guide to GPS positioning, Canadian GPS associates. Frederikton, New Brunswick, Canada

Wikipedia (2004): http://en.wikipedia.org/wiki/Fast_Fourier_transform

Willmann, L. (1968): Luftbilder aus der DDR. VEB F. A. Brockhaus Verlag, Leipzig

Wyszecki, G. (1960): Farbsysteme. Musterschmidt-Verlag, Göttingen

Yotsumata, T., M. Okagawa, Y. Fukuzawa, K. Tachibana and T. Sasagawa (2002): 'Investigation for Mapping Accuracy of the Airborne Digital Sensor ADS 40'; ISPRS Commission I Conference, Denver, CO, 10–14 Nov 2002

Z/I Imaging (2003): http://www.ziimaging.de/Products/AuxiliaryContent/dmcspecsheet.pdf

Zimmermann, B. (2004): Bildsensorik. Universität Ulm, Revision: 13. Februar 2004

Index